Development of new peptide conjugates as biosensors and imaging tools and investigations into their interactions with prostate cancer cells

Giuffrida, Simone Giuseppe

Award date:
2020

Awarding institution:
University of Bath

Development of new peptide conjugates as biosensors and imaging tools and investigations into their interactions with prostate cancer cells

Simone Giuseppe Giuffrida

A thesis submitted for the degree of Doctor of Philosophy

University of Bath

Department of Chemistry

March 2020

TABLE OF CONTENT

Acknowledgements

Firstly, I would like to thank my supervisor Prof Sofia Pascu for giving me the opportunity to work in her group and laboratories. Her support and advice have been fundamental for the completion of this work, giving me stimulating ideas and freedom to explore different ones. In addition, I thank the postdocs of SIP group (Dr Fernando Cortezon-Tamarit, Dr Vincenzo Mirabello, Dr Sara Aguiar and Dr Haobo Ge) which worked with me and gave me professional and non-professional advice throughout this PhD. I thank my fellow PhD students in the group (particularly, Marina, Sophia, Federico and Sam) for their helpful advice in the labs and the time spent with them at Bath.

I also would like to thank Dr Pedro Estrela and his group members Şerife, Uroš and Josh for introducing me to the electrochemical side of the Chemistry which has been an unexplored field for me so far. Most importantly, his mentoring in biosensing has been essential to understand different techniques and carry out experiments.

I also thank Dr Dan Pantos for some organic chemistry-related advice and his group members Simone, Dora and Tiberiu for helping me with some of their equipment.

Prof Stanley Botchway has been helpful with his explanation and advice to understand and perform FLIM experiments during two weeks on his laboratories in RAL.

I would like to thank Andrea, Fernando and Vincenzo which have been supportive and helpful in developing some ideas. Most importantly, they have bonded with me and create a friendship during these years in Bath. I will always remember the fun, the gossip and the drinking nights with them. I also thank some other people I met at University and around Bath which I spent some joyful days.

My long-time friends Fernanda, Giorgio, Martina, Gabriele, Michela and Irene have always been very essential in making some decisions, besides their support and fun.

Last but not least, I would like to thank my family for their support throughout the years and always believed in me and be proud of me.

Abstract

This Thesis describes the design, synthesis and investigation of novel fluorescent imaging probes for prostate cancer cells detection. Such probes are based on the naphthalenediimides (NDIs) core which was used hereby as a synthetic scaffold to link different building blocks such as ligands for metals, peptide and fluorophore. The naphthalenediimide core is well-known to form supramolecular architectures such as rotaxane and fluorogenic composite materials and these functionalities were also explored in this work. New fluorescent probes were synthesised, characterised spectroscopically and investigated by fluorescent microscopies to evaluate the uptake, localisation and targeting in living prostate cancer cell lines for their potential use as imaging agents.

Chapter 1 is the Introduction to the state-of-art and summarises the burden of non-communicable diseases and their connection with cancer and prostate cancer. Current diagnostic tests and imaging methods are briefly described for their application in prostate cancer detection. The use of biosensing, both optical and electrochemical, as an alternative method for cancer detection is pointed out as a sensitive, reliable and low-cost tool.
The chemical and supramolecular characteristics of naphthalenediimides are discussed as the use of a scaffold for biological and imaging applications. The chemistry of thiosemicarbazones and their metal complexes is described with their use in cancer imaging and therapy, both under normoxic conditions and under reduced oxygen concentration (or hypoxia). Finally, the importance of receptor-targeting peptides of relevance to the therapy of prostate cancers is highlighted.

Chapter 2 presents the design, synthesis and characterisation of NDI-based thiosemicarbazone ligands and their metal complexes are presented. Such fluorescent metal complexes are investigated by confocal microscopy in living cell lines in both normoxic and hypoxic conditions.

In **Chapter 3**, novel *psuedo*rotaxanes consisting of 1,5-dinaphtho[38]crown-10, as a "wheel", and different naphthalenediimide-based "axles" with fluorescent properties are presented as a proof-of-concept bioimaging tools for prostate cancer detection.

Chapter 4 explores the design, synthesis and characterisation of naphthalenediimide derivatives which incorporate one or two units of a targeting peptide (fragment [7-13] of bombesin peptide) for gastrin-releasing peptide receptors (GRPRs).

The effect of both stereochemistry and number of peptide moieties are investigated by fluorescent microscopy to evaluate their different uptake and interaction with prostate cancer cells.

Chapter 5 provides a summary of the work described throughout during this Thesis and some proposals for future work arising from the research findings described herein.

Chapter 6 is the Experimental Section and contains detailed synthetic procedure and characterisation data for the compounds investigated hereby.

Appendices A provide selected spectroscopic, mass spectrometry as well as optical imaging data in support of the characterisation and discussions regarding the compounds described. **Appendices B** discusses the design and formation of fluorogenic composite materials consisting of graphene oxide and fluorescent, flat aromatic compounds. Preliminary investigations on their aggregation and optical characteristics were carried out as proof-of-concept for future application in optical imaging applications. **Appendices C** explores the design and preliminary tests of an electrochemical biosensor able to discriminate cell lines with a high density of gastrin-realising peptide receptors (GRPRs). Electrochemical impedance spectroscopy (EIS) is used in this work as the analytical method to measure the binding and interactions of the biosensor with different prostate cancer cell lines, and a comparison with a standard healthy cell line.

List of abbreviations

ACP	Anticancer peptide
ATSM	Diacetyl *bis*(N^4-methylthiosemicarbazone)
BBN	Bombesin
Boc	N-tertbutoxycarbonyl
BODIPY	Boron-dipyrromethene
BTSC	*Bis*-(thiosemicarbazone)
CHO	Chinese hamster ovary cell line
CLSM	Confocal laser scanning microscopy
COSY	Correlation spectroscopy
CT	Computed tomography
DCM	Dichloromethane
DIPEA	*N*,*N*-diisopropylethylamine
DMF	Dimethylformamide
DMSO	Dimethylsulfoxide
DRE	Digital rectal examination
EDC	N-(3-Dimethylaminopropyl)-N′-ethylcarbodiimide
EEM	Excitation-emission matrix
EIS	Electrochemical impedance spectroscopy
EMT6	Murine mammary carcinoma cell line
ESI	Electrospray ionisation
FCM	Fluorogenic composite material
FLIM	Fluorescence lifetime imaging
Fmoc	Fluorenylmethyloxycarbonyl
FRET	Föster resonance energy transfer
FT-IR	Fourier transform infrared spectroscopy
GO	Graphene oxide
GRP	Gastrin-releasing peptide
GRPR	Gastrin-releasing-peptide receptor
HBTU	*N*,*N*,*N*′,*N*′-Tetramethyl-*O*-(1*H*-benzotriazol-1-yl)uronium hexafluorophosphate

HeLa	Human cervical cancer cell line
HMBC	Heteronuclear multiple bond correlation spectroscopy
HOBt	1-Hydroxybenzotriazole
HPLC	High Performance Liquid Chromatography
HSQC	Heteronuclear single quantum coherence spectroscopy
LNCap	Human metastatic prostate carcinoma cell line
MIM	Mechanically interlocked molecule
MRI	Magnetic resonance imaging
MTT	3-(4,5-dimethylthiazol-2-yl)-2,5-diphenyltetrazolium bromide
NDA	1,4,5,8-naphthalenetetracarboxylic dianhydride
NIR	Near infrared
NMR	Nuclear Magnetic Resonance
PBS	Phosphate Buffered Saline
PC-3	Human prostatic adenocarcinoma cell line
PCa	Prostate cancer
PCR	Polymerase chain reaction
PET	Positron emission tomography7
POCT	Point-of-care test
PSA	Prostate specific antigen
ROI	Region-of-interest
RPMI	Roswell Park Memorial Institute medium
R_t	Retention time
SAED	Selected area electron diffraction
SEM	Scanning electron microscopy
TCSPC	Time-correlated single photon counting
TFA	Trifluoroacetic acid
TIPS	Triisopropylsilane
TOCSY	Total Correlated Spectroscopy
TRUS	Transrectal ultrasound
TSC	Thiosemicarbazone

List of compounds

(*) Novel synthesised compounds

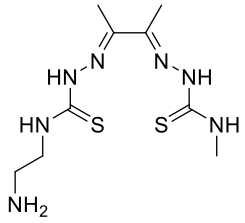

1

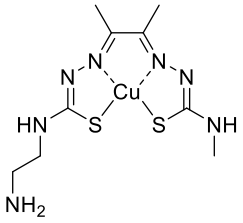

1a

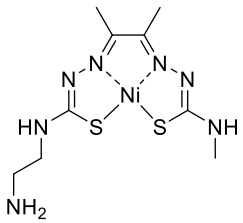

1b

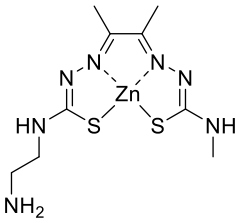

1c

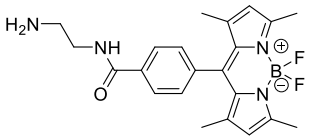

2

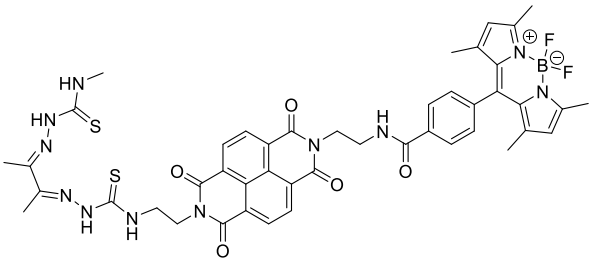

3 (*)

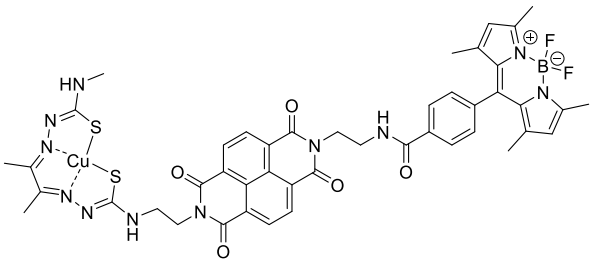

3a (*)

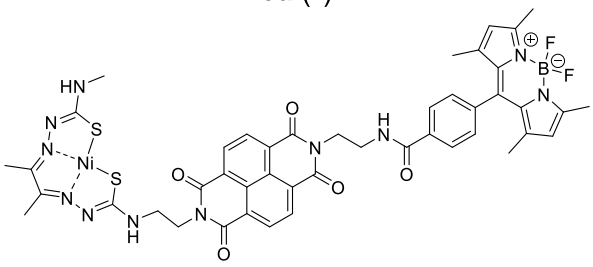

3b (*)

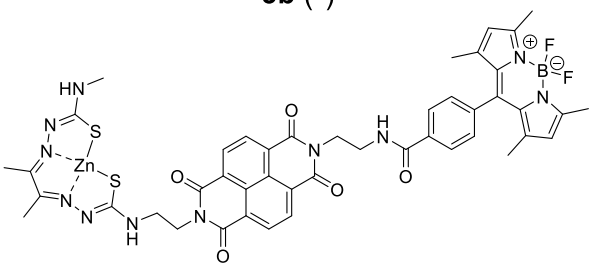

3c (*)

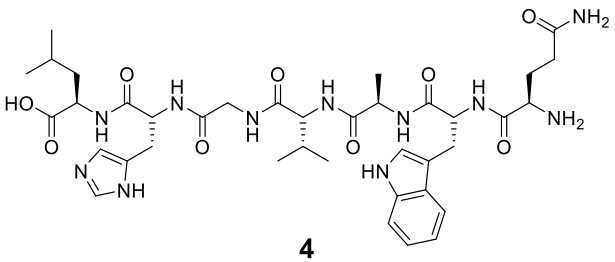

4

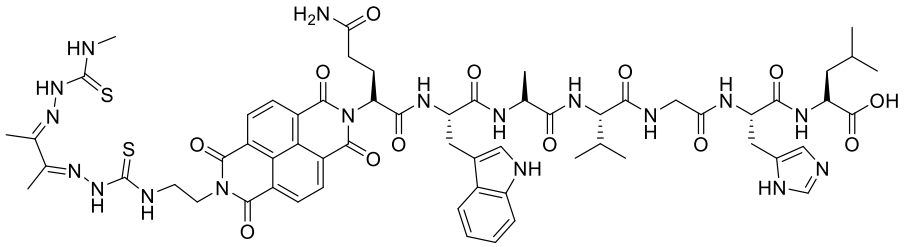

5 (*)

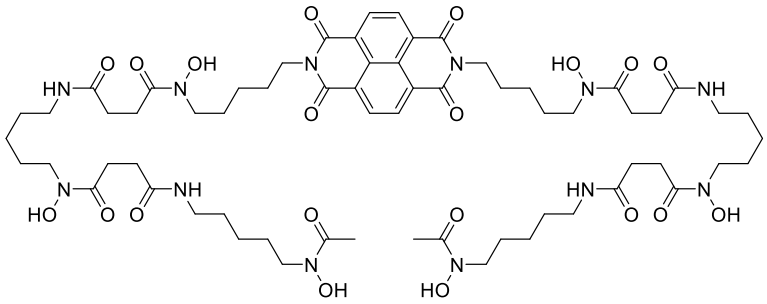

6 (*)

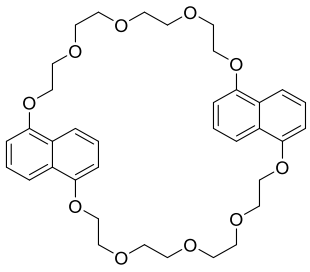

7

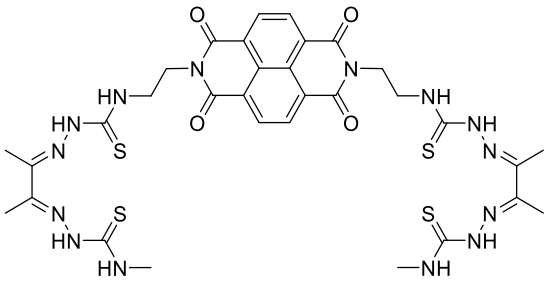

8 (*)

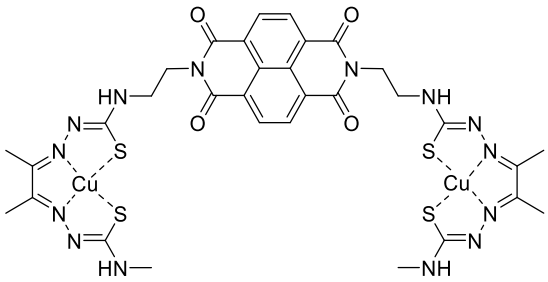

8a (*)

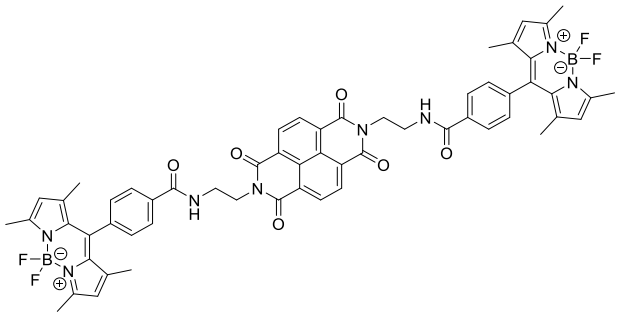

9 (*)

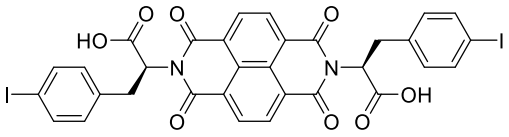

***L*-10**

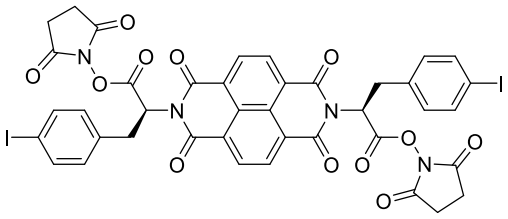

***L*-10**

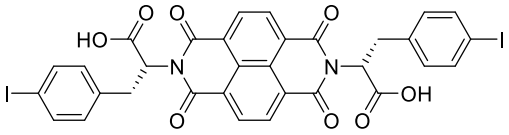

***D*-11** (*)

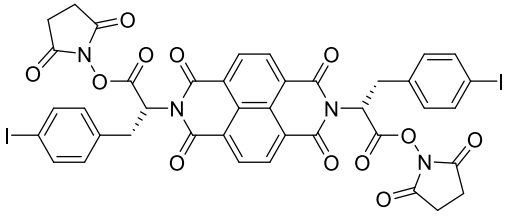

***D*-11** (*)

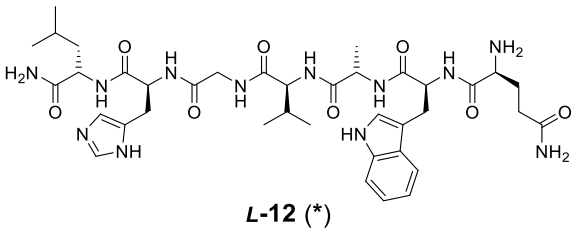

***L*-12** (*)

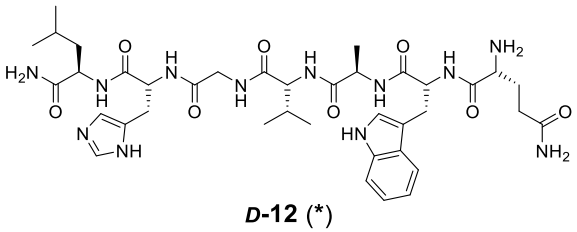

***D*-12** (*)

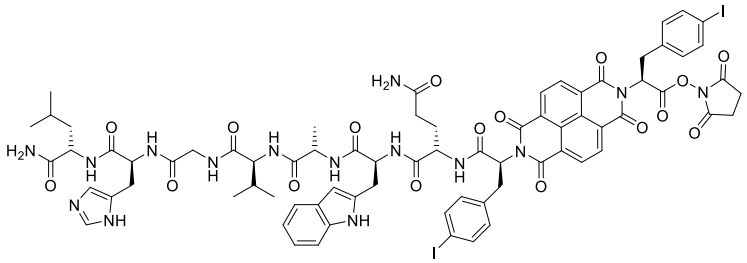

***L*-13** (*)

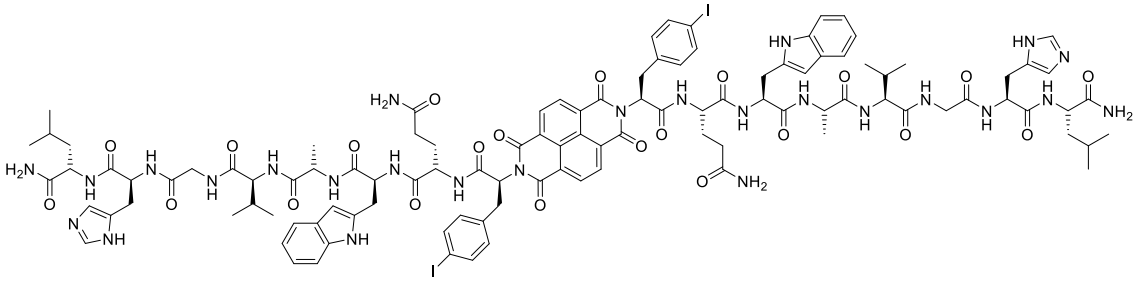

***L*-14** (*)

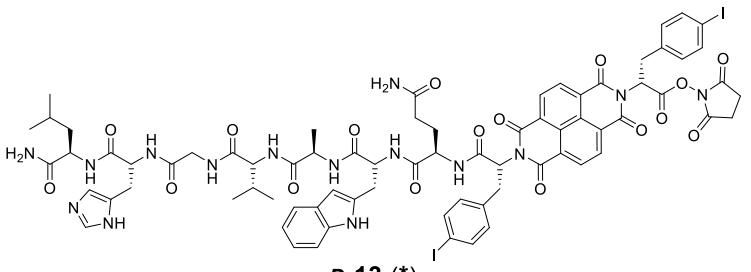

***D*-13 (*)**

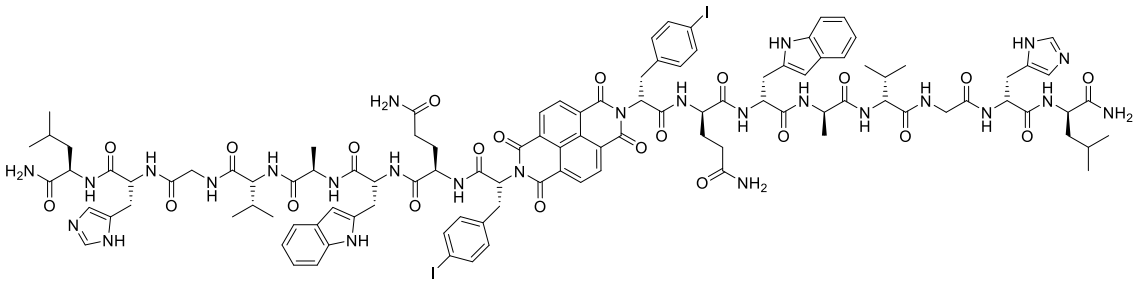

***D*-14 (*)**

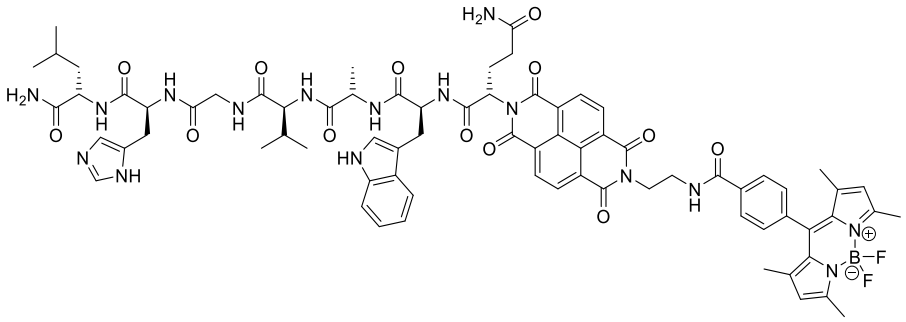

15 (*)

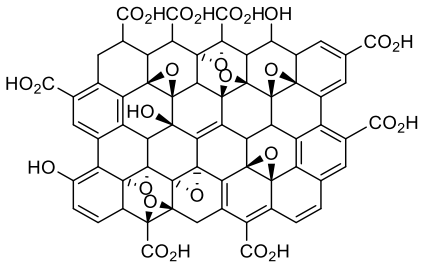

GO

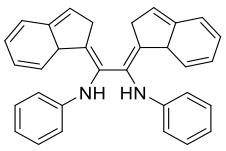

16

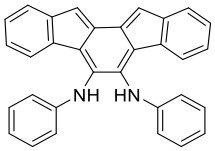

17

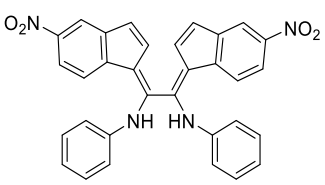

18 (*)

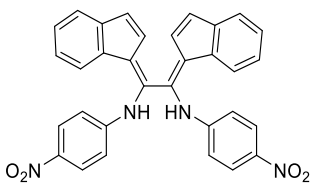

19 (*)

Chapter 1: Introduction

1.1. Impact of non-communicable diseases on society

1.1.1. Correlation between non-communicable diseases and cancer

Non-communicable diseases (NCDs) are a group of medical conditions or diseases which are not infectious or transmissible. Autoimmune diseases, heart diseases, stroke, cancers, diabetes, chronic kidney disease, osteoporosis, Alzheimer's disease, cataracts are the most common NCDs spread worldwide. In many cases, they are referred to as "chronic diseases" for their long periods of persistence and slow progression which can also lead to death[1].

NCDs represented the main cause of death worldwide for centuries in which these diseases remained medically uncontrolled. After the Second World War[2], the most industrialised countries established some medical research outcomes (vaccination, antibiotics and healthcare) and allocated funding in health and education, leading to important improvements in living conditions. However, NCDs were connected to economic and lifestyle conditions in the most developed countries which were considered as "diseases of the rich". NCDs started to spread also in less advanced countries where previously infectious diseases and malnutrition were the top causes of death[3,4]. Nowadays, NCDs kill 38 million people worldwide[5] and therefore represent one of the most important causes of premature death (Figure 1.1).

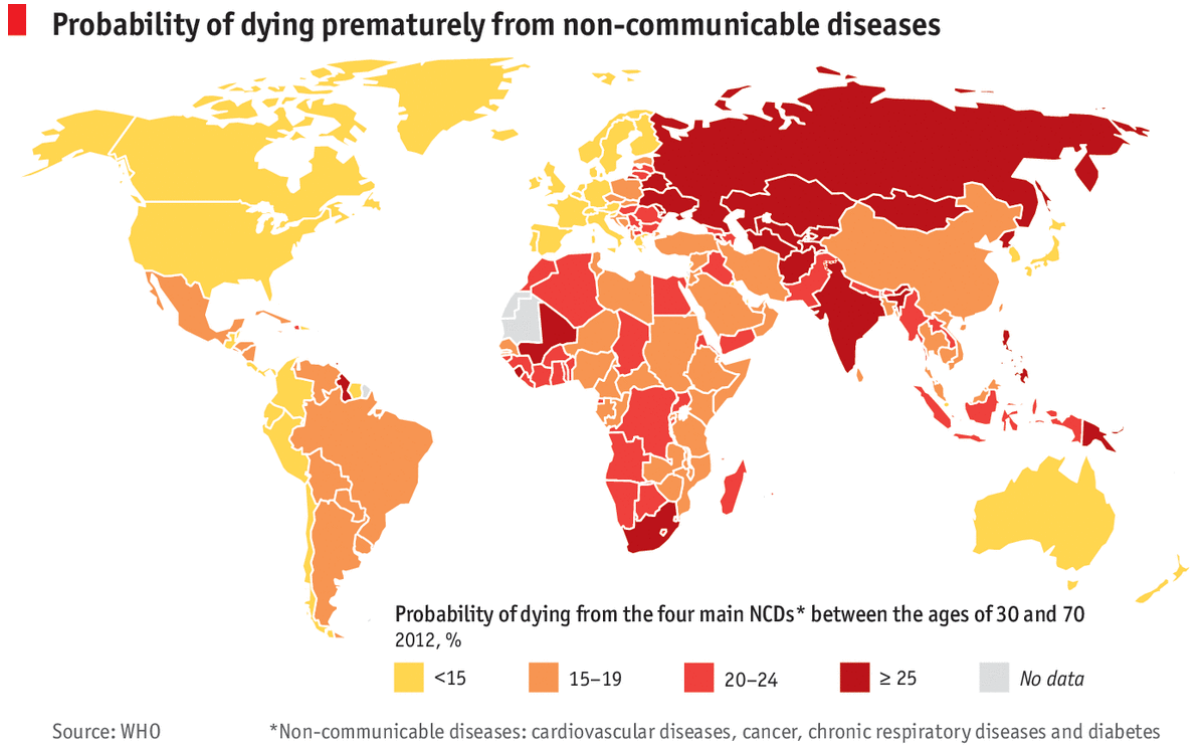

Figure 1.1. Percentages of death by country due to non-communicable diseases, in 2012 (figure adapted from World Health Organisation[6]).

Recent studies have shown that the NCDs are associated with risk factors, attributed to behavioural models[7,8]. The most common risk factors found in the studies during these last 20 years are unhealthy diet, physical inactivity[9], alcohol[10], and tobacco[11,12]. Unhealthy dietary habits can lead to different disorders such as obesity, dietary disorders, cardiovascular diseases, diabetes and can also be associated with different forms of cancer. Physical inactivity is connected to dietary habits and play a key role in the lifestyle of a person. Regular physical activity could reduce by 30% the risk of heart problems, decreases by 27% chances to develop diabetes and prevent breast and colon cancers by 21-25%[13]. Lifestyle choices including alcohol consumption and excessive use of cigarettes have been highlighted as causes for several different health conditions such as liver cirrhosis, cardiovascular disease, stroke, hypertension and some forms of cancer[13].

All these four main risk factors of NCDs have in common, in the worst case, cancer. Cancer is generated by complex mixtures of chemical, called *carcinogens*, which can indirectly help the progression of cancer, interfering the biochemical process[14-16].

1.1.2. Basic considerations regarding cancer and prostate cancer

The word *cancer* was used for the first time by Hippocrates (*circa* 460 BC-370 BC), the Greek physician considered the "Father of Medicine". He referred with this term the non-ulcer and ulcer forming tumours[17,18]. The etymology of the words, according to the linguists, derives from the Greek term *karkinos* which means "crab" or "crayfish" because of the shape of patients' veins[19].

Cancer is used to define a large class of diseases involving abnormal growth of cells which can invade or spread to other parts of the body. These cells are called *neoplasm* which can uncontrollably grow and diffuse in other parts of the body[20]. When cancerous cells form mass or lump, they are referred to *tumour*[21]. Particular diagnostic tests and therapeutic solutions should be considered to intervene precautionarily[22] because of the different nature of cancer. However, different forms of cancer present similar properties and features in common, which can be treated with general therapeutic approaches[23].

Generally speaking, cancer is generated from uncontrolled cells which lose properties and gain others, starting to multiply and spread in other tissues and/or organs. "Regulatory genes" control the replication mechanism of cells and avoid the survival and origin of abnormal cells, generating a neoplasm or tumour.

A failure on the replication mechanism can lead to an uncontrolled cell division and lead to the occurrence of an enormous number of cells with deregulated metabolic problems[24]. This failure of the regulatory process produces "benign tumour cells", remaining in the originating organ, and "malignant tumour cells", moving in other parts of the organism. The "migration" of the malignant tumour cells can last several years, extending in different organs such as lungs, liver and brain, compromising their normal functionality. The name of this process is *metastasis* and the *metastases* are the latest stage of tumour progression and the cause of death because of cancer[25,26].

As mentioned before, cancer cells can spread in other parts of the body and invade organs. This mechanism can be promoted by risk factors and carcinogens. Genetic risk factors such as age, sex and ethnicity can play a role in the occurrence of cancer. For example, latest statistics[27] in the United Kingdom in 2014 (Figure 1.2) revealed that the most common forms of cancer in females are breast, lung and bowel cancers; on the other hand, lung, prostate and bowel cancers are commonly found in males. Such forms of cancer are considered the deadliest categories.

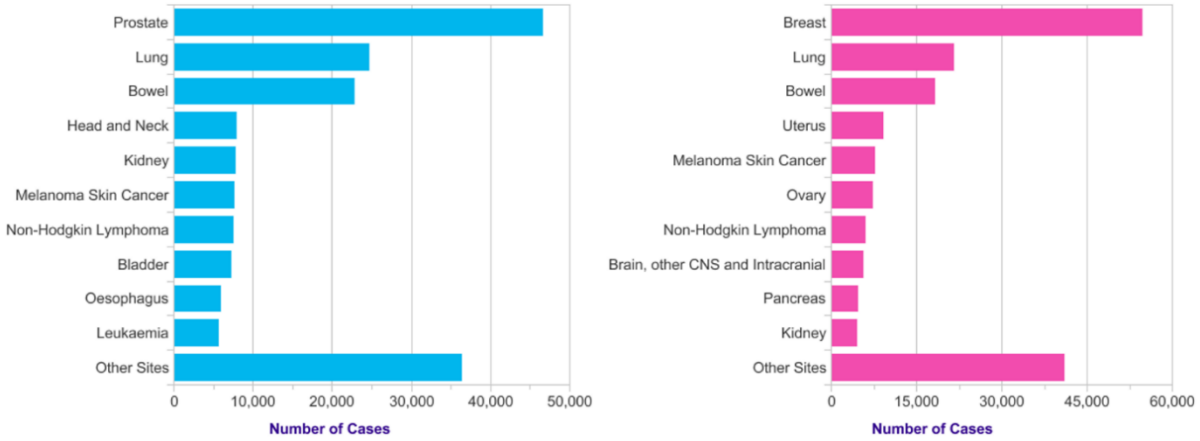

Figure 1.2. On the left, the 10 most common cancer in males; on the left, the most common cancer in females (data obtained in the United Kingdom, in 2014[27]).

Prostate cancer (PCa) is the second most common type of cancer worldwide, found in male over 50 years old. Such malignancy counted about 1.3 million new cases and caused around 360000 deaths in 2018[28]. In the early stage, prostate cancer can not cause any symptoms, but in the later stage, it can produce difficulties urinating, blood in the urine, pain in the pelvis or when urinating.

The main causes of prostate cancer remain unclear to date. However, obesity, age and family history are the main risk factors for this disease (Figure 1.3).

The risk of developing this cancer can be related to age. In fact, males over 50 years old are common patients with a high risk of developing prostate cancer; rare cases have been found in men under 50. Genetic background related to ethnic, family and specific gene variants could contribute to the risk of the development of prostate cancer. Different researches[29,30] have shown that patients with a first-degree relative are prone to such diseases. For instance, father or brother with diagnosed prostate cancer has twice the risk to develop this condition than men with no family history. Black men are the most subjected to PCa due to a large amount of testosterone produced more than other males of other ethnicity[31]. Other factors can increase the risk of developing prostate cancer. For instance, recent researches[32,33] have reported that consuming red meat and processed meat could lead to a high risk of prostate cancer. Most sexually transmitted diseases, such as chlamydia, gonorrhoea and syphilis[34,35], and prostatitis can also be considered risk factors of prostate cancer. Conversely, the latest pubblications[36-39] support eating fruit and vegetables as a prevention method to reduce the risk of prostate cancer. In addition, having frequent sexual intercourses could reduce the chance to develop PCa[40,41]. However, all these suppositions about the factors that could increase or decrease the risk of prostate cancer are still not clear.

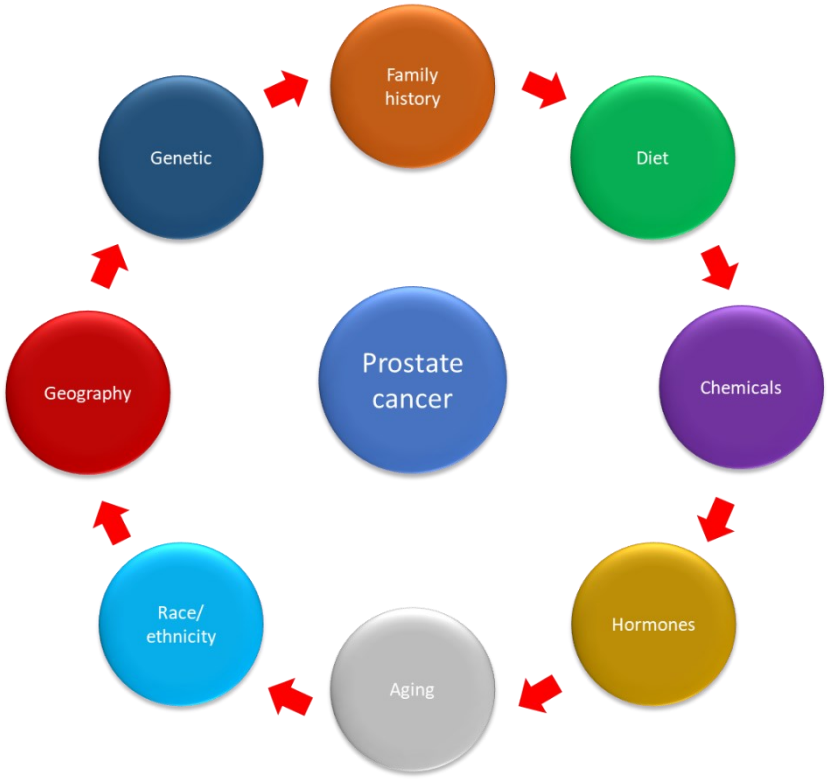

Figure 1.3. Common risk factors which could affect the onset of prostate cancer (figure adapted from Ramakrishnan *et al.*[42]).

The prostate gland is an organ of the male reproductive system that produces and stores seminal fluid. It is located under the bladder, in front of the rectum, and encloses part of the urethra. Usually, the prostate can reach 3 centimetres in length and 20 grams in weight[43] in adult males. This organ works thanks to male hormones, known as *androgens*. Examples of important androgens are testosterone, which is essential for the development of testis and prostate; dehydroepiandrosterone, a metabolic intermediate for the biosynthesis of androgens; dihydrotestosterone, important for sexual differentiation in embryonal stage and precursor of testosterone. Furthermore, such androgens are responsible also for secondary sex characteristics such as facial hair and increased muscle mass.

Prostate cancer develops a mass of cells which can spread and invade other parts of the human body such as bones, lymph nodes, rectum, bladder and lower ureters. Prostate cancer has become the deadliest form of cancer in men because of this characteristic.
PCa can be detected with preliminary tests such as DRE test (digital rectal examination). DRE is a tactile method used by doctors to find abnormal parts on the prostate and, at last, diagnose occurring cancer. Different substances can be produced in response to cancer and can be used as biomarkers for detecting prostate cancer in an early stage. For instance, the PSA (prostate-specific antigen) test is used to measure the level of the enzyme PSA in male blood. Usually, a high level of PSA may indicate a risk of PCa and doctors recommend regular tests over time to evaluate if a biopsy is needed. Similarly, 4Kscore and the PHI (prostate health index) are other tests[44] used to evaluate the developing of prostate cancer. Unfortunately, these methods can lack sensitivity and specificity, resulting in false-positive or negative responses, and can be invasive for patience. Imaging and biosensing have been emerging as powerful tools to detect and localise prostate cancer cells in both early and late stage of the disease.

1.2. Bioimaging methods and biosensing tools for detecting prostate cancer

1.2.1. Current imaging methods for prostate cancer diagnosis

Nowadays clinical imaging methods have become crucial techniques for detection and localisation of prostate cancer. Thanks to these methods, the stage and spreading of the cancer cells can be known which are crucial for the appropriate treatment. Several improvements for each technique have recently been accomplished; however, the choice of imaging modality depends on the biological behaviour of the tumour[45,46].

Transrectal ultrasound imaging (TRUS) is the first method used when PCa is suspected[47]. The analysis consists of introducing an ultrasound probe in the patient's rectum. This probe sends and receives sound waves through the rectal walls into the prostate which are elaborated by a computer. The elaboration of the sound waves creates an image of the prostate and the tissues nearby[48] (Figure 1.4). This technique determines the volume of the prostate and can help to evaluate if cancer is involved.

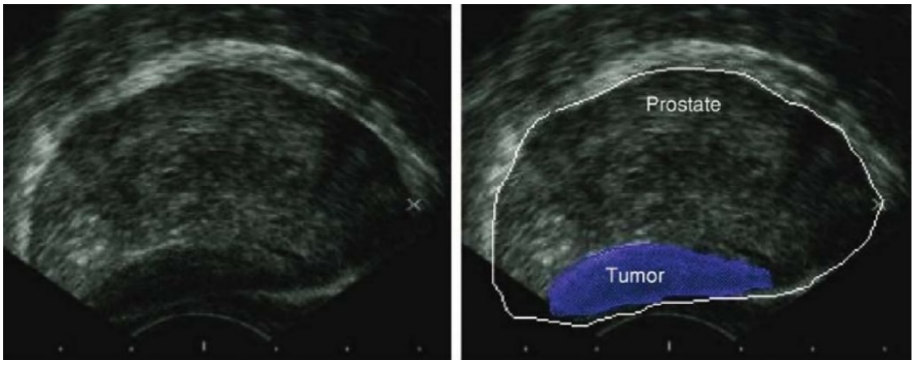

Figure 1.4. TRUS images of a prostate affected by cancer (figure adapted from Theodorescu *et al.*[49]).

The following imaging methods are minimally invasive and deemed to be precise and accurate to detect and localise cancerous tissues.

Magnetic resonance imaging (MRI) is based on nuclear magnetic resonance (NMR)[50]. The involved physical process depends on adsorption and emission of energy by an atomic nucleus, placed in a magnetic field. In MRI, the nuclei of hydrogen atoms are used as probes for the detection of tissues because of natural abundance in fat and water. Varying parameters of the pulse sequence, different contrasts of the surrounding tissues can be obtained which are processed as images. This method is used to evaluate if the cancer is confined in the prostate or has metastasised in other parts of the body[51] (Figure 1.5).

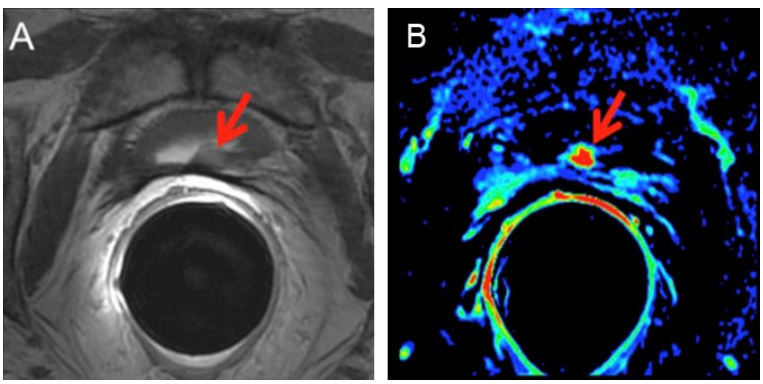

Figure 1.5. MRI images of the prostate with cancer (arrows). **A)** Axial T2-weighted fast spin-echo image and **B)** axial gradient-echo T1-weighted colour map image (figure adapted from Maurer *et al.*[52]).

Positron-emission tomography (PET) and computed tomography (CT) are used to obtain information about the structure and function of cells and tissues in the body.

In PET, a radiolabeled compound is administrated in microgram amounts to the patient's bloodstream while the patient is placed on a circular scanner. This targeting drug presents a radioactive isotope with a half-life enough long to be absorbed by the targeted tissues and/or organs and afterwards a scanned image of the involved body part can be recorded[207].

The radioisotope emits a positron through a positron emission decay (β^+-decay) which travels in tissue for a short distance, typically 1 mm. During this path, the positron interacts with an electron (annihilation), producing a couple of photons (γ-photons). The annihilated photons travel along the line of the annihilation event, in the opposite directions. Both γ-photons are detected by a scintillator, coupled to a photomultiplier tube, in which a dedicated electronic system can determine the energy, the precise timing and position inside the body of the annihilation[207]. This information is elaborated and computed as an image (Figure 1.6a).

On the other hand, computed tomography works with X-rays. The patient is placed in a toroidal scanner. Narrow beams of X-rays are shot by the rotating tube around the patient and 2D image slice of the organ or tissue are generated by each scan. The collected image slices are elaborated by a computer which generates a 3D image of the scanned patient's body part (Figure 1.6b).

At the beginning of 2000s[207], PET and CT had become important medical techniques thanks to their multimodal application. In addition, accurate and detailed images are obtained in a single scan. Information about the body's anatomy can be obtained from CT scans; on the other hand, metabolic information can be determined from PET scans, using for instance [^{18}F]FDG (2-deoxy-2-[^{18}F]fluoroglucose) or ^{18}F-fluorocholine (Figure 1.6c). [^{18}F]FDG competes with glucose and other hexoses in tissues with a great metabolic rate such as tumours, brain, myocardium and gastrointestinal tract[208]. Nevertheless, the limitation of the use of PET/CT with [^{18}F]FDG is due to lack of specificity for cancerous tissues. Despite this drawback, this methodology offers functional information about the metabolic state of the tissue[208]. To overcome the problem of specificity, several targeting radiotracers have been designed and synthesised in the past decades for different kinds of cancer. In particular, the detection of prostate cancer *via* PET/CT has been improved by the use of prostate-specific membrane antigen (PSMA)-based radiotracer. For instance, ^{68}Ga-PSMA-11 Glu-NH-CO-NH-Lys-(Ahx)-[^{68}Ga-*N*,*N'-bis*[2-hydroxy-5-(carboxyethyl)benzyl]ethylenediamine-*N*,*N'*diacetic acid] has demonstrated promising sensitivity and specificity for imaging the prostate cancer and its spread thanks to the selectivity of PSMA on the surface of prostate cancer cells.

The overexpression of PSMA has been found in either locally or metastatic lesions in bones, lymph nodes and soft tissues[209].

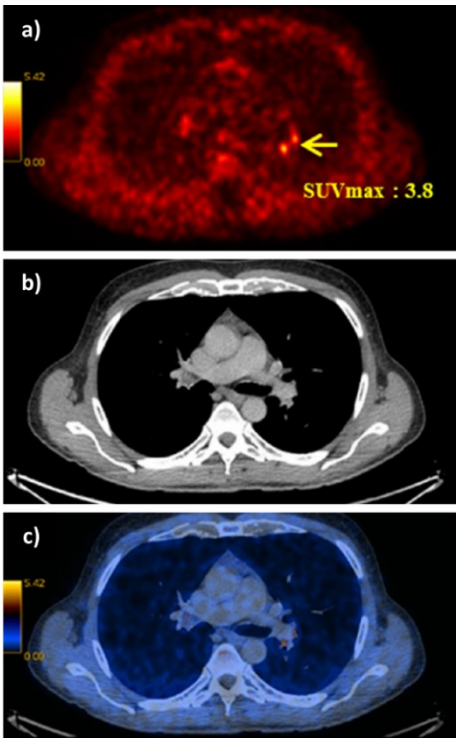

Figure 1.6. a) PET image, **b)** CT image and **c)** PET/CT images of a male body with prostate cancer[54]. (SUV: standardised uptake value[55] of ^{18}F-fluorocholine).

TRUS, MRI and PET/CT differ from each other for their use, obtained information and clinical aim. For instance, TRUS determines the volume of the prostate and can be used in a guided biopsy, giving real-time images[209]. In addition, this technique is inexpensive and portable which can be deemed accessible to patients[210]. Nevertheless, TRUS images can show some speckle and shadow artefacts and sometimes in low contrast. On the other hand, the use of MRI is focused on diagnostic and treatment planning for diseases in the prostate gland, thanks to its better tissue contrast, lesion detection and staging of prostate cancer[210]. The main disadvantages of this method are the cost of the analysis, the instrument can not be portable and difficult to reach real-time imaging. Finally, PET/CT is mainly used for determining the stage and the spreading of prostate cancer and the effectiveness of the radiotherapy[211]. In addition, this modality presents high sensitivity, spatial resolution and it is able to quantify the uptake[212]. Despite these advantages, PET/CT involves the exposure of the patient to radiations of the injected radiotracer, costs of the analysis and require trained personnel.

In addition, MRI and PET/CT are minimally invasive to patients, accurate, sensible and precise compared to TRUS, they are considered expensive for many patients, accessible only for few medical structures and require expert medical staff. One of the most important disadvantages of these imaging methods is the diagnosis of early-stage prostate cancer.

1.2.2. Overview of biosensing and applications for the detection of prostate cancer

The detection of cancer in the early stage is a key point for preventing and treating such diseases. Fortunately, point-of-care tests (POCTs) have become widely used as early-stage diagnostic methods to detect specific biomarkers on the occurrence of a disease. POCTs are affordable, quick and ready-to-use solutions which do not need a specialised medical centre and/or staff. For example, the PSA test is one of the most common POCTs used by doctors to assess the occurrence of PCa in the early stage. Although the PSA test has helped to decrease the mortality for PCa[56], it can lack accuracy and specificity for prostate cancer. In fact, other non-cancerous diseases of the prostate, such as benign prostatic hyperplasia (BPH)[57], can also increase the level of released PSA in the blood, giving a false-positive result for prostate cancer. The burden of research field on PCa is to recognise selectively and in low concentration some biomarkers produced in the early stage by cancer cells. Generally, these tests are based on biosensors which are capable to interact with a specific biomarker produced during a disease.

The most common parts in a biosensor are *i*) a biorecognition element (*i.e.* antibodies, saccharides or peptide fragments) which selectively recognises and binds the analyte; *ii*) a transducing component converts the interaction of biomolecules in a quantifiable signal; *iii*) a readout system is used to read the results (Figure 1.7).

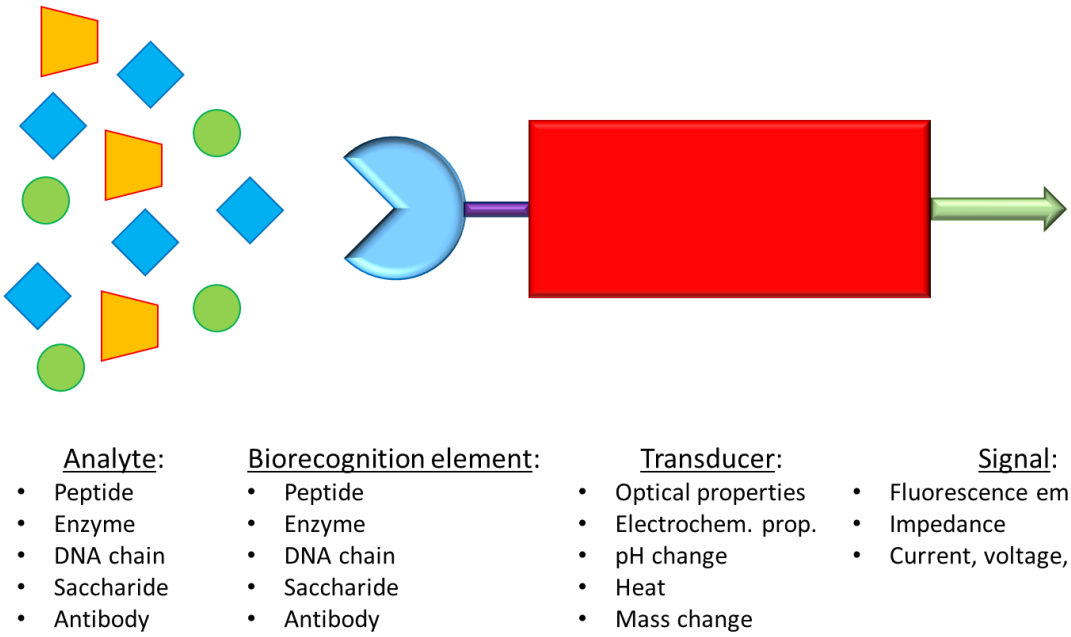

Figure 1.7. Schematic representation of a biosensor.

The transduced signals obtained by the biosensor can be an electrochemical signal or a variation of fluorescence feature (*i.e.* intensity, emission wavelength or lifetime)[58-62]. For example, different fluorescence probes have demonstrated a significant variation of the fluorescence emission upon a binding event. Generally, such probes present weak or none fluorescence emission in solution, but once they respond to binding events with the targeted biomarker, their fluorescence intensity increases[213]. Recently, coumarin-based fluorophores have been synthesised and studied for their large Stokes shifts[214]. Specifically, such fluorescence probes undergo to intramolecular spirocyclisation in presence of esterase enzymes which shows a strong fluorescence activation and a large Stokes shift[214]. The lifetime variation of a ratiometric fluorescent probe has been recently studied in living cells[215]. The proposed probe monitors the variation of the concentration of HOCl in living cells which can be responsible for the occurrence of chronic diseases. This fluorescent biosensor, in presence of HOCl, changes its structure and shows a variation in a lifetime, passing from a non-FRET to a FRET sensitive molecule[215]. A definite variation in fluorescence characteristics of a fluorescence biosensor is significantly important to allow a clear and straightforward read of the results obtained by the analysis. On the other hand, electrochemical biosensors employ electrical property changes (for instance, voltage, current or impedance) to detect the binding event with the targeting analyte. Such produced signal by these types of biosensors is proportional to the concentration[63,64] of the targeting analytes.

This property has been challenging the research field of biosensor design and construction to reach sensitivity and specificity at low concentration of the analyte. In this regards, different research groups have reported novel molecular biosensors, either fluorescent or electrochemical[65,66], able to detect specific biomarkers related to a disease, for instance, the PSA level for prostate cancer[67]. In addition, these biosensors can be embedded in inexpensive, portable and ready-to-use devices able to perform point-of-care tests at any time without specialised staff[68].

In the past decades, novel electrochemical biosensors, which use electrical impedance spectroscopy (EIS) as a method for prostate cancer detection, have been increasingly exploited in the research field. EIS can use label-free detection which consists of direct, sensitive and real-time sensing of the binding event between the biorecognition element and analyte[69] measured in the form of either capacitance or resistance changes[70]. In particular, a recently studied PSA biosensor uses an interdigitated microelectrode (IDE). This biosensor presented an anti-PSA immobilised through a self-assembled monolayer (SAM) on the surface of the IDE. The bovine serum albumin was bonded to the SAM to prevent non-specific adsorption on the surface of the electrode. EIS was used to estimate the PSA concentration and the concentration range. Such biosensor was analysed in solutions at different PSA concentrations. The variation in the EIS spectra can be related to changes in the properties on the interface between the solution and electrode which are due to pure interactions between the free PSA in solution and the immobilised anti-PSA of the IDE. This study has revealed a linear trend in the concentration range of PSA between 1 pg/mL and 100 ng/mL and a sensitivity of 0.444 mL/g[70].

Capacitance and resistance are related, through mathematical equations (detailed in Chapter 6), to impedance. EIS measurements are based on the detection of the impedance in an electrochemical cell which works in the alternate current regime. Impedance can be explained as the opposing force to the electrical current (in alternate current circuits) as well as the resistance (in direct current circuits). The electrochemical cell employed for the EIS measurements consists of a 3-electrode cell with a counter electrode (CE), a reference electrode (RE) and a working electrode (WE)[71] (Figure 1.8)

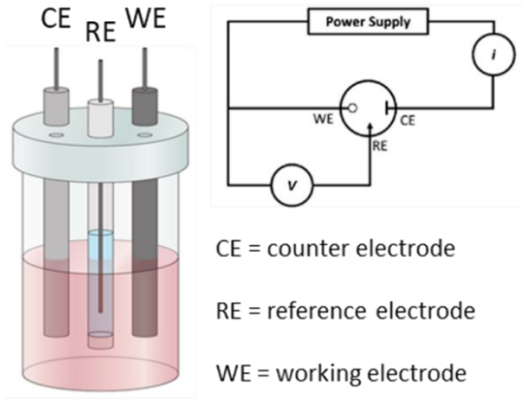

Figure 1.8. Electrochemical 3-electrodes cell and its relative electric circuit (adapted from Raccichini *et al.*[72] and Fischer *et al.*[73]).

The function of the CE is to close the circuit and maintains the reference potential ideally constant; on the other hand, the RE presents a known potential and is used to obtain the potential difference between the WE and RE. The WE presents a biorecognition element on the electrode surface, generally gold, which binds the target molecules in the solution. A potentiostat is used to apply a desired alternate potential between WE and RE. In the last decade, this setup has been increasingly revised in order to build miniaturised electronic devices to perform point-of-care diagnosis for the detection of PCa biomarkers[74-76]. One of the recent miniaturised EIS-based biosensors[77] has shown excellent responses for the detection of PSA level in human serum, comparable to the clinical threshold of 4 ng mL^{-1}. Such biosensor can represent an example for the development of novel devices for early-stage detection of PCa biomarkers thanks to the small size, low-cost, sensitivity, reproducibility and reliability[77].
More details regarding the biosensing design and testing are being discussed in Chapter 6.

1.3. Molecular characteristics of naphthalenediimides as synthetic scaffolds for biosensing

The construction of a biosensor requires a transducer which links the biorecognition element and generates the physical property to be converted in a signal, for example, electrochemical[78] or optical[79] responses.
In the last 30 years, 1,4,5,8-naphthalenetetracarboxylic diimides (NDIs) have been widely explored in different research fields such as electronics, material science, biology and medicinal chemistry[80] as a potential scaffold to link different moieties on the construction of molecular devices.

Such compounds are derived from naphthalene dianhydride (NDA) (Figure 1.9) and an amine and represent the smallest homologue of rylenediimides (RDIs). The first application of NDI derivatives was as synthetic pigments and dyes[81] because of their vivid colours.

NDIs present an electron-deficient aromatic π system which can be extended to show a wide range of absorption and fluorescence emission wavelengths[81]. Simple NDI derivatives present absorption maxima at around 350 nm[82] which can reach a range from 500 to 760 nm[81] with proper derivatisation. In addition, their main characteristic is high fluorescence quantum yield and fluorescence emissions in a range between 650 and 780 nm[81].

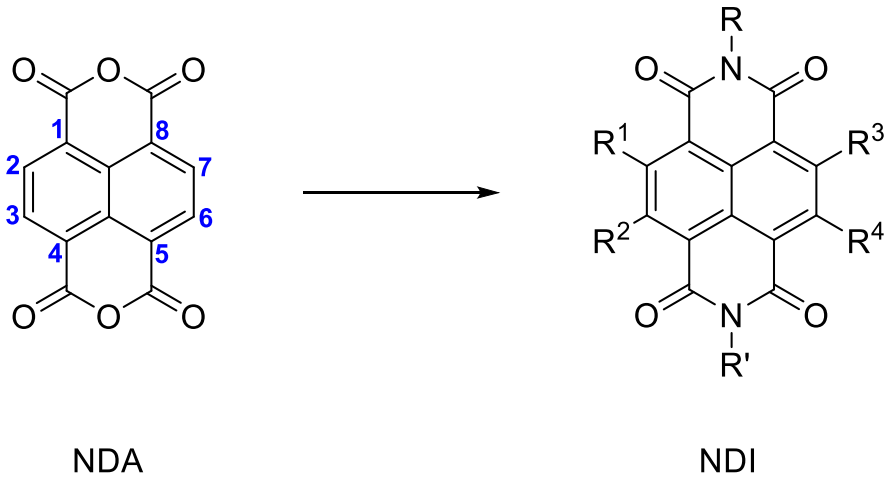

Figure 1.9. Structure of naphthalene dianhydride (NDA) with numbered positions and structure of naphthalenediimide with possible positions of substitution.

As previously mentioned, the ease of functionalisation of NDIs has been increasingly exploited for modulating their optical characteristics, suitable for the different applications.

The major contribution of the characteristics of NDIs is due to modifications through the derivatisation of the aromatic core which can vary both electrochemical and optical properties. For instance, aryl derivatisation in the positions 2, 3, 6 and 7 can lead to a species with a quantum yield close to 1 in solvents of various nature (*i.e.* aliphatic, aromatic, chlorinated and dipolar)[80]. On the other hand, the derivatisation with a variety of groups in the imide bonds results in little effects on the absorption and fluorescence spectra of NDIs. However, such derivatives show high solubility in different solvents. The presence of aromatic substituents on the NDI-core causes aggregation of these molecules in solution due to π-π stacking which leads to aggregation-caused quenching (ACQ). However, the electronic properties of these aggregates facilitate the electron transfer which is useful for the development of an electronic device[216].

On the other hand, disrupting the π-π stacking of core-substituted NDIs enhances the fluorescence emission at the expense of electronic features. The derivatisation with alkyl groups, either in the core or in the N-amide positions, suppresses ACQ. The modulation of the substituents is the main focus of researchers to balance optical and electronic characteristics, according to the use of such aromatic compounds[216]. Generally, the solubility of NDI derivatives can be modulated by the long and bulky aliphatic substituents in the N-amide position. Those substituents can promote the creation of aggregates by weak interactions[80]. Several substituents have been studied to modulate either optical or electronic characteristics to create devices soluble in different solvent systems depending on the aim of the design of such NDI derivatives.

1.3.1. Amino acid- and peptide-tagged naphthalenediimides in biological applications

Various moieties have been introduced in the imide group such as alkyl chains, aromatic groups and amino acids. The introduction of amino acids on the NDI core have been investigated for water solubility and application in biological media. Such amino acids-tagged NDIs can be obtained by microwave-assisted synthesis which has become a fast, reliable, efficient and high yield method to symmetrise and asymmetrise the NDI core[83,84]. In the last decades, different amino acid-tagged NDIs have been studied in aqueous solutions to investigate their aggregation and behaviour in such media[85-87]. These species tend to aggregate with themselves and other aromatic compounds thanks to the presence of the extended electron-deficient π-system on the NDI-core. This characteristic has been explored with electron-rich aromatic materials such as carbon nanotubes[88] and graphene congeners[89] to create supramolecular aggregates for novel bioimaging probes (Figure 1.10a). In these works, the fluorescence and aggregation properties of such amino acids-tagged NDIs have been explored in addition to their biocompatibility in living cells. The fluorescence properties in living cells of such compounds have been extended to the NDI core which links peptide moieties on its sides (Figure 1.10c). Such peptide, cyclo(RGDfK), has shown an affinity to $\alpha_v\beta_3$ integrins which are overexpressed during the angiogenesis of some kind of cancers, such as prostate[82]. Such peptide-tagged NDI has shown a high fluorescence emission at around 605 nm (excited at 405 nm) and a quantum yield of 0.002 (compared to fluorescein in aqueous 0.1 N NaOH) in 10 mM solution in DMSO. Time-correlated single-photon counting (described in Chapter 4) experiments showed that the peptide-tagged NDI tends to aggregate in DMSO solution.

Fluorescence lifetime imaging microscopy (described in Chapter 4) demonstrated that such aggregates are biocompatible and predominantly localised in the cytoplasm of the prostate cancer cells.

The biocompatibility, water solubility and capacity to aggregate with electron-rich species of amino acid-functionalised NDIs have also inspired some works to bind G-quadruplexes as potential anticancer therapies[90] (Figure 1.10b). These species have shown recognition and affinity to such G-quadruplexes which are driven thanks to aromatic stacking and hydrophobic interactions to create supramolecular aggregates.

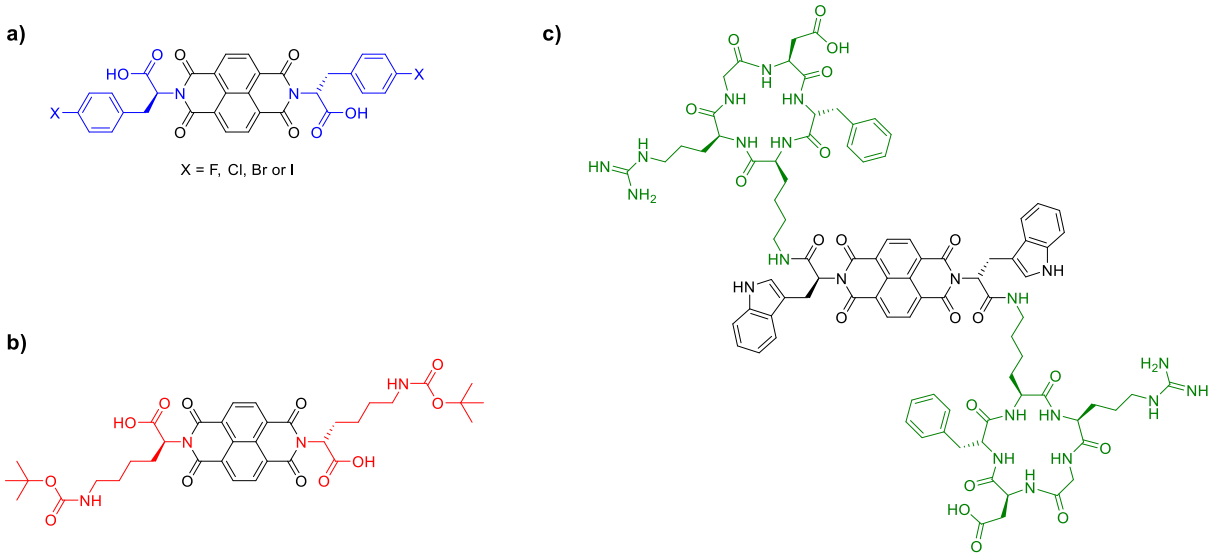

Figure 1.10. Some examples of amino acid/peptide-tagged NDIs. **a)** NDI core tagged with halo-*L*-phenylalanine[88,89] (in blue); **b)** NDI core derivatised with *L*-lysine, protected with *tert*-butoxy carbonyl protecting group[90] (in red); **c)** NDI core tagged with cyclo(RGDfK) peptide[82] (in green).

1.3.2. Supramolecular characteristics of naphthalenediimides

The planar aromatic system of NDIs is responsible for aromatic π-stacking and Van der Waals interactions with other aromatic species. In fact, most aromatic rings present a quadrupole moment created by their electron density with a partial negative charge above and below the face and a partial positive charge around the periphery[91].

Electron-deficient NDIs can form ‘‘donor-acceptor’’ complexes thanks to the pairing with complementary electron-rich species. Such association between π-donor and π-acceptor molecules results in more favourable π-π interactions than the self-association of either “donor-donor” or “acceptor-acceptor” species[91].

An example of a π-π donor-acceptor formed by an amino acid-NDI derivative, used as an acceptor (A), and a cysteine-naphtalene derivative, used as a donor (D), was reported Sanders et al.[217] Dynamic combinatorial approach was used to form a [2]-catenane in aqueous medium and the assembly was driven by adding a templating guest, stochiometry, adding an inert salt. The results of this experiment lead to different stacking configuration of the donor and acceptors. The DADA stack of the building blocks revealed to be favourable, however, either DAAD or DADD sequences were found in the mixure[218].

The association of species with different electronic characteristics is used in supramolecular chemistry which is focused on the design, synthesis and study of complex architectures formed by weak interactions such as hydrogen bonds, electrostatic and Van der Waals forces[92]. The basic concept of supramolecular chemistry is the "lock and key" notion which was hypothesised by Emil Fischer[93]. Since its discovery in 1894, this concept is a milestone of molecular recognition and host-guest chemistry. The supramolecular chemistry has been also explored in different systems consisting of NDIs self-assemblies or supramolecular complexes. In different fields, the interactions created by both the planar aromatic core and substituents on the NDIs have generated different devices such as organic solar cells[94,95], field-effect transistors[96,97], sensors[98,99] and catalysts[100,101] alongside their use as imaging probes[82,88,89].

Another application of supramolecular complexes based on NDI is the formation of mechanically interlocked molecules (MIMs). Despite these aggregates are not considered supramolecular architectures[102,103], there are held by non-covalent interactions which lead to self-organisation, self-assembly and recognition of the participant parts. Rotaxanes are MIMs which consist of kinetically trapped architectures between an "axle" and a "wheel". In some cases, the "axle" can present sterically hindered groups at the end which prevent the dissociation of the complex.

In the last decade, rotaxanes have been explored in a wide range of applications such as catalysts[104], chemical sensors[105], polymers[106], molecular switches[107] and motors[108]. In addition, such MIMs have also found application in the biological field as a system for drug delivery[109], target bacterial protein[110] and release of bioactive peptides[111]. Recently, the optical and fluorescent properties of rotaxanes have been exploited for the design and synthesis of imaging agents such as MRI agent[112], mitochondrial stainer[113] and fluorescent dye[114]. For instance, Fredy *et al.*[112] developed a one-pot mechanoselective synthesis of [3]rotaxanes, formed by an α-cyclodextrin *mono*- or *bi*-functionalised by Gd(III) complexes, useful as MRI contrast agents. Gadolinium(III) complexes are well-established contrast agents for MRI thanks to the large magnetic momentum and long electron spin relaxation time of the metal ion[219].

Such [3]rotaxanes showed minimal toxicity *in vivo* and exhibited higher temporal resolution, contrast enhancement and retention than the commercially available Gd-DOTA. The use of these supramolecular architectures can be a viable approach to produce contrast agents with better efficiency, modularity and versatility compared to conventional covalent strategies[112]. The optical characteristics of some *pseudo*rotaxanes can be changed upon different conditions. Recently, 2 different *pseudo*rotaxanes have been studied in presence of Li^+ and Na^+ solutions. One of those rotaxanes was formed by a hexylamine-NDI, representing the "axle", and 1,5-dinaphtho[38]crown-10, representing the "wheel" (Figure 1.11a). The solution of the formed *pseudo*rotaxanes showed a significant red shift in presence of $Li(CF_3SO_3)$ (from 428 nm to 500 nm). The possibility to changes the optical characteristics by adding or removing Li^+ cations in the solution of such *pseudo*rotaxane can lead to the development of molecular switches for imaging purposes.

Naphthalenediimides have increasingly become interesting components for the design and formation of rotaxanes thanks to their interactions which can create with aromatic electron-rich counterparts. Such compounds have been derivatised for taking part as "axles" because of their electron-deficient π-system which can interact with aromatic electron-rich "wheels" to form different MIMs[102,115,116] (Figure 1.11).

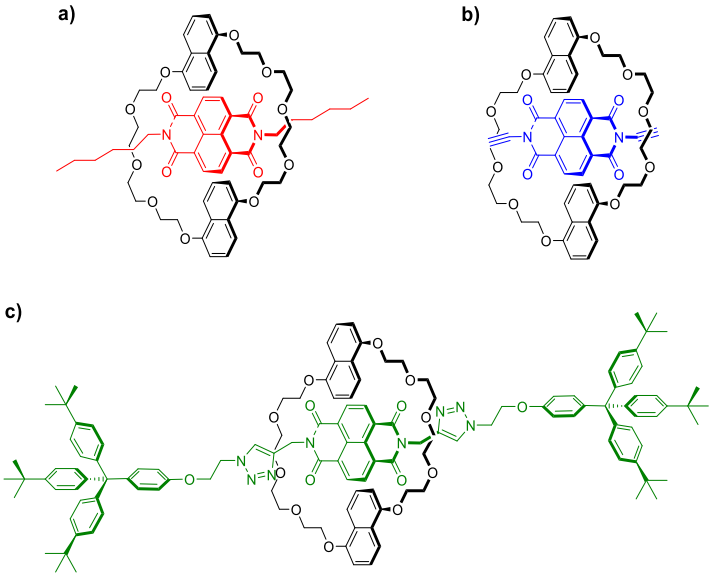

Figure 1.11. Examples of NDI-based *pseudo*rotaxanes. **a)** *Pseudo*rotaxane with alkyl chains on the NDI core as UV-visible molecular switch[117]; **b)** NDI-based *psuedo*rotaxane intermediate for the formation of [2]-catenane[118]; **c)** NDI-based [2]rotaxane as electrochemical induced shuttle[119].

1.4. Overview on thiosemicarbazone metal complexes in cancer imaging and therapy

Thiosemicarbazones (TSCs) have become important molecular building blocks for the development of novel biosensors[120,121], imaging probes and therapeutic agents. One of their main characteristics is the ease of synthesis and functionalisation which have been interested a lot of researchers worldwide to find biological applications. These ligands have also been explored for their ability to complex different metal cations which can improve other characteristics such as cytotoxicity, fluorescence emission or biocompatibility. One of the most representative examples of TSC is diacetyl *bis*(N^4-methylthiosemicarbazonato) copper(II) ([Cu(ATSM)]) (Figure 1.12). Such TSC metal complex has been employed as therapeutic agents to recover the copper imbalance caused by neurodegenerative diseases such as Alzheimer's[122] and represents the first case of thiosemicarbazone complex in clinical trials. This complex has become the starting point for researchers worldwide to synthesise and study either different ligands or metal cations for therapeutic and imaging applications.

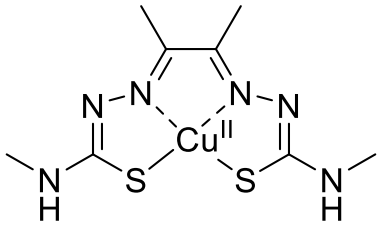

Figure 1.12. Structure of diacetyl *bis*(N^4-methylthiosemicarbazonato) copper(II), well known as [Cu(ATSM)].

TSC ligands were discovered in the 1950s[123] from the condensation of a ketone or aldehyde with a thiosemicarbazide. From the 1970s, their interest in synthesis and functionalisation started to increase, leading to their metal-TSCs complexes chemistry in the late 1980s[123]. From the 1990s, the studies of TSCs as a free ligand or in metal complexes considerably raised and a lot of characteristics have been highlighted from their crystal structures, biological applications and optical properties.

TSC ligands are classified as Schiff bases synthesised from an aldehyde, or a ketone, which is condensed with a thiosemicarbazide. Two main class of TSC ligands can be distinguished. *Mono*-TSCs present different substituents on their backbone (R_1, R_2, R_3 and R_4 indicated in structure **I** Figure 1.13a) which can be alkyl, aryl or heterocyclic groups. On the other hand, *bis*-TSCs present two symmetric, or dissymmetric, arms which can be also bridged (R''_1 in structure **IIb** Figure 1.13a) by a C-C bond or an aromatic ring.

Aliphatic substituents in R'_1 and R'_2, as well as in R''_1 and R''_2, confer flexibility on the structure of the thiosemicarbazone and therefore stability to their metal complexes. On the other hand, aromatic substituents provide a variety of metal complexes with other metal ions such as Ga(II), Ni(II) and In(III) and present fluorescence emissions. In addition, such aromatic TSC have showed higher stability in biological media and lipophilicity compared to their aliphatic counterparts[132].

Both *mono*- and *bis*-TSCs ligands can generate a thione-thiol equilibrium which can bind a metal cation in neutral form. In addition, after the loss of a proton, either in the amino or thiol groups, TSCs can complex metal centres in anionic form[123] (Figure 1.13b).

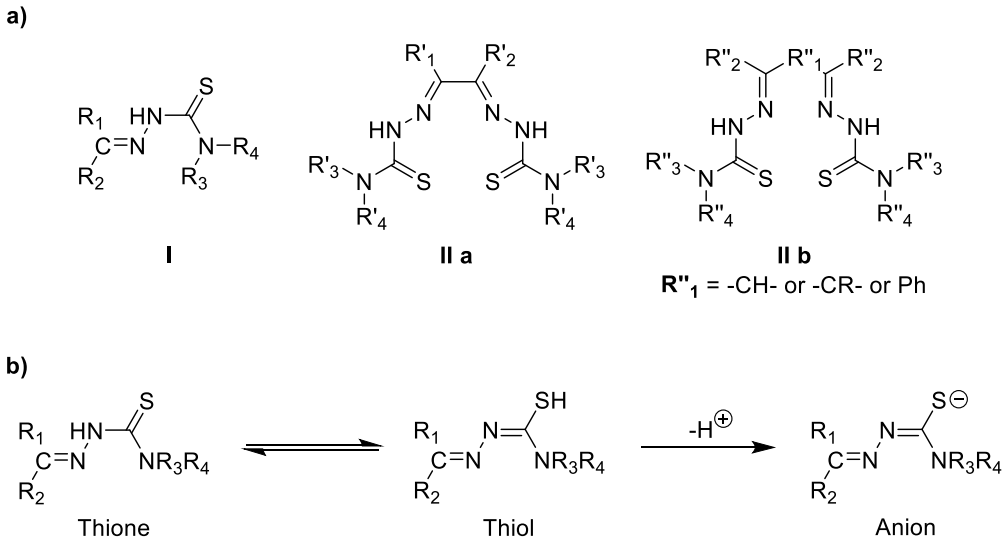

Figure 1.13. a) Structural representation of common TSC backbones: mono-TSC (I), non-bridged *bis*-TSC (IIa) and bridged TSC (IIb). **b)** Thione-thiol equilibrium of TSC which can lead to the anionic form.

The presence of donor atoms, such as nitrogen and sulphur, in the TSCs backbone, confers a wide range of binding modes of metal cations[123]. This characteristic has been explored with different transition metals such as copper[124], zinc[125], cobalt[126], iron[127], manganese[128], gold[129], gallium[130], ruthenium[131] and many others.

In particular, these TSCs metal complexes have been widely studied as therapeutic agents because of their cytotoxicity and biocompatibility[132]. In recent years, TSC derivatives with Zn(II) have been proposed as cytotoxic agents able to localise in the lysosomes and trans-metallate with Cu[133]. In particular, a series of aromatic *mono*-TSCs ligands complexing Zn(II) were formed and studied in different tumor cell lines. In this work, Stacy *et al.*[133] demostarted that such Zn(II) complex was able to penetrate the cell membrane and lysosomes sequestrated it.

Inside such organelles, intralysosomal copper(II) ions transmetallated with zinc(II), forming a redox-active complex. Such newly formed copper TSC complex generated reactive oxygen species which lead to cytotoxicity. In addition, nickel(II) complexes of TSCs have found different applications such as antiretroviral agents for HIV[134], antimicrobial drugs[135] and can induce apoptosis in different cell lines[136]. The proposed Ni(II) TSC metal complex useful as apoptosis-inducer agent presented an aromatic *mono*-thiosemicarbazonato ligand. Cell cycle analysis of these metal complex showed that the compound is able to arrest the cycle of reproduction of IM-9 cells (human multiple myeloma) in the phase between G0 and G1.

Another characteristic which becomes important for TSCs metal complexes is the ability to be selective for "hypoxia". Hypoxia is a condition which indicates the lack of oxygen in a region of the body or the entire body which was discovered by Thomlinson and Gray in the 1950s[137]. The concentration of oxygen in normal tissues is higher closest to a blood vessel (2-9% pO_2) which gradually declines with the distance from the vessel (0.02-2% pO_2) (Figure 1.14)[141]. In cancerous tissues, this concentration drops drastically near zero[138] and cells can adapt to this condition because of hypoxia-inducible factor-1 (HIF-1)[139]. HIF-1 develops responses that make cells to survive under hypoxia. These processes can promote the invasion, growth and metastasis of cancer cells in tissues and organs[140].

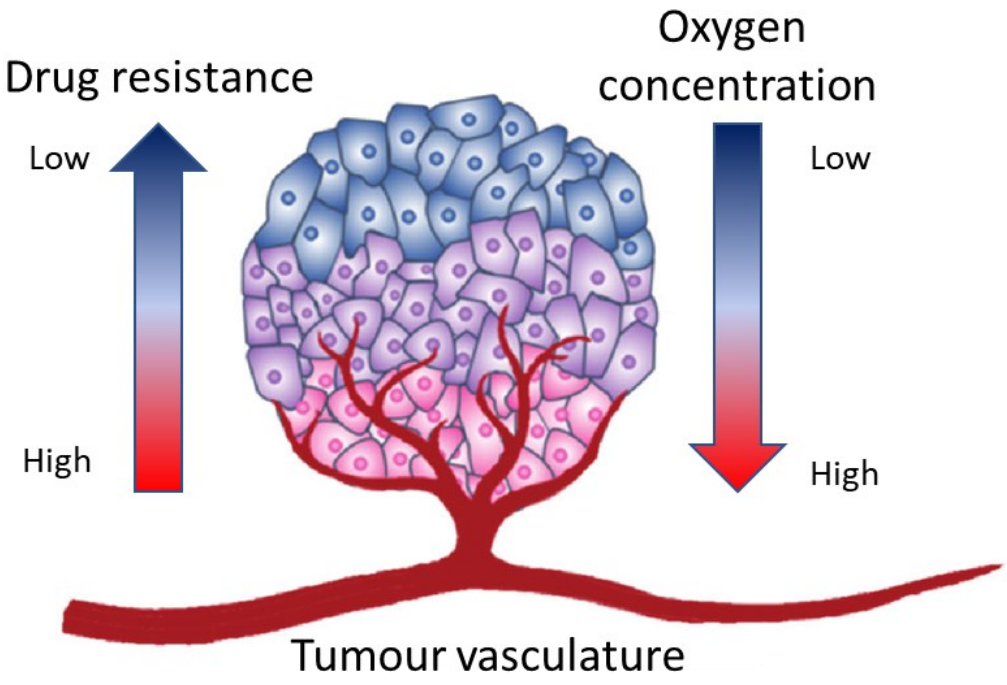

Figure 1.14. Microenvironment of hypoxic tumour. The oxygen supply becomes restricted in cells once the rate of growth of tumour cells is progressing. Cancerous cells in hypoxic conditions can develop aggressiveness, metastasis, and resistance to therapeutic agents (figure adapted from Sharma *et al.*[141]).

In the past, different therapeutic agents have been revealed ineffective as the resistance and aggression of cancer grow under hypoxia conditions[141]. In this regard, the main target of cancer research in the last decades is to find compounds which are able to target HIF-1[142] and being activated by hypoxia condition[143]. [Cu(ATSM)] is one example of *bis*-TSCs which has shown selectivity for cells under hypoxia compared to normal cells[144]. Such hypoxia selectivity is due to its irreversible reduction of Cu(II) in Cu(I) in lack of oxygen which traps the monovalent ions inside the cells[144]. At high concentration of oxygen, Cu(I) can be reoxidised in Cu(II) and be expelled from the cells (Figure 1.15). Similarly, the couple cobalt(III)/cobalt(II) has been investigated with bis-thiosemicarbazone ligands as hypoxia-targeting complexes[145].

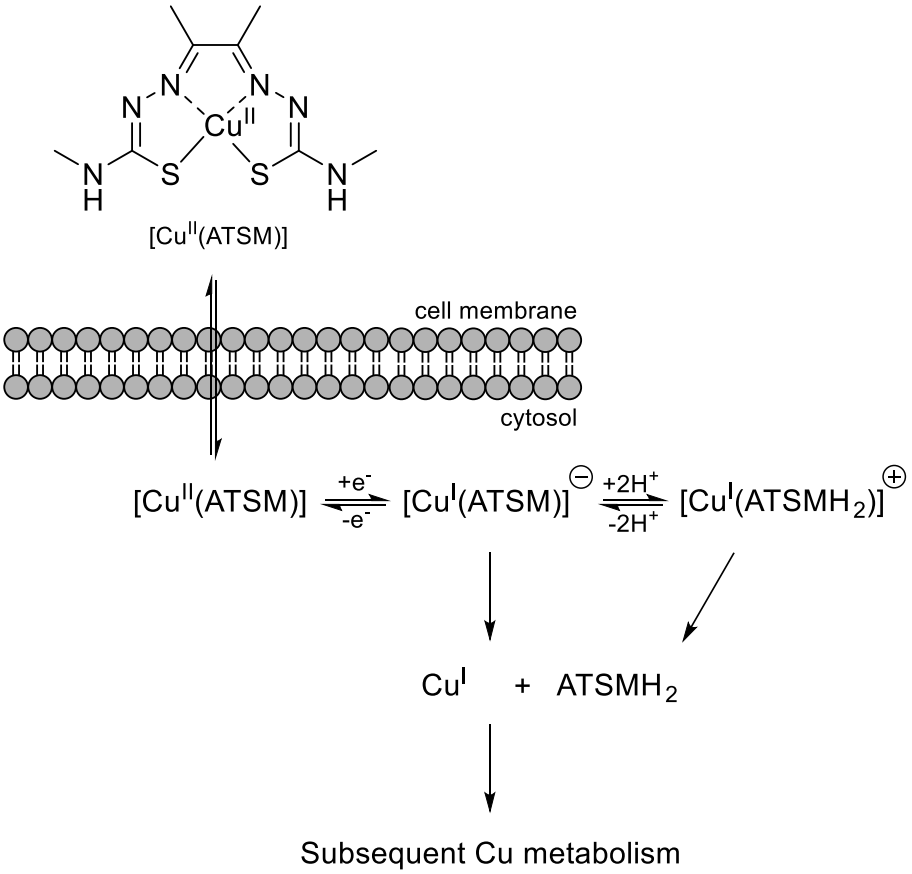

Figure 1.15. Schematic representation of the uptake of [Cu(ATSM)] and release of Cu(I) ions in hypoxic conditions (figure adapted from Challapalli *et al.*[146]).

In recent years, radiopharmaceuticals have been playing an important role in cancer diagnosis and therapy[147,148]. These agents are designed molecules which incorporate radioisotopes of specific atoms able to emit doses of ionising radiation to cancerous cells, able to kill them. Considering the radiation emission of radioisotopes, such radiopharmaceutical can be also used for imaging for example for PET.

Among radiolabelled compounds, copper(II) *bis*-thiosemicarbazones, labelled with ^{60}Cu, ^{62}Cu and ^{64}Cu, have increasingly considered valid agents for *in vivo* imaging in hypoxic tissues[149]. This interest has raised thanks to the simple coordination and redox chemistry of copper, its biochemistry and metabolism in human[150] which is also reflected in its isotopes. In addition, the isotopes of copper, such as ^{60}Cu, ^{62}Cu and ^{64}Cu, present versatile positron decay schemes (^{60}Cu: half-life ($t_{1/2}$)=0.40 h, positron emission (β^+)=93%, electron capture (EC)=7%); ^{62}Cu: $t_{1/2}$=0.16 h, β^+=98%, EC=2%; ^{64}Cu: $t_{1/2}$=12.7 h, β^+=17.4%, EC=43%)[150] which have been revealing to be important for PET imaging. These isotopes can be produced using reliable, reproducible and commercial production systems, available in few medical centres.

Copper-64 has been extensively used in PET imaging for its long half-life, long enough to allow the distribution of this nuclide from the production centre to the imaging centre without a cyclotron. Despite these interesting features of ^{64}Cu, its half-life can result excessive for patients who are exposed to large and long doses of radiation[151]. In the last decades, gallium-68 has become a valid alternative to copper-64 thanks to its shorter half-life ($t_{1/2}$=68 min)[151] and its potential use as a therapeutic and imaging agent under hypoxic condition[151]. Despite its different coordination chemistry, ^{68}Ga has been incorporated to thiosemicarbazone derivatives[151-153] which has shown an increase of activity of TSCs ligands[152]. Besides, Ga(III) is the most relevant metal ion because of its interactions with iron(III) metabolism. In fact, gallium(III) has a similar ionic radius and binding to transferrin with iron(III) which can be uptaken into cells. An analogous mechanism is shown also for its radioisotope gallium-68[220]. TSC complexes with ^{68}Ga can be used in fluorescence *in vivo* imaging because of the radioisotope of Ga is diamagnetic and do not interfere with fluorescence emission, which copper-64 complexes suffers[152]. This dual-modality of fluorescence and positron emissions of ^{68}Ga has brought researchers to increase the range of metal radioisotopes useful in fluorescence and PET imaging. Indium-111, zirconium-89 and technetium-99m are other examples of radioisotopes have been using in both fluorescence and PET imaging[154]. ^{68}Ga is produced in ionic form (^{68}Ga(III)) by commercial generators consisting of a small chromatographic column[221]. On the other hand, ^{64}Cu, ^{111}In, ^{89}Zr and ^{99m}Tc require the use of cyclotrons. The production of such radioisotope sometime requires a specific facility, specialised personnel and the production centre can be far from the imaging centre. Considering such problems, different fluorescent TSC metal complexes have been introduced as an alternative to radiolabelled compounds.

In recent years, the versatility and ease of the synthesis of these TSC metal complexes have been widely explored for their optical properties, cytotoxicity and biocompatibility[155]. Most of these metal complexes present fluorescence emission in different ranges of wavelengths which can be modulated by introducing fluorophores linked to the backbone[156-158] or being part of the backbone[159,160].

Nowadays, PET and PET/CT have reached high sensitivity, specificity and accuracy. In recent work, the detection of colorectal cancer using PET/CT showed a sensitivity of 89%, a specificity of 92% and an accuracy of 90% of the diagnosed patients, compared to 80%, 69 and 75% obtained by FDG-PET[222]. However, this technique presents some limitations such as availability and costs of the analysis, the presence of false-positive due to inflammatory reaction and false-negative results when chemotherapy interferes with the contrast agent. In addition, the patient is exposed to doses of radiation[223]. An early-stage detection of the occurrence of cancer *via* fluorescence imaging has become a fast, sensitive and low-cost alternative to PET imaging. For instance, the sensitivity, specificity and accuracy of the detection of colorectal cancer *via* near-infrared fluorescence imaging using indocyanine green have been recently found at about 74%, 100% and 76% respectively[224]. The use of fluorescent methodologies has increased and developed along with the design and synthesis of fluorescent molecules which can also target hypoxic tissues or specific biomarker in cancerous cells.

1.5. Small-sized peptides as alternative therapeutic and targeting agents

In the late 1990s, monoclonal antibody-based therapy was established and used to treat patients with solid tumours[161]. This strategy is considered one of the most successful and important to target specifically and effectively antigens/receptors which are overexpressed, mutated or selectively expressed by human cancer cells[162]. Most of the approved monoclonal antibody therapeutics can inhibit tumour growth, target specific antibodies and deliver radionucleotides or toxins to cancer cells[161]. The continuous expansion of the market of monoclonal antibodies is due to the increase in the number of approvals, evaluate the efficiency of the existing therapeutic antibodies for other diseases, improvement in formulations and dosage[225]. However, monoclonal antibodies have been showing some limitations such as poor diffusion into tumoral cell membranes due to their large sizes and non-specific uptake by liver or bone marrow[163] of radionucleotides, cytotoxic drugs or toxins[161]. The efficiency of any local therapy for cancer relies on the accurate exclusion of any untreated areas of the disease, using imaging methods.

For instance, in some cases, the recurrence of prostate cancer can be a challenge to be detected in early-stage due to the lack of a sensitive and specific biomarker for a recurrent PCa[225].
In recent years, prostate-specific membrane antigen (PSMA) has increasingly interested the research of a specific either diagnostic or therapeutic agents for early-stage PCa or recurrent PCa. This antigen is a type II membrane protein which is expressed in all forms of prostate tissues, including cancerous tissues[226]. This protein is formed by 3-part structure: an internal portion of 19 amino acid chain, a transmembrane portion of 24 amino acid chain and an external portion of 707 amino acid chain[226]. Its gene expression in chromosome 11 commonly remains in patients with the occurrence of prostate cancer[226]. In the past decade, the targeting of PSMA and therefore the use of PSMA-based conjugates for PET/CT and fluorescence imaging has rapidly increased. For instance, ^{68}Ga-PSMA-11 has given a huge impact on the imaging detection of regional and distant metastatic recurrent prostate cancer at low PSA levels with high specificity and reproducibility[225]. Another example is given by ^{177}Lu-PSMA-617. This PSMA-based radiotherapeutic has been proven to be an effective and safe alternative for prostate cancer treatment[227]. Nevertheless, several patients do not respond to PSMA-targeting compounds and in some cases, patients have no expression of PSMA[228]. Another limitation of PSMA-based radiotherapeutic is the lack of overexpression of PSMA in primary tumoral or metastatic cells in patients with primary PCa or patients in an advanced disease whose show decreased expression[229].

Considering these restrictions of monoclonal antibodies and PSMA-based radio-compounds, cancer research has moved to design and synthesise small-sized peptides (*circa* 3000 Da[161] or below 50 amino acids[164]) which can mimic a portion of antibodies or being complementary to receptors on the surface of cancerous cells. These peptides have shown many advantages such as ease to synthesis[165,166], better penetrability into tumoral tissues due to their small size[167], capacity to target specific receptors on cancer cells surface and have lower toxicity to liver and bone marrow[163,165]. These characteristics have been increasingly exploited for different applications for biomedical purposed such as anticancer and antimicrobial agents and tumour targeting (Figure 1.16).

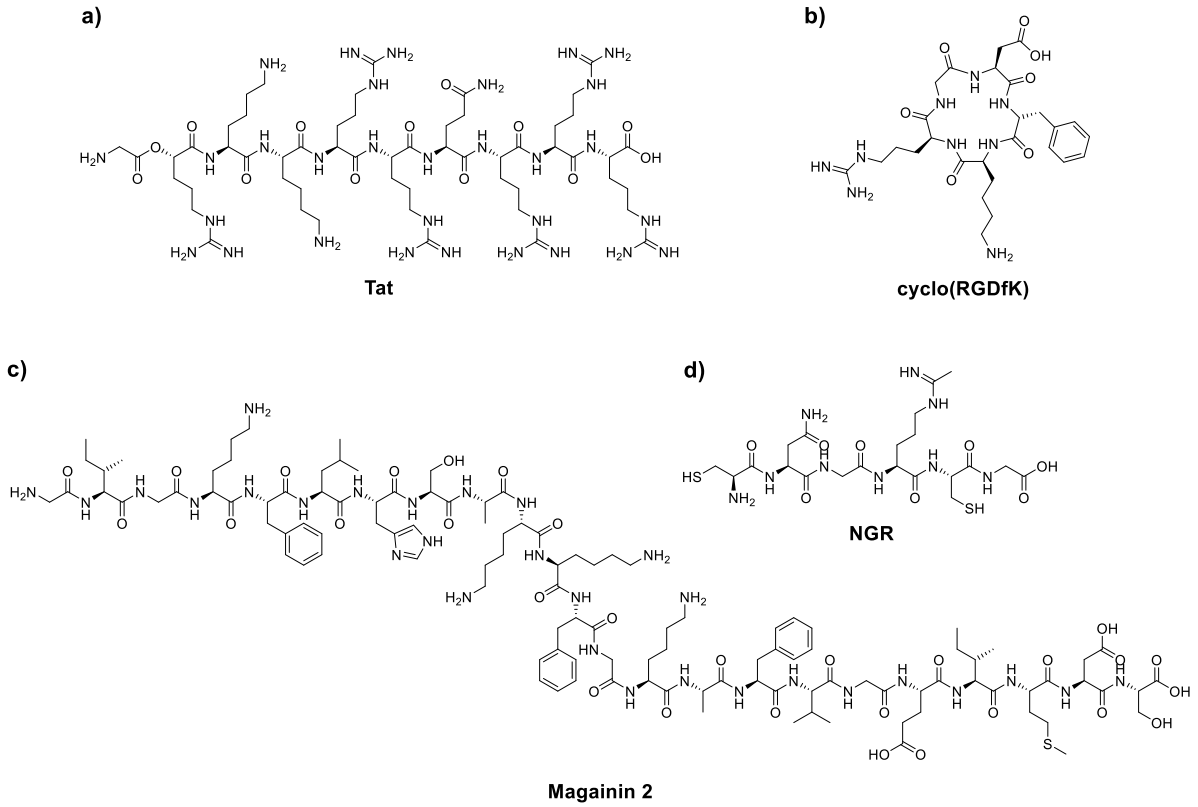

Figure 1.16. Examples of small-sized peptides in pre-clinical and clinical trials of therapeutic agents. **a)** Tat peptide for HIV therapeutic use; **b)** cyclo(RGDfK) peptide for anticancer therapy such as breast, ovarian and prostate; **c)** magainin 2 peptide for bladder anticancer agent and antimicrobial for diabetic ulcers; **d)** NGR anticancer therapy such as ovarian, lung and colon (figure adapted from Boohaker *et al.*[168]).

Another application of small-peptides is the use as carries for drug delivery of bioactive portion into the cells thanks to the affinity and recognition of receptors on cell surface[169-172]. Once the peptide is recognised by the cell receptors, it can go into the cells and releases the active drug which can kill the cancerous cell. Moreover, small-sized peptides have been studied as potential alternatives to synthetic drugs to anticancer treatment.

Anticancer peptides (ACPs) have shown some advantages such as low toxicity for healthy cells and tissues, efficacy, selectivity and specificity for cancerous cells[173]. Different anticancer peptides have been designed to interact with the cellular membrane, able to disrupt it[174] and penetrate inside the cell[175]. This peptide can interfere with necrotic and/or apoptotic mechanisms of the cancerous cells, leading to the cell death[175] (Figure 1.17).

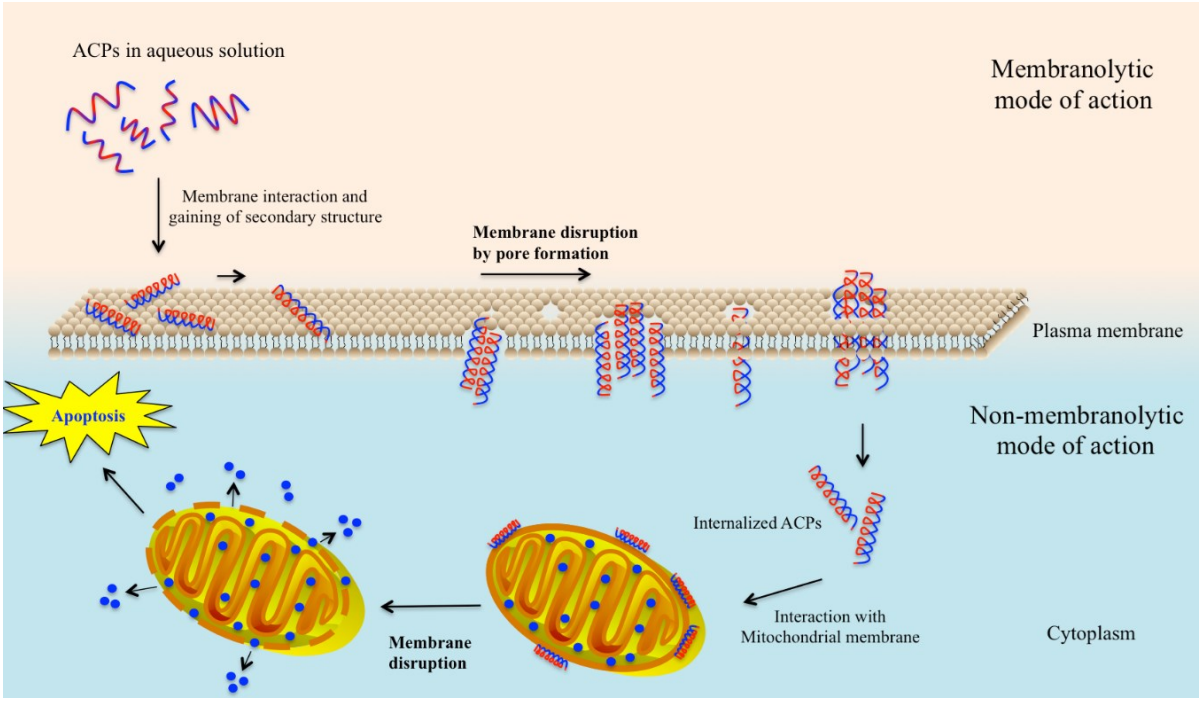

Figure 1.17. Proposed mechanism of action of anticancer peptides into cancerous cells (figure adapted from Tyagi *et al.*[176]).

Despite such characteristics, these peptides require an accurate and specific design to perform those processes. Another class of anticancer peptides has been developed to target specific markers placed on the cellular membrane which can be expressed or overexpressed by cancerous cells[164]. Such targeting-peptides present portion of the receptors of cancer cells which can be selectively recognised and show high affinity to receptors in only cancerous cells. These criteria in addition to retention in the target, rapid clearance from healthy tissues or cells and high stability *in vivo*[177] have made targeting-peptides ideal candidates for the design and synthesis of imaging probes for clinical use.

In recent years, targeting-peptides have been increasingly combined with different fluorescent scaffolds such as nanoparticles[178], fluorophores[179] and ligands for metals[180,181] to be detected through radionuclide-based and/or fluorescence imaging. The advantages of peptides anchored to such scaffolds have been inspired researchers to find novel targeting-imaging probes for cancer cells detection. In particular, multimodal imaging (*e.g.* PET/MRI and PET/CT) have become an important method to cancer detection thanks to the advantage to administrate a single contrast agent for different imaging modalities and signal consistency at the target region without a difference in biodistribution which could occur using two different contrast agents[182].

Several multimodal peptide-based imaging probes[182-185] have been reported in the last decades able to work in multimodal imaging for both *in vitro* and *in vivo* studies. For instance, ^{64}Cu has been the most common radioisotopes exploited in PET imaging for years thanks to its sufficiently long half-life and forms stable complexes with different ligands[186]. Such characteristics have been combined with various peptides to design and synthesise PET imaging probes able to target specific receptors such as gastrin-releasing peptide receptors and integrins[186].

Despite the advantages due to the use of peptides which make these imaging probes safer, the risk of radiations in the human body can persist. In addition, MRI and PET/CT can still lack specificity and sensitivity and moreover be invasive and expensive to patients. Moreover, PET/CT is mainly used to determine the stage and the spreading of cancer and the efficacy of the radiotherapy. On the other hand, fluorescence imaging methods have been considered promising alternatives to early-stage cancer detection thanks to some advantages such as non-invasiveness, real-time, high resolution and low-cost[179]. In addition, the range of wavelength of the near-infrared (NIR) (700-1000 nm) has increasingly become fundamental in fluorescence imaging due to low absorption and autofluorescence of cells and/or cells, deep penetration in cancerous tissues, non-invasiveness and sensitivity in image[179]. NIR fluorescence has been widely employed by clinicians to diagnose diseases, locate tumours and assist surgical procedures[230]. The ability of small-sized peptides to target specifically cancerous cells, the tuneable fluorescence property of the scaffolds where such peptides are attached and use NIR wavelength range have widely increased the number of published works on imaging probes for cancer detection.

1.5.1. Bombesin-related peptides as potential targeting groups for prostate cancer detection

Among small-sized peptides, the fragments 7-13 and 7-14 of bombesin peptide have become important targeting species for prostate cancer. Such fragments are part of the bombesin peptide family, a 14 *L*-amino acids chain, discovered in 1971 in the skin of the frog's species *Bombina bombina*[187-189]. Since its discovery, such peptide has particularly received interest in the biological research field because of mammals present bombesin receptors which are abnormally expressed and/or overexpressed in some malignancies[190].

Mammalian bombesin receptors are classified in 3 subtypes: neuromedin B (NMB), gastrin-releasing peptide (GRP) and bombesin receptor subtype 3 (BB3)[191]. Such subtypes of receptors are involved in specific physiological processes such as immune defence, thyroid and adrenocortical function, deglutition, weight regulation and cognition for NMB; on the other hand, GRP releases gastrointestinal hormones, secretes pancreatic and gastric fluids and smooths muscle contraction[192]. Gastrin-releasing peptide receptors (GRPR) have been discovered in a variety of solid tumours such as breast, colon lung and prostate. In prostate cancer, their expression rates are in the range between 63-100%[193] and moreover, they upregulate promoters of angiogenesis, essential for the metastasis of the cancerous cells[192]. In recent years, GRPRs have increasingly received a lot of interest for being targeted to treat and image prostate cancer. These receptors have shown a high affinity to two natural peptides. GRP consists of 27 amino acids, found in mammals, which is homologous to the amphibian bombesin (BBN) peptide, a 14 amino acids chain[193, 194]. Thanks to their high affinity to the GRPR, such peptides have become important targeting compounds for prostate cancer cells. In particular, bombesin shares the same amino acid sequence (Gln-Trp-Ala-Val-Gly-His-Leu-Met-NH_2) of the human GRP which has been found responsible for the high affinity to the receptors[195] (Figure 1.18).

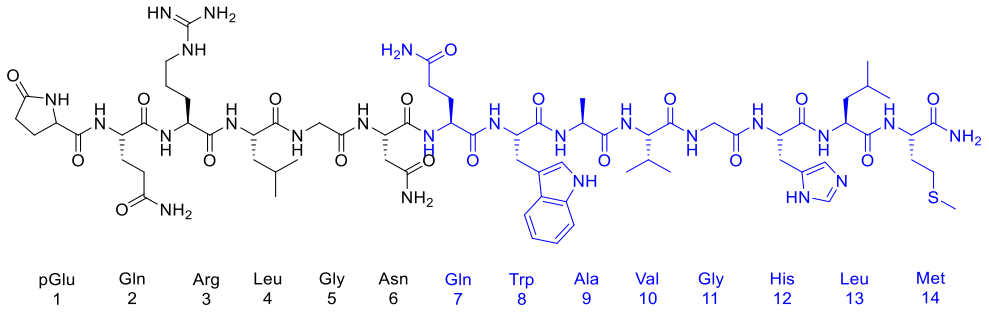

Figure 1.18. Structure of bombesin peptide with the fragment 7-14 highlighted in blue.

The affinity and binding of such sequence, called BBN [7-14], has been recently exploited in different works to design and synthesise targeting therapeutic and/or imaging agents for prostate cancer. In addition, the fragment 7-13 of the bombesin peptide has shown a similar affinity to the GRPR. In these regards, different imaging probes have recently been reported which uses the affinity of either the fragments [7-13] or [7-14] of the bombesin peptide thanks to their affinity to the GRPR. In addition, the emission of the radiations of the transition metal radioisotopes for PET/CT[194,198] and the magnetic characteristic of MRI[196,197] contrast agents have been exploited to design and synthesise several imaging probes.

Moreover, such combined radiolabelled targeting-peptide compounds have also been studied as therapeutic agents which can interfere with cellular growth in prostate cancer[199-201].

Considering the potential use of thiosemicarbazones as therapeutic and imaging agents, in the last decade, different research groups have explored the combination of TSC metal complexes and the fragments of bombesin for targeting specifically GRPR and able to exploit either therapy or imaging[122,195,202]. Recently, a copper-64 ATSM-derivative has been conjugated, through an aliphatic spacer, to the BBN [7-14] peptide to be evaluated as potential therapeutic agents to target specifically prostate cancer cells[231]. This compound showed a similar IC_{50} value in PC-3 cells compared to the BBN peptide alone.

As previously mentioned, radioactive compounds can be still considered a risk for the patients' health and moreover, imaging methods, such as PET and MRI, result expensive to patients, require sophisticated instruments and specialised staff. In the last decades, fluorescence methodologies have become important tools to investigate biological processes and detect cancerous cells thanks to their sensitivity, low-cost and ready-to-use equipment. Novel fluorescent imaging probes have been reported in the last 10 years which present the targeting unit of bombesin peptide to detect the GRPRs on the prostate cancer cells and image them in different fluorescent techniques[203-206]. These fragments of the bombesin peptide need to be anchored to a fluorescent scaffold to be detected by fluorescence methodologies because of such peptide are weakly fluorescent to be imaged accurately.

1.6. Aim of the PhD Thesis

The main aim of this Thesis is the design and synthesis of biosensing systems for prostate cancer detection *via* fluorescence imaging or electrochemical techniques.

The majority of the synthetic scaffolds explored in this work have in common the napthalenediimide (NDI) core which was used either as the fluorescent tag or as a synthon incorporated into the probe prototypes due to its capacity to form supramolecular interaction.

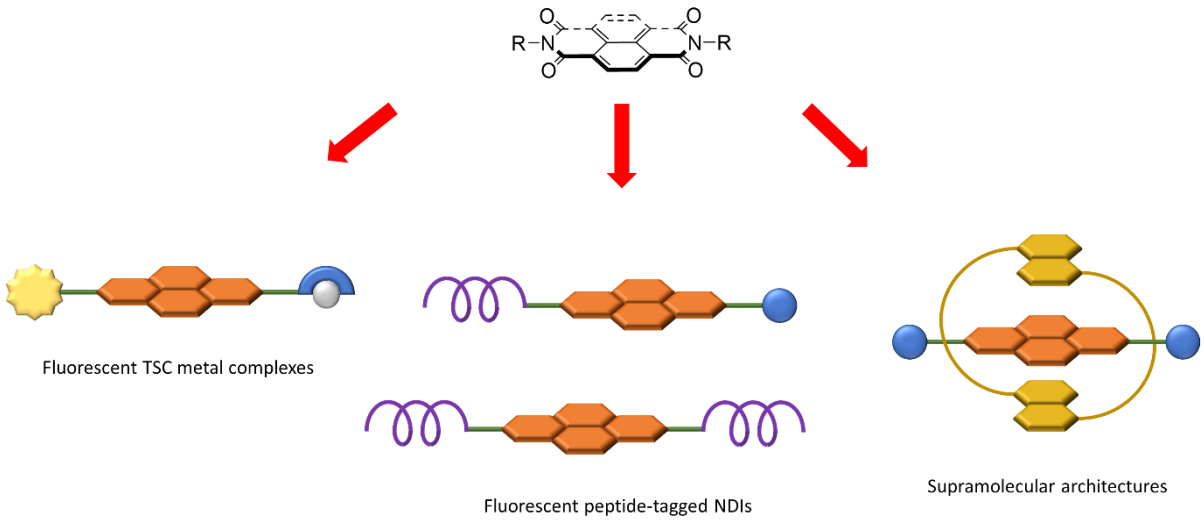

Figure 1.19. Schematic representation of the use of the naphthalenediimide core in this Thesis.

The Objectives of this Thesis are:

- To synthesise and characterise new thiosemicarbazone metal complexes anchored to the NDI scaffold to obtain imaging and therapeutic agents for prostate cancer.
- To evaluate the potential use of Cu-complex in hypoxic condition *via* fluorescence microscopies.
- The design and proof-of-concept testing onwards new *pseudo*rotaxanes for fluorescence imaging.
- To design and characterise novel peptide-tagged NDI conjugates.
- To evaluate the influence of stereochemistry and number of peptide units in their optical properties, cellular uptake and interactions *via* fluorescence microscopies.

1.7. References to Chapter 1

1. A. S. Daar, P. A. Singer, D. Leah Persad, S. K. Pramming, D. R. Matthews, R. Beaglehole, A. Bernstein, L. K. Borysiewicz, S. Colagiuri, N. Ganguly, R. I. Glass, D. T. Finegood, J. Koplan, E. G. Nabel, G. Sarna, N. Sarrafzadegan, R. Smith, D. Yach and J. Bell, *Nature*, 2007, **450**, 494-496.
2. A. Boutayeb, *Trans. R. Soc. Trop. Med. Hyg.*, 2006, **100**, 191-199.
3. C. M. Schooling and G. M. Leung, *J. Epidemiol. Community Health*, 2010, **64**, 941.
4. M. Di Cesare, Y.-H. Khang, P. Asaria, T. Blakely, M. J. Cowan, F. Farzadfar, R. Guerrero, N. Ikeda, C. Kyobutungi, K. P. Msyamboza, S. Oum, J. W. Lynch, M. G. Marmot and M. Ezzati, *The Lancet*, 2013, **381**, 585-597.
5. G. N. Nyaaba, K. Stronks, A. de-Graft Aikins, A. P. Kengne and C. Agyemang, *BMC Public Health*, 2017, **17**, 297.
6. World Health Organization, Non-communicable diseases: Russian roulette, http://cdn.static-economist.com/sites/default/files/images/2015/01/blogs/graphic-detail/20150131_gdm905.png (accessed on 23/01/2020).
7. A. Singh, S. Bassi, G. P. Nazar, K. Saluja, M. Park, S. Kinra and M. Arora, *BMC Public Health*, 2017, **17**, 292.
8. D. J. Hunter and K. S. Reddy, *N. Engl. J. Med.*, 2013, **369**, 1336-1343.
9. G. R. F. Collaborators, *The Lancet*, 2016, **388**, 1659-1724.
10. C. D. Parry, J. Patra and J. Rehm, *Addiction*, 2011, **106**, 1718-1724.
11. S. A. French, M. Story and R. W. Jeffery, *Annu. Rev. Public Health*, 2001, **22**, 309-335.
12. J. O. Hill and J. C. Peters, *Science*, 1998, **280**, 1371-1374.
13. World Health Organization, http://www.emro.who.int/noncommunicable-diseases/causes/index.html, (accessed 23/01/2020).
14. M. Daniel and T. O. Tollefsbol, *J. Exp. Biol.*, 2015, **218**, 59-70.
15. S. S. Hecht, S. G. Carmella, D. Kotandeniya, M. E. Pillsbury, M. Chen, B. W. S. Ransom, R. I. Vogel, E. Thompson, S. E. Murphy and D. K. Hatsukami, *Nicotine Tob. Res.*, 2014, **17**, 704-709.
16. V. Fedirko, I. Tramacere, V. Bagnardi, M. Rota, L. Scotti, F. Islami, E. Negri, K. Straif, I. Romieu, C. La Vecchia, P. Boffetta and M. Jenab, *Ann. Oncol.*, 2011, **22**, 1958-1972.
17. G. B. Faguet, *Int. J. Cancer*, 2015, **136**, 2022-2036.
18. R. B. Robey, *JAMA*, 2014, **311**, 202-203.
19. A. P. Feinberg, R. Ohlsson and S. Henikoff, *Nat. Rev. Genet.*, 2006, **7**, 21-33.
20. A. Birbrair, T. Zhang, Z.-M. Wang, M. L. Messi, J. D. Olson, A. Mintz and O. Delbono, *Am. J. Physiol., Cell Physiol.*, 2014, **307**, C25-C38.

21. W. A. Newman Dorland, *Dorland's illustrated medical dictionary*, W.B. Saunders, Philadelphia, PA, 2007.

22. C. Pucci, C. Martinelli and G. Ciofani, *Ecancermedicalscience*, 2019, **13**, 961-961.

23. M. Arruebo, N. Vilaboa, B. Sáez-Gutierrez, J. Lambea, A. Tres, M. Valladares and A. González-Fernández, *Cancers (Basel)*, 2011, **3**, 3279-3330.

24. G. M. Cooper, *The Cell: A Molecular Approach*, Sinauer Associates, Sunderland (MA), 2nd edn., 2000.

25. C. A. Klein, *Science*, 2008, **321**, 1785-1787.

26. A. C. Chiang and J. Massagué, *N. Engl. J. Med.*, 2008, **359**, 2814-2823.

27. Cancer Research UK, Cancer Statistics for the UK, http://www.cancerresearchuk.org/health-professional/cancer-statistics-for-the-uk, (accessed 23/01/2020).

28. P. Rawla, *World J. Onc.*, 2019, **10**, 63-89.

29. G. D. Steinberg, B. S. Carter, T. H. Beaty, B. Childs and P. C. Walsh, *Prostate*, 1990, **17**, 337-347.

30. E. M. Ledet, E. M. Ernst, J. Schiff, S. Li, B. E. Lewis and A. O. Sartor, *J. Clin. Oncol.*, 2017, **35**, e16548-e16548.

31. J. Schiff, E. M. Ledet, E. M. Ernst, C. E. Garvey, P. Cotogno and O. Sartor, *J. Clin. Oncol.*, 2017, **35**, 225-225.

32. S. F. Peisch, E. L. Van Blarigan, J. M. Chan, M. J. Stampfer and S. A. Kenfield, *World J. Urol.*, 2017, **35**, 867-874.

33. J. A. Lane, S. E. Oliver, P. N. Appleby, M. A. H. Lentjes, P. Emmett, D. Kuh, A. Stephen, E. J. Brunner, M. J. Shipley, F. C. Hamdy, D. E. Neal, J. L. Donovan, K. T. Khaw and T. J. Key, *Eur. J. Clin. Nutr.*, 2017, **71**, 274-283.

34. L. K. Dennis, C. F. Lynch and J. C. Torner, *Urology*, 2002, **60**, 78-83.

35. A. V. Sarma, J. C. McLaughlin, L. P. Wallner, R. L. Dunn, K. A. Cooney, D. Schottenfeld, J. E. Montie and J. T. Wei, *J. Urology*, 2006, **176**, 1108-1113.

36. T. J. Key, *Br. J. Cancer*, 2011, **104**, 6-11.

37. J. Petimar, K. M. Wilson, K. Wu, M. Wang, D. Albanes, P. A. van den Brandt, M. B. Cook, G. G. Giles, E. L. Giovannucci, G. G. Goodman, P. J. Goodman, N. Håkansson, K. Helzlsouer, T. J. Key, L. N. Kolonel, L. M. Liao, S. Männistö, M. L. McCullough, R. L. Milne, M. L. Neuhouser, Y. Park, E. A. Platz, E. Riboli, N. Sawada, J. M. Schenk, S. Tsugane, B. Verhage, Y. Wang, L. R. Wilkens, A. Wolk, R. G. Ziegler and S. A. Smith-Warner, *Cancer Epidemiol. Biomarkers Prev.*, 2017, **26**, 1276-1287.

38. A. Perez-Cornago, R. C. Travis, P. N. Appleby, K. K. Tsilidis, A. Tjønneland, A. Olsen, K. Overvad, V. Katzke, T. Kühn, A. Trichopoulou, E. Peppa, M. Kritikou, S. Sieri, D. Palli, C. Sacerdote, R. Tumino, H. B. Bueno-de-Mesquita, A. Agudo, N. Larrañaga, E. Molina-Portillo, E. Ardanaz, M.-D. Chirlaque, C. Lasheras, P. Stattin, M. Wennberg, I. Drake, J. Malm, J. A. Schmidt, K.-T. Khaw, M. Gunter, H. Freisling, I. Huybrechts, D. Aune, A. J. Cross, E. Riboli and T. J. Key, *Int. J. Cancer*, 2017, **141**, 287-297.

39. M. Taborelli, J. Polesel, M. Parpinel, C. Stocco, S. Birri, D. Serraino and A. Zucchetto, *Mol. Nutr. Food Res.*, 2017, **61**.

40. P. T. Scardino, W. M. Linehan, M. J. Zelefsky, N. J. Vogelzang, B. I. Rini, B. H. Bochner and J. Sheinfeld, *Comprehensive Textbook of Genitourinary Oncology*, Lippincott Williams & Wilkins, Fourth edition edn., 2005.

41. N. P. Papa, R. J. MacInnis, D. R. English, D. Bolton, I. D. Davis, N. Lawrentschuk, J. L. Millar, J. Pedersen, G. Severi, M. C. Southey, J. L. Hopper and G. G. Giles, *Urol. Oncol.: Seminars and Original Investigations*, 2017, **35**, 530e537-530e513.

42. R. Elancheran, V. L. Maruthanila, K. Mahesh, J. Jibon and S. Kabilan, *Urol. Res. Ther. J.*, 2017, **1**.

43. K. H. Leissner and L. E. Tisell, *Scand. J. Urol. Nephrol.*, 1979, **13**, 137-142.

44. J. Eastham, *Investig. Clin. Urol.*, 2017, **58**, 217-219.

45. A. H. Hou, D. Swanson and A. B. Barqawi, *Adv. Urology*, 2009, 1-12.

46. S. Sarkar and S. Das, *Biomed. Eng. Comput. Biol.*, 2016, **7**, 1-15.

47. P. A. Pinto, P. H. Chung, A. R. Ardeshir, A. A. Baccala, J. Kruecker, C. J. Benjamin, S. Xu, P. Yan, S. Kadoury, C. Chua, J. K. Locklin, B. Turkbey, J. H. Shih, S. P. Gates, C. Buckner, G. Bratslavsky, W. M. Linehan, N. D. Glossop, P. L. Choyke and B. J. Wood, *J. Urol.*, 2011, **186**, 1281-1285.

48. M. K. Terris and T. A. Stamey, *J. Urol.*, 1991, **145**, 984-987.

49. D. Theodorescu and B. Ehdaie, *Prostate Cancer, Clinical Oncology*, Springer Berlin Heidelberg, Berlin, Heidelberg, 2009.

50. S. Rais-Bahrami, M. M. Siddiqui, B. Turkbey, L. Stamatakis, J. Logan, A. N. Hoang, A. Walton-Diaz, S. Vourganti, H. Truong, J. Kruecker, M. J. Merino, B. Wood, J., P. L. Choyke and P. A. Pinto, *J. Urol.*, 2013, **190**, 1721-1727.

51. M. de Rooij, E. H. J. Hamoen, J. J. Fütterer, J. O. Barentsz and M. M. Rovers, *Am. J. Roentgenol.*, 2014, **202**, 343-351.

52. T. Maurer, M. Eiber, S. Fanti, L. Budäus and V. Panebianco, *Eur. Urol. Focus*, 2016, **2**, 139-150.

53. D. W. Townsend, *Semin. Ultrasound CT MR*, 2008, **29**, 232-235.

54. R. Vali, W. Loidl, C. Pirich, W. Langesteger and M. Beheshti, *Am. J. Nucl. Med. Mol. Imaging*, 2015, **5**, 96-108.

55. P. E. Kinahan and J. W. Fletcher, *Semin Ultrasound CT MR*, 2010, **31**, 496-505.

56. M. J. Barry, *N. Engl. J. Med.*, 2001, **344**, 1373-1377.

57. K. M. C. Verhamme, J. P. Dieleman, G. S. Bleumink, J. van der Lei and M. C. J. M. Sturkenboom, *Eur. Urol.*, 2002, **42**, 323-328.

58. O. Yavas, M. Svedendahl, P. Dobosz, V. Sanz and R. Quidant, *Nano Lett.*, 2017, **17**, 4421-4426.

59. L.-H. Pan, S.-H. Kuo, T.-Y. Lin, C.-W. Lin, P.-Y. Fang and H.-W. Yang, *Biosens. Bioelectron.*, 2017, **89**, 598-605.

60. M. Devillers, L. Ahmad, H. Korri-Youssoufi and L. Salmon, *Biosens. Bioelectron.*, 2017, **96**, 178-185.

61. S. Mittal, H. Kaur, N. Gautam and A. K. Mantha, *Biosens. Bioelectron.*, 2017, **88**, 217-231.

62. V. S. P. K. S. A. Jayanthi, A. B. Das and U. Saxena, *Biosens. Bioelectron.*, 2017, **91**, 15-23.

63. M. Pohanka and P. Skládal, *J. Appl. Biomed.*, 2008, **6**, 57-64.

64. J. L. Hammond, N. Formisano, P. Estrela, S. Carrara and J. Tkáč, *Essays Biochem.*, 2016, **60**, 69-80.

65. S. N. Topkaya, M. Azimzadeh and M. Ozsoz, *Electroanalysis*, 2016, **28**, 1402-1419.

66. Y. Zhu, H. Wang, L. Wang, J. Zhu and W. Jiang, *ACS Appl. Mater. Interfaces*, 2016, **8**, 2573-2581.

67. P. Jolly, N. Formisano and P. Estrela, *chempap*, 2015, **69**, 77.

68. Y. Leng, H.-P. Wei, Z.-P. Zhang, Y.-F. Zhou, J.-Y. Deng, Z.-Q. Cui, D. Men, X.-Y. You, Z.-N. Yu, M. Luo and X.-E. Zhang, *Angew. Chem., Int. Ed.*, 2010, **49**, 7243-7246.

69. S. Mehrabani, A. J. Maker and A. M. Armani, *Sensors*, 2014, **14**, 5890-5928.

70. S. Arya and S. Bhansali, *Biosens. J.*, 2012, **1**, 1-7.

71. K. J. Lee, N. Elgrishi, B. Kandemir and J. L. Dempsey, *Nat. Rev. Chem.*, 2017, **1**, 0039.

72. R. Raccichini, M. Amores and G. Hinds, *Batteries*, 2019, **5**.

73. L. M. Fischer, M. Tenje, A. R. Heiskanen, N. Masuda, J. Castillo, A. Bentien, J. Émneus, M. H. Jakobsen and A. Boisen, *Microelectron. Eng.*, 2009, **86**, 1282-1285.

74. G. Chornokur, S. K. Arya, C. Phelan, R. Tanner and S. Bhansali, *J. Sens.*, 2011, **2011**, 1-7.

75. M. S. Chiriacò, E. Primiceri, A. Montanaro, F. de Feo, L. Leone, R. Rinaldi and G. Maruccio, *Analyst*, 2013, **138**, 5404-5410.

76. D. Pihíková, Š. Belicky, P. Kasák, T. Bertok and J. Tkac, *Analyst*, 2016, **141**, 1044-1051.

77. C. Ibau, M. K. Md Arshad, S. C. B. Gopinath, M. Nuzaihan M.N, M. F. M. Fathil and P. Estrela, *Biosens. Bioelectron.*, 2019, **136**, 118-127.

78. N. J. Ronkainen, H. B. Halsall and W. R. Heineman, *Chem. Soc. Rev.*, 2010, **39**, 1747-1763.

79. P. Damborský, J. Švitel and J. Katrlík, *Essays Biochem.*, 2016, **60**, 91-100.

80. M. Al Kobaisi, S. V. Bhosale, K. Latham, A. M. Raynor and S. V. Bhosale, *Chem. Rev.*, 2016, **116**, 11685-11796.

81. C. Thalacker, C. Röger and F. Würthner, *J. Org. Chem.*, 2006, **71**, 8098-8105.

82. Z. Hu, R. L. Arrowsmith, J. A. Tyson, V. Mirabello, H. Ge, I. M. Eggleston, S. W. Botchway, G. Dan Pantos and S. I. Pascu, *Chem. Comm.*, 2015, **51**, 6901-6904.

83. K. Tambara, N. Ponnuswamy, G. Hennrich and G. D. Pantoş, *J. Org. Chem.*, 2011, **76**, 3338-3347.

84. P. Pengo, G. D. Pantoş, S. Otto and J. K. M. Sanders, *J. Org. Chem.*, 2006, **71**, 7063-7066.

85. L.-H. Hsu, S.-M. Hsu, F.-Y. Wu, Y.-H. Liu, S. R. Nelli, M.-Y. Yeh and H.-C. Lin, *RSC Advances*, 2015, **5**, 20410-20413.

86. M. B. Avinash and T. Govindaraju, *Adv. Mater.*, 2012, **24**, 3905-3922.

87. K. P. Nandre, S. V. Bhosale, K. V. S. Rama Krishna, A. Gupta and S. V. Bhosale, *Chem. Comm.*, 2013, **49**, 5444-5446.

88. Z. Hu, G. D. Pantoş, N. Kuganathan, R. L. Arrowsmith, R. M. J. Jacobs, G. Kociok-Köhn, J. O'Byrne, K. Jurkschat, P. Burgos, R. M. Tyrrell, S. W. Botchway, J. K. M. Sanders and S. I. Pascu, *Adv. Funct. Mater.*, 2012, **22**, 503-518.

89. J. A. Tyson, V. Mirabello, D. G. Calatayud, H. Ge, G. Kociok-Köhn, S. W. Botchway, G. Dan Pantoş and S. I. Pascu, *Adv. Funct. Mater.*, 2016, **26**, 5641-5657.

90. D. M. Răsădean, B. Sheng, J. Dash and G. D. Pantoş, *Chem. Eur. J.*, 2017, **23**, 8491-8499.

91. G. M. Prentice, L. Emmett, V. Luxami and G. D. Pantoş, in *Naphthalenediimide and its Congeners: From Molecules to Materials*, ed. G. D. Pantoş, The Royal Society of Chemistry, 2017, 1-36.

92. J.-M. Lehn, *Science*, 1985, **227**, 849-856.

93. E. Fischer, *Berichte der deutschen chemischen Gesellschaft*, 1894, **27**, 2985-2993.

94. T. Earmme, Y.-J. Hwang, N. M. Murari, S. Subramaniyan and S. A. Jenekhe, *J. Am. Chem. Soc.*, 2013, **135**, 14960-14963.

95. Y.-J. Hwang, T. Earmme, B. A. E. Courtright, F. N. Eberle and S. A. Jenekhe, *J. Am. Chem. Soc.*, 2015, **137**, 4424-4434.

96. X. Guo, F. S. Kim, M. J. Seger, S. A. Jenekhe and M. D. Watson, *Chem. Mater.*, 2012, **24**, 1434-1442.

97. Z. Yuan, Y. Ma, T. Geßner, M. Li, L. Chen, M. Eustachi, R. T. Weitz, C. Li and K. Müllen, *Org. Lett.*, 2016, **18**, 456-459.

98. L. Zong, Y. Song, Q. Li and Z. Li, *Sens. Actuators B Chem.*, 2016, **226**, 239-244.

99. R. P. Cox, H. F. Higginbotham, B. A. Graystone, S. Sandanayake, S. J. Langford and T. D. M. Bell, *Chem. Phys. Lett.*, 2012, **521**, 59-63.

100. J. F. Martinez, N. T. La Porte, C. M. Mauck and M. R. Wasielewski, *Faraday Discuss.*, 2017, **198**, 235-249.

101. V. Senkovskyy, R. Tkachov, H. Komber, M. Sommer, M. Heuken, B. Voit, W. T. S. Huck, V. Kataev, A. Petr and A. Kiriy, *J. Am. Chem. Soc.*, 2011, **133**, 19966-19970.

102. C. J. Bruns, J. Li, M. Frasconi, S. T. Schneebeli, J. Iehl, H.-P. Jacquot de Rouville, S. I. Stupp, G. A. Voth and J. F. Stoddart, *Angew. Chem., Int. Ed.*, 2014, **53**, 1953-1958.

103. K. E. Griffiths and J. F. Stoddart, *pac*, 2008, **80**, 485.

104. X.-S. Du, C.-Y. Wang, Q. Jia, R. Deng, H.-S. Tian, H.-Y. Zhang, K. Meguellati and Y.-W. Yang, *Chem. Comm.*, 2017, **53**, 5326-5329.

105. A. Brown, T. Lang, K. M. Mullen and P. D. Beer, *Org. Biomol. Chem.*, 2017, **15**, 4587-4594.

106. B. N. Ahamed, P. Van Velthem, K. Robeyns and C.-A. Fustin, *ACS Macro Lett.*, 2017, **6**, 468-472.

107. N. Zhu, K. Nakazono and T. Takata, *Chem. Lett.*, 2016, **45**, 445-447.

108. M. R. Wilson, J. Solà, A. Carlone, S. M. Goldup, N. Lebrasseur and D. A. Leigh, *Nature*, 2016, **534**, 235-240.

109. J. Shi, Y. Xu, X. Wang, L. Zhang, J. Zhu, T. Pang and X. Bao, *Org. Biomol. Chem.*, 2015, **13**, 7517-7529.

110. S. P. Vincent, K. Buffet, I. Nierengarten, A. Imberty and J.-F. Nierengarten, *Chem. Eur. J.*, 2016, **22**, 88-92.

111. A. Fernandes, A. Viterisi, F. Coutrot, S. Potok, D. A. Leigh, V. Aucagne and S. Papot, *Angew. Chem., Int. Ed.*, 2009, **48**, 6443-6447.

112. J. W. Fredy, J. Scelle, G. Ramniceanu, B.-T. Doan, C. S. Bonnet, É. Tóth, M. Ménand, M. Sollogoub, G. Vives and B. Hasenknopf, *Org. Lett.*, 2017, **19**, 1136-1139.

113. G. Yu, D. Wu, Y. Li, Z. Zhang, L. Shao, J. Zhou, Q. Hu, G. Tang and F. Huang, *Chem. Sci.*, 2016, **7**, 3017-3024.

114. J.-J. Lee, A. G. White, D. R. Rice and B. D. Smith, *Chem. Comm.*, 2013, **49**, 3016-3018.

115. M. Pan, X.-M. Lin, G.-B. Li and C.-Y. Su, *Coord. Chem. Rev.*, 2011, **255**, 1921-1936.

116. B. J. Slater, E. S. Davies, S. P. Argent, H. Nowell, W. Lewis, A. J. Blake and N. R. Champness, *Chem. Eur. J.*, 2011, **17**, 14746-14751.

117. S. I. Pascu, C. Naumann, G. Kaiser, A. D. Bond, J. K. M. Sanders and T. Jarrosson, *Dalton Trans.*, 2007, DOI: 10.1039/B706043B, 3874-3884.

118. D. G. Hamilton, J. E. Davies, L. Prodi and J. K. M. Sanders, *Chem. Eur. J.*, 1998, **4**, 608-620.

119. H.-P. Jacquot de Rouville, J. Iehl, C. J. Bruns, P. L. McGrier, M. Frasconi, A. A. Sarjeant and J. F. Stoddart, *Org. Lett.*, 2012, **14**, 5188-5191.

120. H. Yildirim, E. Guler, M. Yavuz, N. Ozturk, P. Kose Yaman, E. Subasi, E. Sahin and S. Timur, *Mater. Sci. Eng. C*, 2014, **44**, 1-8.

121. B. Seven, T. Demirdoven, H. Yildirim, D. O. Demirkol, E. Subasi, E. Sahin and S. Timur, *J. Macromol. Sci. A*, 2013, **50**, 392-398.

122. B. M. Paterson and P. S. Donnelly, *Chem. Soc. Rev.*, 2011, **40**, 3005-3018.

123. T. S. Lobana, R. Sharma, G. Bawa and S. Khanna, *Coord. Chem. Rev.*, 2009, **253**, 977-1055.

124. D. X. West, A. E. Liberta, S. B. Padhye, R. C. Chikate, P. B. Sonawane, A. S. Kumbhar and R. G. Yerande, *Coord. Chem. Rev.*, 1993, **123**, 49-71.

125. W. E. Antholine, J. M. Knight and D. H. Petering, *Inorg. Chem.*, 1977, **16**, 569-574.

126. D. X. West, A. A. Nassar, F. A. El-Saied and M. I. Ayad, *Transit. Met. Chem.*, 1999, **24**, 617-621.

127. A. Walcourt, M. Loyevsky, D. B. Lovejoy, V. R. Gordeuk and D. R. Richardson, *Int. J. Biochem. Cell Biol.*, 2004, **36**, 401-407.

128. A. H. Othman, K.-L. Lee, H.-K. Fun and B.-C. Yip, *Acta Cryst. C*, 1996, **52**, 602-605.

129. U. Abram, K. Ortner, R. Gust and K. Sommer, *J. Chem. Soc., Dalton Trans.*, 2000, DOI: 10.1039/A908712E, 735-744.

130. C. R. Kowol, R. Berger, R. Eichinger, A. Roller, M. A. Jakupec, P. P. Schmidt, V. B. Arion and B. K. Keppler, *J. Med. Chem.*, 2007, **50**, 1254-1265.

131. F. Basuli, S.-M. Peng and S. Bhattacharya, *Inorg. Chem.*, 1997, **36**, 5645-5647.

132. J. R. Dilworth and R. Hueting, *Inorganica Chim. Acta*, 2012, **389**, 3-15.

133. A. E. Stacy, D. Palanimuthu, P. V. Bernhardt, D. S. Kalinowski, P. J. Jansson and D. R. Richardson, *Journal of Medicinal Chemistry*, 2016, **59**, 4965-4984.

134. A. E. Stacy, D. Palanimuthu, P. V. Bernhardt, D. S. Kalinowski, P. J. Jansson and D. R. Richardson, *J. Med. Chem.*, 2016, **59**, 4965-4984.

135. G. Pelosi, F. Bisceglie, F. Bignami, P. Ronzi, P. Schiavone, M. C. Re, C. Casoli and E. Pilotti, *J. Med. Chem.*, 2010, **53**, 8765-8769.

136. A. Akbari, H. Ghateazadeh, R. Takjoo, B. Sadeghi-Nejad, M. Mehrvar and J. T. Mague, *J. Mol. Struct.*, 2019, **1181**, 287-294.

137. C. Balachandran, J. Haribabu, K. Jeyalakshmi, N. S. P. Bhuvanesh, R. Karvembu, N. Emi and S. Awale, *J. Inorg. Biochem.*, 2018, **182**, 208-221.

138. G. L. Semenza, *Oncogene*, 2010, **29**, 625-634.

139. X. Lu and Y. Kang, *Clin. Cancer Res.*, 2010, **16**, 5928.

140. G. L. Semenza, *Cancer Metastasis Rev.*, 2007, **26**, 223-224.

141. A. Sharma, J. F. Arambula, S. Koo, R. Kumar, H. Singh, J. L. Sessler and J. S. Kim, *Chem. Soc. Rev.*, 2019, **48**, 771-813.

142. Y. Xia, H.-K. Choi and K. Lee, *Eur. J. Med. Chem.*, 2012, **49**, 24-40.

143. W. R. Wilson and M. P. Hay, *Nat. Rev. Cancer*, 2011, **11**, 393-410.

144. D. Palanimuthu, S. V. Shinde, K. Somasundaram and A. G. Samuelson, *J. Med. Chem.*, 2013, **56**, 722-734.

145. A. P. King, H. A. Gellineau, J.-E. Ahn, S. N. MacMillan and J. J. Wilson, *Inorg. Chem.*, 2017, **56**, 6609-6623.

146. A. Challapalli, L. Carroll and E. O. Aboagye, *Clin. Transl. Imaging*, 2017, **5**, 225-253.

147. J. L. J. Dearling and P. J. Blower, *Chem. Comm.*, 1998, 2531-2532.

148. W. A. Volkert and T. J. Hoffman, *Chem. Rev.*, 1999, **99**, 2269-2292.

149. J. L. Dearling, J. S. Lewis, G. E. Mullen, M. J. Welch and P. J. Blower, *J. Biol. Inorg. Chem.*, 2002, **7**, 249-259.

150. A. L. Vāvere and J. S. Lewis, *Dalton Trans.*, 2007, 4893-4902.

151. I. S. Alam, R. L. Arrowsmith, F. Cortezon-Tamarit, F. Twyman, G. Kociok-Köhn, S. W. Botchway, J. R. Dilworth, L. Carroll, E. O. Aboagye and S. I. Pascu, *Dalton Trans.*, 2016, **45**, 144-155.

152. J. Chan, A. L. Thompson, M. W. Jones and J. M. Peach, *Inorganica Chim. Acta*, 2010, **363**, 1140-1149.

153. N. S. Al-Hokbany, B. Alotaibi, S. Bin Amer, S. M. Okarvi and I. Al-Jammaz, *J. Chem.*, 2014, **2014**, 6.

154. F. L. Thorp-Greenwood and M. P. Coogan, *Dalton Trans.*, 2011, **40**, 6129-6143.

155. F. Cortezon-Tamarit, S. Sarpaki, D. G. Calatayud, V. Mirabello and S. I. Pascu, *Chem. Rec.*, 2016, **16**, 1380-1397.

156. Y. Li, Z.-Y. Yang and J.-C. Wu, *Eur. J. Med. Chem.*, 2010, **45**, 5692-5701.

157. A. R. Cowley, J. Davis, J. R. Dilworth, P. S. Donnelly, R. Dobson, A. Nightingale, J. M. Peach, B. Shore, D. Kerr and L. Seymour, *Chem. Comm.*, 2005, DOI: 10.1039/B417206J, 845-847.

158. A. N. Kate, A. A. Kumbhar, A. A. Khan, P. V. Joshi and V. G. Puranik, *Bioconjugate Chem.*, 2014, **25**, 102-114.

159. R. L. Arrowsmith, P. A. Waghorn, M. W. Jones, A. Bauman, S. K. Brayshaw, Z. Hu, G. Kociok-Köhn, T. L. Mindt, R. M. Tyrrell, S. W. Botchway, J. R. Dilworth and S. I. Pascu, *Dalton Trans.*, 2011, **40**, 6238-6252.

160. D. Udhayakumari, S. Suganya and S. Velmathi, *J. Lumin.*, 2013, **141**, 48-52.

161. O. H. Aina, R. Liu, J. L. Sutcliffe, J. Marik, C.-X. Pan and K. S. Lam, *Mol. Pharm.*, 2007, **4**, 631-651.

162. A. M. Scott, J. D. Wolchok and L. J. Old, *Nat. Rev. Cancer*, 2012, **12**, 278-287.

163. X.-X. Zhang, H. S. Eden and X. Chen, *J. Control. Release*, 2012, **159**, 2-13.

164. S. Marqus, E. Pirogova and T. J. Piva, *J. Biomed. Sci.*, 2017, **24**, 21.

165. J. Thundimadathil, *J. Amino Acids*, 2012, **2012**, 13.

166. R. J. Boohaker, M. W. Lee, P. Vishnubhotla, J. L. M. Perez and A. R. Khaled, *Current Medicinal Chemistry*, 2012, **19**, 3794-3804.

167. J. L. Lau and M. K. Dunn, *Bioorg. Med. Chem.*, 2018, **26**, 2700-2707.

168. J. R. Boohaker, W. M. Lee, P. Vishnubhotla, L. M. J. Perez and R. A. Khaled, *Curr. Med. Chem.*, 2012, **19**, 3794-3804.

169. N. Svensen, J. G. A. Walton and M. Bradley, *Trends Pharmacol. Sci.*, 2012, **33**, 186-192.

170. Jitendra, P. K. Sharma, S. Bansal and A. Banik, *Indian J. Pharm. Sci.*, 2011, **73**, 367-375.

171. E. Ruoslahti, *Adv. Drug Deliv. Rev.*, 2017, **110-111**, 3-12.

172. S. A. Nasrollahi, C. Taghibiglou, E. Azizi and E. S. Farboud, *Chem. Biol. Drug Des.*, 2012, **80**, 639-646.

173. W. Chen, H. Ding, P. Feng, H. Lin and K.-C. Chou, *Oncotarget*, 2016, **7**, 16895-16909.

174. L. Wang, C. Dong, X. Li, W. Han and X. Su, *Oncol. Rep.*, 2017, **38**, 637-651.

175. D. Gaspar, A. S. Veiga and M. A. R. B. Castanho, *Front. Microbiol.*, 2013, **4**.

176. A. Tyagi, A. Tuknait, P. Anand, S. Gupta, M. Sharma, D. Mathur, A. Joshi, S. Singh, A. Gautam and G. P. S. Raghava, *Nucleic Acids Res.*, 2014, **43**, D837-D843.

177. S. Lee, J. Xie and X. Chen, *Biochemistry*, 2010, **49**, 1364-1376.

178. N. F. Steinmetz, A. L. Ablack, J. L. Hickey, J. Ablack, B. Manocha, J. S. Mymryk, L. G. Luyt and J. D. Lewis, *Small*, 2011, **7**, 1664-1672.

179. S. Luo, E. Zhang, Y. Su, T. Cheng and C. Shi, *Biomaterials*, 2011, **32**, 7127-7138.

180. M. Fani, H. R. Maecke and S. M. Okarvi, *Theranostics*, 2012, **2**, 481-501.

181. F. C. Gaertner, H. Kessler, H. J. Wester, M. Schwaiger and A. J. Beer, *Eur. J. Nucl. Med. Mol. Imaging*, 2012, **39**, 126-138.

182. J. Lee, T. S. Lee, J. Ryu, S. Hong, M. Kang, K. Im, J. H. Kang, S. M. Lim, S. Park and R. Song, *J. Nucl. Med.*, 2013, **54**, 96-103.

183. J. M. Kinsella, R. E. Jimenez, P. P. Karmali, A. M. Rush, V. R. Kotamraju, N. C. Gianneschi, E. Ruoslahti, D. Stupack and M. J. Sailor, *Angew. Chem., Int. Ed.*, 2011, **50**, 12308-12311.

184. I.-C. Sun, D.-K. Eun, H. Koo, C.-Y. Ko, H.-S. Kim, D. K. Yi, K. Choi, I. C. Kwon, K. Kim and C.-H. Ahn, *Angew. Chem., Int. Ed.*, 2011, **50**, 9348-9351.

185. J. Key, D. Dhawan, C. L. Cooper, D. W. Knapp, K. Kim, I. C. Kwon, K. Choi, K. Park, P. Decuzzi and J. F. Leary, *Int. J. Nanomedicine*, 2016, **11**, 4141-4155.

186. M. T. Ma and P. S. Donnelly, *Curr. Top. Med. Chem.*, 2011, **11**, 500-520.

187. A. Anastasi, V. Erspamer and M. Bucci, *Experientia*, 1971, **27**, 166-167.

188. E. Spindel, *Trends Neurosci.*, 1986, **9**, 130-133.

189. M. C. Lee, S. S. Schiffman and T. N. Pappas, *Neurosci. Biobehav. Rev.*, 1994, **18**, 313-323.

190. V. Sancho, A. Di Florio, T. W. Moody and R. T. Jensen, *Curr. Drug Deliv.*, 2011, **8**, 79-134.

191. D. Pooja, A. Gunukula, N. Gupta, D. J. Adams and H. Kulhari, *Int. J. Biochem. Cell Biol.*, 2019, **114**, 105567.

192. S. M. Elshafae, B. B. Hassan, W. Supsavhad, W. P. Dirksen, R. Y. Camiener, H. Ding, M. F. Tweedle and T. J. Rosol, *The Prostate*, 2016, **76**, 796-809.

193. M. Beer, M. Montani, J. Gerhardt, P. J. Wild, T. F. Hany, T. Hermanns, M. Müntener and G. Kristiansen, *The Prostate*, 2012, **72**, 318-325.

194. R. P. J. Schroeder, W. M. van Weerden, E. P. Krenning, C. H. Bangma, S. Berndsen, C. H. Grievink-de Ligt, H. C. Groen, S. Reneman, E. de Blois, W. A. P. Breeman and M. de Jong, *Eur. J. Nucl. Med. Mol. Imaging*, 2011, **38**, 1257-1266.

195. B. M. Paterson, J. A. Karas, D. B. Scanlon, J. M. White and P. S. Donnelly, *Inorg. Chem.*, 2010, **49**, 1884-1893.

196. A. Jafari, M. Salouti, S. F. Shayesteh, Z. Heidari, A. B. Rajabi, K. Boustani and A. Nahardani, *Nanotechnology*, 2015, **26**, 075101.

197. P. J. Koo, J. J. Kwak, S. Pokharel and P. L. Choyke, *Curr. Oncol. Rep.*, 2015, **17**, 56.

198. J. Inkster, K.-S. Lin, S. Ait-Mohand, S. Gosselin, F. Bénard, B. Guérin, M. Pourghiasian, T. Ruth, P. Schaffer and T. Storr, *Bioorg. Med. Chem. Lett.*, 2013, **23**, 3920-3926.

199. L. Cui, Z. Liu, X. Jin, B. Jia, F. Li and F. Wang, *Nucl. Med. Biol.*, 2013, **40**, 182-189.

200. P. Moreno, I. Ramos-Álvarez, T. W. Moody and R. T. Jensen, *Expert Opin. Ther. Targets*, 2016, **20**, 1055-1073.

201. C. Morgat, A. K. Mishra, R. Varshney, M. Allard, P. Fernandez and E. Hindié, *J. Nucl. Med.*, 2014, **55**, 1650-1657.

202. R. Hueting, M. Christlieb, J. R. Dilworth, E. G. Garayoa, V. Gouverneur, M. W. Jones, V. Maes, R. Schibli, X. Sun and D. A. Tourwé, *Dalton Trans.*, 2010, **39**, 3620-3632.

203. J.-C. Tseng, N. Narayanan, G. Ho, K. Groves, J. Delaney, B. Bao, J. Zhang, J. Morin, S. Kossodo, M. Rajopadhye and J. D. Peterson, *PLoS One*, 2017, **12**, e0182689.

204. A. Sturzu, S. Sheikh, H. Echner, T. Nägele, M. Deeg, B. Amin, C. Schwentner, M. Horger, U. Ernemann and S. Heckl, *Invest. New Drugs*, 2014, **32**, 37-46.

205. C.-M. Lee, H.-J. Jeong, S.-J. Cheong, E.-M. Kim, D. W. Kim, S. T. Lim and M.-H. Sohn, *Pharm. Res.*, 2010, **27**, 712-721.

206. A. Shrivastava, H. Ding, S. Kothandaraman, S.-H. Wang, L. Gong, M. Williams, K. Milum, S. Zhang and M. F. Tweedle, *Mol. Imaging Biol.*, 2014, **16**, 661-669.

207. G. Delso, E. ter Voert, P. Veit-Haibach, *Abdom. Imaging*, 2015, **40**, 1352-1357.

208. H. O'Neill, V. Malik, C. Johnston, J. V. Reynolds, J. O'Sullivan, *Pharmaceuticals (Basel)*, 2019, **12**, 16.

209. J. J. Morigi, P. D. Stricker, P. J. van Leeuwen, R. Tang, B. Ho, Q. Nguyen, G. Hruby, G. Fogarty, R. Jagavkar, A. Kneebone, A. Hickey, S. Fanti, L. Tarlinton, L. Emmett, *J. Nucl. Med.*, 2015, **56**, 1185-1190.

210. S. Ghose, A. Oliver, R. Martí, X. Lladó, J. C. Vilanovac, J. Freixenet, J. Mitraa, D. Sidibé, F. Meriaudeau, *Comput. Meth. Prog. Bio.*, 2012, **108**, 262-287.

211. R. Li, G. C. Ravizzini, M. A. Gorin, T. Maurer, M. Eiber, M. R. Cooperberg, M. Alemozzaffar, M. K. Tollefson, S. E. Delacroix, B. F. Chapin, *Prostate Cancer P. D.*, 2018, **21**, 4-21.

212. K. Bouchelouche, S. T. Tagawa, S. J. Goldsmith, B. Turkbey, J. Capala, P. Choyke, *Semin. Nucl. Med.*, 2011, **41**, 29-44.

213. F. Hu, Y. Huang, G. Zhang, R. Zhao, H. Yang, D. Zhang, *Anal. Chem.*, 2014, **86**, 7987-7995.

214. H. Fujioka, S. Uno, M. Kamiya, R. Kojima, K. Johnsson, Y. Urano, *Chem. Commun.*, 2020, **56**, 5617-5620.

215. L. Tian, H. Ma, B. Song, Z. Dai, X. Zheng, R. Zhang, K. Chen, J. Yuan, *Talanta*, 2012, **212**, 120760.

216. N. Kumari, S. Naqvi, M. Ahuja, K. Bhardwaj, R. Kumar, *J. Mater. Sci.: Mater. Electron.*, 2020, **31**, 4310-4322.

217. H. Y. Au-Yeung, G. D. Pantos- and J. K. M. Sanders, *J. Am. Chem. Soc.*, 2009, **131**, 16030–16032.

218. H. Y. Au-Yeung, G. D. Pantos- and J. K. M. Sanders, *J. Org. Chem.*, 2011, **76**, 1257–1268.

219. S. Aime, C, Cabella, S. Colombatto, S. Geninatti Crich, E. Gianolio, F. Maggioni, *J. Magn. Reson. Imaging*, 2002, **16**, 394-406.

220. C. R. Chitambar, W. E. Antholine, *Antioxid. Redox Sign.*, 2013, **1**, 956-972.

221. I. Velikyan, *Molecules*, 2015, **20**, 12913-12943.

222. A. Zhu, D. Lee, H. Shim, *Semin. Oncol.*, 2011, **38**, 55-69.

223. W. Hetta , G. Niazi, M. H. Abdelbary, *E. J. R. N. M.*, 2020, **51**, 1-8.

224. S. H. Emile, H. Elfeki, M. Shalaby, A. Sakr, P. Sileri, S. Laurberg, S. D. Wexner, *J. Surg. Oncol.*, 2017, **116**, 730-740.

225. J. Clais, J. Czernin, W. P. Fendler, D. Elashoff, N. G. Nickols, *BMC Cancer*, 2019, **19**, 1-11.

226. S. S. Chang, *Rev. Urol.*, 2004, **6**, S13-S18.

227. M. P. Yadav, S. Ballal, C. Bal, R. K. Sahoo, N. A. Damle, M. Tripathi, A. Seth, *Clin. Nucl. Med.*, 2020, **45**, 19-31.

228. H. Goldberg, *35th Annual EAU Congress*, 2020 Virtual Program #EAU20, July 17-19, 2020.

229. S. M. Schwarzenboeck, I. Rauscher, C. Bluemel, W. P. Fendler, S. P. Rowe, M. G. Pomper, A. Asfhar-Oromieh, K. Herrmann, M. Eiber, *J. Nucl. Med.*, 2017, **58**, 1545-1552.

230. G. Deng, S. Li, Z. Sun, W. Li, L. Zhou, J. Zhang, P. Gong, L. Cai, *Theranostics*, 2018, **8**, 4116-4128.

231. B. M. Paterson, P. S. Donnelly, *Chem. Soc. Rev.*, 2011, **40**, 3005-3018.

Chapter 2: Novel fluorescent metal complexes based on naphthalenediimide for prostate cancer imaging

2.1. Overview of Chapter 2

In this Chapter, the design, synthesis and characterisation of thiosemicarbazone (TSC) ligands and their metal complexes of Cu(II), Ni(II) and Zn(II) are presented. Such metal complexes are investigated by confocal microscopy to evaluate their interaction with living prostate cancer cells (PC-3) and other cell lines.

Thiosemicarbazones have found an important role in imaging and disease therapy thanks to their ease of synthesis and derivatisation. Their main characteristic relies on their N/S-donor's nature which adapts to the oxidation state and therefore coordination sphere of the complexed metal. Tridentate *mono*- and tetradentate *bis*-thiosemicarbazones (BTSC) represent the main class of chelating agents widely studied since 1950s[1].

Bis-thiosemicarbazones have been widely explored because of their cytotoxicity in different murine and human tumour cells[2,3], finding different applications in biological processes. Copper(II) complexes of TSCs have been studied in neurogenerative diseases, such as Alzheimer's, for their potential therapeutic applications[4]. [Cu(ATSM)] was one of the first TSC-based compounds to be used in clinical trials. [^{64}Cu][Cu(ATSM)] has been used as radiotherapeutic agent thanks to its effective, non-invasive and hypoxia-selectivity upon tumoral cells[5]. In fact, [Cu(ATSM)] and its radiolabeled version are neutral lipophilic molecules which can easily permeate the cell membrane and diffuse from the bloodstream to the cells[83]. Under hypoxia conditions, the copper(II) can be reduced in copper(I). In cancer cells, this phenomenon occurs in the abnormally reduced state of the mitochondria. The formed Cu(I) formed in hypoxic cells slowly dissociates from the ATSM ligand and remains irreversibly trapped[84] and bonded to Cu-bonded proteins[85]. Moreover, it has demonstrated that this compound can be used as a diagnostic marker for human cancers with imaging methods such as PET and SPECT[2,5,6].

Other metals have been complexed with different TSC derivatives for imaging and therapy purposes. In particular, zinc(II)-based complexes of TSCs have been demonstrated to be promising alternatives for imaging thanks to their fluorescent properties and cytotoxicity[7]. Furthermore, a recent study has shown that Zn(II), complexed with a TSC derivative, localises in the lysosomes and is able to trans-metallate with Cu to induce cytotoxicity[8].

This aromatic *mono*-TSCs ligands complexing Zn(II) was able to penetrate the cell membrane and lysosomes sequestrated the zinc(II) ions. Inside the lysosomes, the intralysosomal copper(II) ions were exchanged with zinc(II) which formed a redox-active complex with the TSC ligand. The formed copper TSC complex generated reactive oxygen species which led to cytotoxicity[8]. Besides, nickel(II) complexes of TSCs have found applications as therapeutic agents. Recent studies have demonstrated that TSC derivatives with Ni(II) able to show antiretroviral activity for HIV[9], antimicrobial activity[10] and induce apoptosis in different cell lines[11].

4,4-difluoro-4-bora-3a,4a-diaza-s-indacene (BODIPY) and its derivatives are well-known fluorophores and dyes widely employed for biological labelling[12]. Such fluorescent compounds have become popular thanks to their stability in biological conditions, compatibility in living cells and absorbing/emitting in a broad spectral range[13].
In recent years, BTSCs have been embedded with different BODIPY derivatives to evaluate their stability *in vitro*. In one of these studies[14], [Cu(ATSM)] was linked to a BODIPY derivative to increase the fluorescence emission of the molecule. Such fluorescent compound was studied *in vitro* by fluorescence lifetime imaging microscopy[15] to evaluate its stability and interaction with living cancer cells (HeLa).

The NDI-core is chosen as a scaffold to link proposed moieties because of its ease functionalisation, spectroscopic features[16,17], inertness, tunability for water solubility[18] and ability to form supramolecular aggregates[19].

Taking into account such considerations, novel fluorescent probes which include a BTSC-ligand, linked in one side of an NDI scaffold are reported. On the other side of the NDI core is covalently bonded to a derivative of the BODIPY fluorophore (*N*-(2-aminoethyl)-4-(5,5-difluoro-1,3,7,9-tetramethyl-5*H*-4λ^4,5λ^4-dipyrrolo[1,2-c:2',1'-f][1,3,2]diazaborinin-10-yl) benzamide) (Scheme 2.1). This compound was designed to present: *i*) an high efficiency of fluorescence emission due to the BODIPY derivative moiety; *ii*) incorporate a well-known ligand for copper(II) able to complex different metal ions; *iii*) exploit the supramolecular interactions which the NDI scaffold can create to form aggregates.
The ability of the chosen TSC ligand to complex different metals has been exploited to create a library of metal complexes such as Cu(II), Ni(II) and Zn(II). Such novel metal complexes will be explored by confocal laser-scanning and fluorescence lifetime imaging microscopies and evaluated by cytotoxicity assay for potential cancer therapy *in vitro*.

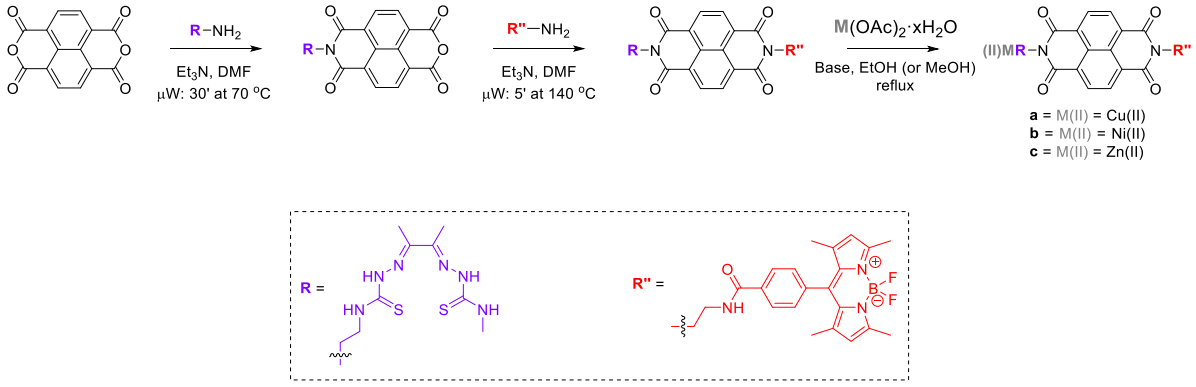

Scheme 2.1. Generic reaction scheme of the fluorescent ATSM-based metal complexes.

In Scheme 2.1, the naphthalene dianhydride (NDA) reacted with one equivalent of the desired amine under specific temperature and time in a microwave system. The control of the reaction temperature and time led to the *mono*-imide derivative. In the second step, the second amine was reacted with the *mono*-imide derivative which led to an asymmetric NDI derivative. In the first step, the selectivity of the formation of the *mono*-imide over a *bis*-derivative is due to the chemical nature of the chosen amine nucleophile[26]. Moreover, the overall control of the asymmetric formation of the NDI derivative is due to the specific temperature and time of the reaction, the stepwise process and the stoichiometric quantity of the used amines[26].

2.2. Synthesis and characterisation of BODIPY-tagged metal complexes based on thiosemicarbazone

The fluorescent TSC ligand, based on the NDI scaffold, is represented in Figure 2.1. This molecule presents a derivative of the well-known ATSM ligand and a BODIPY derivative (*N*-(2-aminoethyl)-4-(5,5-difluoro-1,3,7,9-tetramethyl-5*H*-4λ^4,5λ^4-dipyrrolo[1,2-c:2',1'-f][1,3,2] diazaborinin-10-yl)benzamide), covalently linked to the NDI platform. [Cu(ATSM)] has been studied in phase 1 of the clinical trial for neurodegenerative diseases[20], moreover, its ^{64}Cu version has found applications as radiotherapeutic treatment[5] and imaging agent for PET[6]. The choice of a derivative of BODIPY relies on its stability in biological conditions, compatibility in living cells and absorbing/emitting in a broad spectral range[13].

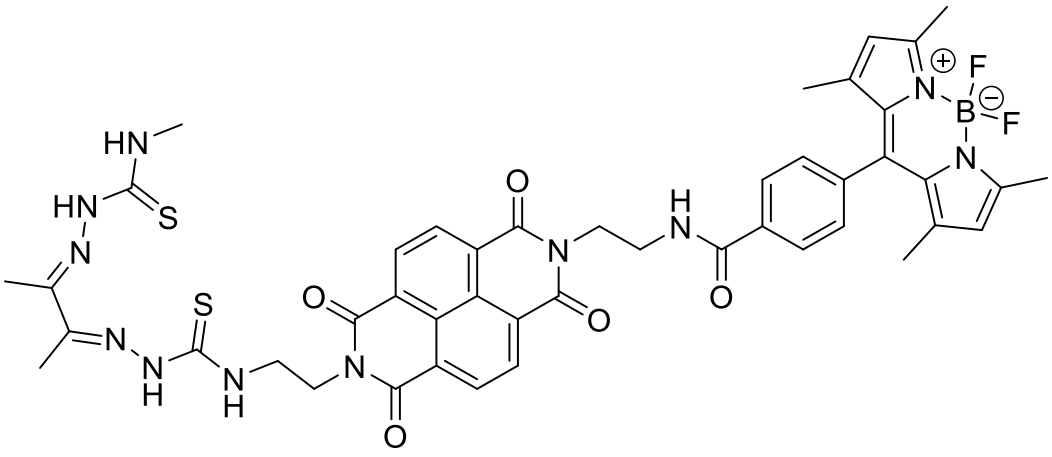

3

Figure 2.1. The structural representation of the desired of ligand **3**.

The chosen *bis*-(thiosemicarbazonate) (BTSC) is a derivative of diacetyl *bis*(*N*^{4}-methylthiosemicarbazonate) (ATSM), well-known ligand for copper(II) in this class of compounds. Such ligand has been also investigated with different divalent metal cations such as Ni(II)[21] and Zn(II)[22]. The proposed ATSM derivative is an asymmetric BTSC in which an ethylenediamino moiety is used as a linker to bond the NDI-core. The synthetic plan of ATSM derivative **1** involves the syntheses of two different moieties. The first unit is a thiosemicarbazide with an ethylenediamino chain, protected by *tert*-butiloxycarbonyl (BOC) (Scheme 2.2a); the second unit is a 2,3-butanedione backbone, derivatised with the thiosemicarbazide (Scheme 2.2b). The protocol was adapted from previous works[23-25] which synthetic scheme is fully reported in Scheme 2.2.

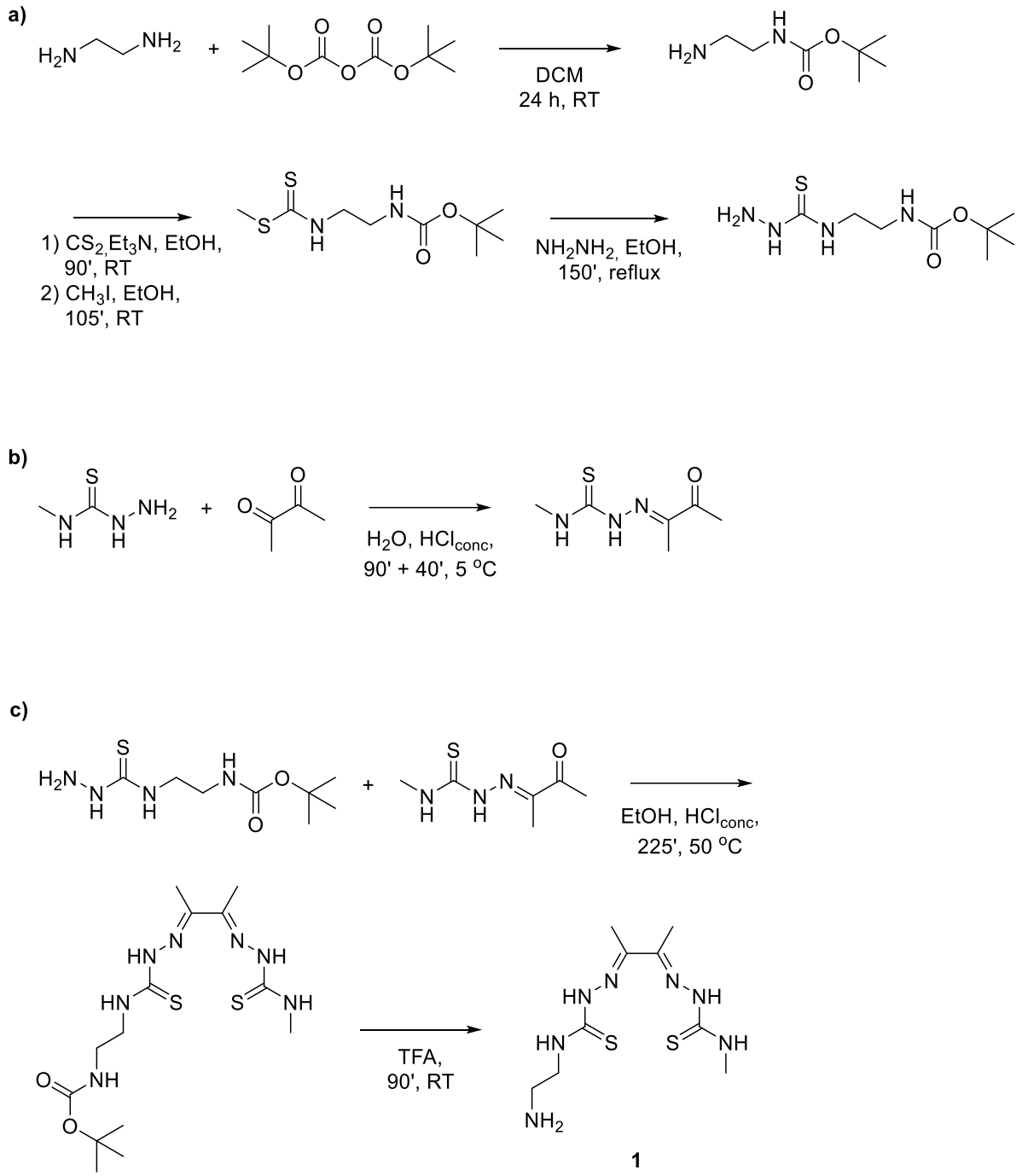

Scheme 2.2. Reaction scheme for the synthesis of compound 1. **a)** Synthetic path of the thiosemicarbazide with the diethylamino unit, protected by BOC; **b)** synthetic path of the 2,3-butanedione backbone; **c)** condensation of the asymmetric thiosemicarbazide units and deprotection step of the BTSC from the BOC protecting group.

The condensation of the two thiosemicarbazide units led to an asymmetric ATSM derivative, protected by BOC. The deprotection step was carried out in concentrated trifluoroacetic acid (Scheme 2.2c). Compound **1** was obtained as yellow solid by filtration and washings with deionised water and diethyl ether, without any further purification. The ^{1}H-NMR of ligand **1** as triflate salt is shown in Figure 2.2.

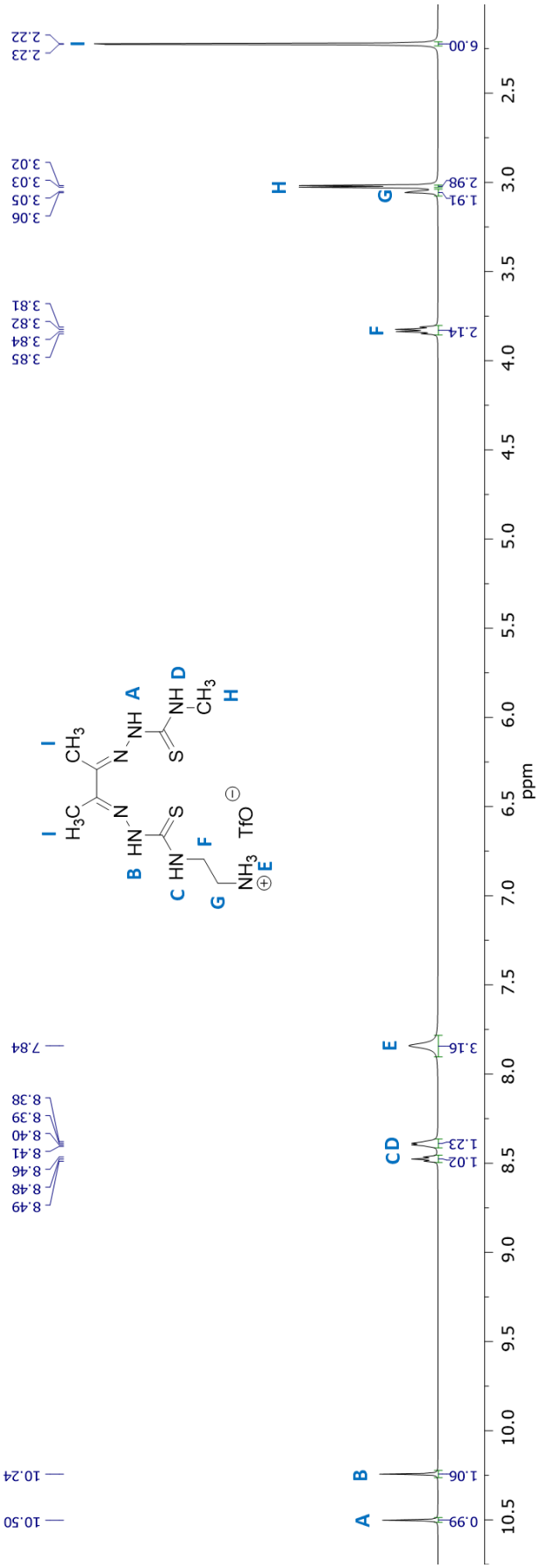

Figure 2.2. ^{1}H-NMR spectrum of triflate salt of compound **1** (DMSO-d_6, 500 MHz).

The asymmetric structure of ligand **1** is reflected on the splitting of signals of the two different units. The signals of the protons in the thiosemicarbazide derivatised with the ethylenediamino linker appeared at 10.24, 8.41, 3.83 and 3.05 (indicated by *B*, *D*, *F* and *G* respectively). The resonance of the ammonium salt protons was attributed to the broad singlet at 7.84 ppm (*E*) with an integration area of 3. The signals of the methyl-derivatised thiosemicarbazide moiety appear at 10.50, 8.46 and 3.03 ppm (*A*, *C* and *H* respectively). The *pseudo*-doublet at 2.22 ppm, integrating for 6 protons, was attributed to the methyl groups on the imine bridge.

The synthesis of compound **3** was carried out using a two-steps microwave reaction. Such a method has revealed a fast, efficient and high yield method to derivatise NDI-core, symmetrically and asymetrically[26]. Scheme 2.3 reports the synthetic approach, adapted from a previous work[26].

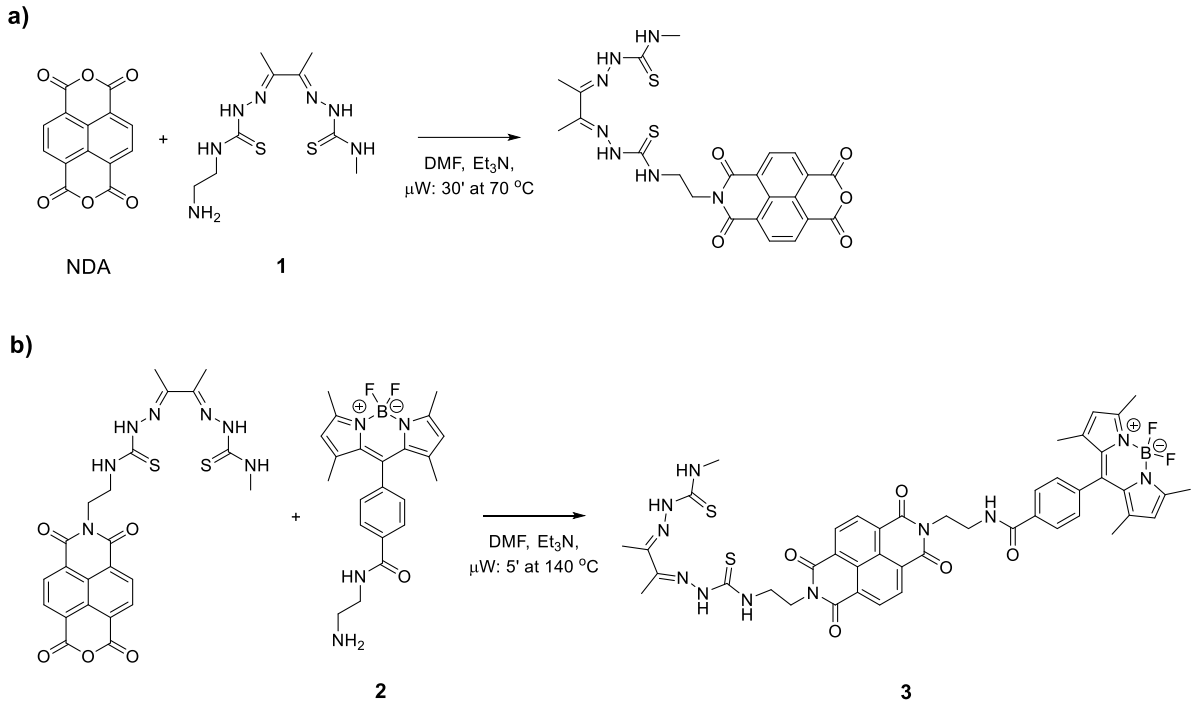

Scheme 2.3. Reaction scheme for the synthesis of compound **3**. **a)** Condensation of naphthalene dianhydride (NDA) with **1**; **b)** coupling between the ATSM/NDI intermediate with the BODIPY-derivative **2**.

The first step involved the formation of imide bond between the naphthalene dianhydride (NDA) and the ligand **1**. The mixture of the two compounds was dissolved in dimethylformamide and triethylamine, used as a basic catalyst, and then heated at 70 °C for 30 minutes (Scheme 2.3a). Under these conditions, less than one equivalent of the nucleophilic ATSM-derivative is added in the mixture of the NDA, DMF and triethylamine.

The excess of the NDA rather than the ATSM derivative determines the formation of a *mono*-ATSM intermediate[26]. The conditions were modified from Tambara *et al.*[26] which suggested to heat the reaction mixture at 75±5 ºC for 5 minutes when an alkylamine is used.The product obtained from the Tambara's suggested conditions did not lead to the desired compound. The product obtained from the modified conditions was a *mono*-ATSM derivative which was collected by filtration and analysed by ^{1}H-NMR (Figure A.2 in Appendices A).

The second step (Scheme 2.3b) involves the coupling of the previous intermediate with a BODIPY-derivative (**2**), synthesised according to the procedure of Iwaki *et al.*[27] and provided by Dr Cortezon-Tamarit. Such BODIPY derivative presents an ethylenediamino linker which was previously used by Waghorn *et al.*[14] to label a derivative of [Cu(ATSM)].

The mixture of the *mono*-ATSM/NDI intermediate and compound **2** was dissolved in dimethylformamide and triethylamine, used as a basic catalyst. The reaction mixture was heated at 140 ºC for 5 minutes, according to the work of Tambara *et al.*[26]. Compound **3** was obtained as dark red solid by removing the solvent under reduced pressure without any further purification. Figure 2.3 shows the mass spectrum of compound **3** with its chemical structure, chemical formula and exact mass.

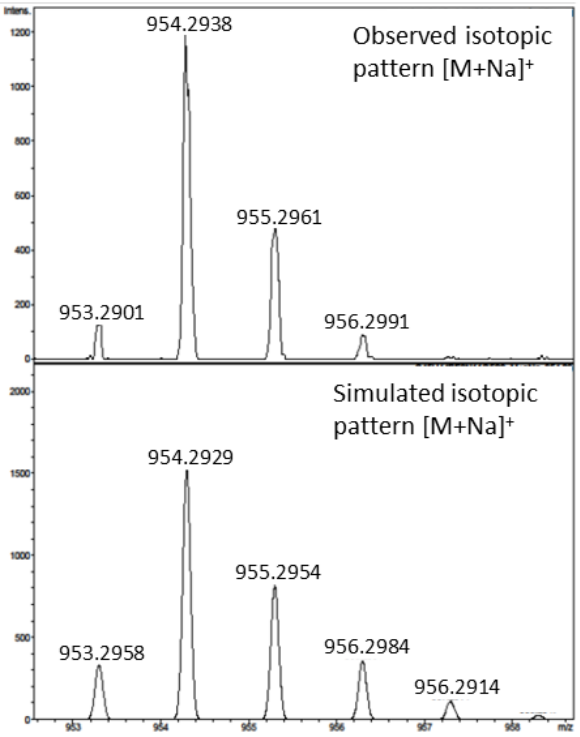

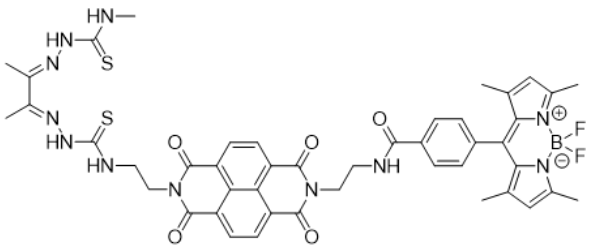

3

Chemical Formula: $C_{45}H_{44}BF_2N_{11}O_5S_2$
Exact mass: 931.3029

Figure 2.3. Isotopic patterns for $[M+Na]^+$ ion of compound **3**. Observed (top) and theoretical data (bottom) (ESI^+-TOF in MeOH).

The fluorescent ligand **3** was used to complex three different divalent transition metal cations. In particular, the chosen divalent cations are copper(II), nickel(II) and zinc(II). The TSC metal complexes of Cu(II) and its radioisotopes (^{60}Cu, ^{62}Cu, ^{64}Cu) has been studied for their potential therapeutic properties and their use as PET imaging agents[4]. Recently, different TSC ligands have been designed and synthesised to complex Ni(II) cation. Such Ni(II) complexes have shown antiretroviral activity for HIV[9], antimicrobial activity[10] and induced apoptosis in different cell lines[11]. The BTSC complexes of Zn(II) have been considered a valid alternative to their copper(II) counterparts thanks to their fluorescent properties[22], suitable for fluorescence microscopy imaging. In additions, some BTSC complexes with Zn(II) have shown low cytotoxicity[7] in a healthy cell line which has been considered good imaging probes.

Taking into account these considerations, ligand **3** was used to complex Cu(II), Ni(II) and Zn(II) as a proof-of-concept for novel fluorescent diagnostic and therapeutic agents. The synthetic protocol for the complexation by the ligand **3** of the three metal cations is reported in Scheme 2.4.

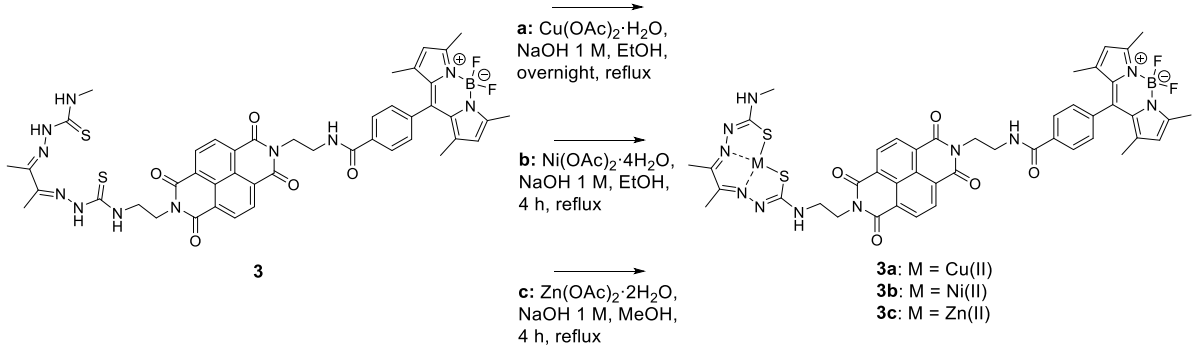

Scheme 2.4. Reaction scheme for the synthesis of the metal complexes **3a**, **3b** and **3c**.

The metal complexes of **3** with Cu(II) (**3a**), Ni(II) (**3b**) and Zn(II) (**3c**) were obtained from similar reaction conditions. The complexation step involves the dissolution of the hydrated acetate salts of the divalent cations in alcoholic solution, basified with sodium hydroxide. Ligand **3** was added after complete dissolution of the acetate salts. The reaction mixture was heated and left under reflux for the required time. The protocol was adapted from the synthesis of [Cu(ATSM)][28], [Ni(ATSM)][29] and [Zn(ATSM)][22], reported in the corresponding literature. These metal complexes were obtained hereby by analogous protocols followed in each case by simple filtrations and washings with deionised water and hexane. The obtained compounds were analysed by NMR, specifically, the Ni(II) complex **3b** was analysed by ^{1}H-NMR inasmuch it is paramagnetic and **3a** and **3c** were analysed by paramagnetic ^{1}H-NMR.

All three metal complexes were analysed by ^{19}F- and ^{11}B-NMR. However, the quantities obtained from the synthesis were not suitable for a clear analysis by those techniques. Mass spectrometry was considered a reasonable method to detect the presence of those metal complexes.

The mass spectra of compound **3a**, **3b** and **3c** are reported in Figure 2.4 with chemical structure, chemical formula and exact mass.

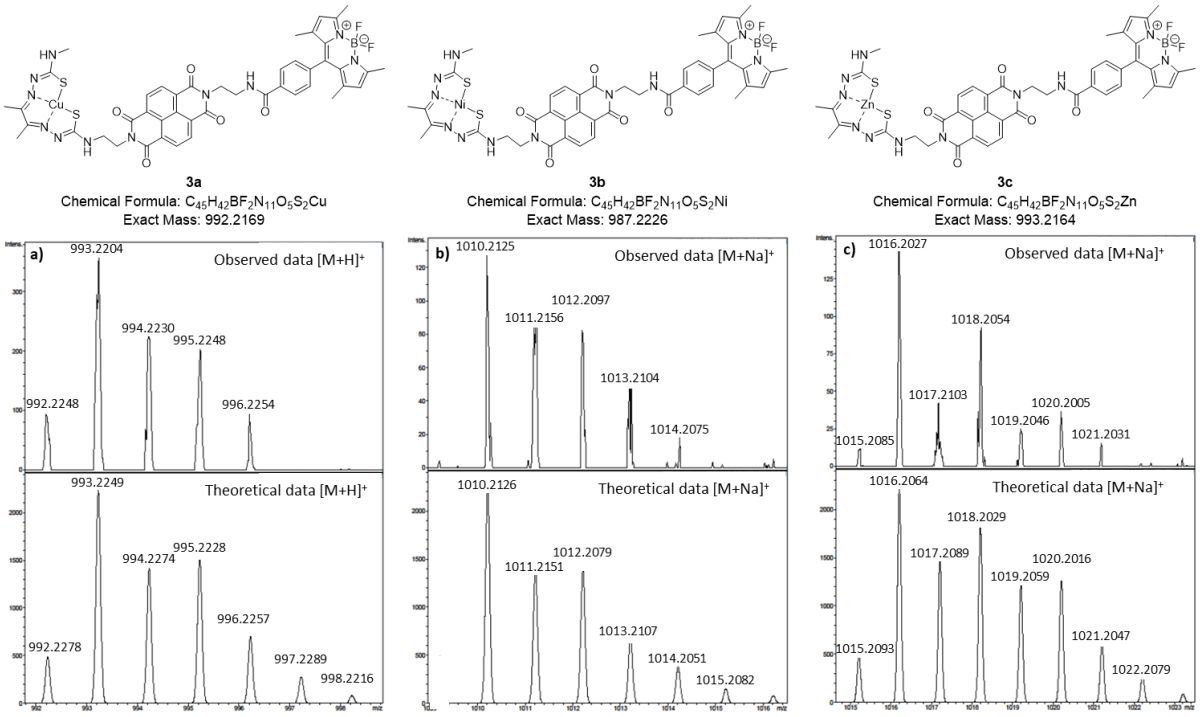

Figure 2.4. Isotopic patterns for **a)** $[M+H]^+$ ion of **3a**, **b)** $[M+Na]^+$ ion of **3b** and **c)** $[M+Na]^+$ ion of **3c**. Observed (top) and theoretical data (bottom) (ESI^+-TOF in MeOH).

In the following discussions, compounds **3a**, **3b** and **3c** will be compared with the ethylennediamino-ATSM metal complexes of Cu(II), Ni(II) and Zn(II) to evaluate their chemical properties and afterwards their different behaviour *in vitro*. Scheme 2.5 reports the synthetic conditions for **1a**[28], **1b**[29] and **1c**[22]. Figure 2.5 shows the mass spectrum of **1a** with the observed (a) and the theoretical data (b) of the $[M+H]^+$ adduct. The mass spectra of **1b** and **1c** can be found in Appendices A (Figure A.5).

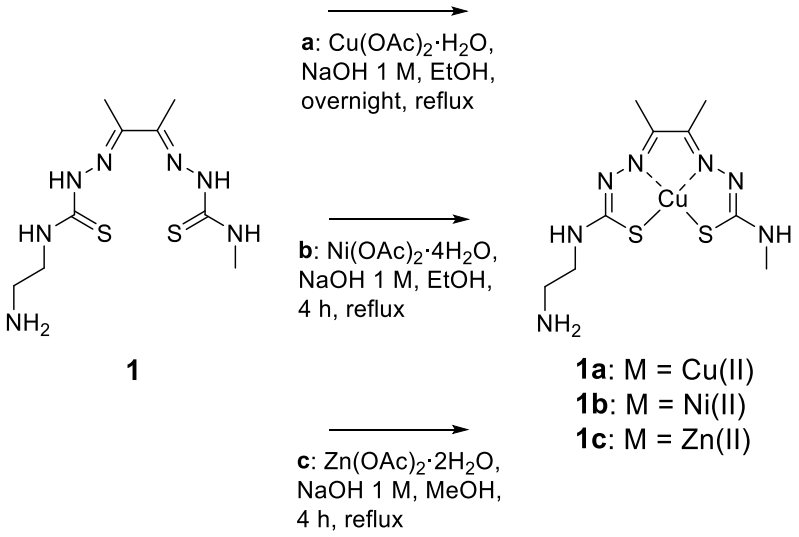

Scheme 2.5. Reaction scheme for the synthesis of ATSM-derivative metal complexes **1a**, **1b** and **1c**.

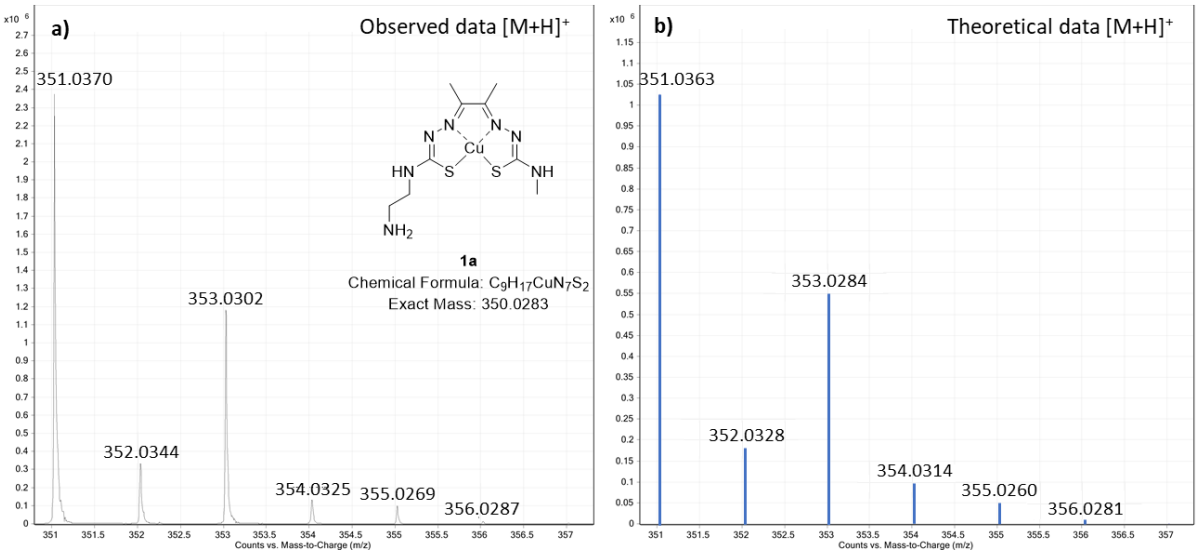

Figure 2.5. Observed (**a**) and theoretical (**b**) isotopic patterns for $[M+H]^+$ ion of compound **1a** (ESI^+-TOF in MeOH).

Compounds **3**, **3a**, **3b** and **3c** and their ATSM precursors **1**, **1a**, **1b** and **1c** were analysed by infrared spectroscopy. In Figure 2.6 and 2.7, the spectra of **1** *vs* **1a** and **3** *vs* **3a** are shown as an example with the main functional group bands highlighted. The IR spectra of **1b**, **1c**, **3b** and **3c** are shown in Appendices A (Figures A.12 and A.13 respectively).

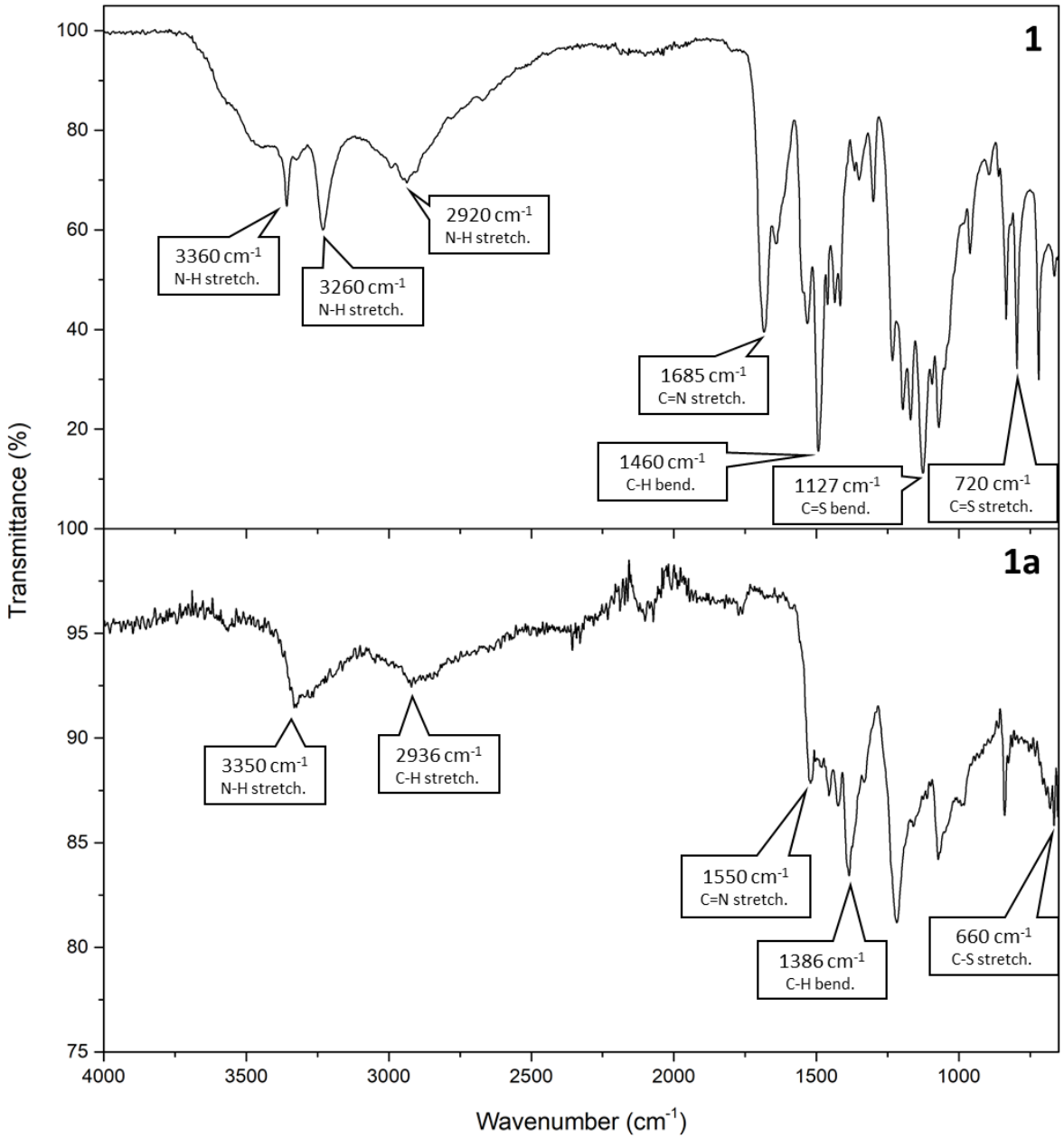

Figure 2.6. FT-IR spectra of compounds **1** (on the top) and **1a** (on the bottom) with the main functional group bands highlighted.

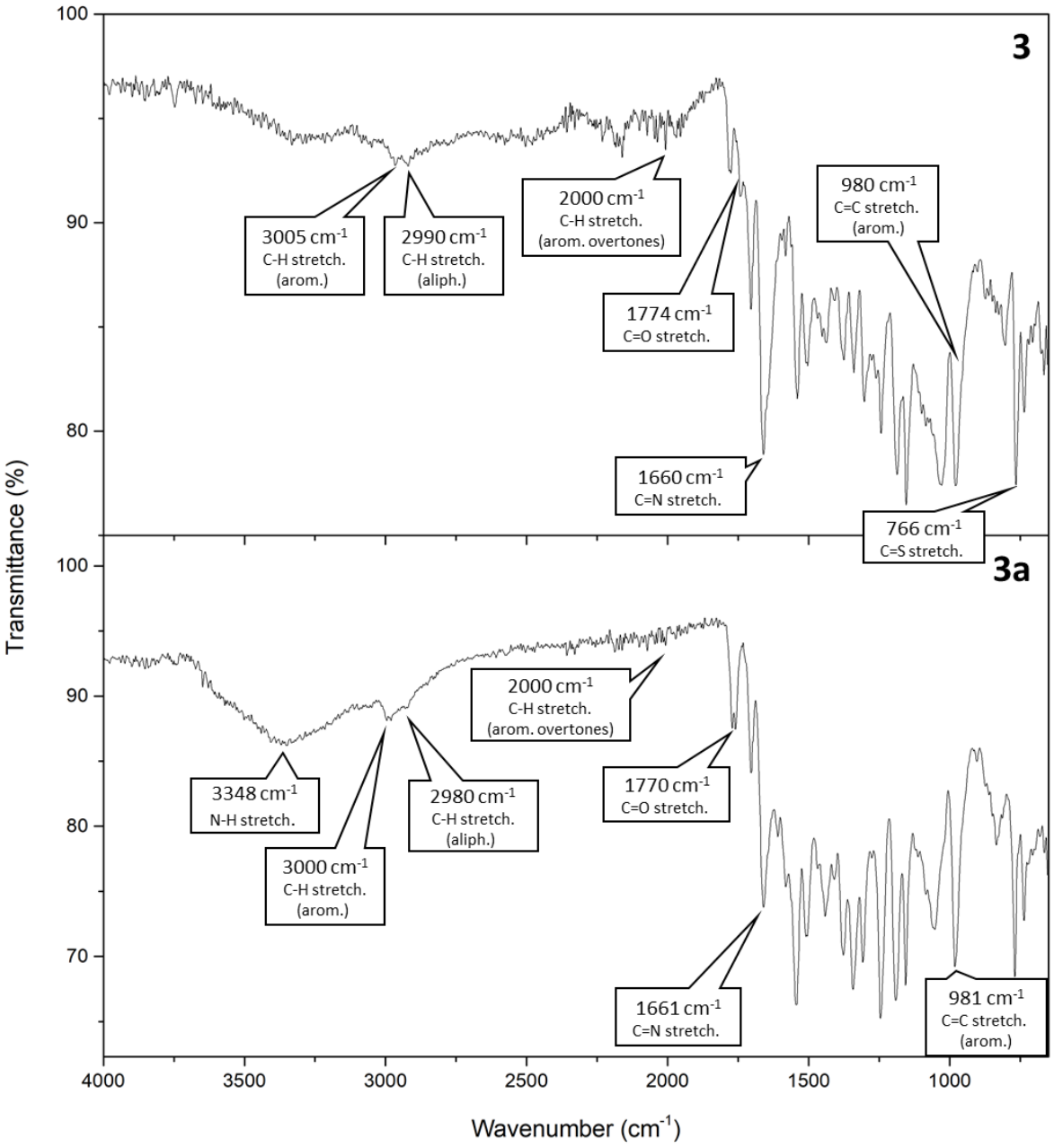

Figure 2.7. FT-IR spectra of compounds **3** (on the top) and **3a** (on the bottom) with the main functional group bands highlighted.

The spectrum of ligand **1** (Figure 2.6) shows the characteristic bands of the stretching of the primary amine N-H bonds at around 3360 cm^{-1} and the N-H stretching of the thiourea moieties at 3260 cm^{-1}. The aliphatic portions are confirmed by the bands at 2920 cm^{-1} (C-H stretching) and 1460 cm^{-1} (C-H bending). The diagnostic peaks of C=N stretching are at 1685 cm^{-1}, whilst the C=S stretching presents 2 bands at 1127 and 720 cm^{-1}.

The complexation of the metals in **1a**, **1b** and **1c** can be confirmed by the shift of the band of the C=N bond from 1685 cm^{-1} to around 1550 cm^{-1}. Moreover, a band at around 660 cm^{-1} appears which is due to the C-S stretching.

The IR spectra of the NDI-based ligand **3** (Figure 2.7) and its metal complexes **3a**, **3b** and **3c**, presents the characteristic bands of aromatic rings due to the presence of the NDI core and the BODIPY derivative. In particular, the aromatic C-H stretching bands are at around 3000 cm^{-1} with their overtone bands at around 2000 cm^{-1}. The aromatic C-H bending is confirmed by complex bands between 800 and 700 cm^{-1}. In addition, the aromatic C=C stretching can be noticed at around 980 cm^{-1}. The imide bond formed on the NDI-core is confirmed by the following bands: *i*) between 1770 and 1760 cm^{-1} due to the asymmetric and symmetric C=O stretching; *ii*) at around 1660 cm^{-1} due to the C=N stretching; *iii*) at 1550 cm^{-1} due to the C-N stretching. Unfortunately, the complexation with the metals could not be evaluated due to complex bands in the region of 1650-1600 cm^{-1}. The characteristics bands for the N-Metal and S-Metal[30] are situated below 600 cm^{-1} which could not be analysed under the conditions applied hereby.

The NDI-based metal complexes **3a**, **3b** and **3c** were analysed by cyclic voltammetry in 1 mM solution in methanol and compared with their ATSM-complexes **1a**, **1b** and **1c**. Besides, the acetate form of the divalent metal cations of Cu(II), Ni(II) and Zn(II) were used as referring thermodynamic data. Such analysis was used to evaluate the thermodynamic stability and study the redox processes undergoing on the different species, especially the redox parameters for the different metal ions. Table 2.1 summarises the average cathodic and anodic potentials (E_{pc} and E_{pa} respectively), the peak-to-peak separation potential ($\Delta E_p = E_{pa} - E_{pc}$) and formal reduction potential ($E_{1/2}$). The potentials are referred to the Ag/AgCl reference potential (scan rate 50 mV/sec). Complete cyclic voltammetry curves in Appendices A (Figure A.14).

Table 2.1. Summary of the cyclic voltammetry analysis (average E_{pc} and E_{pa} calculated after 10 cycles).

Molecule	**E_{pc}** (V)	**E_{pa}** (V)	**ΔE_p** (V)	**$E_{1/2}$** (V)
1a	0.43±0.02	1.17±0.04	0.74	0.80
1b	0.32±0.04	1.27±0.05	0.95	0.80
1c	0.24±0.02	1.44±0.01	1.20	0.94
3a	-0.14±0.01	1.10±0.01	1.24	0.48
3b	0.26±0.01	0.86±0.01	0.60	0.56
3c	0.05±0.03	0.83±0.01	0.78	0.44
$Cu(OAc)_2 \cdot H_2O$	0.62±0.01	1.72±0.03	1.10	1.17
$Ni(OAc)_2 \cdot 4H_2O$	0.03±0.01	0.95±0.01	0.92	0.49
$Zn(OAc)_2 \cdot 2H_2O$	0.01±0.01	0.96±0.01	0.95	0.49

The data obtained from the cyclic voltammetry analysis suggests that all the redox reactions of the analysed compounds are not reversible as their ΔE_p is greater than 59 mV[31] in this solvent system. Despite this fact, both the reduction and the oxidation reactions are favourable. In the ligands **1a**, **1b** and **1c**, the values of E_{pa} and E_{pc} are higher than the values for **3a**, **3b** and **3c** which could suggest that the metals in ligand **1** could be easily reduced or oxidised. The voltammograms of the species are shown in Figure A.11 in Appendices.

The values of E_{pc} in the acetate form of the metals are lower than the ones of the complexes ATSM metal complexes (**1a**, **1b** and **1c**) and the NDI- based metal complexes (**3a**, **3b** and **3c**) which could suggest that the metals in form of acetate do not easily undergo to reduction and/or oxidation. Comparing the $E_{1/2}$ values with literature data of [Cu(ATSM)] (-0.59 V[28,32]), [Ni(ATSM)] (-1.35 V[33]) and [Zn(ATSM)] (-1.10 V[34]), it can be noticed that the formal reduction potentials of **1a**, **1b**, **1c**, **3a**, **3b** and **3c** are positive which suggest the non-reversibility of the redox reactions. In addition, these species present formal reduction potentials that can suggest a lack of hypoxia selectivity, compared to the well-known [Cu(ATSM)][35,36].

2.2.1. Investigation *via* UV-visible and fluorescence spectroscopies in solution

The NDI-based complexes **3a**, **3b** and **3c** were investigated by UV-visible and fluorescence spectroscopies to assess their optical behaviour in solution. Such compounds were compared to their corresponding ATSM-complexes (**1a**, **1b** and **1c**) and the acetate form of the divalent metal ions, *i.e.* Cu(II), Ni(II) and Zn(II). Figures 2.8 and 2.9 show the normalised absorption spectra of the free ligands (a), the acetate salts of Cu(II), Ni(II) and Zn(II) (b), the ATSM complexes (c) and the NDI-based complexes (d).

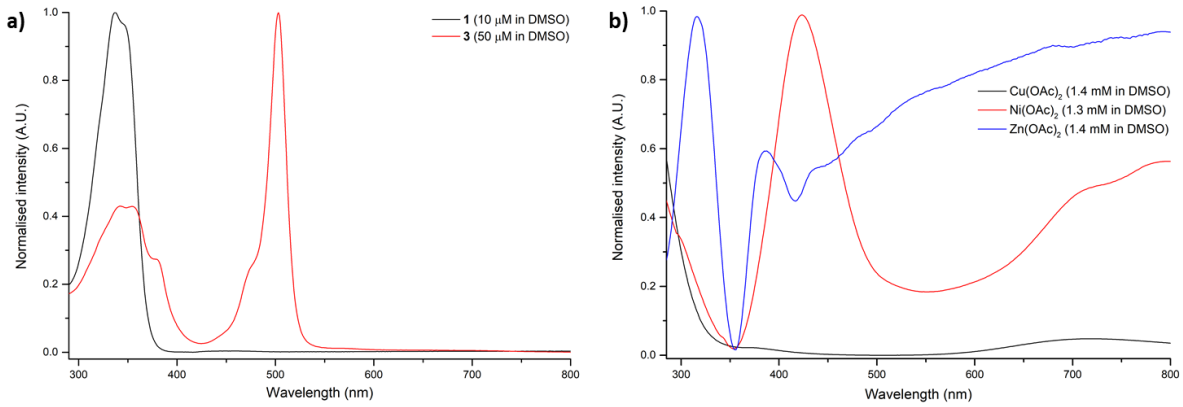

Figure 2.8. Comparative normalised UV-visible spectra. **a) 1** *vs* **3**; **b)** $Cu(OAc)_2$ *vs* $Ni(OAc)_2$ *vs* $Zn(OAc)_2$.

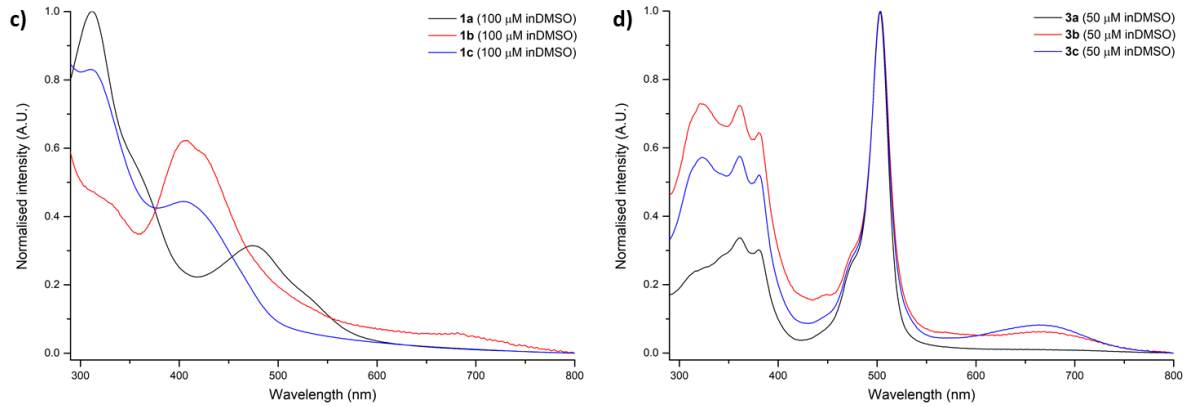

Figure 2.9. Comparative normalised UV-visible spectra. **c) 1a** *vs* **1b** *vs* **1c**; **d) 3a** *vs* **3b** *vs* **3c**.

The absorption maxima of **1** were found at 337 and 347 nm which can be associated with the n-π^* transition of the C=N and C=S functional groups of the molecule (Figure 2.8a in black line). On the other hand, compound **3** presented four characteristics absorption maxima: *i*) the peak at 342 nm, attributed to the ATSM portion of the molecule; *ii*) the two peaks at 355 and 380 nm are associated to the π- π^* transitions of the NDI-core[37,38]; *iii*) the main maximum at 503 nm is due to the π- π^* transitions of the BODIPY moiety[39] (Figure 2.8a in red line).

The spectra in Figure 2.8b show the absorption maxima of the acetate form of the divalent metals. The copper(II) acetate (black line) presented the two absorption maxima at 375 and 713 nm; the absorption maxima for the $Ni(OAc)_2$ (red line) were at 423, 709 and 793 nm, while $Zn(OAc)_2$ (blue line) showed a distinguishable peak at 385 nm.

The spectra of **1a**, **1b** and **1c** (Figure 2.9c) depicts the characteristic peak at 310 nm of the due to the electronic transitions of the ATSM moiety. Such absorption maxima are red-shifted than in the free ligand **1** due to the complexation of the corresponding metal cation. In addition, the *d-d* and ligand-to-metal transitions of the divalent ions can be noticed at 475 and 527 nm for Cu(II), at 408 and 685 nm for Ni(II) and 410 nm for Zn(II).

The NDI-based metal complexes **3a**, **3b** and **3c** in Figure 2.9d present the characteristic peaks of the ATSM unit (λ_{abs}≈320 nm), the NDI-core absorption maxima (λ_{abs}≈360 and 380 nm) and the BODIPY moiety (λ_{abs}≈500 nm).

The emission characteristics of **3**, **3a**, **3b** and **3c** were evaluated by fluorescence spectroscopy, using the excitation-emission matrix (EEM). The corresponding graph obtained by the excitation-emission matrix is a 3-dimensions plot of excitation wavelength *vs* emission wavelength *vs* intensity.

Such plots can qualitatively visualise the fluorescent profile of a given species and indicate similarity among a series of correlated compounds. Such EEM were compared to the fluorescence EEM of the precursor-like compounds **2** and **11**, discussed in details in Chapter 4. Figure 2.11 shows the EEM graphs of **2**, **11**, **3**, **3a**, **3b** and **3c** with normalised intensities.

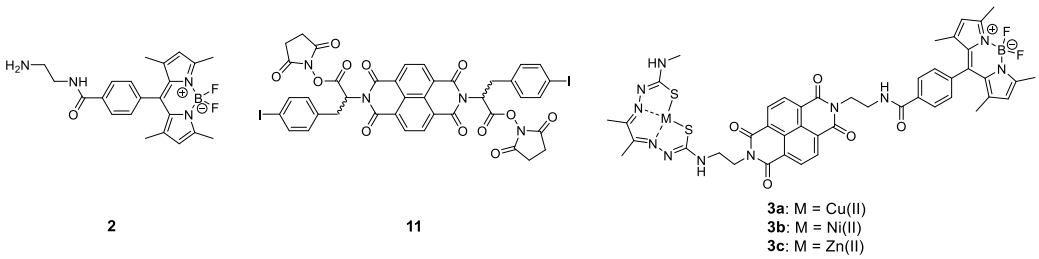

Figure 2.10. Structure of compounds **2**, **11** and the series of metal complexes **3a**, **3b** and **3c**.

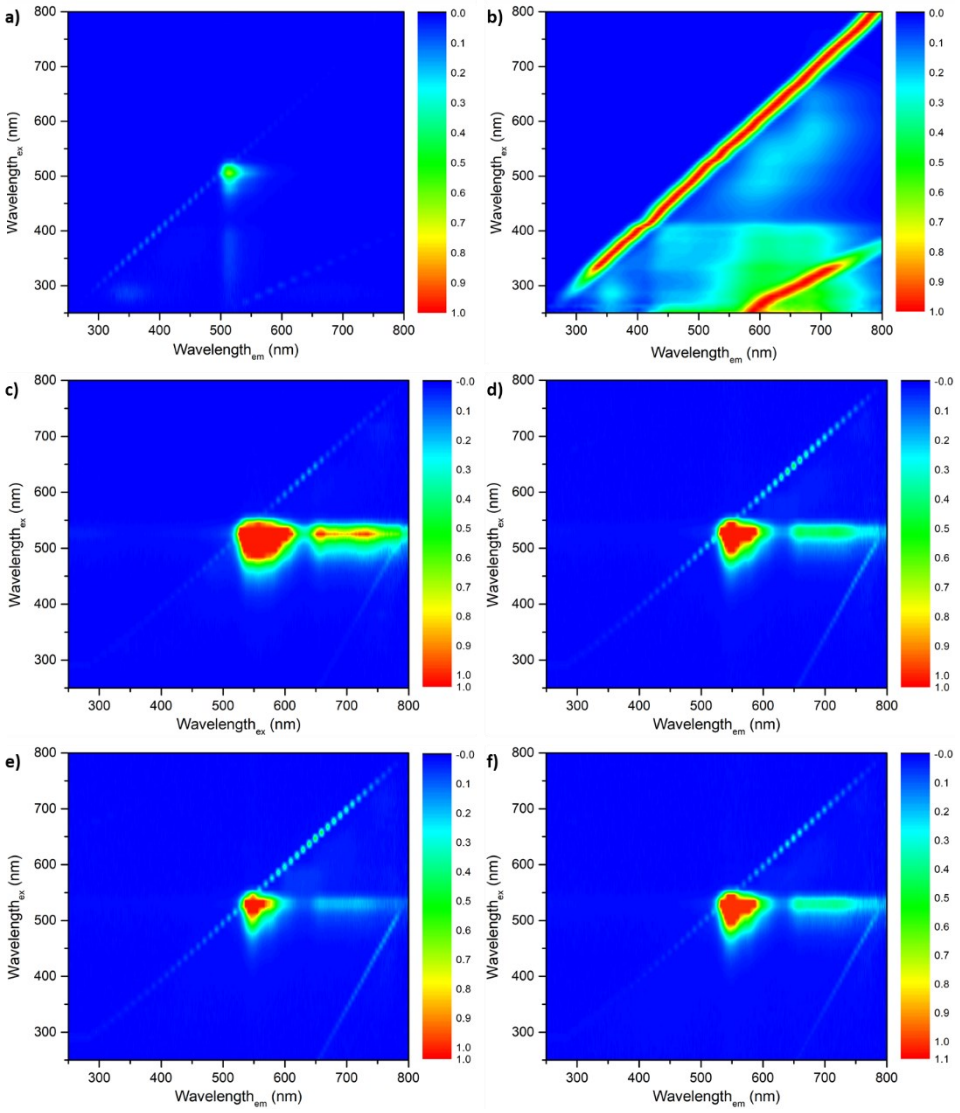

Figure 2.11. Normalised excitation-emission matrix maps of **a) 2**, **b) 11**, **c) 3**, **d) 3a**, **e) 3b** and **f) 3c**. (50 µM solutions in DMSO).

The EEM maps of **3**, **3a**, **3b** and **3c** showed two main emission regions, appearing when the species were excited between 450 and 550 nm. The first region (between 500 and 600 nm) can be attributed to the fluorescence emission of the portion of the molecules with the BODIPY derivative **2**[40] (Figure 2.11a). The second region (between 650 and 800 nm) can be also attributed to the BODIPY moiety[40]. The fluorescence emissions of ligand **3** and its metal complexes **3a**, **3b** and **3c** present intense regions compared to the fluorophore **2**. In addition, the quantum yield of the proposed fluorescent probes is higher than compound **2** (Table 2.2). Comparing the compounds **3**, **3a**, **3b** and **3c** with an NDI-derivative (**11**), the weak fluorescence emission in the region between 400 and 500 nm can not be discriminated in the EEM of **3**, **3a**, **3b** and **3c**. Recently, an aromatic copper(II) bis-thiosemicarbazone[86] has been designed and synthesised to monitor the cellular uptake of Cu(II) and he showed a quantum yield of 0.04 which is 8.5 times lower than the quantum yield found in compound **3a** (Table 2.2). Cowley *et al.*[87] reported a fluorescent Zn(II) *bis*-thiosemicarbazone which had a lower quantum yield (0.02) than the one calculated from compound **3c** presented hereby (Table 2.2).

Such comparisons with existing fluorescent BTSCs metal complexes, the well-known BODIPY derivatives and the NDI-based compounds may indicate that the proposed compounds hereby can be useful for the development of fluorescent probes for *in vitro* imaging.Besides, the emission ranges are close to the near-infrared region (650-1350 nm) of the spectrum of the light which can be particularly useful for imaging purposes due to the deep penetrability and non-invasiveness in cells and tissues[41].

Table 2.2 reports the molar extinction coefficients (ε) and quantum yields (Φ) of the fluorescent NDI-based metal complexes **3a**, **3b** and **3c**. The ε is calculated from Beer's law:

$$A = \varepsilon \cdot c \cdot l$$

where A is the maximum absorbance at its corresponding wavelength, c is the concentration in molarity and l is the path length in cm. On the other hand, the Φ_x is calculated as follow, according to literature[42]:

$$\Phi_x = \Phi_S \cdot \frac{A_S}{A_x} \cdot \frac{E_x}{E_S} \cdot \frac{I_S}{I_x} \cdot \frac{{n_x}^2}{{n_S}^2}$$

where Φ_S is the quantum yield of the standard, A is the absorbance of the solution, E is the corrected emission intensity, I is the relative intensity of the exciting light and n is the average refractive index of the solution.

Table 2.2. Summary table of ε and Φ, referred to fluorescein 2.3 nM in 0.1 M $NaOH_{(aq)}$ (Φ=0.95±0.03; λ_{ex}=496 nm; η=1.33)[43].

Molecule (50 μM DMSO)	ε_{max} ($\cdot 10^3$ L mol^{-1} cm^{-1}) (λ_{max}=503 nm)	**Φ**
2	849.9	0.02
3	119.0	0.82
3a	40.0	0.34
3b	13.0	0.19
3c	30.0	0.31

The values of ε and Φ of the metal complexes **3a**, **3b** and **3c** are lower than the values of the free ligand **3**. This phenomenon suggests that the presence of the divalent cations in the species can affect the absorption and emission properties of the entire molecule.

2.2.2. Preliminary investigation *via* fluorescence microscopies in living cancer cells

The fluorescent NDI-based metal complexes were preliminarily studied, using confocal laser-scanning microscopy (CLSM) in prostate cancer cells (PC-3 cell line) to study their localisation and their emission properties in living cells. Moreover, they were compared with their ATSM metal complexes. The compounds were incubated for 20 minutes in PC-3 cells at 37 °C and then studied by confocal laser-scanning microscopy. Such species were excited with a wavelength of 488 nm and their fluorescence emissions were recorded in the green channel (emission wavelength range between 500 and 550 nm).

Figure 2.12 shows the micrographs of the ATSM metal complexes **1** (a_1-b_1), **1a** (a_2, b_2), **1b** (a_3-b_3) and **1c** (a_4-b_4); on the right, the micrographs of **3** (a'_1-b'_1), **3a** (a'_2-b'_2), **3b** (a'_3-b'_3) and **3c** (a'_4-b'_4). Complete confocal laser-scanning microscopy micrographs are shown in Appendices A (from Figure A.16 to A.23).

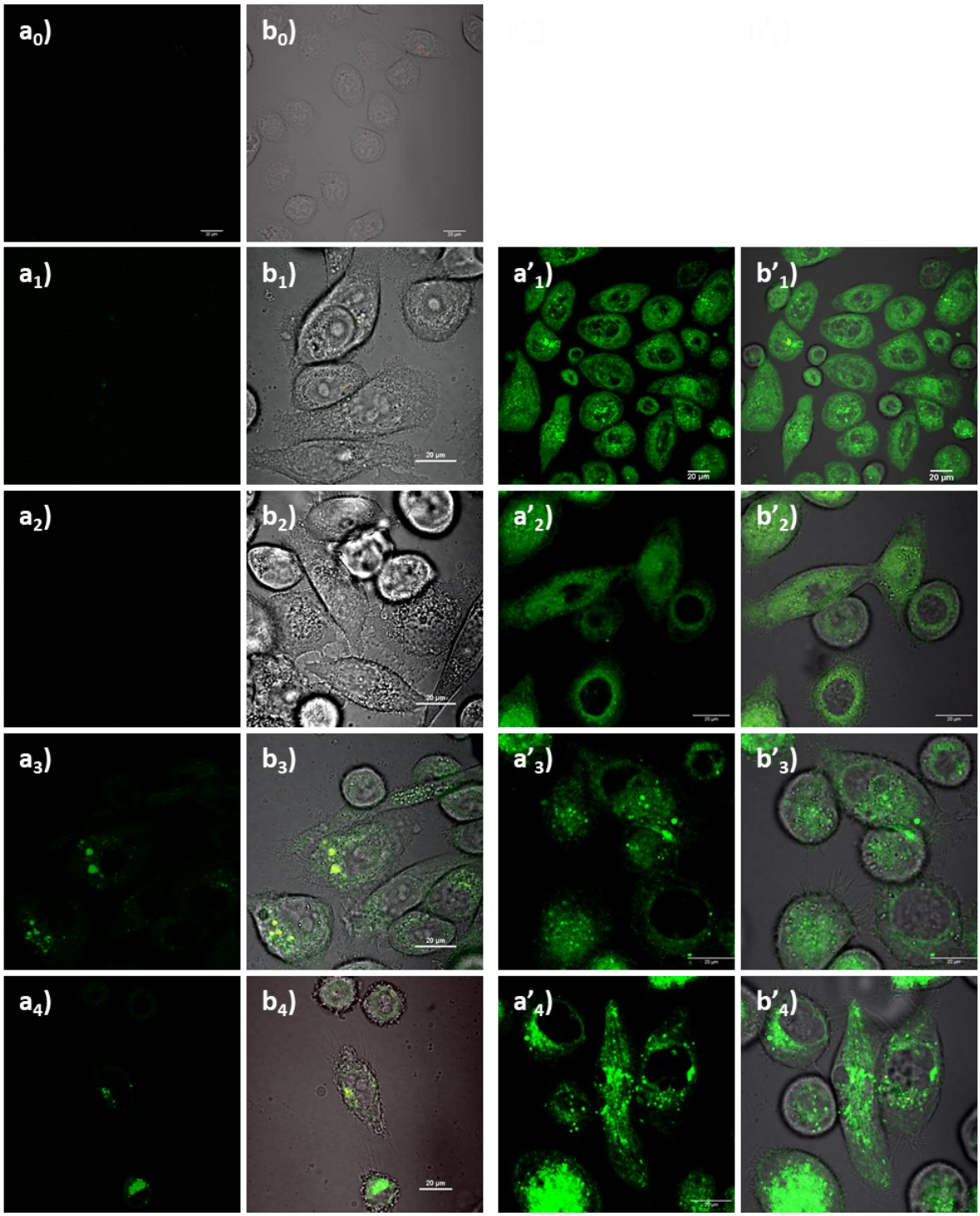

Figure 2.12. Single-photon confocal laser-scanning microscopy of PC-3 cells incubated at 37 °C for 20 min with **a_0-b_0)** DMSO (1:99 DMSO:serum-free medium); **a_1-b_1) 1**; **a_2-b_2) 1a**; **a_3-b_3) 1b**; **a_4-b_4) 1c**; **a'_1-b'_1) 3**; **a'_2-b'_2) 3a**; **a'_3-b'_3) 3b**; **a'_4-b'_4) 3c** (100 µM solutions in 1:99 DMSO:serum-free medium). **a_{0-4}** and **a'_{1-4})** green channel (λ_{em}=500–550 nm); **b_{0-4}** and **b'_{1-4})** overlay of TD-green channels. λ_{ex}=488.0 nm. Scale bar: 20 µm.

The micrographs were acquired with the same laser power in the same day after 20 minutes incubation at 37 °C with the compounds at 100 µM in 1:99 DMSO:serum-free medium and processed with same parameters using *Nikon Elements-AR Analysis 4.30.02* software.

Figure 2.12a_0-b_0 shows the negative control of PC-3 cells incubated with DMSO diluted 99 times in serum-free medium and excited at 488 nm to exclude autofluorescence of the cells. The free ligand **1** and the copper complex **1a** did not show any fluorescence emission in the green channel at the excitation wavelength of 488 nm. Such phenomenon is expected as compound **1** do not present any fluorophore unit; whilst **1a** complexes the Cu(II) ion, a d^9 paramagnetic metal centre that can quench the fluorescence emission[22].

On the other hand, the Ni(II) and Zn(II) ATSM-complexes (**1b** and **1c** respectively) showed weak fluorescence emission in the range between 500 and 500 nm when excited at 488 nm.

The fluorescence ligand **3** and its metal complexes **3a**, **3b** and **3c** showed intense emission in the green channel at the excitation wavelength of 488 nm. The fluorescence emission of such species can be due to the moiety **2**. As previously mentioned, BODIPY and its derivatives have been widely used as fluorophore to label different synthetic molecules thanks to their high molar extinction coefficient and quantum yield[27]. Overall, compounds **3**, **3a**, **3b** and **3c** localise in the cytosol of the cells, showing appreciable fluorescence emission in living PC-3 cells.

Time-correlated single-photon counting (TCSPC) and multiphoton fluorescence lifetime imaging microscopy (FLIM) have become powerful tools to investigate biological processes, cellular uptake and distribution of species *in vitro*[44]. TCSPC records the statistical distribution of lifetimes of the studied compound in an environment; on the other hands, FLIM can produce an image of the distribution of lifetimes of the fluorophore in the studied environment. Details about such techniques are explained in Chapter 4. The analyses were carried out with the assistance of Prof Stanley Botchway at the Rutherford Appleton Laboratory.

The fluorescent NDI-based complex of copper (**3a**) was preliminarily studied and compared to its free ligand **3** *via* TCSPC in solution. In Figure 2.13, the lifetime decays of **3** and **3a** are presented in a 1 mM solution in DMSO (a) and 2.5 mM in DMSO:H_2O (1:1) mixture (b).

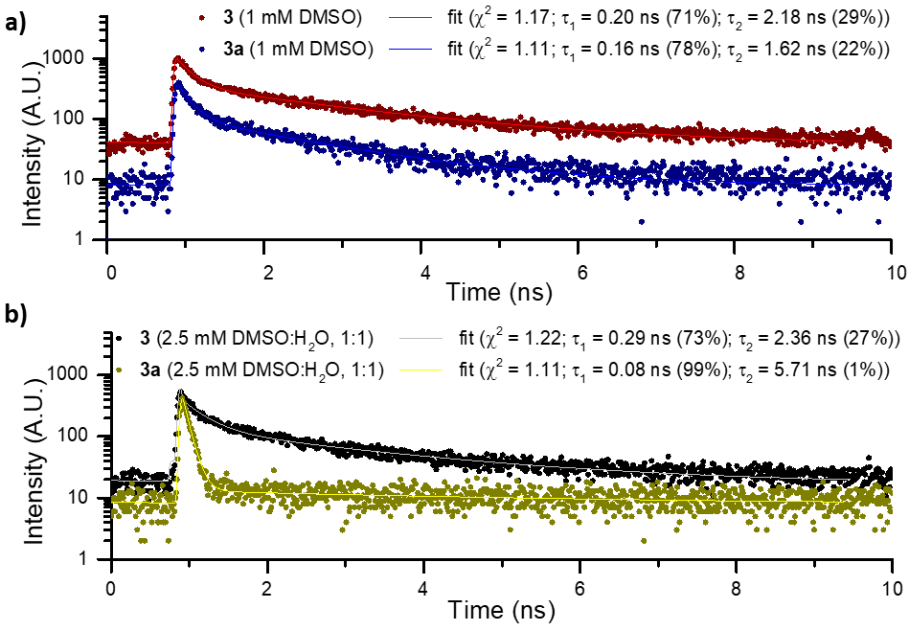

Figure 2.13. Two-photon time-correlated single-photon counting (λ_{ex} = 910 nm). **a) 3** (in red) and **3a** (in blue) in 1 mM in DMSO; **b) 3** (in black) and **3a** (in yellow) in 2.5 mM in DMSO:H_2O (1:1).

TCSPC produces lifetime decay distributions which are characterised by some parameters. χ^2 indicates the fitting between the obtained data points with an exponential model. If the fitting model is a double-exponential, two-lifetime components are generated. τ_1 (fast or short-lifetime component) represents molecules interacting each other and therefore provoke a Förster resonance energy transfer (FRET) events[45,46]; whilst, τ_2 (slow or long-lifetime component) represents the population of non-interacting molecules[47]. The parameters a_1 and a_2 represent the amplitude of the components.

Both compounds present a double-exponential fitting model with a value of χ^2 close to 1 which generates two-lifetime components. In DMSO solution (Figure 2.13a), both species presented similar lifetime distribution decays. The short-lived component in **3** is 0.20 ns and represent the 71% of the entire distribution; on the other hands, **3a** presents a τ_1=0.16 ns which is 78% of the distribution. The long-lived components in compound **3** are about 2 ns, representing the 29% of the lifetime decay; while for compound **3a**, τ_2 is about 1.6 ns (22%). The presence of the divalent copper ion does not affect the aggregation and lifetime properties in this solvent system. On the other hand, in DMSO:H_2O (Figure 2.13b), **3** and **3a** present different lifetime distributions. The free ligand **3** showed two-lifetime components with the short-lived component at 0.29 ns (73%), whilst the Cu(II) complex **3a** presented a lifetime distribution approximated to a one-lifetime component at 0.08 ns (99%).

The presence of a shorter τ_1 in **3a** than **3** can be attributed to the quenched emission of the ligand; on the other hand, the long decay of the complex is due to the residual unquenched ligand-based processes[88].

Fluorescence lifetime imaging microscopy was used to evaluate and compare the interaction between the fluorescent probes (**3** and **3a**) and the cellular environment. In addition, such technology can estimate the localisation and fluorescence lifetime behaviour of the molecular probes in living cancerous cells. The chosen cell lines to investigate the compounds **3** and **3a** were the Chinese hamster ovary (CHO) cells, used as a model of a healthy cell line to preliminarily study such species *via* FLIM.

The compounds were incubated at 37 ºC for 20 minutes in CHO cells and then analysed by FLIM. The FLIM analysis produces a fluorescence intensity image in greyscale; a fluorescence lifetime micrograph with a related colour bar indicating the time; a statistical distribution of lifetimes related to the fluorescence lifetime micrograph. Figure 2.14 shows the FLIM information of compounds **3** (a_1-c_1) and **3a** (a_2-c_2), obtained by the software *SCImage 7.4*. Complete FLIM data are shown in Appendices A (Figure A.26 and A.27).

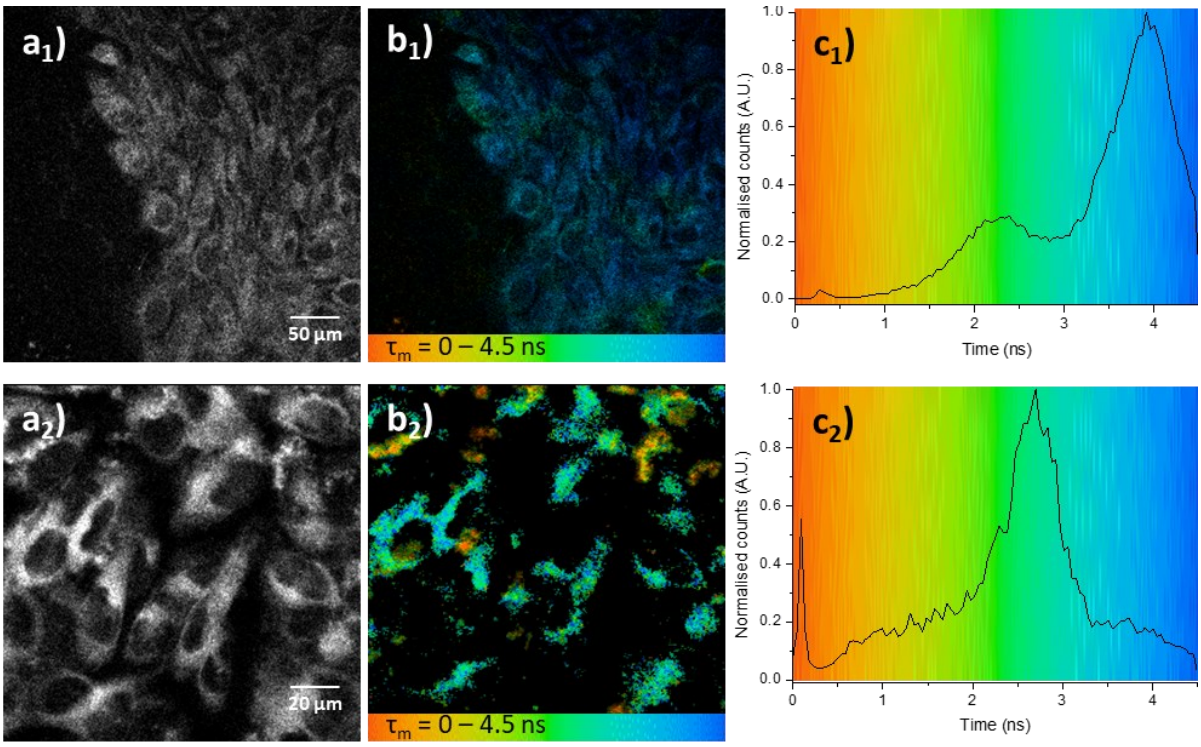

Figure 2.14. Two-photon fluorescence lifetime imaging in CHO cells line including **$a_{1,2}$)** intensity map, **$b_{1,2}$)** lifetime maps in coloured code and **$c_{1,2}$)** lifetime distribution. **a_1-c_1) 3** (τ_m=3.91±0.17 ns) and **a_2-c_2) 3a** (τ_m=2.70±0.05 ns). Compounds **3** and **3a** incubated in CHO cells for 20 min at 37 ºC (0.05 mM in 1:99 DMSO:serum-free medium). λ_{ex}=910 nm; **a_1-c_1)** laser power 1.2 mW, acquisition time 30 s; **a_2-c_2)** laser power 4.4 mW, acquisition time 60 s.

The intensity image (a_1) and lifetime map (b_1) show that the distribution of compound **3** is mainly in the cytosol of the cells. The statistical distribution of lifetime of **3** found in the image is at 3.91±0.17 ns. This data is very different from the solution data obtained by TCSPC in the studied solvent systems (Figure 2.11).

The fluorescent copper complex **3a** shows a homogeneous distribution inside the cells (b_2) with a lifetime statistical distribution at 2.70±0.05 ns. In addition, **3** and **3a** presented lifetime distributions differing from about 1.2 ns. This phenomenon suggests that the presence of Cu(II) in **3a** can affect the interaction of the molecule with the cellular environment, which is denoted on the decrease of the average lifetime of the species.

Overall, the use of TCSPC and FLIM as methods to preliminarily investigate the interaction of such fluorescent probes has revealed informative for the different behaviour that the compounds showed either in solution or *in vitro*. The different lifetime distributions found in solution and *in vitro* can indicate a different interaction of the compound with the cellular environment, which can affect the lifetime of the species. The presence of copper(II) ions can play a role on the interaction with the cells, reflected on the difference in lifetime distribution of the free ligand **3** and its Cu(II) metal complex **3a**.

2.2.3. Cytotoxicity assays in prostate cancer cells

The fluorescent metal complexes **3a**, **3b** and **3c**, along with the fluorescent free ligand **3**, were preliminarily tested in cytotoxicity assays, using 3-(4,5-dimethylthiazol-2-yl)-2,5-diphenyltetrazolium bromide (MTT). Such a colourimetric assay is based on the reduction of the yellow MTT in the purple formazan by the mitochondrial enzymes in living cells. The quantity of formed formazan is proportional to the number of viable cells. This measure is performed by a UV-visible spectrometer, recording the changes in absorbance at 570 nm. The changes in absorbance are due to the cell death which loses the ability to convert MTT to formazan and therefore the absorbance at 570 nm is proportional to the viable cells[48].

Figure 2.15 shows the normalised cell viabilities of **3** (a), **3a** (b), **3b** (c) and **3c** (d) after 30 minutes, 24- and 48-hours incubations into prostate cancer cells line (PC-3). MTT assays were carried out with the assistance of Dr Haobo Ge.

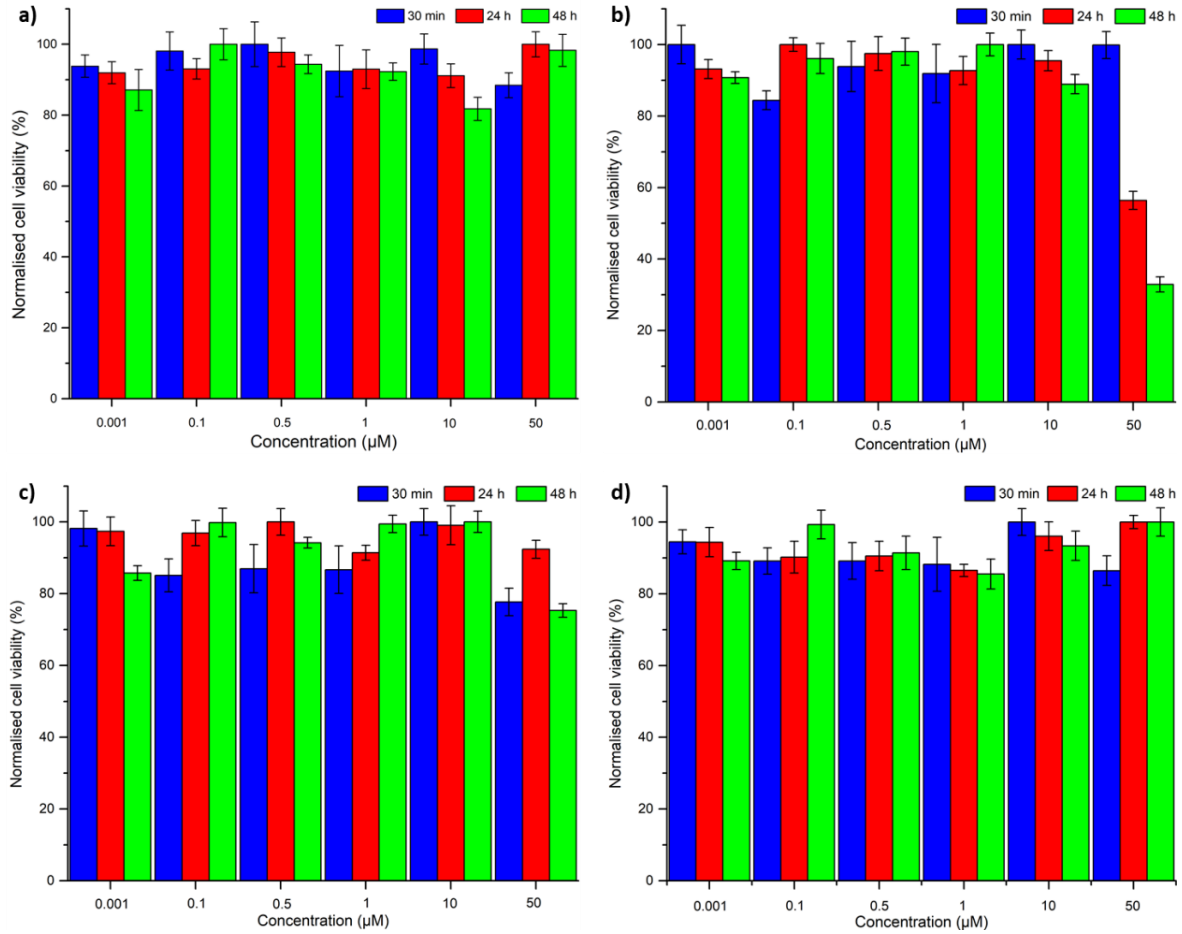

Figure 2.15. MTT assay results over 30 min (blue bars), 24 h (red bars) and 48 h (green bars) incubation of compounds **a) 3**, **b) 3a**, **c) 3b** and **d) 3c** into PC-3 cells line. (The data were collected from 3 repeated measurements on the same day, N=1).

Overall the normalised cell viabilities of compound **3** were above 80% which suggested its mild cytotoxicity in PC-3 cells (Figure 2.15a). At 48 hours incubation, 10 μM concentration of the compound killed 20% of the cells. The copper complex **3a** (b) presents mild toxicity until 10 μM which values are above 80%. The 50 μM concentration killed almost 40% of the cells after 24 hours of incubation and after 48 hours, the viability of the cells decreased to about 30%. The fluorescent Ni(II) complex **3b** (c) showed cell viabilities above 80% at almost all concentrations and incubation times. At 50 μM, the dead cells were 20% after 30 minutes and 48 h. The Zn(II) complex **3c** (d) presents weak cytotoxicity at all concentrations and at all incubation times which killed almost the 10-15% of the cells.

2.3. Preliminary investigation of fluorescence "turn-on" effect under hypoxia

Some diseases and tumours, such as cardiovascular, liver, lung and kidney diseases[49] and breast, cervix and prostate cancers[50], are associated with lack of oxygen, called hypoxia.
Over 60% of solid tumours are related to hypoxia because of the ability of the tumoral cells to grow fast and big in the existing vasculature. In recent years, conventional medical imaging techniques (PET, SPECT and MRI) have been developed to detect hypoxic tissues in early-stage once the diameter of solid tumour reaches 350 μm[51]. However, these hypoxia imaging methods require specialised personnel and dedicated environment which few clinical structures are provided and they could result expensive to the patients and long waiting lists. Fluorescence imaging has gradually become a powerful method to detect hypoxia thanks to easy operation, high sensitivity and good resolution.
In recent years, two categories of fluorescent probes have been developed which the first group is based on the biomolecules related to hypoxia (hypoxia-inducible factor 1 and carbonic anhydrase) and the second group is based on the low partial pressure of oxygen and strong ability bio-reduction in the hypoxic tissues[51]. [Cu(ATSM)] and its radiolabelled versions with ^{60}Cu, ^{61}Cu, ^{62}Cu and ^{64}Cu have been studied for being selective for hypoxia tissues and therefore used for medical imaging[6]. Recently, different TSC-based systems[14,32,52] have been developed to be used in fluorescence imaging *in vitro* and *in vivo* to detect hypoxic cancers.
In the last decade, some hypoxia-sensitive fluorescence probes[53-55] have been studied in living cells able to turn-on the fluorescence when in hypoxic conditions. A molecular device able to tun-on the fluorescence when it is in hypoxic tissues could be a powerful tool to detect diseases and/or cancer in the early stage.

The fluorescent NDI-based complex **3a** was preliminarily studied by confocal laser-scanning microscopy to qualitatively evaluate the effect of lack of oxygen on the fluorescence emission of such species in the cellular environment. Supposedly, the reduction of Cu(II) in Cu(I) under hypoxic cellular environment can affect the fluorescence emission of the molecular probe.
The three cell lines chosen in this study represent models of the most common form of cancer in men and women in UK[56]. EMT6 cells are murine mammary carcinoma cells, HeLa cells are human breast cancer cells and PC-3 cells are human prostate cancer cells. To reproduce the hypoxic conditions, such cells lines were incubated overnight at 37 ^{o}C in a concentration of 5% of oxygen and 95% of carbon dioxide. The subsequent day, compound **3a** was incubated under the recreated hypoxic condition for 20 minutes with the cells and analysed by CLSM.

The cells were excited with a wavelength of 488 nm, using the same laser power. Figure 2.16 reports the micrographs of the green channel in both normoxic and hypoxic conditions for **3** and **3a** in the different cell lines.

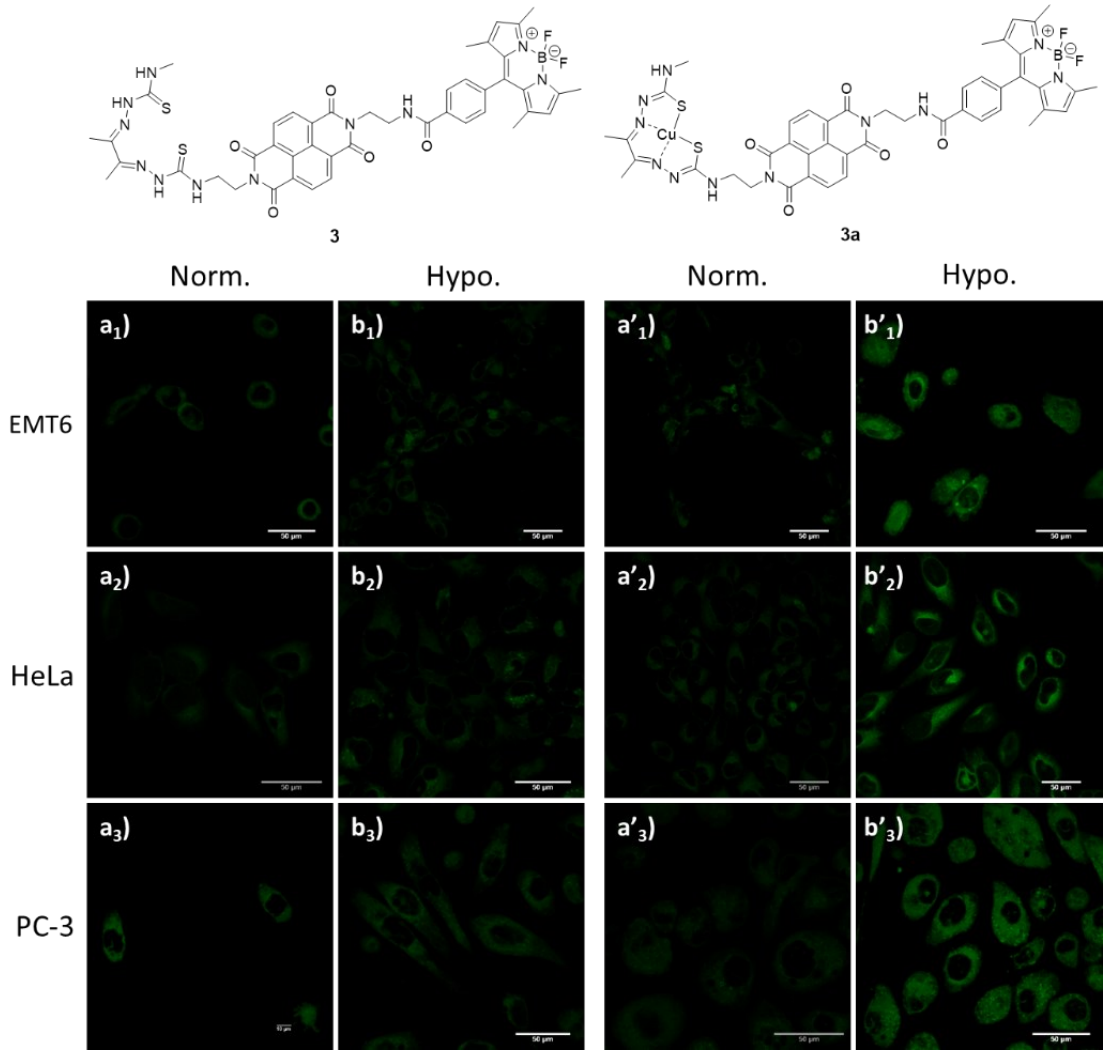

Figure 2.16. Single-photon confocal laser-scanning microscopy of EMT6 (**a_1-b_1** and **a'_1-b'_1**), HeLa (**a_2-b_2** and **a'_2-b'_2**) and PC-3 (**a_3-b_3** and **a'_3-b'_3**) cells incubated at 37 °C for 20 min with compounds **3** (**$a_{1\text{-}3}$-$b_{1\text{-}3}$**) and **3a** (**$a'_{1\text{-}3}$-$b'_{1\text{-}3}$**). Solutions 0.1 µM in 1:99 DMSO:serum-free medium; λ_{ex}=488.0 nm; λ_{em}=500–550 nm; scale bar: 50 µm. (Normoxia: 20% pO_2; hypoxia: 5% pO_2 and 95% CO_2).

The obtained micrographs in Figure 2.15 of the fluorescence emission channel (λ_{em}=500-550 nm) were processed by *Nikon Elements-AR Analysis 4.30.02* software. The same procedure was carried out on compound **3**. Compound **3** and **3a** were incubated in the selected cell lines in both normoxic (20% pO_2) and recreated hypoxic conditions (5% pO_2). The different oxygen concentration di not qualitatively affect the fluorescence emission of the free ligand **3** (Figure 2.16$a_{1\text{-}3}$ and $b_{1\text{-}3}$). On the other hand, compound **3a** qualitatively showed different fluorescence emission intensity between the analysis under normoxia and hypoxia on the cells.

In fact, the fluorescence intensity in the micrographs seemed increasing on EMT6, HeLa and PC-3 cells under hypoxia.

The used software (*Nikon Elements-AR Analysis 4.30.02*) can produce the mean fluorescence intensity, associated with its standard deviation, of the region of the image. This method has been recently used[57-59] to estimate the fluorescence emission changes in a particular environment and can help to visualise numerically the changes in the fluorescence emission on the selected area of analysis. The graph in Figure 2.17 reports the mean fluorescence emission intensities with standard deviations, produced by software on the investigated areas on the micrographs in Figure 2.15.

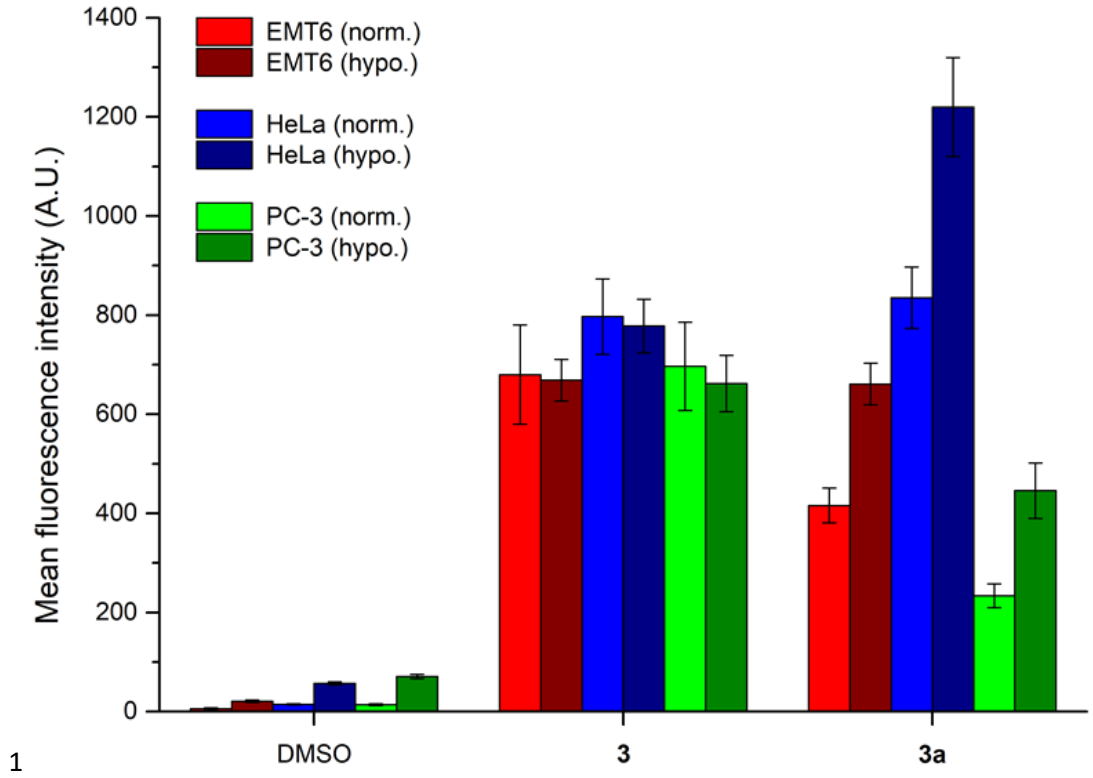

Figure 2.17. Representation of the mean fluorescence intensities with error bars of the green channel (λ_{em}=500-550 nm) for DMSO control, **3** and **3a** in EMT6 (red bars), HeLa (blue bars) and PC-3 (green bars) cells in normoxia (bright colours) and hypoxia (dark colours). (The means and standard deviations were obtained by *Nikon Elements-AR Analysis 4.30.02* on the micrographs in Figure 2.15).

The graph compares the mean fluorescence intensity of the free ligand **3** and its Cu(II) complex **3a** under normoxia (5% pO_2) and hypoxia (20% pO_2) in EMT6, HeLa and PC-3 cell lines. The cells were also incubated with a concentration of 1:99 of dimethyl sulfoxide in serum-free medium and analysed by CLSM. Such data were used as a negative control.

The mean fluorescence emission intensities of compound **3** in the three cell lines are similar in under both normoxia and hypoxia. This phenomenon suggests that the fluorescence of the species is not affected by the different concentration of oxygen and the probe can be detected in both conditions. On the other hand, compound **3a** presents substantial differences in fluorescence emissions in the different oxygen concentrations. In fact, the mean fluorescence intensity under hypoxia is higher than under normoxia, independently of the cell line. This fact suggests that the presence of Cu(II), undergoing the reduction in lack of oxygen, can affect the fluorescence emission of the probe **3a**. The "turn on" process of the fluorescence emission of compound **3a** can be dependent on the concentration of oxygen presented on cancerous cells.

The fluorescence "turn-on" effect under hypoxia was preliminarily investigated over time using confocal laser-scanning microscopy. The analysis was carried out on CHO cells which were previously incubated under recreated hypoxic conditions with a continuous flux of nitrogen. The NDI-base complex **3a** was incubated in CHO cells for 20 minutes at 37 ^{o}C and then exited with a wavelength of 488 nm, under continuous nitrogen flux on the instrument. The fluorescence emissions were recorded on the green channel (emission wavelength between 500 and 550 nm) of the selected region-of-interest (ROI) at established time intervals. Figure 2.18 shows the processed micrographs obtained by the CLSM analysis of compound **3a** in CHO cells line.

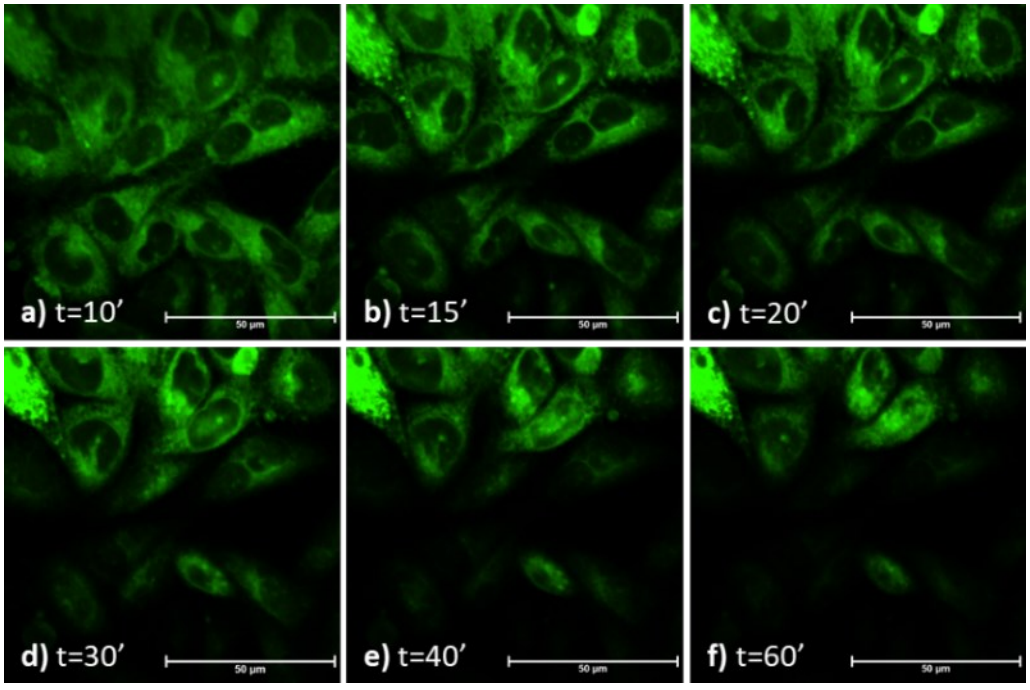

Figure 2.18. Single-photon confocal laser-scanning microscopy of CHO incubated for 20 min at 37 °C with compound **3a** (0.1 mM in 1:99 DMSO:serum-free medium). **a-f)** λ_{ex}=488.0 nm and λ_{em}=500–550 nm; scale bar: 50 µm.

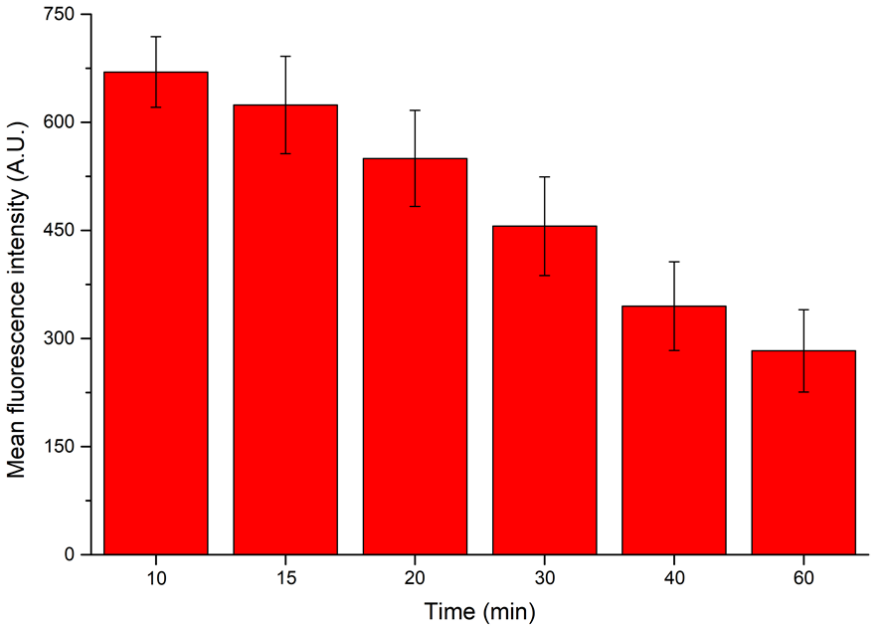

Figure 2.19. Plot of mean fluorescence intensities of micrographs *vs* time of hypoxic condition. (The means and standard deviations were obtained by *Nikon Elements-AR Analysis 4.30.02* on the micrographs in Figure 2.17).

Similar to the previous discussion, the software *Nikon Elements-AR Analysis 4.30.02* produced mean fluorescence emission intensities with their standard deviations on the micrographs shown in Figure 2.18. The plot in Figure 2.19 depicts the mean fluorescence intensity of compound **3a** over regular intervals of time. This analysis showed that the fluorescence emission of compound **3a** decreases overtime. This phenomenon suggests that the ligand can release the copper(II) ions inside the cells[60]and, therefore, decrease the fluorescence emission of the probe as it has been demonstrated in a previous report with a similar cell line[60]. In a future perspective, complex **3a** will be compared to the free ligand **3** in the same hypoxic conditions over time to evaluate the turn-on effect of the fluorescence emission over time. Compound **3** presented a longer lifetime decay than **3a** which could suggest a longer retaining of fluorescence emission.

Fluorescence lifetime imaging microscopy was used to preliminarily investigate the effect of hypoxia on the fluorescence lifetime of compound **3a**. The used instrument was able to record both CLSM and FLIM on the same selected ROIs in Figure 2.18. The FLIM analysis was recorded at similar time intervals as before.

Figure 2.20 shows the intensity micrographs (a-f), lifetime maps in colour scale (a'-f') and statistical distribution of lifetime of **3a** in CHO cells overt regular time intervals in hypoxic conditions (continuous flux of nitrogen)

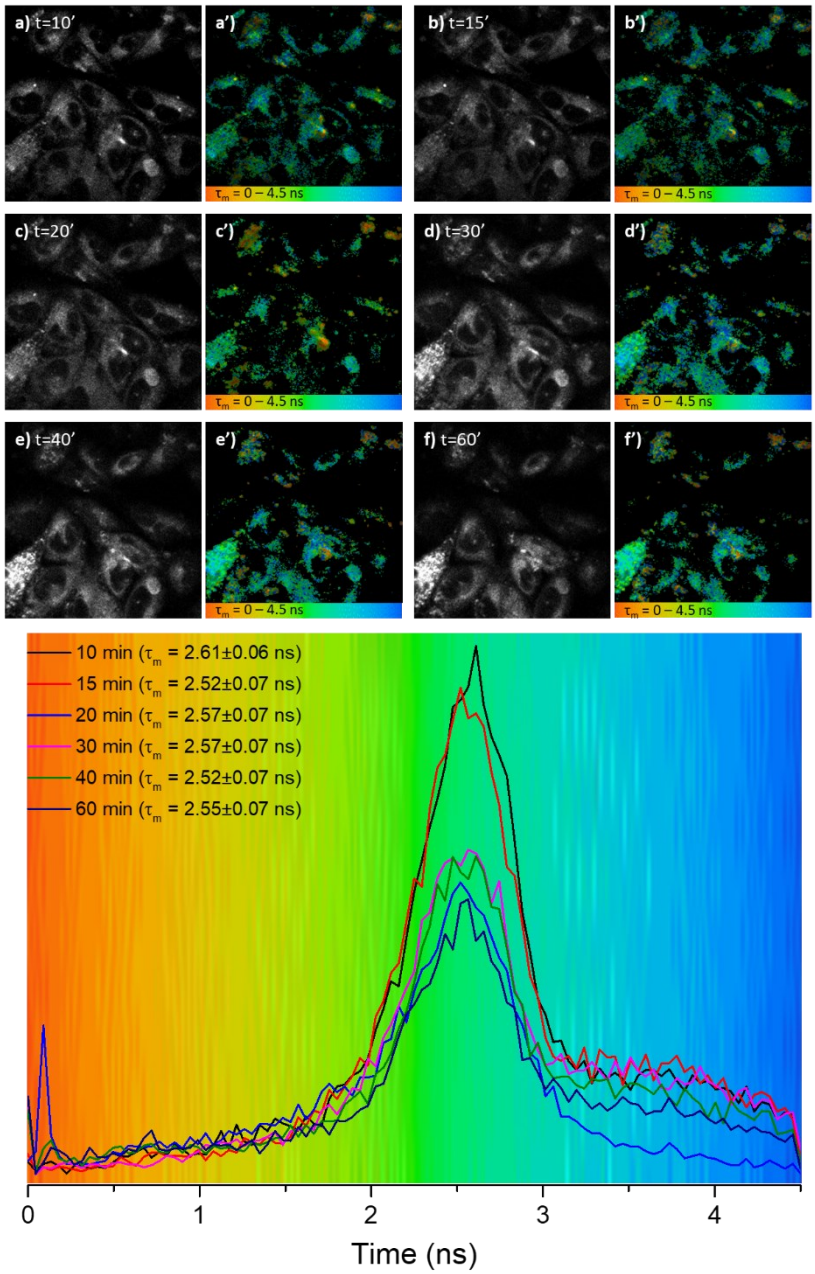

Figure 2.20. Two-photon fluorescence lifetime imaging in CHO cells line including **a-f)** intensity map, **a'-f')** lifetime maps in coloured code and lifetime distributions of **3a** overtime in hypoxic conditions. Compound **3a** incubated in CHO cells for 20 min at 37 °C (0.05 mM solution in 1:99 DMSO:serum-free medium). λ_{ex}=910 nm; **a-f)** laser power: 1.2 mW, acquisition time 30 s.

The statistical distributions of lifetimes (Figure 2.20) of **3a,** incubated in CHO cells under hypoxic conditions, shows that the average value is 2.50 ns. Overall the fluorescence lifetime of **3a** remains unchanged overtime under hypoxic condition.

These preliminary analyses obtained by CLSM and FLIM have been qualitatively revealed promising for a fluorescent "turn-on" process which the NDI-based probe **3a** undergoes, passing from normoxia to hypoxia.

However, further investigation will be carried out in both normoxic and hypoxic conditions to understand the mechanism involved in this process. Considering the molecule **3a** presents both derivatives of [Cu(ATSM)] and BODIPY, some recent studies have demonstrated that the reduction of [Cu(ATSM)] occurs in a cellular environment lacking oxygen, mainly in the cytosol of the cells[6] which is trapped in copper chaperones proteins[89]. Besides, Sunahara *et al.* have studied different BODIPY derivatives in living cells under hypoxia conditions[61] showing that this moiety could be affected by environment lacking oxygen which leads to change of fluorescence emission. The NDI-core was taken into consideration in the design of such fluorescent metal complexes to be used as a scaffold for linking both the ATSM and BODIPY derivatives. In addition, the combination of the NDI and the BODIPY may interact electronically to result in a fluorescent signal.

2.4. Peptide-conjugate of thiosemicarbazone-based ligand for potential targeting application under hypoxia

In recent years, small fragments of bombesin peptide, either 7-13 or 7-14 fragments, has become particularly interesting because of their high affinity to bind selectively the gastrin-releasing peptide receptors (GRPRs)[62]. Such receptors have been studied for localising, detecting and treating prostate cancer[63,64]. Considering the potential target of the bombesin [7-13] peptide on prostate cancer cells and the ability of the ATSM to "turn-on" the fluorescence emission in hypoxic conditions, a new NDI-based targeting compound is presented in this part of the essay.

2.4.1. Synthesis and characterisation of bombesin [7-13] peptide

In the state-of-the-art prior to this Thesis, the bombesin fragment 7-13 had already the focus of some limited research interest due to its potential applications in imaging and drug design for its targeting nature[63] for the gastrin-releasing peptide receptors (GRPRs). The fragment 7-13 of bombesin peptide has shown biological activity and affinity to GRPRs similarly to the well-known fragment 7-14 of bombesin[90,91].

The complete bombesin peptide is a 14-amino acids chain and the portion from 7th to 13th amino acid is chosen in this essay (highlighted in blue in Figure 2.21).

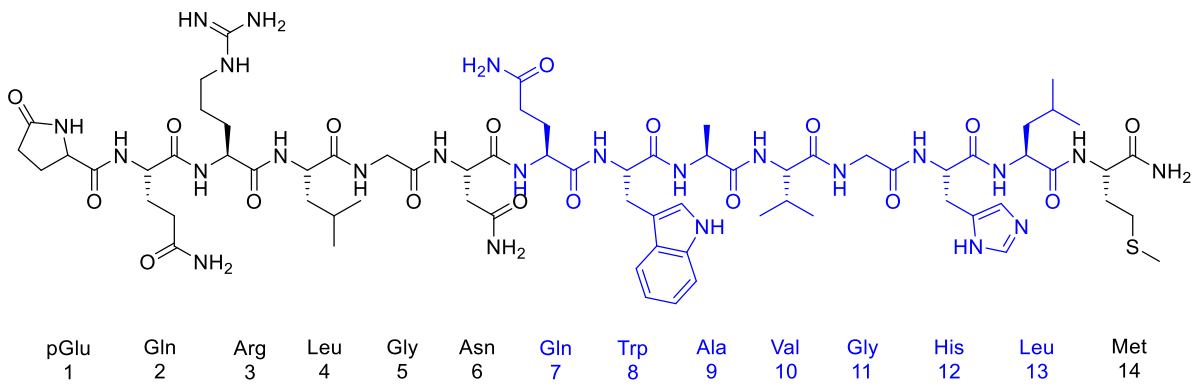

Figure 2.21. Structure of bombesin peptide with the fragment [7-13] highlighted in blue.

The synthesis of this 7-amino acids peptide was performed *via* solid-phase peptide synthesis (SPPS), introduced by Bruce Merrifield in 1963[65]. Recent reports showed that peptides can be prepared thanks to automated systems[66], interfaced with microwave radiations[67], which increased the efficiency of the couplings and reduced the reaction times.

A 2-chlorotrityl chloride resin was used as solid support which was swelled in dimethylformamide for 20 minutes at 70 ºC, under microwave radiation. All the amino acids were employed in their *L*-configuration and fluorenylmethyloxycarbonyl (Fmoc) protected in their amino groups. Each coupling step involves the deprotection of the amino group from the Fmoc, achieved by piperidine 20% in dimethylformamide[68], and the activation of the carboxylic group of the subsequent amino acid. The activation step is performed by *N,N,N′,N′*-tetramethyl-*O*-(1*H*-benzotriazol-1-yl)uronium hexafluorophosphate (HBTU), assisted by 1-hydroxybenzotriazole (HOBt)[67,69] in basic conditions. Scheme 2.6 shows the activation mechanism of the carboxylic acid group of generic amino acid, using HBTU and HOBt, base catalysed.

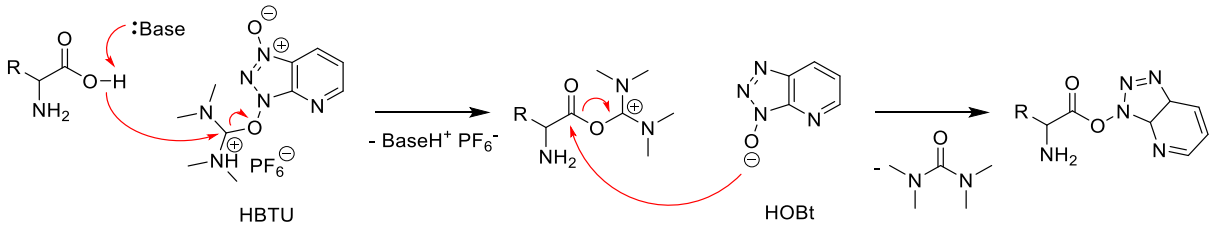

Scheme 2.6. Activation mechanism of the carboxylic group of a generic α-amino acid.

The first coupling reaction between the resin and leucine was performed at 75 °C for 5 minutes under microwave radiation in which the carboxylic group was activated by the mixture of HBTU/HOBt/DIPEA (1:1:2). After this coupling, the Fmoc protecting group was removed by piperidine 20% in dimethylformamide for 10 minutes at room temperature.

The second amino acid (histidine) was introduced in the reaction mixture and activated for 60 minutes at room temperature. This deprotection/activation protocol was followed for all the remaining amino acids which are schematically depicted in Scheme 2.7. After the coupling of the last amino acid (glutamine), its Fmoc protective group was removed by piperidine 20% in dimethylformamide and the amino acid sequence was ready to be cleaved from the resin. The cleavage of the peptide from the resin was obtained by stirring the resin for 2.5 hours at room temperature in a mixture of trifluoroacetic acid, phenol, water and triisopropylsilane (88:5:5:2). This step allows also to deprotect the side chains of tryptophan, glutamine and histidine (*tert*-butoxycarnonyl and trityl respectively)[70]. The peptide (**4**) was precipitated from cold diethyl ether and centrifuged/washed with the same solvent and then freeze-dried overnight.

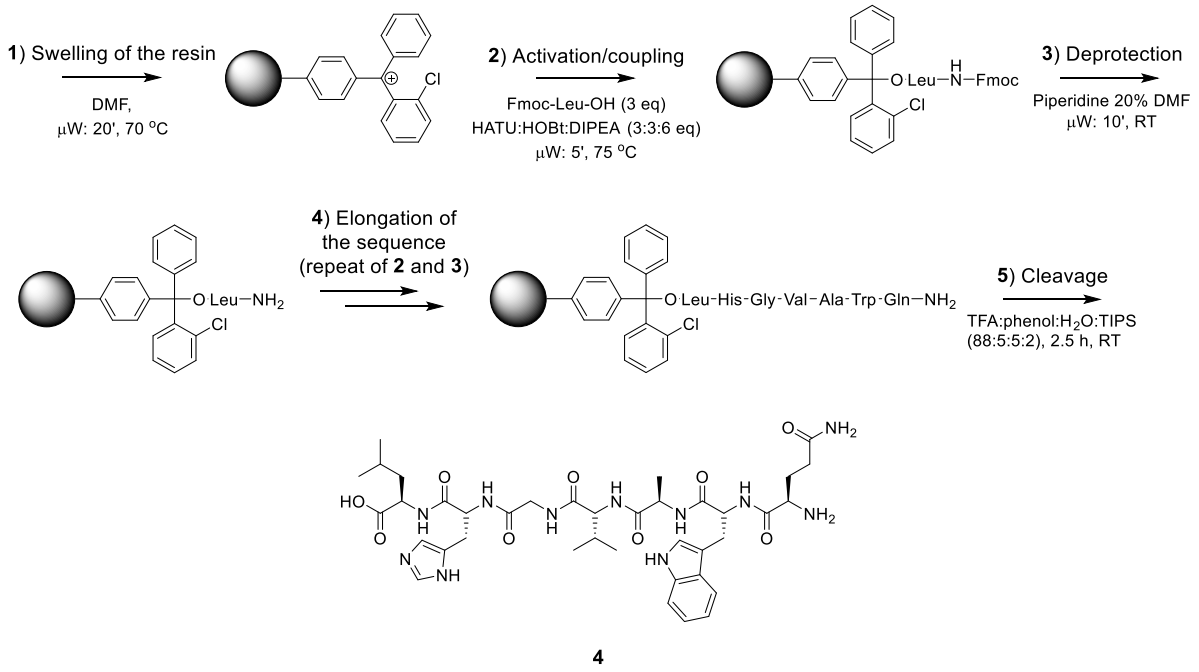

Scheme 2.7. Reaction scheme of the microwave-assisted SPPS of bombesin [7-13] peptide (**4**).

The crude peptide was purified by semi-preparative HPLC (method B, details in Experimental Section) and afterwards analysed by analytical HPLC (method A, details in Experimental Section). The pure peptide was characterised by ESI^+-TOF mass spectrometry (Figure 2.22).

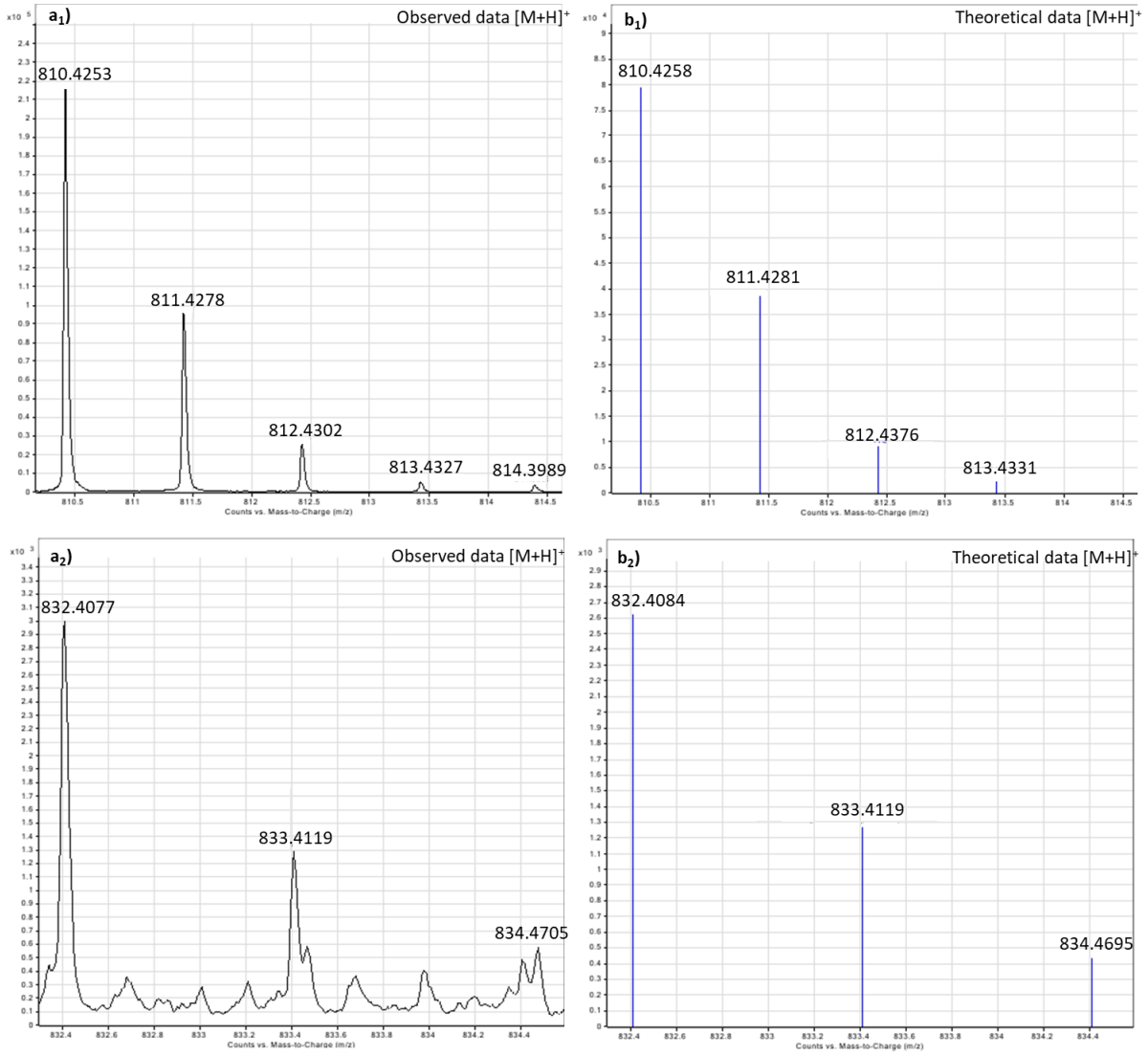

Figure 2.22. a1) Observed and **b1)** theoretical isotopic patterns for the ion $[M+H]^+$; **a2)** observed and **b2)** theoretical isotopic patterns for the ion $[M+Na]^+$.

The mass spectra in Figure 2.21 show the $[M+H]^+$ (b_1-c_1) and $[M+Na]^+$ (b_2-c_2) ions for **4** (calculated mass=809.4184 Da). In both ions, the theoretical data are within 5 mDa of error which confirms the analysed species.

2.4.2. Synthesis and characterisation of the peptide-tagged ATSM-based ligand

The ATSM-based compound with potential application as targeting probe under hypoxia conditions, presented in this part of the Chapter, consists of an asymmetric NDI scaffold with the ATSM derivative **1** and the peptide **4**. The synthesis of the proposed molecule **5** was carried out using a microwave-assisted reaction, modified by the previous work of Tambara *et al.*[26]. Scheme 2.8 shows the synthetic pathway of compound **5.**

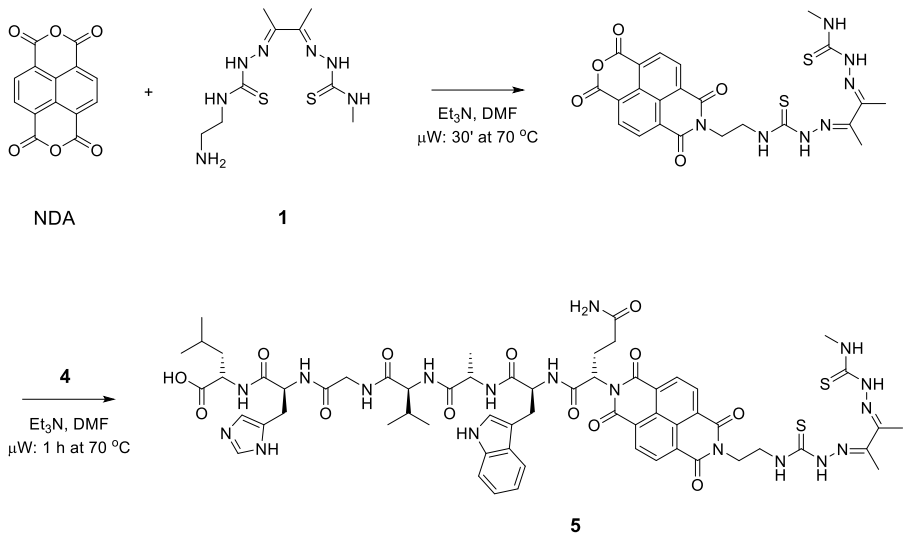

Scheme 2.8. Reaction scheme for the synthesis of compound **5**.

The adapted protocol involves a 2-step microwave-assisted reaction. The first step consists of the coupling between the NDA and **1** in dimethylformamide and triethylamine. A pure conjugate between ATSM and the NDI-core was obtained as an intermediate (^{1}H-NMR spectrum in Figure A.2 in Appendices A), controlling the stoichiometric quantities of the reagents and the reaction condition as suggested in literature[26]. This intermediate was then dissolved in dimethylformamide and triethylamine, adding the bombesin peptide **4**. The temperature of these reactions was decreased compared to the one suggested by Tambara *et al.*[26] to avoid the degradation of either the ATSM derivative and the peptide. Compound **5** was obtained by centrifugation and washing in cold diethyl ether. The pure product was analysed by mass spectrometry (Figure 2.23).

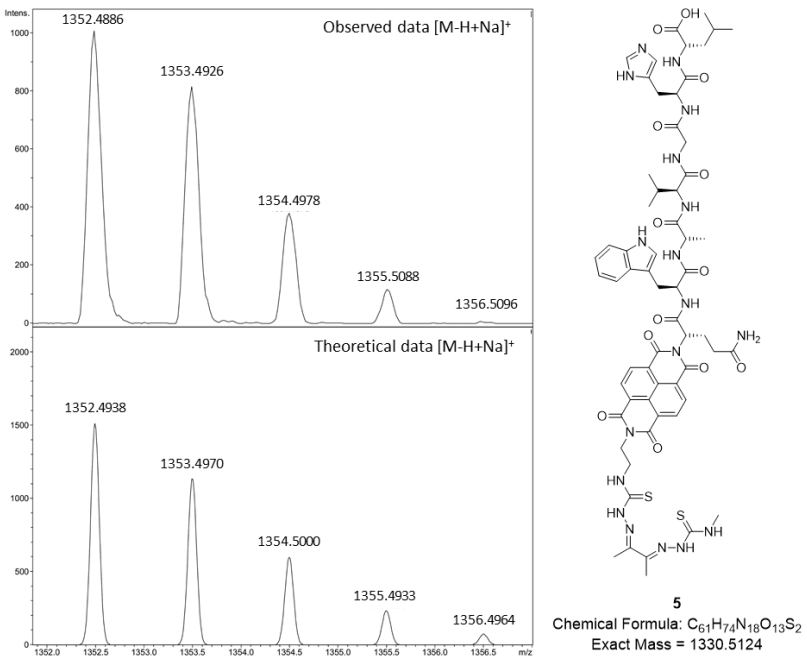

Figure 2.23. Isotopic patterns for the $[M-H+Na]^+$ ion of compound **5** (ESI^+-TOF in MeOH). Observed (top) and theoretical data (bottom).

The mass spectrometry analysis showed an isotopic pattern belonging to $[M-H+Na]^+$ ion of compound **5**. According to the theoretical isotopic pattern, the observed ion is consistent within 5 mDa of error and with the exact mass of the compound's chemical formula: $C_{61}H_{74}N_{18}O_{13}S_2$.

This proposed compound needs further analysis to assess the achieved synthesis. In future work, the optical characteristics will be evaluated by UV-visible and fluorescence spectroscopies in solution. Compound **5** can be considered as a proof-of-concept for potential targeting species for prostate cancer cells thanks to the presence of GRPRs-targeting peptide **4**. In addition, such molecule presents the ATSM moiety **1** which can complex the copper(II) ions and be hypoxia-selective, as previously described in Subchapter 2.3.

2.5. Bioconjugation with siderophore with potential applications for radiolabelling with metal isotopes

As previously mentioned, clinical medicine has benefited from radioisotopes since the 1950s[71] for imaging and therapy purposes. Nuclear medicine has been widely used in cancer early detection and early treatment thanks to the ability to image the tissues non-invasively and treat specifically diseased tissues, without damaging the healthy ones[72]. Commonly used isotopes are ^{18}F, ^{15}O, ^{13}N, ^{11}C and ^{131}I which have been integrated into small organic drug mimetics.

However, the incorporation of these nucleotides requires covalent bond linkages into the organic agents through long and complex syntheses which can sacrifice the radioactivity of these short half-lived isotopes[73]. On the other hand, radiometal-based pharmaceuticals have been started to gain importance in cancer imaging and therapy thanks to their half-lives, which is sufficient to carry out the synthesis and accumulate in the patients' targeted tissues, and moreover for their costs and availability[71].

Among the studied radiometals, ^{68}Ga and ^{89}Zr have been widely incorporated in various organic ligands for PET imaging thanks to their ease and cost of production, half-lives suitable for the synthesis and use, stability in physiological environment and safety to handle[74-76].

Both 1,4,7-triazacyclononane-1,4,7-triacetic acid (NOTA)- and 1,4,7,10-tetraazacyclododecane-1,4,7,10-tetraacetic acid (DOTA)-based chelating agents have been widely designed and synthesised to incorporate ^{68}Ga for PET/CT cancer imaging because they can be derivatised with biomolecules such as peptides and antibodies to target tumoral tissues[74,77,78]. In addition, TSC ligands have been recently proposed as kinetically stable chelators for ^{68}Ga for *in vitro* imaging in hypoxia condition[79]. On the other hand, ^{89}Zr has been incorporated in different derivatives of ethylenediaminetetraacetic acid (EDTA), DOTA and desferrioxamine B (DFO) which can suit the octahedral geometry of its tetravalent ion. DFO is a natural microbial siderophore which is formed as a metabolite of a soil bacterium *Streptomyces pilosus*[92,93]. This ligand can strongly chelate with Fe(III) with a binding constant of $10^{30.6}$ and for this reason, is used to treat acute iron poisoning[94] and transfusion-dependent blood disorderers[92]. Besides, such siderophore has shown a good capacity to coordinate other metal ions[92]. In the last decade, several DFO-based agents have been designed and synthesised for different applications such as treatment of metal ion dyshomeostasis, radiometals imaging, metal ions sensing, inhibiting metal ion-dependent processes and releasing other antibiotics exploiting the Fe(III)-mediated uptake pathways[92]. DFO has been proved to be promising to chelate both ^{68}Ga(III) ^{89}Zr(IV) ions because of its hexadentate nature, rapid and efficient labelling and has a free primary amine tail which can be derivatised[75]. Recently, an ^{89}Zr(IV)-DFO moiety has been incorporated to a monoclonal antibody for the development of a dual-modality imaging probe (PET and NIR imaging) as a potential agent for diagnosis and image-guided resection of solid tumors[94].

In this part of the Chapter, an NDI-based chelator is proposed which covalently link 2 units of DFO. This compound was preliminarily studied by UV-visible and fluorescence spectroscopies

to assess its optical features. The uptake, localisation and fluorescence emission in living prostate cancer cells was preliminarily evaluated by confocal laser scanning microscopy. Scheme 2.9 shows the reaction path of the synthesis of compound **6**.

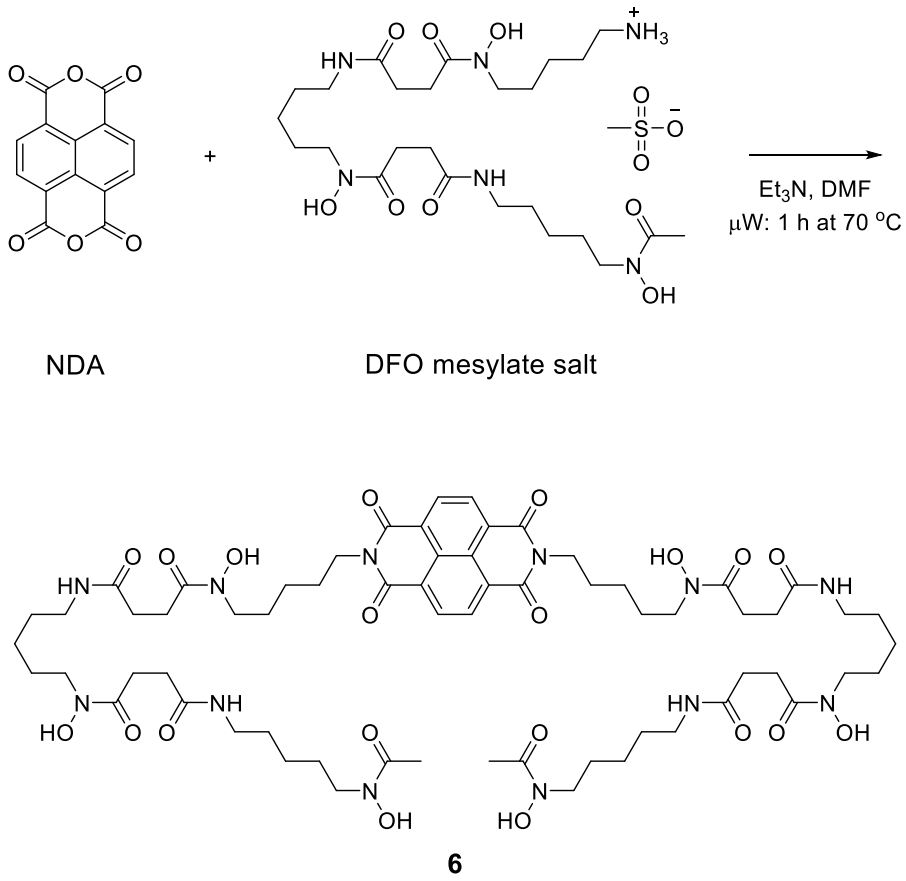

Scheme 2.9. Reaction scheme for the synthesis of compound **6**.

Compound **6** was obtained by a microwave-assisted reaction, adapted from the previous work[26]. NDA and two equivalents of DFO mesylate salt were solubilised in dimethylformamide and triethylamine was added to ensure the basic pH. The resulting mixture was sonicated for 5 minutes and heated at 70 °C for 1 hour. The product was filtered and washed with Et_2O without any further purification. Compounds **6** was analysed by mass spectrometry and ^{1}H-NMR (yield 54%). Figure 2.24 shows the observed and theoretical isotopic patterns of compound **6**.

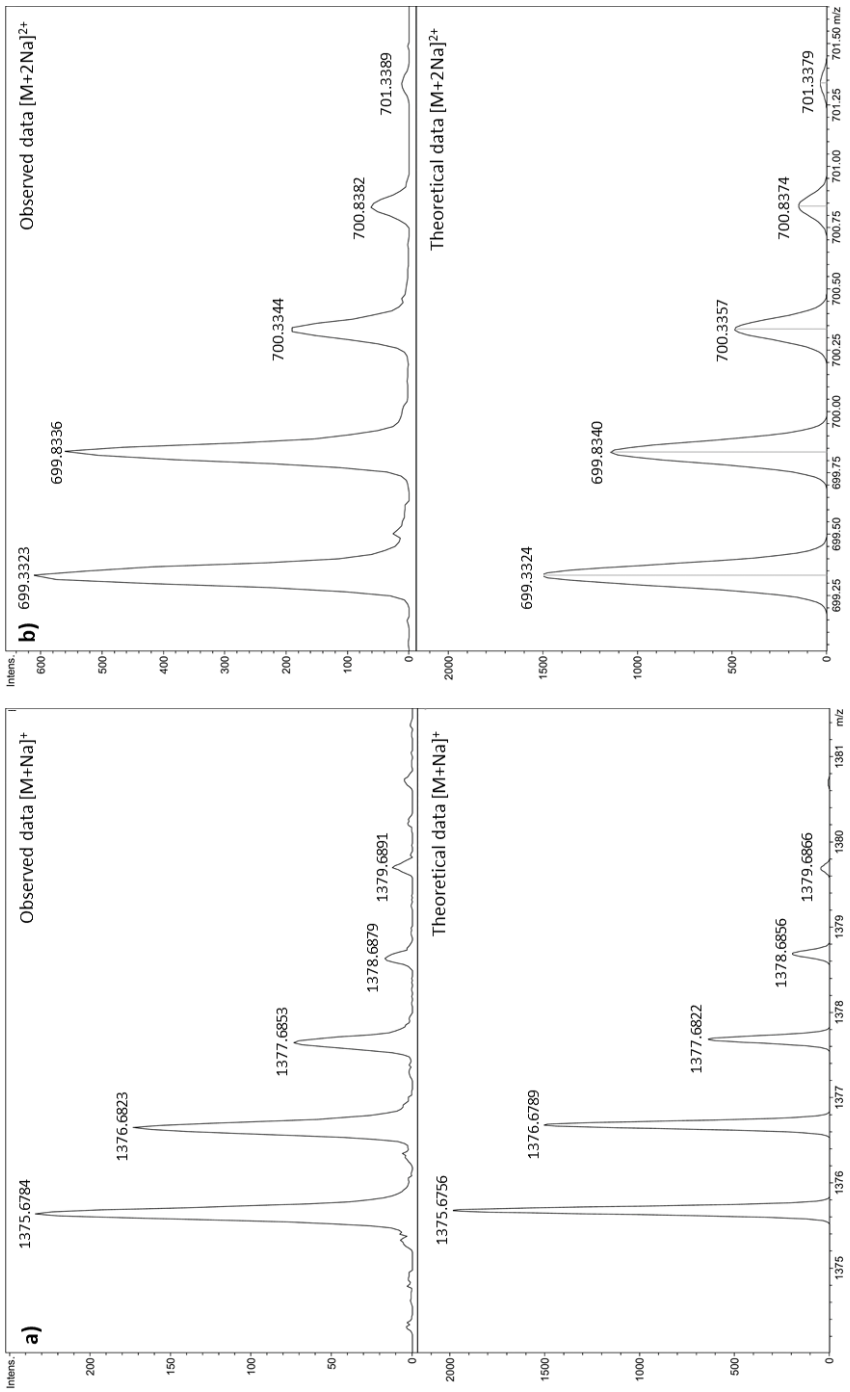

Figure 2.24. Isotopic patterns for the **a)** $[M+Na]^+$ and **b)** $[M+2Na]^+$ ions of compound **6** (ESI^+-TOF in MeOH). Observed (top) and theoretical data (bottom).

The found isotopic patterns by mass spectrometry belongs to the ions $[M+Na]^+$ (Figure 2.23a) and $[M+2Na]^{2+}$. These data were within 5 mDa agreement with respect to their theoretical isotopic patterns shown below and deemed indicative of the formation of the desired compound with the expected exact mass of 1352.6864 Da.

The ^{1}H-NMR spectrum of compound **6** is shown in Figure 2.25 with the corresponding assignments in the structure.

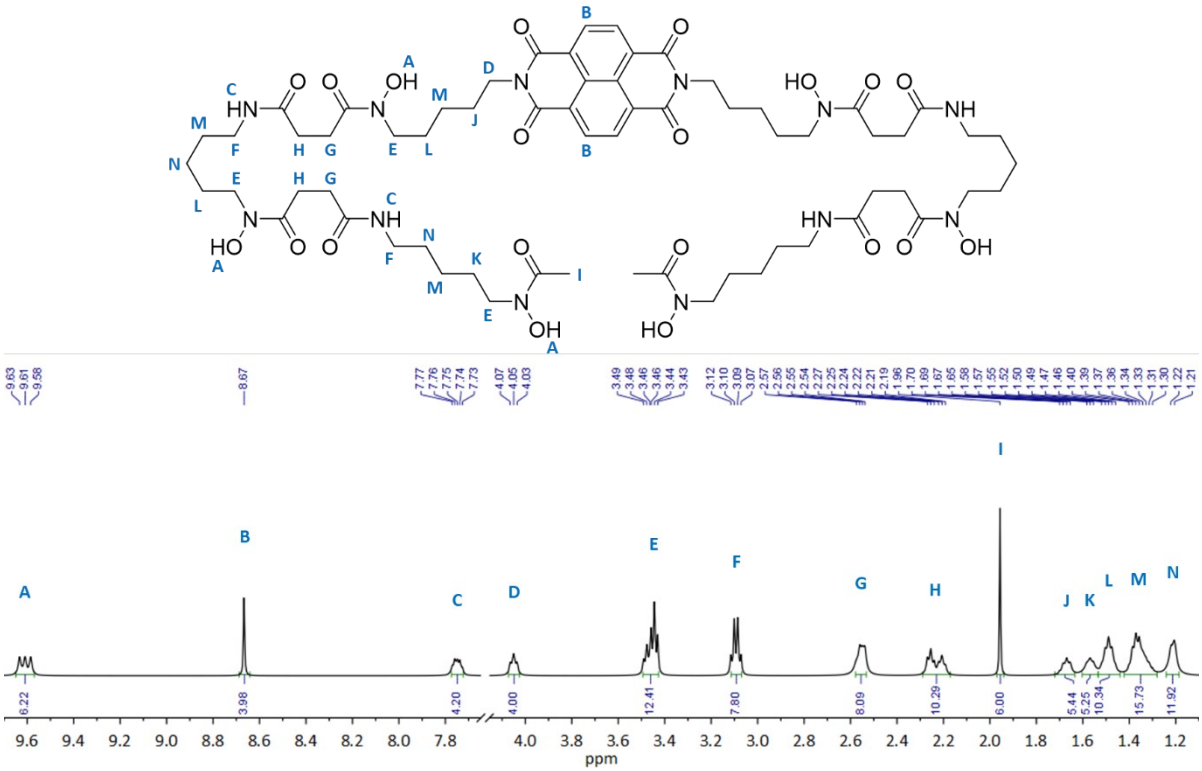

Figure 2.25. ^{1}H-NMR spectrum of compound **6** with assignments (500 MHz, DMSO-d_6).

The signals detected on the ^{1}H-NMR spectrum are assignable to a symmetric NDI structure because of the singlet at 8.67 ppm (*B*), belonging to the 4 aromatic protons of the NDI-core. The signal appearing at 9.61 ppm was attributed to the 6 hydroxyl protons (*A*). The pentyl chain, linked to NDI-core, is characterised by the signals at 4.05 (*D*), 1.68 (*J*), 1.34 (*M*), 1.47 (*L*) and 3.46 (*E*) ppm. The signals of the ethyl group labelled with *G* and *H* appeared at 2.55 and 2.25 ppm. The propyl group presented signals at 1.32 (*M*), 1.22 (*N*) and 1.34 ppm (*L*). The signals of the final pentyl chain appeared at 3.09 (*F*), 1.22 (*N*), 1.32 (*M*), 1.56 (*K*) and 3.46 ppm (*E*). Some signals presented accidental isochrony, noticeable from their multiplicity and integration areas. The resonances were assigned by observing the correlations in the ^{1}H-^{1}H COSY spectrum shown in Appendices (Figure A.3). In addition, the signal of the methyl group of the mesylate anion was found in the spectrum. Such residual anion was present in commercially available DFO, brought from Sigma.

Compound **6** was analysed by FT-IR in ATR mode which spectrum is shown in Figure 2.26 with the characteristic bands signed.

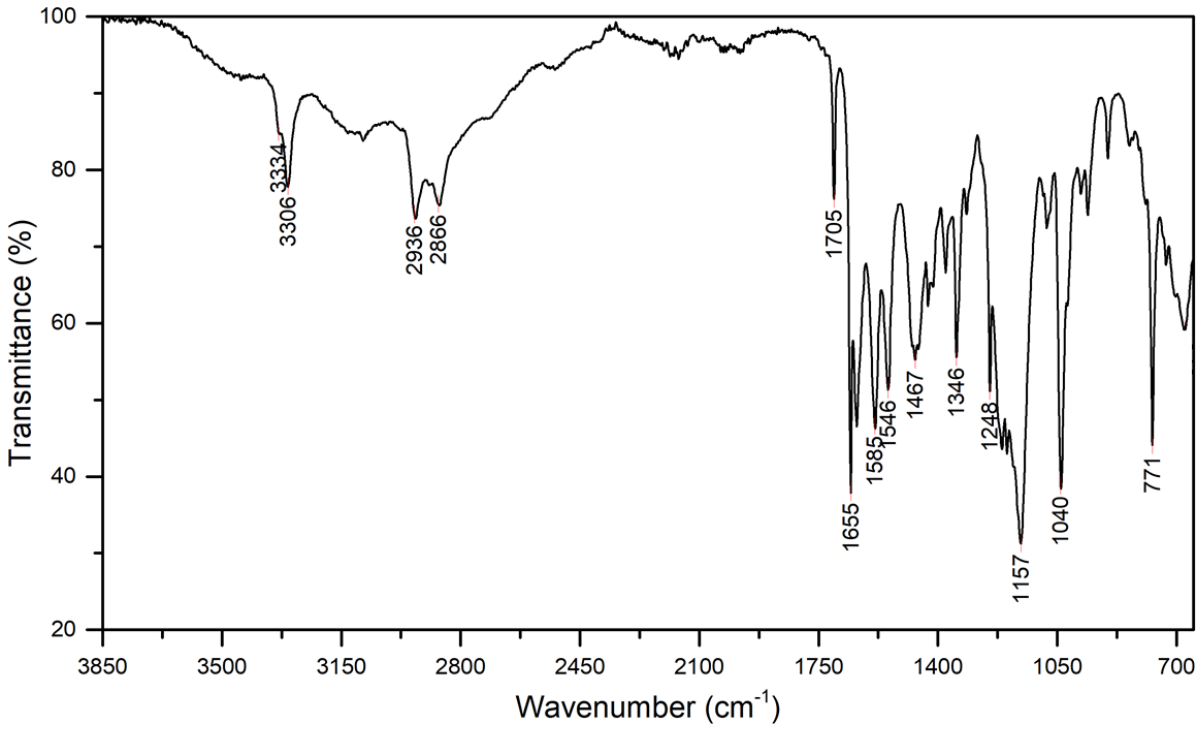

Figure 2.26. FT-IR spectrum of compound **6** with the main bands labelled.

In the IR spectrum, it can be noticed the characteristic bands of the amide N-H stretching at 3334 and 3306 cm^{-1} which presents their corresponding bending bands at 1585 and 1546 cm^{-1}. Broad bands at around 3500 and 3150 cm^{-1} can be attributed to the O-H stretching. The C-H stretching of the aliphatic chains was at 2936 and 2866 cm^{-1}. The aromatic C-H bending overtones are at about 2000 cm^{-1} which their C-H bending signals were at 771 cm^{-1}. The imide C=O stretching signal was at 1705 cm^{-1} with the corresponding CO-N-CO stretching at 1040 cm^{-1}. The bands of the amide moieties were at 1655 cm^{-1} (C=O stretching) and 1248 cm^{-1} (C-N stretching).

The optical properties of **6** were investigated by UV-visible and fluorescence spectroscopies in DMSO solution. In Figure 2.27, the absorption (a) and the excitation-emission matrix (EEM) map (b) are depicted.

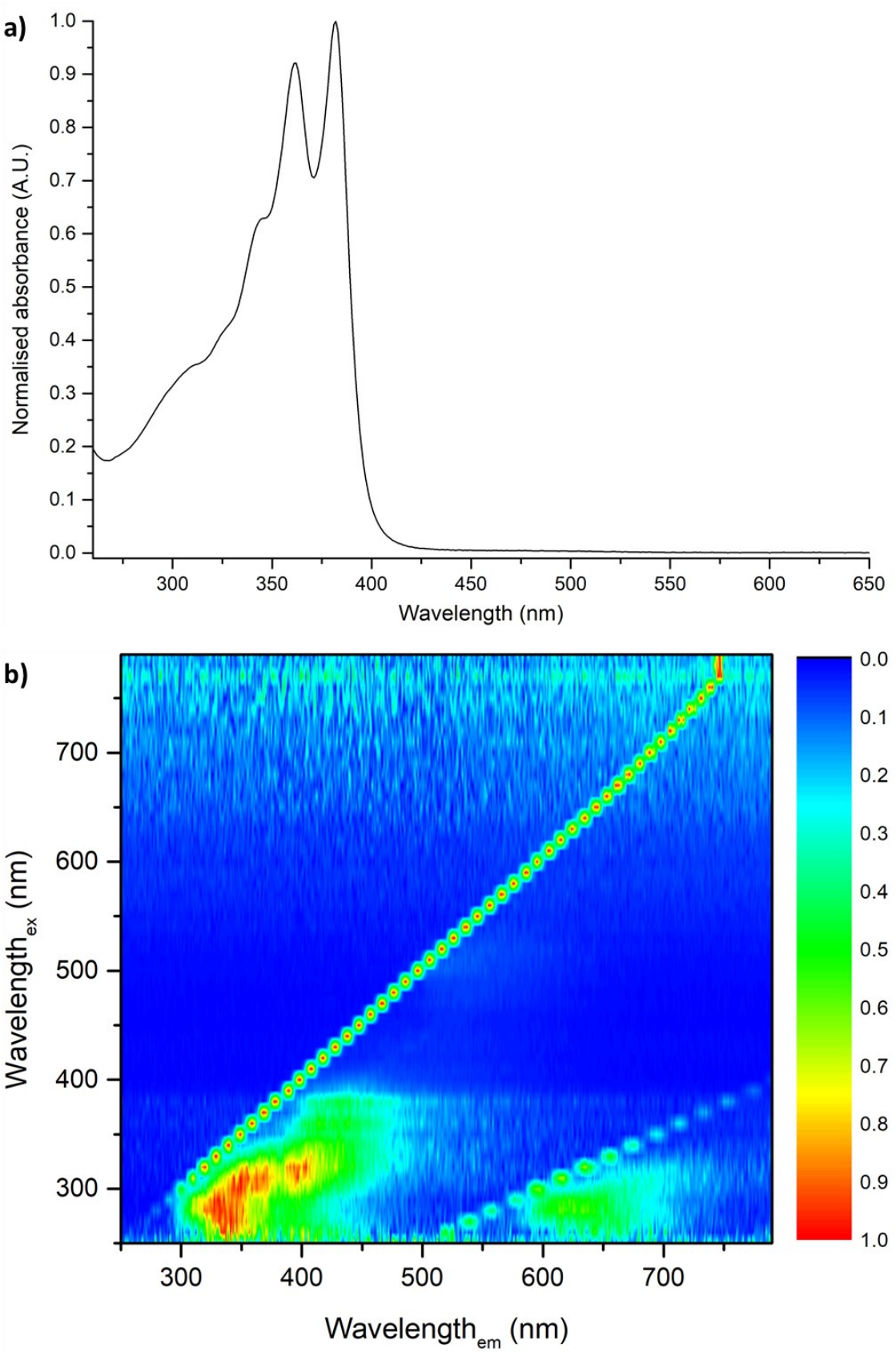

Figure 2.27. a) UV-visible and **b)** fluorescence excitation-emission matrix map of compound **6** (10 µM in DMSO).

The absorption spectrum (a) of compound **6** shows the characteristic bands of the NDI-core at around 360 and 380 nm. The band belonging to the DFO at 225 nm[80] is not shown because of the experimental setup of the used spectrometer.

The fluorescence EEM map (b) highlights strong emissions between 300 and 400 nm when excited between 250 and 400 nm. These emissions can be attributed to the NDI core which can be compared to the spectra of the NDI derivative (**11**) shown in Figure 2.11b. In this DFO-derivative the emission bands of the NDI core are less intense than compound **11**. The ranges above 500 nm and onwards are affected by the second-order Rayleigh scattering[81], whilst the region above 600 nm was due to noise. The molar extinction coefficient (ε) is 69000 L mol^{-1} cm^{-1}, calculated at the maximum absorbance (382 nm); whilst the quantum yield (Φ) is 0.32, using rhodamine B as standard (2.6 nM in MeOH; Φ=0.70±0.02; λ_{ex}=348 nm; η=1.33)[43].

Compound **6** could be used as a ligand to complex radiometals such as ^{68}Ga and ^{89}Zr. In particular, ^{68}Ga has shown dual modality of use for either PET and fluorescence imaging for prostate cancer detection. Preliminary studies in living prostate cancer (PC-3) were carried out using confocal laser-scanning microscopy to evaluate the cellular uptake and fluorescence emission of the compound **6**. Figure 2.28 shows the micrographs obtained by CLSM of compound **6** incubated for 20 minutes in PC-3 cells at 37 ºC.

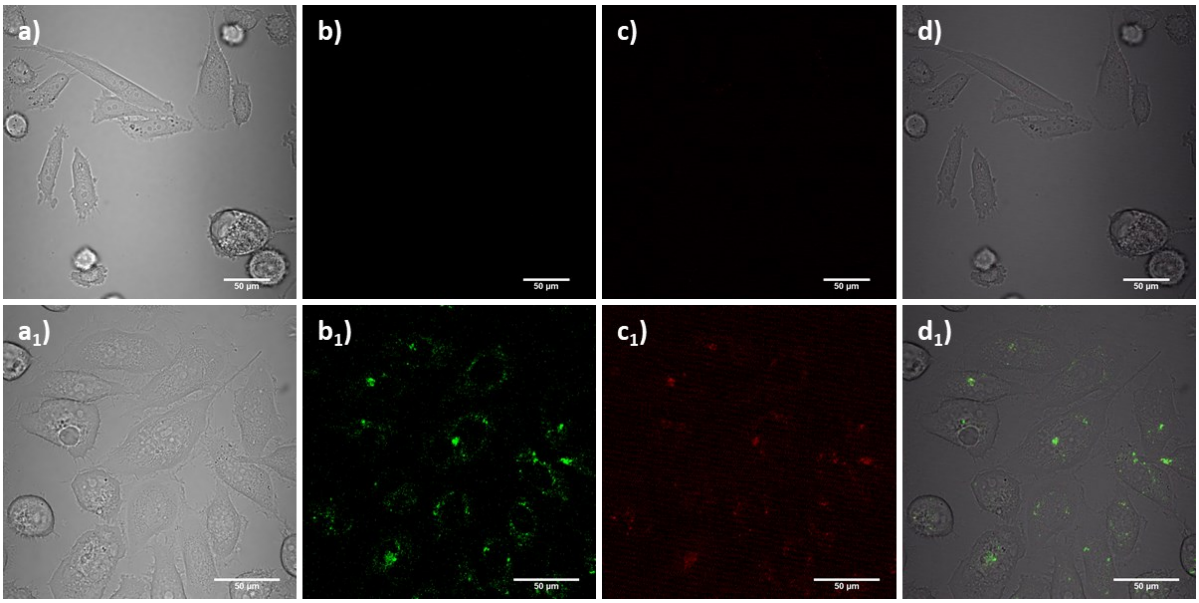

Figure 2.28. Single-photon confocal laser-scanning microscopy of PC-3 cells incubated at 37 °C for 20 min with **a-d)** DMSO (1:99 DMSO: serum free-medium) and **a1-d1)** compound **6** (0.1mM, 1:99 DMSO: serum free-medium). **a,a1)** TD channel; **b,b1)** green channel (λ_{em}=500–550 nm); **c,c1)** red channel (λ_{em}=570–750 nm; **d,d1)** overlay of TD-green-red channels. λ_{ex}=488.0 nm. Scale bar: 50 µm.

The micrographs a-c) in Figure 2.28 shows the negative control of PC-3 cells incubated with DMSO in serum-free medium to exclude any autofluorescence of the cells. The compound presents weak fluorescence emissions in the range of 500 and 550 nm (green channel) and 570-750 nm (red channel) at the excitation wavelength of 488 nm (complete CLSM micrographs in Appendices, Figure A.21). However, compound **6** can distribute on the cytosol of the cells, noticeable from the micrographs in Figure 2.28d$_1$. These results can be used for future work to compare the free ligand **6** with a Ga metal complex to evaluate the fluorescence emission in prostate cancer cells.

The complexation of the Zr(IV) was attempted as a proof-of-concept for the radiolabelling with ^{89}Zr(IV) for PET imaging application. The synthesis was adapted from Patra *et al.*[82] which is schematically shown in Scheme 2.10. The protocol involved the dissolution of the ligand **6** in anhydrous methanol and zirconium(IV) chloride under anhydrous conditions. The mixture was left to react for 2 hours at room temperature. The species isolated from the synthesis was characterised by mass spectrometry and ^{1}H-NMR with no positive result with the proposed species.

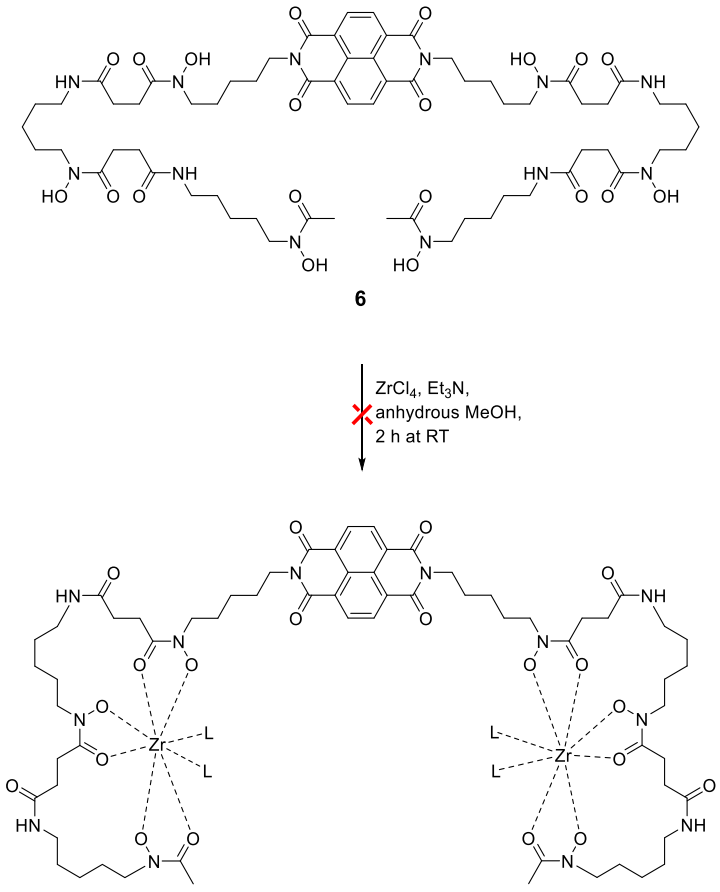

Scheme 2.10. Reaction scheme of the attempted complexation of Zr(IV).

2.6. Conclusions to Chapter 2

In this Chapter, the synthesis of novel fluorescent and functionalised ATSM-based ligand, linked in a naphthalenediimide scaffold, was reported. Besides, a previously studied BODIPY-derivative was incorporated on the NDI-core which was used for fluorescent labelling of molecules. Thiosemicarbazones have been studied since 1950s thanks to their ability to complex different metal cations and their cytotoxicity. Such proposed ligand was obtained thanks to microwave-assisted reactions which has revealed a fast, reliable and high yield method.

Considering the potential therapeutic and imaging applications of divalent ions of copper, nickel and zinc, such cations were complexed by the proposed fluorescent ligand and compared with their well-known ATSM versions by infrared, UV-visible and fluorescence spectroscopies and cyclic voltammetry.

Confocal laser scanning microscopy was used to assess the fluorescence emission of such fluorescent metal complexes in living prostate cancer cells and in addition to evaluate qualitatively their localisation and uptake into the cells.

Two-photon time-correlated single-photon counting (TCSPC) and fluorescence lifetime imaging microscopy (FLIM) have recently become powerful tools to investigate biological processes and distribution of novel fluorophores. In this regard, the free fluorescent ligand and its copper(II) complex were investigated by TCSPC to estimate their lifetime and aggregation in solutions in different solvent systems. In the mixture of 1:1 DMSO:H_2O, the lifetime distributions of the free ligand and its Cu(II) complex presented a substantial difference which was not noticed in the DMSO solutions. The FLIM study of these species in living CHO cells revealed that the copper(II) complex statistically presents a shorter lifetime distribution than the free ligand.

The Cu(II), Ni(II) and Zn(II) fluorescent complexes were evaluated by MTT assays to evaluate their cytotoxicity in living prostate cancer cells. Such metal complexes and their free ligand presented low toxicity in those cell line.

[Cu(ATSM)] is a well-known therapeutic agent which exploit its redox feature in hypoxic conditions. The proposed fluorescent copper(II) complex was investigated by confocal laser-scanning microscopy in both normoxia and hypoxia conditions in different cell lines.

This study revealed that such metal complex undergoes to a fluorescence enhance when in lack of oxygen conditions.

Another study was carried out by confocal laser scanning microscopy interfaced with FLIM in which the copper(II) metal complex was incubated in CHO cell line under hypoxic conditions and analysed over time. The mean fluorescence intensity of this complex decreased within 1 hour of investigation; on the other hand, its lifetime distribution did not change in this period of time.

To improve the targeting of these ATSM complexes, a novel targeting NDI-based ATSM ligand was proposed. This compound presents the [7-13] fragment of bombesin peptide which has been studied to detect and target prostate cancer cells. This proposed compound will be further analysed to assess its optical characteristics by UV-visible and fluorescence spectroscopies in solution. Thanks to the presence of GRPRs-targeting peptide and the ATSM moiety which can complex the copper(II) ions, this novel compound will be studied for its potential targeting for PCa cell under hypoxic conditions, using fluorescence microscopies.

Since recent years, ^{68}Ga and ^{89}Zr have been used for molecular imaging applications upon incorporation within different ligands (as potential imaging probes for PET/CT), their coordination chemistry towards the new ligands of interest have been explored in model studies. One of the most used ligands is DFO for both radioisotopes thanks to its hexadentate nature which fit the coordination sphere of ^{68}Ga(III) and ^{89}Zr(IV). In this regard, a double DFO moiety on an NDI scaffold is proposed and preliminarily investigated as a proof-of-concept for future radiolabelling.

2.7. References to Chapter 2

1. T. S. Lobana, R. Sharma, G. Bawa and S. Khanna, *Coord. Chem. Rev.*, 2009, **253**, 977-1055.
2. J. R. Dilworth and R. Hueting, *Inorg. Chim. Acta*, 2012, **389**, 3-15.
3. I. H. Hall, C. B. Lackey, T. D. Kistler, J. S. Ives, H. Beraldo, L. J. Ackerman and D. X. West, *Arch. Pharm.*, 2000, **333**, 217-225.
4. B. M. Paterson and P. S. Donnelly, *Chem. Soc. Rev.*, 2011, **40**, 3005-3018.
5. J. S. Lewis, R. Laforest, T. L. Buettner, S.-K. Song, Y. Fujibayashi, J. M. Connett and M. J. Welch, *Proc. Natl. Acad. Sci. USA*, 2001, **98**, 1206-1211.
6. A. L. Vāvere and J. S. Lewis, *Dalton Trans.*, 2007, 4893-4902.
7. D. Dayal, D. Palanimuthu, S. V. Shinde, K. Somasundaram and A. G. Samuelson, *J. Biol. Inorg. Chem.*, 2011, **16**, 621-632.
8. A. E. Stacy, D. Palanimuthu, P. V. Bernhardt, D. S. Kalinowski, P. J. Jansson and D. R. Richardson, *J. Med. Chem.*, 2016, **59**, 4965-4984.
9. G. Pelosi, F. Bisceglie, F. Bignami, P. Ronzi, P. Schiavone, M. C. Re, C. Casoli and E. Pilotti, *J. Med. Chem.*, 2010, **53**, 8765-8769.
10. A. Akbari, H. Ghateazadeh, R. Takjoo, B. Sadeghi-Nejad, M. Mehrvar and J. T. Mague, *J. Mol. Struct.*, 2019, **1181**, 287-294.
11. C. Balachandran, J. Haribabu, K. Jeyalakshmi, N. S. P. Bhuvanesh, R. Karvembu, N. Emi and S. Awale, *J. Inorg. Biochem.*, 2018, **182**, 208-221.
12. G. Ulrich, R. Ziessel and A. Harriman, *Angew. Chem. Int. Ed.*, 2008, **47**, 1184-1201.
13. T. Kowada, H. Maeda and K. Kikuchi, *Chem. Soc. Rev.*, 2015, **44**, 4953-4972.
14. P. A. Waghorn, M. W. Jones, M. B. M. Theobald, R. L. Arrowsmith, S. I. Pascu, S. W. Botchway, S. Faulkner and J. R. Dilworth, *Chem. Sci.*, 2013, **4**, 1430-1441.
15. F. Cortezon-Tamarit, S. Sarpaki, D. G. Calatayud, V. Mirabello and S. I. Pascu, *Chem. Rec.*, 2016, **16**, 1380-1397.
16. M. Al Kobaisi, S. V. Bhosale, K. Latham, A. M. Raynor and S. V. Bhosale, *Chem. Rev.*, 2016, **116**, 11685-11796.
17. C. L. Lyall, C. C. Shotton, M. Pérez-Salvia, G. Dan Pantoş and S. E. Lewis, *Chem. Comm.*, 2014, **50**, 13837-13840.
18. P. Pengo, G. D. Pantoş, S. Otto and J. K. M. Sanders, *J. Org. Chem.*, 2006, **71**, 7063-7066.
19. G. M. Prentice, L. Emmett, V. Luxami and G. D. Pantoş, in *Naphthalenediimide and its Congeners: From Molecules to Materials*, ed. G. D. Pantoş, The Royal Society of Chemistry, 2017.
20. R. Rowe, S. Mathers, G. Smith, E. Windebank, M.-L. Rogers, K. Noel and C. S. Rosenfeld, *Amyotroph. Lat. Scl. Fr.*, 2018, **19**, 264-281.

21. C. A. Calvary, O. Hietsoi, J. M. Strain, M. S. Mashuta, J. M. Spurgeon, R. M. Buchanan and C. A. Grapperhaus, *Eur. J. Inorg. Chem.*, 2019, **2019**, 3782-3790.

22. E. Palma, H. M. Botelho, G. R. Morais, I. Rodrigues, I. C. Santos, M. P. C. Campello, P. Raposinho, A. Belchior, S. S. Gomes, M. F. Araújo, I. Correia, N. Ribeiro, S. Gama, F. Mendes and A. Paulo, *J. Biol. Inorg. Chem.*, 2019, **24**, 71-89.

23. P. D. Bonnitcha, S. R. Bayly, M. B. M. Theobald, H. M. Betts, J. S. Lewis and J. R. Dilworth, *J. Inorg. Biochem.*, 2010, **104**, 126-135.

24. D. Muller, I. Zeltser, G. Bitan and C. Gilon, *J. Org. Chem.*, 1997, **62**, 411-416.

25. B. M. Paterson, J. A. Karas, D. B. Scanlon, J. M. White and P. S. Donnelly, *Inorg. Chem.*, 2010, **49**, 1884-1893.

26. K. Tambara, N. Ponnuswamy, G. Hennrich and G. D. Pantoş, *J. Org. Chem.*, 2011, **76**, 3338-3347.

27. S. Iwaki, K. Hokamura, M. Ogawa, Y. Takehara, Y. Muramatsu, T. Yamane, K. Hirabayashi, Y. Morimoto, K. Hagisawa, K. Nakahara, T. Mineno, T. Terai, T. Komatsu, T. Ueno, K. Tamura, Y. Adachi, Y. Hirata, M. Arita, H. Arai, K. Umemura, T. Nagano and K. Hanaoka, *Org. Biomol. Chem.*, 2014, **12**, 8611-8618.

28. J. L. Dearling, J. S. Lewis, G. E. Mullen, M. J. Welch and P. J. Blower, *J. Biol. Inorg. Chem.*, 2002, **7**, 249-259.

29. D. X. West, J. S. Ives, G. A. Bain, A. E. Liberta, J. Valdés-Martínez, K. H. Ebert and S. Hernández-Ortega, *Polyhedron*, 1997, **16**, 1895-1905.

30. D. A. Köse and H. Necefoğlu, *J. Therm. Anal. Calorim.*, 2008, **93**, 509-514.

31. N. Elgrishi, K. J. Rountree, B. D. McCarthy, E. S. Rountree, T. T. Eisenhart and J. L. Dempsey, *J. Chem. Educ.*, 2018, **95**, 197-206.

32. S. I. Pascu, P. A. Waghorn, B. W. C. Kennedy, R. L. Arrowsmith, S. R. Bayly, J. R. Dilworth, M. Christlieb, R. M. Tyrrell, J. Zhong, R. M. Kowalczyk, D. Collison, P. K. Aley, G. C. Churchill and F. I. Aigbirhio, *Chem. Asian J.*, 2010, **5**, 506-519.

33. C. J. Jones and J. A. McCleverty, *J. Chem. Soc. A*, 1970, 2829-2836.

34. J. J. Sirois, L. Padgitt-Cobb, M. A. Gallegos, J. S. Beckman, C. M. Beaudry and J. K. Hurst, *Inorg. Chem.*, 2018, **57**, 8923-8932.

35. J. P. Holland, J. C. Green and J. R. Dilworth, *Dalton Trans.*, 2006, 783-794.

36. A. R. Cowley, J. R. Dilworth, P. S. Donnelly and J. M. White, *Inorg. Chem.*, 2006, **45**, 496-498.

37. N. V. Ghule, D. D. La, R. S. Bhosale, M. Al Kobaisi, A. M. Raynor, S. V. Bhosale and S. V. Bhosale, *ChemistryOpen*, 2016, **5**, 157-163.

38. F. Salerno, J. A. Berrocal, A. T. Haedler, F. Zinna, E. W. Meijer and L. Di Bari, *J. Mater. Chem. C*, 2017, **5**, 3609-3615.

39. V. Saravanan and P. Rajakumar, *New J. Chem.*, 2018, **42**, 2504-2512.

40. C. Göl, M. Malkoç, S. Yeşilot and M. Durmuş, *Dalton Trans.*, 2014, **43**.

41. A. Periasamy and R. M. Clegg, *FLIM microscopy in biology and medicine*, Chapman and Hall (CRC press), Boca Raton, Florida, 2009.

42. A. T. R. Williams, S. A. Winfield and J. N. Miller, *Analyst*, 1983, **108**, 1067-1071.

43. A. M. Brouwer, *Pure Appl. Chem.*, 2011, **83**, 2213-2228.

44. H. Ge, F. Cortezon-Tamarit, H.-C. Wang, A. C. Sedgwick, R. L. Arrowsmith, V. Mirabello, S. W. Botchway, T. D. James and S. I. Pascu, *Nanoscale*, 2019, **11**, 9498-9507.

45. T. Förster, *Ann. Phys.*, 1948, **437**, 55-75.

46. S. E. Braslavsky, *pac*, 2007, **79**, 293.

47. W. Becker, in *The bh TCSPC Handbook*, Becker & Hickl GmbH, Berlin, Germany, 2017.

48. T. L. Riss, R. A. Moravec, A. L. Niles, S. Duellman, H. A. Benink, T. J. Worzella and L. Minor, *Cell Viability Assays*, Eli Lilly & Company and the National Center for Advancing Translational Sciences; 2004-, 2013.

49. J. W. Lee, J. Ko, C. Ju and H. K. Eltzschig, *Exp. Mol. Med.*, 2019, **51**, 68.

50. P. Vaupel and A. Mayer, *Cancer Metastasis Rev.*, 2007, **26**, 225-239.

51. Q. Cai, T. Yu, W. Zhu, Y. Xu and X. Qian, *Chem. Comm.*, 2015, **51**, 14739-14741.

52. S. Lim, K. A. Price, S.-F. Chong, B. M. Paterson, A. Caragounis, K. J. Barnham, P. J. Crouch, J. M. Peach, J. R. Dilworth, A. R. White and P. S. Donnelly, *J. Biol. Inorg. Chem.*, 2010, **15**, 225-235.

53. S. Takahashi, W. Piao, Y. Matsumura, T. Komatsu, T. Ueno, T. Terai, T. Kamachi, M. Kohno, T. Nagano and K. Hanaoka, *J. Am. Chem. Soc.*, 2012, **134**, 19588-19591.

54. K. Kiyose, K. Hanaoka, D. Oushiki, T. Nakamura, M. Kajimura, M. Suematsu, H. Nishimatsu, T. Yamane, T. Terai, Y. Hirata and T. Nagano, *J. Am. Chem. Soc.*, 2010, **132**, 15846-15848.

55. Z. Xiao, P. S. Donnelly, M. Zimmermann and A. G. Wedd, *Inorg. Chem.*, 2008, **47**, 4338-4347.

56. Cancer Research UK, https://www.cancerresearchuk.org/health-professional/cancer-statistics/incidence/common-cancers-compared, (accessed 23/01, 2019).

57. C. Conte, F. Mastrotto, V. Taresco, A. Tchoryk, F. Quaglia, S. Stolnik and C. Alexander, *J. Control. Release*, 2018, **277**, 126-141.

58. E. J. Sayers, J. P. Magnusson, P. R. Moody, F. Mastrotto, C. Conte, C. Brazzale, P. Borri, P. Caliceti, P. Watson, G. Mantovani, J. Aylott, S. Salmaso, A. T. Jones and C. Alexander, *Bioconjugate Chem.*, 2018, **29**, 1030-1046.

59. H. Chen, Q. Bi, Y. Yao and N. Tan, *J. Mater. Chem. B*, 2018, **6**, 4351-4359.

60. P. S. Donnelly, A. Caragounis, T. Du, K. M. Laughton, I. Volitakis, R. A. Cherny, R. A. Sharples, A. F. Hill, Q.-X. Li, C. L. Masters, K. J. Barnham and A. R. White, *J. Biol. Chem.*, 2008, **283**, 4568-4577.

61. H. Sunahara, Y. Urano, H. Kojima and T. Nagano, *J. Am. Chem. Soc.*, 2007, **129**, 5597-5604.

62. R. Mansi, R. Minamimoto, H. Mäcke and A. H. Iagaru, *J. Nucl. Med.*, 2016, **57**, 67S-72S.

63. D. Pooja, A. Gunukula, N. Gupta, D. J. Adams and H. Kulhari, *Int. J. Biochem. Cell Biol.*, 2019, **114**, 105567.

64. L. B. Retzloff, L. Heinzke, S. D. Figureoa, S. V. Sublett, L. Ma, G. L. Sieckman, T. L. Rold, I. Santos, T. J. Hoffman and C. J. Smith, *Anticancer Res.*, 2010, **30**, 19-30.

65. R. B. Merrifield, *J. Am. Chem. Soc.*, 1963, **85**, 2149-2154.

66. S. L. Pedersen, K. K. Sørensen and K. J. Jensen, *J. Pept. Sci.*, 2010, **94**, 206-212.

67. S. L. Pedersen, A. P. Tofteng, L. Malik and K. J. Jensen, *Chem. Soc. Rev.*, 2012, **41**, 1826-1844.

68. D. A. Wellings and E. Atherton, in *Methods in Enzymology*, Academic Press, 1997, vol. 289, pp. 44-67.

69. E. Valeur and M. Bradley, *Chem. Soc. Rev.*, 2009, **38**, 606-631.

70. A. Biosystems, *Technical Bulletin*, 1998, 1-12.

71. C. J. Anderson and M. J. Welch, *Chem. Rev.*, 1999, **99**, 2219-2234.

72. C. F. Ramogida and C. Orvig, *Chem. Comm.*, 2013, **49**, 4720-4739.

73. M. Conti and L. Eriksson, *Eur. J. Nucl. Med. Mol. Imaging Phys.*, 2016, **3**, 8-8.

74. W. A. P. Breeman, E. de Blois, H. Sze Chan, M. Konijnenberg, D. J. Kwekkeboom and E. P. Krenning, *Seminars in Nuclear Medicine*, 2011, **41**, 314-321.

75. M. A. Deri, B. M. Zeglis, L. C. Francesconi and J. S. Lewis, *Nuclear Medicine and Biology*, 2013, **40**, 3-14.

76. T. Almasi, K. Jabbari, N. Gholipour, A. Mokhtari Kheirabadi, D. Beiki, P. Shahrokhi and M. Akhlaghi, *Int. J. Biol. Macromol.*, 2019, **125**, 915-921.

77. W. A. P. Breeman, M. de Jong, E. de Blois, B. F. Bernard, M. Konijnenberg and E. P. Krenning, *Eur. J. Nucl. Med. Mol. Imaging*, 2005, **32**, 478-485.

78. Z. Liu, G. Niu, F. Wang and X. Chen, *Eur. J. Nucl. Med. Mol. Imaging*, 2009, **36**, 1483-1494.

79. I. S. Alam, R. L. Arrowsmith, F. Cortezon-Tamarit, F. Twyman, G. Kociok-Köhn, S. W. Botchway, J. R. Dilworth, L. Carroll, E. O. Aboagye and S. I. Pascu, *Dalton Trans.*, 2016, **45**, 144-155.

80. T. Filipský, M. Říha, R. Hrdina, K. Vávrová and P. Mladěnka, *Bioorg. Chem.*, 2013, **49**, 1-8.

81. Y.-Q. Li, F. Qian and Z. Li, *Chemical Journal on Internet*, 2000, **2**, 29-36.

82. M. Patra, A. Bauman, C. Mari, C. A. Fischer, O. Blacque, D. Häussinger, G. Gasser and T. L. Mindt, *Chem. Comm.*, 2014, **50**, 11523-11525.

83. S. E. Lapi, J. S. Lewis, F. Dehdashti, *Semin. Nucl. Med.*, 2015, **45**, 177-185.

84. E. A. Pérès, J. Toutain, L.-P. Paty, D. Divoux, M. Ibazizène, S. Guillouet, L. Barré, A. Vidal, M. Cherel, M. Bourgeois, M. Bernaudin, S. Valable, *EJNMMI Research*, 2019, **9**, 1-15.

85. Z.Xiao, P. S. Donnelly, M.Zimmermann, A. G. Wedd, *Inorg. Chem.*, 2008, **47**, 4338-4347.

86. A. N. Kate, A. A. Kumbhar, A. A. Khan, P. V. Joshi, V. G. Puranik, *Bioconjugate Chem.*, 2014, **25**, 102-114.

87. A. R. Cowley, J. Davis, J. R. Dilworth, P. S. Donnelly, R. Dobson, A. Nightingale, J. M. Peach, B. Shore, D. Kerrb, L. Seymour, *Chem. Comm.*, 2005, 845-847.

88. J. L. Hickey, J. L. James, C. A. Henderson, K. A. Price, A. I. Mot, G. Buncic, P. J. Crouch, J. M. White, A. R. White, T. A. Smith, P. S. Donnelly, *Inorg. Chem.*, 2015, **54**, 9556-9567.

89. M. Colombié, S. Gouard, M.Frindel, A. Vidal, M. Chérel, F. Kraeber-Bodéré, C. Rousseau, M. Bourgeois, *Front. Med.*, 2015, **2**, 58.

90. B. E. Rogers, M. E. Rosenfeld, M. B. Khazaeli, G. Mikheeva, M. A. Stackhouse, T. Liu, D. T. Curiel and D. J. Buchsbaum, *J. Nucl. Med.*, 1997, **38**, 1221-1229.

91. A. Safavy, K. P. Raisch, M. B. Khazaeli, D. J. Buchsbaum and J. A. Bonner, *J. Med. Chem.*, 1999, **42**, 4919-4924.

92. R. Codd, T. Richardson-Sanchez, T. J. Telfer, M. P. Gotsbacher, *ACS Chem. Biol.*, 2018, **13**, 11-25.

93. Y. Wu, T. Qiu, Y. Wang, H. Liu, W. Sun, W. Dong, G. Mailhot, *Environ. Sci. Pollut. Res. Int.*, 2020, 1-7.

94. Y. Zhang, H. Hong, G. W. Severin, J. W. Engle, Y. Yang, S. Goel, A. J. Nathanson, G. Liu, R. J. Nickles, B. R. Leigh, T. E. Barnhart, W. Cai, *Am. J. Transl. Res.*, 2012, **4**, 333-346.

Chapter 3: *Pseudo*rotaxanes for potential imaging application

3.1. Overview to Chapter 3

In this Chapter, the design of novel *pseudo*rotaxane consisting of a 1,5-dinaphtho-crown ether and different symmetric NDI-based "axles" with fluorescent properties will be presented. The formation of two *pseudo*rotaxanes will be preliminarily investigated as a proof-of-concept of a useful tool for bioimaging.

Rotaxanes are complex architectures held by weak interactions such as hydrogen bonds, electrostatic and Van der Waals forces[1] able to spontaneously assembly and organise[2]. A rotaxane is a kinetically trapped architecture between an "axle" and a "wheel". Generally, the "axle" presents bulky terminal groups, larger than the internal diameter of the "wheel", which prevent the dissociation of the complex. Such complex architectures have been classified as mechanically interlocked molecules (MIMs).

In the last decade, rotaxanes have been found a wide range of applications such as catalysts[3], chemical sensors[4], polymers[5], molecular switches[6] and motors[7]. Recently, rotaxanes have been explored in biological systems for drug delivery[8], targeting bacterial protein[9] and releasing bioactive peptides[10]. These architectures have also exhibited chemiluminescent properties and found applications in the field of biological imaging. Different works have explored the optical and fluorescent properties of rotaxane for MRI agent[11], mitochondrial stainer[12] and fluorescent dye[13].

In recent publications, derivatives of dinaphtho-crown ether have been widely used to create different assemblies[14]. The peculiarity of such supramolecular building blocks is the presence of the dinaphthalene units which can interact with aromatic electron-deficient "axles"[14]. In addition, the ethylene glycol chains act as a template for the formation of catenanes or *pseudo*-rotaxane[15] thanks to their nature as hydrogen bond acceptors.

Figure 3.1 presents the designed *pseudo*rotaxanes consisting of a common "wheel", *i.e.* 1,5-dinaphtho-crown ether, and different symmetric NDI-based "axles" with fluorescent properties.

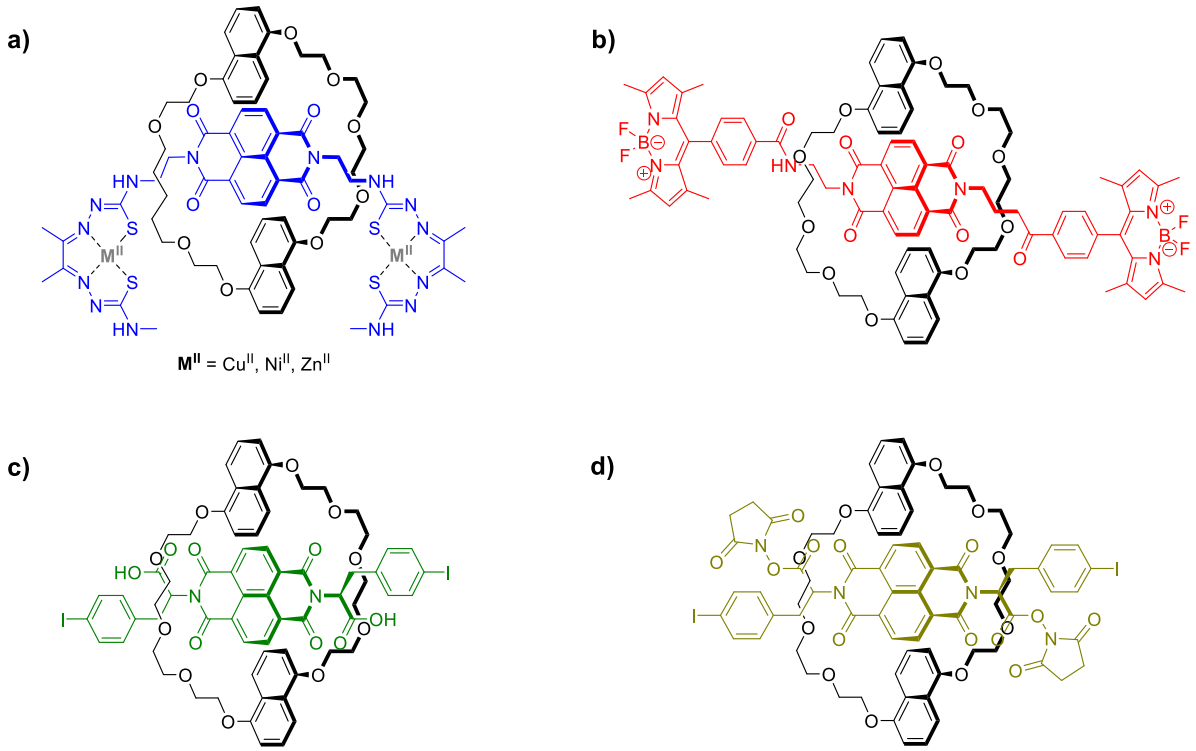

Figure 3.1. Structural representation of the *pseudo*rotaxanes proposed in this Chapter with a 1,5-dinaphtho-crown ether "wheel" (in black). **a)** NDI-based "axle" with ATSM tags (in blue); **b)** NDI-based "axle" labelled with the BODIPY derivative **2** (in red); **c** and **d)** NDI-based "axles" with amino acid-derivative tags (in green and yellow).

3.2. Synthesis and characterisation of the dinaphtho-crown ether "wheel"

The discovery of crown ethers, over 40 years ago by Pedersen, has brought the concept of host-guest chemistry in the research field. This class of compound can complex Group I and II metal cations and participate in molecular recognition and self-assembly processes. Particularly, crown ethers with fused aromatic rings, which are π electron-rich, can act as receptors for π electron-poor species[14]. Among the popular aromatic crown ethers, 1,5-dinaphtho[38]crown-10 has been explored with different aromatic electron-deficient substrates to create mechanically interlocked molecules (MIMs).

Scheme 3.1 reports the reaction pathway for the synthesis of 1,5-dinaphtho[38]crown-10 (**7**), based on Stoddart *et al.*[14] and Sanders' *et al.*[15] works.

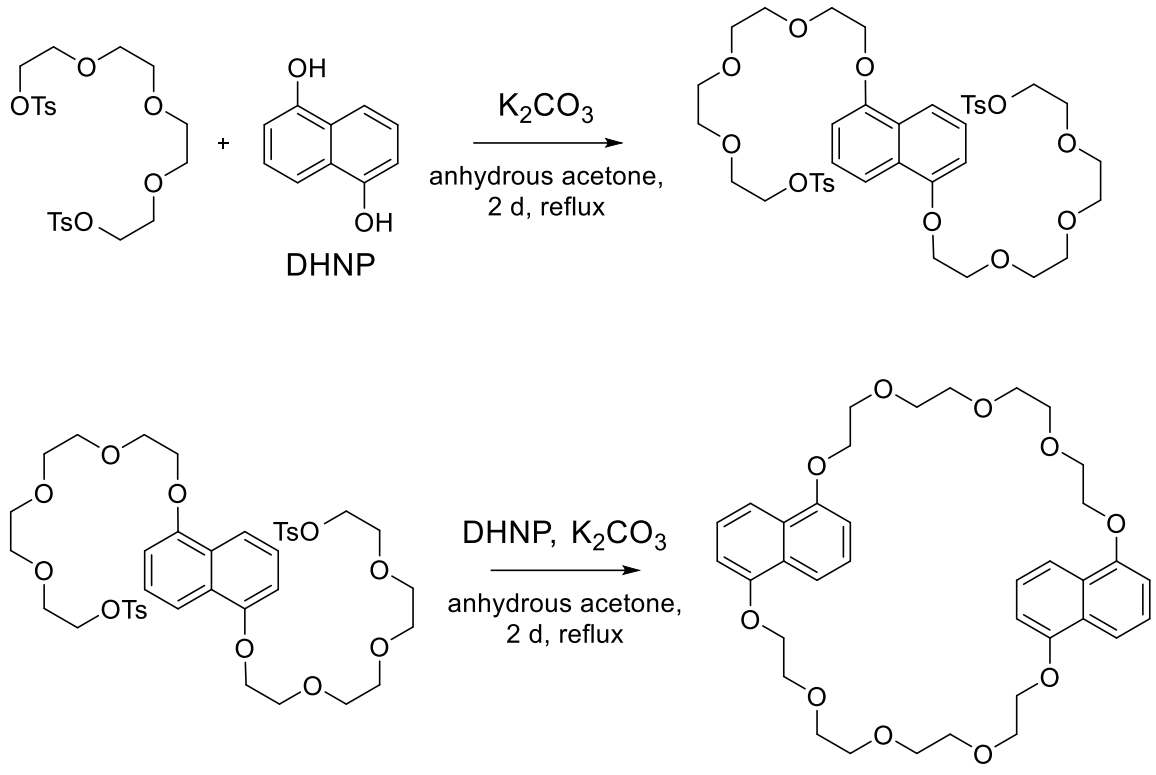

Scheme 3.1. Reaction scheme of the synthesis of the "wheel" **7.**

The synthesis of **7** involves a two-step reaction, consisting of the coupling of tetraethylene glycol ditosylate in a large excess of dihydroxynaphthalene (DHNP), in basic conditions. The presence of K^+ ions may have a template effect and control the formation of a monomeric species rather than polymeric species. The open version of **7** was purified by chromatographic column and then reacted with an equivalent of dihydroxynaphthalene in basic conditions.

The pure **7** was obtained by column chromatography and recrystallisation in methanol. Figure 3.2 shows the ^{1}H-NMR spectrum of pure "wheel" **7**.

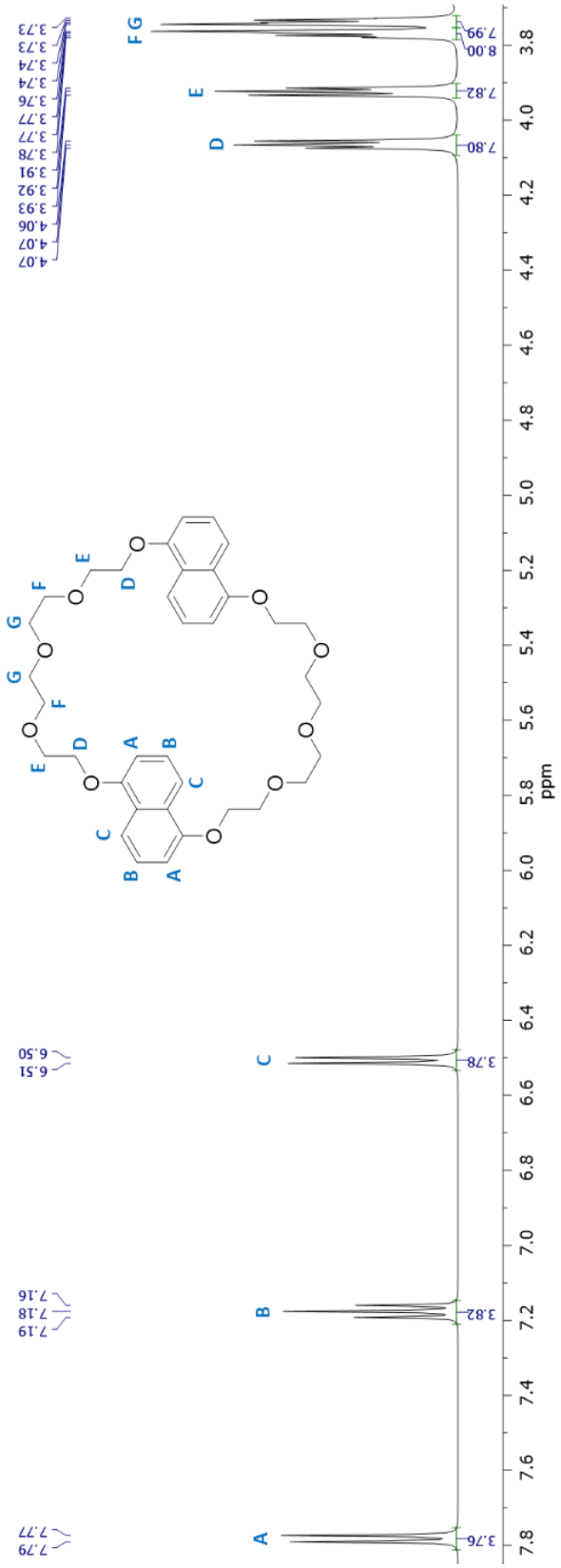

Figure 3.2. ^{1}H-NMR spectrum of compound **7** with corresponding assignments (500 MHz, $CDCl_3$).

The ^{1}H-NMR spectrum shows a pattern of resonances attributable to a symmetric compound. The signals of the naphthalene rings were assigned to: *i*) the doublet at 7.78 ppm (4 protons in *ortho*-position, *A*); *ii*) the double doublet at 7.18 ppm (4 protons in *meta*-position, *B*); *iii*) the doublet at 6.50 ppm is due to the 4 protons in *para*-position (*C*). The ethylene glycol chains directly linked to the naphthalene ring are characterised by the two triplets at 4.07 and 3.92 ppm (*D* and *E*, respectively). On the other hand, the two triplets at 3.77 and 3.73 ppm (F and G, respectively) are assignable to the central ethylene glycol moieties. The assignments were attributed through the correlations found in the ^{1}H-^{1}H COSY-NMR spectrum (shown in Appendices A, Figure A.28). Mass spectroscopy was used to assess the formation of a single unit of compound **7** (Appendices A, Figure A.36).

The optical features of **7** were investigated by UV-visible and fluorescence spectroscopies (spectra are shown in Appendices A, Figure A.41). The absorption spectrum shows four relative maxima at 287, 298, 313 and 327 nm; on the other hand, the emission spectrum presents two relative maxima at 333 and 347 nm. The molar extinction coefficient and quantum yield are 30000 L mol^{-1} cm^{-1} and 0.001 (referred to *L*-tryptophan 0.1 μM in deionised H_2O at pH 6)[16].

3.3. Symmetric naphthalenediimide-based “axles” with fluorescent properties

The π electron-deficient aromatic rings of NDIs can suit the rich aromatic π-system of 1,5-dinaphtho-crown ether to create MIMs. In the last decade[14,15,17-20], several works have reported the formation of rotaxanes with NDI-based “axles” thanks to π-stacking interaction with the aromatic crown ether “wheels”. In this part of the Chapter, different NDI-based “axles” are presented as a proof-of-concept to create MIMs with the synthesised “wheel” **7** for potential biological applications.

3.3.1. Synthesis and characterisation of an ATSM-tagged “axle”

This NDI-based “axle” presents two TSC moieties in its two sides which could complex metal cations. The chosen TSC moiety is a derivative of the ligand diacetyl *bis*(N^4-methylthiosemicarbazone) (ATSM) which is well-known to be able to chelate different metal ions. The rationale to design such “axle” is to use metal ions to prevent the threading/de-threading equilibrium of the rotaxane, forming a molecular interlocked system.

The proposed "axle" (**8**) consists of two units of the ATSM-derivative **1**, synthesised and described in Chapter 2. Scheme 3.2 reports the synthesis of compound **8**.

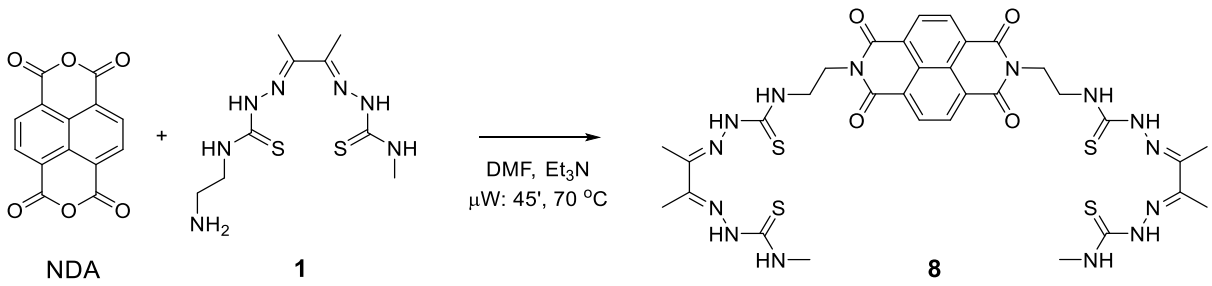

Scheme 3.2. Reaction scheme of the synthesis of the "axle" **8.**

The synthesis involved a microwave-assisted reaction of naphthalene dianhydride (NDA) and three equivalents of the ATSM-derivative **1** in dimethylformamide and catalytic triethylamine. The protocol was adapted from the work of Tambara *et al.*[21]. Compound **8** was obtained by filtration and characterised by ^{1}H-NMR spectroscopy (yield 61%) (Figure 3.3). Low-resolution mass spectrometry was used to characterise preliminarily the formed species (Appendices A, Figure A.37).

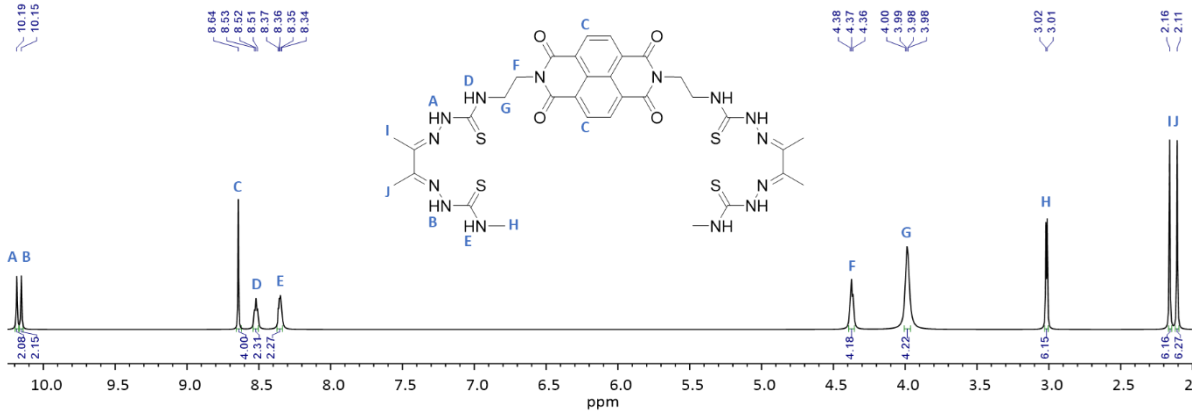

Figure 3.3. ^{1}H-NMR spectrum of compound **8** with assignments (500 MHz, DMSO-d_6).

The successful synthesis was demonstrated by the occurrence of a symmetric pattern in the NMR spectroscopy of this compound whereby resonances assignable to the 4 protons of the NDI core appeared as a singlet at 8.64 ppm. The protons assignable to the thiourea functional group were found as the singlets at 10.19 and 10.15 ppm and the quartets at 8.53 and 8.35 ppm. The signals assignable to the ethyl protons were presented as a triplet at 4.37 and a quartet at 3.99 ppm.

The methyl groups are characterised by the doublet resonance at 3.02 ppm and the two singlets at 2.16 and 2.11 ppm. The assignments were attributed through the correlations found in the ^{1}H-^{1}H COSY-NMR spectrum (shown in Appendices, Figure A.26)

Compound **8** was investigated by UV-visible and fluorescence spectroscopies (spectra are shown in Appendices A, Figure A.42). The UV-visible spectrum showed an intense absorption peak at 340 nm which belongs to the two moieties of **1** (Chapter 2, Figure 2.8a); on the other hand, the bands due to the electronic transition of the NDI core were covered by the absorption of the ATSM moiety. Only the band at 381 nm was slightly visible. The emission profile of **8** with an excitation wavelength of 340 nm presented a band centred at 423 nm. The molar extinction coefficient and quantum yield are 51800 L mol^{-1} cm^{-1} and 0.002 (referred to rhodamine B 2.6 nM in MeOH)[16].

The "axle" **8** was investigated in living prostate cancer cells (PC-3) by confocal laser-scanning microscopy in 0.1 mM (1:99 DMSO:serum-free medium), after overnight incubation at 37 °C. The collected micrographs are shown in Appendices A, Figure A.44. Compound **8** shows weak fluorescence emissions in living PC-3 cells. The main emissions are in the emission ranges of the blue (417-477 nm), green (500-550 nm) and red channels (570-750 nm) when excited at 405 nm. Other emissions were found in the green and red channels of the excitation wavelength at 488 nm. The only emissions at the excitation wavelength of 561 nm were in the red channel.

The "axle" **8** was designed to incorporate the ATSM moieties, the well-known ligand for copper(II) ions and similar cations as described in Chapter 2. The complexation of Cu(II) followed the adapted protocol[22] presented in Chapter 2. Scheme 3.3 reports the synthetic conditions for the Cu(II) metal complex **8a**.

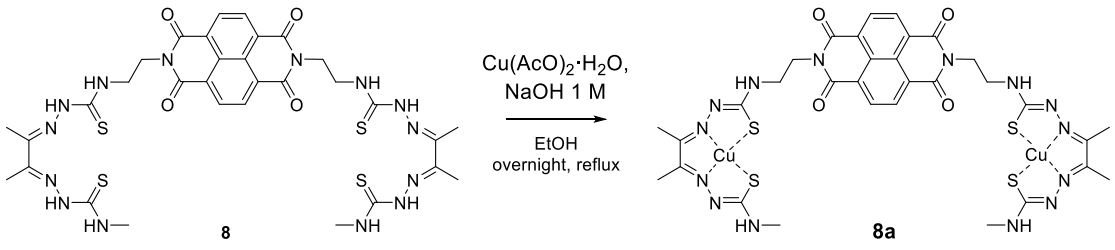

Scheme 3.3. Reaction scheme for the synthesis of compound **8a.**

The "axle" **8** was dissolved in ethanol and two equivalents of copper(II) acetate monohydrate were added. The mixture was basified with sodium hydroxide and left to react overnight under reflux.

Compound **8a** was obtained by filtration and preliminarily characterised by mass spectrometry (yield 42%). Figure 3.4 shows the theoretical (a) and observed data (b) of the $[M]^+$ ion for the exact mass of **8a** equals to 932.0362 Da. The observed isotopic pattern is similar to the theoretical data, suggesting the success of the incorporation of the two equivalent of Cu(II) cations.

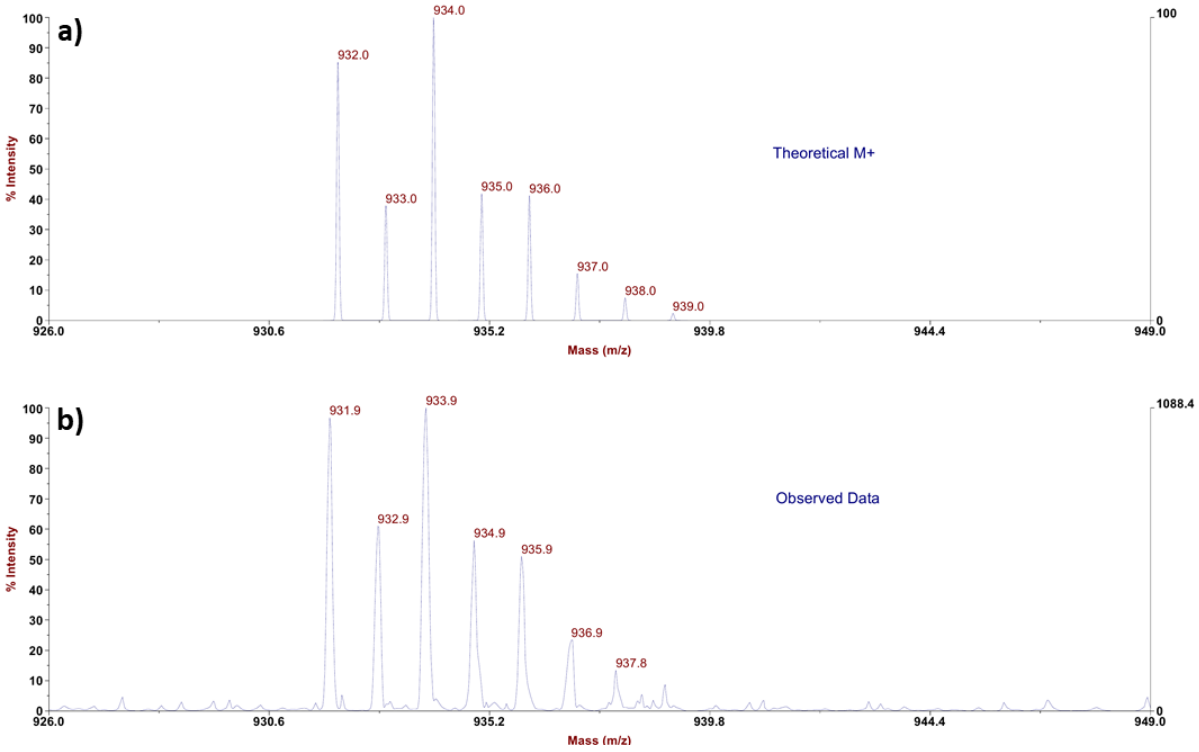

Figure 3.4. Solvent-free MALDI mass spectra with theoretical (a) and observed (b) isotopic patterns for $[M+H]^+$ ion of compound **8a**.

3.3.2. Synthesis and characterisation of a BODIPY-tagged "axle"

The following "axle" incorporates two units of the BODIPY derivative **2** investigated in Chapter 2. Such fluorescent labels are of interest as they are sufficiently bulky as to generate a thread/de-thread equilibrium with the "wheel" **7**. Moreover, the fluorescent BODIPY derivative **2** could enhance the fluorescent emission of the entire rotaxane. Scheme 3.4 reports the adapted synthetic protocol[21] for the fluorescent "axle" **9**.

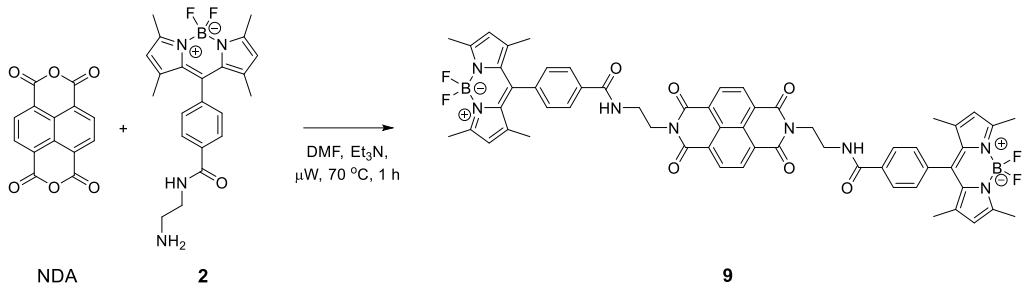

Scheme 3.4. Reaction scheme for the synthesis of the "axle" **9.**

The synthesis of **9** involved the coupling of NDA and two equivalents of the BODIPY derivative **2** in a microwave system in dimethylformamide and catalytic triethylamine. Compound **9** was obtained by filtration and characterised by ^{1}H-NMR (yield 73%) (Figure 3.5).

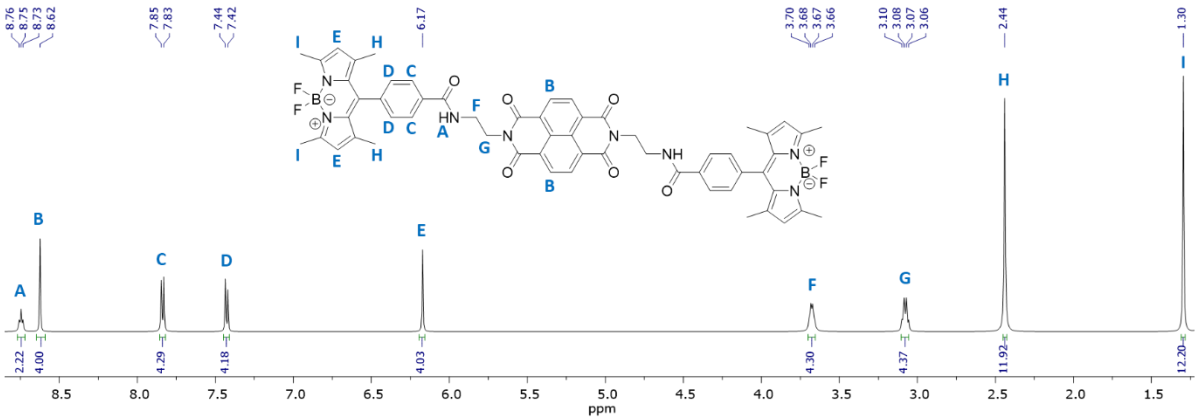

Figure 3.5. ^{1}H-NMR spectrum of compound **9** with assignments (500 MHz, DMSO-d_6).

The ^{1}H-NMR spectrum shows a symmetric pattern of signals which suggest the presence of two moieties of **2** linked to the NDI-core. The singlet at 8.62 belongs to the 4 protons of the aromatic rings of the NDI. The characteristic signals of the BODIPY core are the singlets at 6.17, 2.44 and 1.30 ppm which are assignable to the protons *E* and the 4 methyl groups (*H* and *I*)[23,24]. The triplet at 8.75, the doublets at 7.84 and 7.43 ppm, the quartet at 3.68 and the triplet at 3.08 ppm are signals of the aminoethyl benzamide spacer.

The optical characteristics of **9** were investigated by UV-visible and fluorescence spectroscopies. The absorption and emission spectra of **9** (10 μM solution in DMSO) are reported in Appendices A (Figure A.43). The UV-visible spectrum shows the bands of the aromatic transitions of the NDI core at 360 and 379 nm and the intense absorption band of the BODIPY-derivative **2** moieties at 500 nm.

The emission spectrum presents an intense band at 511 nm when excited at 500 nm. The molar extinction coefficient and quantum yield are 80000 L mol^{-1} cm^{-1} and 0.65, respectively (referred to fluorescein 2.3 nM in $NaOH_{(aq)}$ 0.1M)[16]. Comparing these data with the BODIPY and NDI derivatives (compounds **15** and **11** respectively discussed in Chapter 4), the axle **9** present higher quantum yield than **15** and **11** which can be more efficiently detectable *via* fluorescence microscopies. In addition, the spectral characteristics of the precursors (**15** and **11**) are maintained in compound **9**.

The fluorescence emission, uptake and localisation of compound **9** were preliminarily investigated by confocal laser-scanning microscopy (CLSM). The fluorescent "axle" **9** was incubated in PC-3 cells line for 20 minutes at 37 ºC and then analysed by CLSM. Figure 3.6 shows the obtained micrographs. The chosen cell line is used as a model to preliminarily evaluate the uptake and fluorescence emission of compound **9** in the cellular environment.

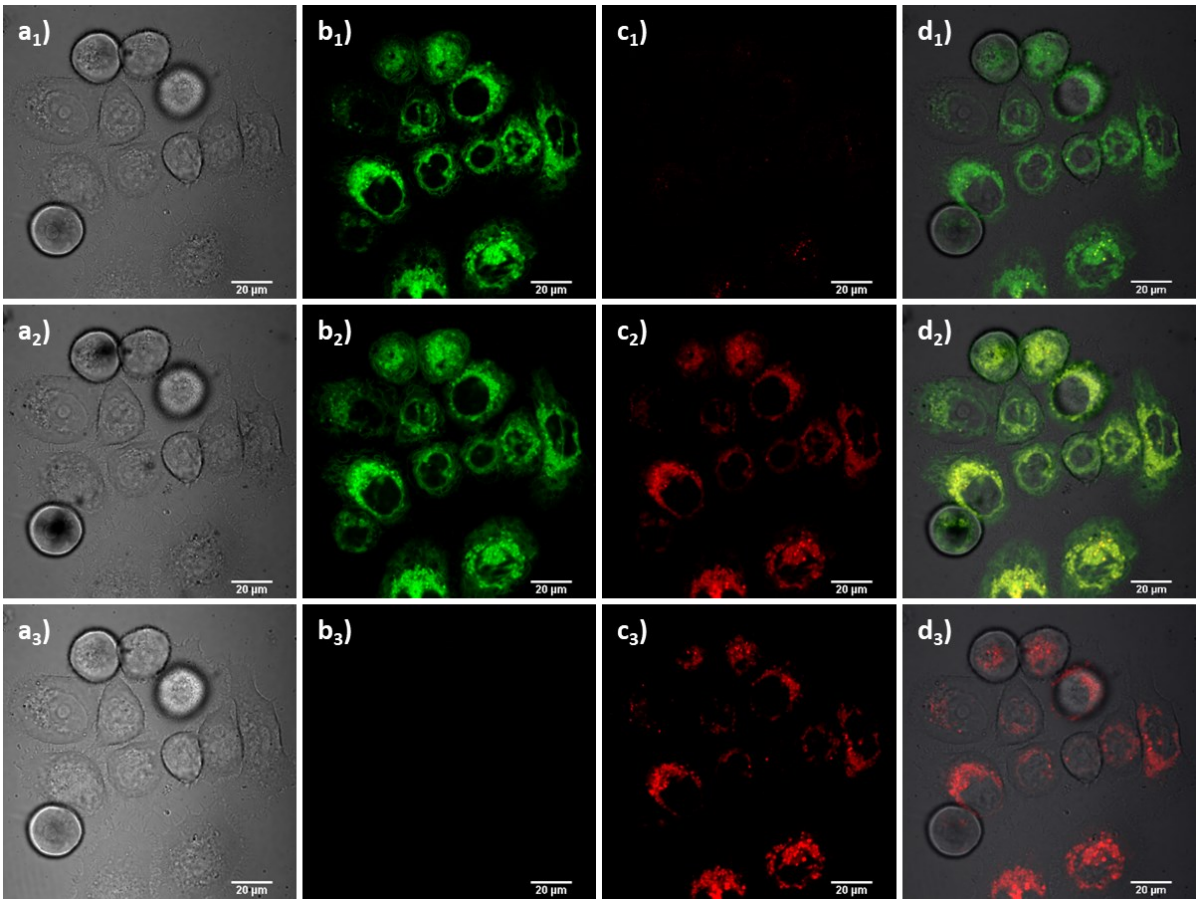

Figure 3.6. Single-photon confocal laser-scanning microscopy of PC-3 cells incubated with compound **9** (100 µM, 1:99 DMSO:serum-free medium). **a_{1-3})** TD channel; **b_{1-3})** green channel (λ_{em}=550-550 nm); **c_{1-3})** red channel (λ_{ex}=405; λ_{em}=570-750 nm); **d_{1-3})** overlay of TD-green-red channels. **a_1-d_1)** λ_{ex}=405 nm; **a_2-d_2)** λ_{ex}=488 nm; **a_3-d_3)** λ_{ex}=561 nm; scale bar: 50 µm.

The micrographs a_1-e_1 are referred to the excitation wavelength of 405 nm which showed an intense fluorescence emission in the green channel (fluorescence emission range between 500 and 550 nm) and it is distributed in the cytoplasm of the cells. At the excitation wavelength of 488 nm (a_2-d_2), the compound emitted in the green and red channels (emission wavelengths between 570 and 750 nm). On the other hand, at the excitation wavelength of 561 nm (a_3-d_3), compound **9** showed fluorescence emissions in the red channel.

3.3.3. Synthesis and characterisation of amino acid-tagged "axles"

Amino acid-tagged NDIs has been previously studied as potential imaging probes[25] as well as supramolecular architecture with carbon-based materials[26]. In this part of the Chapter, two amino acid-tagged NDI "axles" are presented, consisting of iodo-*L*-phenylalanine derivative moieties. Scheme 3.5 shows the reaction scheme of the amino acid-tagged "axles".

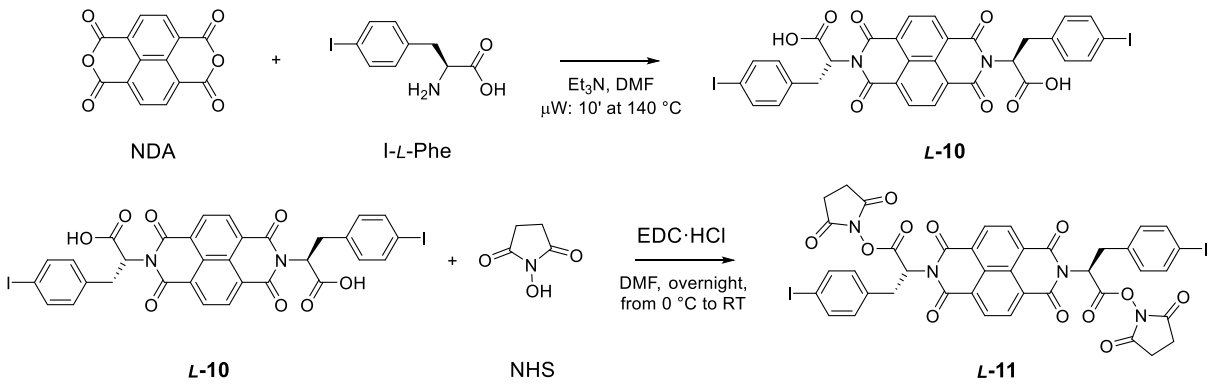

Scheme 3.5. Reaction scheme of the synthesis of the amino acid-tagged NDI "axles" ***L*-10** and ***L*-11**.

The reaction was carried out using a microwave-assisted synthesis and the protocol was adapted from a literature procedure[21]. Two equivalents of iodo-*L*-phenylalanine were added to the suspension of naphthalene dianhydride (NDA) in anhydrous dimethylformamide. The reaction mixture was heated at 140 ºC for 10 minutes. This method provided a fast, efficient, well-yielded and pure synthesis of ***L*-10** (yield 59%).

The carboxylic group of ***L*-10** was protected by a succinimide moiety to decrease potential hydrogen bonds with the "wheel" **7** which could interfere with the formation of an interlocked rotaxane. This protection step was achieved by reacting compound ***L*-10** with 1-ethyl-3-(3-dimethylaminopropyl) carbodiimide hydrochloride (EDC·HCl) (8 equivalents) and *N*-hydroxysuccinimide (NHS) (5.5 equivalents). Compound **11** was obtained after filtration and washing with n-pentane with no further purification (yield 83%).

Figure 3.7 shows the comparative ^{1}H-NMR spectra of compounds ***L*-10** and ***L*-11**. Mass spectra of the compounds are shown in Appendices A in Figure A.55 and A.56. Iodo-phenylalanine was incorporated to the NDI core to be used as a stain to enhance contrast in TEM analysis of the system[32].

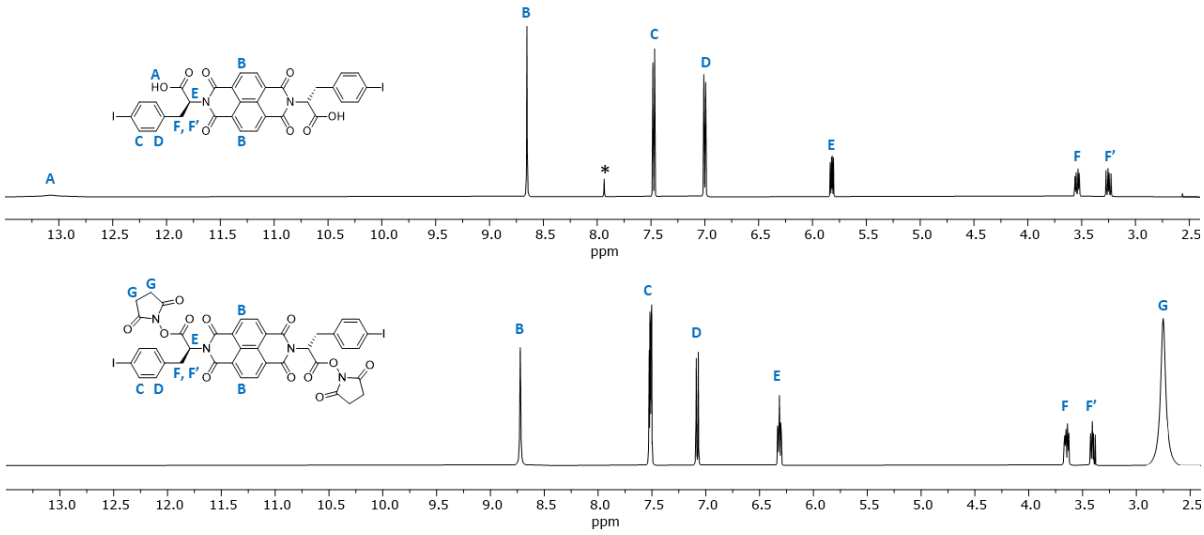

Figure 3.7. Comparative ^{1}H-NMR spectra of compounds ***L*-10** (on the top) and ***L*-11** (on the bottom) (500 MHz, $CDCl_3$, *DMF residual signal).

Both ^{1}H-NMR spectra show a pattern attributable to symmetric NDI-derivatives, deductible from the signals appeared at around 8.65 ppm (*B*) due to the resonance of the 4 aromatic protons on the NDI core. The resonances of the protons in the phenylalanine aromatic rings appeared at 7.55 and 7.07 ppm (*C* and *D*, respectively). The signal at 6.32 ppm (*E*) was attributed to the α-protons of ***L*-11**. Such resonance is more deshielded than the signal due to the hydrogen in α-position of the natural phenylalanine in ***L*-10**. The diastereotopic protons in β-position of ***L*-11** are attributed to the signals at 3.65 and 3.38 ppm (*F* and *F'*, respectively) with a multiplicity of double doublets. In the spectrum of ***L*-11**, the signal, attributed to the hydroxyl group, disappeared; whilst a resonance at 2.73 ppm (*G*) appeared. Such signals confirmed the successful transformation of ***L*-10** in ***L*-11**.

The optical characteristics of ***L*-10** and ***L*-11** were investigated by UV-visible and fluorescence spectroscopy. The absorption spectra of ***L*-11** presents two maxima at around 360 and 380 nm are attributed to the allowed π-π* transitions due to the electric dipole moment polarised along the long axis of the NDI-core[27,28]. The fluorescence emissions of ***L*-11** were found in the range of wavelength between 400 and 500 nm when excited from 350 to 400 nm.

Compound ***L*-11** will be discussed in detail in Chapter 3 with the UV-visible spectrum and fluorescence excitation-emission map depicted in Figure 4.10b and 4.11b respectively.

The fluorescence emission, uptake and localisation into living prostate cancer cells (PC-3) were investigated using confocal laser-scanning microscopy (CLSM) to evaluate such characteristics in a cell line model. Compound ***L*-11** was incubated overnight at 37 °C in PC-3 cells line and then analysed by CLSM.

Figure 3.8 shows the micrographs of compound ***L*-11** up taken into PC-3 cells, excited with a wavelength at 488 nm. Such compound showed good fluorescence emissions in the green and red channels and is spread localised in the cytosol of the cells.

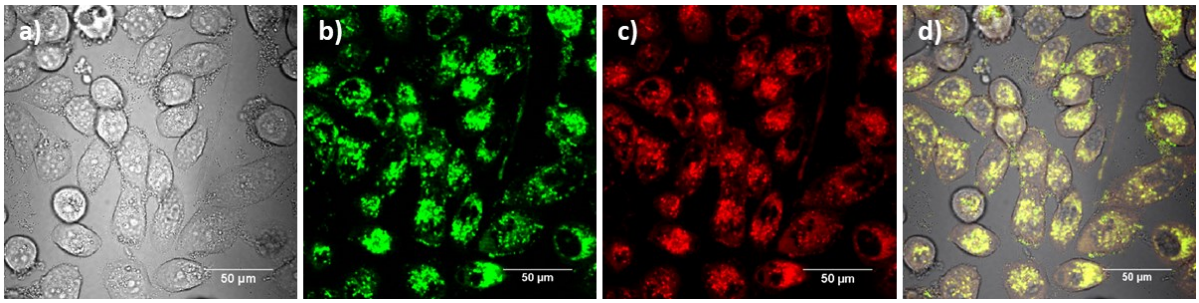

Figure 3.8. Single-photon confocal laser-scanning microscopy of PC-3 cells incubated at 37 °C for 24 h with compound ***L*-11**. Solution 100 µM, in 1:99 DMSO:serum-free medium. **a)** TD channel; **b)** green channel (λ_{em}=500–550 nm); **c)** red channel (λ_{em}=570–750 nm); **d)** overlay of TD-green-red channels. λ_{ex}=488.0 nm; scale bar: 50 µm.

3.4. Preliminary investigations into the formation of new *pseudo*rotaxanes in solution

In this part of the Chapter, preliminary results on the formation of two *pseudo*rotaxanes, consisting of the amino acid-tagged NDI-based "axles" (***L*-10** and ***L*-11**) and the "wheel" **7**, are presented. The electron-rich naphthalene ring on the 1,5-dinaphtho[38]crown-10 (**7**) may interact with the electron-deficient NDI core of both ***L*-10** and ***L*-11**.

Figure 3.9 proposes the *pseudo*rotaxane formed by the NDI-based "axles" ***L*-10** (highlighted in blue) and ***L*-11** (highlighted in red) the "wheel" **7** (highlighted in black).

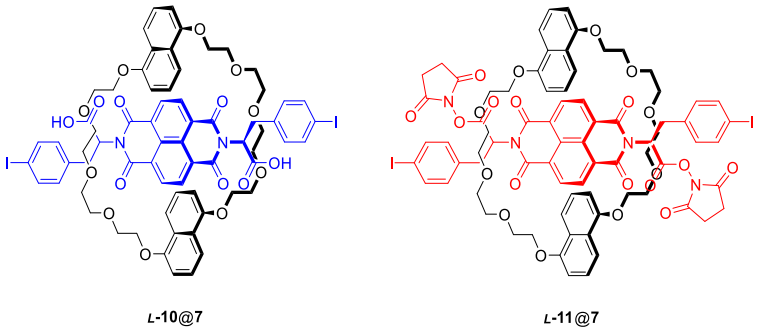

Figure 3.9. Proposed *pseudo*rotaxanes consisting of amino acid-tagged NDI "axles" and dinaphtho-crown ether "wheel".

The formation of the *pseudo*rotaxane was attempted mixing a solution of 1 mg mL^{-1} in chloroform of ***L*-10** (coloured yellow) with a solution 1 mg mL^{-1} in chloroform of **7** (coloured pink). Such mixture suddenly became red and then analysed by ^{1}H-NMR spectroscopy.

Figure 3.10 shows the comparative ^{1}H-NMR spectra of ***L*-10**, **7** and ***L*-10@7** with the corresponding assignments.

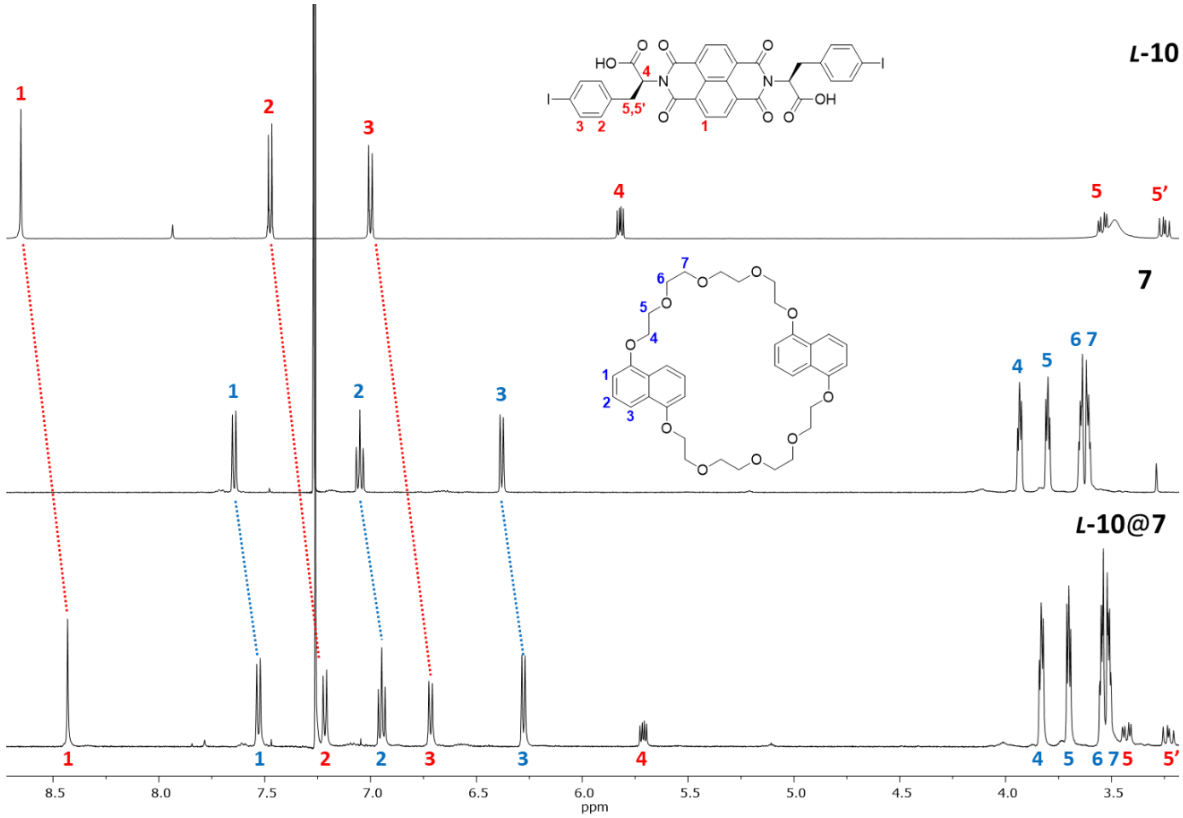

Figure 3.10. Comparative ^{1}H-NMR spectra of ***L*-10**, **7** and ***L*-10@7** (500 MHz, $CDCl_3$:DMSO-d_6, 1:1).

The ^{1}H-NMR spectrum of ***L*-10@7** shows the characteristic pattern of signals of both ***L*-10** and **7**. In the spectrum of the *pseudo*rotaxane, the signals of both species are upfield. Particularly, the 4 aromatic protons (*1*) of the NDI-core of ***L*-10** are shifted from 8.65 ppm to 8.42 ppm. Moreover, the *ortho*- and *meta*-protons of the phenylalanine (*2* and *3*, respectively) are shielded of about 0.3 ppm. The aromatic protons of the naphthalene rings of **7** are shifted upfield of about 0.1 ppm. Such shifting of signals upfield suggests an interaction ongoing between the aromatic rings of the two species and possibly the thread of the "axle" ***L*-10** into the macrocycle **7**. An analogous system was synthesised by Choudhary *et al.*[33] which was formed by an NDI derivative used as an "axle" and the "wheel" used hereby. From the ^{1}H-NMR spectrum of such *pseudo*rotaxane, a downshift of the signals of both the "axle" and the "wheel" can be noticed. The magnitude of these variations is about 0.45 ppm, for the axle (from the complexed to the uncomplexed species) and 0.4-1.0 ppm for the wheel (from the complexed to the uncomplexed species). The data showed in Choudhary *et al.*'s work suggest that the *pseudo*rotaxane presented in this work has formed and interactions between the "axle" and the "wheel" may have been established[33]. The shift of the signals in the phenylalanine moiety can be attributed to a transient interaction with the wheel.

^{1}H DOSY-NMR experiment was carried out on ***L*-10@7** to investigate the diffusion in solution as interlocked species (Figure 3.11). The signals marked with green dots represent the protons attributed to the "axle" ***L*-10**, whilst the blue dots are the signals due to the "wheel" **7**. The system diffuses with a diffusion coefficient of $5.30 \cdot 10^{-6}$ m^2/s.

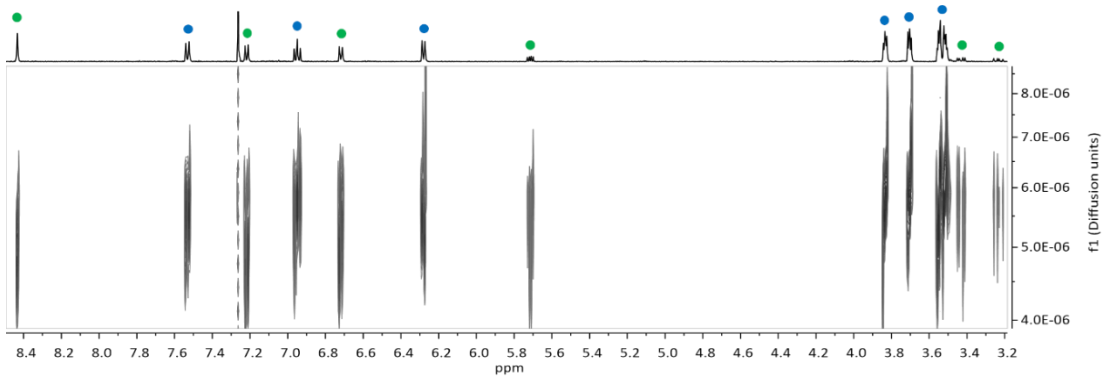

Figure 3.11. ^{1}H DOSY-NMR spectrum of ***L*-10@7** (500 MHz, $CDCl_3$).

The *pseudo*rotaxane consisting of the "axle" ***L*-11** and the "wheel" **7** was formed by mixing the two solutions (1 mg mL^{-1} in chloroform) of the two building blocks. Such mixture became red once the species were mixed.

The comparative ^{1}H-NMR spectra of ***L*-11**, **7** and ***L*-11@7** with the corresponding assignments are depicted in Figure 3.12.

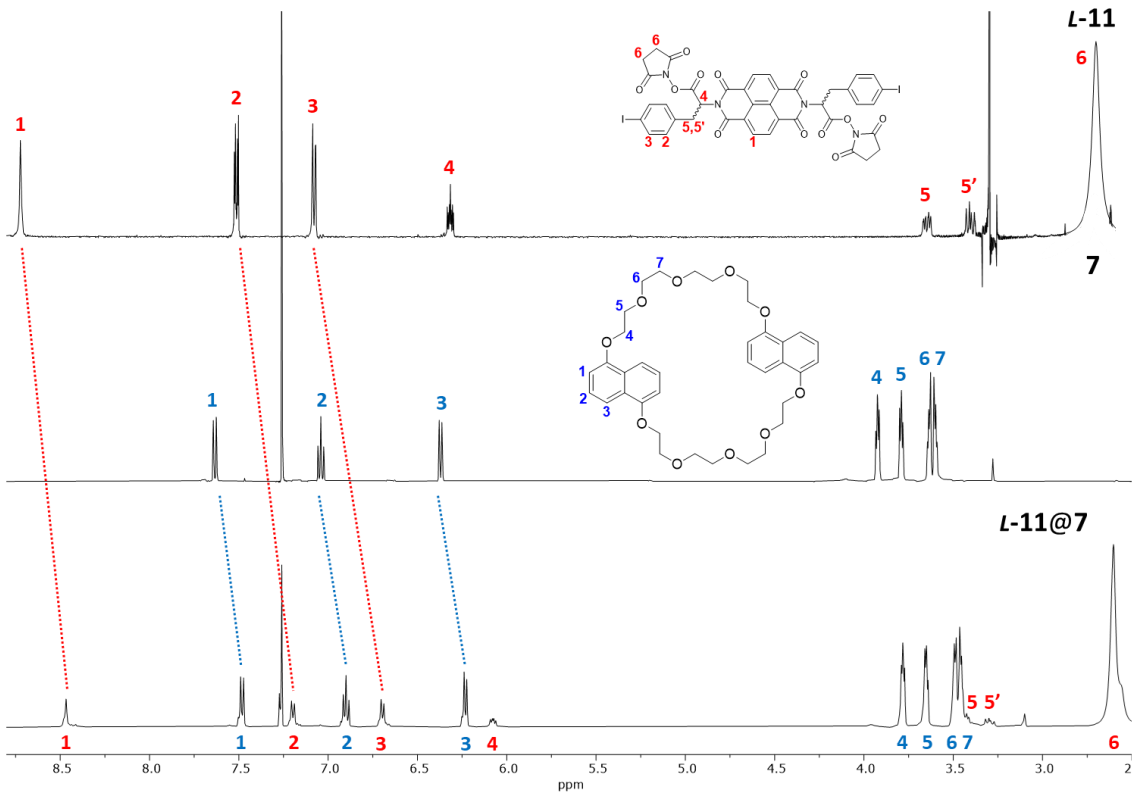

Figure 3.12. Comparative ^{1}H-NMR spectra of ***L*-11**, **7** and ***L*-11@7** (500 MHz, $CDCl_3$).

Similarly to the previous case, the ^{1}H-NMR spectrum of ***L*-11@7** shows the characteristic pattern of signals of both ***L*-11** and **7**. Once the rotaxane is formed, the signals of both species are shifted upfield. The signals belonging to ***L*-11** (highlighted in red) shift of about 0.2 ppm, whilst the signals of the **7** are shifted by 0.1 ppm.

Variable temperature ^{1}H-NMR experiment was carried out on ***L*-10@7**, as well as ***L*-11@7**, to investigate a possible threading/de-threading equilibrium. Figure 3.13 and 3.14 show the NMR spectra at different temperature of the two *pseudo*rotaxanes, from 50 °C to -60 °C. The green dots indicated the signals attributed to the NDI-based "axles", whilst the blue dots were assigned to the aromatic protons of the "wheel" **7**. The signals of the tetraethylene glycol chains are not reported because there was not a significant change.

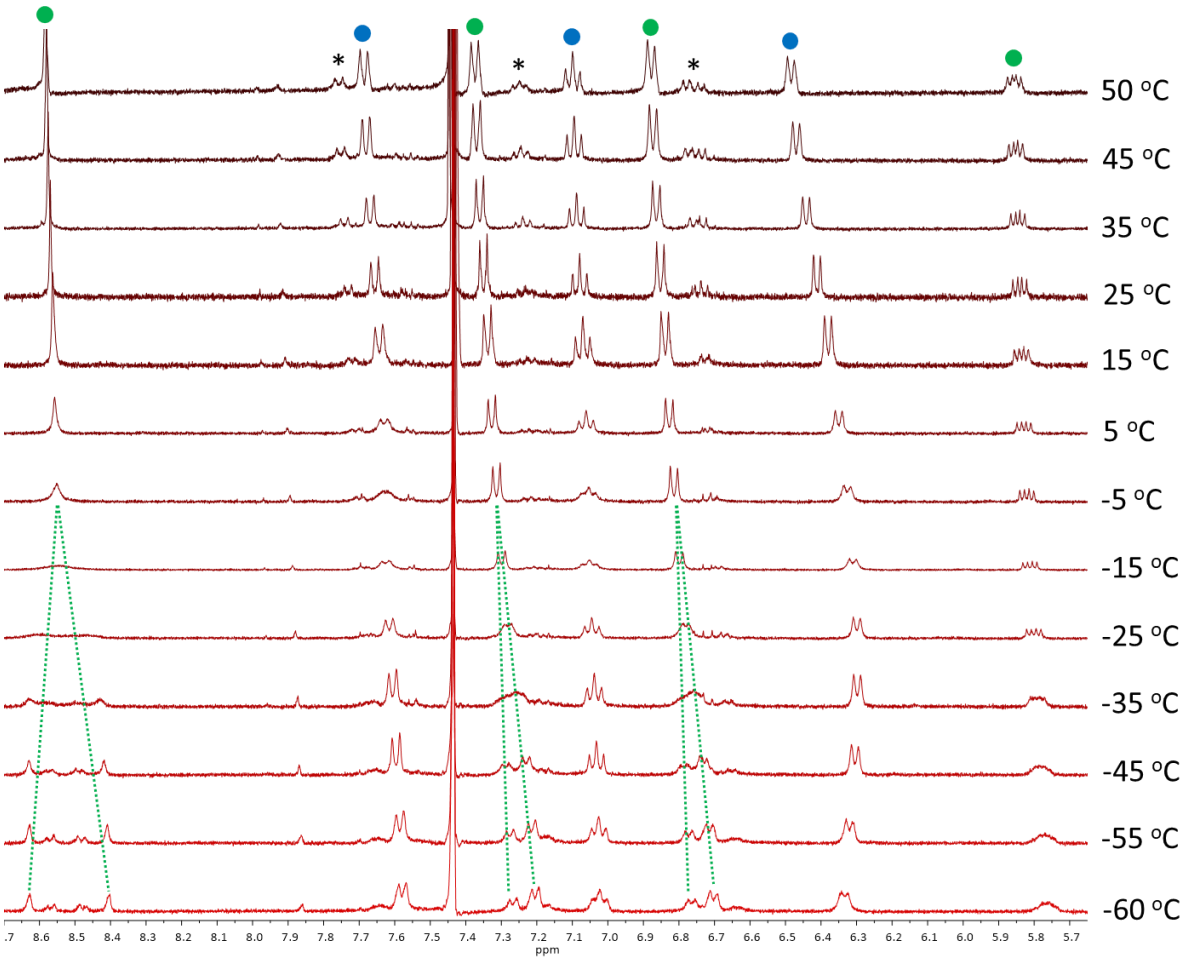

Figure 3.13. ^{1}H-NMR spectra of ***L*-10@7** at variable temperature (400 MHz, $CDCl_3$:DMSO-d_6, 1:1).

The variable temperature ^{1}H-NMR spectra show that the signals attributed to the "axle" ***L*-10** (in green dots) are splitting into two sets when the temperature decrease. Such phenomenon suggests the existence of two species in solution, which at high temperature the equilibrium is fast for the NMR acquisition time. Domoto *et al.*[34] observed a splitting of the diimide protons of the NDI-core in a similar *pseudo*rotaxane, consisted of an NDI derivative "axle" and the dinaphtho-crown ether "wheel", during variable temperature ^{1}H-NMR. In their system, the protons of the NDI-core remained under the same signal until -40 °C. At -50 °C, it was possible to distinguish two signals for those protons. This phenomenon was attributed to a limited movement of the "wheel" compared to the "axle" which is affected by low temperature[34]. In the pseudorotaxane presented hereby, two different species could be seen at low temperature which can be attributed to different positions of the "wheel" **7** on the "axle" ***L*-10**. On a closer look on the variable temperature spectra in Figure 3.13, the ^{1}H-NMR spectrum at -60 °C of ***L*-10@7** shows two different sets of protons for the NDI core hydrogens (signals between 8.65 and 8.40 ppm).

Such splitting may be due to the presence of two possible configurations of **7** around ***L*-10** shown in Figure 3.14.

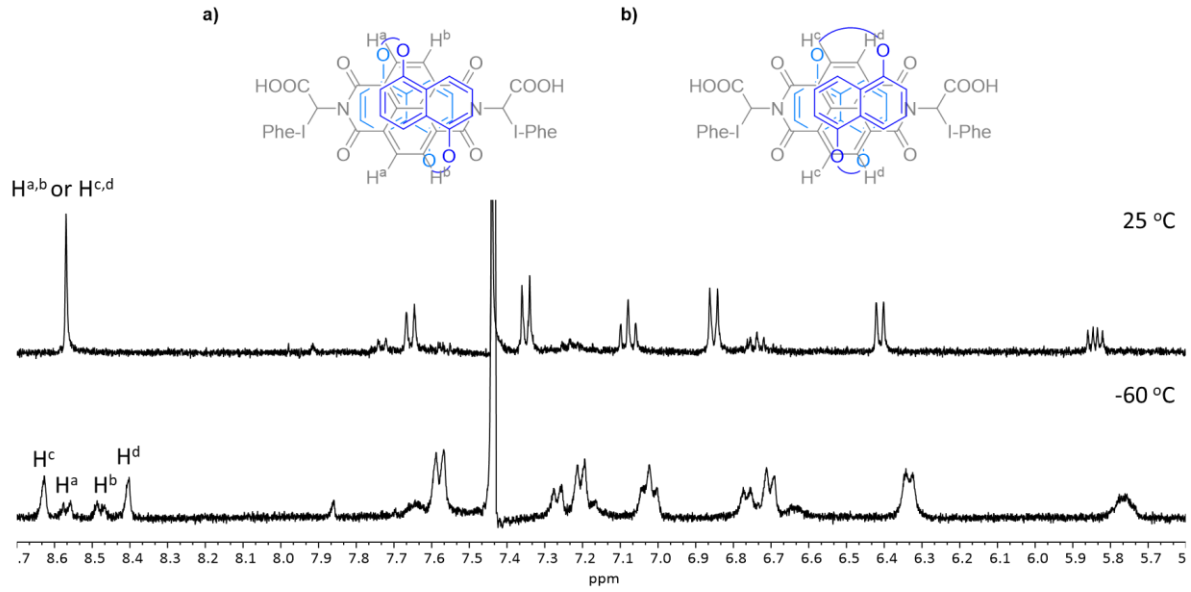

Figure 3.14. On the top: hypothesised conformers between the "axle" ***L*-10** and the "wheel" **7**. In the conformer A (a), the dinaphthyl rings face specularly the NDI-core. In conformer B (b), the dinaphthyl rings face the NDI-core in opposite directions. On the bottom: ^{1}H-NMR spectra of the *pseudo*rotaxane at 25 and -60 °C.

In the isomer showed in Figure 3.14 (conformer A), the protons in the NDI core labelled H^a and H^b at 25 °C are equivalent and their signal is a singlet at around 8.6 ppm. At -60 °C, H^a and H^b become chemically inequivalent and split into two doublets. On the other hypothesised isomer (conformer B, Figure 3.14b), at -60 °C the protons H^c and H^d split into two singlets because of the substituents in the nitrogen atoms (the iodo-phenylalanine moieties). Such phenylalanine rings spacially point to the same side and are hindered by the "wheel" to rotate because of closer interaction between the NDI core and the dinaphthol rings. The conformer A presents phenylalanine moieties which can allow the "wheel" **7** to expand more than in the conformer B and therefore presents a closer π-π stacking. This equilibrium has been already observed in different rotaxanes[29-31] in which the "wheel" at high temperature is able to move fast through the "axle", causing the coalescence of a particular signal of the "axle". On the other hand, at low temperature and under the NMR timescale, the "axle" shuttles slowly. Such movement can place this "axle" in a different position with respect of the "wheel", causing the observations of different resonance sets.

From the observation of the dynamic process, line shape analysis was performed to extract thermodynamic data from the ^{1}H-NMR spectra at variable temperatures.

The significative signals used in this analysis were H^c and H^d for conformer A and the protons H^a and H^b for conformer B. Figure 3.15 depicts the experimental and simulated ^{1}H-NMR spectra of the region between 8.7 and 8.3 ppm from -60 ºC to 25 ºC.

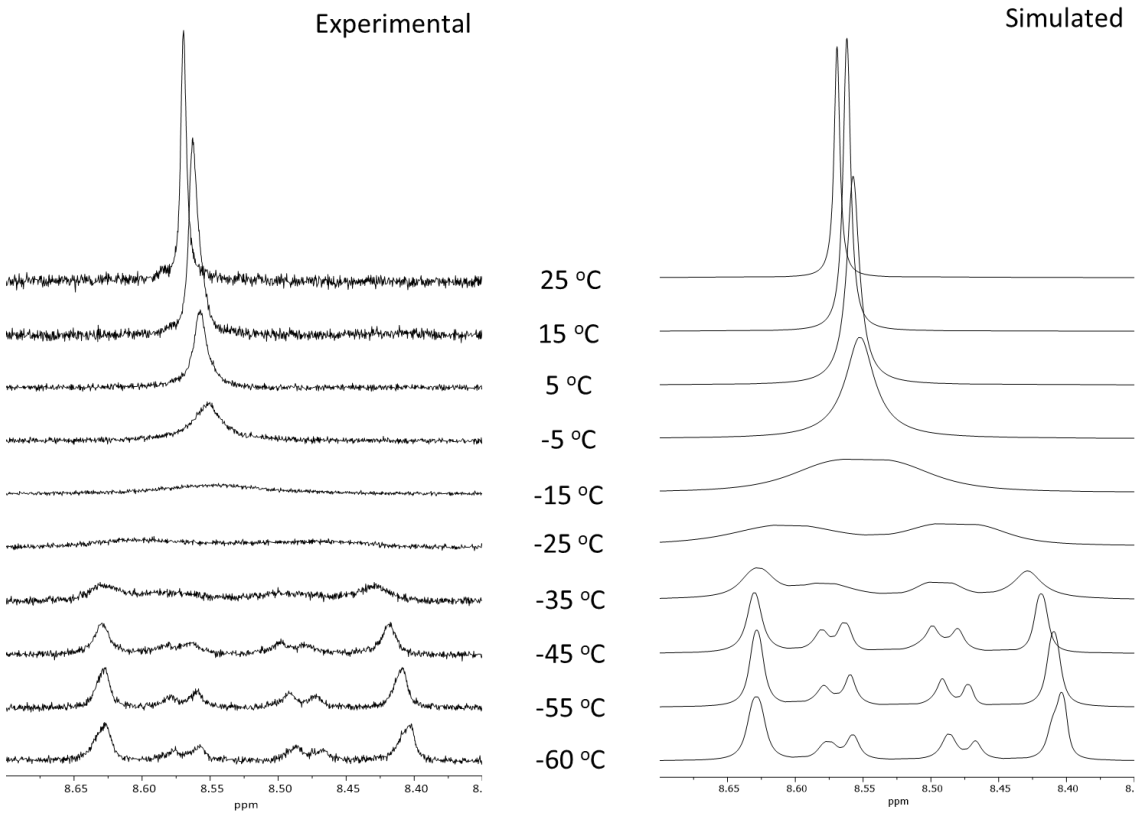

Figure 3.15. On the left: experimental expansions of the ^{1}H-NMR spectra in the region between 8.7 and 8.3 ppm from -60 to 25 ºC. On the right: simulated expansions of the ^{1}H-NMR spectra in the region between 8.7 and 8.3 ppm from -60 to 25 ºC.

The simulated ^{1}H-NMR spectra were used to extrapolated the necessary parameters to apply the Eyring's equation and obtain the relative plot to determine the $\Delta G^{\ddagger}$, $\Delta H^{\ddagger}$ and $\Delta S^{\ddagger}$ of the process[35,36]. The rate of the process (k) was previously calculated for each conformer at the reported temperatures[37] which are summarised in Table 3.1. The spectrum at -60 ºC was used as a reference for the no-exchange process.

Table 3.1. Summary table of the dynamic rates of the process for the *pseudo*rotaxane ***L*-10@7** at different temperatures.

Temperature	Conformer a	Conformer b
(K)	***k*** **(s^{-1})**	***k*** **(s^{-1})**
218	3.27	12.57
228	10.02	12.57
238	25.87	25.13
248	168.49	85.64
258	204.24	88.80
268	1887.57	1887.57
278	2863.90	2863.90
288	12777.38	12777.38
298	88589.87	88589.87

In this dynamic process, the coalescence temperature was 258 K (-15 ºC) in both cases in which the signals collapsed in one broad singlet. The values of *k* from 268 K to 298 K are in common in both conformers because of the extensive overlap of the signals. From the rate *k* of such processes, the Eyring's plots were extrapolated and fitted for both conformers (Figure 3.16).

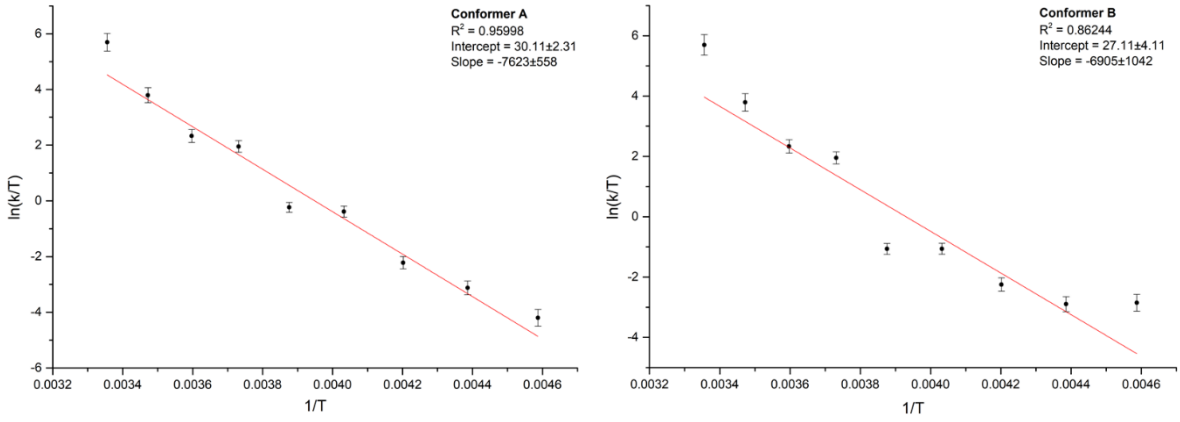

Figure 3.16. Eyring's plots for conformer A (on the left) and conformer B (on the right) for the *pseudo*rotaxane ***L*-10@7**.

From the slope and intercept of the plot, it was possible to apply th following equations to calculate $\Delta G^{\ddagger}$, $\Delta H^{\ddagger}$ and $\Delta S^{\ddagger}$ of the process[35,36]. The Eyring's equation used in the plots is: $\ln\frac{k}{T} = \frac{\Delta S^{\ddagger}}{R} - \ln\frac{h}{k_B} - \frac{\Delta H^{\ddagger}}{RT}$ where *k* is the rate of the process (in s^{-1}), T is the temperature (in kelvin), h

is the Plank's constant ($6.626 \cdot 10^{-34}$ J s), k_b is the Boltzmann's constant ($1.381 \cdot 10^{-23}$ J mol^{-1}) and R is the molar gas constant (8.314 J K^{-1} mol^{-1}). Calculated $\Delta H^{\ddagger}$ and $\Delta S^{\ddagger}$ from the Eyring's plot, the $\Delta G^{\ddagger}$ was determined by the equation $\Delta G^{\ddagger}=\Delta H^{\ddagger}-T\Delta S^{\ddagger}$. Table 3.2 reports the thermodynamic data for both conformers involved in the dynamic process.

Table 3.2. Summary table of the thermodynamic parameters extrapolated from the Eyring's plots.

	Conformer A	**Conformer B**
$\Delta G^{\ddagger}$	49±10 kJ mol^{-1}	50±18 kJ mol^{-1}
$\Delta H^{\ddagger}$	63±5 kJ mol^{-1}	57±9 kJ mol^{-1}
$\Delta S^{\ddagger}$	53±19 J mol^{-1} K^{-1}	28±34 J mol^{-1} K^{-1}

Figure 3.17 shows the variable temperature ^{1}H-NMR spectra of ***L*-11@7**. The green dots indicate the protons of ***L*-11**, whilst the signals of the aromatic protons of **7** are marked with blue dots. The resonances of the tetraethylene glycol chains were not affected by significant shifting.

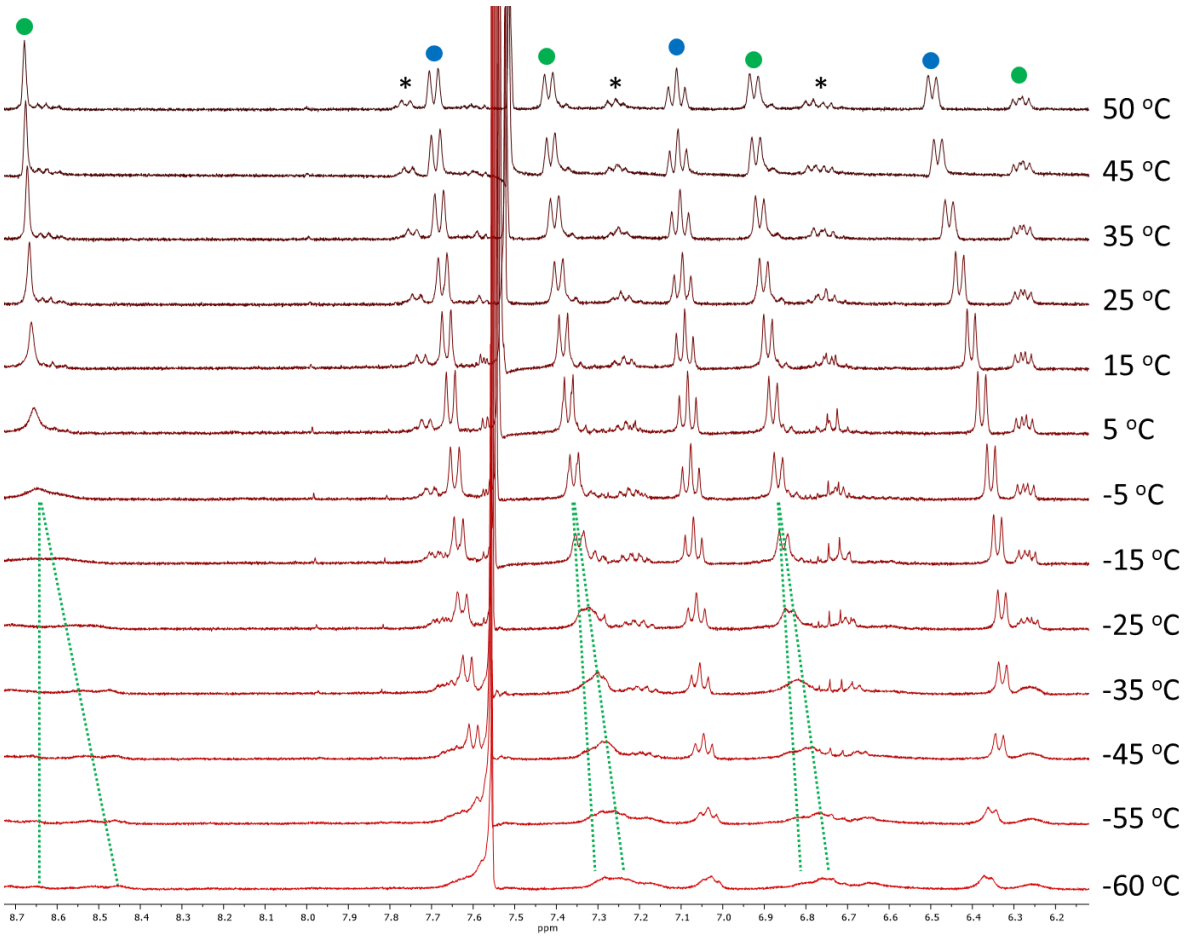

Figure 3.17. ^{1}H-NMR spectra of ***L*-11@7** at variable temperature (400 MHz, $CDCl_3$:DMSO-d_6, 1:1).

The signals of the "axle" ***L*-11** started to split in two sets at -15 °C. As previously seen in ***L*-10@7**, in solution the equilibrium between ***L*-11** and **7** is fast at high temperature; whilst at low temperature, two different species exist which could be due to different position of **7** on the "axle" ***L*-11**. In this case, the line shape analysis was not performed and the relative dynamic parameters were not calculated due to the difficulty to simulate the spectra from the experimental ones.

The *pseudo*rotaxanes ***L*-10@7** and ***L*-11@7** were investigated by UV-visible and fluorescence spectroscopies which spectra are shown in Figure 3.18 (a and b for ***L*-10@7** and c and d for ***L*-11@7**). The absorption spectrum of ***L*-10@7** shows the characteristic bands of the transitions belonging to the "wheel" **7** and the "axle" ***L*-10**. Despite a visible change of colour during the formation of the system ***L*-10@7**, no substantial changes in the absorbance spectrum were found in the region between 400 and 500 nm. In the similar *pseudo*rotaxane synthesised in the work of Choudhary *et al.*[33], an absorbance around the region between 425 and 575 nm was expected. ***L*-10@7** was analysed with a concentration of 0.025 mM in DMSO which may affect this electronic band due to a charge transfer phenomenon between the aromatic cores of the axle" ***L*-10** and the "wheel" **7**[33,34]. The excitation-emission matrix map shows weak fluorescence emissions in the range between 320-350 nm when excited from 270 to 320 nm. Similar absorption characteristics were highlighted in ***L*-11@7**. The electronic transitions of "wheel" **7** and the "axle" ***L*-11** are the predominant bands on the UV-visible spectra. Weak fluorescence emissions were noticed in the range between 320 and 360 nm when excited from 270 to 320 nm.

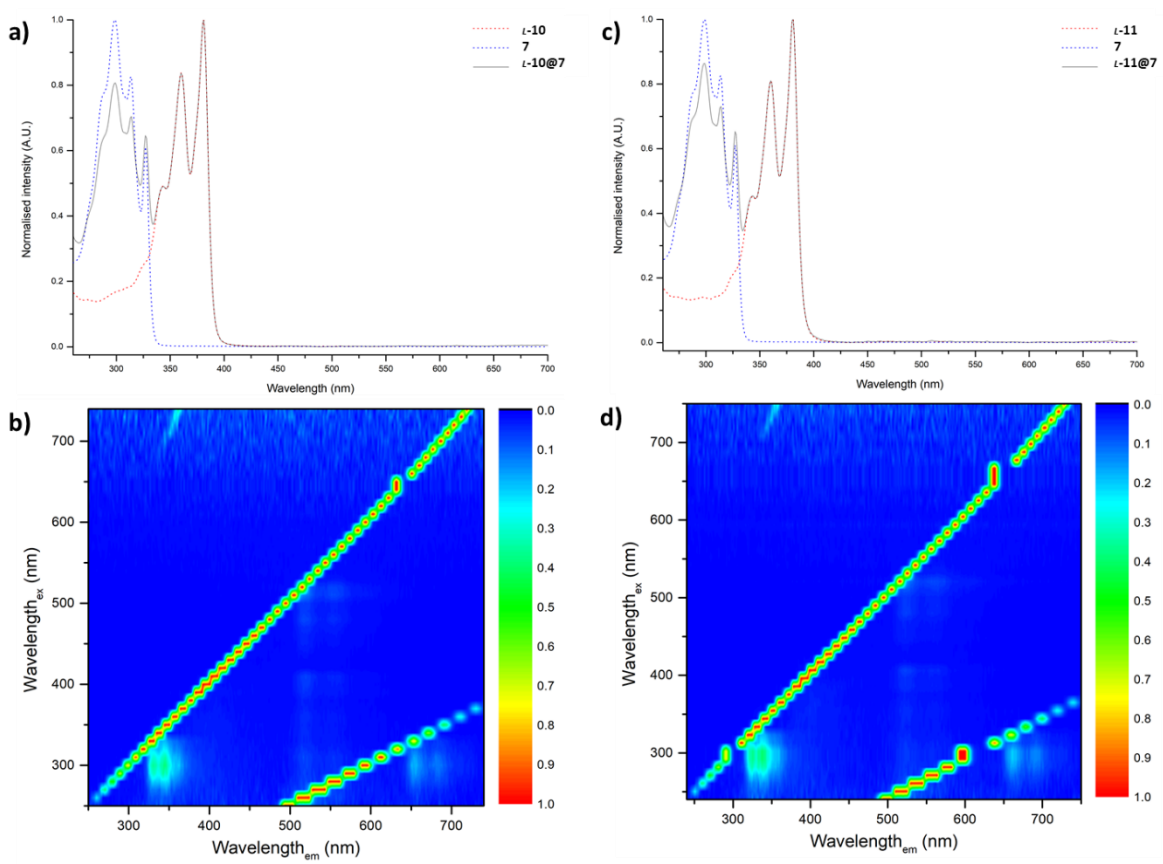

Figure 3.18. a) Normalised UV-visible spectra of ***L*-10** (red dotted line), **7** (blue dotted line) and ***L*-10@7** (grey line); **b)** normalised EEM map of ***L*-10@7**. **c)** Normalised UV-visible spectra of ***L*-11** (red dotted line), **7** (blue dotted line) and ***L*-11@7** (grey line); **d)** normalised EEM map of ***L*-11@7**. Solutions 0.025 mM in DMSO.

3.5. Conclusions to Chapter 3

In this Chapter, different NDI-based "axles" and a dinaphtho tetraethylene glycol "wheel" were investigated as potential mechanically interlocked molecules (MIMs) for prostate cancer imaging.

The chosen "wheel" has been already reported for its intermolecular interactions with aromatic electron-deficient "axles", such as NDIs. The "wheel" was synthesised and characterised by ^{1}H-NMR and optical spectroscopies.

The first proposed "axle" consists of two moieties of ATSM derivative, linked to and NDI-core. This molecule was chosen thanks to its ability to complex Cu(II) which this ion could act as a stopper for an interlocked system with the synthesised "wheel". The ATSM-based "axle" was characterised by ^{1}H-NMR and optical spectroscopies and in addition, was preliminarily investigated by confocal laser scanning microscopy in living prostate cancer cells. Copper(II) ions were incorporated to such "axle" which species was analysed by mass spectrometry.

The second synthesised "axle" presents two BODIPY moieties on an NDI scaffold. This fluorescent species was characterised by ^{1}H-NMR and its optical properties were investigated by UV-visible and fluorescence spectroscopies. This "axle" was also preliminarily investigated in living prostate cancer by confocal laser scanning microscopy.

The third set of "axles" consists of amino acids-tagged NDIs, presenting two iodo-phenylalanine moieties. One of the two "axles" has the carboxylic group of the phenylalanine protected by succinimide, whilst the second "axle" has hydroxyl groups. This protection could increase the aromatic stacking between the NDI and the naphthalene rings on the "wheel", blocking the threading/dethreading equilibrium of the rotaxane. These "axles" were characterised by NMR and investigated by UV-visible and fluorescence spectroscopy.

Two different *pseudo*rotaxanes were formed using the amino acid-tagged NDIs which were preliminarily investigated by ^{1}H-NMR. Variable temperature ^{1}H-NMR and DOSY-NMR experiments were carried out to investigate the possible threading/dethreading equilibrium. In one of the proposed *pseudo*rotaxane, the existence of two possible conformers was supposed by the ^{1}H-NMR spectra at variable temperature. Kinetic and thermodynamic data were extrapolated using the line shape analysis of the spectra. These NMR preliminary studies seem promising for further analysis and studies for the conformational equilibrium which such *pseudo*rotaxane can undergo in solution.

3.6. References to Chapter 3

1. J.-M. Lehn, *Science*, 1985, **227**, 849-856.
2. J.-M. Lehn, *Chem. Soc. Rev.*, 2007, **36**, 151-160.
3. X.-S. Du, C.-Y. Wang, Q. Jia, R. Deng, H.-S. Tian, H.-Y. Zhang, K. Meguellati and Y.-W. Yang, *Chem. Comm.*, 2017, **53**, 5326-5329.
4. A. Brown, T. Lang, K. M. Mullen and P. D. Beer, *Org. Biomol. Chem.*, 2017, **15**, 4587-4594.
5. B. N. Ahamed, P. Van Velthem, K. Robeyns and C.-A. Fustin, *ACS Macro Letters*, 2017, **6**, 468-472.
6. N. Zhu, K. Nakazono and T. Takata, *Chem. Lett.*, 2016, **45**, 445-447.
7. M. R. Wilson, J. Solà, A. Carlone, S. M. Goldup, N. Lebrasseur and D. A. Leigh, *Nature*, 2016, **534**, 235-240.
8. J. Shi, Y. Xu, X. Wang, L. Zhang, J. Zhu, T. Pang and X. Bao, *Org. Biomol. Chem.*, 2015, **13**, 7517-7529.
9. S. P. Vincent, K. Buffet, I. Nierengarten, A. Imberty and J.-F. Nierengarten, *Chem. Eur. J.*, 2016, **22**, 88-92.
10. A. Fernandes, A. Viterisi, F. Coutrot, S. Potok, D. A. Leigh, V. Aucagne and S. Papot, *Angew. Chem. Int. Ed.*, 2009, **48**, 6443-6447.
11. J. W. Fredy, J. Scelle, G. Ramniceanu, B.-T. Doan, C. S. Bonnet, É. Tóth, M. Ménand, M. Sollogoub, G. Vives and B. Hasenknopf, *Org. Lett.*, 2017, **19**, 1136-1139.
12. G. Yu, D. Wu, Y. Li, Z. Zhang, L. Shao, J. Zhou, Q. Hu, G. Tang and F. Huang, *Chem. Sci.*, 2016, **7**, 3017-3024.
13. J.-J. Lee, A. G. White, D. R. Rice and B. D. Smith, *Chem. Comm.*, 2013, **49**, 3016-3018.
14. C. J. Bruns, S. Basu and J. Fraser Stoddart, *Tetrahedron Lett.*, 2010, **51**, 983-986.
15. D. G. Hamilton, J. E. Davies, L. Prodi and J. K. M. Sanders, *Chem. Eur. J.*, 1998, **4**, 608-620.
16. A. M. Brouwer, *Pure Appl. Chem.*, 2011, **83**, 2213-2228.
17. T. Iijima, S. A. Vignon, H.-R. Tseng, T. Jarrosson, J. K. M. Sanders, F. Marchioni, M. Venturi, E. Apostoli, V. Balzani and J. F. Stoddart, *Chem. Eur. J.*, 2004, **10**, 6375-6392.
18. S. I. Pascu, C. Naumann, G. Kaiser, A. D. Bond, J. K. M. Sanders and T. Jarrosson, *Dalton Trans.*, 2007, 3874-3884.
19. D. Cao, M. Amelia, L. M. Klivansky, G. Koshkakaryan, S. I. Khan, M. Semeraro, S. Silvi, M. Venturi, A. Credi and Y. Liu, *J. Am. Chem. Soc.*, 2010, **132**, 1110-1122.
20. A.-J. Avestro, D. M. Gardner, N. A. Vermeulen, E. A. Wilson, S. T. Schneebeli, A. C. Whalley, M. E. Belowich, R. Carmieli, M. R. Wasielewski and J. F. Stoddart, *Angew. Chem. Int. Ed.*, 2014, **53**, 4442-4449.

21. K. Tambara, N. Ponnuswamy, G. Hennrich and G. D. Pantoş, *J. Org. Chem.*, 2011, **76**, 3338-3347.

22. J. L. Dearling, J. S. Lewis, G. E. Mullen, M. J. Welch and P. J. Blower, *J. Biol. Inorg. Chem.*, 2002, **7**, 249-259.

23. S. Iwaki, K. Hokamura, M. Ogawa, Y. Takehara, Y. Muramatsu, T. Yamane, K. Hirabayashi, Y. Morimoto, K. Hagisawa, K. Nakahara, T. Mineno, T. Terai, T. Komatsu, T. Ueno, K. Tamura, Y. Adachi, Y. Hirata, M. Arita, H. Arai, K. Umemura, T. Nagano and K. Hanaoka, *Org. Biomol. Chem.*, 2014, **12**, 8611-8618.

24. P. A. Waghorn, M. W. Jones, M. B. M. Theobald, R. L. Arrowsmith, S. I. Pascu, S. W. Botchway, S. Faulkner and J. R. Dilworth, *Chem. Sci.*, 2013, **4**, 1430-1441.

25. Z. Hu, R. L. Arrowsmith, J. A. Tyson, V. Mirabello, H. Ge, I. M. Eggleston, S. W. Botchway, G. Dan Pantos and S. I. Pascu, *Chem. Comm.*, 2015, **51**, 6901-6904.

26. J. A. Tyson, V. Mirabello, D. G. Calatayud, H. Ge, G. Kociok-Köhn, S. W. Botchway, G. Dan Pantoş and S. I. Pascu, *Adv. Funct. Mater.*, 2016, **26**, 5641-5657.

27. N. V. Ghule, D. D. La, R. S. Bhosale, M. Al Kobaisi, A. M. Raynor, S. V. Bhosale and S. V. Bhosale, *ChemistryOpen*, 2016, **5**, 157-163.

28. F. Salerno, J. A. Berrocal, A. T. Haedler, F. Zinna, E. W. Meijer and L. Di Bari, *J. Mater. Chem. C*, 2017, **5**, 3609-3615.

29. T. Ogoshi, D. Kotera, S. Nishida, T. Kakuta, T.-a. Yamagishi and A. M. Brouwer, *Chem. Eur. J.*, 2018, **24**, 6325-6329.

30. K. Hirose, K. Ishibashi, Y. Shiba, Y. Doi and Y. Tobe, *Chem. Eur. J.*, 2008, **14**, 5803-5811.

31. T. Prakasam, M. Lusi, E. Nauha, J.-C. Olsen, M. Sy, C. Platas-Iglesias, L. J. Charbonnière and A. Trabolsi, *Chem. Comm.*, 2015, **51**, 5840-5843.

32. L. E. Franken, E. J. Boekema, M. C. A. Stuart, *Adv. Sci.*, 2017, **4**, 1600476.

33. U. Choudhary, B. H. Northrop, *Org. Lett.*, 2012, **14**, 2082-2085.

34. Y. Domoto, S. Sase, K. Goto, *Chem. Eur. J.*, 2014, **20**, 15998-16005.

35. M. Teng, Y. Liu, S. Li, G. Huang, J. Jiang, L. Wang, *RSC Advances*, 2013, **3**, 9016.

36. J. Rönnols, M. T. C. Walvoort, G. A. van der Marel, J. D. C. Codée, G. Widmalm, *Org. Biomol. Chem.*, 2013, **11**, 8127.

37 F. P. Gasparro, N. H. Kolodny, *J. Chem. Educ.*, 1977, **54**, 258.

Chapter 4: Naphthalenediimide-based peptide conjugates and their investigation in living cancer cells *via* fluorescence microscopies

4.1. Overview

This Chapter describes the design, synthesis and characterisation of naphthalenediimide (NDI) derivatives which incorporate one or two units of the fragment [7-13] of bombesin peptide which can target selectively the gastrin-realising peptide receptors (GRPRs) on the prostate cancer cells.

Here, the naphthalenediimide-core was chosen as the connecting building block between the peptide strands due to its facile functionalisation, spectroscopic features with UV-visible[1,2], inertness, tune-ability for water solubility[3] and ability to form supramolecular aggregates in organic solvents[4]. Amino acid-tagged NDIs have been studied in cancerous cell lines to show efficient cellular uptake and traceable fluorescence emissions within the cytoplasm[5,6].

A particular interest in small fragments of bombesin peptide, specifically both 7-13 and 7-14 peptide fragments, has come to light because of their high affinity to bind selectively the GRPRs[7] which have emerged in localising, detecting and treating prostate cancer[8,9].

The choice of a derivative of 4,4-difluoro-4-bora-3a,4a-diaza-s-indacene (BODIPY) relies on its stability in biological conditions, compatibility in living cells and absorbing/emitting in a broad spectral range[10].

Considering such evidence, different types of fluorescent probes able to interact with prostate cancer cells are designed and shown in Scheme 4.1. The reaction pathway in Scheme 4.1a represents the synthesis of *mono*- and *bis*-peptide NDI-derivatives. An amino acid-derivative linker (iodo-phenylalanine) is used in between the NDI moiety and the bombesin [7-13]. A library of peptide conjugates as the *L*-/*D*-enantiomers was created and the different stereochemistry presented on both the linker and the constituent amino acids of the peptide fragment was investigated. The route b in the Scheme 4.1 describes the synthesis of an asymmetrical NDI-core which links the BODIPY-derivative [*N*-(2-aminoethyl)-4-(5,5-difluoro-1,3,7,9-tetramethyl-5*H*-4λ^4,5λ^4-dipyrrolo[1,2-c:2',1'-f][1,3,2]diazaborinin-10-yl)benzamide][11], in one side, and the *L*-version of the targeting bombesin [7-13], in the other side.

The spectroscopy investigations of probe-conjugates synthesised hereby, intended as prototypes for future molecular imaging probes were carried out. UV-visible and fluorescence spectroscopies assessed their absorption and emission characteristics in common organic solvents.

The fluorescence emission and localisation in the cellular environment are evaluated by confocal laser scanning microscopy. In addition, the lifetime distributions, aggregation and localisation of these fluorescent probes are estimated by one- and two-photon fluorescence lifetime techniques both in solution and *in vivo*. In the one-photon fluorescence experiment, the wavelengths involved in the process are between 300 and 700 nm; on the other hand, the wavelengths in two-photon fluorescence techniques are between 800 and 1000 nm. The energy involved in the two-photon fluorescence methods is weaker and can deeply penetrate tissues and organs. In recent years, these characteristics have widely employed to detect cancerous cells in patients with prostate cancer in early-stage.

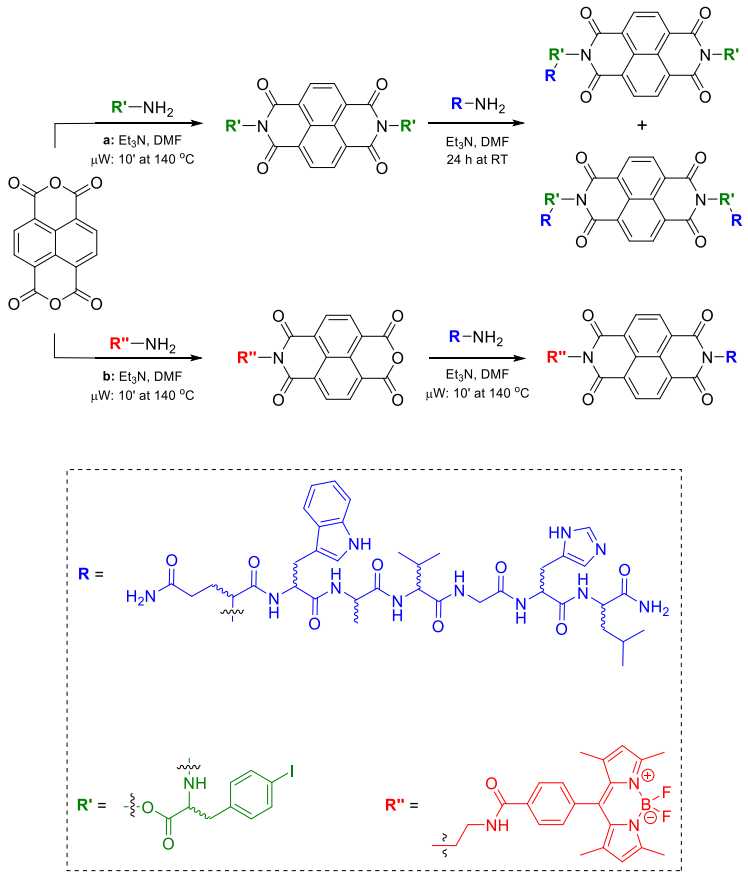

Scheme 4.1. Schematic synthetic pathways for the designed imaging probes. The NDI-core is represented in black; the fragment of the bombesin [7-13] is displayed in blue (stereochemistry is not shown); the green moiety is the iodo-phenylalanine; the chosen BODIPY-derivative is shown in red.

4.2. Synthesis and characterisation of the peptide-tagged imaging probes

The starting point for obtaining the PCa-targeted imaging probes was the synthesis of the fragment [7-13] of the bombesin peptide. In this Chapter, two enantiomers of the chosen peptide fragment were generated considering either *L*- or *D*-amino acids. In recent years, *D*-peptides have found an important role in cancer immunotherapy thanks to their higher stability *in vivo* and oral bioavailability[45] than *L*-peptides[44]. Taxol-conjugated with a *D*-peptide presented a higher antitumor efficacy than the corresponding *L*-peptide used as control after the injection. Taking into account these considerations, the enantiomers of proposed imaging probes were synthesised and compared. In addition, the fragment 7-13 of bombesin peptide has shown biological activity and affinity to GRPRs similarly to the well-known fragment 7-14 of bombesin[12,46,47].

The fragment 7-13 has become an object of study for its applications in imaging and drug design for its targeting nature[8]. As shown in Figure 4.1, the complete bombesin peptide is a 14-amino acids chain which in which the fragment from 7 to 13 is chosen in this essay (depicted in blue).

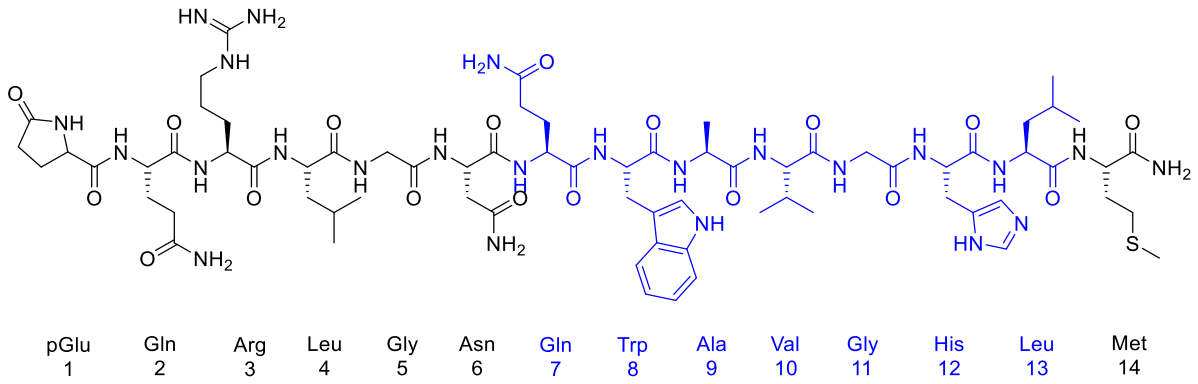

Figure 4.1. Structure of bombesin peptide with the fragment 7-13 highlighted in blue.

The synthesis of either *L*- or *D*-bombesin [7-13] peptide was carried out *via* an automated microwave-assisted solid-phase peptide synthesis (SPPS). In this case, a rink amide resin was used as solid support and, after the cleavage of the peptide from the resin, an imide group remains on the C-terminus of the peptide (specifically on the leucine amino acid residue).
The protocol employed for the synthesis of *L*- and *D*-bombesin [7-13] (***L*-12** and ***D*-12**, respectively) was adapted from the previous procedure, described in Chapter 2. Scheme 4.2 represents the generic synthetic protocol for the microwave-assisted SPPS of ***L*-12** and ***D*-12**.

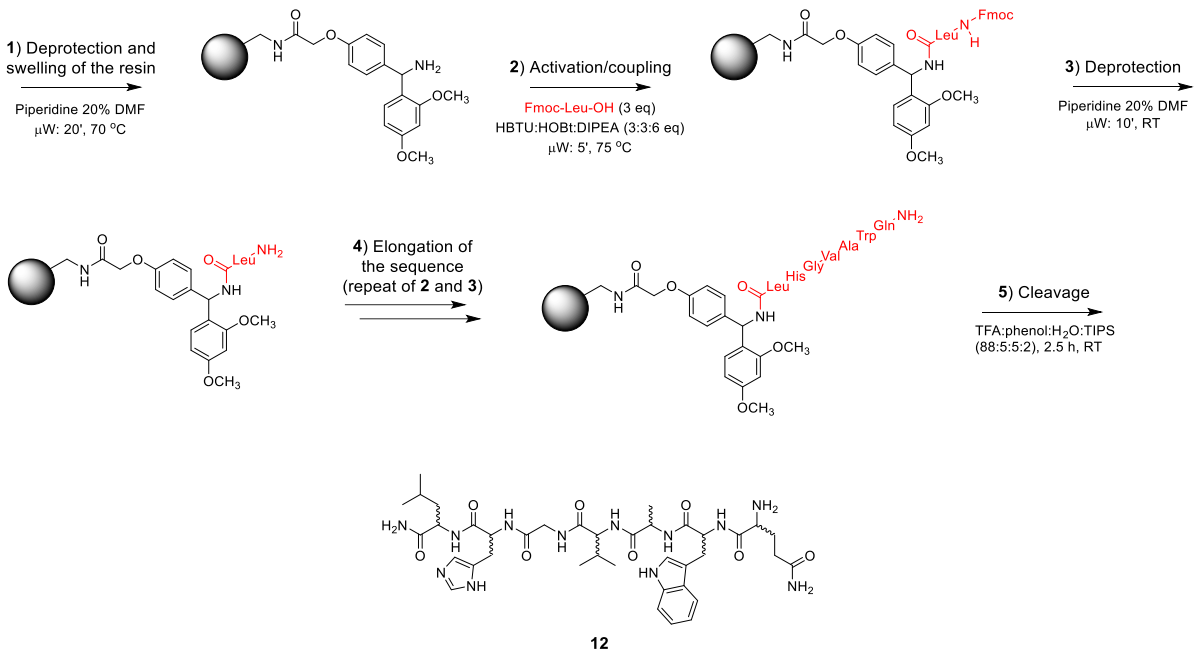

Scheme 4.2. Generic reaction scheme of the microwave-assisted SPPS of fragment 7-13 of bombesin peptide **12**. (Stereochemistry not indicated).

Figure 4.2 shows the α-amino acid sequence, from the C-terminus to the N-terminus, of the two enantiomers ***L*-12** and ***D*-12** with the proper stereochemistry indicated. Each amino acid is highlighted with different colours. Scheme 4.2 describes the generic reaction protocol followed to synthesise the peptides. 3 equivalents of each amino-acid were added at each coupling step with HBTU 0.6 M in DMF, HOBt 3 M in DMF and concentrated DIEA in ratio 3:3:6. The deprotection of the fluorenylmethyloxycarbonyl (Fmoc) protecting group was performed with piperidine 20% in DMF. The leucine presents the amide group due to the cleavage from the rink amide resin. The cleveage of the peptide from the resin was obtained with TFA/H_2O/TIPS (95:2.5:2.5).

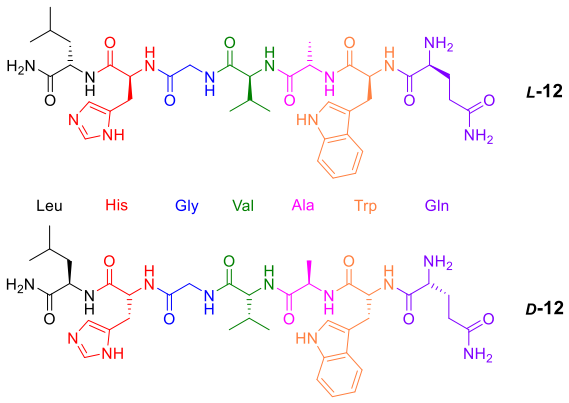

Figure 4.2. Structure of the two synthesised enantiomers of the synthesised bombesin [7-13] peptide (**12**) with the corresponding stereochemistry and α-amino acids sequence.

Both 7-amino acids sequences were characterised by mass spectrometry after purification *via* HPLC (analytical HPLC shown in Figure 4.3, method A described in Experimental Section) (yields: 20% for ***L*-12** and 15% for ***D*-12**).

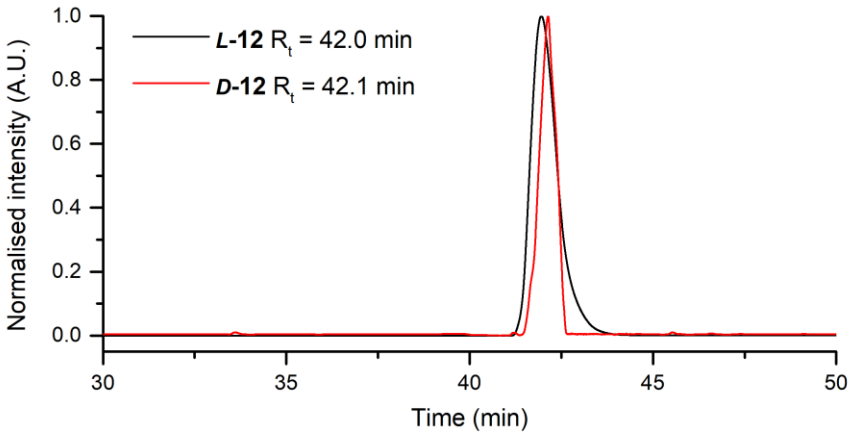

Figure 4.3. Comparative analitycal HPLC of both enantiomers of the fragment [7-13] of the bombesin peptide (method A described in Experimental Section).

Figures 4.4a and 4.4b show the observed and theoretical isotopic patterns for the ion $[M+H]^+$ of ***L*-12** and ***D*-12**, respectively. Both detected patterns fit within 5 mDa error with the simulated data.

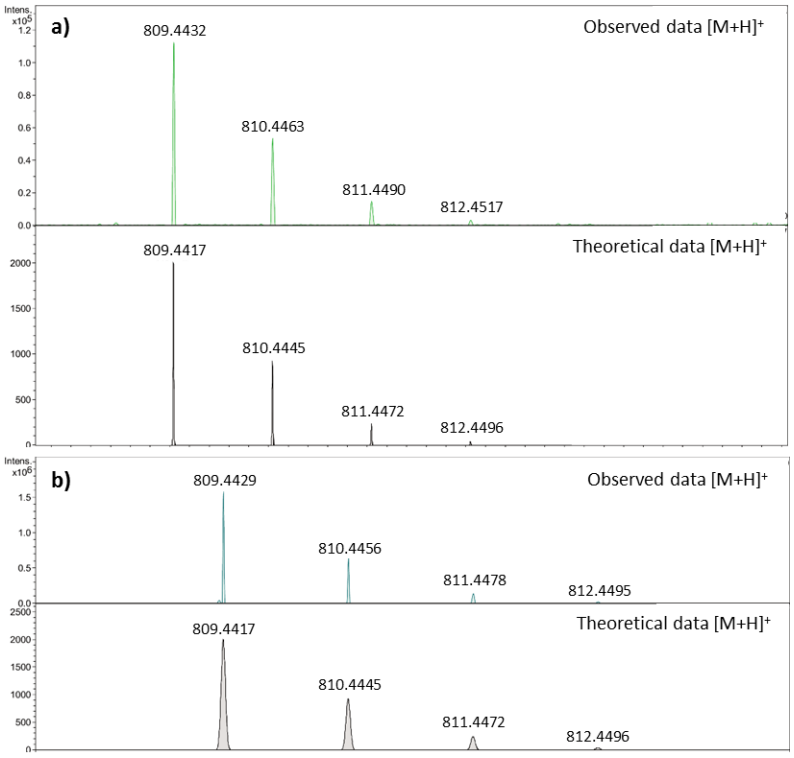

Figure 4.4. Mass spectrometry analysis of **a)** ***L*-12** and **b)** ***D*-12**. The observed data of the $[M+H]^+$ ion is shown on top, whilst its simulated isotopic pattern is below.

The second part of the synthesis of the targeted-imaging probes was the derivatisation of the NDI core. Such protocol involved the symmetric derivatisation naphthalene dianhydride (NDA) with an α-amino acid-derivative (iodo-phenylalanine). The procedure adapted from the work of Pengo *et al.*[3] is shown in Scheme 4.3.

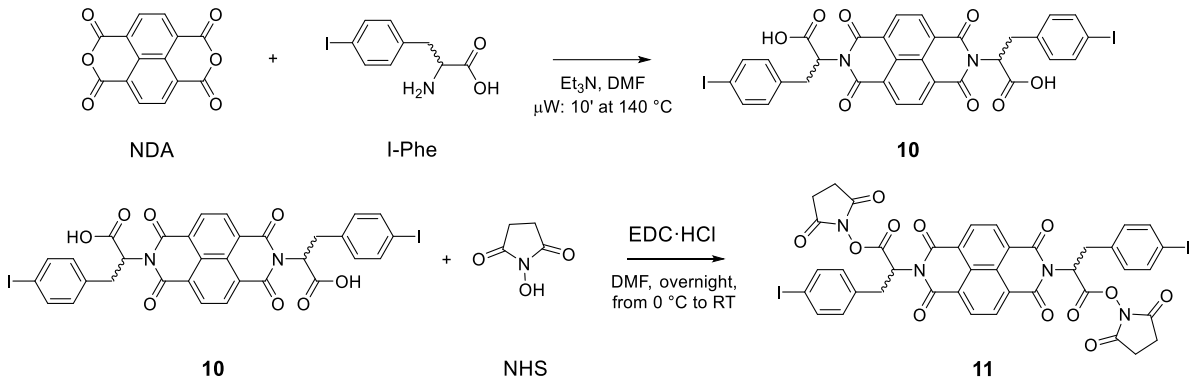

Scheme 4.3. Reaction scheme of the synthesis of the building block **11**. (Stereochemistry is indicated in the List of compounds).

The condensation of the NDA reaction with either *L*- or iodo-*D*-phenylalanine (I-*L*/*D*-Phe) was carried out on a microwave system. 1 equivalent of NDA (200.2 mg) and 2 equivalents of iodo-phenylalanine (438.8 mg) were suspended in dimethylformamide and a catalytic quantity of triethylamine (0.2 mL) and sonicated until complete homogenisation. The reaction mixture was heated at 140 ºC for 10 minutes. Such method provided a fast, efficient, well-yielded and pure synthesis of either ***L*-10** or ***D*-10** (yields: 59% for ***L*-10** and 60% for ***D*-10**). The carboxylic group of **10** was activated by 8 equivalents of 1-ethyl-3-(3-dimethylaminopropyl) carbodiimide hydrochloride (EDC·HCl, 232.8 mg) in the presence of 5.5 equivalents of *N*-hydroxysuccinimide (NHS, 94.9 mg). Such reagent has been considered a good leaving group for the next coupling with the reactive amino group of the peptide[13]. This step generated the molecules **11** shown in Scheme 4.4, valid either for the *L*- or *D*-enantiomer (yields: 83% for ***L*-10** and 84% for ***D*-10**).

Figure 4.5 shows the comparative ^{1}H-NMR spectra of compounds **10** and **11**. Such ^{1}H-NMR spectra of the *L*-enantiomers of compounds **10** and **11** were already described in Chapter 3, here the main resonances will be briefly mentioned and analytical HPLC is shown in Figure 4.6 (method A described in Experimental Section).

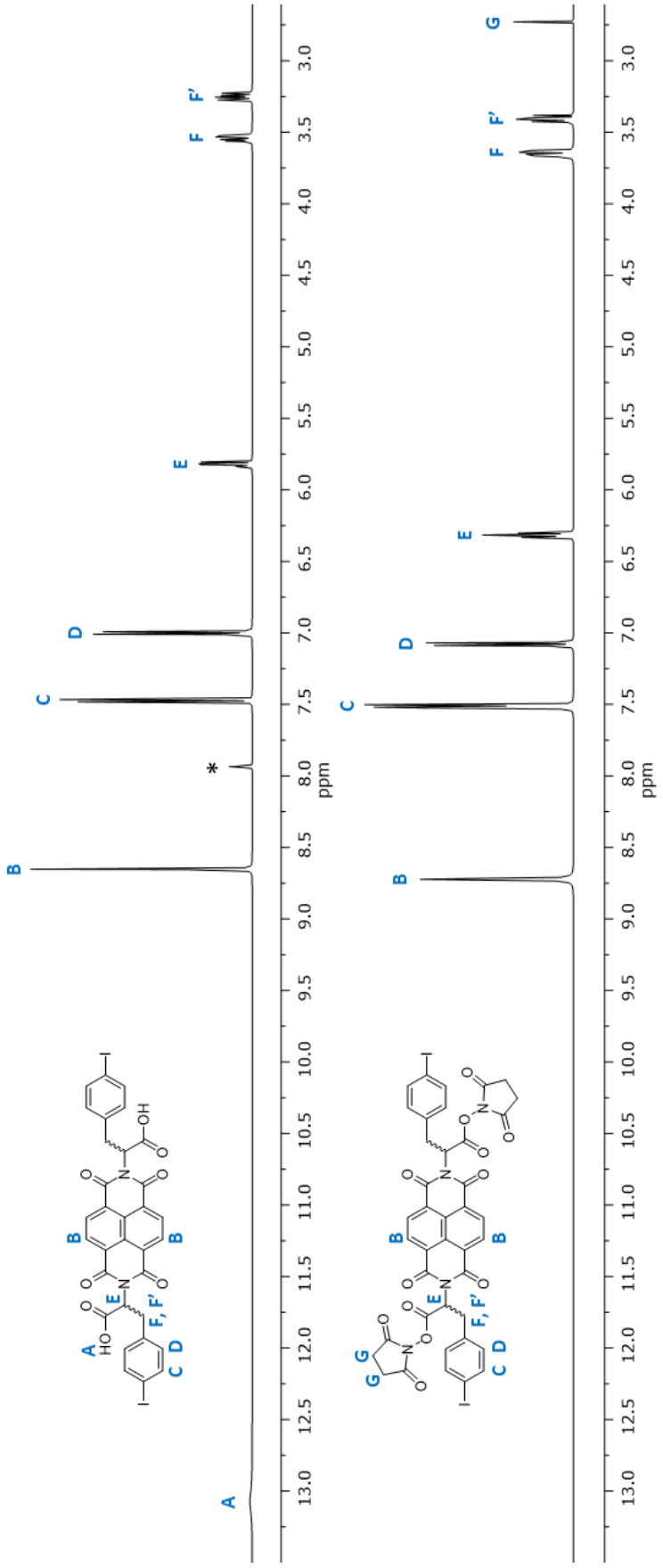

Figure 4.5. Comparative ^{1}H-NMR spectra of compounds **10** (on the top) and **11** (on the bottom). (* DMF residual signal).

The characteristic singlet of the 4 protons on the NDI core appeared at around 8.65 ppm (*B*). The signals at 7.55 and 7.05 ppm (*C* and *D*, respectively) were attributed to the aromatic ring of the iodo-phenylalanine moiety. The resonance of the protons in α-position of the amino acid appeared at 6.32 ppm (***L*-11**) and 5.85 (***L*-10**). The diastereotopic protons in β-position of the phenylalanine are located at 3.65 and 3.38 ppm (*F* and *F'*). The spectrum of ***L*-10** shows a broad singlet at 13.10 ppm (*A*) attributed to the hydrogen on the carboxylic group. On the other hand, the spectrum of ***L*-11** shows a singlet at 2.73 (*G*) attributed to the 4 protons on the NHS moiety.

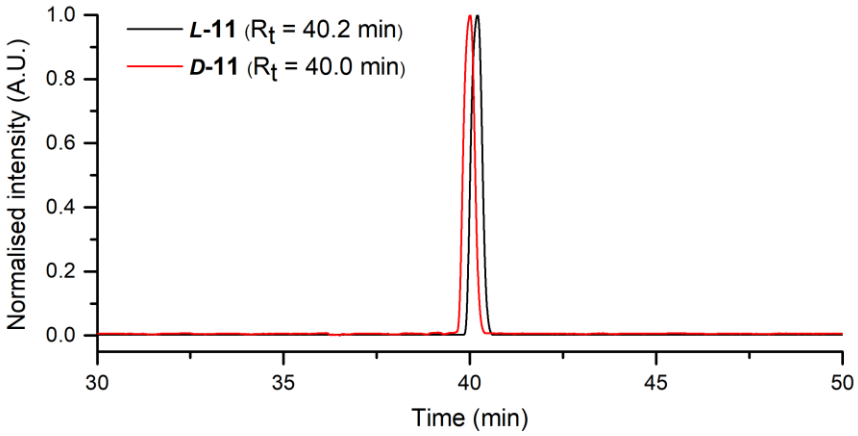

Figure 4.6. Comparative analytical HPLC of ***L*-11** and ***D*-11** (method A described in Experimental Section).

The third and last step to form the NDI-based peptide-conjugates involves the coupling of peptide **12** with amino acid-tagged NDI **11**. Scheme 4.4 reports the conditions employed for both enantiomers.

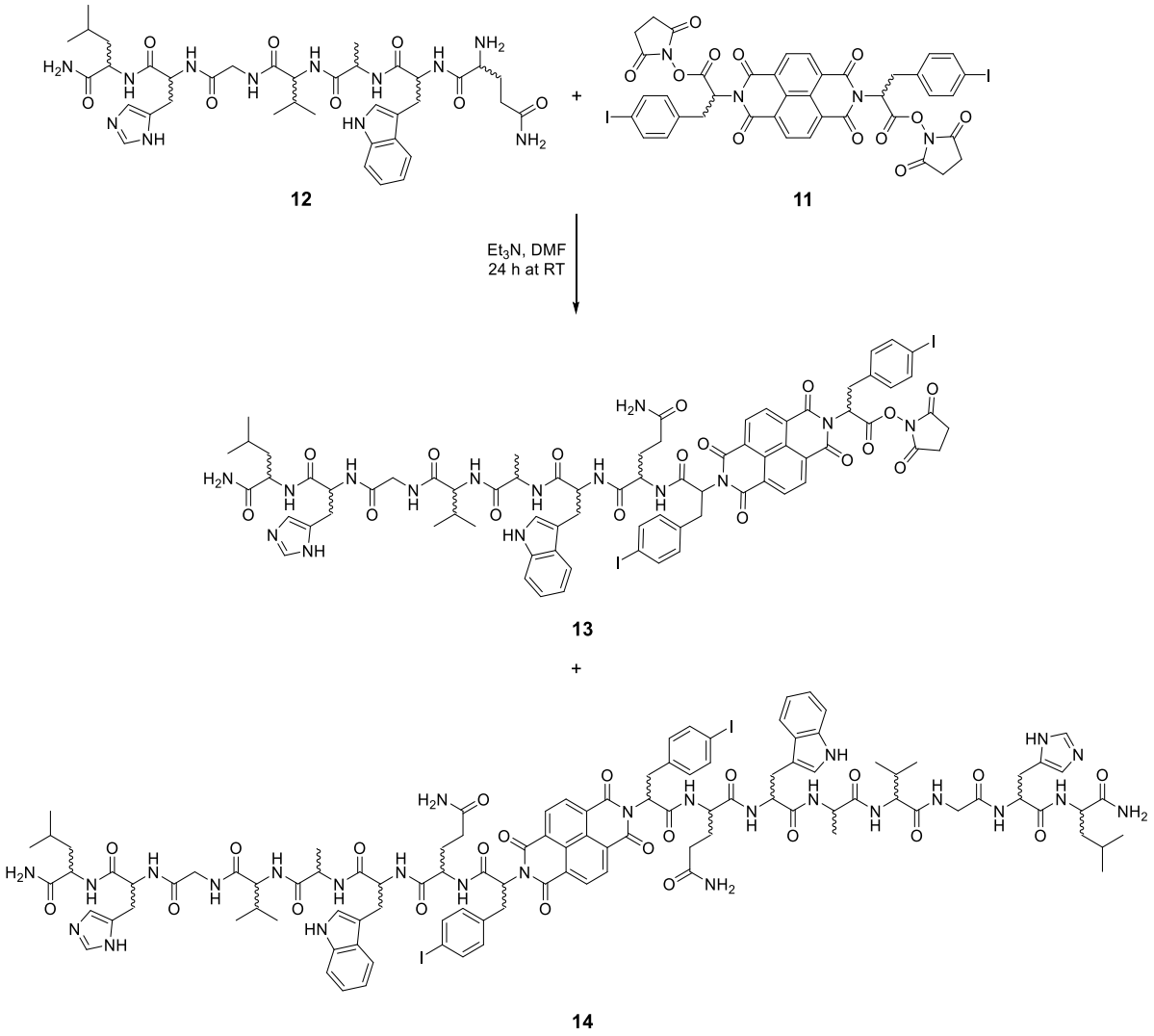

Scheme 4.4. Reaction scheme of the synthesis of the NDI-based peptide-conjugates **13** and **14**. (Stereochemistry is indicated in the List of compounds).

The suspension of 2 equivalents of **12** (110.0 mg) and 1 equivalent of **11** (68.6 mg) in anhydrous dimethylformamide and a catalytic amount of triethylamine (0.2 mL) was sonicated until complete homogenisation. The mixture reacted at room temperature for 24 hours. The same reaction was also attempted using the microwave-assisted synthesis. In this case, the mixture of the reagents was heated at 70 °C for 45 minutes. Such method revealed an efficient and quick procedure to obtain **13** and **14** (yields: 1.0% for ***L*-13**; 3.9% for ***L*-14**; 1.2% for ***D*-13**; 1.1% for ***D*-14**). The *mono*-peptide derivative **13** presents a succinyl moiety in one side of the structure. Such a unit can be used for further modification of the compound. In both cases, the crude materials **13** and **14** were precipitated by cold diethyl ether and purified via HPLC (method B in Experimental Section).

To assure that the room temperature and microwave-assisted syntheses worked comparably, the semi-preparative HPLC chromatograms are reported in Figure A.63 in Appendices A (method B described in Experimental Section). Comparing the chromatograms of the microwave-assisted and room temperature reactions, no substantial differences in the retention times in the two different reaction conditions were noticed. Such comparison confirms that the microwave-assisted reaction can be used for the coupling of such building blocks to form quickly and efficiently these peptide-tagged probes. Two main fractions, which belong to **13** and **14**, were found after the HPLC purification. Surprisingly, another compound (mass spectrum shown in Figure A.57 in Appendices A) was found in the chromatograms attributed to a *mono*-peptide molecule without the NHS group on the other side. Thanks to the mass spectrometry analysis of this fraction, it was possible to hypothesise that the TFA buffer in the HPLC solvents may hydrolyse the carbonyl group during the purification. The proposed structure of the compound found (**13'**) is shown in Figure 4.7.

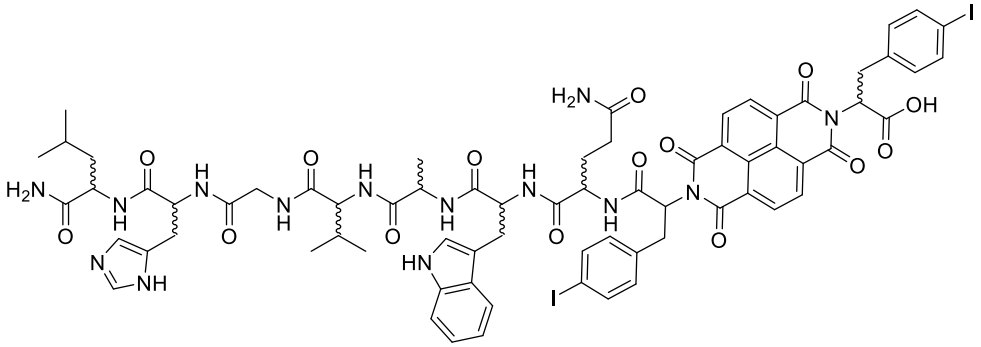

Figure 4.7. The proposed structure of the found compound (*L*- or *D*-enantiomer) by mass spectrometry analysis. (Stereochemistry not indicated here).

The mass spectra of **13** and **14** are reported in Figure 4.8 with their observed and theoretical isotopic patterns with related structure, chemical formula and exact masses.

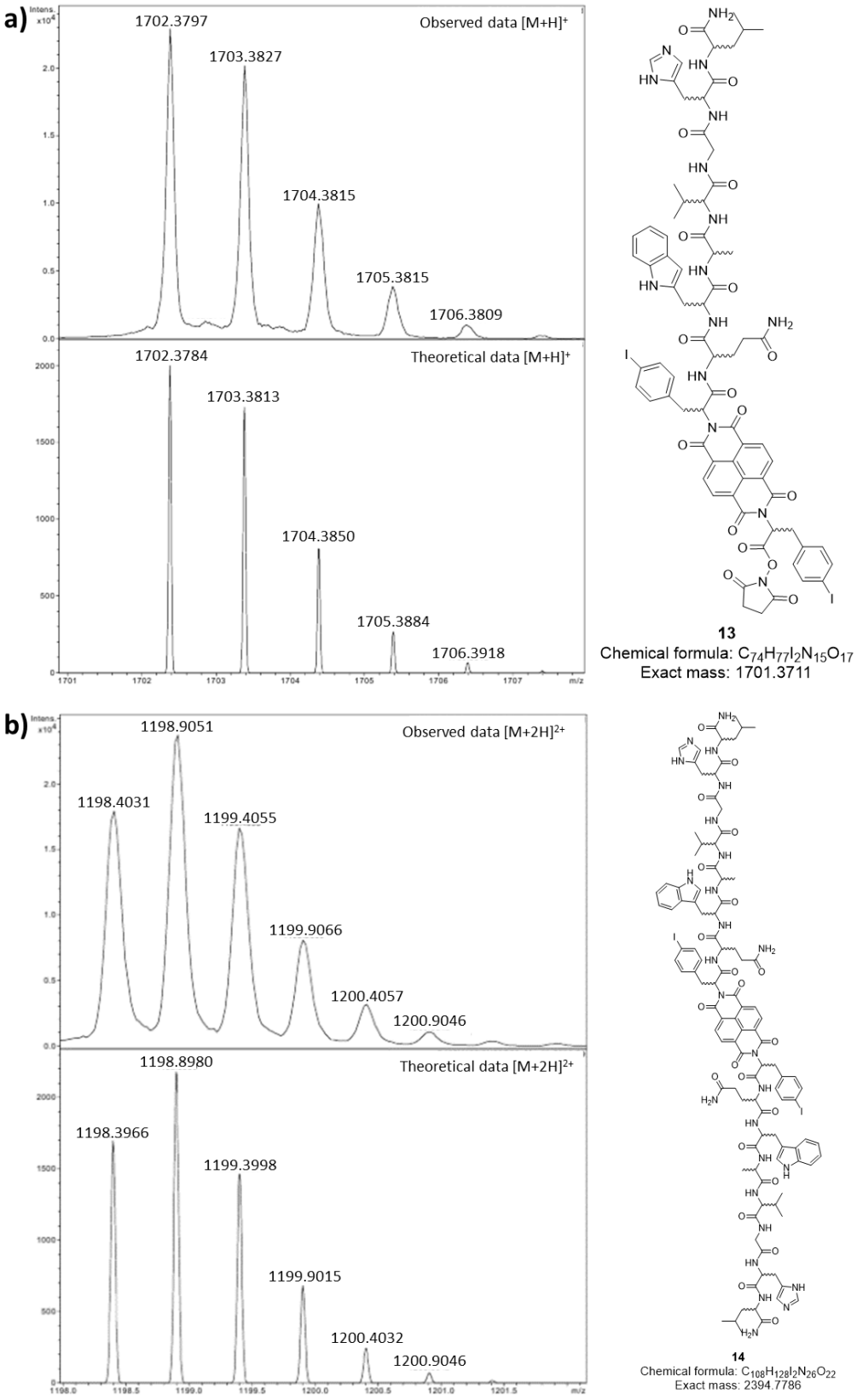

Figure 4.8. Observed and theoretical isotopic patterns of compounds **a) 13** and **b) 14**.

The chirality of ***L*-13** *vs* ***D*-13** and ***L*-14** *vs* ***D*-14** was evaluated using circular dichroism (Figure 4.9 and 4.10). The analysis was focused on one of the maximum absorption wavelengths of the NDI-core which corresponds to about 380 nm. DMSO was the used solvent throughout this Chapter and its cut off wavelength is 268 nm. This solvent is used in this analysis for concistency to the cellular studies undertaken with DMSO. The CD spectra were recorded excluding wavelengths below 300 nm to avoid the cut-off wavelength of DMSO.

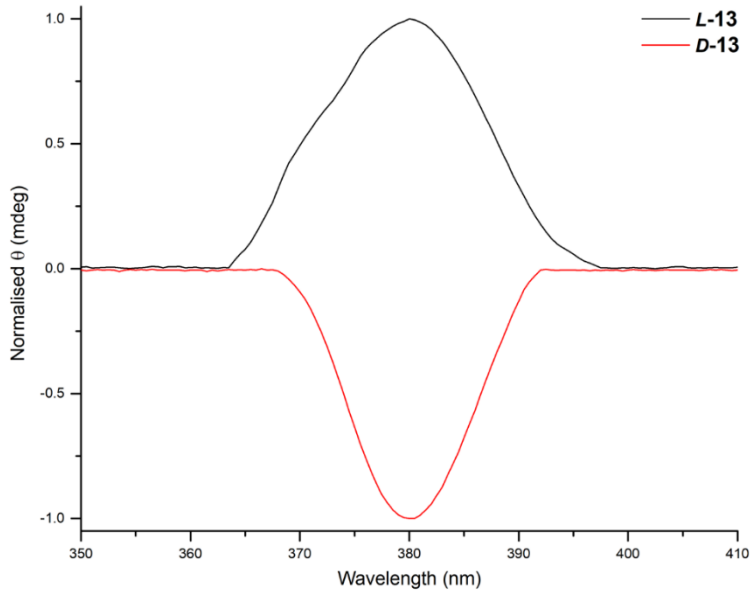

Figure 4.9. Circular dichroism spectra of compounds ***L*-13** and ***D*-13** at their absorption maxima (λ_{max}=380 nm, solutions 50 µM in DMSO).

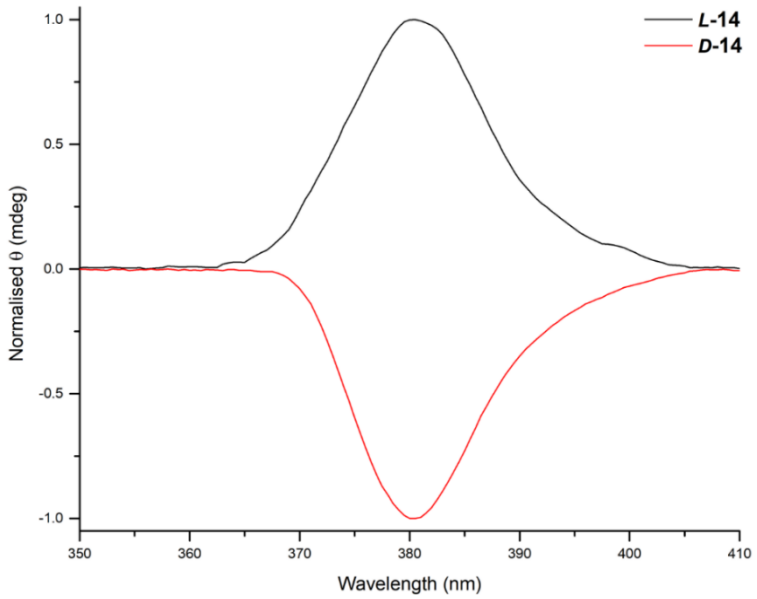

Figure 4.10. Circular dichroism spectra of compounds ***L*-14** and ***D*-14** at their absorption maxima (λ_{max}=381 nm, 50 µM in DMSO).

Figures 4.9 and 4.10 shows that the *L*-enantiomers (depicted in black curves) present a positive rotatory behaviour rather than the negative feature of their *D*-enantiomers (red curves). Afterwards, variable temperature circular dichroism experiments were carried out to evaluate the effect of temperature on thechirality of the compounds and temperature-induced structural changes are present in the secondary structure of such peptide-based molecules[48]. . From these results, no substantial changes were noticed in their chirality and secondary structure which remain unchanged until 75 °C (spectra are shown in Appendices A, from Figure A.59 to A.62).

Scheme 4.5 reports the synthetic protocol of another type of fluorescent probe. NDA was asymmetrised, introducing a well-known small fluorescent moiety (derivative of BODIPY (**2**), described in Chapter 2) and the *L*-version of the bombesin [7-13] (***L*-12**). Specifically, this strategy was chosen to increase the fluorescence emission and biocompatibility of the NDI derivative thanks to the presence of the moiety of the BODIPY derivative **2**. As mentioned previously, derivatives of BODIPY have found a lot of *in vivo* applications due also to their ease of functionalisation[10,11].

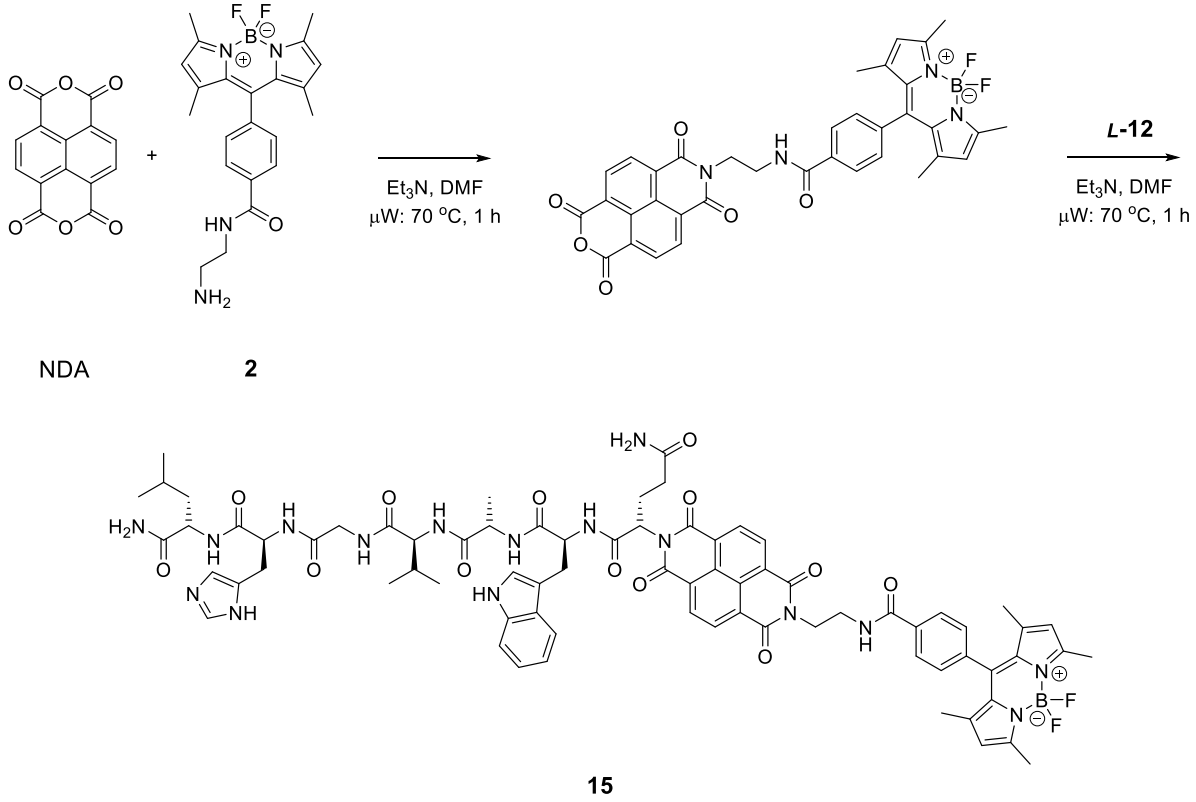

Scheme 4.5. Reaction scheme of the synthesis of compound **15**.

This synthesis involved a two-step microwave-assisted reaction which asymmetrised the NDI-core with two different moieties[14]. NDA (0.16 mmol) was added in excess of **2** (0.12 mmol) to avoid the formation of a disubstituted-derivative and Et_3N (0.02 mL) was added in the mixture to guarantee that the amino group of **2** was deprotonated.

After the homogenisation of the reaction mixture by sonication, it was heated at 70 ºC for 1 hour. Afterwards, the crude product was purified by flash chromatography and the pure *mono*-intermediate was used without further purification in the second step with ***L*-12** (0.07 mmol). The mixture was heated at 70 ºC for 1 hour and the pure product was obtained by centrifugation/washings with cold Et_2O (yield: 30%). Figure 4.11 shows the isotopic pattern of the $[M+H]^+$ ion of compound **15**.

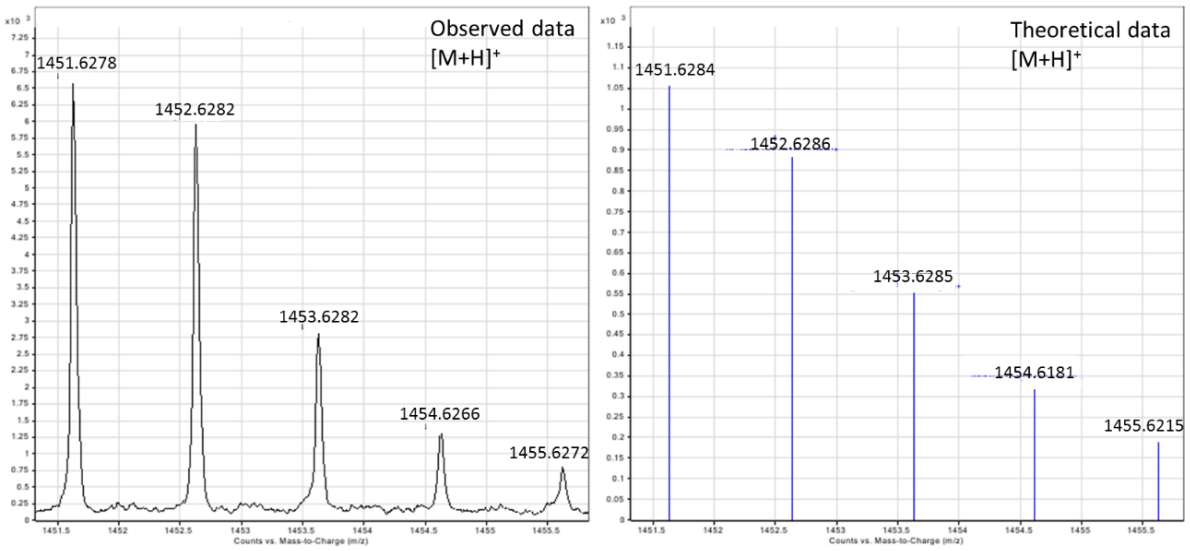

Figure 4.11. Mass spectra of compound **15**. Observed data is reported on the left, whilst the simulated isotopic pattern is shown on the right.

The mass spectrometry analysis shows an observed isotopic pattern at 1451.6278 m/z which can be associated with the ion $[M+H]^+$ of **15**. This data is within 5 mDa of error with the simulated isotopic pattern of this molecule.

All the proposed imaging probes (*i.e.* **13**, **14** and **15**) were compared by analytical HPLC with their main precursors: the NDI-core and the bombesin [7-13] (method A described in the Experimental Section). Figure 4.12 shows the chromatograms and retention times of such compounds. As precursors were used ***L*-11** and ***L*-12** which present similar retention times of their *D*-variants.

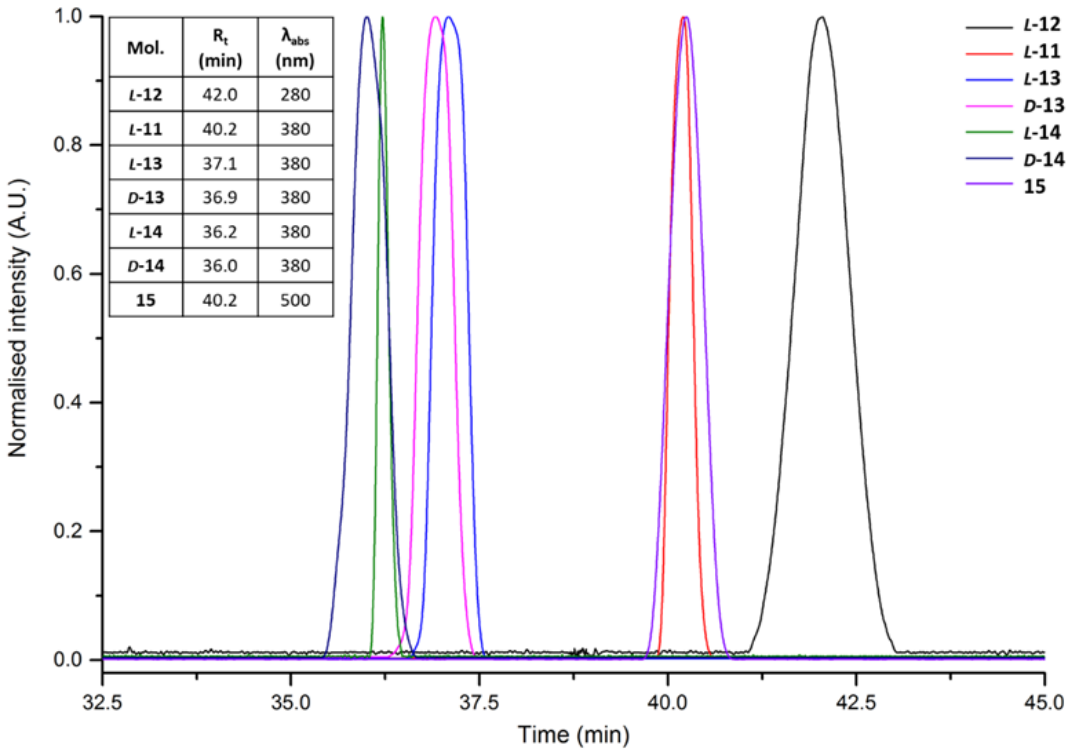

Figure 4.12. Comparative analytical HPLC chromatograms of ***L*-12** (black, monitored wavelength 280 nm), ***L*-11** (red, monitored wavelength 380 nm), ***L*-13** (blue, monitored wavelength 380 nm), ***D*-13** (purple, monitored wavelength 380 nm), ***L*-14** (green, monitored wavelength 380 nm), ***D*-14** (navy blue, monitored wavelength 380 nm) and **15** (dark purple, monitored wavelength 500 nm). The table shows the corresponding retention times and the wavelengths of the recorded chromatograms (method A described in Experimental Section).

At first glance, the *mono*-peptide probes (***L*-13** and ***D*-13**) present retention times at around 37 minutes which differ from the elution time of their *bis*-variants ***L*-14** and ***D*-14**. Furthermore, it can be noticed that the enantiomers (***L*-13** *vs* ***D*-13** and ***L*-14** *vs* ***D*-14**) show similar retention times which is expected as enantiomers have similar physical properties. On the other hand, the retention time of **7** is very different from the other probes. Overall, these molecules show retention times very distinct from their precursors ***L*-11** and ***L*-12**.

4.2.1. Investigation *via* UV-visible and fluorescence spectroscopies in solution

The optical spectroscopic features of the peptide-tagged probes were assessed by UV-visible and fluorescence spectroscopies before they were studied *in vitro*. These analyses were performed in DMSO solutions which is the solvent used throughout this Chapter to incubate compounds into living cells. The following Figures show the absorption spectra of **11** and **12** (Figures 4.13b and 4.13a), **13** and **14** (Figures 4.14c and 4.14d) and **2** and **15** (Figures 4.15e and 4.15f).

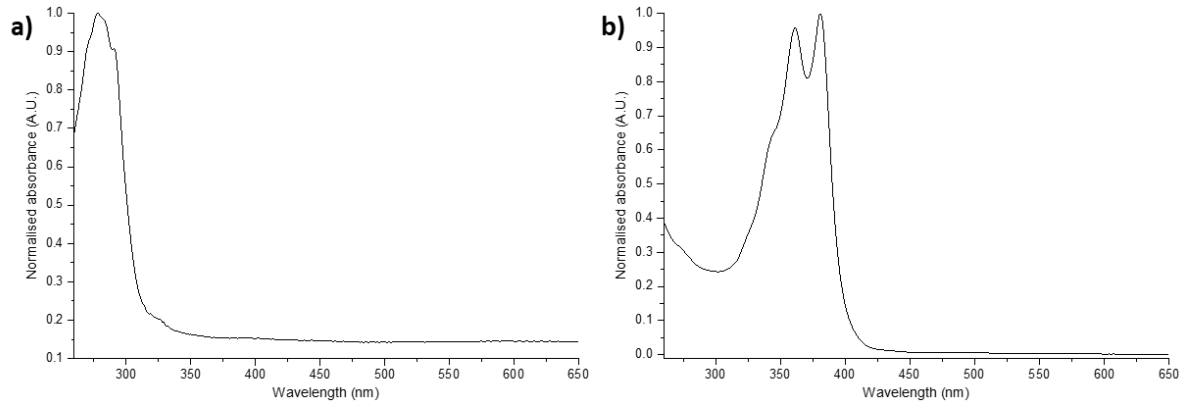

Figure 4.13. Normalised UV-Vis spectra of compounds **a) *D*-12** (50 µM in DMSO) and **b) *D*-11** (2.5 µM in DMSO).

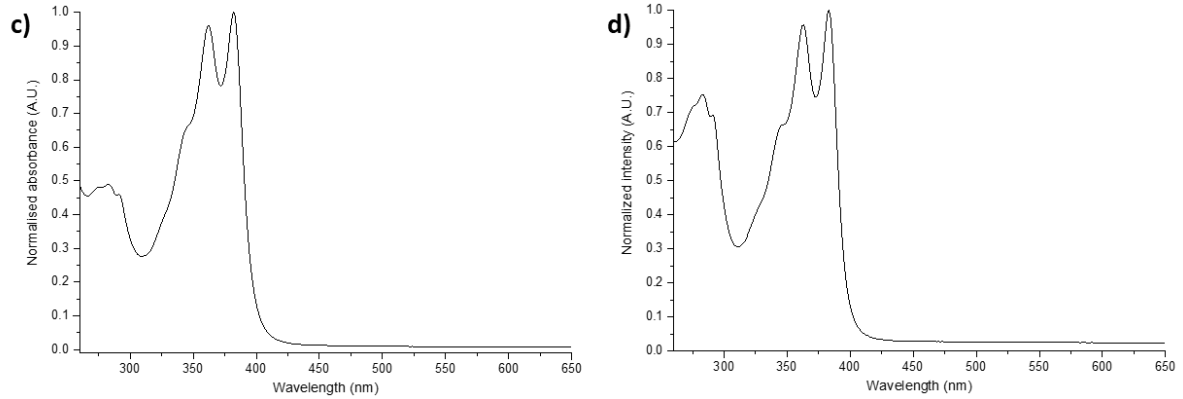

Figure 4.14. Normalised UV-Vis spectra of compounds **c) *D*-13** (10 µM in DMSO) and **d) *D*-14** (200 µM in DMSO).

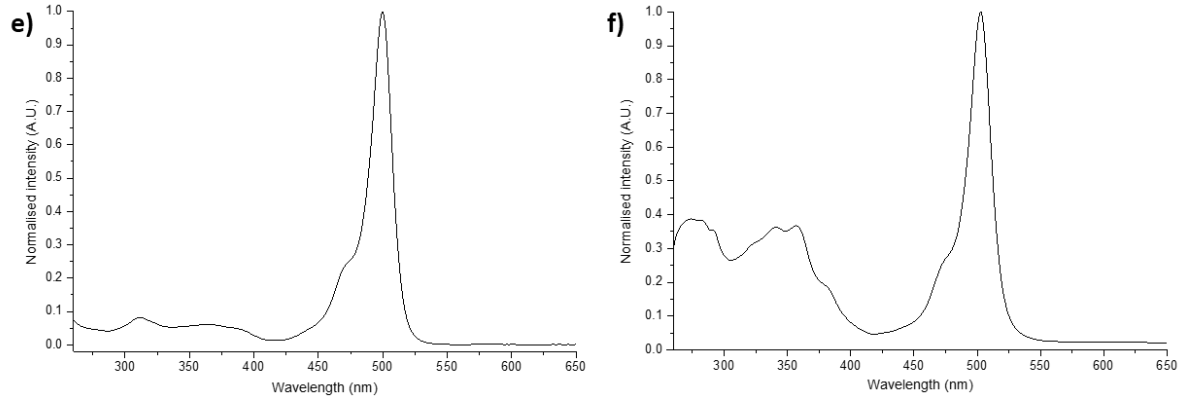

Figure 4.15. Normalised UV-Vis spectra of compounds **e) 2** (10 µM in DMSO) and **f) 15** (50 µM in DMSO).

The absorption spectrum of **13** (Figure 4.14c) shows three relative maxima. The first maximum at around 280 nm was attributed to the absorption of the fragment [7-13] of bombesin peptide (spectrum shown in Figure 4.13a). Such absorption is due to the n-π^* and π-π^* transitions of the aromatic rings of the histidine and tryptophan residues. On the other hand, the maxima at around 360 and 380 nm are attributed to the allowed π-π^* transitions due to the electric dipole moment polarised along the long axis of the NDI-core[15,16] (spectrum in Figure 4.13b). The same trend can be noticed in the UV-visible spectrum of **14** (Figure 4.14d). Besides, the absorption at about 280 nm is more intense (almost twice) than in ***D*-13**. This fact can be referred to as the presence of two bombesin [7-13] moieties in the molecule. The spectrum of **15** (Figure 4.15f) displays the characteristic absorption bands of the bombesin [7-13] (maximum at *circa* 280 nm, Figure 4.13a) and the NDI-core (maxima at approximately 360 and 380 nm). Moreover, the strongly intense maximum at 500 nm is due to π-π^* transitions the BODIPY moiety[17].

The fluorescence emission characteristics of the proposed imaging probes were estimated by fluorescence spectroscopy, particularly *via* fluorescence excitation-emission matrix (EEM). This method allows visualising the emission wavelengths ranges and their relative intensities of the studied solutions in particular excitation wavelength ranges.

The fluorescence emission maps of both enantiomers of **13** and **14** (Figure 4.16c, d, e, f, respectively) are reported with their precursors **12** and **11** (4.16a and 3.16b, respectively).

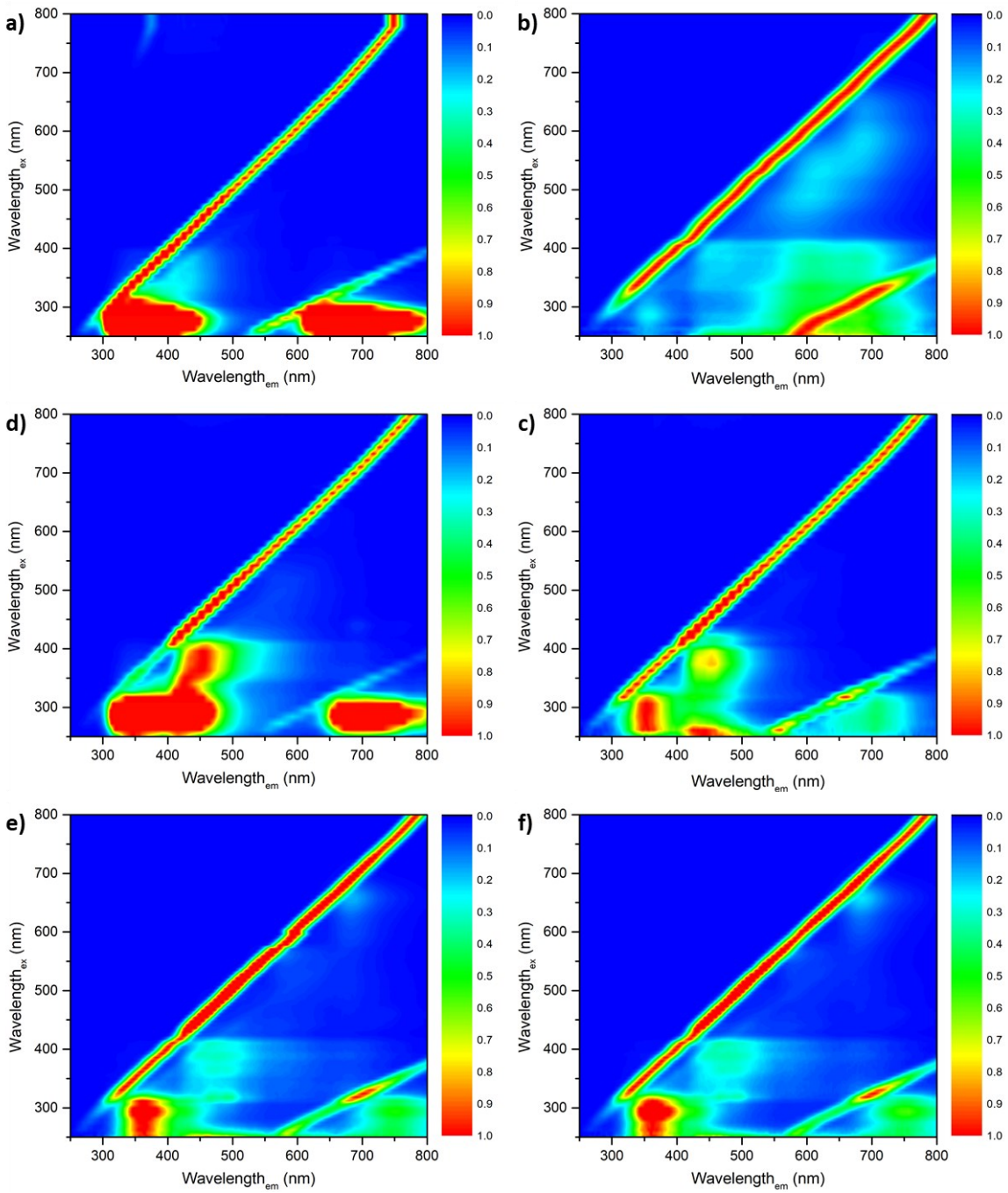

Figure 4.16. Normalised fluorescence excitation-emission matrix maps of **a) *D*-12** (50 μM in DMSO); **b) *D*-11** (2.5 μM in DMSO); **c) *L*-13** (200 μM in DMSO); **d) *L*-14** (200 μM in DMSO); **e) *D*-13** (200 μM in DMSO); **f) *D*-14** (200 μM in DMSO).

In both enantiomer sets (***L*-13** and ***L*-14**, ***D*-13** and ***D*-14**), strong emissions can be found in the range between 300 and 450 nm when they are excited by wavelengths between 250 nm and 300 nm. The different stereochemistry does not affect substantially the range of the fluorescence emission. However, the intensities of the fluorescence emissions of the *D*-enantiomers are slightly weaker than their *L*-version.

The fluorescence emissions are mainly due to the presence of aromatic rings of the tryptophan and histidine residues presented on the bombesin [7-13] peptide moiety. (EEM map is depicted in Figure 4.16a). On the other hand, weak emission bands can be noticed at around 400-500 nm when excited from 350 to 400 nm. As shown in Figure 4.16b, these emissions are typically attributed to the NDI-core which presents also emissions at around 350 nm (λ_{ex}≈270 nm).

All four compounds showed good fluorescence emissions at around 450 nm when they are excited at 405 nm. The ranges above 550 nm and onwards are affected by the second-order Rayleigh scattering[18].

Molecule **15** was also analysed by fluorescence excitation-emission fluorescence matrix in DMSO solution which map is shown in Figure 4.17.

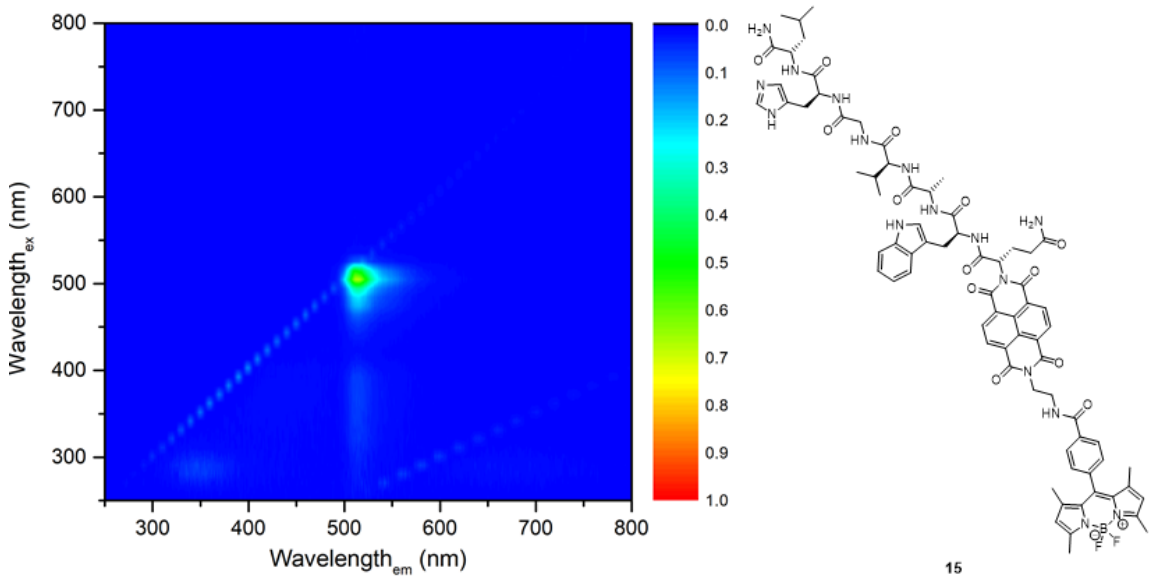

Figure 4.17. Normalised fluorescence excitation-emission matrix of compound **15** (50 µM in DMSO).

Molecule **15** showed an intense relative emission range at around 500 and 560 nm when it is excited between 470 and 520 nm. This range is particularly interesting for the *in vitro* studies through confocal microscopy in which the auto-fluorescence emission of cells is avoided. Furthermore, the fluorescence emission in this range can be typically attributed to the BODIPY moiety[11]. Besides, the emission ranges assignable to the aromatic residues of the bombesin [7-13] and the typical emission of NDI-core are only slightly perceptible (Figure 4.16a and 4.16b, respectively).

The molar extinction coefficients (ε) and the quantum yields (Φ) of the imaging probes and their precursors are summarised in Table 4.1.

Table 4.1. Summary table with molar extinction coefficients and quantum yields of the synthesised molecules. The Φ were calculated using the following standards: **a)** rhodamine B 2.6 nM in MeOH (Φ=0.70±0.02; λ_{ex}=348 nm; η=1.33); **b)** *L*-tryptophan 0.1 μM in H_2O (pH=6) (Φ=0.12±0.01; λ_{ex}=280 nm; η=1.33); **c)** fluorescein 2.3 nM in 0.1 M $NaOH_{(aq)}$ (Φ=0.95±0.03; λ_{ex}=496 nm; η=1.33). Data obtained from literature[20].

Molecule (conc.)	ε_{max} ($\cdot 10^3$ L mol^{-1} cm^{-1}) (λ_{max})	**Φ** (λ^{em}_{max})
***L*-12** (50 μM DMSO)	4.4 (278 nm)	0.037 (340 nm)[b]
***D*-12** (50 μM DMSO)	3.1 (278 nm)	0.037 (341 nm)[b]
***L*-11** (2.5 μM DMSO)	472.0 (361 nm)	0.092 (427 nm)[a]
***D*-11** (2.5 μM DMSO)	493.3 (361 nm)	0.094 (426 nm)[a]
***L*-13** (200 μM DMSO)	14.9 (362 nm)	0.015 (429 nm)[a]
***D*-13** (200 μM DMSO)	16.6 (362 nm)	0.023 (428 nm)[a]
***L*-14** (200 μM DMSO)	16.7 (363 nm)	0.050 (433 nm)[a]
***D*-14** (200 μM DMSO)	14.7 (363 nm)	0.058 (434 nm)[a]
2 (100 nM DMSO)	849.9 (503 nm)	0.017 (510 nm)[c]
15 (50 μM DMSO)	26.2 (503 nm)	0.003 (514 nm)[c]

The enantiomers of **12** and **11** present molar extinction coefficients and quantum yields comparable which is expected from optical features of enantiomers. In addition, molecules **11** have molar extinction coefficients almost 100-fold than peptides **12** which is well assessed in NDI-derivatives.

Comparing the enantiomers of **13** and **14**, it can be noticed that their ε values are similar. On the other hand, the quantum yields of the *bis*-peptide derivatives are higher than their *mono*-versions. The presence of two moieties of the peptide on the same structure may play an important role in enhancing the quantum yield of the entire molecule.

Compound **15** showed values of ε and Φ very different from the ones of its precursor **2**. In particular, the molar extinction coefficient of **15** is almost 35-fold less than **2** and the quantum yield is 5 times lower.

4.2.2. Preliminary investigations *via* confocal laser-scanning microscopy in living cancer cells

The spectroscopic features and aggregation behaviours of the five fluorescent imaging probes, which were studied through UV-visible and fluorescence spectroscopies may be used as a benchmark for *in vitro* imaging assays. These compounds were incubated with living prostate cancer cells line (PC-3) under physiological conditions to visualise their uptake and bio-localisation in a cellular environment, using single- and multi-photon fluorescence imaging methods. In particular, the PC-3 cells present an expression of GRPR of approximately $4 \cdot 10^5$ receptors/cell[49] and have been demonstrated to be responsive to bombesin-based compounds[50]. The used confocal microscope is equipped with three excitation wavelengths, *i.e.* 405, 488 and 561 nm, in which present three different emission channels (blue channel: λ_{em}=417–477 nm; green channel: λ_{em}=500–550 nm; red channel: λ_{em}=570–750 nm). The 405 nm excitation wavelength may be the optimal investigation wavelength for those compounds, considering that they manifested good fluorescence emissions in solution at around 450 nm when they are excited at this wavelength (EEM maps in Figure 4.17). However, in some cases, PC-3 cells could emit auto-fluorescence when they are excited by an energy corresponding to 405 nm, misleading the evaluation of the fluorescence emission due to the cells and/or the compounds. Despite this inconvenience, exciting the cells incubated with the probes with an excitation wavelength of 488 nm showed a good compromise to investigate these species in the cellular environment.

In the first instance, the precursors of the proposed imaging probes were studied by CLSM to evaluate their fluorescence emissions and localisation into prostate cancer cells. In these regards, the following figures show the micrographs of the targeting peptides **12** (both enantiomers, Figure 4.18) and the phenylalanine-tagged NDIs **11** (both enantiomers, Figure 4.19). The compounds were incubated overnight in PC-3 cells at 37 °C and then excited at 488 nm at the same laser power in the same day. The considered emission channels are the green (fluorescence emission range between 500 and 550 nm) and red channels (fluorescence emission range between 570 and 750 nm).

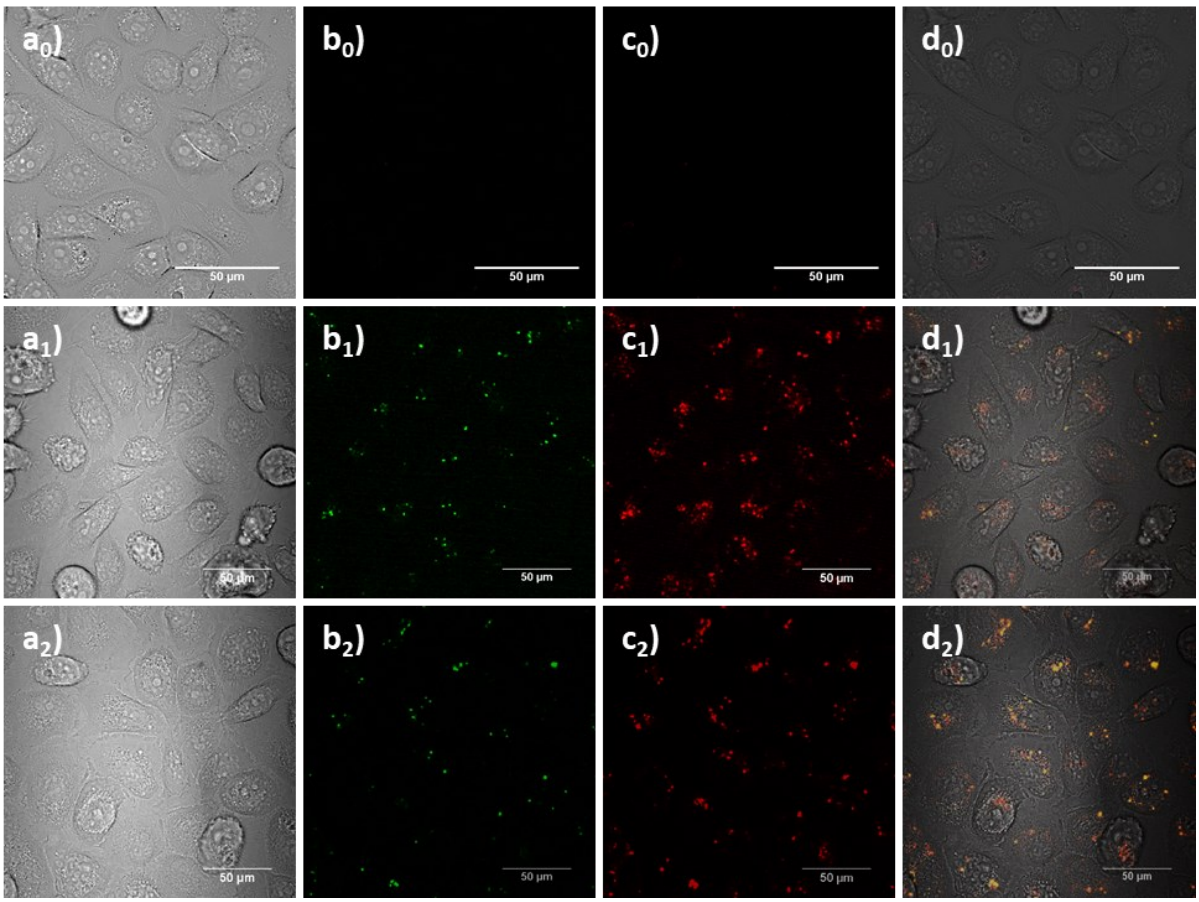

Figure 4.18. Single-photon confocal laser-scanning microscopy of PC-3 cells incubated at 37 °C for 24 h with compounds **a_1-d_1) *L*-12** and **a_2-d_2) *D*-12**. Solutions 100 µM, in 1:99 DMSO:serum-free medium. **a_0-d_0)** PC-3 cells incubated for 24 h at 37 °C with DMSO in serum-free medium (1:99) used as negative control. **$a_{0\text{-}2}$)** TD channel; **$b_{0\text{-}2}$)** green channel (λ_{em}=500–550 nm); **$c_{0\text{-}2}$)** red channel (λ_{em}=570–750 nm); **$d_{0\text{-}2}$)** overlay of TD-green-red channels. λ_{ex}=488.0 nm. Scale bar: 50 µm.

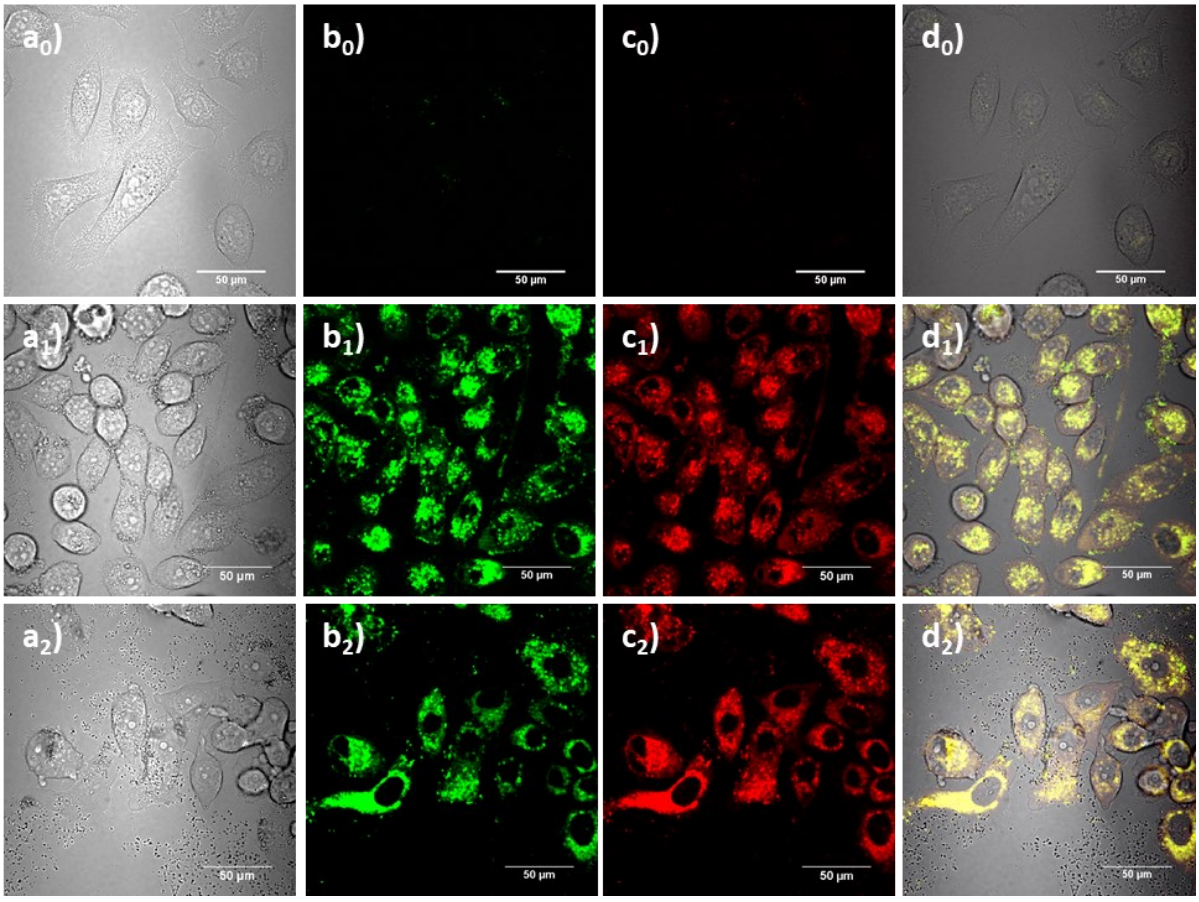

Figure 4.19. Single-photon confocal laser-scanning microscopy of PC-3 cells incubated at 37 °C for 24 h with compounds **a$_1$-d$_1$) *L*-11** and **a$_2$-d$_2$) *D*-11**. Solutions 100 µM, in 1:99 DMSO:serum-free medium. **a$_0$-d$_0$)** PC-3 cells incubated for 24 h at 37 °C with DMSO in serum-free medium (1:99) used as negative control. **a$_{0-2}$)** TD channel; **b$_{0-2}$)** green channel (λ_{em}=500–550 nm); **c$_{0-2}$)** red channel (λ_{em}=570–750 nm); **d$_{0-2}$)** overlay of TD-green-red channels. λ_{ex}=488.0 nm. Scale bar: 50 µm.

In Figure 4.18a$_1$-d$_1$ and a$_2$-d$_2$, it can be noticed the *in vitro* fluorescence emission and uptake of ***L*-12** and ***D*-12** into the PC-3 cells. The fluorescence emissions of the peptides were compared with a control consisted of the PC-3 cells incubated overnight with DMSO in serum-free medium. This comparison was used to exclude any fluorescence due to the cells instead of the compounds. In fact, both enantiomers of the bombesin [7-13] peptide **12** emitted mainly in the green and red channels of the 488 nm excitation wavelength. In addition, they showed weak fluorescence emission in all three emission channels of the excitation wavelength at 405 nm (CLSM micrographs shown in Appendices A, Figures A.71 and A.72). On the other hand, the enantiomers of **11** showed good fluorescence emissions in the green and red channels (Figure 4.19b$_3$/b$_4$ and c$_3$/c$_4$ respectively) which were compared with the fluorescence emission of the negative control.

The EEM data in solution (Figure 4.17b) of such NDI-based compounds showed emissions in the range of 550-650 nm when excited at around 480 nm which is consistent with the observed data acquired by CLSM. The different stereochemistry in both **12** and **11** did not qualitatively affect the uptake into the cells; in fact, the enantiomers of the same compound, either **12** or **11**, seem to be absorbed comparably after overnight incubation with cells. Besides, NDI-derivatives have been studied in the cellular environment thanks to their solubility in water and lipophilicity for crossing the cellular membrane[51]. The uptake showed by the enantiomers of **11** may due to passive diffusion into the cells.

Figure 4.20 and 4.21 displays the micrographs of **13** and **14** (both enantiomers) incubated into PC-3 cells line at 37 ºC overnight. The cells with the compound were excited at 488 nm at the same laser power and the micrograph collected on the same day.

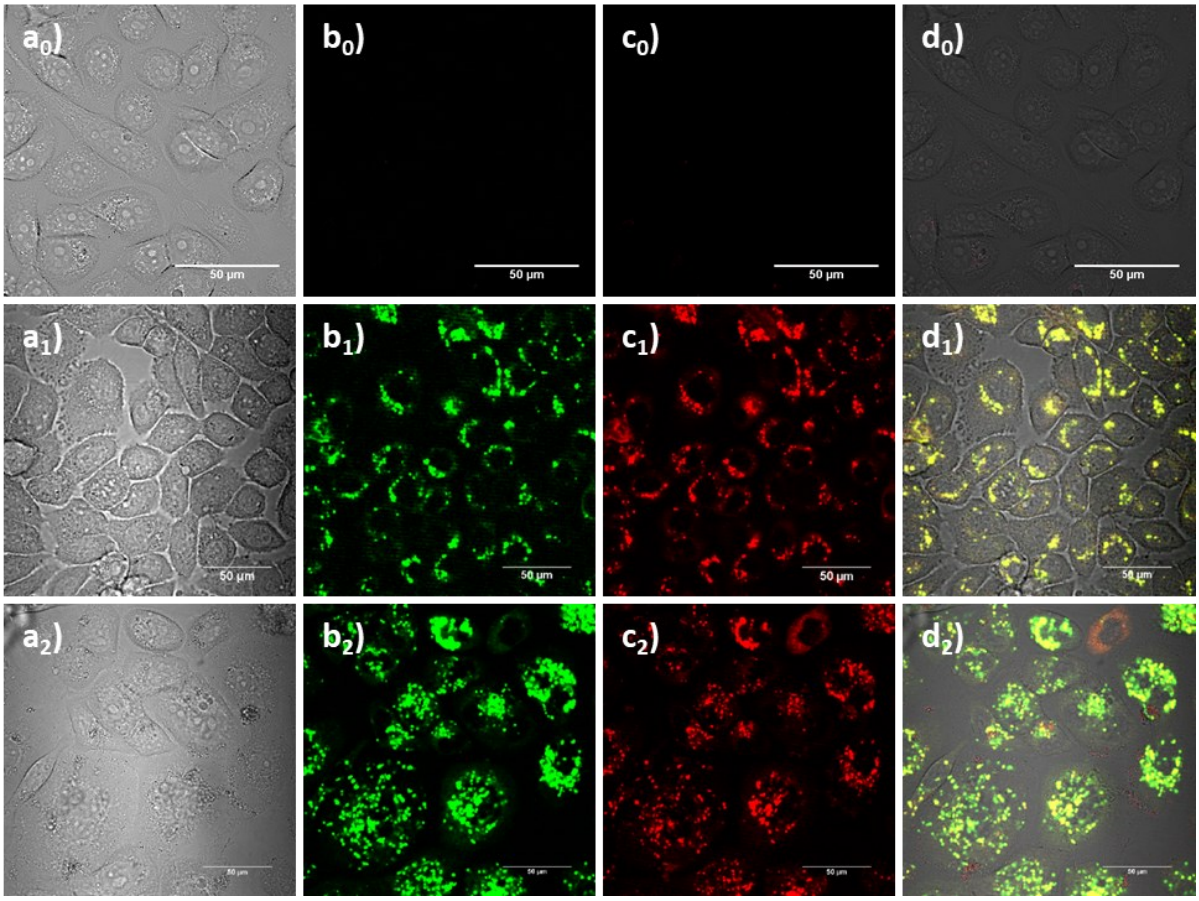

Figure 4.20. Single-photon confocal laser-scanning microscopy of PC-3 cells incubated at 37 °C for 24 h with compounds **a1-d1)** ***L*-13** and **a2-d2)** ***L*-14**. Solutions 100 µM, in 1:99 DMSO:serum-free medium. **a0-d0)** PC-3 cells incubated for 24 h at 37 °C with DMSO in serum-free medium (1:99) used as negative control. **a0-2)** TD channel; **b0-2)** green channel (λ_{em}=500–550 nm); **c0-2)** red channel (λ_{em}=570–750 nm); **d0-2)** overlay of TD-green-red channels. λ_{ex}=488.0 nm. Scale bar: 50 µm.

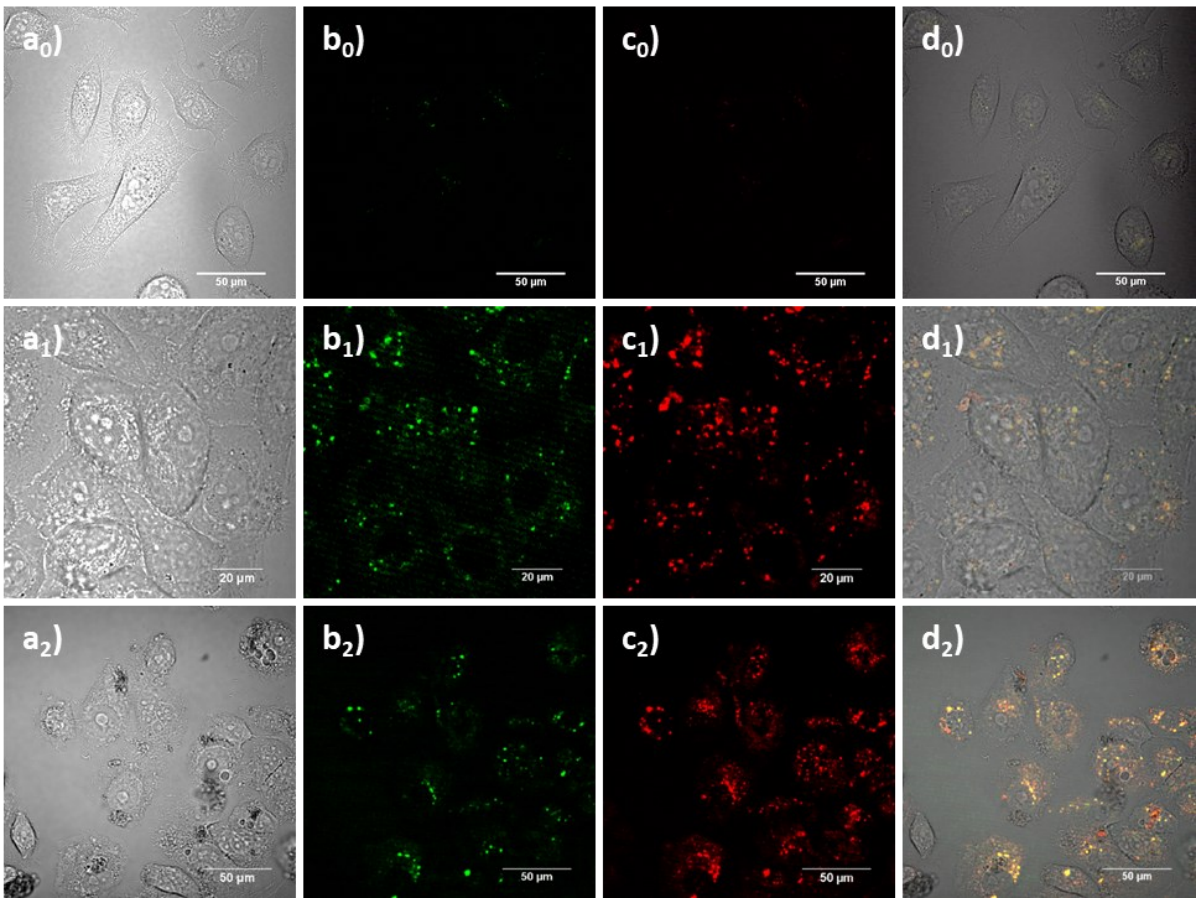

Figure 4.21. Single-photon confocal laser-scanning microscopy of PC-3 cells incubated at 37 °C for 24 h with compounds **a$_1$-d$_1$) *D*-13** and **a$_2$-d$_2$) *D*-14**. Solutions 100 µM, in 1:99 DMSO:serum-free medium. **a$_0$-d$_0$)** PC-3 cells incubated for 24 h at 37 °C with DMSO in serum-free medium (1:99) used as negative control. **a$_{0-2}$)** TD channel; **b$_{0-2}$)** green channel (λ_{em}=500–550 nm); **c$_{0-2}$)** red channel (λ_{em}=570–750 nm); **d$_{0-2}$)** overlay of TD-green-red channels. λ_{ex}=488.0 nm. Scale bar: 50 µm.

In Figures 4.20 and 4.21, it can be noticed that all four compounds presented higher fluorescence emissions than the control consisting of PC-3 cells incubated with DMSO in serum-free medium (Figures 4.20a$_0$-d$_0$ and 4.21a$_0$-d$_0$). Auto-fluorescence due to the cells can be excluded and therefore the emissions are due to the injected compounds. The compounds ***L*-13**, ***L*-14**, ***D*-13** and ***D*-14** emit in the green (λ_{em}=500–550 nm) and red channels (λ_{em}=570–750 nm) in which surprisingly these emission wavelengths were slightly visible the EEM maps shown in Figure 4.17c-f. Figure 4.20a$_1$-d$_1$ shows the confocal micrographs of ***L*-13** which presented intense emissions in the green and red channels and also was mainly localised in the cellular cytoplasm. On the other hand, ***L*-14** (Figure 4.20a$_2$-d$_2$) showed stronger fluorescence emissions than ***L*-13** in those channels and it can be speculated that its qualitative uptake is more accentuated than ***L*-13**, suggesting that the presence of two peptide moieties could improve the affinity with the cellular receptors[23].

Further analyses to quantify the effective uptake of the *mono*-peptide *vs bis*-peptide molecule are in progress to assess the increased uptake due to the presence of two peptide moieties. To verify the effect of the stereochemistry in cellular uptake, the *D*-enantiomers ***D*-13** and ***D*-14** (Figures 4.21a_1-d_1 and 4.21a_2-d_2, respectively) were incubated in the same cells line and investigated by confocal microscopy. First of all, the fluorescence emissions of the *D*-enantiomers were compared with the PC-3 cells incubated with DMSO in the serum-free medium used as a negative control to exclude auto-fluorescence of the cells (Figure 4.21a_0-d_0). Overall, ***D*-13** and ***D*-14** showed fluorescence emissions in the green and red channels and, as in the previous case, these fluorescence emissions were slightly perceptible in the EEM maps (Figure 4.17e-f). Qualitatively, *D*-enantiomers seemed to be less taken up into PC-3 cells than their *L*-enantiomers. Such phenomenon suggests that *L*-enantiomers of **13** and **14** can be more assimilated than their *D*-enantiomers which may be reasonable as living cells prefer the uptake of *L*-amino acids[24-27]. Further analyses are in progress to verify the quantitative uptake of *L*- *vs* *D*-enantiomers into PC-3 cells. These experiments may demonstrate that *L*-enantiomers are more effectively absorbed by the cells and follow Nature's preference for *L*-amino acids[24-27]. All four compounds were also incubated with another typical prostate cell line, derived from the left metastatic supraclavicular lymph node site of human prostate (LNCaP) which presents less than 500-fold gastrin-releasing peptide receptors compared to PC-3 cells and they are androgen sensitive[52].The following investigation was carried out to evaluate qualitatively any difference in cellular uptake of the compounds compared with PC-3 cells. The micrographs of ***L*-13** (Figure 4.22a_1-d_1), ***L*-14** (Figure 4.22a_2-d_2), ***D*-13** (Figure 4.23a_3-d_3) and ***D*-14** (Figure 4.23a_4-d_4), analysed after their incubation overnight in LNCaP cells at 37 ºC and excited at 488 nm at the same laser power.

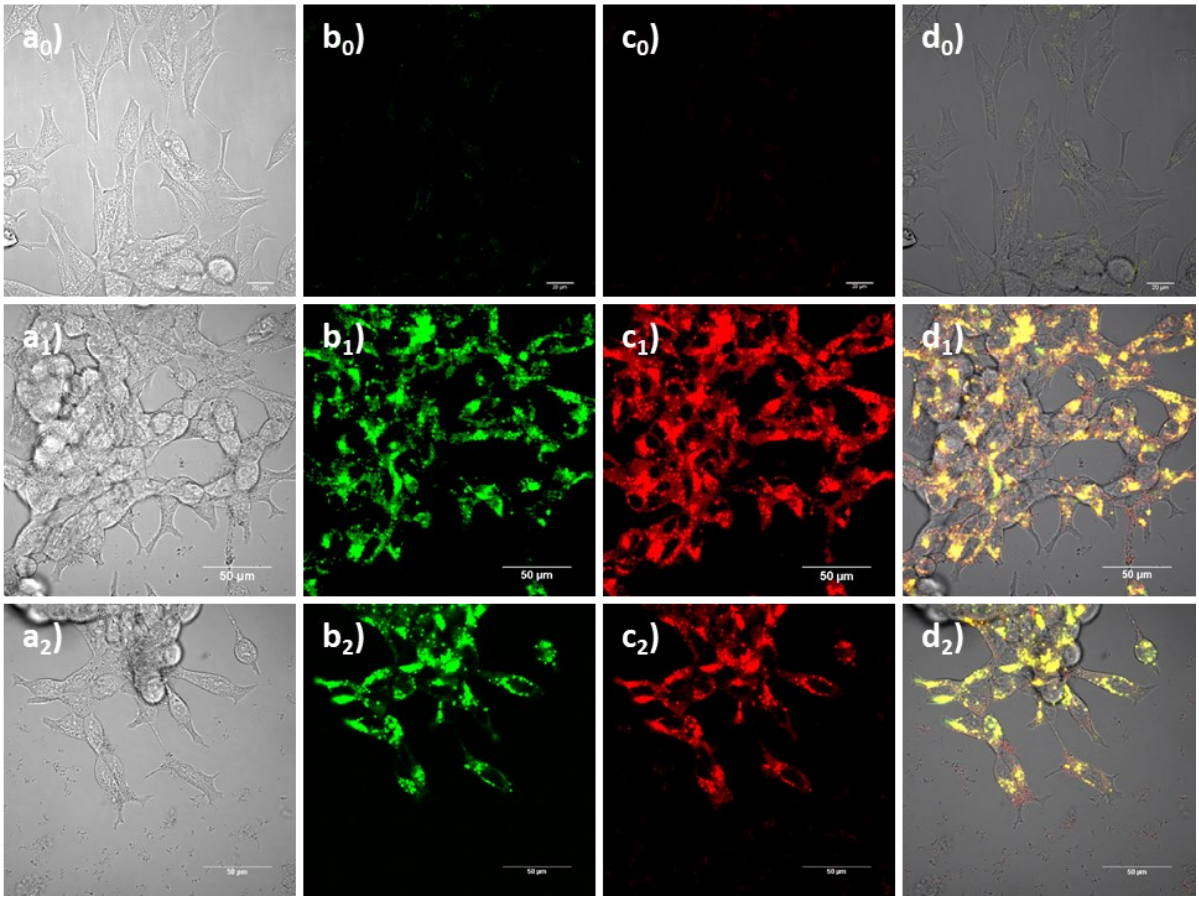

Figure 4.22. Single-photon confocal laser-scanning microscopy of LNCap cells incubated at 37 °C for 24 h with compounds **a$_1$-d$_1$) *L*-13** and **a$_2$-d$_2$) *L*-14**. Solutions 100 µM, in 1:99 DMSO:serum-free medium. **a$_0$-d$_0$)** LNCap cells incubated for 24 h at 37 °C with DMSO in serum-free medium (1:99) used as negative control. **a$_{0-2}$)** TD channel; **b$_{0-2}$)** green channel (λ_{em}=500–550 nm); **c$_{0-2}$)** red channel (λ_{em}=570–750 nm); **d$_{0-2}$)** overlay of TD-green-red channels. λ_{ex}=488.0 nm. Scale bar: 50 µm.

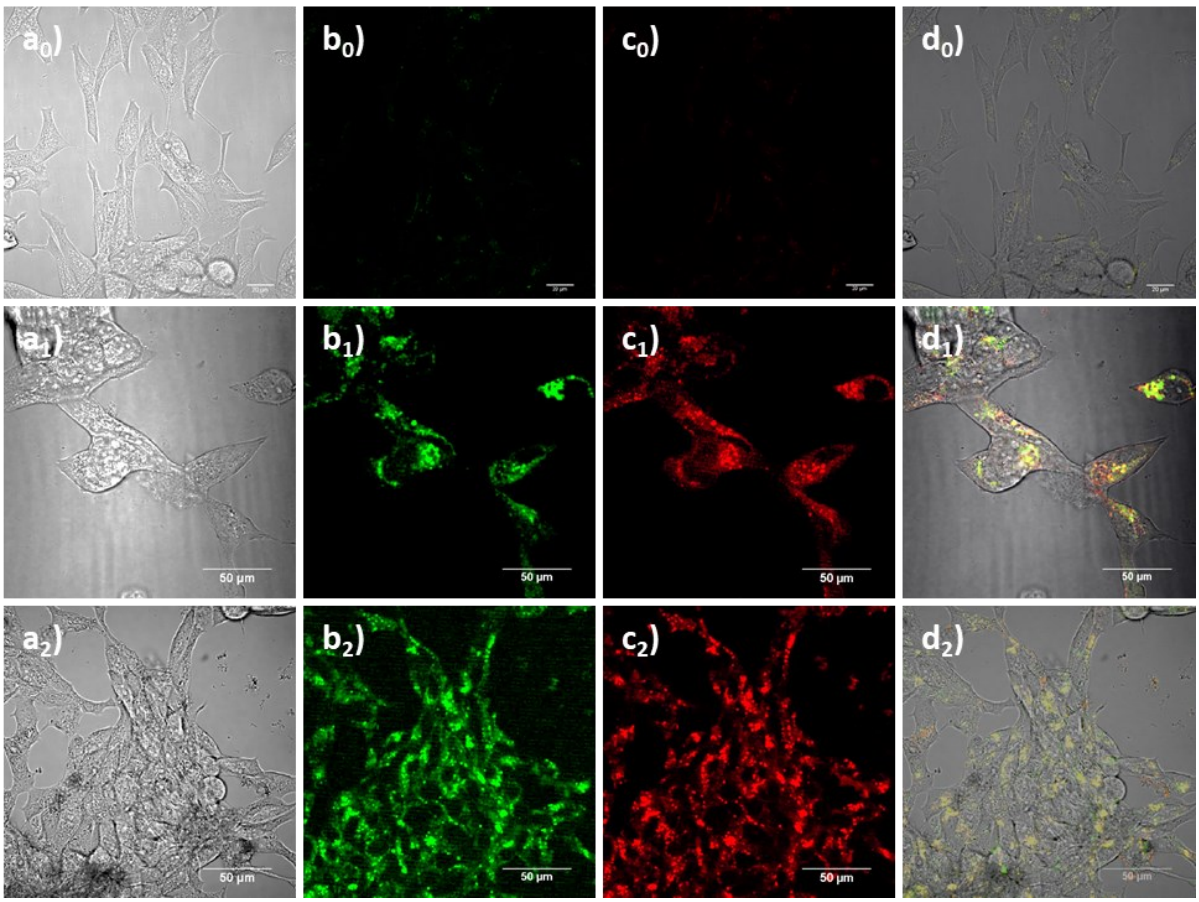

Figure 4.23. Single-photon confocal laser-scanning microscopy of LNCap cells incubated at 37 °C for 24 h with compounds **a1-d1)** ***D*-13** and **a2-d2)** ***D*-14**. Solutions 100 µM, in 1:99 DMSO:serum-free medium. **a0-d0)** LNCap cells incubated for 24 h at 37 °C with DMSO in serum-free medium (1:99) used as negative control. **a0-2)** TD channel; **b0-2)** green channel (λ_{em}=500–550 nm); **c0-2)** red channel (λ_{em}=570–750 nm); **d0-2)** overlay of TD-green-red channels. λ_{ex}=488.0 nm. Scale bar: 50 µm.

The *L*- and *D*-enantiomers of **13** and **14** were compared to a control constisting of LNCap cells incubated with DMSO in serum-free medium to exclude any auto-fluorescence due to the cells (Figure 4.22a_0-d_0 and 4.23a_0-d_0). These peptide-based probes showed fluorescence emissions in the green (λ_{em}=500–550 nm) and red channels (λ_{em}=570–750 nm) when excited at 488 nm, after overnight incubation into LNCaP cells. Qualitatively, the *L*-enantiomers of **13** and **14** presented similar fluorescence intensity and distribution in the cytoplasm to each other. Their *D*-versions qualitatively showed homogeneous distribution in the cytoplasm of the cells. No substantial differences in uptake and fluorescence intensity were qualitatively observed. Further analysis is in progress to compare quantitatively the effective uptake of these compounds into the LNCaP cells and evaluate these data with PC-3 cells. Such analysis can be useful to understand any specific uptake in those cells line.

Besides, quantitative CLSM studies have been considered with either cell lines which doesn't express GRPR or cell lines which such receptors are blocked by a non-fluorescent compound to block receptor-mediated uptake.

Despite these compounds showed good uptake and acceptable fluorescence emissions in the cellular environment, the uptake of such probes into cells requires a long time. This feature is important for a quick, responsive and fluorescent biosensor which can detect prostate cancer cells. To improve the fluorescence emission and the uptake time, molecule **15** was designed to fulfil these expectations. The bombesin [7-13] moiety is made by all *L*-amino acids which it was assed to be effectively absorbed into cells; on the other hand, the BODIPY derivative, like its congeners, is well known to be used for imaging different types of cancer thanks to their optical characteristics, their biocompatibility and stability in physiological conditions[28] and it also showed quick uptake into cells[29].

The following figures show the micrograph of the probe **15**, incubated 20 minutes at 37 °C in PC-3 (Figure 4.25a_1-d_1), A431 (Figure 4.25a_2-d_2), CHO (Figure 4.25a_3-d_3) and MCF7 (Figure 4.25a_4-d_4) cells lines to assess its fluorescence emission and absorption in different cancerous cells. In particular, the PC-3 cells are human prostate cancer cells, A431 cells are human epidermoid carcinoma; MCF7 cells are human breast cancer cells; CHO cells are epithelial cell line derived from the ovary of Chinese hamsters. This qualitative analysis using CLSM was performed to assess any specific uptake of compound **15** in either GRPR-responsive cell line (PC-3) and non-GRPR-responsive cell lines (A431, MCF-7 and CHO). In Figure 4.24, the micrographs of the aforementioned cell lines incubated with DMSO in the serum-free medium are reported to exclude any autofluorescence due to the cells.

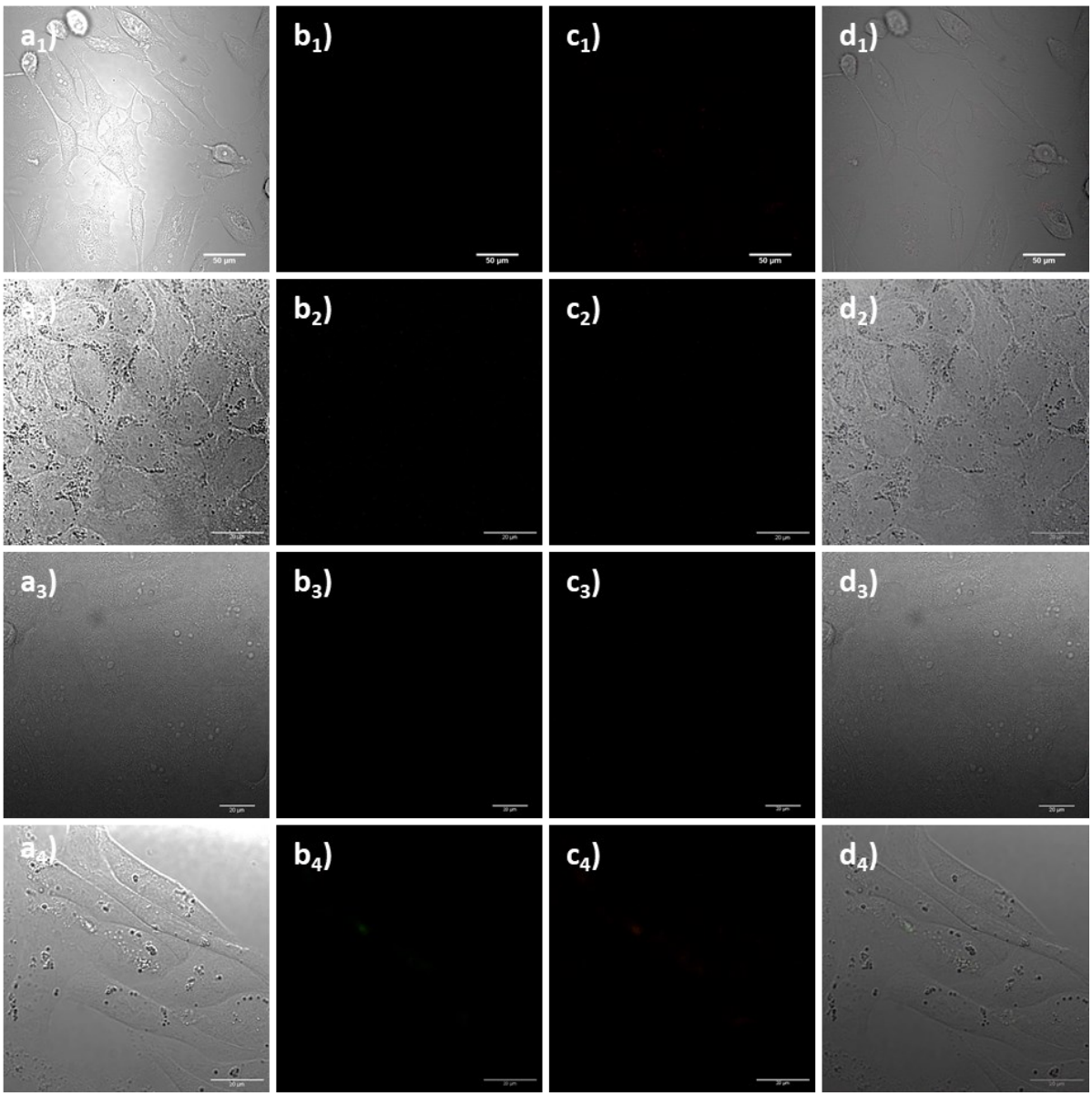

Figure 4.24. Single-photon confocal laser-scanning microscopy of DMSO in sereum-free medium (1:99) incubated at 37 °C for 20 minutes to **a_1-d_1)** PC-3, **a_2-d_2)** A431, **a_3-d_3)** MCF-7 and **a_4-d_4)** CHO cells lines. Solutions 100 μM, in 1:99 DMSO:serum-free medium. **a_{1-4})** TD channel; **b_{1-4})** green channel (λ_{em}=500–550 nm); **c_{1-4})** red channel (λ_{em}=570–750 nm); **d_{1-4})** overlay of TD-green-red channels. λ_{ex}=488.0 nm. Scale bar: 10 μm.

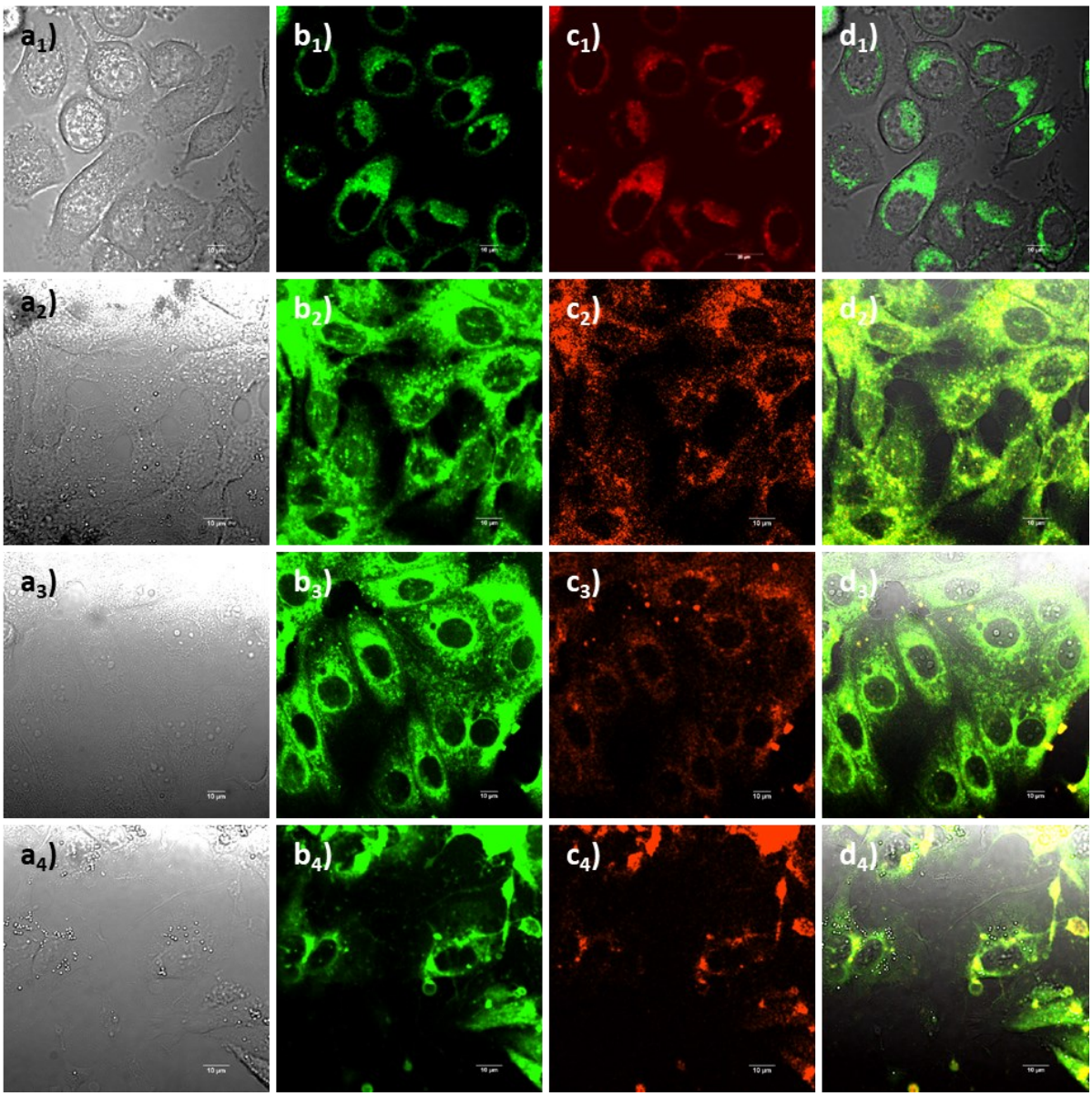

Figure 4.25. Single-photon confocal laser-scanning microscopy of compound **15** incubated at 37 °C for 20 minutes to **a_1-d_1)** PC-3, **a_2-d_2)** A431, **a_3-d_3)** MCF-7 and **a_4-d_4)** CHO cells lines. Solutions 100 µM, in 1:99 DMSO:serum-free medium. **a_{1-4})** TD channel; **b_{1-4})** green channel (λ_{em}=500–550 nm); **c_{1-4})** red channel (λ_{em}=570–750 nm); **d_{31-4})** overlay of TD-green-red channels. λ_{ex}=488.0 nm. Scale bar: 10 µm.

The micrographs in Figure 4.25 display the uptake and the fluorescence emission of **15** into PC-3 (a_1-d_1), A431 (a_2-d_2), MCF-7 (a_3-d_3) and CHO cells (a_4-d_4) after 20 minutes incubation at 37 °C. Autofluorescence of the cells can be excluded due to the lack of any fluorescence emissions in the micrographs depicted in Figure 4.24. The micrographs in Figure 4.25a_1-d_1 shows qualitative strong fluorescence emissions of compound **15** in the green (λ_{em}=500–550 nm) and red channels (λ_{em}=570–750 nm) when excited at 488 nm.

This observation is consistent with the EEM maps of the compound showed in Figure 4.18 wherein DMSO solution showed intense fluorescence emissions in the range between 500 and 570 nm when excited at around 500 nm. Qualitatively, the compound seems well distributed in the cytoplasm of the cells and well taken up. Surprisingly, the probe **15** was also adsorbed in the other cell lines in which there are no GRPR. This phenomenon may confirm that the compound is taken up non-specifically into the cells. Further quantitative analyses in specific and non-specific uptake have been considered to assess the selectivity and specificity of the compound for the cells.

4.2.3. Preliminary investigations into cellular co-localisation in prostate cancer cells

The co-localisation of two dyes into targeted cellular organelles can be estimated qualitatively by software graphic analysis of micrographs obtained by CLSM. Such an approach consists of overlaying the emission channels of the two dyes which emit in different regions of the UV-visible light spectrum. The software generates scatterplots in terms of pixel intensity emissions of a particular region-of-interest (ROI) in the corresponding emission channels of the dyes, one *vs* the other. A correlation between the fluorescence emission intensities of the two compounds may reflect in a direct or indirect molecular interaction with each other, a third molecule or a subdomain in a cellular compartment[30]. If the scatterplot shows a linear distribution of the pixel intensities of the two compounds' emission channels, it could mean that the two species can interact with each other or be localised in the same cellular compartment. Otherwise, there is none of the above events[30].

In this part of the Chapter, the cellular localisation of **13**, **14** and **15** was established using the aforementioned graphical approach, using *Nikon Elements-AR Analysis 4.30.02* software for the analysis. Lysotracker Blue DND-22 was used to stain the lysosomes of PC-3 cells. These organelles have been recently studied as a potential target to induce apoptotic and lysosomal cell death in cancerous cells[31] and, besides, may inhibit the cytoprotective autophagy[32]. The chosen dye localises in the lysosomes of the studied prostate cancer cells and emits between 417 and 470 nm (blue channel) when excited with a wavelength of 405 nm. On the other hand, the studied compounds mainly emit between 500 and 550 nm (green channel) when excited with an energy corresponding at 488 nm.

The following analysis was performed to assess any targeting for lysosomes which may contribute to further studies of such compounds as therapeutic agents to induce cancer cell death.

Figure 4.26 shows the overlaid micrograph and the scatterplots of the three selected ROIs of ***L*-12** (a_1-d_1) and ***D*-12** (a_2-d_2). In the first instance, bio-localisation of both enantiomers of peptide **12** was assessed into PC-3 cells to verify any qualitative targeting for the lysosomes of such cell line. In addition, the effect of the stereochemistry on the targeting of the lysosomes was considered. The obtained results for the enantiomers of the fragment [7-13] of the bombesin peptide (**12**) will be used as a reference to compare the proposed probes **13**, **14** and **15** each other.

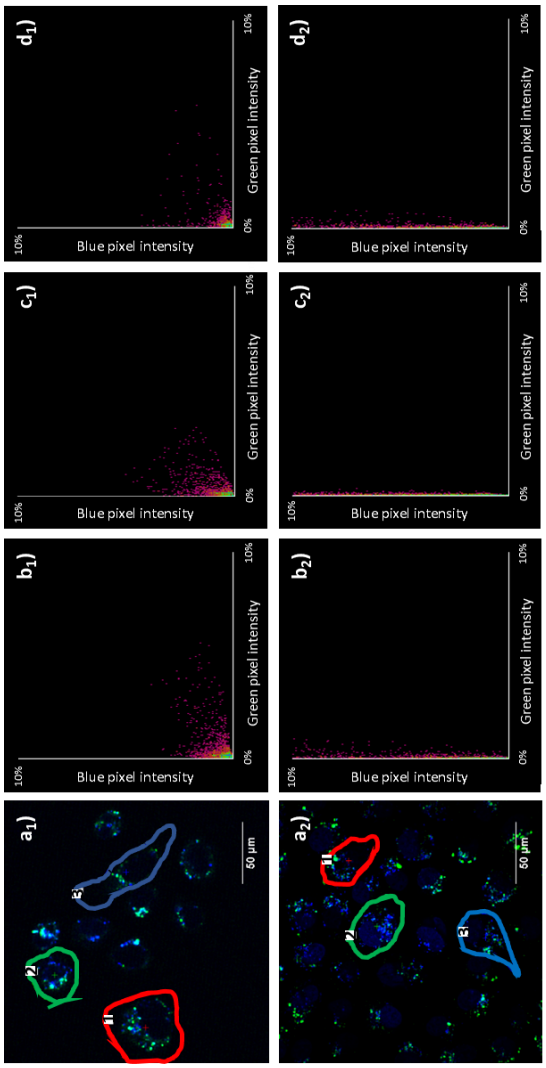

Figure 4.26. Co-localisation analysis of the enantiomers of the bombesin [7-13] peptide. Superimposed confocal micrographs of ***L*-12** (**a**$_1$) and ***D*-12** (**a**$_2$) and Lysotracker Blue DND-22. Scatterplots of ROI 1 (**b**$_{1\text{-}2}$, represented in red), ROI 2 (**c**$_{1\text{-}2}$, represented in green); ROI 3 (**d**$_{1\text{-}2}$, represented in blue). Solutions of the probes and the stain were 100 µM in 1:99 DMSO:serum-free medium. The peptides were excited with a wavelength of 488 nm (λ_{em}=500–550 nm) and the Lysotracker with a wavelength of 405 nm (λ_{em}=417–470 nm).

The cells were incubated with the compounds and the lysosomal dye overnight at 37 ºC and the micrographs were acquired with the same laser power. In all cases, the scatterplots analysis of the blue and green channels was performed with *Nikon Elements-AR Analysis 4.30.02*. The visual analysis was performed in three different cells with a comparable surface area to obtain a meaningful homogeneity of the results. The analysis of the scatterplots b_1 (ROI 1, red) c_1 (ROI 2, green) and d_1 (ROI 3, blue) showed that in the three cells the pixel intensities of the blue and green channels are in linear correlation, suggesting that both the lysosomal dye and ***L*-12** qualitatively colocalise in the lysosomes of the cells. The visual analysis of ***D*-12** (a_2-d_2) presents a different distribution of the pixel intensities in the investigated ROIs (b_2: ROI 1; c_2: ROI 2; d_2: ROI 3). It seems that there is no significant co-distribution with the Lysotracker Blue, therefore, this peptide may not interact and/or localise in the lysosomes. These preliminary results suggested that the *L*-enantiomer interacts and target the lysosomes better than the *D*-enantiomer, which is consistent with the previous qualitative observation on the uptake of such peptides seen *via* CLSM in Figure 4.18. In addition, these results may confirm the living being's preference for *L*-amino acids[24-27].

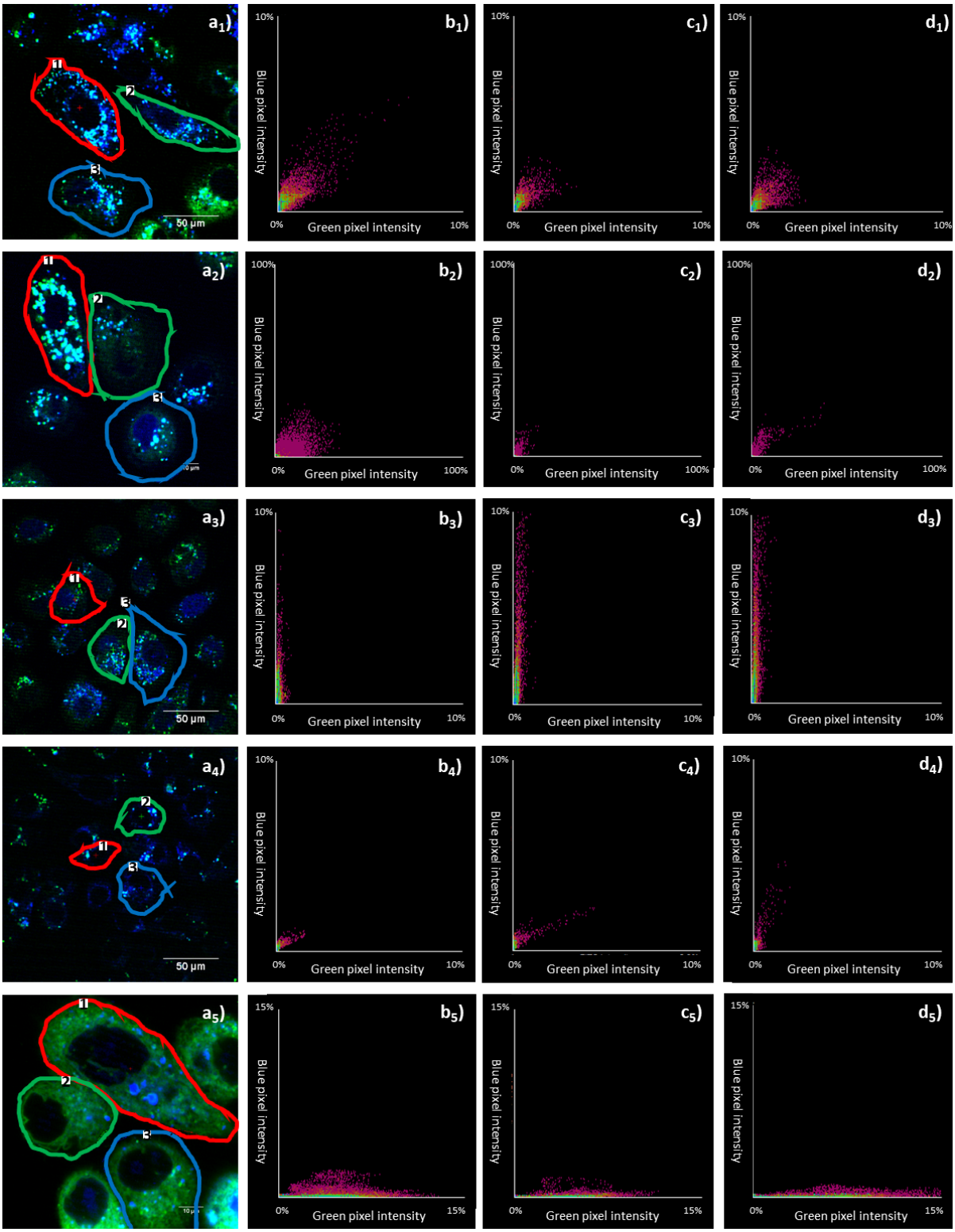

Figure 4.27. Co-localisation analysis of the five proposed probes. Superimposed confocal micrographs of ***L*-13** (**a**$_1$), ***L*-14** (a$_2$), ***D*-13** (**a**$_3$), ***D*-14** (**a**$_4$) and **15** (**a**$_5$) and Lysotracker Blue DND-22. Scatterplots of ROI 1 (**b**$_{1\text{-}5}$: represented in red), ROI 2 (**c**$_{1\text{-}5}$: represented in green); ROI 3 (**d**$_{1\text{-}5}$: represented in blue). Solutions of the probes and the stain were 100 µM in 1:99 DMSO:serum-free medium. The probes were excited with a wavelength of 488 nm (λ_{em}=500–550 nm) and the Lysotracker with a wavelength of 405 nm (λ_{em}=417–470 nm).

The compounds **13** (both enantiomers), **14** (both enantiomers) and **15** were incubated into the PC-3 cells and Lysotracker Blue DND-22 overnight at 37 ºC. The micrographs were obtained with the same excitation laser power of the selected area of cells. The scatterplots analysis was performed with *Nikon Elements-AR Analysis 4.30.02*, choosing three different cells (ROIs) with similar areas to obtain reasonable results. Despite the weak fluorescence emission of both enantiomers of **13** and **14**, this analysis was possible to be carried out and give some meaningful observations. In Figure 4.27a_1-d_1, the scatterplots b_1 (ROI 1, red) c_1 (ROI 2, green) and d_1 (ROI 3, blue) of ***L*-13** present a linear correlation between the blue and green channels which can suggest that either the lysosomal dye and ***L*-13** colocalise in the lysosomes of the cells. The visual analysis of ***L*-14** (Figure 4.27a_2-d_2) showed a similar linear trend in the scatterplots of the selected ROIs (b_2, red ROI; c_2, green ROI; d_2, blue ROI) as previously seen in ***L*-13**. On the other hand, ***D*-13** (Figure 4.27a_3-d_3) presents a different trend in its scatterplots of the investigated ROIs (b_3: ROI 1; c_3: ROI 2; d_3: ROI 3). ***D*-14** (Figure 4 27a_4-d_4) showed a linear correlation which can mean that it localises in the lysosome of the selected cells (ROI 1, ROI 2 and ROI 3) as well as the lysosomal stain. Species **15** (Figure 4.27a_5-d_5) showed a non-linear correlation between the emission intensities of the blue and green channel, suggesting a lack of localisation in the cellular lysosomes. The qualitative scatterplot analysis for the *L*-enantiomers of **13** and **14** showed that such compounds may efficiently localise and interact with the lysosomes of PC-3 cells. Such phenomenon may be driven by the presence of the fragment [7-13] of the bombesin peptide which can presumably be degraded in the lysosome[53,54]. Surprisingly, compound **15** qualitatively showed that has no linear correlation in the scatterplots with the lysosomal dye, despite the molecule presents the *L*-enantiomer of peptide **12** in its structure.

Such method revealed useful to qualitatively estimate the localisations of the probes in the lysosomes. However, such visual approach often lacks comparability in terms of co-localisation in different experimental conditions and may mislead the amount of co-distribution due to random coincidence[30]. Two main analytical parameters were introduced to measure the co-distribution between fluorophores[33]. These parameters can be also obtained by software analysis of the micrograph of the emission channels of the probes. *Pearson's correlation coefficient* (PCC) establishes a quantification parameter between the merged micrographs of the studied probe and organelle stain. This coefficient values range is from +1, a perfect and linear relationship between the fluorescence intensities, to -1, where the fluorescence intensities are perfect, but inversely, related to one another[30].

Sometimes the negative values are difficult to be interpreted and for this reason, another statistical quantification parameter was introduced: *Mander's overlap coefficient* (MOC). Its values range is from 0, which means an absence of correlation, to +1, a perfect correlation and, therefore, a potential localisation and/or interaction with the specific organelle.

In these perspectives, the graph below (Figure 4.28) summarises the average PCC and the MOC for each compound, considering their corresponding micrographs shown in Figure 4.26 and 4.27 with their selected cells (ROIs).

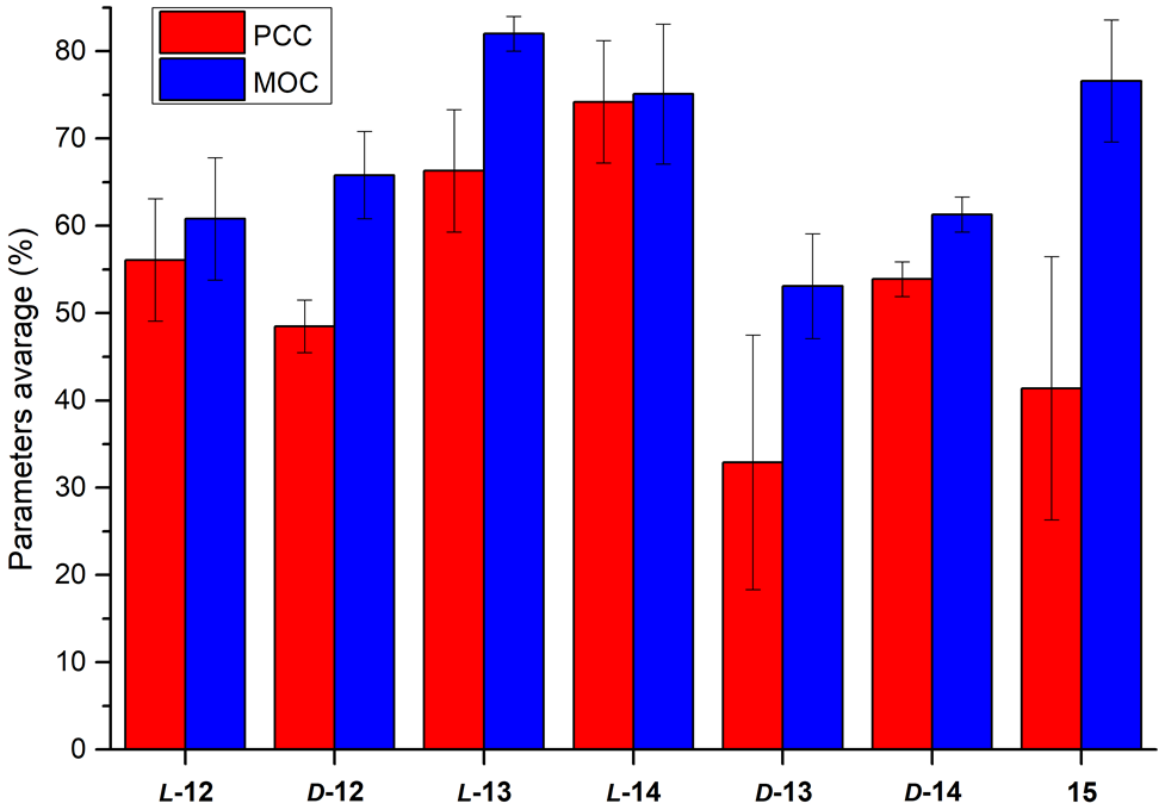

Figure 4.28. Summary plot of average Pearson's correlation coefficient (PCC) and Mander's overlap coefficient (MOC) parameters of the studied compounds, referring to the merged micrographs shown in Figure 4.28 and 4.29. (The means and standard deviations were obtained by the *Nikon Elements-AR Analysis 4.30.02* software on the selected ROIs in the micrographs shown in Figure 4.26 and 4.27).

The percentage average PCC and MOC values are presented in the graph in Figure 4.28, calculated from the selected ROIs of the enantiomers of peptide **12** and the fluorescent probes **13**, **14** and **15**. In the first instance, it can be noticed that the average PCC and MOC have similar values to each other, within their standard deviations. . This analysis showed that the PCC of ***D*-12** is slightly lower than ***L*-12**; however, the MOC of ***D*-12** is slightly higher than ***L*-12**.

Considering these results together, it can be speculated that both peptides comparably localise in the lysosomes of PC-3 cells. The *L*-enantiomer of **13** presents both PCC and MOC parameters significantly higher than their *D*-versions. In addition, the presence of two moieties of the peptide **12** effect the targeting for such organelles. Such observation can be also noticed between the *D*-enantiomers of **13** and **14**. Compound **15** showed a significative deviation between its average PCC and MOC parameters which can be due to the lack of sensitivity of PCC in different emission intensities between the components of an image caused by different dyes and/or photobleaching[33]. However, its MOC value can be considered a valid parameter to speculate that such probe can target the lysosome of PC-3 cells.

The *L*-enantiomers of **13** and **14** and also compound **15** showed an overall better localisation in the lysosomes of PC-3 cells which suggests that such compounds may target these organelles and being considered as potential targets to induce cellular and lysosomal death and/or inhibit cytoprotective autophagy.

4.2.4. Cytotoxicity assays in prostate cancer cells

The compounds with an *L*-stereochemistry, *i.e.* ***L*-13**, ***L*-14** and **15**, previously showed an effective uptake in the cellular environment into PC-3 cells (Figure 4.20 and 4.25a_1-d_1, respectively), and a good probability of localising in the lysosomes of these cells (Figure 4.27a_1-d_1, a_2-d_2 and a_5-d_5). In these regards, crystal violet assays were performed to assess the cellular viability, after staining the cells with a cellular dye (crystal violet). Such method indirectly quantifies cell death and determines differences in proliferation due to death-inducing agents[34] *via* optical detection. Crystal violet assay consists of the detection of adherent cells in the plate which are stained by the crystal violet dye (λ_{abs}=590 nm), which is bound to proteins and DNA. In the presence of a cell death-inducing agent, the death cells lose their adherence on the plate which is subsequently washed and therefore they reduce the number of stained cells on the plate. This screening method is quick and reliable for evaluating the impact on cell survival and growth inhibition due to proposed synthetic agents[34].

Figures 4.29 and 4.30 reports the normalised cellular viabilities of ***L*-13**, ***L*-14** and **15**, estimated *via* crystal violet assay, after 24- and 48-hours incubation of the compounds in PC-3 cells.

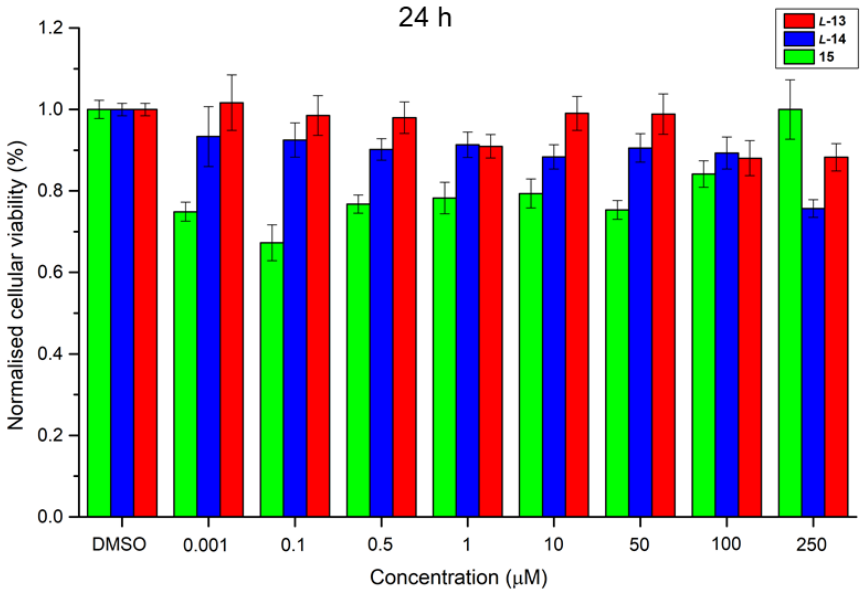

Figure 4.29. Normalised cellular viability graphs over 24 h obtained by crystal violet assays. Data for compounds ***L*-13** are represented in red bars, ***L*-14** in blue bars and **15** in green bars. (The data were collected from 3 repeated measurements on the same day, N=1).

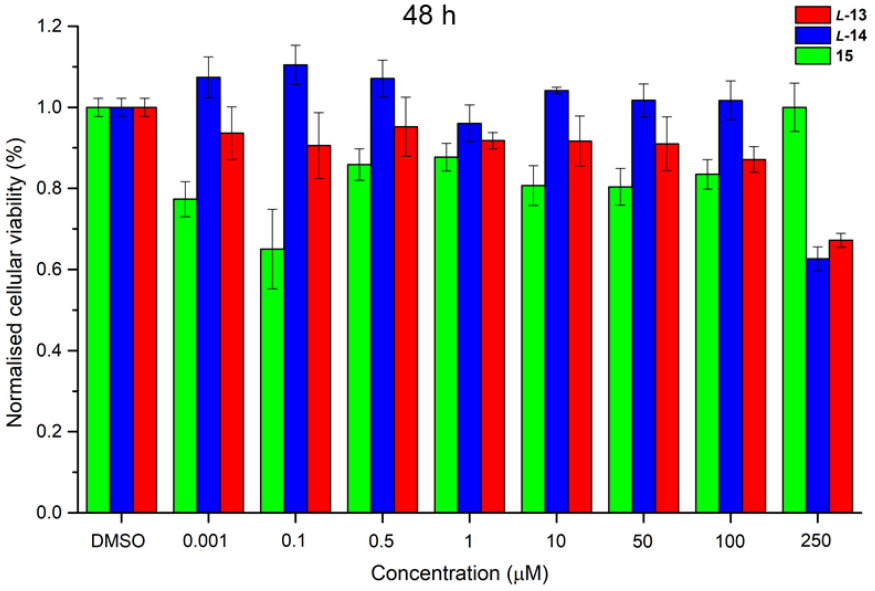

Figure 4.30. Normalised cellular viability graphs over 48 h obtained by crystal violet assays. Data for compounds ***L*-13** are represented in red bars, ***L*-14** in blue bars and **15** in green bars. (The data were collected from 3 repeated measurements on the same day, N=1).

Figures 4.29 and 4.30 display the normalised cellular viabilities of ***L*-13** (red bars), ***L*-14** (blue bars) and **15** (green bars), after 24- and 48-hours screening. ***L*-13** showed above 95% of cellular viability at all concentrations after 24 hours. Only the highest concentrations (100 and 250 μM) showed a decrease in values in which they reached approximately 90%. ***L*-14** present the same trend which shows values around 90% and therefore lower than ***L*-13**.

Only 250 μM concentration reached about 75% of cellular viability. In this case, overall ***L*-14** showed lower values than ***L*-13** at 24 hours which may suggest higher toxicity than the latest compound. On the other hand, after 48 hours, ***L*-13** presents approximatively 90% of cellular viability at all concentrations, except at 250 μM which value decreased to 65%. Instead, ***L*-14** presented approximately 95% of cellular viability at all concentrations with the only exception at 250 μM (about 60%). Molecule **15** presented a different trend in which, after 24 hours, its cellular viability is around 80% at all concentrations. Only at 0.1 μM, the cellular viability of **15** decreased to about 70%. After 48 hours, **7** maintained the cellular viability at around 85% until 0.5 μM; at 0.1 μM, the value reached 65%.

Overall, ***L*-13**, ***L*-14** and **15** showed mild toxicity overtime which can suggest that they do not present a significant therapeutic potential for inducing cell death or growth inhibition.

4.2.5. Multiphoton fluorescence lifetime imaging microscopy (FLIM) investigations of living cancer cells

Over the past decade, fluorescence lifetime microscopy (FLIM) has found a wide range of applications in biomedical science thanks to the investigation of biochemical processes which can study. Such a technique is used to determine the spatial distribution of the excited state lifetime of a sample in determined environments. FLIM has found its origin in two research fields: microscopy and fluorescence spectroscopy[35]. From the first method, FLIM has in common the investigation of a sample on a microscopic scale by a light microscope. From the second one, FLIM uses the physical principle of fluorescence. In fact, this technique excites the sample *via* a certain wavelength in which the ground electronic state of the species passes to a primary excited electronic state. The fluorophore remains in this state in the range from picoseconds to nanoseconds before it will return on its ground electronic state, accordingly to the Jablonski's diagram. The average time that the molecule spends in the excited electronic state is called "fluorescence lifetime"[36]. The fluorescence lifetime can be affected by different factors, such as energy transfer from another nearby excited molecule (Foster resonance energy transfer, FRET)[37,38] and chemical/biochemical processes[36], which can be a measure of the molecular interactions/changes of the fluorophore with the surrounding environment. The main advantages of FLIM are independence of the species concentration, fluorescence excitation and photobleaching[39]. Thanks to such benefits, FLIM has become a new, powerful and potential tool to investigate biological processes such as cellular metabolism[40], biological O_2 sensing[41] and cellular uptake and distribution of species *in vitro*[42].

Particularly, multi-photon FLIM has been widely used in biomedical science thanks to the use of near-infrared (NIR) wavelengths range (650-1350 nm) which can penetrate cells and tissues in depth and avoid one-photon absorption in most of cells[36]. In addition, the NIR energy powers used in this technique are sufficient to image the cell monolayers and also is non-invasive. Another advantage of using multi-photon FLIM is to record time-correlated single-photon counting (TCSPC) decay curve. Such technique records the time difference between the excitation/emission event for every single photon and over multiple emission events. The statistical distribution of lifetimes of the studied species in a particular environment is generated by this technique.

Considering the advantages of FLIM and TCSPC, data from such techniques are presented in this part of the Chapter. TCSPC was used to assess the lifetime decays of the imaging probes **13**, **14** and **15** in different solvent conditions and how this property can be affected by their aggregation. In addition, data of their precursors (**2**, **11** and **13**) are also presented as a comparison. Furthermore, this technique allows the evaluation of the FRET efficiency of fluorescent probes. FLIM was also used for studying the lifetime changes in the cellular environment and evaluate the interactions and localisation of the compounds into different cancerous cells lines.

Figure 4.31 shows the TCSPC lifetime decays of **2**, **11** (both enantiomers) and **12** (both enantiomers) in different solvent conditions and concentrations. The χ^2 quantifies the goodness of the fit with the data points obtained in the experiments. The fast (or short) lifetime component (τ_1) is due to molecules which are interacting each other and therefore provoke a FRET event; whilst the slow (or long) component (τ_2) represents the population of non-interacting molecules[43]. The parameters a_1 and a_2 represent the amplitude of the components.

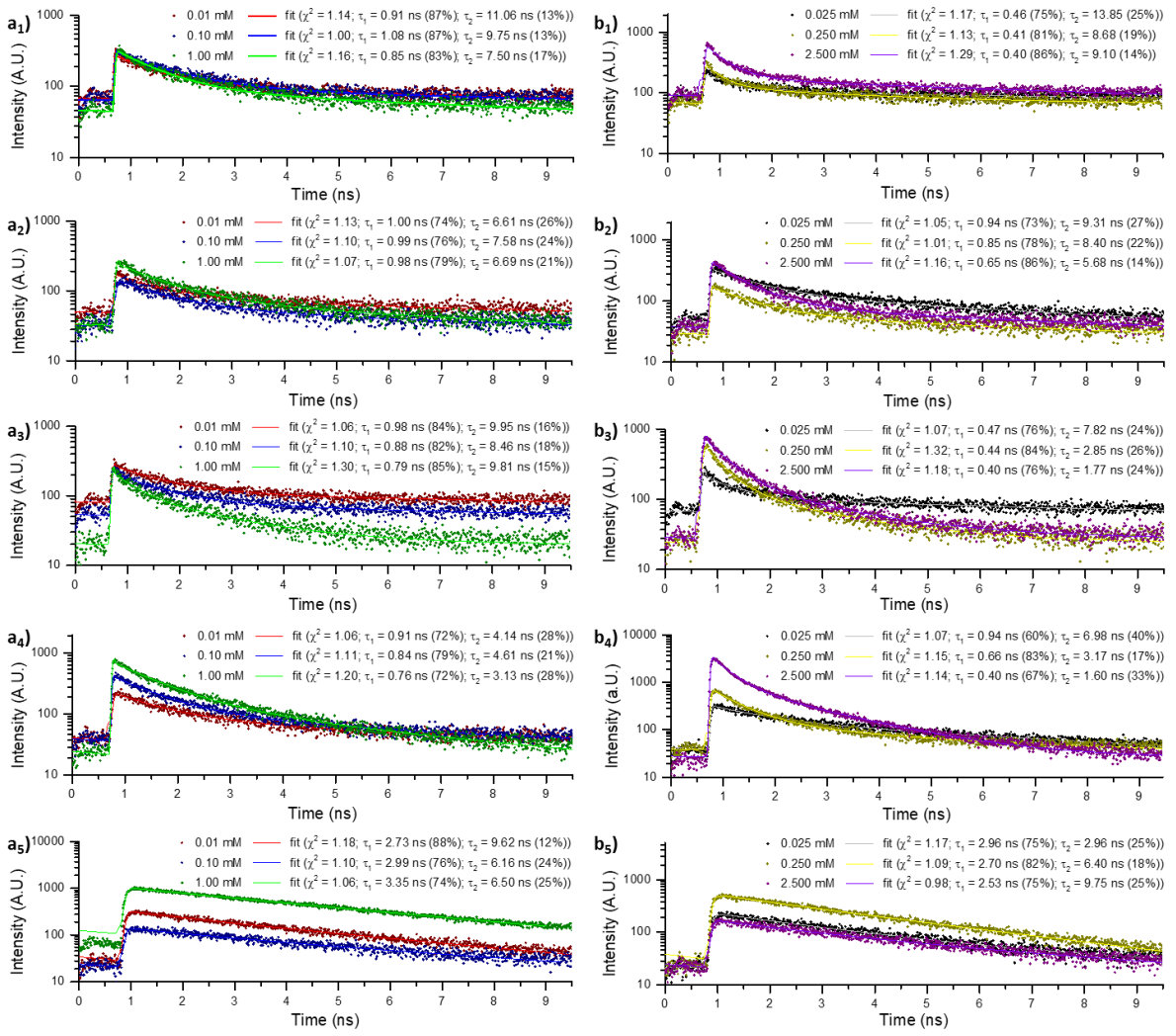

Figure 4.31. Two-photon time-correlated single-photon counting (λ_{ex}=810 nm from **a$_1$-b$_1$** to **a$_4$-b$_4$** and λ_{ex}=910 nm for **a$_5$-b$_5$**). **a$_1$-b$_1$) *L*-12**; **a$_2$-b$_2$) *D*-12**; **a$_3$-b$_3$) *L*-11**; **a$_4$-b$_4$) *D*-11**; **a$_5$-d$_5$) 2**. **a$_{1\text{-}5}$** in DMSO; **b$_{1\text{-}5}$** in DMSO:H_2O (1:1).

The lifetime decays of **2**, **11** and **12** were studied in two solvent systems, *i.e.* DMSO ($a_{1\text{-}5}$) and DMSO:H_2O (1:1) ($b_{1\text{-}5}$) at different concentrations. All the precursors presented a double-exponential fitting model with a value of χ^2 close to 1 which generates two-lifetime components. Comparing the lifetimes of the peptide ***L*-12** in DMSO (a_1), it can be noticed that the short-lived lifetime component (τ_1) maintain approximately the same value in different concentrations of the solvent. This suggests that the aggregation of the molecules in solution is not affected by the concentration, which can be confirmed by the percentage of its amplitude a_1. Moreover, from the value of τ_1, it can be speculated that the molecule interacts each other, increasing the lifetime component. In the second solvent system (1:1 DMSO:H_2O, b_1), compound ***L*-12** presented the same values of τ_1 which represent the main contribution of the overall lifetime decay of this molecule. Besides, their values are halved than in DMSO solution.

The DMSO and H_2O mixture could affect the FRET events in solutions which can lead to a different short-lived lifetime component. The behaviour of ***D*-12** in DMSO solution (a_2) is similar to the same conditions previously described in ***L*-12**. In fact, the τ_1 is around 1.0 ns at all different concentrations which represent the major component of the lifetime decay. The similar behaviour of these enantiomers may suggest that the stereochemistry does not affect the physical properties and the aggregation of the molecules in this solvent is analogous. On the other hand, in DMSO:H_2O mixture (b_2), the values of τ_1 slightly decrease when the concentration increases. This decrease could be due to some FRET events, occurring at high concentration of ***D*-12**. ***L*-11** (a_3-b_3) and ***D*-11** (a_4-b_4) showed similar trends in both solvent systems. In particular, they presented a slight decrease of τ_1 when concentration increases, either in DMSO (a_3 and a_4) or DMSO:H_2O mixture (b_3 and b_4). The aggregation of these molecules could be due to their π-π interactions which can change their lifetime decays. As in the previous case, the different stereochemistry of the species does not affect their physical properties in different solvent conditions. The short-lifetime component of the BODIPY derivative **2** presented values above 2.5 ns in both solvent conditions which represent the major contribution in the lifetime decay. Interestingly, in DMSO, the τ_1 values increase at the increment of the concentration; contrarily, τ_1 decreases passing from 0.025 to 2.5 mM in DMSO:H_2O. Such phenomenon suggested that the aggregation of the molecules is affected by the solvent system, changing the lifetime property.

The lifetime decays of the probes **13** (both enantiomers), **14** (both enantiomers) and **15** were studied by TCSPC in the same solvent conditions as their precursors and the TCSPC results are presented in Figure 4.32.

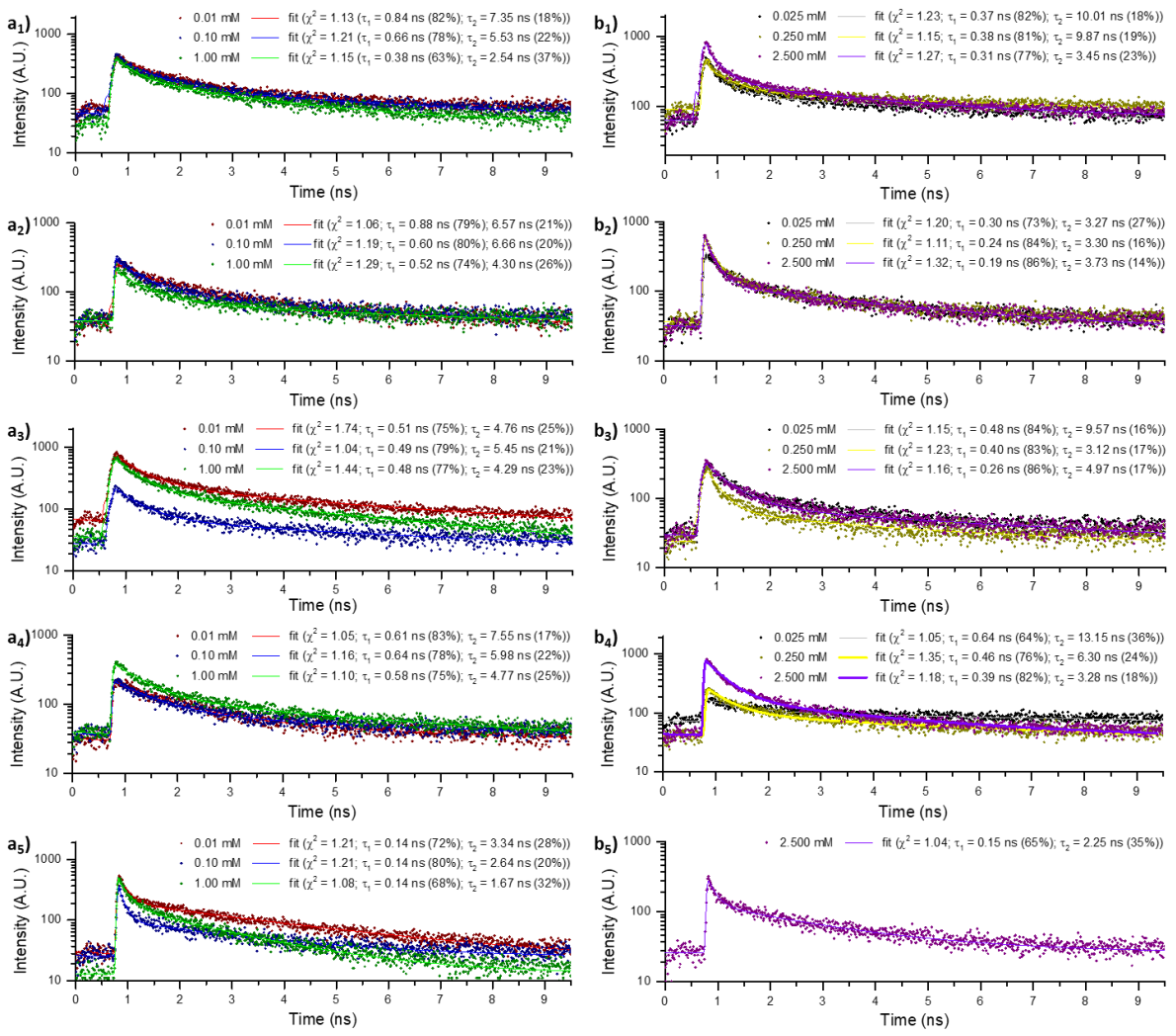

Figure 4.32. Two-photon time-correlated single-photon counting (λ_{ex}=810 nm from **a$_1$-b$_1$** to **a$_4$-b$_4$** and λ_{ex}=910 nm for **a$_5$-b$_5$**). **a$_1$-b$_1$) *L*-13**; **a$_2$-b$_2$) *D*-13**; **a$_3$-b$_3$) *L*-14**; **a$_4$-b$_4$) *D*-14**; **a$_5$-d$_5$) 15**. **a$_{1\text{-}5}$** in DMSO; **b$_{1\text{-}5}$** in DMSO:H_2O (1:1).

All the fluorescent probes can be fitted by a double-exponential model for their lifetime decays, independently of the solvent system with a χ^2 close to 1. ***L*-13** presented a decrease of the short-lived component when the concentration in DMSO (a_1) decreases which this behaviour has also been found in ***D*-13** (a_2). In the DMSO:H_2O mixture (b_1 and b_2), on the other hand, the τ_1 remained approximatively the same. For the *bis*-peptide species (***L*-14** and ***D*-14**), the first lifetime component remained unchanged at the increase of the concentration in DMSO (a_3 and a_4, respectively). Differently, in the 1:1 mixture of DMSO and H_2O (b_3 and b_4), this parameter decreased when the concentration rises. This phenomenon was shown for the peptides ***L*-12** and ***D*-12** (Figure 4.31 a_1-b_1/a_2-b_2) in whichthe lifetime of molecule **13** may be affected by the predominance of the presence of two moieties of the bombesin peptide, linked to the NDI-core.

In **13** and **14**, the stereochemistry did not affect the lifetime decays of the molecules in different solvent conditions. Species **15** presented similar behaviour passing from DMSO to DMSO:H_2O (1:1). Particularly, it showed similar slow components approximatively 0.1 ns both in DMSO (a_5) and DMSO:H_2O (b_5) solutions. Surprisingly, the τ_1 values obtained for **15** are ten-fold lower than the ones for the BODIPY derivative **2** (Figure 4.31a_5-b_5). This fact could be due to a different aggregation of the species in solution, despite the different solvent system.

From the values of τ_1 and τ_2 can be calculated the FRET efficiency (E_{FRET}), *i.e.* the probability of an energy transfer arising from the excitation event of each molecule[43]. It can be expressed as follow:

$$E_{FRET} = 1 - \frac{\tau_{FRET}}{\tau_0}$$

where τ_{FRET} correspond to the fast component (τ_1) and τ_0 is associated with the slow component (τ_2). The following tables resume the E_{FRET} of the building blocks **12**, **11** and **2** (Table 4.2) and the proposed fluorescent probes **13**, **14** and **15** (Table 4.3).

Table 4.2. Calculated FRET efficiency (E_{FRET}) values for compounds **12**, **11** and **2** in different solvent systems.

	DMSO				DMSO:H_2O (1:1)			
Molecule	**Conc. (mM)**	**τ_{FRET} (ns)**	**τ_0 (ns)**	**E_{FRET} (%)**	**Conc. (mM)**	**τ_{FRET} (ns)**	**τ_0 (ns)**	**E_{FRET} (%)**
***L*-12**	0.01	0.91	11.06	91.77	0.025	0.46	13.85	96.68
	0.1	1.08	9.75	88.92	0.25	0.41	8.68	95.28
	1	0.85	7.50	88.67	2.5	0.40	9.10	95.60
***D*-12**	0.01	1.00	6.61	84.87	0.025	0.94	9.31	89.90
	0.1	0.99	7.58	86.94	0.25	0.85	8.40	89.88
	1	0.98	6.69	85.35	2.5	0.65	5.68	88.56
***L*-11**	0.01	0.98	9.95	90.15	0.025	0.47	7.82	93.99
	0.1	0.88	8.46	89.60	0.25	0.44	2.85	84.56
	1	0.79	9.81	91.95	2.5	0.40	1.77	77.40
***D*-11**	0.01	0.91	4.14	78.02	0.025	0.94	6.98	86.53
	0.1	0.84	4.61	81.78	0.25	0.66	3.17	79.18
	1	0.76	3.13	75.72	2.5	0.40	1.60	75.00
2	0.01	2.73	9.62	71.62	0.025	2.96	2.96	0.00
	0.1	2.99	6.16	51.46	0.25	2.70	6.40	57.81
	1	3.35	6.50	48.46	2.5	2.53	9.75	74.05

Table 4.3. Calculated FRET (E_{FRET}) values for compounds **13**, **14** and **15** in different solvent systems.

	DMSO				DMSO:H_2O (1:1)			
Molecule	**Conc. (mM)**	**τ_{FRET} (ns)**	**τ_0 (ns)**	**E_{FRET} (%)**	**Conc. (mM)**	**τ_{FRET} (ns)**	**τ_0 (ns)**	**E_{FRET} (%)**
***L*-13**	0.01	0.84	7.35	88.57	0.025	0.37	10.01	96.30
	0.1	0.66	5.53	88.07	0.25	0.38	9.87	96.15
	1	0.38	2.54	85.04	2.5	0.31	3.45	91.01
***D*-13**	0.01	0.88	6.57	86.61	0.025	0.30	3.27	90.83
	0.1	0.60	6.66	90.99	0.25	0.24	3.30	92.73
	1	0.52	4.30	87.91	2.5	0.19	3.73	94.91
***L*-14**	0.01	0.51	4.76	89.29	0.025	0.48	9.57	94.98
	0.1	0.49	5.45	91.01	0.25	0.40	3.12	87.18
	1	0.48	4.29	88.81	2.5	0.26	4.97	94.77
***D*-14**	0.01	0.61	7.55	91.92	0.025	0.64	13.15	95.13
	0.1	0.64	5.98	89.30	0.25	0.46	6.30	92.70
	1	0.58	4.77	87.84	2.5	0.39	3.28	88.11
15	0.01	0.14	3.34	95.81	2.5	0.15	2.25	93.33
	0.1	0.14	2.64	94.70				
	1	0.14	1.67	91.62				

The values of the calculated FRET efficiency of the proposed probes (Table 4.4) are overall close to 90%. In particular, in DMSO:H_2O mixture, these values are slightly higher than in pure DMSO. This result suggested that such solvent mixture increases the interactions among molecules than in pure DMSO and therefore increases their FRET events. Comparing the data obtained from **13** and **14** against **12** and **11**, it can be noticed that the FRET efficiency values of the NDI-based probes are slightly higher than their precursors **12** and **11**. The presence of both building blocks in the same structure may help the interactions of the molecules thanks to a combination of weak interactions as H-bonds and π-π stackings. On the other hand, **15** showed higher E_{FRET} values in both solvent systems than its precursor **2**. In this case, the presence of the peptide ***L*-12** and the NDI-core in the structure may improve the interactions among molecules as a result of more FRET events in solution.

FLIM was used to investigate the distribution and localisation of the probes in living cells (A431 cells line). Such cell line was used to assess the targeting of such probes to the lysosomes of the cells and also verify non-specific uptake of the compounds. In Figure 4.33, the intensity images, the fluorescence lifetime micrographs and τ_m lifetime statistical distribution curves of A431 cells incubated with: DMSO (a_1-c_1), ***L*-13** (a_2-c_2), ***L*-14** (a_3-c_3), ***D*-13** (a_4-c_4), ***D*-14** (a_5-c_5) and **15** (a_6-c_6) are presented. τ_1 and τ_2 are reported in Appendices A, from Figure A.90 to A.95.

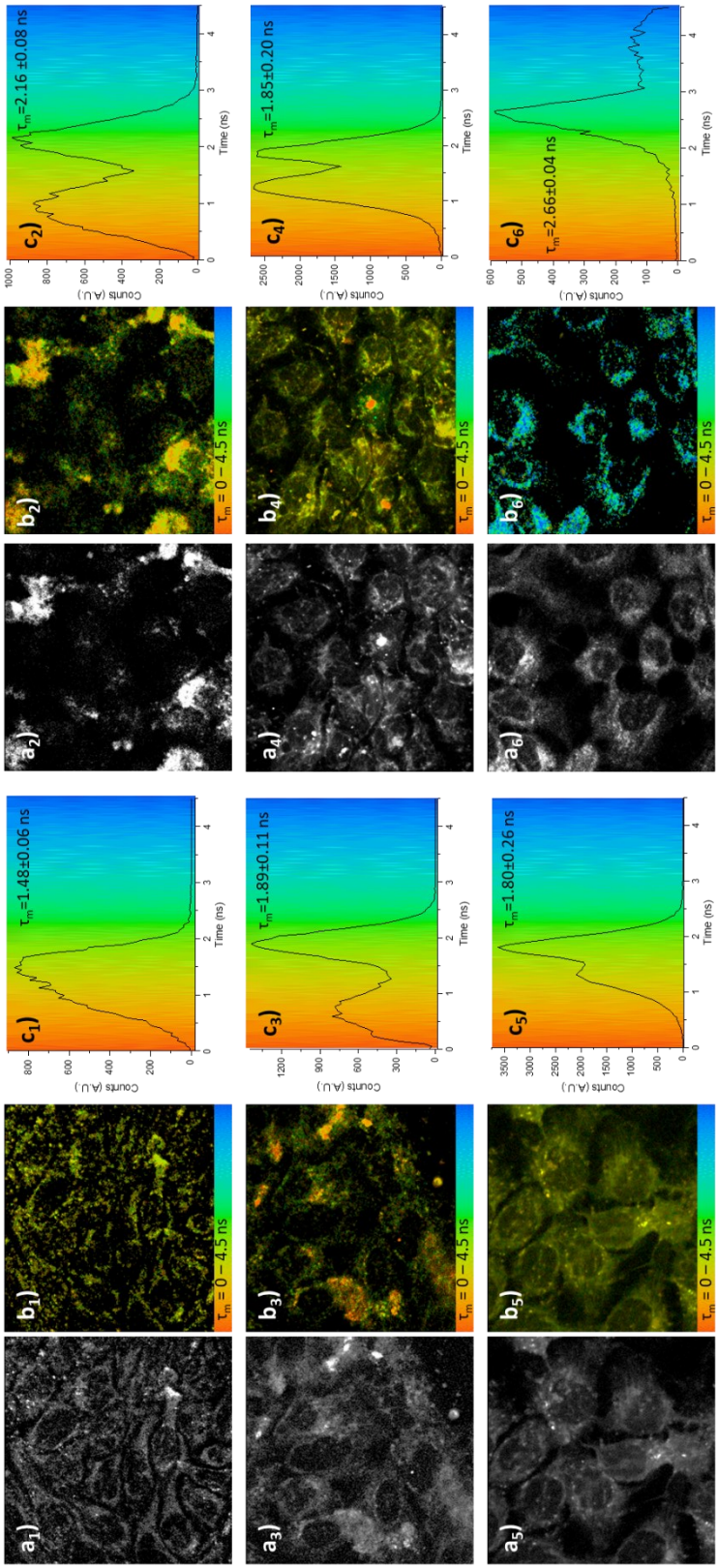

Figure 4.33. Two-photon fluorescence lifetime imaging in A431 cells line including **$a_{1\text{-}6}$)** intensity map, **$b_{1\text{-}6}$)** lifetime maps in coloured code and **$c_{1\text{-}6}$)** lifetime distribution (λ_{ex}=810 nm from **a_1-b_1** to **a_5-b_5** and λ_{ex}=910 nm for a_6-b_6). **a_1-c_1)** DMSO control (laser power 6.6 mW, acquisition time 20 s); **a_2-c_2)** ***L*-13** (laser power 5.0 mW, acquisition time 90 s); **a_3-c_3)** ***L*-14** (laser power 4.7 mW, acquisition time 60 s); **a_4-c_4)** ***D*-13** (laser power 4.9 mW, acquisition time 60 s); **a_5-c_5)** ***D*-14** (laser power 4.9 mW, acquisition time 90 s); **a_6-d_6) 15** (laser power 1.2 mW, acquisition time 40 s).

The images depicted in Figure 4.33a_1-c_1 refer to the A431 cells incubated with DMSO and used as FLIM control for the comparison with the fluorescent probes. The lifetime distribution (c_1) is centred in value of τ_m=1.48±0.06 ns which can be used as a reference for studying the interaction with the probes. The decay time distribution of ***L*-13** (c_2) showed two distinct groups of lifetimes: the first has a τ_m=0.95±0.06 ns and the second is centred at 2.16±0.08 ns. The long lifetime contribution can be due to the interaction of the probe with the compartments of the cells, whilst the short-lived contribution is due to parts of the cells which are not interacting with the probe. ***L*-14** (c_3) showed also two groups of lifetime distributions which the first is at around 0.72±0.05 ns and the second at 1.89±0.11 ns. This molecule showed a short-lived lifetime distribution than in ***L*-13** which may suggest that the number of peptide moieties can affect the interactions with the compartment of the cells. The *D*-enantiomers (***D*-13** and ***D*-14**) showed also two groups of lifetime distributions. In particular, ***D*-13** (c_4) present a short-lived lifetime distribution centred at 1.26±0.19 ns and the long distribution is at 1.85±0.20 ns. Similarly, ***D*-14** (c_5) showed a slow lifetime distribution at 1.30±0.15 ns and the faster at 1.80±0.26 ns. The *D*-enantiomers of the *mono*- and *bis*-peptide derivatives showed consistently the same values for both lifetime distributions which may result in a similar interaction with cells as their *L*-versions. The different stereochemistry of **13**, as well as **14**, was reflected in different short lifetime distributions which can suggest that the *L*-enantiomers can interact better with cells than their *D*-enantiomers, confirming the preference[24-27] of living cells for *L*-enantiomers already assessed previously. Different lifetime behaviour was found for compound **15**. It showed only one-lifetime decay distribution (c_6), centred at 2.66±0.04 ns. It can be supposed that the molecule is distributed into the cells and the interactions with the cellular environment increase the lifetime of **15**. In addition, the BODIPY moiety may lead the overall lifetime of the molecule. In recent works[55,56], the lifetime distribution of BODIPY derivatives is between 2.5 and 3.0 ns which is consistent with the results obtained hereby. Globally, a substantial difference in lifetime decays can be noticed between the solutions and the studies of the living cell. In the last environment, statistically long lifetime decays were found which can confirm that these molecules may interact with the cellular compartments, encouraging the FRET events.

Further FLIM investigations were carried out in PC-3 cells line to assess the effect of the presence of one or two moieties of the bombesin peptide on the NDI-core. In addition, these analyses were performed to evaluate any targeting on the lysosomes and GRPR of the cells.

Figure 4.34 reports the intensity images, fluorescence lifetime micrographs and lifetime distribution curves of ***L*-13** (a_1-c_1) and ***L*-14** (a_2-b_2). τ_1 and τ_2 are reported in Appendices A, Figures A.98 and A.99.

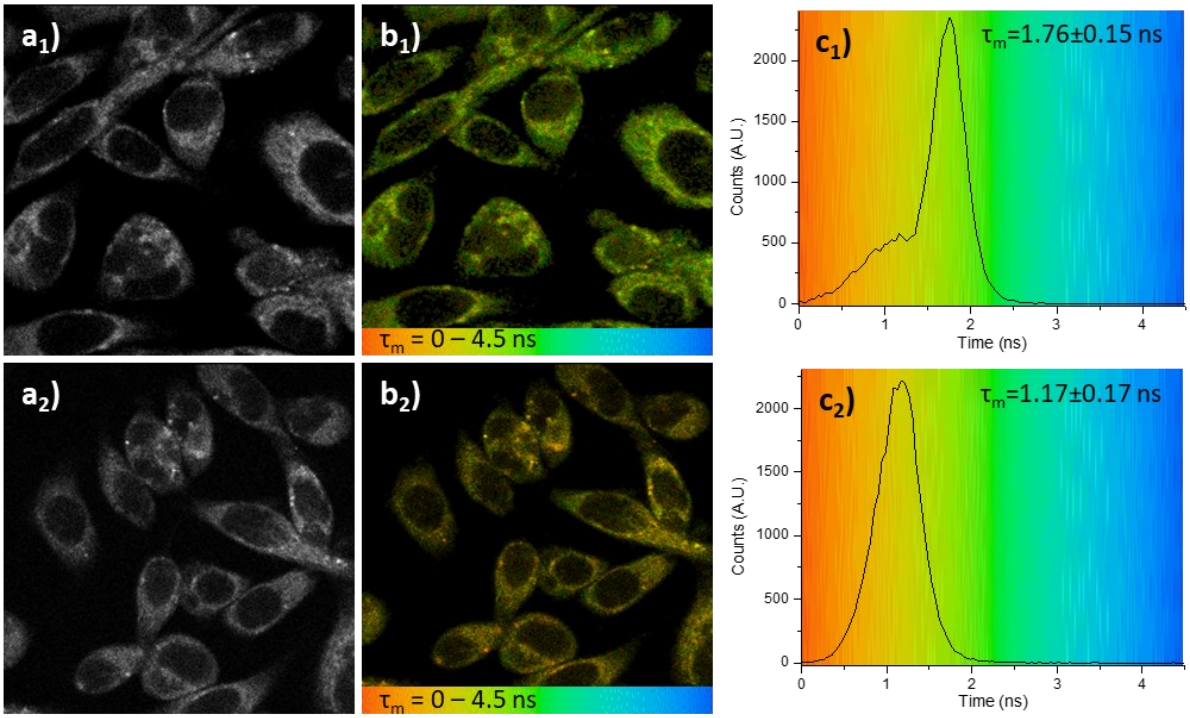

Figure 4.34. Two-photon fluorescence lifetime imaging in PC-3 cells line including **$a_{1,2}$)** intensity map, **$b_{1,2}$)** lifetime maps in coloured code and **$c_{1,2}$)** lifetime distribution (λ_{ex}=810 nm). **a_1-c_1)** ***L*-13** (laser power 3.9 mW, acquisition time 30 s); **a_2-c_2)** ***L*-14** (laser power 4.9 mW, acquisition time 30 s).

The lifetime distribution of ***L*-13** (Figure 4.34c_1) in PC-3 cells shows two groups of distributions. The less intense distribution is centred at 1.12±0.13 ns, whilst the second one is 1.76±0.15 ns. The fast component could be due to the number of molecules that interacts with the cellular compartment. On the other hand, the long-lived lifetime distribution can be attributed to free molecules on the cytosol of the cells which interacts with each other. Differently, ***L*-14** showed only one lifetime distribution curve (c_2) centred at 1.17±0.17 ns. The presence of one lifetime distribution can suggest that ***L*-14** interacts more efficiently with cells thanks to the presence of 2 peptide moieties in its structure.

Compounds **2** and **15** were investigated by FLIM in CHO cell line to assess the contribution of the BODIPY derivative moiety on the interaction and lifetime characteristics into the cellular environment. Figure 4.35 reports the FLIM investigation of **2** (a_1-c_1) and **15** (a_2-b_2) is reported for comparison. τ_1 and τ_2 are reported in Appendices A, Figure A.96 and A.97.

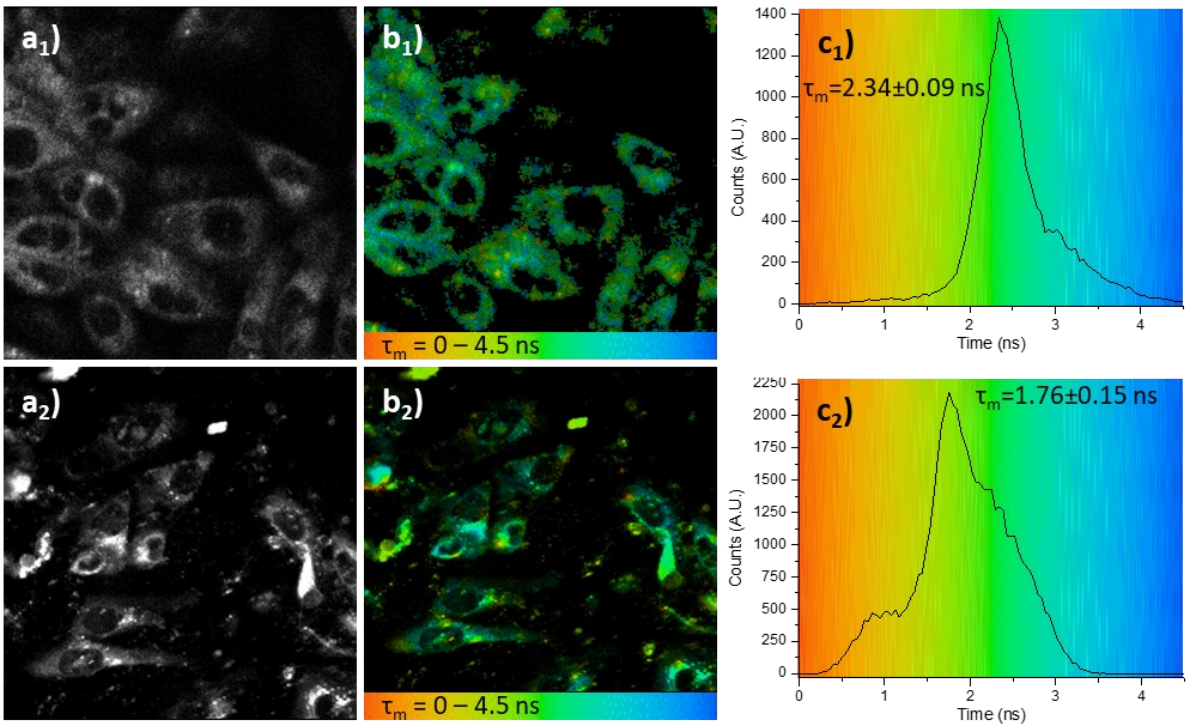

Figure 4.35. Two-photon fluorescence lifetime imaging in CHO cells line including **$a_{1,2}$)** intensity map, **$b_{1,2}$)** lifetime maps in coloured code and **$c_{1,2}$)** lifetime distribution (λ_{ex}=910 nm). **a_1-c_1) 2** (laser power 4.9 mW, acquisition time 90 s); **a_2-c_2) 15** (laser power 4.2 mW, acquisition time 40 s).

In the distribution c_1, it can be noticed a value of 2.34±0.09 ns which belongs to **2**. As shown in the fluorescence lifetime micrographs b_1, this compound localises in the cytosol of the cells and interacts with some cellular compartments. On the other hand, **15** shows a single distribution of lifetimes centred at 1.76±0.15 ns. The presence of the peptide in the structure may increase the interactions with the cellular compartments.

4.3. Conclusions to Chapter 4

In this Chapter, two different types of naphthalenediimide (NDI)-based compounds were prepared. The first group of molecules presented one or two targeting-peptide moieties covalently bound on the NDI core. It was possible to synthesise different enantiomers thanks to the different stereochemistry available from both the spacer (*L*- or *D*-phenylalanine) and the chain of the amino acid on the chosen peptide. On the other hand, the second type of molecule present the NDI core linked with the peptide moiety (only *L*-amino acids), in one side, and a BODIPY derivative, in the other side.

Their optical features in solution were widely explored by UV-visible and fluorescence spectroscopies. The *L*- and *D*-enantiomers of the NDI-based targeting peptides showed a good fluorescence emission in the range at around 400-500 nm when they are excited in the range between 300 and 400 nm. On the other hand, the unsymmetrised NDI showed an intense fluorescence emission at around 500 nm, when excited at 500 nm which is suitable for the confocal imaging studies in living cells.

The uptake and bio-distribution of these fluorescent probes were assessed by confocal laser scanning microscopy. The stereochemistry of the targeting-peptide played a fundamental role in the absorption into the prostate cancer cells. In fact, the *L*-enantiomers seemed qualitatively more absorbed than the *D*-enantiomers. Besides, the presence of one or two peptide moieties made the difference as well. The *bis*-peptide species (regardless of the nature of the stereoisomers considered) were more effectively internalised by cells than their *mono*-counterparts. Further analyses to assess the effective amount of compound may be taken up by the cells have been considered. In addition, further studies to evaluate the specific/non-specific uptake of the compounds in different cell lines with a high density of GRPRs and non-GRPR responsive have been planned to be carried out.

On the other hand, the BODIPY-functionalised showed an uptake after 20 minutes of incubation which can be due to the presence of the BODIPY moiety. This group was extensively studied in cellular environments in terms of fluorescence properties and biocompatibility. In addition, the presence of the peptide moiety within the molecular framework allowed a specific localisation into the cellular compartment namely lysosomes. Even in this case, further analysis to compare the effective amount of compound taken up and specific/non-specific uptake into the cells have been considered to be performed in the future.

The bio-localisation of these probes was studied by confocal laser scanning microscopy, using image statistical analysis. In particular, the prostate cancer cells were stained with a lysosomal dye. These organelles have recently been studied as a potential target to induce cells death and inhibit the cytoprotective autophagy. All the probes showed good localisation into these organelles, despite their different uptake rate and time. To assess their cytotoxicity into the cells, crystal violet assays were carried out at different incubation times. These compounds showed mild toxicity over time which suggests that these compounds can be used as fluorescence probes instead of therapeutic agents.

TCSPC and FLIM were used as powerful tools to evaluate the lifetime decay of these molecules, the FRET and their interactions with living cells. Particularly, the lifetime decays analysis in the solution obtained by TCSPC showed that these fluorescent probes tend to aggregate and cause FRET events in solutions, despite the solvent system involved. On the other hand, FLIM confirmed the absorption, distribution and interactions of these molecules with the cellular environment, showing the substantial difference between the behaviour in solution and the cells.

4.4. References to Chapter 4

1. M. Al Kobaisi, S. V. Bhosale, K. Latham, A. M. Raynor and S. V. Bhosale, *Chem. Rev.*, 2016, **116**, 11685-11796.
2. C. L. Lyall, C. C. Shotton, M. Pérez-Salvia, G. Dan Pantoş and S. E. Lewis, *Chem. Comm.*, 2014, **50**, 13837-13840.
3. P. Pengo, G. D. Pantoş, S. Otto and J. K. M. Sanders, *J. Org. Chem.*, 2006, **71**, 7063-7066.
4. G. M. Prentice, L. Emmett, V. Luxami and G. D. Pantoş, in *Naphthalenediimide and its Congeners: From Molecules to Materials*, ed. G. D. Pantoş, The Royal Society of Chemistry, 2017, 1-36.
5. Z. Hu, R. L. Arrowsmith, J. A. Tyson, V. Mirabello, H. Ge, I. M. Eggleston, S. W. Botchway, G. Dan Pantos and S. I. Pascu, *Chemical Communications*, 2015, **51**, 6901-6904.
6. J. A. Tyson, V. Mirabello, D. G. Calatayud, H. Ge, G. Kociok-Köhn, S. W. Botchway, G. Dan Pantoş and S. I. Pascu, *Adv. Funct. Mater.*, 2016, **26**, 5641-5657.
7. R. Mansi, R. Minamimoto, H. Mäcke and A. H. Iagaru, *J. Nucl. Med.* , 2016, **57**, 67S-72S.
8. D. Pooja, A. Gunukula, N. Gupta, D. J. Adams and H. Kulhari, *Int. J. Biochem. Cell Biol.*, 2019, **114**, 105567.
9. L. B. Retzloff, L. Heinzke, S. D. Figureoa, S. V. Sublett, L. Ma, G. L. Sieckman, T. L. Rold, I. Santos, T. J. Hoffman and C. J. Smith, *Anticancer Res.*, 2010, **30**, 19-30.
10. T. Kowada, H. Maeda and K. Kikuchi, *Chem. Soc. Rev.*, 2015, **44**, 4953-4972.
11. S. Iwaki, K. Hokamura, M. Ogawa, Y. Takehara, Y. Muramatsu, T. Yamane, K. Hirabayashi, Y. Morimoto, K. Hagisawa, K. Nakahara, T. Mineno, T. Terai, T. Komatsu, T. Ueno, K. Tamura, Y. Adachi, Y. Hirata, M. Arita, H. Arai, K. Umemura, T. Nagano and K. Hanaoka, *Org. Biomol. Chem.*, 2014, **12**, 8611-8618.
12. S. M. Elshafae, B. B. Hassan, W. Supsavhad, W. P. Dirksen, R. Y. Camiener, H. Ding, M. F. Tweedle and T. J. Rosol, *The Prostate*, 2016, **76**, 796-809.
13. Z. Hu, R. L. Arrowsmith, J. A. Tyson, V. Mirabello, H. Ge, I. M. Eggleston, S. W. Botchway, G. Dan Pantos and S. I. Pascu, *Chem. Comm.*, 2015, **51**, 6901-6904.
14. K. Tambara, N. Ponnuswamy, G. Hennrich and G. D. Pantoş, *J. Org.Chem.*, 2011, **76**, 3338-3347.
15. N. V. Ghule, D. D. La, R. S. Bhosale, M. Al Kobaisi, A. M. Raynor, S. V. Bhosale and S. V. Bhosale, *ChemistryOpen*, 2016, **5**, 157-163.
16. F. Salerno, J. A. Berrocal, A. T. Haedler, F. Zinna, E. W. Meijer and L. Di Bari, *J. Mater. Chem. C*, 2017, **5**, 3609-3615.
17. V. Saravanan and P. Rajakumar, *New J. Chem.*, 2018, **42**, 2504-2512.
18. Y.-Q. Li, F. Qian and Z. Li, *Chemical Journal on Internet*, 2000, **2**, 29-36.

19. A. T. R. Williams, S. A. Winfield and J. N. Miller, *Analyst*, 1983, **108**, 1067-1071.

20. A. M. Brouwer, *Pure Appl. Chem.*, 2011, **83**, 2213-2228.

21. J. Huff, *Nat. Methods*, 2015, **12**, 1205.

22. J. Huff, I. Kleppe, A. Naumann and R. Nitschke, *Na. Methods*, 2018.

23. X. Dou, T. Nomoto, H. Takemoto, M. Matsui, K. Tomoda and N. Nishiyama, *Sci. Rep.*, 2018, **8**, 8126.

24. F. C. Frank, *Biochim. Biophys. Acta*, 1953, **11**, 459-463.

25. S. Bondy and M. Harrington, *Science*, 1979, **203**, 1243-1244.

26. R. Milton, S. Milton and S. Kent, *Science*, 1992, **256**, 1445-1448.

27. F. Jafarpour, T. Biancalani and N. Goldenfeld, *Phys. Rev. E*, 2017, **95**, 032407.

28. S. Luo, E. Zhang, Y. Su, T. Cheng and C. Shi, *Biomaterials*, 2011, **32**, 7127-7138.

29. J. M. Belitsky, S. J. Leslie, P. S. Arora, T. A. Beerman and P. B. Dervan, *Bioorg. Med. Chem.*, 2002, **10**, 3313-3318.

30. K. W. Dunn, M. M. Kamocka and J. H. McDonald, *Am. J. Physiol. Cell Physiol.*, 2011, **300**, C723-C742.

31. S. Piao and R. K. Amaravadi, *Ann. N. Y. Acad. Sci.*, 2016, **1371**, 45-54.

32. K. Moreau, S. Luo and D. C. Rubinsztein, *Curr. Opin. Cell Biol.*, 2010, **22**, 206-211.

33. J. Adler and I. Parmryd, *Cytom. A*, 2010, **77A**, 733-742.

34. R. Schilling, P. Geserick and M. Leverkus, in *Methods in Enzymology*, eds. A. Ashkenazi, J. A. Wells and J. Yuan, Academic Press, 2014, 545, pp. 83-102.

35. E. B. van Munster and T. W. J. Gadella, in *Microscopy Techniques*, ed. J. Rietdorf, Springer Berlin Heidelberg, Berlin, Heidelberg, 2005, 143-175.

36. A. Periasamy and R. M. Clegg, *FLIM microscopy in biology and medicine*, Chapman and Hall (CRC press), Boca Raton, Florida, 2009.

37. T. Förster, *Ann. Phys.*, 1948, **437**, 55-75.

38. S. E. Braslavsky, *Pure Appl. Chem.*, 2007, **79**, 293.

39. H. Ranawat, S. Pal and N. Mazumder, *Biomed. Eng. Lett.*, 2019, **9**, 293-310.

40. A. Cong, R. M. L. Pimenta, H. B. Lee, V. Mereddy, J. Holy and A. A. Heikal, *Cytom. A*, 2019, **95**, 80-92.

41. R. I. Dmitriev and D. B. Papkovsky, *Cell. Mol. Life Sci.*, 2012, **69**, 2025-2039.

42. H. Ge, F. Cortezon-Tamarit, H.-C. Wang, A. C. Sedgwick, R. L. Arrowsmith, V. Mirabello, S. W. Botchway, T. D. James and S. I. Pascu, *Nanoscale*, 2019, **11**, 9498-9507.

43. W. Becker, in *The bh TCSPC Handbook*, Becker & Hickl GmbH, Berlin, Germany, 2017.

44. H.-N. Chang, B.-Y. Liu, Y.-K. Qi, Y. Zhou, Y.-P. Chen, K.-M. Pan, W.-W. Li, X.-M. Zhou, W.-W. Ma, C.-Y. Fu, Y.-M. Qi, L. Liu, Y.-F. Gao, *Angew. Chem. Int. Ed.*, 2015, **54**, 11760-11764.

45. J. Liu, J. Liu, L. Chu, Y. Zhang, H. Xu, D. Kong, Z. Yang, C. Yang, D. Ding, *ACS Appl. Mater. Interfaces*, 2014, **6**, 5558-5565.

46. B. E. Rogers, M. E. Rosenfeld, M. B. Khazaeli, G. Mikheeva, M. A. Stackhouse, T. Liu, D. T. Curiel and D. J. Buchsbaum, *J. Nucl. Med.*, 1997, **38**, 1221-1229.

47. A. Safavy, K. P. Raisch, M. B. Khazaeli, D. J. Buchsbaum and J. A. Bonner, *J. Med. Chem.*, 1999, **42**, 4919-4924.

48. M. Kjaergaard, A.-B. Nørholm, R. Hendus-Altenburger, S. F. Pedersen, F. M. Poulsen, B. B. Kragelund, *Protein Sci.*, 2010, **19**, 1555-1564.

49. F. Pu, J. Qiao, S. Xue, H. Yang, A. Patel, L. Wei, K. Hekmatyar, M. Salarian, H. E. Grossniklaus, Z.-R. Liu, J. J. Yang, *Sci. Rep.*, 2015, **5**, 16214.

50. X. Wen, C. Chao, K. Ives, M. R. Hellmich, *BMC Mol. Biol.*, 2011, **12**, 29.

51. E. Salvati, F. Doria, F. Manoli, C. D'Angelo, A. Biroccio, M. Freccero, I. Manet, *Org. Biomol. Chem.*, 2016, **14**, 7238.

52. J. Ischia, O. Patel, D. Bolton, A. Shulkes, G. S. Baldwin, *BJU Int.*, 2014, **113**, 40-47.

53. C. A. Fischer, S. Vomstein, T. L. Mindt, *Pharmaceuticals*, 2014, **7**, 662-675.

54. M. Aoki, S. Zhao, K. Takahashi, K. Washiyama, N. Ukon, C. Tan, S. Shimoyama, K. Nishijima, K. Ogawa, *Chem. Pharm. Bull.*, 2020, **68**, 538-545.

55. S. Requena, O. Ponomarchuk, M. Castillo, J. Rebik, E. Brochiero, J. Borejdo, I. Gryczynski, S. V. Dzyuba, Z.Gryczynski, R. Grygorczyk, R. Fudala, *Sci. Rep.*, 2017, **7**, 1-6.

56. M. Kubánková, J. E. Chambers, R. G. Huber, P. J. Bond, S. J. Marciniak, M. K. Kuimova, *Methods Appl. Fluoresc.*, 2019, **7**.

Chapter 5: Summary to Thesis and Outlook

Optical and electrochemical biosensing have increasingly become potent tools to detect cancer in the early stage. Such methods allow developing non-invasive, sensitive and accurate point-of-care tests to localise cancer cells, *e.g.* prostate cancer, through different techniques such as confocal microscopy and electrochemical impedance spectroscopy. This Thesis aimed to design and develop novel molecular systems able to localise in prostate cancer cells and be detected *via* confocal microscopy. Following, it is presented a summary chapter by chapter of the systems explored in this Thesis.

Chapter 2 proposed the design and synthesis of novel fluorescent ligands for *d*-metal cations used in imaging and therapy for different forms of cancer.

The first proposed ligand presented a diacetyl *bis*(N^4-methylthiosemicarbazonate (ATSM) ligand, linked in a naphthalenediimide (NDI) scaffold in which a 4,4-difluoro-4-bora-3a,4a-diaza-s-indacene (BODIPY) derivative was incorporated on the other side of the NDI core. The ATSM ligand was chosen thanks to its ability to complex copper (II) ions, as the well-know [Cu(ATSM)], and similar *d*-group cations such as nickel (II) and zinc(II). In addition, such metal complexes have been widely employed for imaging and therapeutic purposes for different forms of cancer. The NDI core is a versatile scaffold to be derivatised *via* microwave-assisted reactions, considered a fast, efficient and high yielded method. BODIPY and its derivatives have been explored as fluorescent tags for bioimaging thanks to their stability, biocompatibility and high quantum yield in the cellular environment. Three metal complexes (*i.e.* Cu(II), Ni(II) and Zn(II)) were generated from the proposed fluorescent ATSM ligand, based on NDI. Such fluorescent metal complexes were characterised by mass spectrometry and infrared spectroscopy. UV-visible and fluorescence spectroscopy were used to investigate their optical characteristics in DMSO. These fluorescent metal complexes were preliminarily investigated by confocal laser scanning microscopy in living cell lines such as prostate cancer cells (PC-3). Such study revealed that the fluorescent compounds localised into the cytoplasm of the cells, emitting an appreciable signal in the range between 500 and 500 nm.

As known in the literature, [Cu(ATSM)] has been explored for its potential hypoxia selectivity for either imaging or therapy. The proposed fluorescent Cu(II) complex was preliminarily investigated *via* confocal laser-scanning microscopy in both normoxic and hypoxic conditions into different cells to evaluate its fluorescence change in such cellular environment.

This preliminary analysis revealed that the compound increased the fluorescence emission under hypoxia, indifferently from the cells.

Further investigation was carried out preliminarily through fluorescence lifetime imaging to evaluate the lifetime behaviour, passing from normoxia to hypoxia. No substantial changes in lifetime distribution were found under hypoxia.

The second ATSM-based functionalised ligand, incorporating the NDI core, was designed and conjugated to the fragment BBN [7-13] of the bombesin peptide. Such ligand was chosen deliberately aiming to target specifically prostate cancer cells, exploiting the potential hypoxia selectivity of the [Cu(ATSM)] complex.

The third ligand was designed and synthesised with two moieties of desferrioxamine B (DFO) on the NDI-core. Such ligand has been explored to chelate metal radioisotopes such as ^{68}Ga and ^{89}Zr, widely used for PET/CT cancer imaging. The proposed ligand was characterised by NMR and infrared spectroscopies and mass spectrometry. Such proposed ligand was investigated by UV-visible and fluorescence microscopies to assess its characteristics in DMSO and then preliminarily investigated into living prostate cancer cells by confocal laser scanning microscopy. The incorporation of Zr(IV) was attempted on the ligand as a proof-of-concept for future radiolabelling.

Chapter 3 described the design of different *pseudo*rotaxanes as a supramolecular tool for cancer imaging.

The proposed systems were based in a dinaphtho tetraethylene glycol “wheel” with three different NDI-based “axles”. The first designed and synthesised “axle” presented two moieties of the ATSM ligand on the NDI core which incorporated copper(II) ions, useful as potential stoppers on the formation of the *pseudo*rotaxane. The second “axle” presented two BODIPY-derivative moieties on the NDI scaffold. Such molecule was characterised by ^{1}H-NMR and its optical properties were investigated by UV-visible and fluorescence spectroscopies. Such fluorescent “axle” was also preliminarily investigated in living prostate cancer by confocal laser scanning microscopy. The third set of “axles” consisted of amino acids-tagged NDIs with two iodo-phenylalanine moieties. One of the two “axles” presented the carboxylic group of the phenylalanine protected by succinimide, whilst the second “axle” has hydroxyl groups. Such protection could increase the aromatic stacking between the NDI and the naphthalene rings on the “wheel”, blocking the threading/de-threading equilibrium of the rotaxane. Two different *pseudo*rotaxanes were formed, consisting of the amino acid-tagged NDIs “axles” and the dinaphtho tetraethylene glycol “wheel”.

Such species were preliminarily investigated by variable temperature ^{1}H-NMR and DOSY-NMR to assess the possible threading/de-threading equilibrium.
Such preliminary studies on the two *pseudo*rotaxanes revealed the existence of two different species in solution at low temperature which suggest the existence of an equilibrium between the interlocked system and the free components of the rotaxane.

Chapter 4 presented novel peptide-tagged NDIs as potential fluorescent probes to detect and localise prostate cancer cells through confocal microscopy.
The first group of molecules presented one or two targeting-peptide moieties (bombesin [7-13]) covalently linked to the NDI core. Different enantiomers were generated thanks to the different stereochemistry available from both the spacer (*L*- or *D*-phenylalanine) and the amino acid sequence of the peptide. On the other hand, the second type of molecule consisted of an NDI-core linked with the *L*-version of the peptide moiety and a BODIPY-derivative. Their optical features in solution were widely explored by UV-visible and fluorescence spectroscopies which showed appreciable fluorescence emissions in the range between 300 and 500 nm. Confocal laser-scanning microscopy was used to investigate preliminarily the uptake and bio-distribution of these proposed fluorescent probes into living cancer cells. The stereochemistry and the number of the targeting-peptide moieties played a fundamental role in the absorption into the prostate cancer cells. In fact, the *L*-enantiomers were absorbed more rather than the *D*-enantiomers and moreover, the *bis*-peptide species were more absorbed than their *mono*-versions, indifferently from the stereochemistry. The localisation of such peptide-tagged probes was preliminarily studied by confocal laser-scanning microscopy, using image statistical analysis, staining the prostate cancer cells with a lysosomal dye. Lysosomes have been recently studied as a potential target to induce cells death and inhibit the cytoprotective autophagy. Overall, the proposed probes showed good localisation into these organelles, despite their different uptake rate and time. Fluorescence lifetime imaging microscopy has been increasingly explored as a powerful tool to investigate biological processes and study cellular uptake and distribution of fluorescent probes into cells. In addition, such a technique can penetrate tissues and organs in-depth, non-invasively, thanks to the use of near-infrared wavelengths (650-1350 nm). The lifetime distribution and localisation of the proposed peptide-tagged probes were preliminarily investigated in both solution and living cells using two-photon time-correlated single-photon counting (TCSPC) and fluorescence lifetime imaging microscopy (FLIM).

The TCSPC analysis showed that these fluorescent probes tended to aggregate and cause Förster resonance energy transfer (FRET) events in solutions, despite the solvent system involved. On the other hand, FLIM confirmed the absorption, distribution and interactions of these molecules with the cellular environment, showing the substantial difference between the behaviour in solution and the cells.

Chapter 6: Experimental Section

6.1. General information

Reagents were obtained from commercial sources (*Sigma Aldrich*, *Alfa Aesar*, *Acros Organics*, *Merck Chemicals*, *Fluorochem*) and used as received unless otherwise specified. Solvents were reagent or HPLC grade obtained from *Sigma Aldrich* or *VWR*. Water was obtained from a *Millipore Milli-Q* purification system.

Microwave reactions were performed in either 5 or 20 mL pressure-tight vessels in a *Biotage Initiator 2.5* microwave reactor. Reaction mixtures were pre-stirred for 30 s and heated to the desired temperature by applying a maximum power of 400 W which was reduced and kept constant once the required temperature was reached.

Automated flash chromatography purifications were carried out in a *Biotage Isolera Four* system using 10, 25 or 50 g *Biotage SNAP Ultra* silica cartridges.

NMR spectra were acquired in a *500 MHz Bruker Avance II+* or a *500 MHz Agilent* automated system. Spectra were processed using *MestReNova 11.0.2* and referred to the residual solvent peaks. Splitting patterns are identified as singlet (*s*), doublet (*d*), triplet (*t*), quartet (*q*) and multiplet (*m*).

Mass spectra were acquired in *Bruker MicrOTOF Electrospray Time-Of-Flight* mass spectrometer (ESI-TOF) coupled to an *Agilent* HPLC.

HPLC was performed in a *Dionex Ultimate 3000 HPLC* instrument with a UV-visible diode array detector at eight wavelengths between 200 and 800 nm.

Analytical HPLC chromatograms were acquired in reverse phase (RP) mode using a *Dionex Acclaim 120 C18* column (5 µm, 4.6x150 mm). In this case, a 60 min gradient method (method A) was used using MeCN and H_2O, both containing 0.1% of TFA, as mobile phases. The method A consisted in: 0 min 5% MeCN; 1 min 5% MeCN; 31 min 95% MeCN; 41 min 95% MeCN; 51 min 5% MeCN; 58 min 5% MeCN; flow rate: 0.5 mL/min.
Semi-preparative HPLC was performed using *Nucleodur C18 HTEC* (5 µm, 10 x 250 mm) and *Nucleodur C18 HTEC* (5 µm, 21x250 mm) columns. A 36 min gradient method (method B) was used for both columns. Method B conditions were: 0 min 5% MeCN; 1 min 5% MeCN; 21 min 95% MeCN; 26 min 95% MeCN; 31 min 5% MeCN; 36 min 5% MeCN; flow rates:

1.8 and 4.0 mL/min, respectively. IR spectra were acquired in a *Perkin Elmer Frontier FTIR* machine in ATR mode.

UV-visible spectra were acquired in 1 cm quartz cuvettes in a *Perkin Elmer Lambda 650* UV-*vis spectrometer* controlled by *UV-WinLab 6.2.0.0741* software.

Fluorescence spectra were acquired in 1 cm quartz cuvettes in a *Perkin Elmer LS55* luminescence spectrometer controlled by *FL-WinLab 4.00.02* software.

Quantum yields were calculated according to the equation 7.1[1] using $Ru(bpy)_3$, *L*-triptophan, rhodamine B and fluoresceine as standards.

$$\Phi_x = \Phi_S \cdot \frac{A_S}{A_x} \cdot \frac{E_x}{E_S} \cdot \frac{I_S}{I_x} \cdot \frac{{n_x}^2}{{n_S}^2}$$

Equation 6.1

where Φ_S is the quantum yield of the standard, A is the absorbance of the solution, E is the corrected emission intensity, I is the relative intensity of the exciting light and n is the average refractive index of the solution.

HR-TEM was performed using a multi-purpose *Jeol Jem-2100 Plus* Transmission Electron Microscope with a constant accelerating voltage of 200 kV at varying magnifications. Graphene oxide samples were prepared from a dilute THF suspension of the compound deposited onto Lacey carbon TEM meshes (*Agar Scientific* Lacey Carbon Film on 400 Mesh Cu). SAED was also carried out using the same microscope.

SEM images were acquired using a *Jeol JSM-6480 LV* Scanning Electron Microscope with a constant accelerating voltage of 10 kV under high vacuum ($\sim 1.6 \cdot 10^{-5}$ mbar). Graphene oxide samples were prepared from a dilute THF suspension of the compound dropped onto freshly cleaved Ruby Muscovite Mica (*Agar Scientific* Mica Sheets, AGG250) and dried overnight under low vacuum. Compounds ***L*-13**, ***L*-14**, ***D*-13** and ***D*-14** were prepared from a dilute either DMSO or DMSO:H_2O (1:1) suspensions of the compound dropped onto freshly cleaved Ruby Muscovite Mica (*Agar Scientific* Mica Sheets, AGG250) and dried overnight under low vacuum. A conducting gold thin film was deposited on top of samples for standard imaging.

Cells were cultured at 37 ºC in RPMI medium containing foetal calf serum (10%), penicillin/streptomycin (10000 IU mL^{-1}) and *L*-glutamine (200 mM). All steps were performed in the absence of phenol red. Cell culture was carried out by Dr Haobo Ge.

Cell viability tests (MTT and Crystal violet) assays were performed culturing cells as above in 96 well plates (*ca*. $5 \cdot 10^4$ cells/mL). The cells were incubated for 48 h to adhere and then the compounds of interest added in different concentrations in RPMI medium (1% DMSO). The concentrations used were reported in relative Chapter 1, 4 and 5. The compounds were incubated for the described period of time at 37 ºC to be subsequently washed with PBS and MTT or Crystal violet reagents added. The absorbance of the generated colour was measured using a *Molecular Devices VersaMax ELISA* plate reader. Data were calculated from at least six consistent results and IC_{50} values calculated from the fitting obtained with *Origin 9.0* software. The reported error corresponds to the error of the mean. Cell viability studies were carried out by Dr Haobo Ge.

Confocal microscopy images were acquired in a *Nikon Eclipse Ti* instrument equipped with 405, 488 and 561 nm excitations lasers. The obtained images were processed using the *Nikon Elements-AR Analysis 4.30.02* software.

Fluorescence lifetimes and FLIM measurements were conducted at the Rutherford Appleton Laboratory (Central Lasers Facility, Research Complex at Harwell) with the assistance of Prof Stanley Botchway, Dr Fernando Cortezon-Tamarit, Dr Vincenzo Mirabello and Dr Haobo Ge. Lifetime calculations were processed using *SPCImage 7.4* software. The region of interest (ROI) was linked via a time-correlated single-photon counting (TCSPC) module *SPC830* (*Becker and Hickl*) to generate the multiphoton exciting image with the associated characteristic decay at each pixel position. The decays were subsequently analysed to generate the FLIM image. Two-photon (710–1000 nm) wavelength laser light was obtained from the mode-locked titanium-sapphire laser *Mira* (*Coherent Laser Co., Ltd*) producing 180 femtosecond at 75 MHz. This laser-pumped solid-state continuous-wave 532 nm laser (*Verdi V18*, *Coherent Laser Co., Ltd*). This can also be used for the fundamental output of the oscillator 810±2 nm. The laser beam was focused to a diffraction-limited spot by the water immersion UV objective (*Nikon VC×60*, *NA1.2*) at the specimen on a microscope stage of the modified *Nikon TE2000-U*. The focused laser multiphoton beam was raster scanned using a modified *Nikon Eclipse EC2* scan head to allow input of the titanium:sapphire laser.

Fluorescence emission was collected without de-scanning, bypassing the scanning system and passed through a coloured glass (*BG39*) filter. In normal operation mode and line scan frame and pixel clock signal was generated and synchronised with an external fast microchannel plate photomultiplier tube as detector (*R3809-U*, *Hamamatsu*, Japan). These were linked via a time correlated single-photon counting (TCSPC) PC module *SPC830* for the lifetime measurements with 810 and 910 nm excitation and emission in the range between 360 and 580 nm. FLIM images are shown with corresponding intensity images from the same samples with different coded colours representing different lifetime scales. The lifetime of each pixel is obtained by applying a single or multi-exponential fit.

Super-resolution confocal microscopy images were acquired in a *ZEISS LSM-880 Inverted Confocal Laser Scanning Microscope* with MP laser and *Airyscan*. The instrument is equipped with 405, 488 and 561 nm excitations lasers. The obtained images were processed using the *ZEISS ZEN LITE 3.0* software.

Cyclic voltammetry measurements were recorded using a *CompactStat potentiostat* (Ivium Technologies, the Netherlands) with *Ivium* software. A three-electrode cell with an Ag/AgCl reference electrode (BASi, USA) connected *via* a salt bridge filled with buffer and platinum counter electrode (ALS, Japan) was used for all measurements.

The EIS measurements with cells were performed in a *PalmSens* potentiostat (*PalmSens*), incubating the electrodes with the cells for 20 min and then leave in the PBS measure solution for 10 min to stabilise. Time of equilibration of 5 s was used before each measure. The frequencies used were between 1 mHz to 10 kHz with 10 points/decade and fixed potentials of E_{dc}=0 V and E_{ac}=0.01 V. Measurements and E_{dc} were *vs* OCP of 15 s.

6.2. Experimental procedures to compounds in Chapter 2

6.2.1. Synthesis of ATSM-en (**1**)

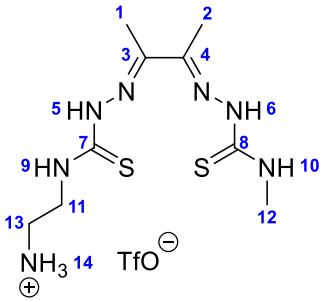

Protocol was adapted from literature procedure[2-4]. A stirring solution of 1.80 mL (27.0 mmol) of ethylenediamine, dissolved in 8.20 mL of DCM, was placed in an ice bath. A solution of 1.02 g (4.6 mmol) of di-*tert*-butyl dicarbonate (*t*-Boc) in 66mL of DCM was added dropwise over 3-4 h to the first one. The mixture was left to react overnight at room temperature. The solvent was removed under reduced pressure and the white solid was suspended in saturated $Na_2CO_{3(aq)}$ and extracted 2 times with $CHCl_3$. The organic layer was dried over $MgSO_4$, filtered and dried under reduced pressure to obtain an orange oil (yield: 1.4223 g, 89%).

The *mono-t*-Boc-protected ethylenediamine (0.7235 g, 4.1 mmol) was dissolved in 10 mL of EtOH and 0.30 mL of CS_2 were added dropwise with 0.60 mL (4.1 mmol) of Et_3N. The resulting mixture reacted for 90 min in a water bath. Iodomethane (0.30 mL, 4.2 mmol) was added to the reaction mixture which was left to react for further 1.75 h. The solvent was removed by rotavapor and the residue was suspended in EtOAc and extracted with $HCl_{(aq)}$ 1 M, saturated $Na_2CO_{3(aq)}$ and deionised H_2O. The yellow solid was obtained from drying the organic over $MgSO_4$, filtered and dried under reduced pressure (yield: 0.8013 mg, 77%).

The previous solid (0.8mg, 3.2 mmol) and hydrazine monohydrate (0.20 mL, 4.4 mmol) were dissolved in 15 mL of EtOH and left to react for 2.5 h under reflux. The solvent was removed under reduced pressure and the pure brown oil (**A**) was obtained by a short plug of silica gel ($CHCl_3$:MeOH, 0-100%) (yield: 0.6 mg, 83%).

A round-bottom flask with 2,3-butadienone (0.90 mL, 10.6 mmol), solubilised in 20 mL of deionised H_2O, was placed in an ice bath. To the stirring solution, 5 drops of $HCl_{(conc.)}$ were added. 1.03 g (9.5 mmol) of 4-methyl-3-thiosemicarbazide was added over 1.5 h in the reaction mixture. The resulting solution was left for a further 40 minutes to react at room temperature. The aqueous phase was extracted 3 times with $CHCl_3$ and the resulting organic layer was dried over $MgSO_4$, filtered and the solvent removed by rotavapor.

The obtained solid was suspended in pentane with few drops of $CHCl_3$ until slight turbidity and left overnight at 4 ºC. The yellow solid (**B**) was obtained by filtration, washing with pentane and drying in air (yield: 1.5236 g, 82%).

In a solution of **A** (0.6 mg, 2.6 mmol) in 15 mL of EtOH, 0.5 mg (2.6 mmol) of **B** were added over 30 min and, at the last addition, 2 drops of $HCl_{(conc.)}$ were added. The solution reacted for 3.5 h under reflux. The reaction mixture was cooled and poured in 50 mL of deionised H_2O. The yellow solid was obtained by washing 2 times with deionised H_2O and 1 time with Et_2O (yield: 0.6 mg, 63%).

The *t*-Boc protecting group was removed by dissolving the previous solid (0.6 mg, 1.6 mmol) in 1.20 mL of TFA which was stirred for 1.5 h at room temperature. The acid was removed under reduced pressure and saturated $Na_2CO_{3(aq)}$ was added. The resulting solution was filtered and washed with deionised H_2O (3x10 mL) and Et_2O (2x10 mL) to obtain a yellow solid (**8**, yield: 0.4 mg, 80%).

^{1}H-NMR (500 MHz, 298 K, DMSO-d_6) δ = 10.50 (*s*, 1H, H-6), 10.24 (*s*, 1H, H-5), 8.48 (*t*, 1H, H-10, *J* = 6.0 Hz), 8.41-8.37 (*m*, 1H, H-9), 7.84 (*bs*, 3H, H-4), 3.83 (*q*, 2H, H-11, *J* = 6.4 Hz), 3.06-3.04 (*m*, 2H, H-13), 3.02 (*d*, 3H, H-12), 2.23 (*s*, 3H, H-1), 2.22 (*s*, 3H, H-2).

^{13}C-NMR (125 MHz, 298 K, DMSO-d_6): δ = 178.49 (C-8), 178.48 (C-7), 148.86 (C-4), 147.74 (C-3), 41.34 (C-11), 38.01 (C-13), 31.24 (C-12), 11.89 (C-2), 12.18 (C-1).

ESI$^+$-TOF (CH_3OH): m/z found: 290.1185 $[M+H]^+$, 312.1002 $[M+Na]^+$; calculated for $C_9H_{19}N_7S_2$: 289.1143 Da.

FT-IR (ATR mode): ῡ (cm^{-1}) = 3360 (N-H stretc.), 3260 (N-H stretch.), 2920 (C-H stretc.), 1685 (C=N stretch.), 1460 (C-H bend.), 1127 and 720 (C=S stretc.).

6.2.2. Synthesis of [Cu(ATSM-en)] (**1a**), [Ni(ATSM-en)] (**1b**) and [Zn(ATSM-en)] (**1c**)

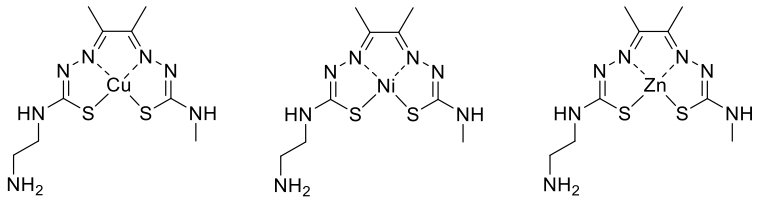

1a **1b** **1c**

Protocols adapted from literature procedure.

1a[5]: in a round-bottom flask, 50.0 mg (0.2 mmol) of **1** were dissolved in 4.00 mL of $NaOH_{(aq)}$ 1 M and a solution of 31.0 mg (0.2 mmol) of $Cu(OAc)_2 \cdot H_2O$ in 1.00 mL of deionised H_2O was added dropwise. The mixture reacted overnight at room temperature. The red solid was obtained by filtration and washing with H_2O and MeOH (yield: 35.0 mg, 70%).

1b[6]: in a round-bottom flask, 30.0 mg (0.1 mmol) of **1** and 31.0 mg (0.1 mmol) of $Ni(OAc)_2 \cdot 4H_2O$ were dissolved in 2.00 mL of EtOH. 0.1 mL of $NaOH_{(EtOH)}$ 1 M were added to the previous mixture which was left to react for 4 h under reflux. The green solid was collected by centrifugation and washing with Et_2O (yield: 23.5 mg, 68%).

1c[7]: in a round-bottom flask, 30.0 mg (0.1 mmol) of **1** and 27.3 mg (0.1 mmol) of $Zn(OAc)_2 \cdot 2H_2O$ were dissolved in 2.00 mL of MeOH. 0.10 mL of $NaOH_{(MeOH)}$ 1 M were added to the previous mixture which was left to react for 4 h under reflux. The yellow solid was collected by centrifugation and washing with Et_2O (yield: 26.3 mg, 75%).

1a) ESI$^+$-TOF (CH_3OH): m/z found: 351.0370 $[M+H]^+$; calculated for $C_9H_{17}N_7S_2Cu$: 350.0283 Da.

FT-IR (ATR mode): ῡ (cm^{-1}): 3325 (N-H stretc.), 2920 (C-H stretc.), 1570 (C=N stretch.), 1384 (C-H bend.), 1074 (C=S stretc.), 665 (C-S strect.).

1b) ESI$^+$-TOF (CH_3OH): m/z found: 346.0457 $[M+H]^+$; calculated for $C_9H_{17}N_7S_2Ni$: 345.0340 Da.

FT-IR (ATR mode): ῡ (cm^{-1}): 3325 (N-H stretc.), 2922 (C-H stretc.), 1520 (C=N stretch.), 1398 (C-H bend.), 1033 (C=S stretc.), 680 (C-S strect.).

1c) ESI$^+$-TOF (CH_3OH): m/z found: 352.0358 $[M+H]^+$; calculated for $C_9H_{17}N_7S_2Zn$: 351.0278 Da.

FT-IR (ATR mode): ῡ (cm^{-1}): 3469 (N-H stretch.), 3319 (N-H stretc.), 3243 (N-H stretch.), 2932 (C-H stretc.), 1521 (C=N stretch.), 1455 (C-H bend.), 1086 (C=S stretc.), 655 (C-S strect.).

6.2.3. Synthesis of 4-(5,5-difluoro-1,3,7,9-tetramethyl-5H-4λ^4,5λ^4-dipyrrolo[1,2 c:2',1'-f][1,3,2]diazaborinin-10-yl)-N-(2-(7-((5E,7E)-6,7-dimethyl-3,10 dithioxo-2,4,5,8,9,11-hexaazatrideca-5,7-dien-13-yl)-1,3,6,8-tetraoxo-3,6,7,8 tetrahydrobenzo[lmn][3,8]phenanthrolin-2(1H)-yl)ethyl)benzamide (**3**)

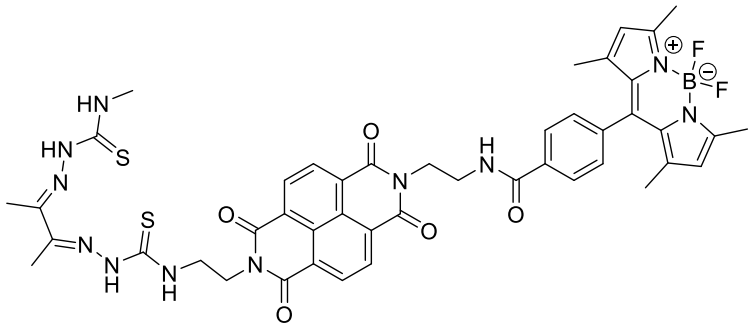

Protocol adapted from literature procedure[8]. In a pressure-tight vessel, 80.2 mg (0.3 mmol) of **1** and 34.3 mg (0.1 mmol) of NDA were dissolved in 5 mL of DMF and 80 µL of Et_3N. The mixture was sonicated 5 min until homogenisation. The reaction mixture was heated at 70 ºC for 1 h and then at 140 ºC for 5 min.

The solvent was removed under reduced pressure, the solid was suspended in acetone and the poured in $HCl_{(aq)}$ 1 M. The yellow solid was filtered and washed with pentane (yield: 35.1 mg, 65%).

The *mono*-ATSM intermediate (50.1 mg, 0.1 mmol) was solubilised in 1.00 mL of DMF and 13 µL of Et_3N with 38.2 mg (0.1 mmol) of **2**. The mixture was sonicated for 5 min and heated for 5 min at 140 ºC. The solvent was removed by rotavapor and the crude product was purified by automated flash chromatography in silica gel (from 20% MeOH in DCM to 50% MeOH in DCM) (yield: 32.3 mg, 35%).

ESI$^+$-TOF (CH_3OH): m/z found: 953.2901 $[M+Na]^+$; calculated for $C_{45}H_{44}BF_2N_{11}O_5S_2$: 931.3029 Da.

FT-IR (ATR mode): ῡ (cm^{-1}): 3309 (N-H stretc.), 3060 (C-H arom. stretch.), 2960 (C-H aliph. stretc.), 2050-2000 (C-H bend. overtone), 1776 (C=O stretch.), 1660 (C-N stretch.), 1537 (C-N stretch.), 762 (C-H arom. bend.).

6.2.4. Synthesis of compounds **3a**, **3b** and **3c**

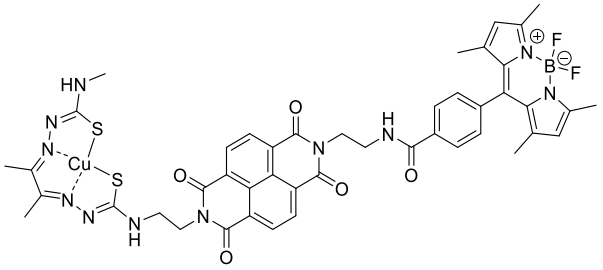

3a

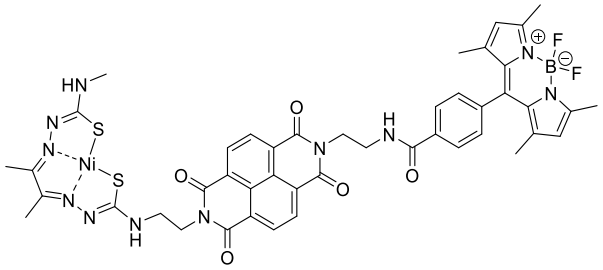

3b

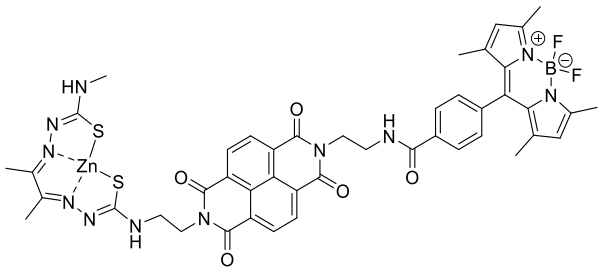

3c

Protocols adapted from literature procedures.

3a[5]: in a pressure tight-vessel, 20.0 mg (22 μmol) of **3** and 8.6 mg (43 μmol) of $Cu(OAc)_2 \cdot H_2O$ were dissolved in 3.00 mL of EtOH and 100 μL of $NaOH_{(EtOH)}$ 1 M. The mixture was heated at 50 ºC for 30 min. The dark red solid was isolated by filtration and washing with H_2O and hexane (yield: 10.9 mg, 50%).

3b[6]: in a round-bottom flask, 20.0 mg (22 μmol) of **3** and 6.4 mg (26 μmol) of $Ni(OAc)_2 \cdot 4H_2O$ were dissolved in 2.00 mL of EtOH. 0.10 mL of $NaOH_{(EtOH)}$ 1 M were added to the previous mixture which was left to react for 4 h under reflux. The dark green solid was collected by centrifugation and washing with Et_2O (yield: 11.3 mg, 52%).

3c[7]: in a round-bottom flask, 20.0 mg (22 μmol) of **3** and 5.7 mg (26 μmol) of $Zn(OAc)_2 \cdot 2H_2O$ were dissolved in 2.00 mL of MeOH. 0.10 mL of $NaOH_{(MeOH)}$ 1 M were added to the previous mixture which was left to react for 4 h under reflux. The dark brown solid was collected by centrifugation and washing with Et_2O (yield: 9.8 mg, 45%).

3a) ESI$^+$-TOF (CH_3OH): m/z found: 993.2204 $[M+H]^+$; calculated for $C_{45}H_{42}BF_2N_{11}O_5S_2Cu$: 992.2169 Da.

FT-IR (ATR mode): ῡ (cm^{-1}): 3348 (N-H stretc.), 2978 (C-H stretc.), 2050-2000 (C-H bend. overtone), 1759 (C=O stretch.), 1654 (C=N stretch.), 1542 (C-N stretch.), 778 (C-H arom. bend.).

3b) ESI$^+$-TOF (CH_3OH): m/z found: 1010.2125 $[M+Na]^+$; calculated for $C_{45}H_{42}BF_2N_{11}O_5S_2Ni$: 987.2226 Da.

FT-IR (ATR mode): ῡ (cm^{-1}): 3346 (N-H stretc.), 2980 (C-H stretc.), 2050-2000 (C-H bend. overtone), 1772 (C=O stretch.), 1655 (C-N stretch.), 1542 (C-N stretch.), 770 (C-H arom. bend.).

3c) ESI$^+$-TOF (CH_3OH): m/z found: 1016.2027 $[M+Na]^+$; calculated for $C_{45}H_{42}BF_2N_{11}O_5S_2Zn$: 991.2164 Da.

FT-IR (ATR mode): ῡ (cm^{-1}): 3347 (N-H stretc.), 2921 (C-H stretc.), 2050-2000 (C-H bend. overtone), 1775 (C=O stretch.), 1657 (C-N stretch.), 1550 (C-N stretch.), 770 (C-H arom. bend.).

6.2.5. Synthesis of *L*-bombesin [7-13] peptide (**4**)

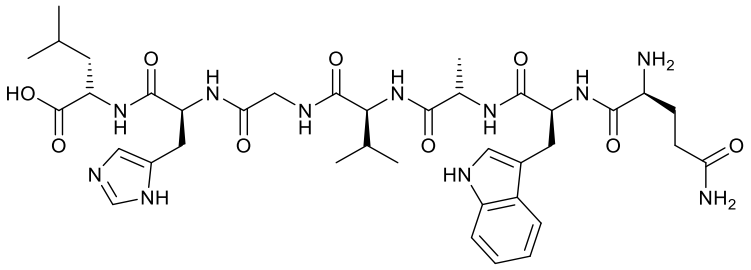

The *L*-fragments (HOOC-Leu-His-Gly-Val-Ala-Trp-Gln-NH_2) (**4**) of the bombesin peptide were obtained by solid-phase peptide synthesis (SPPS), through the automated solid-phase synthesiser, using traditional fluorenylmethoxycarbonyl (Fmoc) chemistry and 2-chlorotrityl resin (1.14 mmol/g). Leucine, glycine, alanine, and valine were used unprotected in their side chains (Fmoc-Leu-OH, Fmoc-Gly-OH, Fmoc-Ala-OH and Fmoc-Val-OH), whilst the side chains of histidine, glutamine and tryptophan were protected by trityl and tert-butoxycarbonyl, respectively (Fmoc-His(Trt)-OH, Fmoc-Gln(Boc)-OH and Fmoc-Trp(Boc)-OH).

For each amino acid 3 equivalents were used, and each coupling step was performed with HBTU (0.6 M in DMF), HOBt (3 M in DMF) and $DIEA_{(conc.)}$ and the deprotection of the Fmoc group was performed with piperidine 20% (v/v) in DMF.

After the coupling of all the amino acids in the sequence, the obtained peptide was cleaved from the resin and deprotected from protecting groups, presented in the side chains, using a cocktail of TFAphenol (88:5:5:2). The resin was mixed with the cocktail (2 mL/100 mg of resin) and left for 3 hours under stirring. The solution was filtered and the peptide was precipitated with Et_2O. The white solid was washed 3 times with Et_2O and centrifuged 3 times at 10000 rpm for 3 min. The white solid was freeze-dried overnight and purified through HPLC.

ESI$^+$-TOF (CH_3OH): 810.4253 $[M+H]^+$, 832.4077 $[M+Na]^+$; calculated for $C_{38}H_{55}N_{11}O_9$: 809.4184 Da.

HPLC (metod A): Rt = 14.0 min.

6.2.6. Synthesis of ((*S*)-5-amino-2-(7-((5E,7E)-6,7-dimethyl-3,10-dithioxo 2,4,5,8,9,11-hexaazatrideca-5,7-dien-13-yl)-1,3,6,8-tetraoxo-3,6,7,8-tetrahydrobenzo[lmn][3,8]phenanthrolin-2(1H)-yl)-5-oxopentanoyl)-*L*-tryptophyl-*L*-alanyl-*L*-valylglycyl-*L*-histidyl-*L*-leucine (**5**)

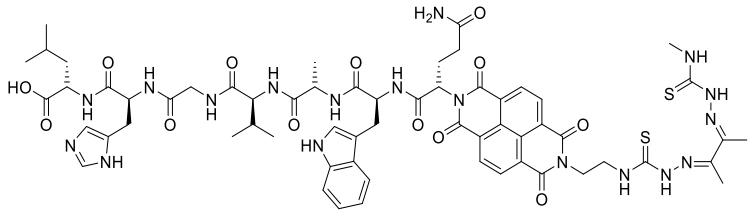

Protocol adapted from literature procedure[8]. In a pressure-tight vessel, 80 mg (0.3 mmol) of **1** and 34 mg (0.1 mmol) of NDA were dissolved in 5.00 mL of DMF and 0.08 mL of Et_3N. The mixture was sonicated 5 min until homogenisation. The reaction mixture was heated at 70 ºC for 1 h and then at 140 ºC for 5 min. The solvent was removed by rotavapor, the solid was suspended in acetone and poured in $HCl_{(aq)}$ 1 M. The yellow solid was filtered and washed with pentane (yield: 25.9 mg, 65%).

The *mono*-ATSM intermediate (13.2 mg, 0.03 mmol) was solubilised in 1.00 mL of DMF and 0.02 mL of Et_3N with 20.0 mg (0.03 mmol) of **4**. The mixture was sonicated for 5 min and heated for 1 h at 70 ºC. The yellow solid was obtained by centrifugation and washing with Et_2O.

ESI$^+$-TOF (CH_3OH): m/z found: 1352.4886 $[M-H+Na]^+$; calculated for $C_{61}H_{74}N_{18}O_{13}S_2$: 1330.5124 Da.

6.2.7. Synthesis of *N*1,*N*1'-((1,3,6,8-tetraoxo-1,3,6,8

6.2.7. tetrahydrobenzo[lmn][3,8]phenanthroline-2,7-diyl)bis(pentane-5,1-diyl)) bis(*N*1-hydroxy-*N*4-(5-(N-hydroxy-4-((5-(*N*-hydroxyacetamido)pentyl) amino)-4-oxobutanamido)pentyl)succinamide) (**6**)

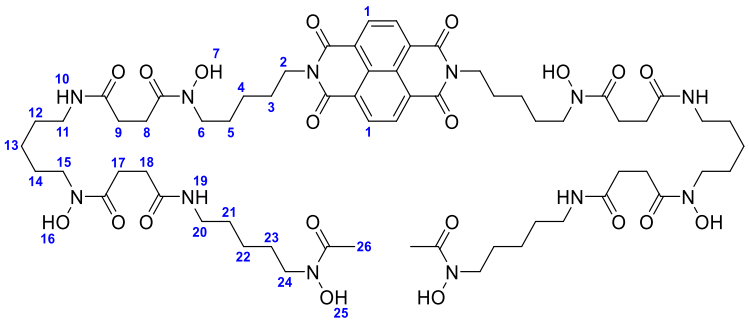

Protocol adapted from literature procedure. In a pressure-tight vessel, 100.0 mg (0.2 mmol) of DFO mesylate salt and 19.1 mg (0.1 mmol) of NDA were dissolved in 2.00 mL of DMF and 0.10 mL of Et_3N. The mixture was sonicated 5 min until homogenisation. The reaction mixture was heated at 70 ºC for 1 h. The yellow solid was centrifuged and washed with Et_2O (yield: 146.0 mg, 54%).

^{1}H-NMR (500 MHz, 298 K, DMSO-d_6) δ = 9.61 (*m*, 6H, H-7, H-16, H-25), 8.67 (*s*, 4H, H-1), 7.77-7.73 (*m*, 4H, H-10, H-19), 4.05 (*t*, 4H, H-2, *J* = 7.6 Hz), 3.49-3.43 (*m*, 12H, H-6, H-15, H-24), 3.09 (*q*, 8H, H-11, H-20 *J* = 7.3 Hz), 2.57-2.52 (*m*, 8H, H-8, H-18), 2.28-2.19 (*m*, 8H, H-9, H-17), 1.96 (*s*, 6H, H-26), 1.72-1.64 (m, 4H, H-3), 1.61-1.53 (m, 4H, H-23), 1.52-1.44 (m, 8H, H-5, H-14), 1.41-1.31 (m, 12H, H-4, H-12, H-22), 1.23-1.20 (m, 8H, H-13, H-21).

ESI$^+$-TOF (CH_3OH): m/z found: 699.3323 $[M+2Na]^{2+}$, 1375.6784 $[M+Na]^+$; calculated for $C_{64}H_{96}N_{12}O_{20}$: 1352.6884 Da.

FT-IR (ATR mode): ῡ (cm^{-1}): 3500 (O-H stretch.), 3334 (N-H stretc.), 3306 (N-H stretch.), 3150 (O-H stretch), 2936 (C-H aliph. stretc.), 2050-2000 (C-H bend. overtone), 1705 (C=O imide stretch.), 1655 (C=O amide stretch.), 1585 (N-H bend.), 1546 (N-H bend.), 1248 (C-N stretch.), 1040 (CO-N-CO stretch.), 771 (C-H arom. bend.).

6.2.8. Attempt of Zr(IV) complexation

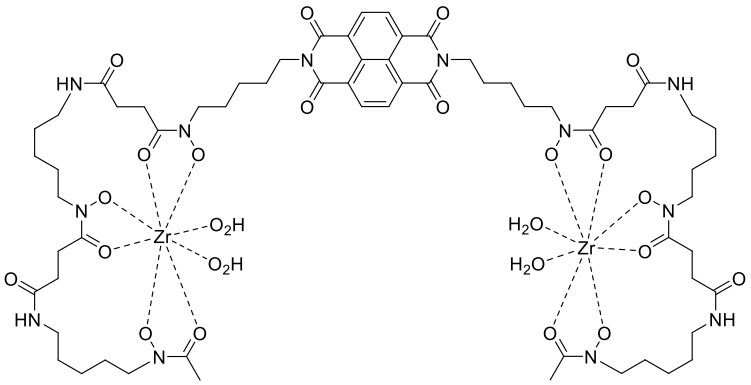

Protocol adapted from literature procedure[9]. In a round-bottom flask, under anhydrous conditions, 60 mg (0.1 mg) of **6** were added to a solution of 28.2 mg (0.13 mmol) of $ZrCl_4$ in 3.00 mL of anhydrous MeOH and 0.10 mL of Et_3N. The reaction was left for 2 h at RT. The brown solid was filtered and washed with MeOH. The brown solid was analysed by ^{1}H-NMR and mass spectrometry which data showed no correspondence with the desired compound.

6.3. Experimental procedures to compounds in Chapter 3

6.3.1. Synthesis of 2,5,8,11,14,16,19,22,25,28-decaoxa-1,15(1,5)-dinaphthalena cyclooctacosaphane (**7**)

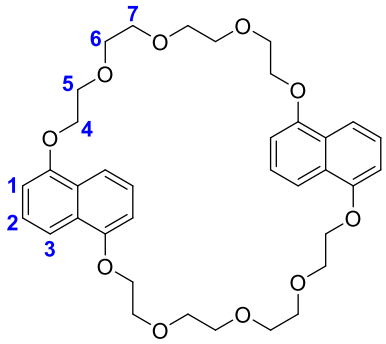

Protocol adapted from literature procedures[10,11]. In a 3-neck round-bottom flask, 1.02 g of K_2CO_3 was dissolved in 40 mL of anhydrous acetone and placed under reflux and N_2 flux. In another round-bottom flask, dihydroxynaphthalene (250.1 mg, 1.6 mmol) and tetraethylene glycol di(*p*-toluenesulfonate) (3.92 g, 7.8 mmol) were dissolved in 40 mL of anhydrous acetone. This last solution was added dropwise over 2 h to the first one. The reaction mixture was left for 2 d under reflux and N_2 flux. The solution was cooled down, filtered and the solvent removed under reduced pressure. The obtained oil was partitioned between DCM and deionised H_2O. The organic layer was washed with $NaOH_{(aq)}$ 3 M and deionised H_2O. The collected organic layer was dried over $MgSO_4$, filtered and concentrated under reduced pressure. The obtained oil was purified by column chromatography in silica gel (petroleum ether:AcOEt, 1:1). (yield: 0.35 g, 25%)

The pure open macrocycle (350.1 mg, 0.4 mmol) and dihydroxynaphthalene (690.2 mg, 0.4 mmol) were dissolved in 20 mL of anhydrous acetone and added dropwise over 2 h to a solution of 3.03 g of K_2CO_3 in 85 mL of anhydrous acetone. The reaction mixture was left for 2 d under reflux and N_2 flux. The solution was cooled down, filtered and the solvent removed under reduced pressure. The obtained oil was extracted from DCM and deionised H_2O and the collected organic layer was dried over $MgSO_4$, filtered and concentrated under reduced pressure. The obtained solid was purified by column chromatography in silica gel (petroleum ether:AcOEt, 1:1). The pure **16** was obtained from recrystallisation in warm MeOH. (Yield: 0.1123 g, 50%)

^{1}H-NMR (500 MHz, 298 K, $CDCl_3$) δ = 7.78 (*d*, 4H, H-1, *J* = 8.4 Hz), 7.18 (*dd*, 4H, H-2, *J* = 8.0 Hz), 6.50 (*d*, 4H, H-3, *J* = 7.6 Hz), 4.07-4.06 (*m*, 8H, H-4), 3.93-3.91 (*m*, 8H, H-5), 3.77 (*t*, 8H, H-6, *J* = 5.9 Hz, *J* = 2.5 Hz), 3.74 (*t*, 8H, H-7, *J* = 5.8 Hz, *J* = 2.5 Hz).

6.3.2. Synthesis of (2E,2'E)-*N*,*N*'-((1,3,6,8-tetraoxo-1,3,6,8-tetrahydrobenzo [lmn][3,8]phenanthroline-2,7-diyl)bis(ethane-2,1-diyl))bis(2-((E)-3-(2-(methylcarbamothioyl)hydrazineylidene)butan-2-ylidene)hydrazine-1-carbothioamide) (**8**)

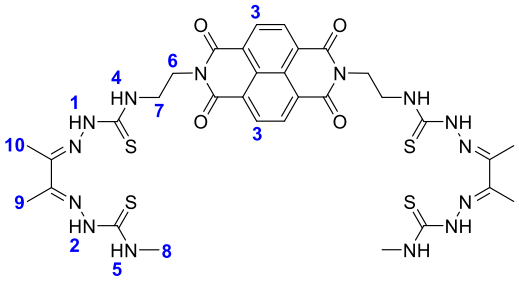

Protocol adapted from literature procedure[8]. In a microwave vessel, 95.2 mg (0.3 mmol) of **1** and 30.1 mg (0.1 mmol) of NDA were dissolved in 5.00 mL of DMF and 0.08 mL of Et_3N. The reaction mixture was sonicated for 5 min and then heated at 70 ºC for 1 h. The solvent was removed under reduced pressure, filtered and washed with hexane. (Yield: 49.2 mg, 61%)

^{1}H-NMR (500 MHz, 298 K, DMSO-d_6) δ = 10.19 (*s*, 2H, H-1), 10.15 (*s*, 2H, H-2), 8.64 (*s*, 4H, H-3), 8.52 (*t*, 2H, H-4, *J* = 5.8 Hz), 8.36 (*q*, 2H, H-5, *J* = 3.7 Hz), 4.38-4.36 (*m*, 4H, H-6), 4.00-3.98 (*m*, 8H, H-7), 3.02 (*d*, 6H, H-8, *J* = 4.6 Hz), 2.16 (*s*, 6H, H-9), 2.11 (*s*, 6H, H-10).

6.3.3. Synthesis of compound **8a**

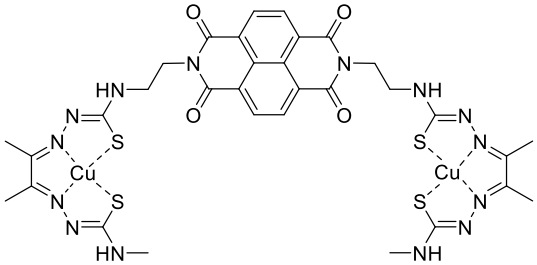

Protocol adapted from literature procedure[5]. In a round-bottomed flask, 10.1 mg (0.01 mmol) of **8** and 4.2 mg (0.02 mmol) of $Cu(OAc)_2 \cdot H_2O$ were dissolved in 1 mL of $NaOH_{(MeOH)}$ 1 M and 1 mL of MeOH. The reaction mixture was left under reflux overnight. The solid was obtained after filtration and washing with MeOH. (Yield: 4.0 mg, 42%)

MALDI (solvent-free): m/z found: 931.9 $[M]^+$, 932.0 $[M]^-$; calculated for $C_{32}H_{34}N_{14}O_4S_2Cu_2$: 932.0362 Da.

6.3.4. Synthesis of 4-(5,5-difluoro-1,3,7,9-tetramethyl-5H-4l4,5l4-dipyrrolo[1,2-c:2',1'-f][1,3,2]diazaborinin-10-yl)-*N*-(2-(7-(2-(4-(5,5-difluoro-1,3,7,9-tetramethyl-5H-4λ^4,5λ^4-dipyrrolo[1,2-c:2',1'-f][1,3,2]diazaborinin-10-yl) benzamido)ethyl)-1,3,6,8-tetraoxo-3,6,7,8-tetrahydrobenzo[lmn][3,8] phenanthrolin-2(1H)-yl)ethyl)benzamide (**9**)

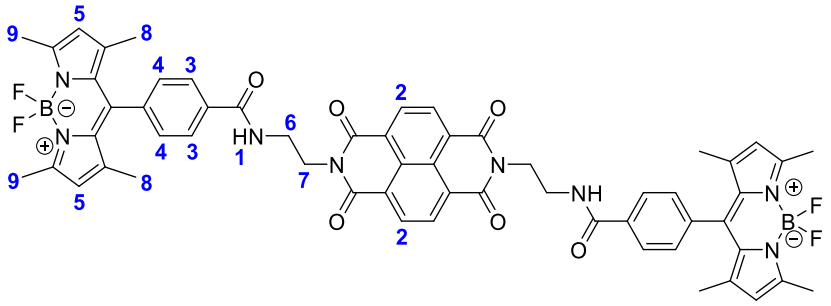

Protocol adapted from literature procedure[12]. In a microwave vessel, 50.0 mg (0.2 mmol) of **2** and 43.1 mg (0.1 mmol) of NDA were dissolved in 5.00 mL of DMF and 0.08 mL of Et_3N. The reaction mixture was sonicated for 5 min and then heated at 40 ºC for 5 min and at 140 ºC for 5 min. The solvent was removed under reduced pressure and purified by flash chromatography in silica gel (MeOH:DCM, 20-100% MeOH). (Yield: 77.0 mg, 73%)

^{1}H-NMR (500 MHz, 298 K, DMSO-d_6) δ = 8.75 (*t*, 2H, H-1, *J* = 6.1 Hz), 8.62 (*s*, 4H, H-2), 7.84 (*d*, 4H, H-3, *J* = 8.1 Hz), 7.43 (*d*, 4H, H-4, *J* = 8.1 Hz), 6.17 (*s*, 4H, H-5), 3.68 (*q*, 4H, H-6, *J* = 3.7 Hz), 3.08 (*d*, 4H, H-7, *J* = 3.6 Hz), 2.44 (*s*, 12H, H-8), 1.30 (*s*, 12H, H-9).

6.3.5. Synthesis of iodo-*L*-phenylalanine-naphthalenediimide (***L*-10**)

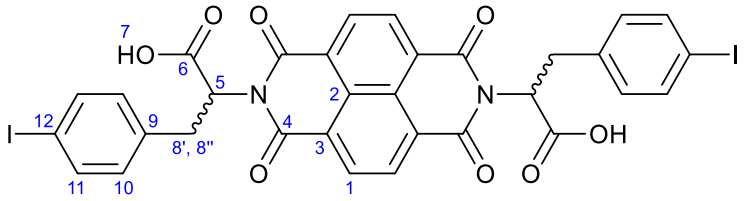

Protocol adapted from literature procedure[12]. In a pressure-tight microwave vial, 1,4,5,8-naphthalenetetracarboxylic anhydride (NDA) (200.2 mg, 0.75 mmol) and iodo-*L*-phenylalanine (438.8 mg, 1.50 mmol) were dissolved in 5.00 mL of anhydrous DMF and afterwards, 0.20 mL of Et_3N was added. The resulting suspension was sonicated until complete homogenisation. The reaction mixture was left to react in the microwave system for 10 min at 140 ºC. Subsequently, the solvent was partially removed under reduced pressure and a yellow precipitate was obtained after the addition of acetonitrile and HCl 1 N.

The solid was filtered and washed with acetonitrile, HCl 1 N, deionised water and *n*-pentane. Iodo-*L*-phenylalanine-naphthalenediimide was obtained without any further purification. (Yields: 360.1 mg, 59%).

^{1}H-NMR (500 MHz, 298 K, DMSO-d_6): δ = 13.11 (*bs*, 2H, H-7), 8.67 (*s*, 4H, H-1), 7.51-7.49 (*m*, 4H, H-11), 7.03-7.01 (*m*, 4H, H-10), 5.84 (*dd*, 2H, H-5, *J* = 5.5 Hz, *J* = 9.3 Hz), 3.56 (*dd*, 2H, H-8', *J* = 5.6 Hz, *J* =14.22 Hz), 3.27 (*dd*, 2H, H-8'', *J* = 9.2 Hz, *J* = 14.3 Hz).
^{13}C-NMR (125 MHz, 298 K, DMSO-d_6): δ = 170.51 (C-4), 162.52 (C-6), 137.37 (C-11), 132.99 (C-10), 131.92 (C-1), 131.78 (C-3), 126.59 (C-9), 126.14 (C-2), 92.68 (C-12), 54.83 (C-5), 34.95 (C-8).
ESI^{-}-TOF (CH_3OH): m/z found: 405.9552 $[M-2H]^{2-}$, 812.9498 $[M-H]^{-}$; calculated for $C_{32}H_{20}I_2N_{12}O_8$: 813.9309 Da.

6.3.6. Synthesis of iodo-*L*-phenylalanine-tagged hydroxusuccinimidyl naphthalenediimide (***L*-11**)

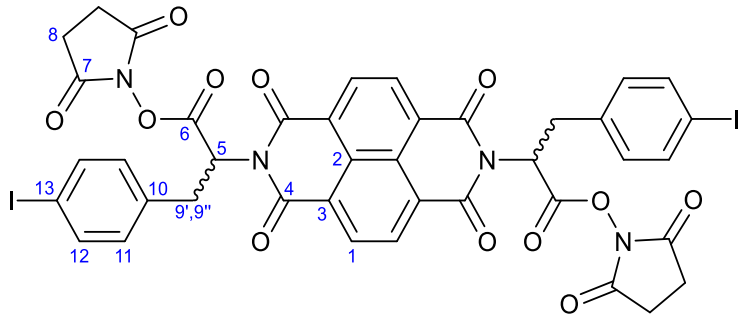

Protocol adapted from literature procedure[12]. Iodo-*L*-phenylalanine-naphthalenediimide (124.15 mg, 0.15 mmol) and *N*-hydroxysuccinimide (94.9 mg, 0.82 mmol) were dissolved in 5 mL of anhydrous DMF. The solution was stirred for 15 min in an ice bath and, in the meantime, a solution of EDC·HCl (232.8 mg, 1.2 mmol) in 5.00 mL of anhydrous DMF was prepared and stirred for 15 minutes. The EDC·HCl solution was added to the imide solution and the resulting reaction mixture was stirred for 15 min. After that time, the ice bath was removed and the mixture was left for 24 h, under stirring, at room temperature. The solvent was partially removed, and the obtained brown syrup was suspended in 2.00 mL of acetonitrile and afterwards, deionised water was added. The dark yellow precipitate was filtered and washed with n-pentane. The yellow fine powder was dried under vacuum and no further purification was required. (Yields: 125.1 mg, 83%).

^{1}H NMR (500 MHz, 298 K, DMSO-d_6): δ = 8.72 (*s*, 4H, H-1), 7.53-7.50 (*m*, 4H, H-12), 7.09-7.07 (*m*, 4H, H-11), 6.32 (*ddd*, 2H, H-5, *J* = 2.7 Hz, *J* = 6.1 Hz, *J* = 8.7 Hz), 3.67-3.63 (*m*, 2H, H-9'), 3.43-3.38 (*m*, 2H, H-9''), 2.73 (*s*, 8H, H-8).

^{13}C NMR (125 MHz, 298 K, DMSO-d_6) δ = 169.66 (C-6), 164.92 (C-7), 161.73 (C-4), 137.07 (C-12), 136.05 (C-10), 131.67 (C-1), 131.59 (C-11), 126.12 (C-3), 125.56 (C-2), 92.86 (C-13), 52. 28 (C-5), 33.36 (C-9), 25.41 (C-8).

ESI^{+}-TOF (CH_3OH): m/z found: 1008.9721 $[M+H]^{+}$, 1030.9542 $[M+Na]^{+}$; calculated for $C_{32}H_{20}I_2N_{12}O_8$: 1007.9637 Da.

HPLC (metod A): Rt = 40.2 min.

6.4. Experimental procedures to compounds in Chapter 4

6.4.1. Synthesis of *L*- or *D*-bombesin [7-13] peptide (**12**)

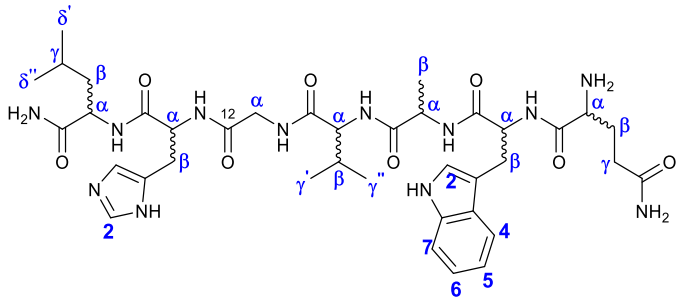

The *L*- or *D*-fragments (H_2NOC-Leu-His-Gly-Val-Ala-Trp-Gln-NH_2) (***L*-12** or ***D*-12**) of the bombesin peptide were obtained by solid-phase peptide synthesis (SPPS), through the automated solid-phase synthesiser, using traditional fluorenylmethoxycarbonyl (Fmoc) chemistry and Rink amide resin (0.59 mmol/g). Leucine, glycine, alanine, and valine were used unprotected in their side chains (Fmoc-Leu-OH, Fmoc-Gly-OH, Fmoc-Ala-OH and Fmoc-Val-OH), whilst the side chains of histidine, glutamine and tryptophan were protected by trityl and tert-butoxycarbonyl, respectively (Fmoc-His(Trt)-OH, Fmoc-Gln(Boc)-OH and Fmoc-Trp(Boc)-OH). For each amino acid 3 equivalents were used and each coupling step was performed with HBTU (0.6 M in DMF), HOBt (3 M in DMF) and $DIEA_{(conc.)}$ and the deprotection of the Fmoc group was performed with piperidine 20% (v/v) in DMF.

After the coupling of all the amino acids in the sequence, the obtained peptide was cleaved from the resin and deprotected from protecting groups, presented in the side chains, using a cocktail of TFA/H_2O/TIPS (95:2.5:2.5). The resin was mixed with the cocktail (2 mL/100 mg of resin) and left for 3 hours under stirring. The solution was filtered, and the peptide was precipitated with Et_2O. The white solid was washed 3 times with Et_2O and centrifuged 3 times at 10000 rpm for 3 min. The white solid was freeze-dried overnight and purified through HPLC.

^{1}H-NMR (500 MHz, 298 K, D_2O) δ = 8.53 (*d*, 1H, His-H2, *J* = 1.4 Hz), 7.62 (*d*, 1H, Trp-H4, *J* = 7.9 Hz), 7.50 (*d*, 1H, Trp-H7, *J* = 8.2 Hz), 7.28-7.23 (*m*, 2H, Trp-H2, Trp-H6), 7.21 (*d*, 1H, His-H4, *J* = 1.2 Hz), 7.17 (*m*, 1H, Trp-H5), 4.74 (*dd*, 1H, Trp-Hα, *J* = 8.8 Hz, *J* = 6.6 Hz), 4.66 (*dd*, 1H, His-Hα, *J* = 7.7 Hz, *J* = 6.7 Hz), 4.37-4.28 (*m*, 2H, Leu-Hα, Ala-Hα), 4.03 (*d*, 1H, Gln-Hα, *J* = 7.3 Hz), 3.99-3.87 (*m*, 3H, Gly-H_2α, Val-Hα), 3.34 (*dd*, 1H, Trp-Hβ, *J* = 14.4 Hz, *J* = 6.4 Hz), 3.30-3.11 (*m*, 3H, Trp-Hβ, His-H_2β), 2.43-2.33 (*m*, 1H, Gln-Hγ), 2.29-2.21 (*m*, 1H, Gln-Hβ), 2.11-2.00 (*m*, 3H, Gln-Hγ, Gln-Hβ, Val-Hβ), 1.71-1.52 (*m*, 3H, Leu-H_2β, Leu-Hγ), 1.34 (*d*, 3H, Ala-CH_3, *J* = 7.2 Hz), 0.98 (*d*, 3H, Val-CH_3, *J* = 6.8 Hz), 0.96 (*d*, 3H, Val-CH_3, *J* = 6.8 Hz), 0.92 (*d*, 3H, Leu-CH_3, *J* = 6.8 Hz), 0.86 (*d*, 3H, Leu-CH_3, *J* = 6.1 Hz).

***L*-1) ESI$^+$-TOF** (CH_3OH): m/z found: 405.2315 $[M+2H]^{2+}$, 809.4465 $[M+H]^+$, 831.4273 $[M+Na]^+$; calculated for $C_{38}H_{56}N_{12}O_8$: 808.4344 Da.

***D*-1) ESI$^+$-TOF** (CH_3OH): m/z found: 405.2252 $[M+2H]^{2+}$,809.4429 $[M+H]^+$; calculated for $C_{38}H_{56}N_{12}O_8$: 808.4344 Da.

HPLC (metod A): Rt = 42.0 min (***L*-12**) and 42.1 min (***D*-12**).

6.4.2. *L*- or iodo-*D*-phenylalanine-naphthalenediimide (**10**)

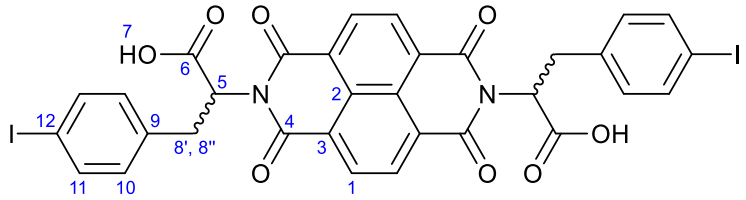

Protocol adapted from literature procedure[12]. In a pressure-tight microwave vial, 1,4,5,8-naphthalenetetracarboxylic anhydride (NDA) (200.2 mg, 0.75 mmol) and iodo-*L*-phenylalanine (438.8 mg, 1.50 mmol) were dissolved in 5 mL of anhydrous DMF and afterwards 0.20 mL of Et_3N was added. The resulting suspension was sonicated until complete homogenisation. The reaction mixture was left to react in the microwave system for 10 min at 140 ºC. Subsequently, the solvent was partially removed under reduced pressure and a yellow precipitate was obtained after the addition of acetonitrile and HCl 1 N. The solid was filtered and washed with acetonitrile, HCl 1 N, deionised water and n-pentane. Iodo-*L*-phenylalanine-naphthalenediimide was obtained without any further purification. The same procedure was applied for iodo-*D*-phenylalanine-naphthalenediimide. Yields: 360.1 mg, 59% for ***L*-10**; 366.3 mg, 60% for ***D*-10**.

^{1}H-NMR (500 MHz, 298 K, DMSO-d_6): δ = 13.11 (*bs*, 2H, H-7), 8.67 (*s*, 4H, H-1), 7.51-7.49 (*m*, 4H, H-11), 7.03-7.01 (*m*, 4H, H-10), 5.84 (*dd*, 2H, H-5, *J* = 5.5 Hz, *J* = 9.3 Hz), 3.56 (*dd*, 2H, H-8', *J* = 5.6 Hz, *J* =14.22 Hz), 3.27 (*dd*, 2H, H-8'', *J* = 9.2 Hz, *J* = 14.3 Hz).

^{13}C-NMR (125 MHz, 298 K, DMSO-d_6): δ = 170.51 (C-4), 162.52 (C-6), 137.37 (C-11), 132.99 (C-10), 131.92 (C-1), 131.78 (C-3), 126.59 (C-9), 126.14 (C-2), 92.68 (C-12), 54.83 (C-5), 34.95 (C-8).

ESI$^-$-TOF (CH_3OH): m/z found: 405.9552 $[M-2H]^{2-}$, 812.9498 $[M-H]^-$; calculated for $C_{32}H_{20}I_2N_{12}O_8$: 813.9309 Da.

6.4.3. *L*- or iodo-*D*-phenylalanine-tagged hydroxusuccinimidyl naphthalenediimide (**11**)

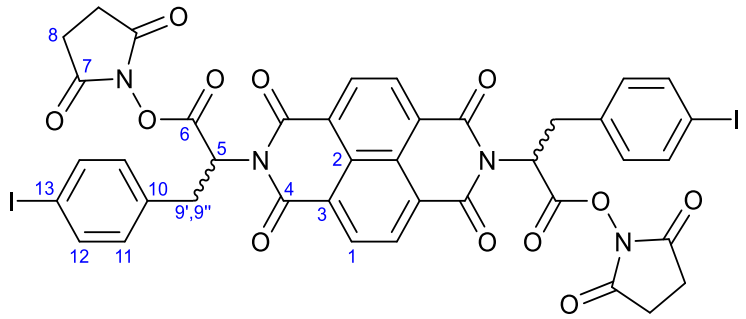

Protocol adapted from literature procedure[12]. Iodo-*L*-phenylalanine-naphthalenediimide (***L*-10**, 124.2 mg, 0.15 mmol) and *N*-hydroxysuccinimide (94.9 mg, 0.82 mmol) were dissolved in 5 mL of anhydrous DMF. The solution was stirred for 15 min in an ice bath and, in the meantime, a solution of EDC·HCl (232.8 mg, 1.2 mmol) in 5 mL of anhydrous DMF was prepared and stirred for 15 minutes. The EDC·HCl solution was added to the solution of the imide and the resulting reaction mixture was stirred for 15 min. After that time, the ice bath was removed and the mixture was left for 24 h, under stirring, at room temperature. The solvent was partially removed, and the obtained brown syrup was suspended in 2 mL of acetonitrile and afterwards, deionised water was added. The dark yellow precipitate was filtered and washed with n-pentane. The yellow fine powder was dried under vacuum and no further purification was required. The same procedure was applied for the *D*-enantiomer. (Yields: 125.5 mg, 83% for ***L*-11**; 126.3 mg, 84% for ***D*-11**).

^{1}H NMR (500 MHz, 298 K, DMSO-d_6): δ = 8.72 (*s*, 4H, H-1), 7.53-7.50 (*m*, 4H, H-12), 7.09-7.07 (*m*, 4H, H-11), 6.32 (*ddd*, 2H, H-5, *J* = 2.7 Hz, *J* = 6.1 Hz, *J* = 8.7 Hz), 3.67-3.63 (*m*, 2H, H-9'), 3.43-3.38 (*m*, 2H, H-9''), 2.73 (*s*, 8H, H-8).

^{13}C NMR (125 MHz, 298 K, DMSO-d_6) δ = 169.66 (C-6), 164.92 (C-7), 161.73 (C-4), 137.07 (C-12), 136.05 (C-10), 131.67 (C-1), 131.59 (C-11), 126.12 (C-3), 125.56 (C-2), 92.86 (C-13), 52. 28 (C-5), 33.36 (C-9), 25.41 (C-8).

ESI^{+}-TOF (CH_3OH): m/z found: 1008.9721 $[M+H]^{+}$, 1030.9542 $[M+Na]^{+}$; calculated for $C_{32}H_{20}I_2N_{12}O_8$: 1007.9637 Da.

HPLC (metod A): Rt = 40.2 min (***L*-11**) and 40.0 min (***D*-11**).

6.4.4. *L*- or iodo-*D*-phenylalanine-tagged hydroxusuccinimidyl naphthalenediimide-(*mono*-bombesin) (**13**) and *L*- or iodo-*D*-phenylalanine-tagged hydroxysuccinimidyl naphthalenediimide-(*bis*-bombesin) (**14**)

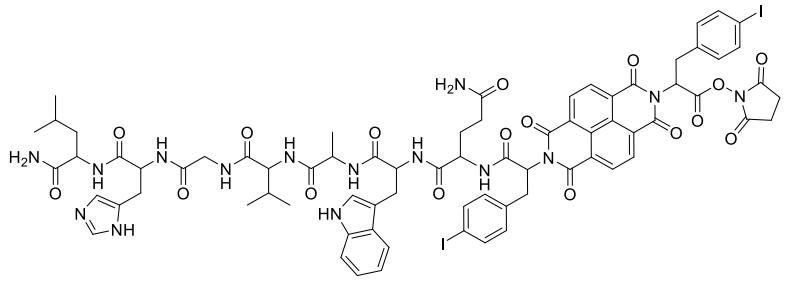

13

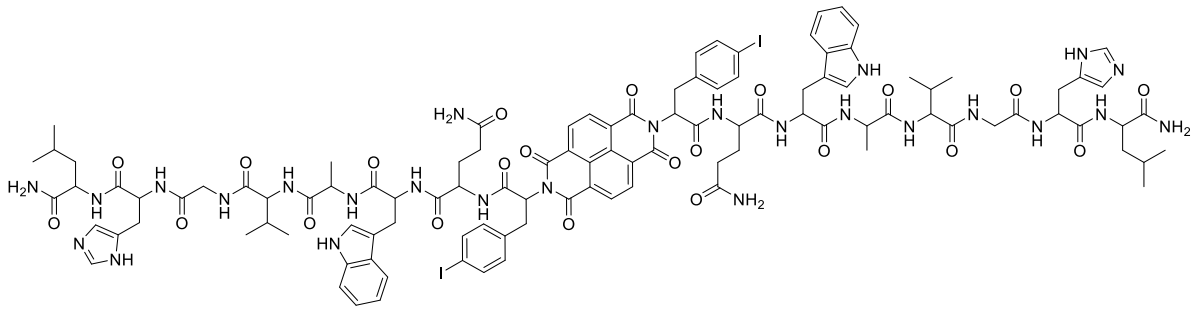

14

Protocol adapted from literature procedure[12]. *L*-bombesin [7-13] (***L*-12**) (110.0 mg, 0.14 mmol) were added to a stirring solution of ***L*-11** (68.6 mg, 0.07 mmol) in 5 mL of DMF. Afterwards, 0.20 mL of Et_3N were added to the previous mixture. The reaction mixture was left under stirring for 24 h at room temperature. The solvent was partially removed under reduced pressure and a light brown precipitate was obtained after the addition of Et_2O. The bright brown solid was washed with Et_2O and centrifuged 3 times at 10000 rpm for 3 min. The bright brown solid was freeze-dried overnight and purified by HPLC. The same procedure was applied to the coupling between ***D*-12** and ***D*-11**. (Yields: 1.2 mg, 1.0% for ***L*-13**; 6.5 mg, 3.9% for ***L*-14**; 1.4 mg, 1.2% for ***D*-13**; 1.8 mg, 1.1% for ***D*-14**).

Alternatively, in a pressure-tight microwave vessel, ***L*-12** (68.6 mg, 0.07 mmol) and ***L*-11** (110.0 mg, 0.14 mmol) were dissolved in 5 mL of anhydrous DMF. To the resulting mixture, 0.20 mL of Et_3N was added and the reaction mixture was heated at 70 ºC for 45 min in the microwave system. The solvent was partially removed under reduced pressure and a light brown precipitate was obtained after the addition of Et_2O. The bright brown solid was washed with Et_2O and centrifuged 3 times at 10000 rpm for 3 min. The bright brown solid was freeze-dried overnight and purified by HPLC. The same procedure was applied to the coupling between ***D*-12** and ***D*-11**. (Yields: 1.4 mg, 1.2% for ***L*-13**; 6.88 mg, 4.1% for ***L*-14**; 1.5 mg, 1.3% for ***D*-13**; 1.8 mg, 1.1% for ***D*-14**).

***L*-4**) **ESI$^+$-TOF** (CH_3OH): m/z found: 1702.3797 $[M+H]^+$, 1724.3672 $[M+Na]^+$; calculated for $C_{74}H_{77}I_2N_{15}O_{17}$: 1701.3711 Da.

***D*-4**) **ESI$^+$-TOF** (CH_3OH): m/z found: 1702.3811 $[M+H]^+$, 1724.3710 $[M+Na]^+$; calculated for $C_{74}H_{77}I_2N_{15}O_{17}$: 1701.3711 Da.

***L*-5**) **ESI$^+$-TOF** (CH_3OH): m/z found: 1198.4002 $[M+2H]^{2+}$, 2395.7806 $[M]^+$; calculated for $C_{108}H_{128}I_2N_{26}O_{22}$: 2394.7786 Da.

***D*-5**) **ESI$^+$-TOF** (CH_3OH): m/z found: 1198.4050 $[M+2H]^{2+}$, 2395.8557 $[M]^+$; calculated for $C_{108}H_{128}I_2N_{26}O_{22}$: 2394.7786 Da.

HPLC (metod A): Rt = 37.1 min (***L*-13** and ***D*-14**), 36.2 min (***L*-13** and ***D*-14**).

6.4.5. *N*-(2-aminoethyl)-4-(5,5-difluoro-1,3,7,9-tetramethyl-5H-4λ^4,5λ^4-dipyrrolo [1,2-c:2',1'-f][1,3,2]diazaborinin-10-yl)benzamide (**2**)

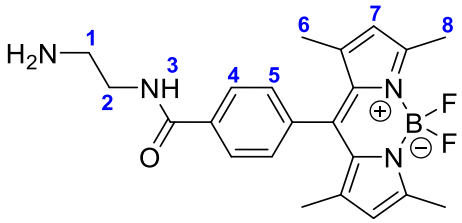

^{1}H NMR (500 MHz, DMSO-d_6) δ 8.67 (*t*, 1H, H-3, *J* = 5.6 Hz,), 8.06 (*d*, 2H, H-4, *J* = 7.8 Hz,), 7.50 (*d*, 2H, H-5, *J* = 7.7 Hz), 6.19 (s, 2H, H-7), 3.35 (*q*, 2H, H-2, *J* = 6.1 Hz), 2.79 (*t*, 2H, H-1, *J* = 6.3 Hz, 1H), 2.46 (s, 6H, H-6), 1.34 (s, 6H, H-8).

6.4.6. (*S*)-*N*1-((2S,5S,8S,14S,17S)-14-((1H-imidazol-5-yl)methyl)-17-carbamoyl-1-(1H-indol-3-yl)-8-isopropyl-5,19-dimethyl-3,6,9,12,15-pentaoxo-4,7,10,13,16-pentaazaicosan-2-yl)-2-(7-(2-(4-(5,5-difluoro-1,3,7,9-tetramethyl-5H-4λ^4,5λ^4-dipyrrolo[1,2-c:2',1'-f][1,3,2]diazaborinin-10-yl)benzamido)ethyl)-1,3,6,8-tetraoxo-3,6,7,8-tetrahydrobenzo[lmn][3,8]phenanthrolin-2(1H)-yl)pentanediamide (**15**)

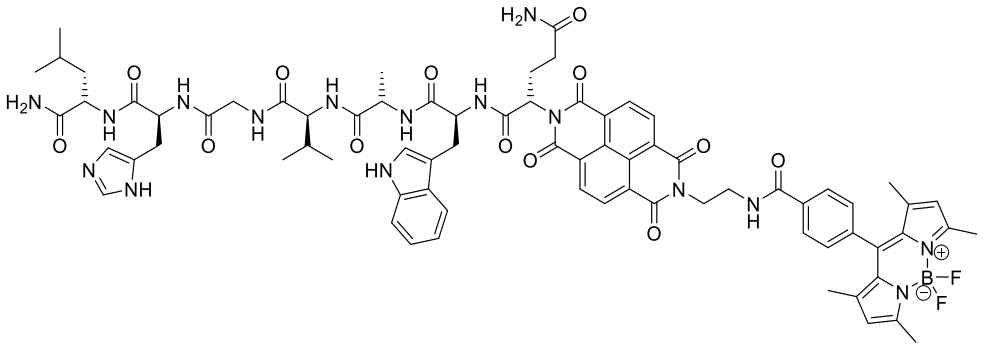

Protocol adapted from literature procedure[8]. In a pressure-tight microwave vessel, NDA (42.5 mg, 0.16 mmol) and **2** (50.0 mg, 0.12 mmol) were dissolved in 1 mL of anhydrous DMF and 0.02 mL of Et_3N. The resulting mixture was sonicated for 5 minutes.

When it was homogenised, the brown solution was heated in the microwave system at 40 ºC for 5 minutes and then at 140 ºC for further 5 minutes. The solvent was removed by rotary evaporation and the resulting light brown solid was obtained by automated flash chromatography (silica gel, gradient from 20% MeOH in DCM to 100% MeOH).

This solid (44 mg, 0.06 mmol) was solubilised in 2 mL of anhydrous DMF with 55 mg (0.07 mmol) of ***L*-12** and 0.01 mL of Et_3N. The mixture was heated at 70 ºC for 1 h in the microwave system. The obtained dark red solution was washed with Et_2O and centrifuged 3 times at 10000 rpm for 3 minutes. The dark solid was freeze dried overnight and purified by HPLC. (Yield: 69.2 mg, 30%).

ESI$^+$-TOF (CH_3OH): m/z found: 1451.6278 $[M+H]^+$; calculated for $C_{74}H_{81}BF_2N_{16}O_{13}$: 1450.6230 Da.

HPLC (metod A): Rt = 40.2 min.

6.5. References to Chapter 8

1. A. T. R. Williams, S. A. Winfield and J. N. Miller, *The Analyst*, 1983, **108**, 1067.
2. P. D. Bonnitcha, S. R. Bayly, M. B. M. Theobald, H. M. Betts, J. S. Lewis and J. R. Dilworth, *J. Inorg. Biochem.*, 2010, **104**, 126-135.
3. D. Muller, I. Zeltser, G. Bitan and C. Gilon, *J. Org. Chem.*, 1997, **62**, 411-416.
4. B. M. Paterson, J. A. Karas, D. B. Scanlon, J. M. White and P. S. Donnelly, *Inorg. Chem.*, 2010, **49**, 1884-1893.
5. J. L. Dearling, J. S. Lewis, G. E. Mullen, M. J. Welch and P. J. Blower, *J. Biol. Inorg. Chem.*, 2002, **7**, 249-259.
6. D. X. West, J. S. Ives, G. A. Bain, A. E. Liberta, J. Valdés-Martínez, K. H. Ebert and S. Hernández-Ortega, *Polyhedron*, 1997, **16**, 1895-1905.
7. E. Palma, H. M. Botelho, G. R. Morais, I. Rodrigues, I. C. Santos, M. P. C. Campello, P. Raposinho, A. Belchior, S. S. Gomes, M. F. Araújo, I. Correia, N. Ribeiro, S. Gama, F. Mendes and A. Paulo, *J. Biol. Inorg. Chem.*, 2019, **24**, 71-89.
8. K. Tambara, N. Ponnuswamy, G. Hennrich and G. D. Pantoş, *J. Org. Chem.*, 2011, **76**, 3338-3347.
9. M. Patra, A. Bauman, C. Mari, C. A. Fischer, O. Blacque, D. Häussinger, G. Gasser and T. L. Mindt, *Chem. Comm.*, 2014, **50**, 11523-11525.
10. C. J. Bruns, S. Basu and J. Fraser Stoddart, *Tetrahedron Lett.*, 2010, **51**, 983-986.
11. D. G. Hamilton, J. E. Davies, L. Prodi and J. K. M. Sanders, *Chem. Eur. J.*, 1998, **4**, 608-620.
12. Z. Hu, R. L. Arrowsmith, J. A. Tyson, V. Mirabello, H. Ge, I. M. Eggleston, S. W. Botchway, G. Dan Pantos and S. I. Pascu, *Chem. Comm.*, 2015, **51**, 6901-6904.
13. W. S. J. Hummers and R. E. Offeman, *J. Am. Chem. Soc.*, 1958, **80**, 1339.
14. D. Voiry, J. Yang, J. Kupferberg, R. Fullon, C. Lee, H. Y. Jeong, H. S. Shin and M. Chhowalla, *Science*, 2016, **353**, 1413-1416.
15. C.-T. Chen, M. E. Fischer, C. Windsor, I. C. Vei, D. G. Calatayud, M. L. H. Green and S. I. Pascu, *Polyhedron*, 2016, **119**, 532-547.
16. X. Guan, P. Luo, Q. He, Y. Hu and H. Ying, *Molecules*, 2017, **22**.
17. J. J. Park, Y.-H. Kim, C. Kim and J. Kang, *Tetrahedron Lett.*, 2011, **52**, 3361-3366.
18. L. M. Fischer, M. Tenje, A. R. Heiskanen, N. Masuda, J. Castillo, A. Bentien, J. Émneus, M. H. Jakobsen and A. Boisen, *Microelectron. Eng.*, 2009, **86**, 1282-1285.

7. Appendices A

7.1. Appendices to Chapter 2

7.1.1. NMR spectroscopy of selected compounds

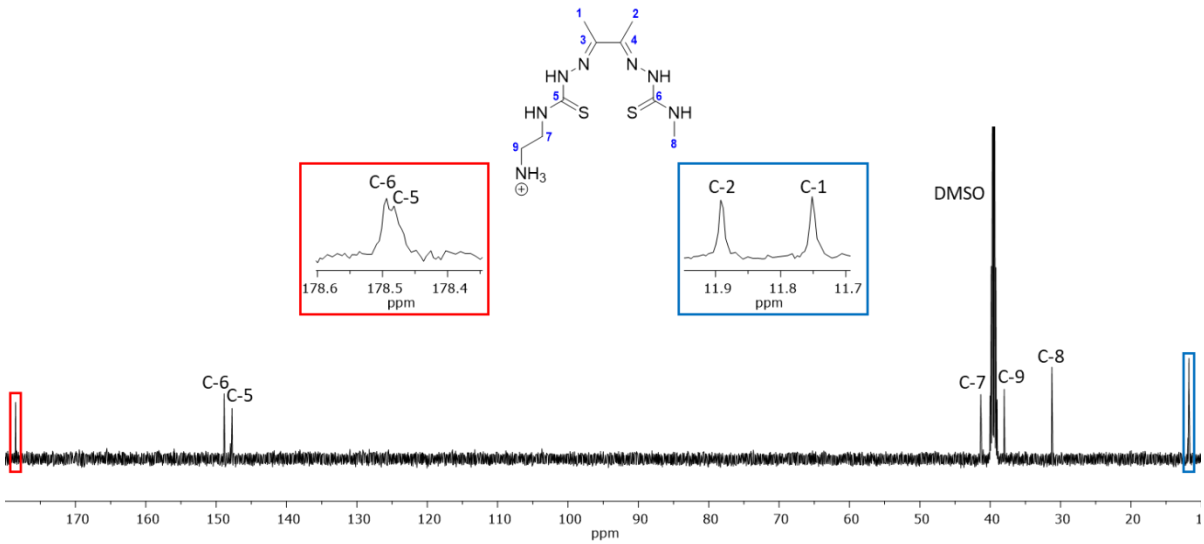

Figure A.1. ^{13}C-NMR spectrum of compound **1** (DMSO-d_6, 125 MHz).

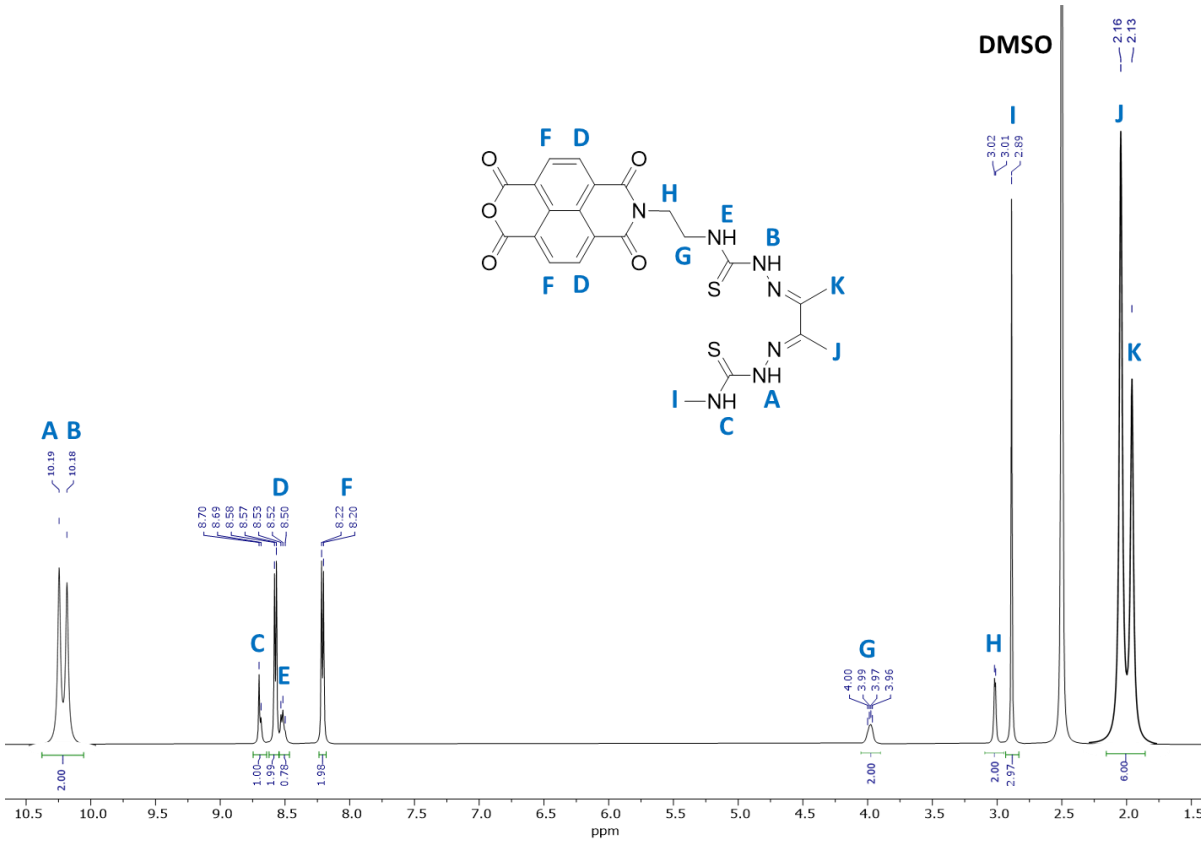

Figure A.2. ^{1}H-NMR spectrum of *mono*-ATSM derivative (DMSO-d_6, 500 MHz).

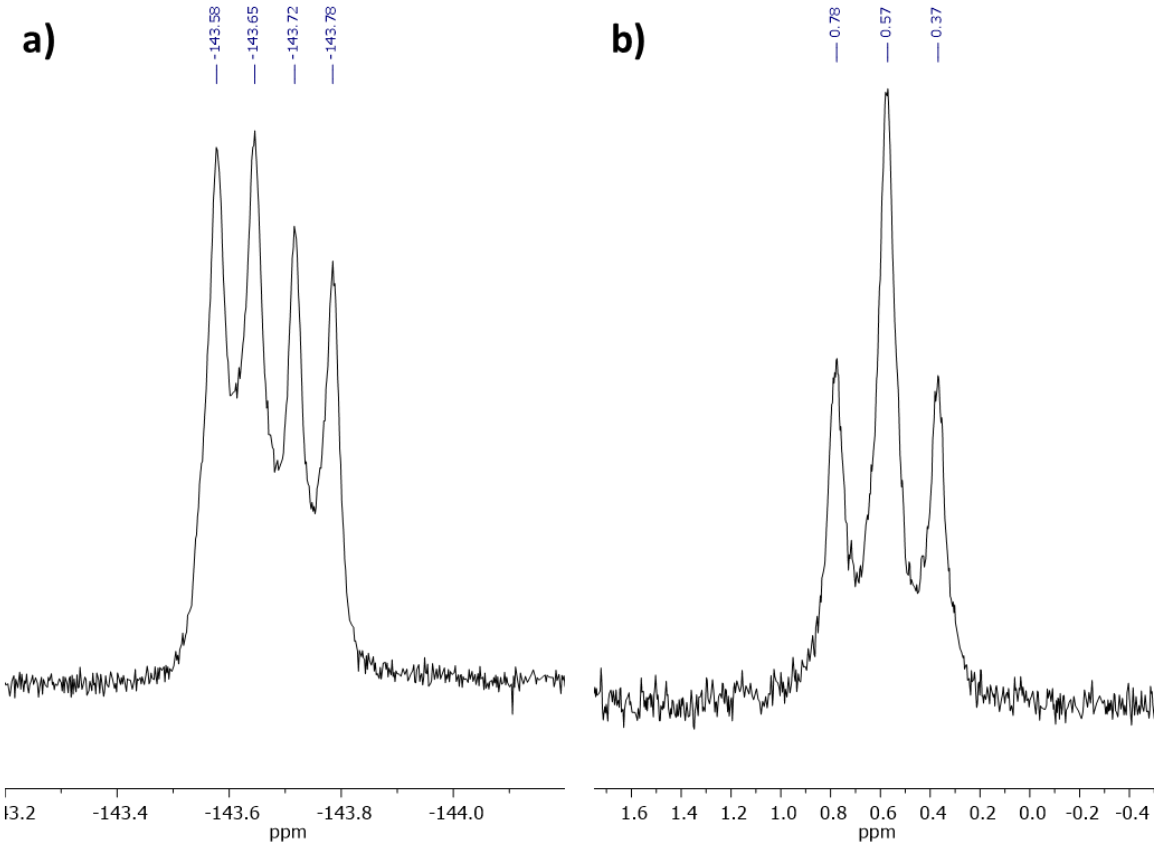

Figure A.3. a) ^{19}F-NMR (DMSO-d_6, 470.4 MHz) and **b)** ^{11}B-NMR (DMSO-d_6, 160.4 MHz) spectra of compound **3**.

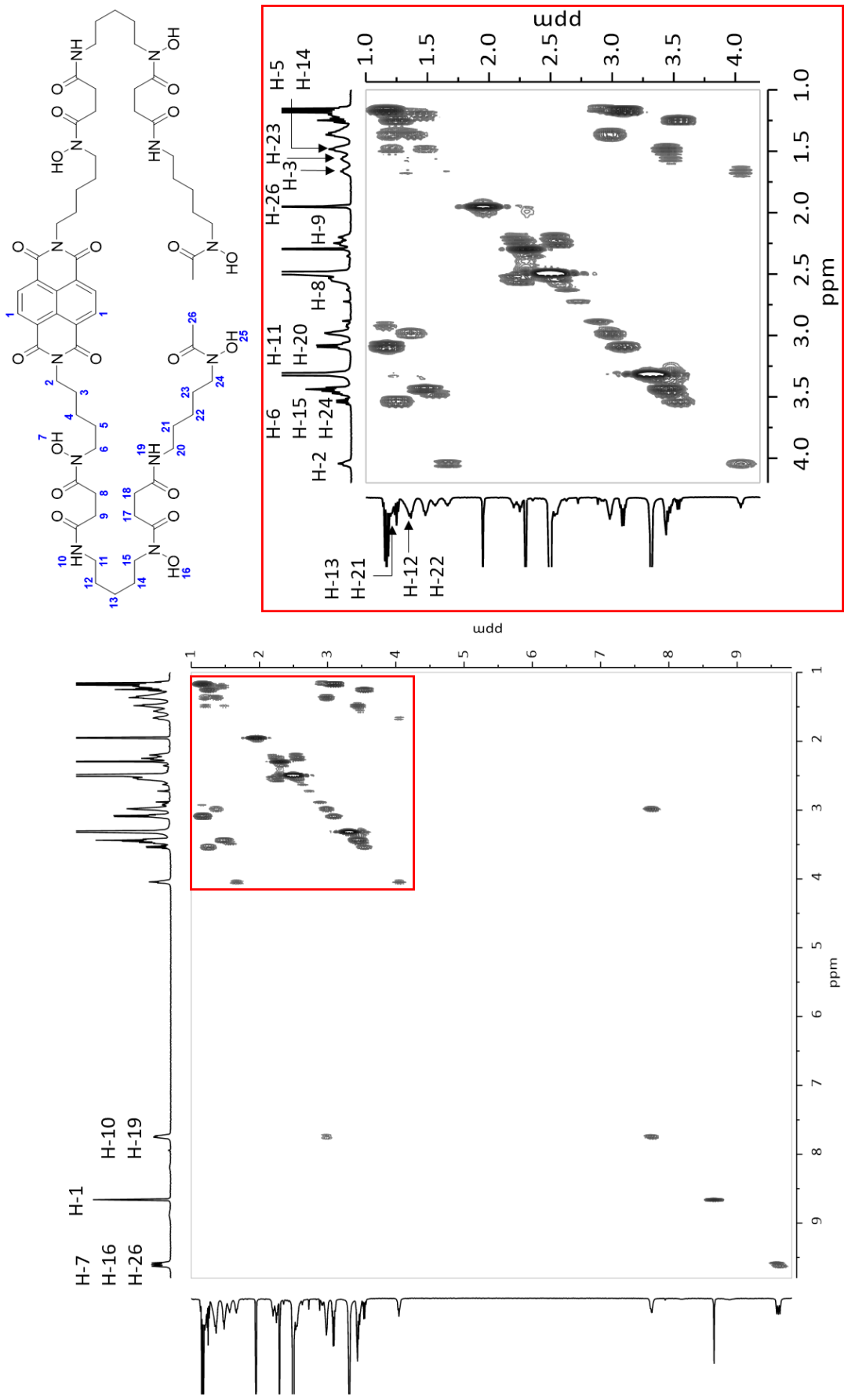

Figure A.4. ^{1}H-^{1}H COSY-NMR spectrum of compound **6** (DMSO-d_6, 500MHz).

7.2.2. Mass spectroscopy of selected compounds

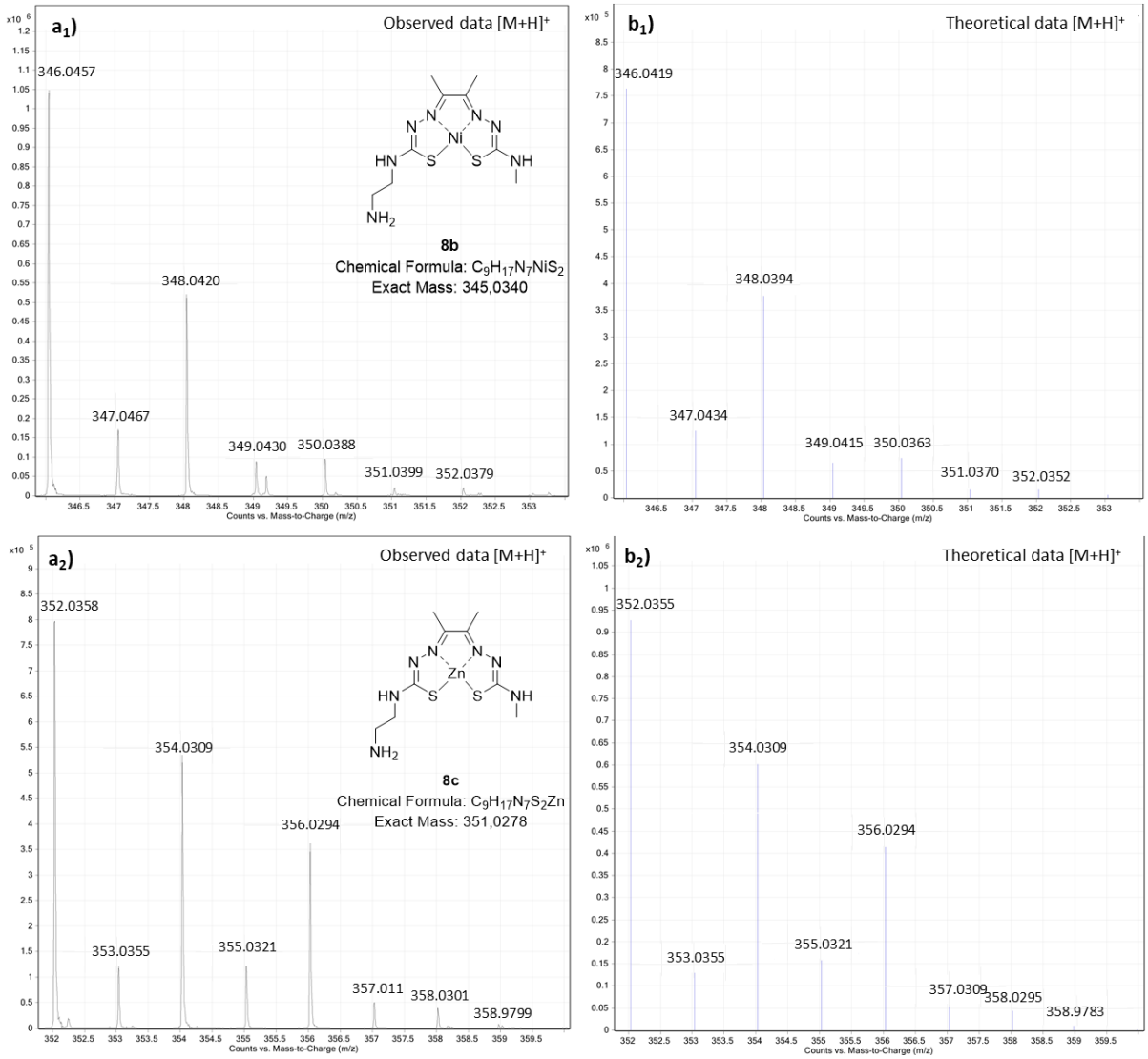

Figure A.5. Observed and theoretical isotopic patterns for $[M+H]^+$ ions of **1b** (a_1-b_1) and **1c** (a_2-b_2) (ESI^+-TOF, MeOH).

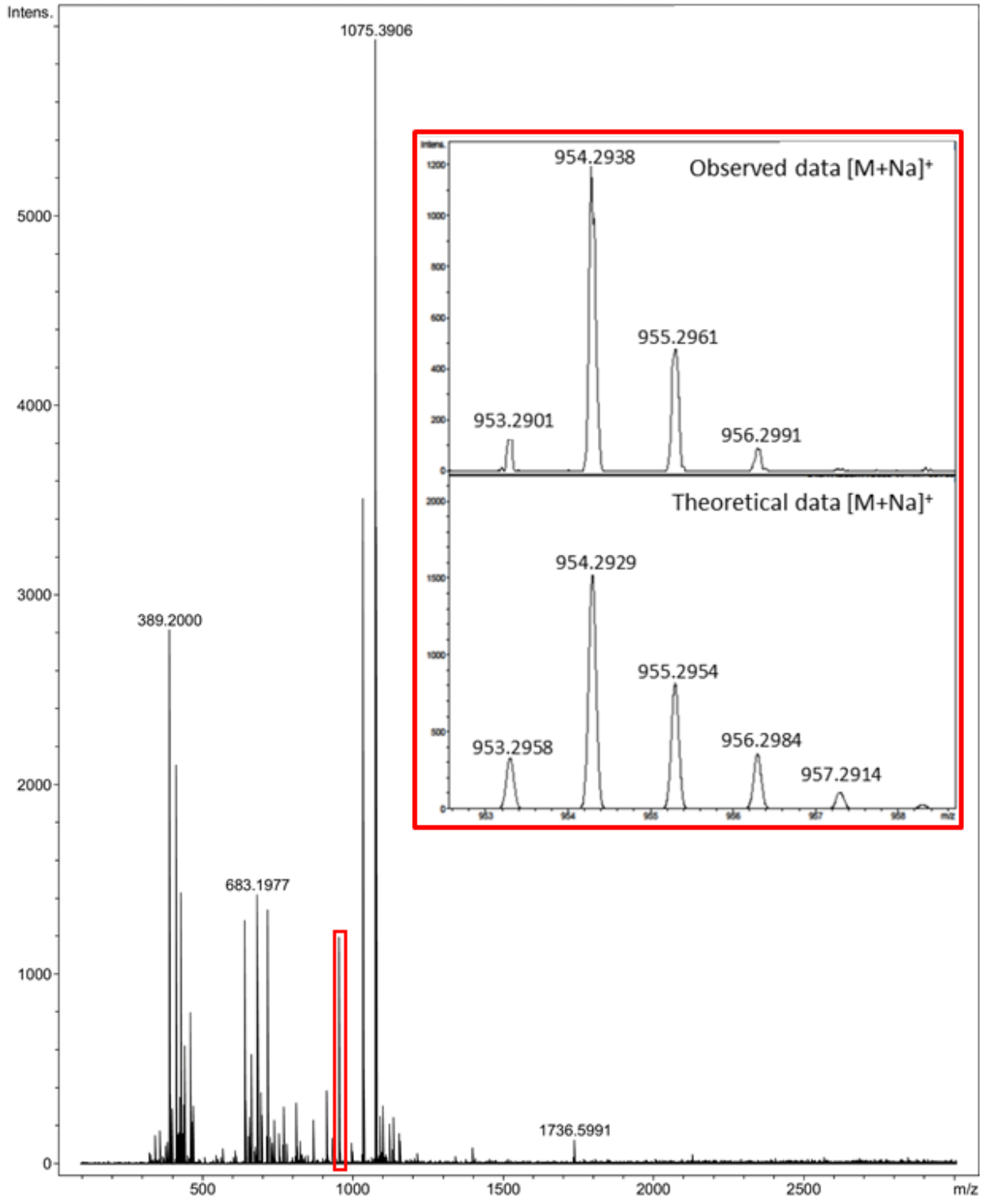

Figure A.6. Mass spectrum of compound **3** (ESI^+-TOF, MeOH).

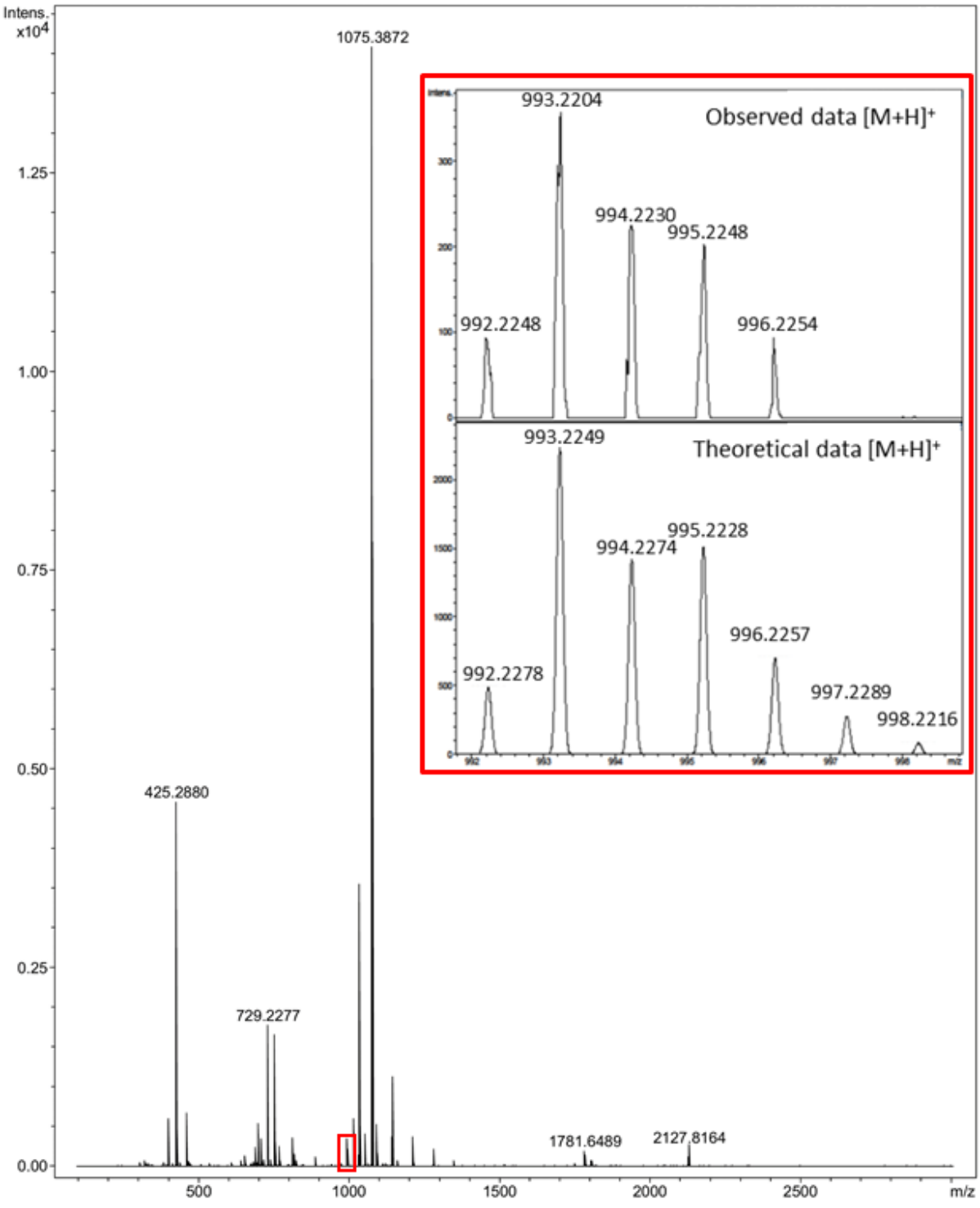

Figure A.7. Mass spectrum of compound **3a** (ESI^+-TOF, MeOH).

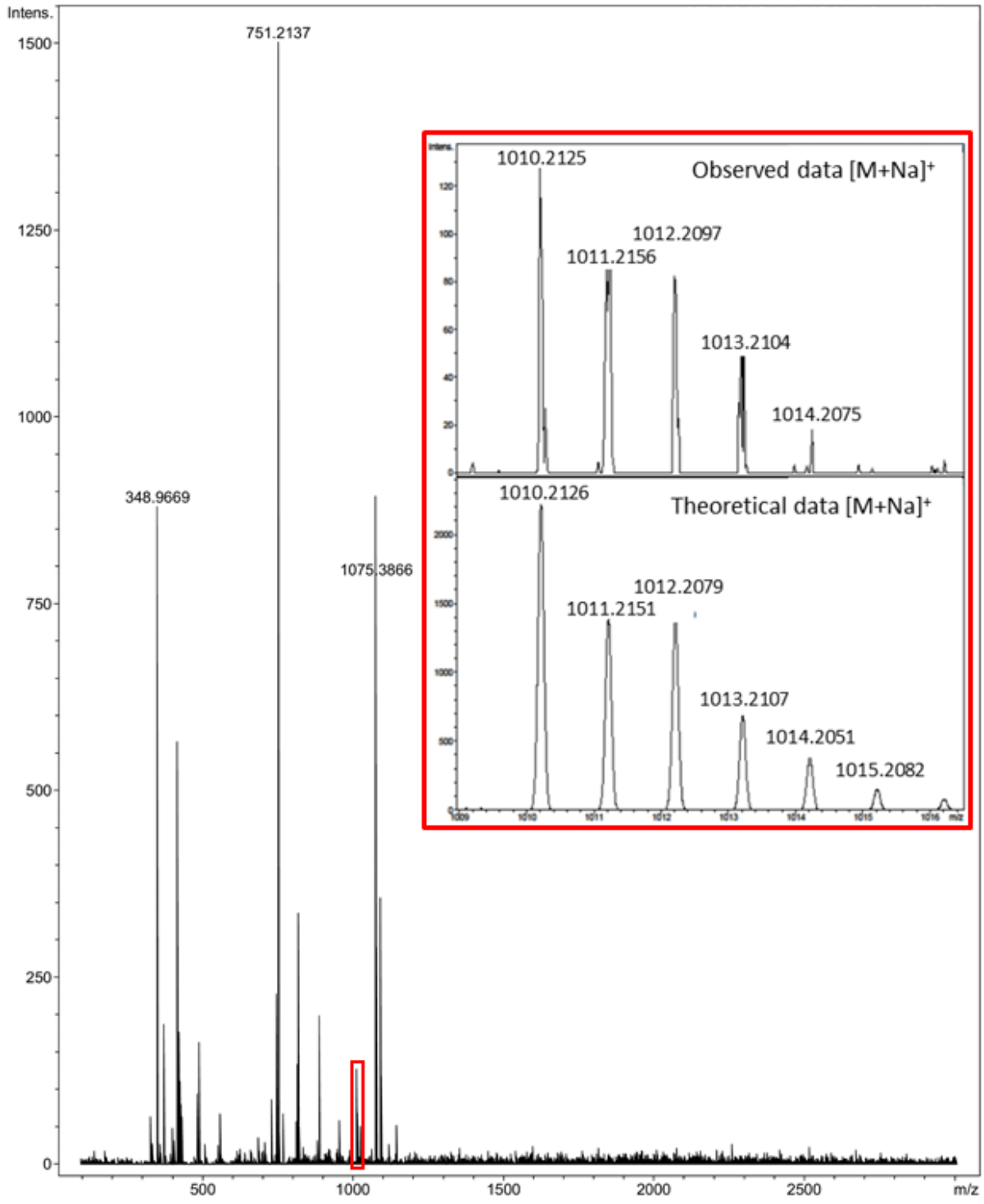

Figure A.8. Mass spectrum of compound **3b** (ESI^+-TOF, MeOH).

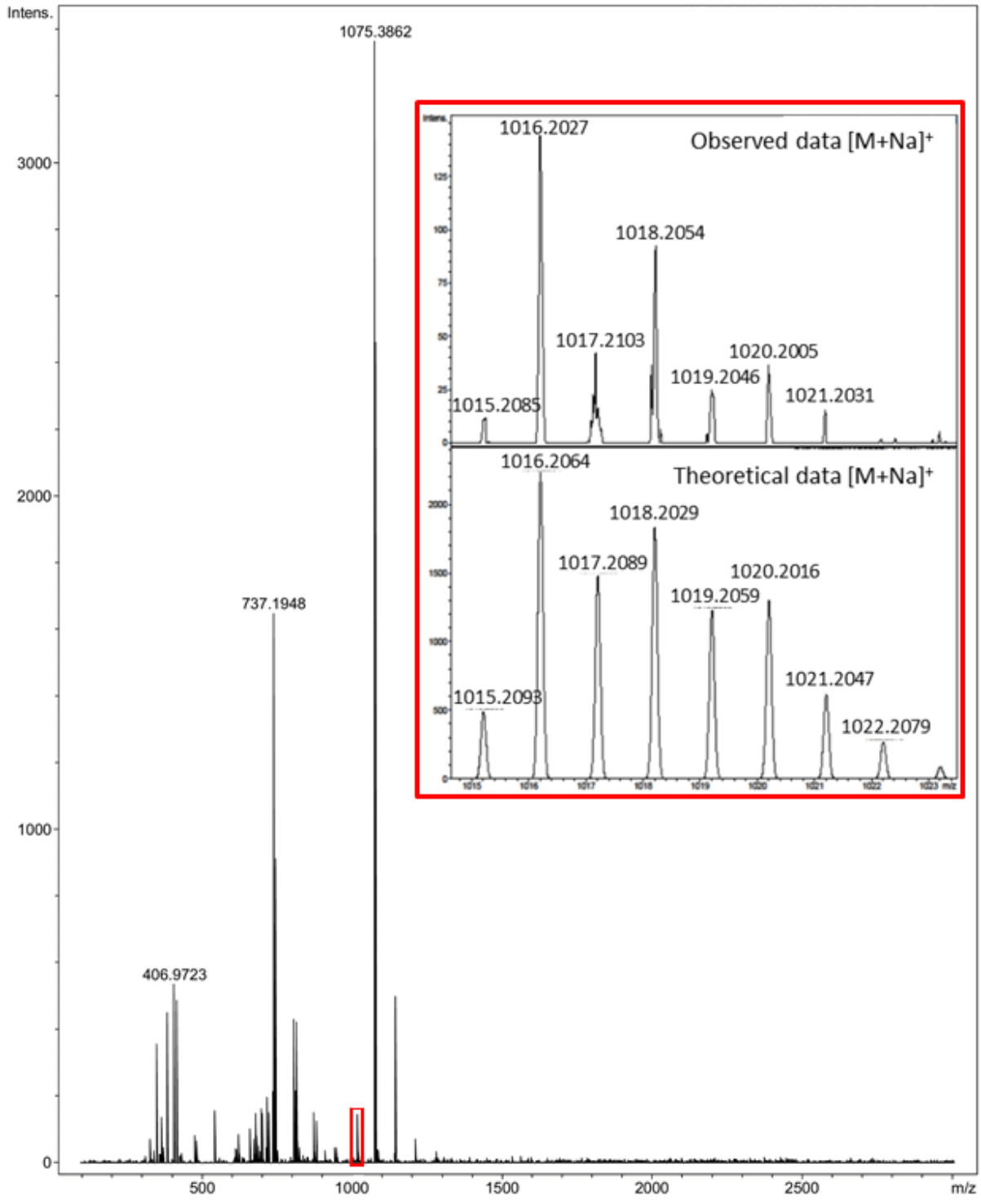

Figure A.9. Mass spectrum of compound **3c** (ESI^+-TOF, MeOH).

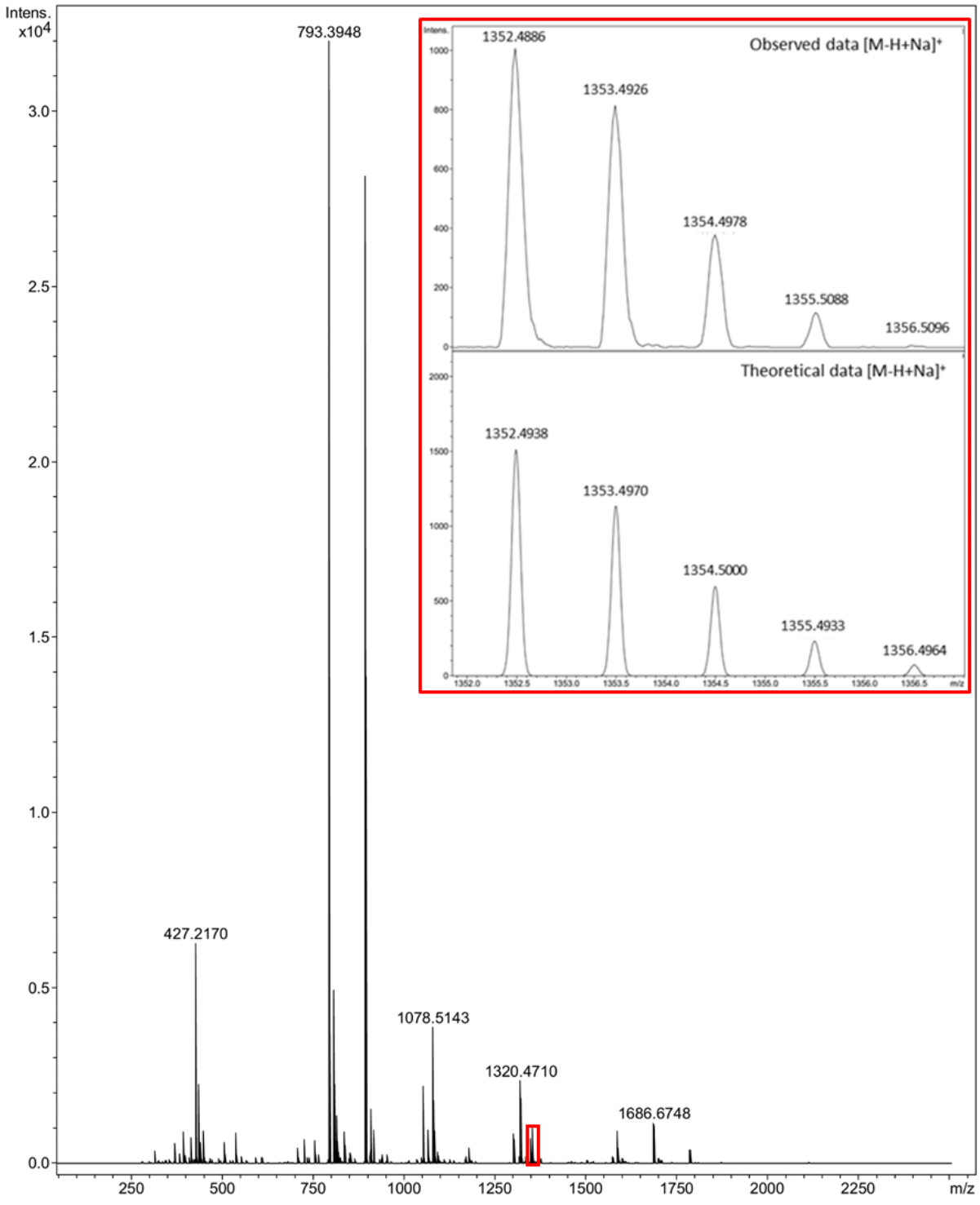

Figure A.10. Mass spectrum of compound **5** (ESI^+-TOF, MeOH).

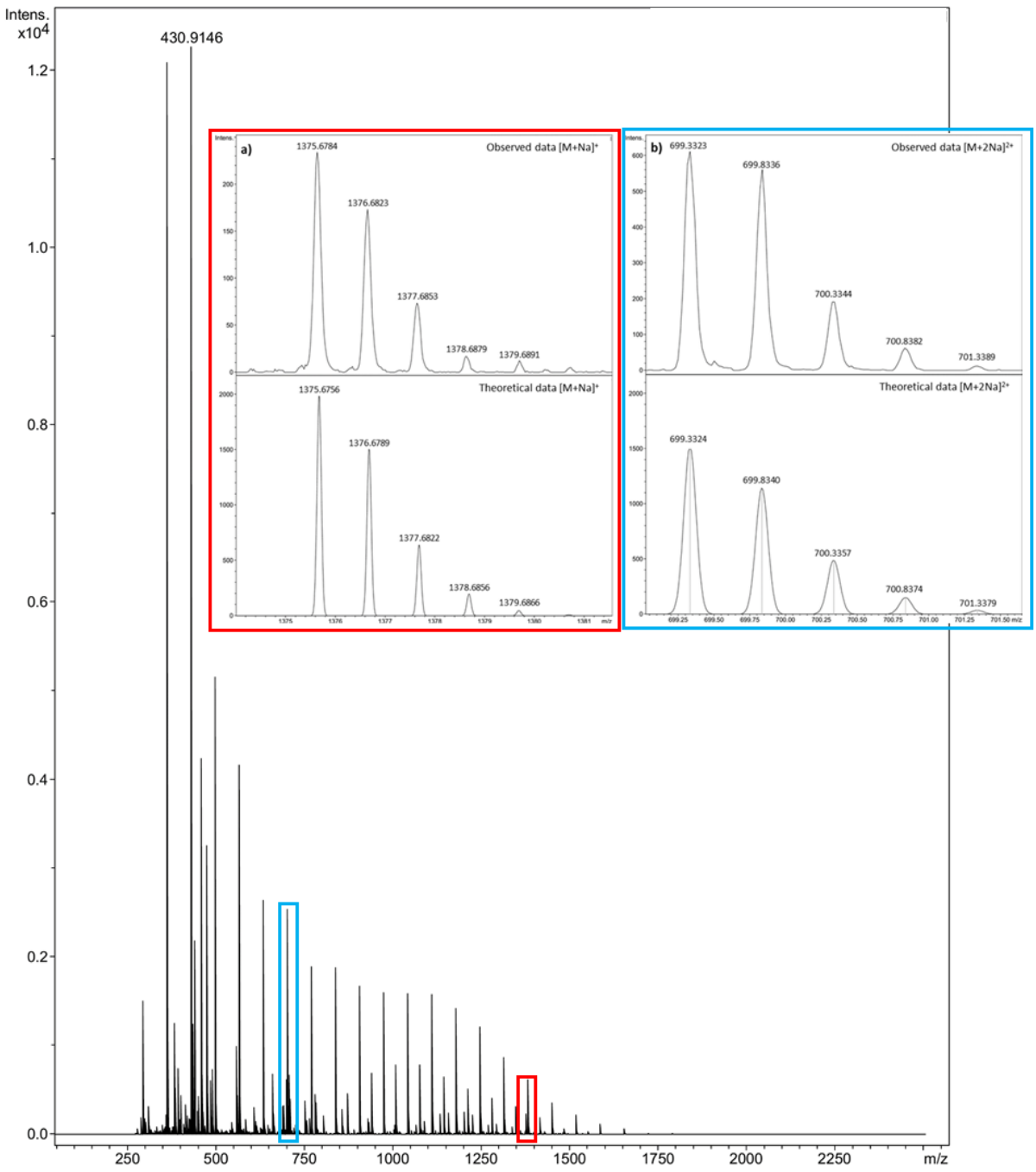

Figure A.11. Mass spectrum of compound **6** (ESI+-TOF, MeOH).

7.1.3. IR spectroscopy

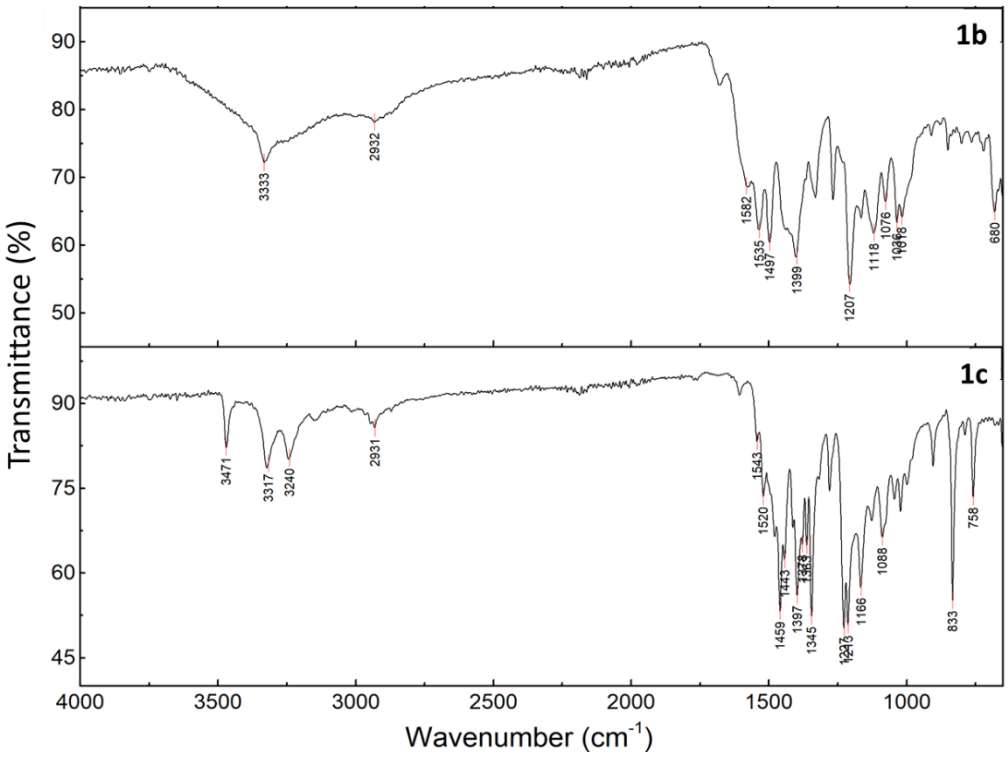

Figure A.12. FT-IR spectra in ATR mode of compounds **1b** (on the top) and **1c** (on the bottom).

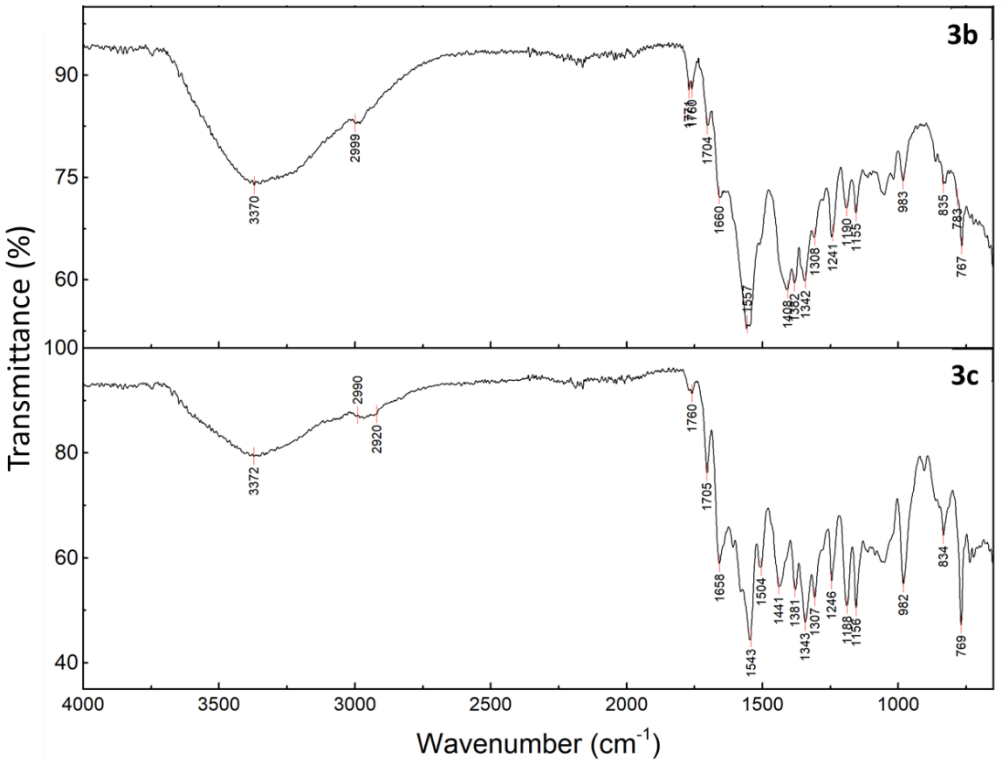

Figure A.13. FT-IR spectra in ATR mode of compounds **3b** (on the top) and **3c** (on the bottom).

7.1.4. Cyclic voltammetry

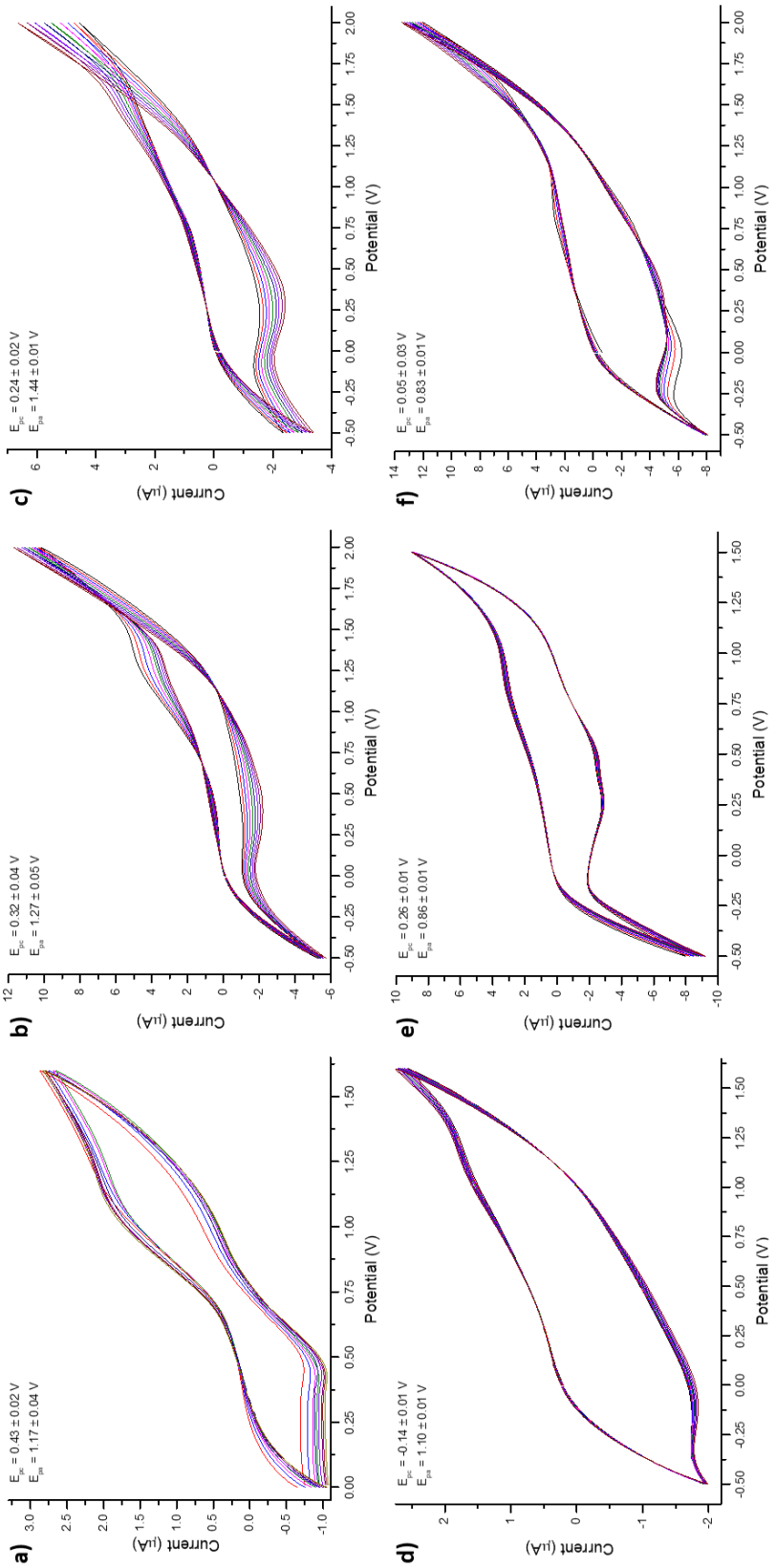

Figure A.14. Cyclic voltammograms of **a) 1a**, **b) 1b**, **c) 1c**, **d) 3a**, **e) 3b** and **f) 3c**. Solutions 1mM in MeOH. The potentials are referred to the Ag/AgCl reference potential (scan rate 50 mV/sec).

7.1.5. Confocal laser-scanning and fluorescence lifetime imaging microscopies

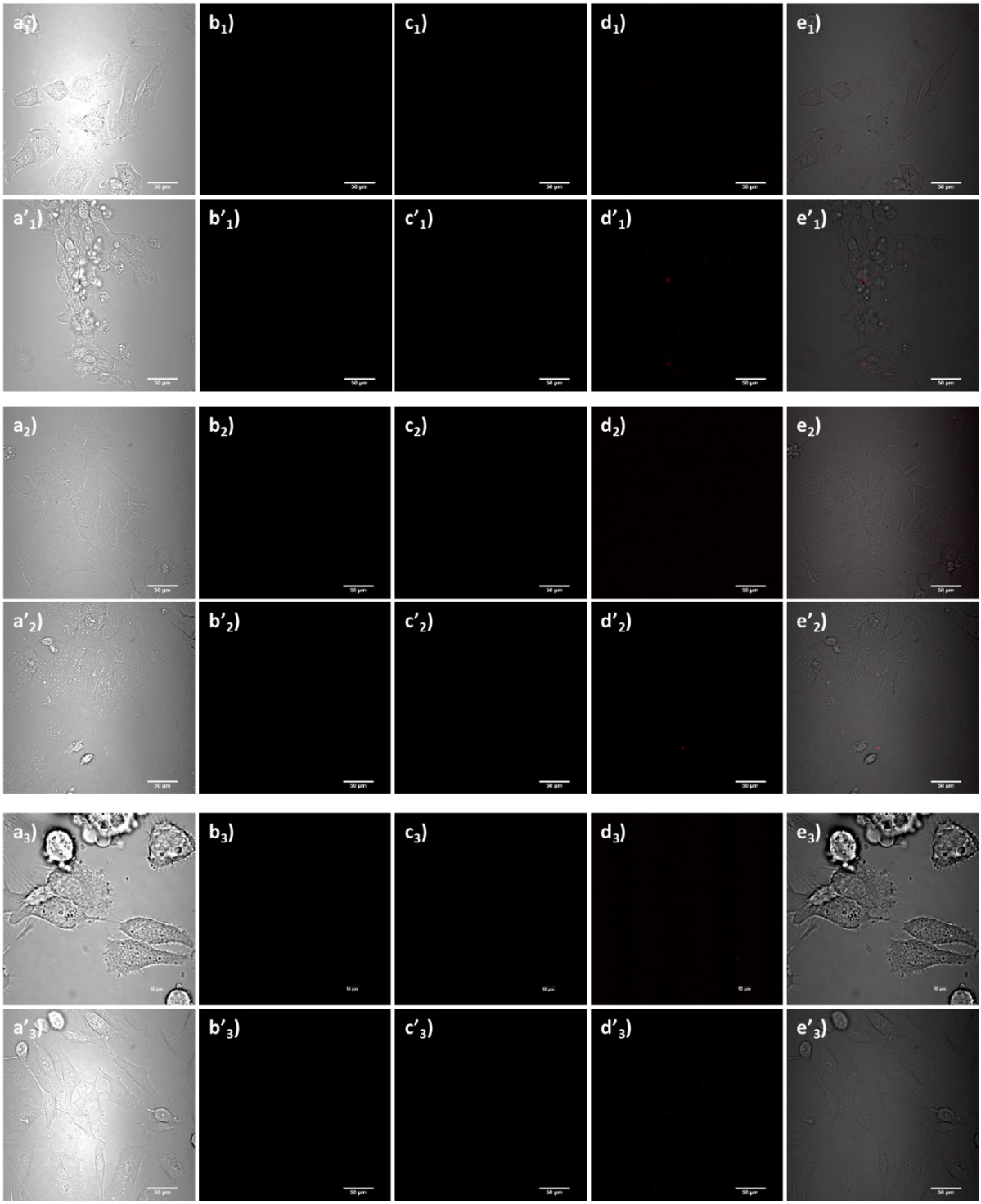

Figure A.15. Single-photon confocal laser-scanning microscopy of DMSO control (1:99 DMSO:serum-free medium) incubated at 37 °C for 20 min in **a$_1$-e$_1$** and **a'$_1$-e'$_1$)** EMT6, **a$_2$-e$_2$** and **a'$_2$-e'$_2$)** HeLa and **a$_3$-e$_3$** and **a'$_3$-e'$_3$)** PC-3 cell lines. **a$_{1-3}$-e$_{1-3}$)** Normoxia and **a'$_{1-3}$-e'$_{1-3}$)** hypoxia (5% pO_2 in 95 % pCO_2) conditions. **a$_{1-3}$** and **a'$_{1-3}$)** TD channel; **b$_{1-3}$** and **b'$_{1-3}$)** blue channel (λ_{em}=417–477 nm); **c$_{1-3}$** and **c'$_{1-3}$)** green channel (λ_{em}=500–550 nm); **d$_{1-3}$** and **d'$_{1-3}$)** red channel (λ_{em}=570–750 nm); **e$_{1-3}$** and **e'$_{1-3}$)** overlay of TD, blue, green and red channels. λ_{ex}=488 nm, scale bar: 50 µm.

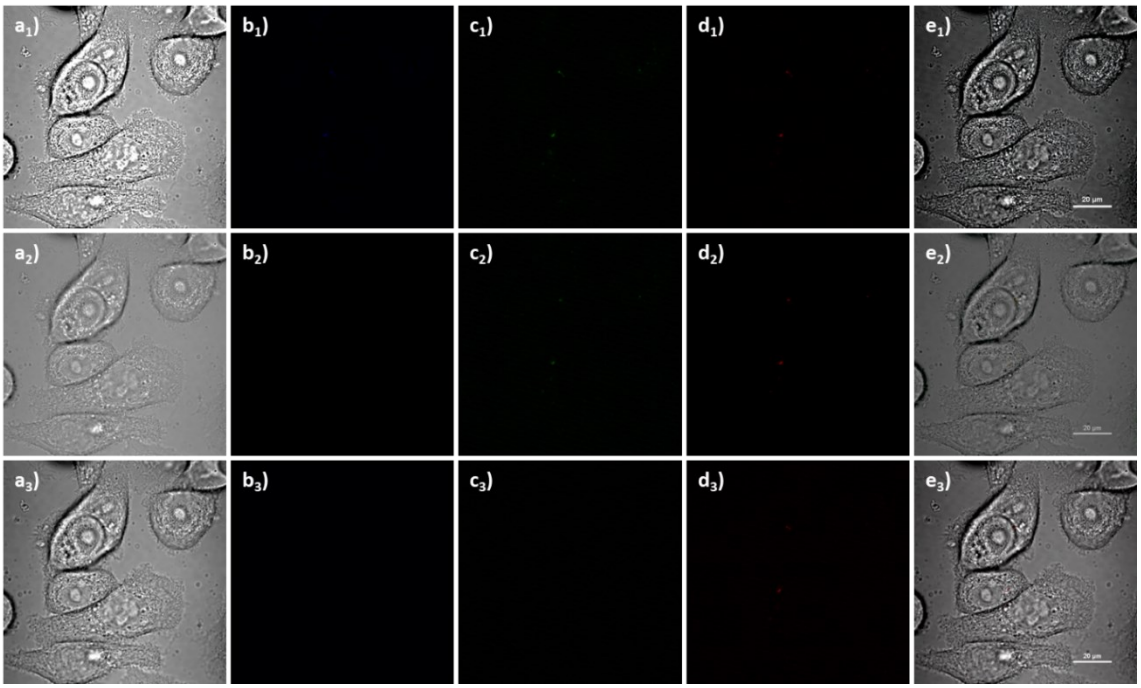

Figure A.16. Single-photon confocal laser-scanning microscopy of PC-3 cells incubated at 37 °C for 20 min with compound **1** (0.1 mM, 1:99 DMSO:serum-free medium). **a_{1-3})** TD channel; **b_{1-3})** blue channel (λ_{em}=417–477 nm); **c_{1-3})** green channel (λ_{em}=500–550 nm); **d_{1-3})** red channel (λ_{em}=570–750 nm); **e_{1-3})** overlay of TD, blue, green and red channels. **a_1-e_1)** λ_{ex}=405 nm, **a_2-e_2)** λ_{ex}=488 nm, **a_3-e_3)** λ_{ex}=561 nm. Scale bar: 20 µm.

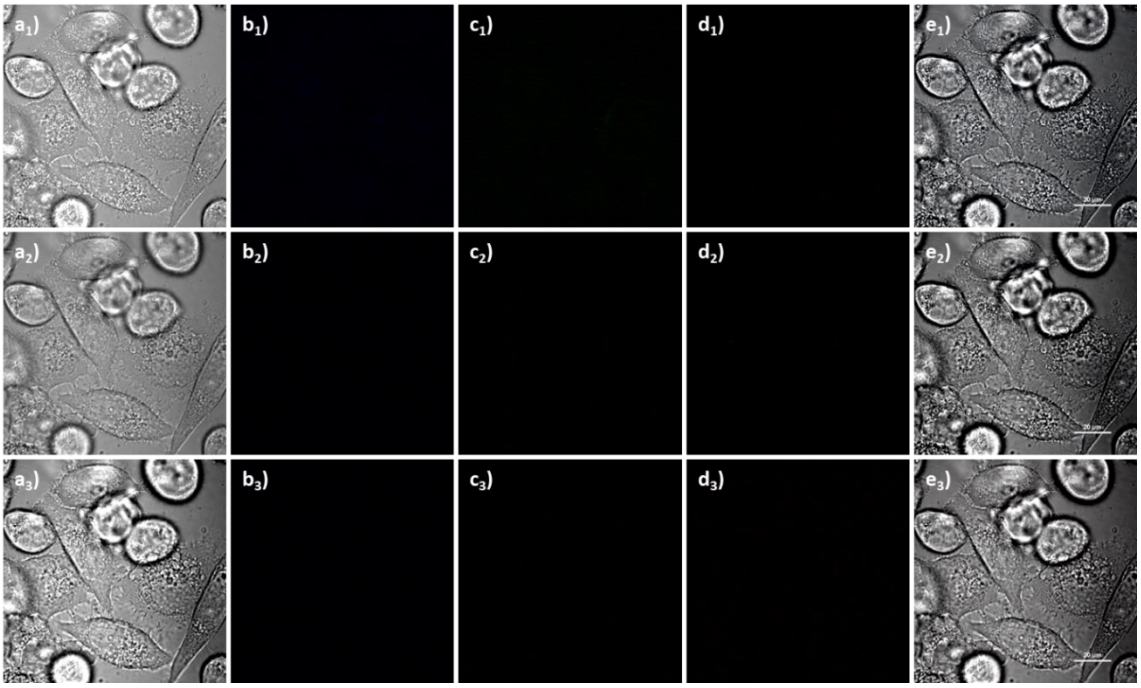

Figure A.17. Single-photon confocal laser-scanning microscopy of PC-3 cells incubated at 37 °C for 20 min with compound **1a** (0.1 mM, 1:99 DMSO:serum-free medium). **a_{1-3})** TD channel; **b_{1-3})** blue channel (λ_{em}=417–477 nm); **c_{1-3})** green channel (λ_{em}=500–550 nm); **d_{1-3})** red channel (λ_{em}=570–750 nm); **e_{1-3})** overlay of TD, blue, green and red channels. **a_1-e_1)** λ_{ex}=405 nm, **a_2-e_2)** λ_{ex}=488 nm, **a_3-e_3)** λ_{ex}=561 nm. Scale bar: 20 µm.

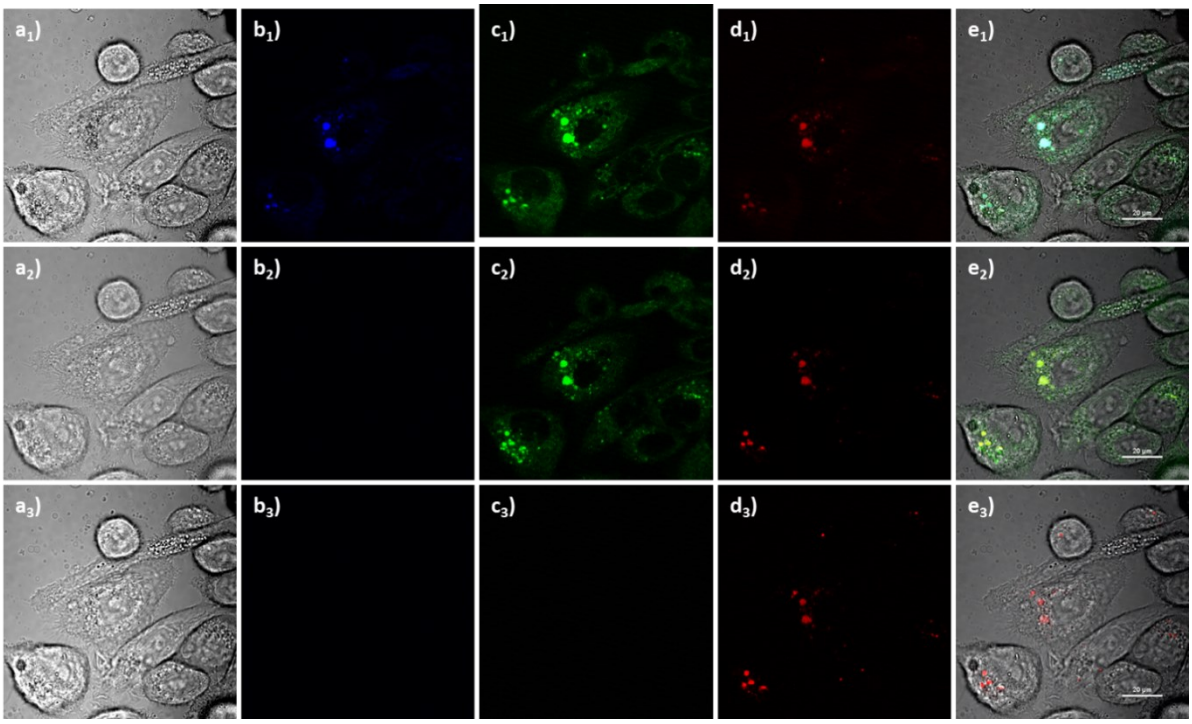

Figure A.18. Single-photon confocal laser-scanning microscopy of PC-3 cells incubated at 37 °C for 20 min with compound **1b** (0.1 mM, 1:99 DMSO:serum-free medium). **a_{1-3})** TD channel; **b_{1-3})** blue channel (λ_{em}=417–477 nm); **c_{1-3})** green channel (λ_{em}=500–550 nm); **d_{1-3})** red channel (λ_{em}=570–750 nm); **e_{1-3})** overlay of TD, blue, green and red channels. **a_1-e_1)** λ_{ex}=405 nm, **a_2-e_2)** λ_{ex}=488 nm, **a_3-e_3)** λ_{ex}=561 nm. Scale bar: 20 µm.

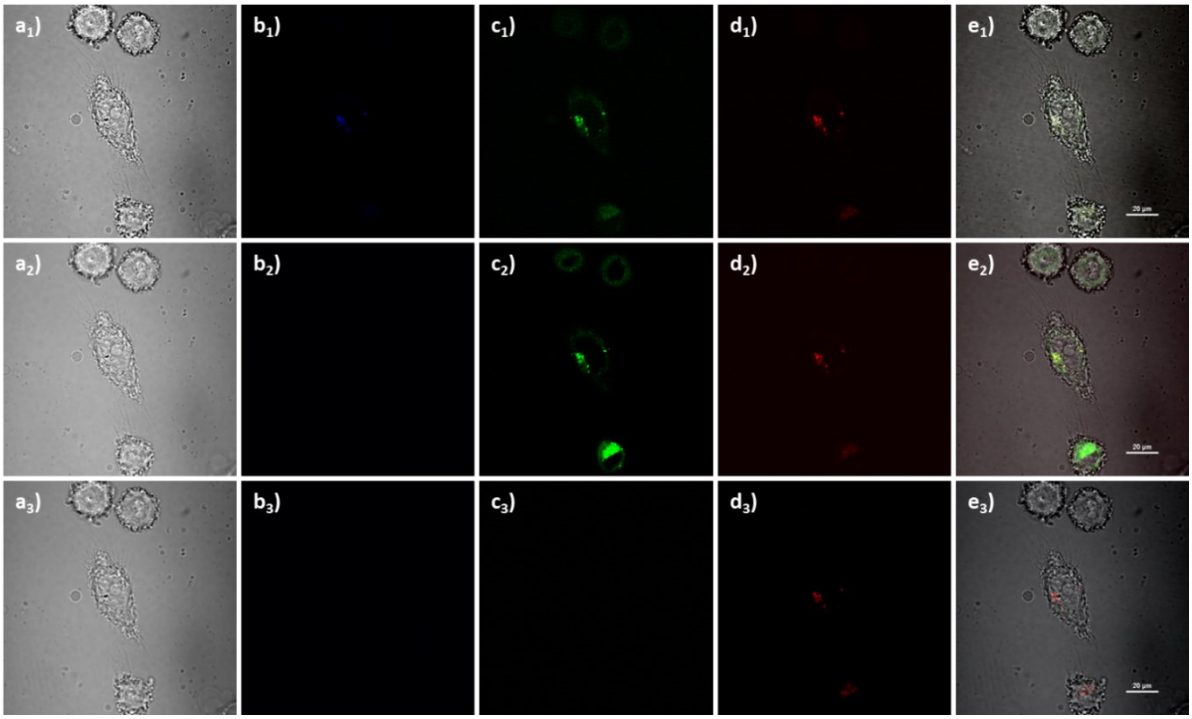

Figure A.19. Single-photon confocal laser-scanning microscopy of PC-3 cells incubated at 37 °C for 20 min with compound **1c** (0.1 mM, 1:99 DMSO:serum-free medium). **a_{1-3})** TD channel; **b_{1-3})** blue channel (λ_{em}=417–477 nm); **c_{1-3})** green channel (λ_{em}=500–550 nm); **d_{1-3})** red channel (λ_{em}=570–750 nm); **e_{1-3})** overlay of TD, blue, green and red channels. **a_1-e_1)** λ_{ex}=405 nm, **a_2-e_2)** λ_{ex}=488 nm, **a_3-e_3)** λ_{ex}=561 nm. Scale bar: 20 µm.

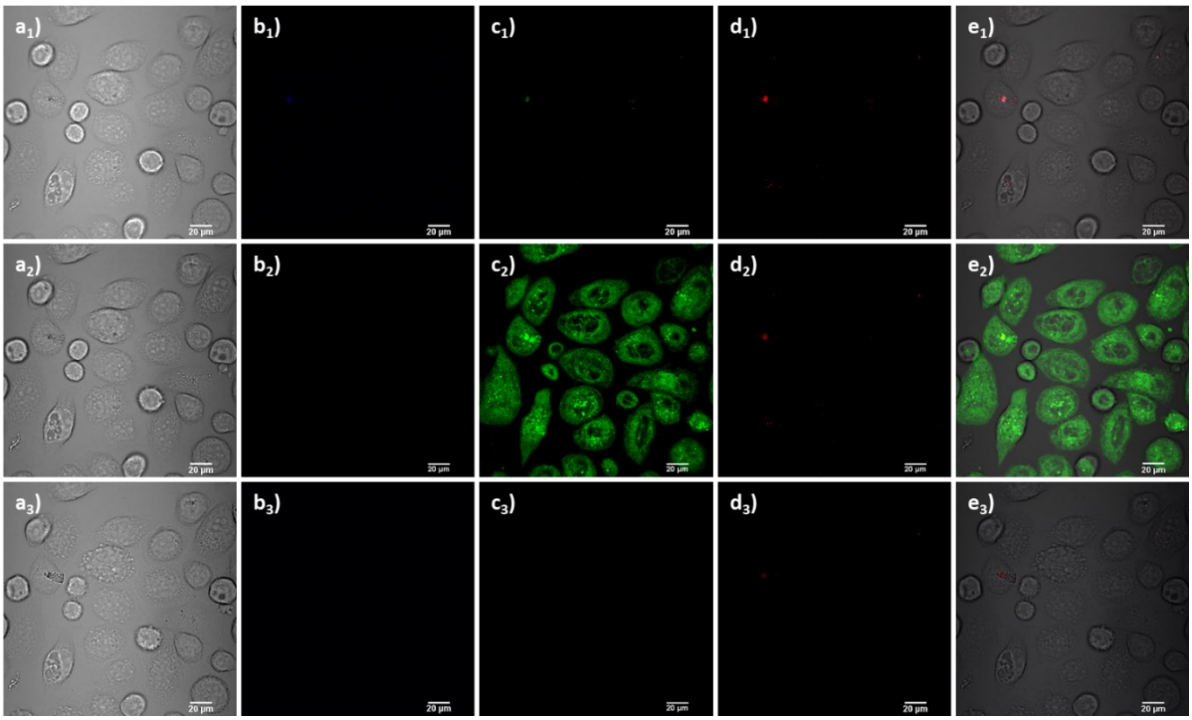

Figure A.20. Single-photon confocal laser-scanning microscopy of PC-3 cells incubated at 37 °C for 20 min with compound **3** (0.1 mM, 1:99 DMSO:serum-free medium). **a$_{1-3}$)** TD channel; **b$_{1-3}$)** blue channel (λ_{em}=417–477 nm); **c$_{1-3}$)** green channel (λ_{em}=500–550 nm); **d$_{1-3}$)** red channel (λ_{em}=570–750 nm); **e$_{1-3}$)** overlay of TD, blue, green and red channels. **a$_1$-e$_1$)** λ_{ex}=405 nm, **a$_2$-e$_2$)** λ_{ex}=488 nm, **a$_3$-e$_3$)** λ_{ex}=561 nm. Scale bar: 50 µm.

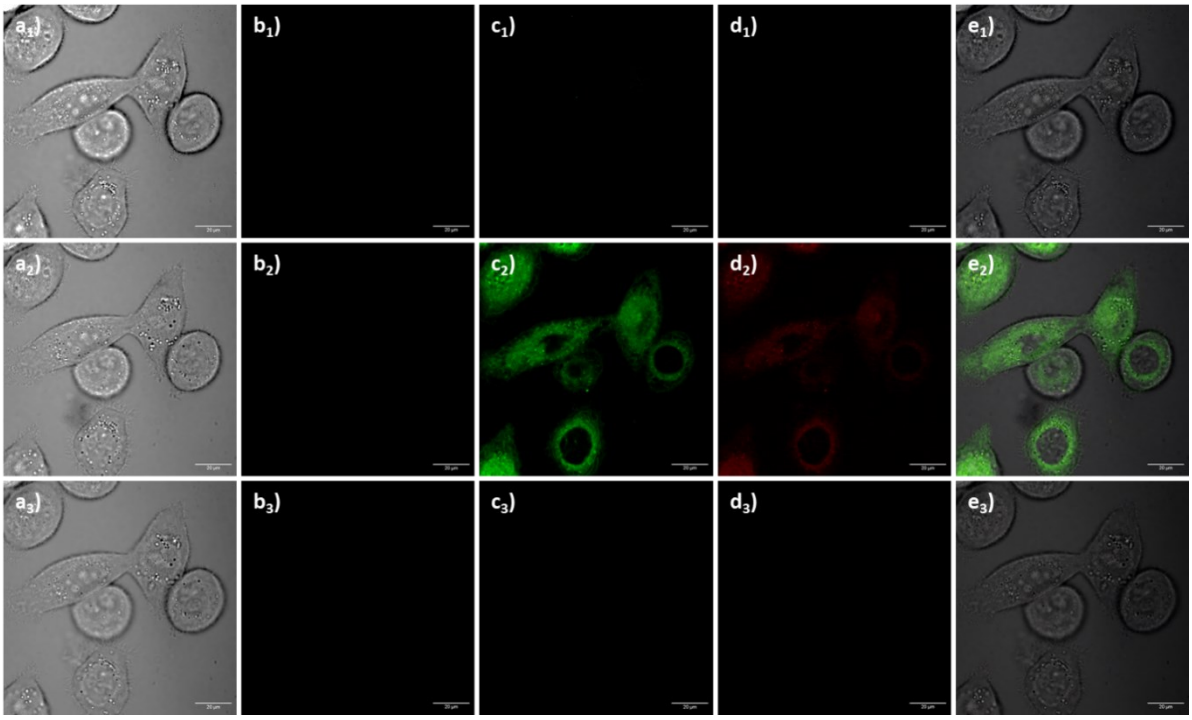

Figure A.21. Single-photon confocal laser-scanning microscopy of PC-3 cells incubated at 37 °C for 20 min with compound **3a** (0.1 mM, 1:99 DMSO:serum-free medium). **a$_{1-3}$)** TD channel; **b$_{1-3}$)** blue channel (λ_{em}=417–477 nm); **c$_{1-3}$)** green channel (λ_{em}=500–550 nm); **d$_{1-3}$)** red channel (λ_{em}=570–750 nm); **e$_{1-3}$)** overlay of TD, blue, green and red channels. **a$_1$-e$_1$)** λ_{ex}=405 nm, **a$_2$-e$_2$)** λ_{ex}=488 nm, **a$_3$-e$_3$)** λ_{ex}=561 nm. Scale bar: 20 µm.

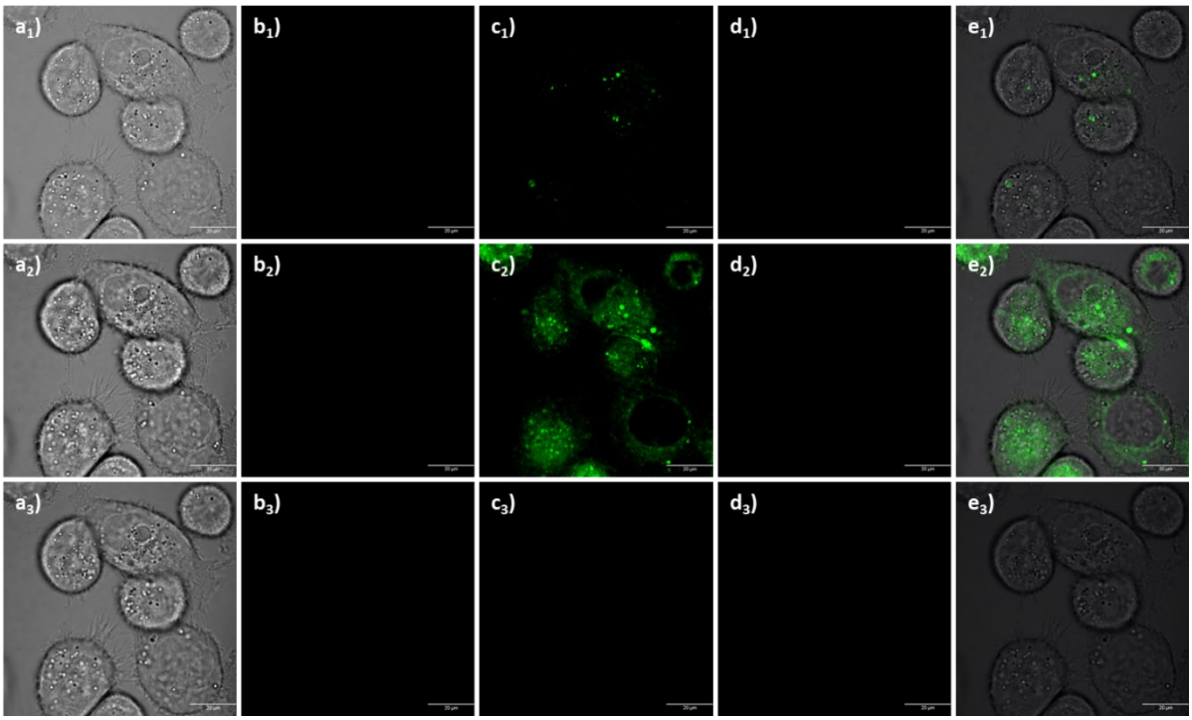

Figure A.22. Single-photon confocal laser-scanning microscopy of PC-3 cells incubated at 37 °C for 20 min with compound **3b** (0.1 mM, 1:99 DMSO:serum-free medium). **a_{1-3})** TD channel; **b_{1-3})** blue channel (λ_{em}=417–477 nm); **c_{1-3})** green channel (λ_{em}=500–550 nm); **d_{1-3})** red channel (λ_{em}=570–750 nm); **e_{1-3})** overlay of TD, blue, green and red channels. **a_1-e_1)** λ_{ex}=405 nm, **a_2-e_2)** λ_{ex}=488 nm, **a_3-e_3)** λ_{ex}=561 nm. Scale bar: 20 µm.

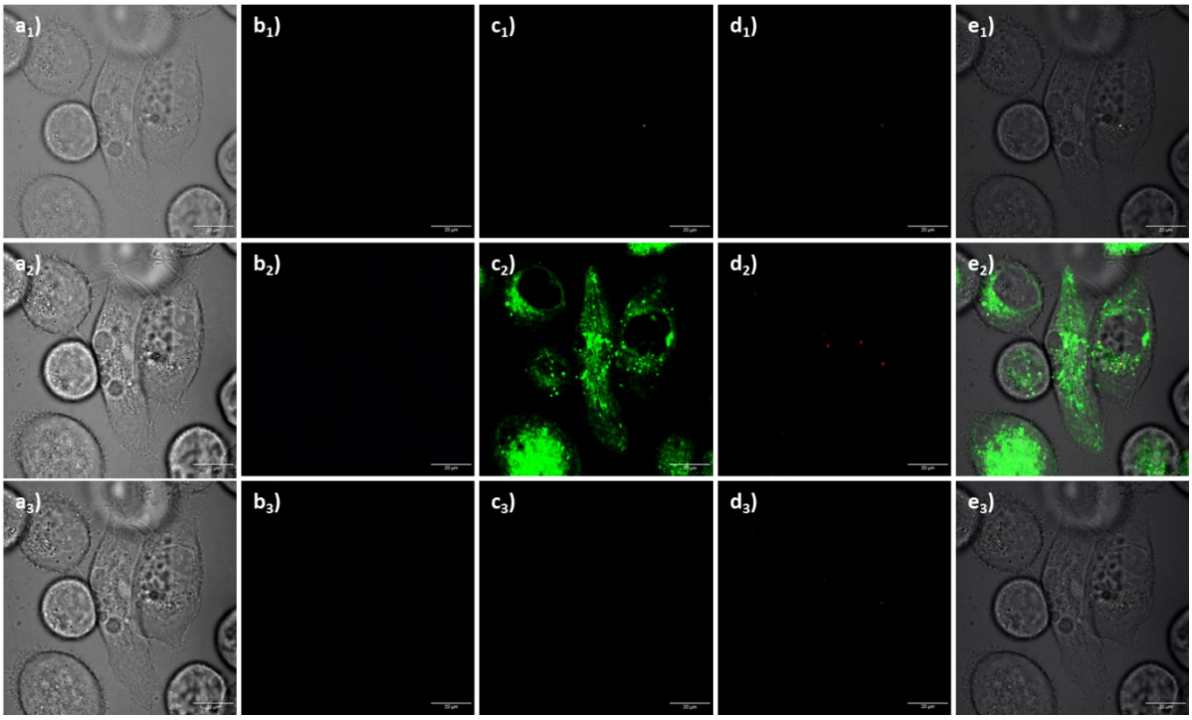

Figure A.23. Single-photon confocal laser-scanning microscopy of PC-3 cells incubated at 37 °C for 20 min with compound **3c** (0.1 mM, 1:99 DMSO:serum-free medium). **a_{1-3})** TD channel; **b_{1-3})** blue channel (λ_{em}=417–477 nm); **c_{1-3})** green channel (λ_{em}=500–550 nm); **d_{1-3})** red channel (λ_{em}=570–750 nm); **e_{1-3})** overlay of TD, blue, green and red channels. **a_1-e_1)** λ_{ex}=405 nm, **a_2-e_2)** λ_{ex}=488 nm, **a_3-e_3)** λ_{ex}=561 nm. Scale bar: 20 µm.

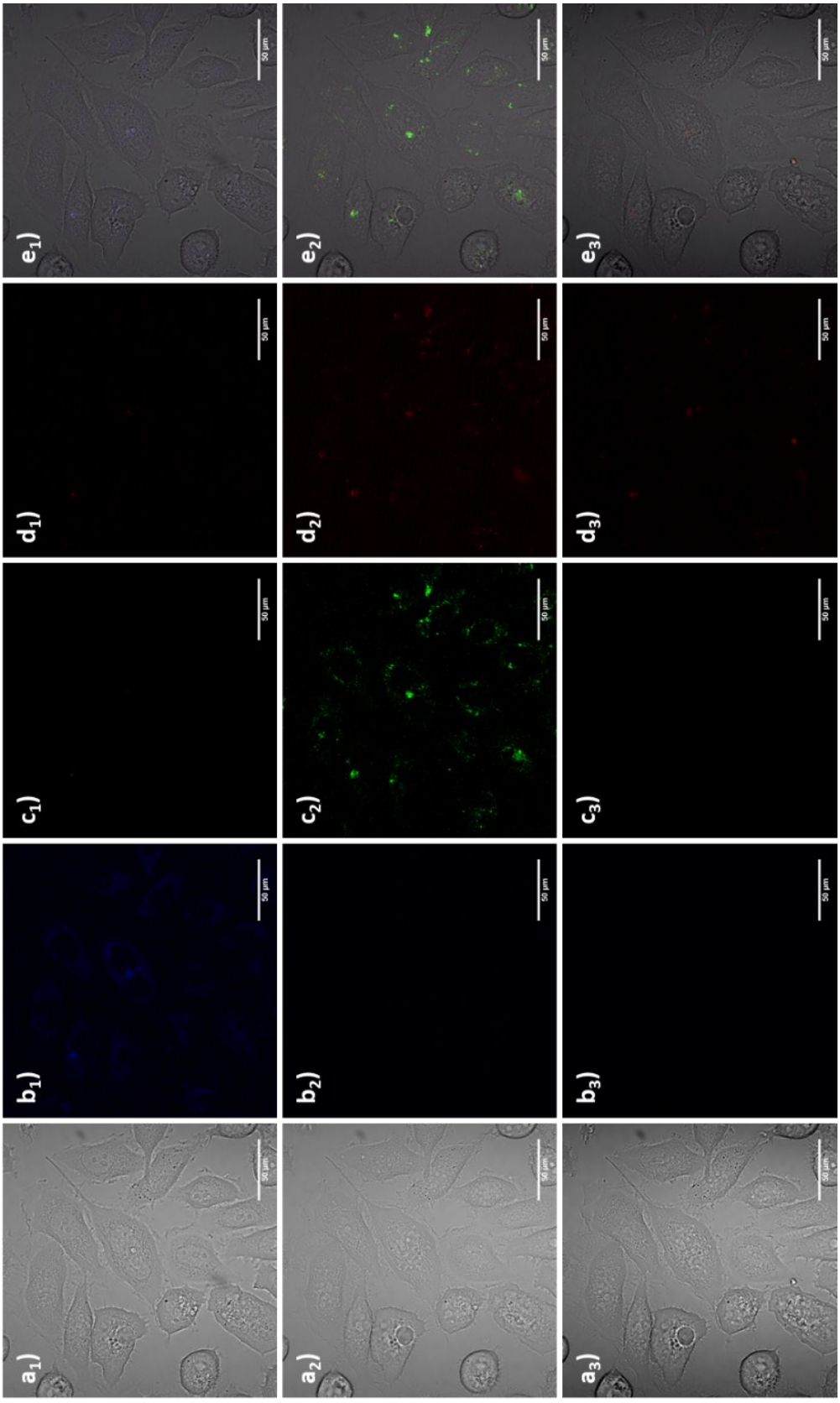

Figure A.24. Single-photon confocal laser-scanning microscopy of PC-3 cells incubated at 37 °C for 20 min with compound **6** (0.1 mM, 1:99 DMSO:serum-free medium). **a_{1-3})** TD channel; **b_{1-3})** blue channel (λ_{em}=417–477 nm); **c_{1-3})** green channel (λ_{em}=500–550 nm); **d_{1-3})** red channel (λ_{em}=570–750 nm); **e_{1-3})** overlay of TD, blue, green and red channels. **a_1-e_1)** λ_{ex}=405 nm, **a_2-e_2)** λ_{ex}=488 nm, **a_3-e_3)** λ_{ex}=561 nm. Scale bar: 50 µm.

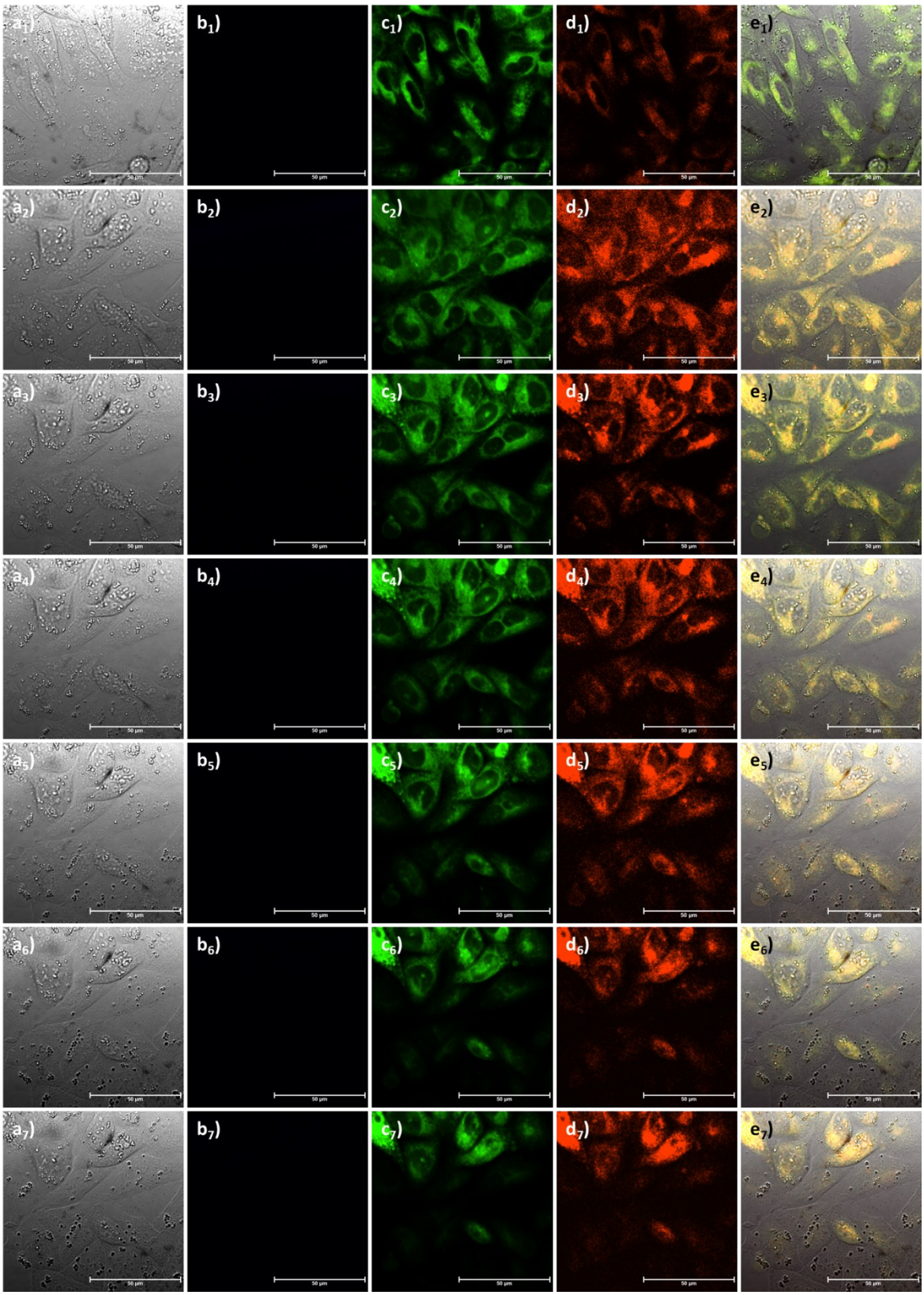

Figure A.25. Single-photon confocal laser-scanning microscopy of CHO cells incubated at 37 °C for 20 min with compound **3a** (0.1 mM, 1:99 DMSO:serum-free medium). **a$_{1\text{-}7}$)** TD channel; **b$_{1\text{-}7}$)** blue channel (λ_{em}=417–477 nm); **c$_{1\text{-}7}$)** green channel (λ_{em}=500–550 nm); **d$_{1\text{-}7}$)** red channel (λ_{em}=570–750 nm); **e$_{1\text{-}7}$)** overlay of TD, blue, green and red channels. Micrographs captured under hypoxic condition (N_2 flux) after **a$_1$-e$_1$)** 0 min, **a$_2$-e$_2$)** 10 min, **a$_3$-e$_3$)** 15 min, **a$_4$-e$_4$)** 20 min, **a$_5$-e$_5$)** 30 min, **a$_6$-e$_6$)** 40 min and **a$_7$-e$_7$)** 60min. λ_{ex}=488 nm. Scale bar: 50 µm.

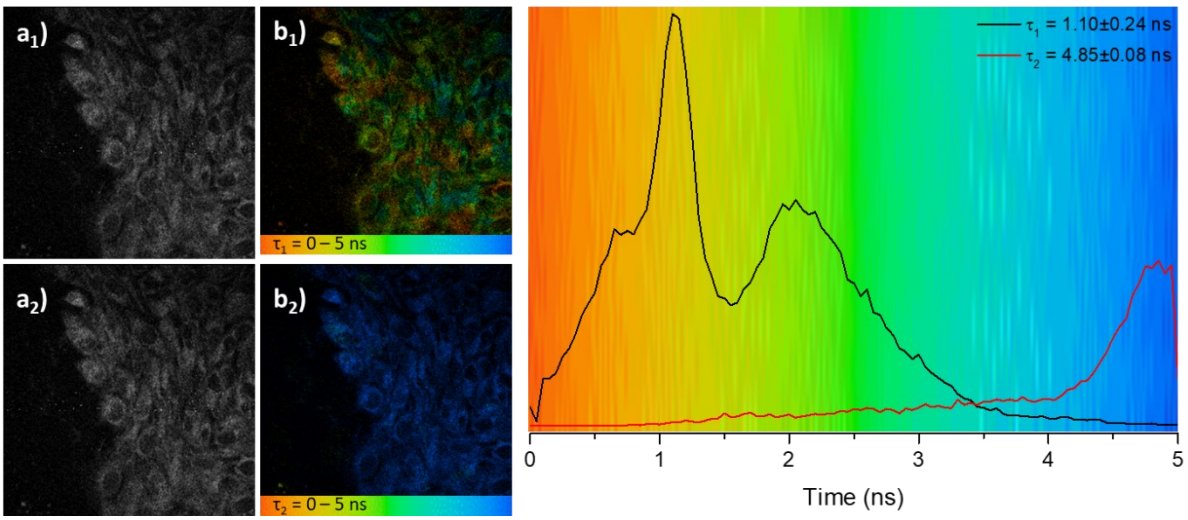

Figure A.26. Two-photon fluorescence lifetime imaging in CHO cells line of compound **3** (0.05 mM in 1:99 DMSO:sereum-free medium) including **$a_{1,2}$)** intensity map, **$b_{1,2}$)** lifetime maps in coloured code and lifetime distribution. **a_1-b_1)** τ_1=1.10±0.24 ns and **a_2-b_2)** τ_2=4.85±0.08 ns. λ_{ex}=910 nm; laser power 4.4 mW; acquisition time 60 s.

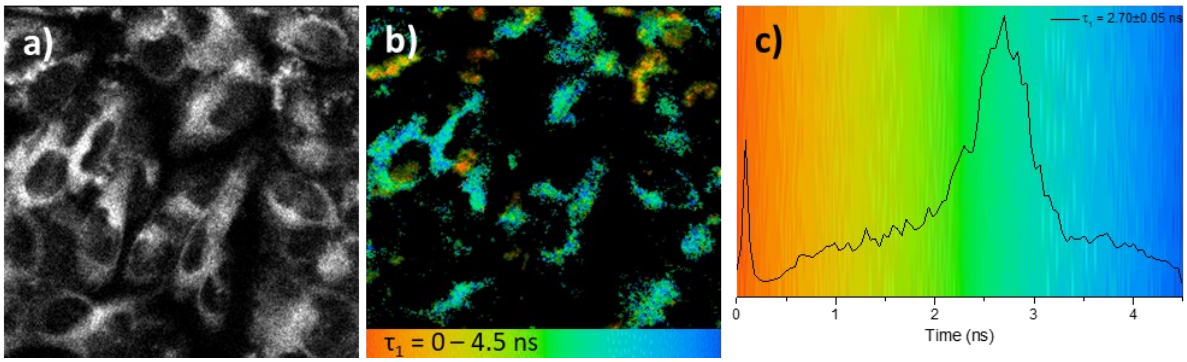

Figure A.27. Two-photon fluorescence lifetime imaging in CHO cells line of compound **3a** (0.05 mM in 1:99 DMSO:sereum-free medium) including **a)** intensity map, **b)** lifetime maps in coloured code and **c)** lifetime distribution. τ_1=2.70±0.05 ns. λ_{ex}=910 nm, laser power 1.2 mW; acquisition time 30 s.

7.2. Appendices to Chapter 3

7.2.1. NMR spectroscopy of selected compounds

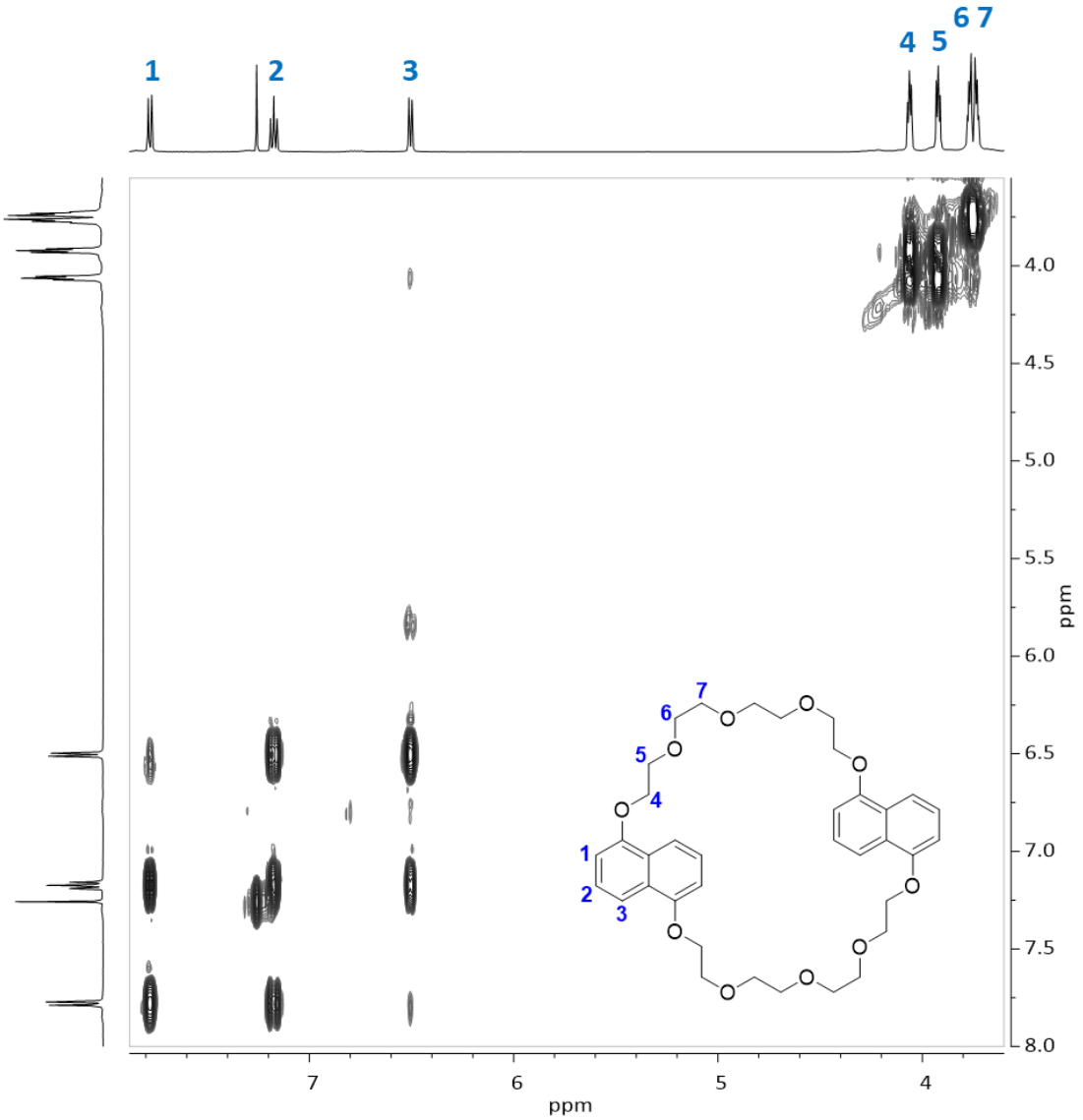

Figure A.28. ^{1}H-^{1}H COSY-NMR spectrum of compound **7** ($CDCl_3$, 500MHz).

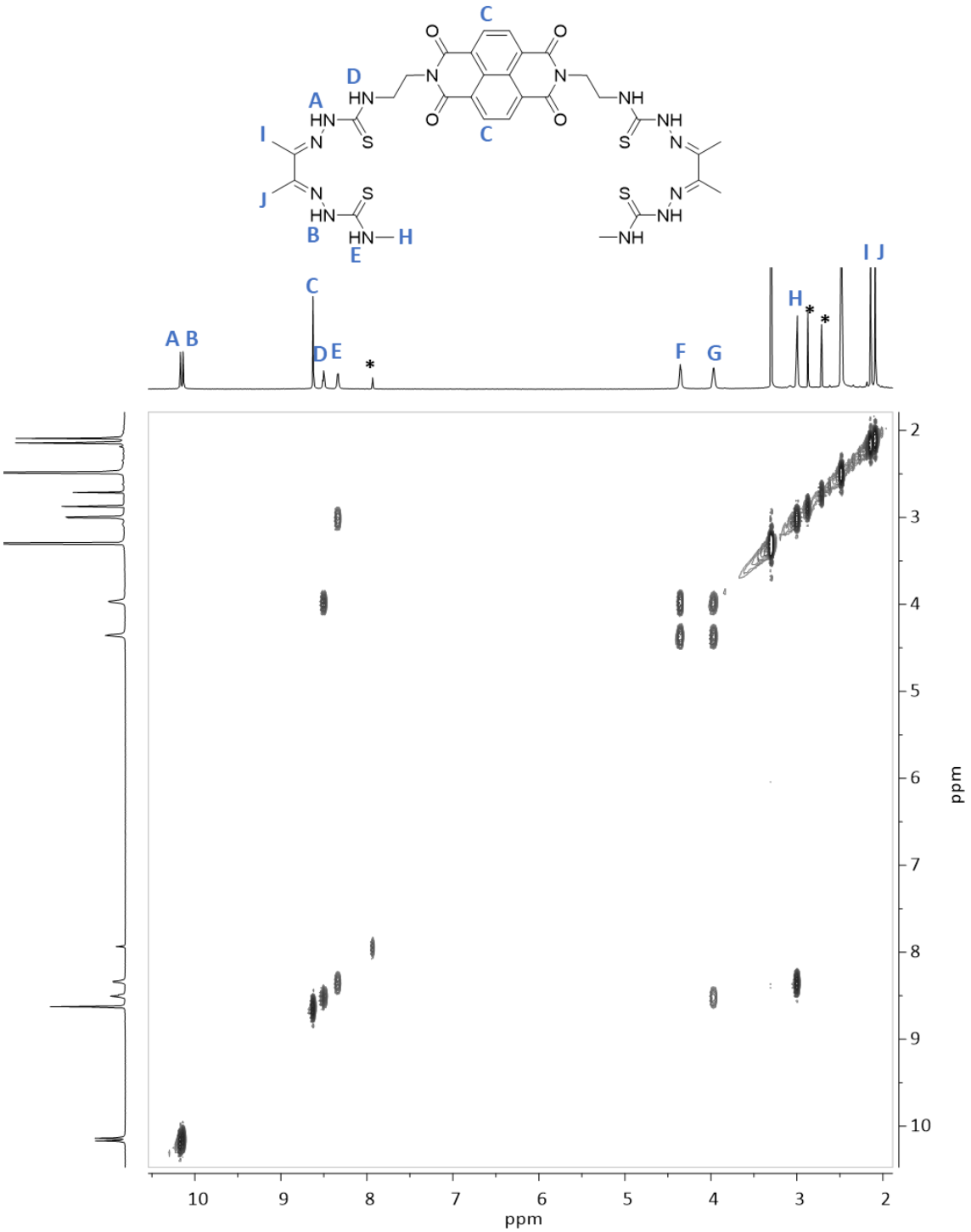

Figure A.29. ^{1}H-^{1}H COSY-NMR spectrum of compound **8** (DMSO-d_6, 500MHz).

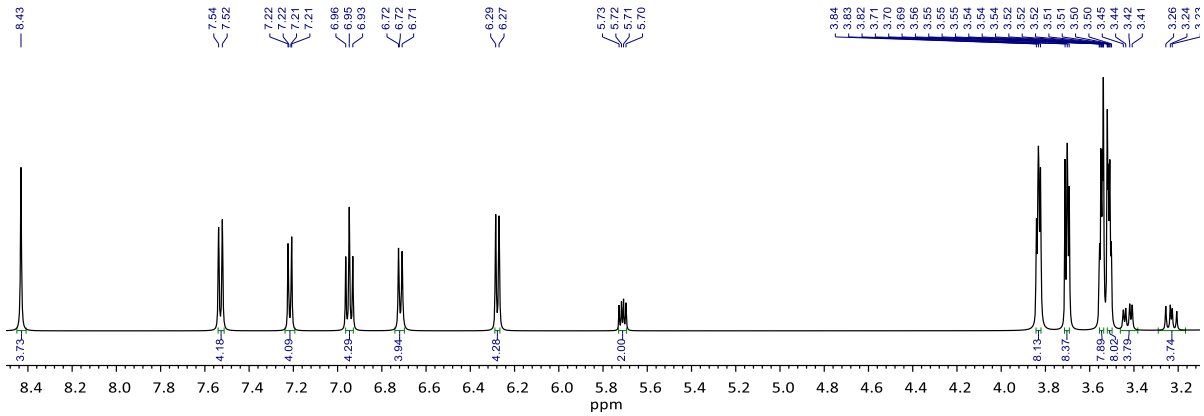

Figure A.30. ^{1}H-NMR spectrum of *pseudo*rotaxane ***L*-10@7** ($CDCl_3$, 500MHz).

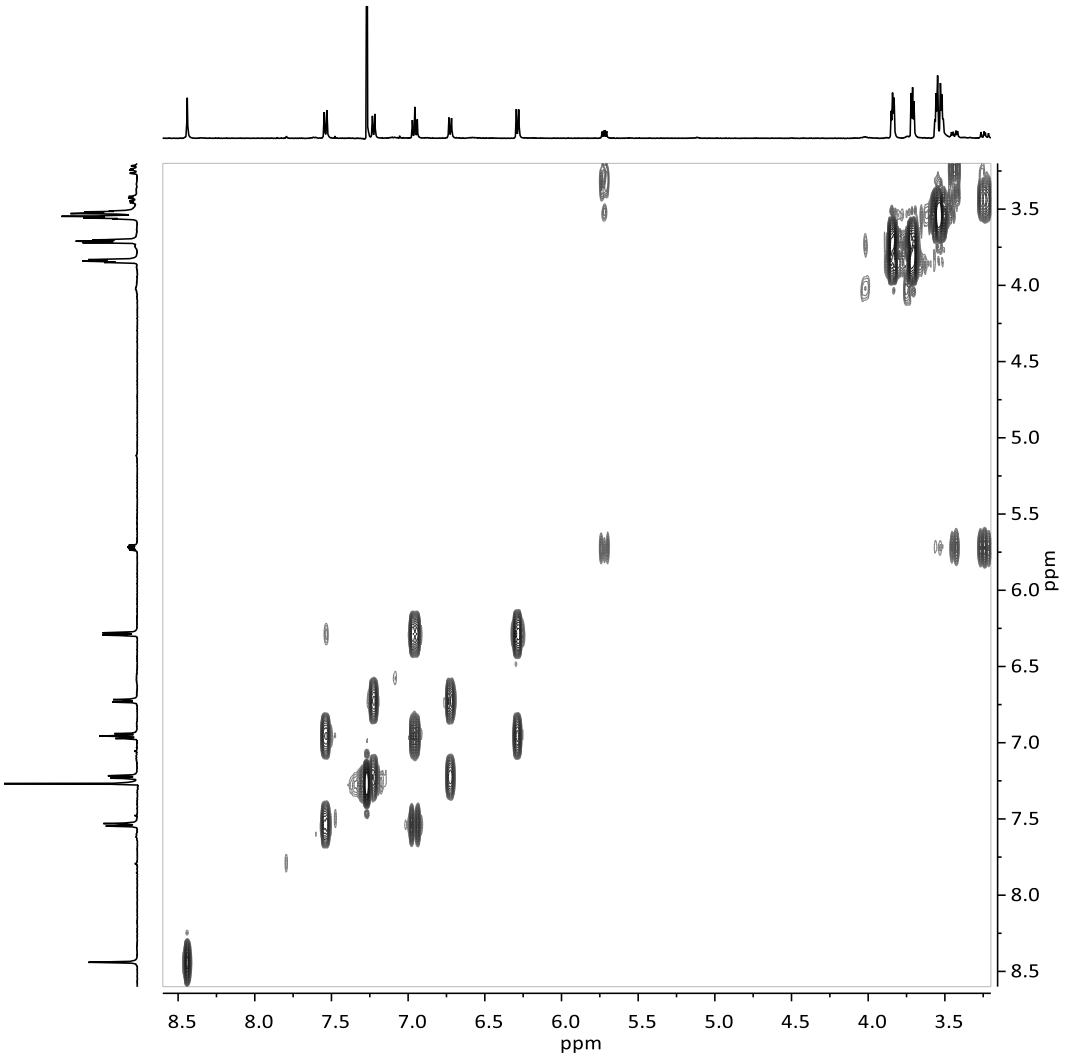

Figure A.31. ^{1}H-^{1}H COSY-NMR spectrum of *pseudo*rotaxane ***L*-10@7** ($CDCl_3$, 500MHz).

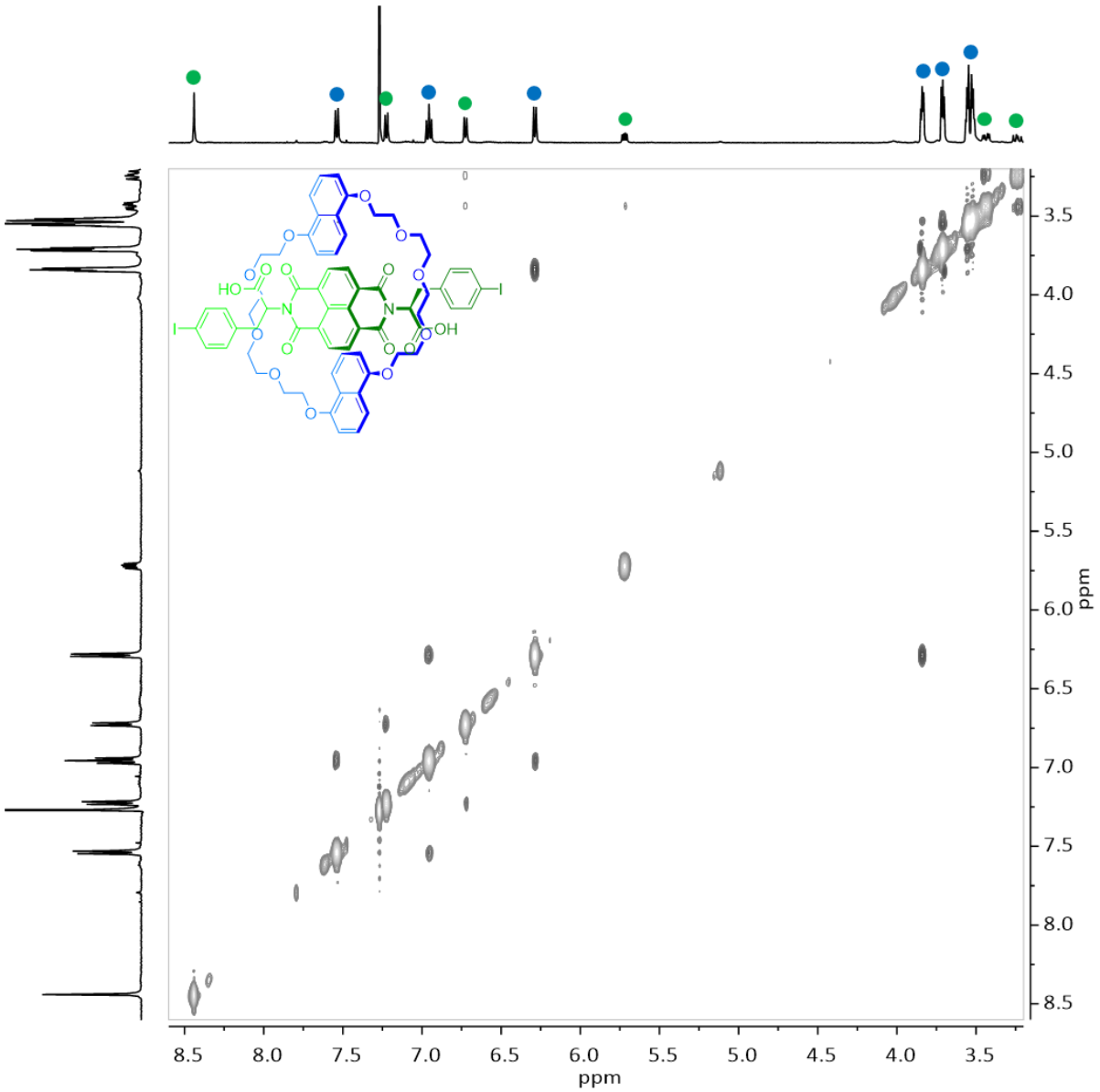

Figure A.32. ^{1}H-^{1}H NOESY-NMR spectrum of *pseudo*rotaxane ***L*-10@7** ($CDCl_3$, 500MHz).

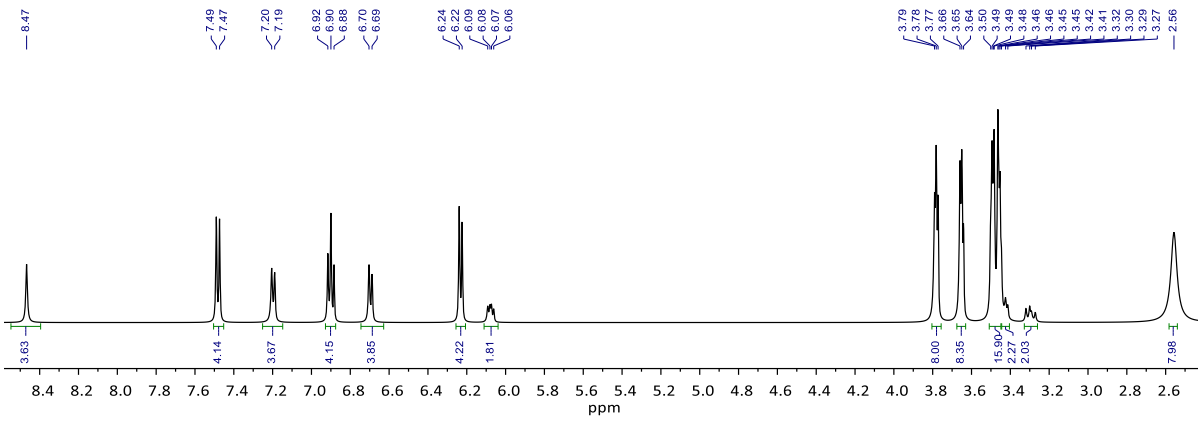

Figure A.33. ^{1}H-NMR spectrum of *pseudo*rotaxane ***L*-11@7** ($CDCl_3$, 500MHz).

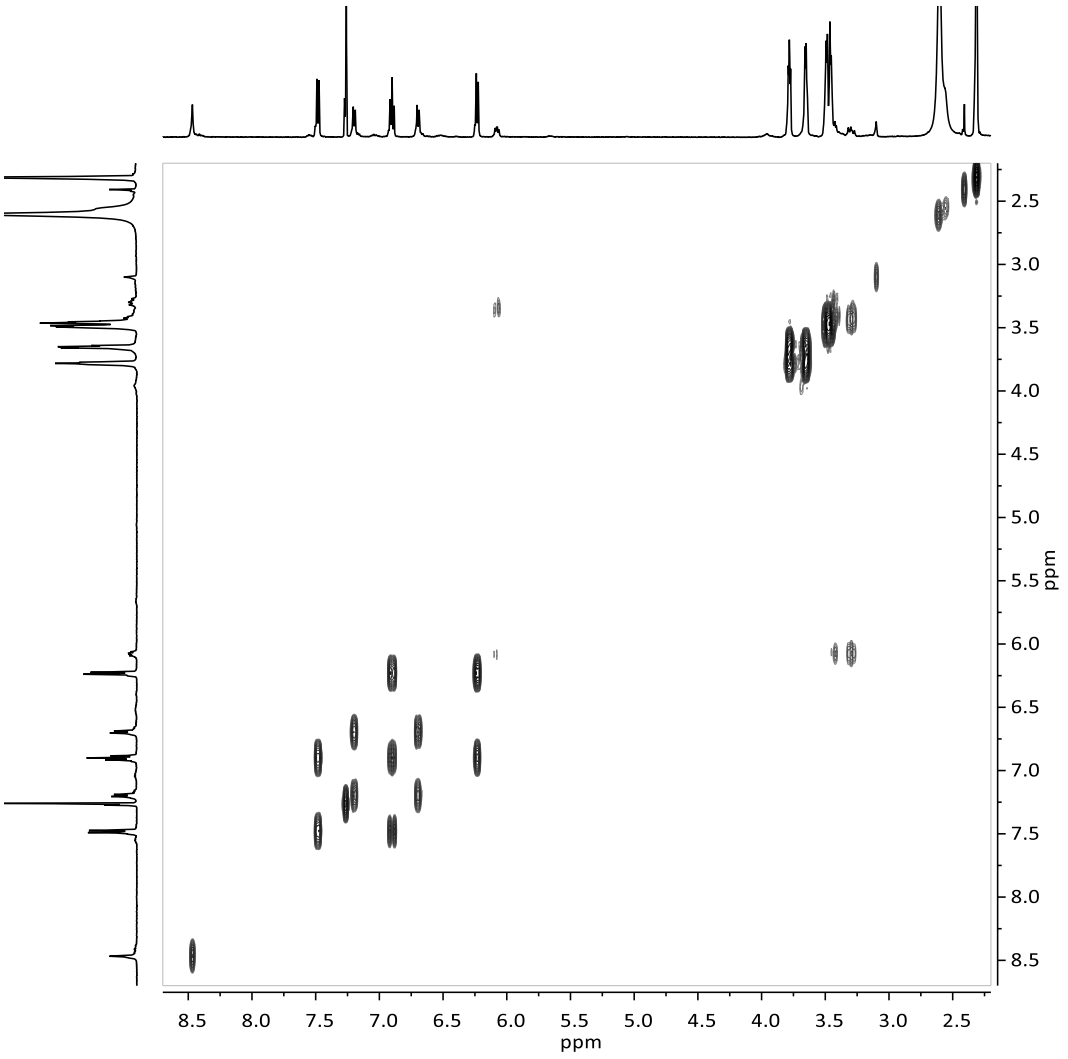

Figure A.34. ^{1}H-^{1}H COSY-NMR spectrum of *pseudo*rotaxane ***L*-11@7** ($CDCl_3$, 500MHz).

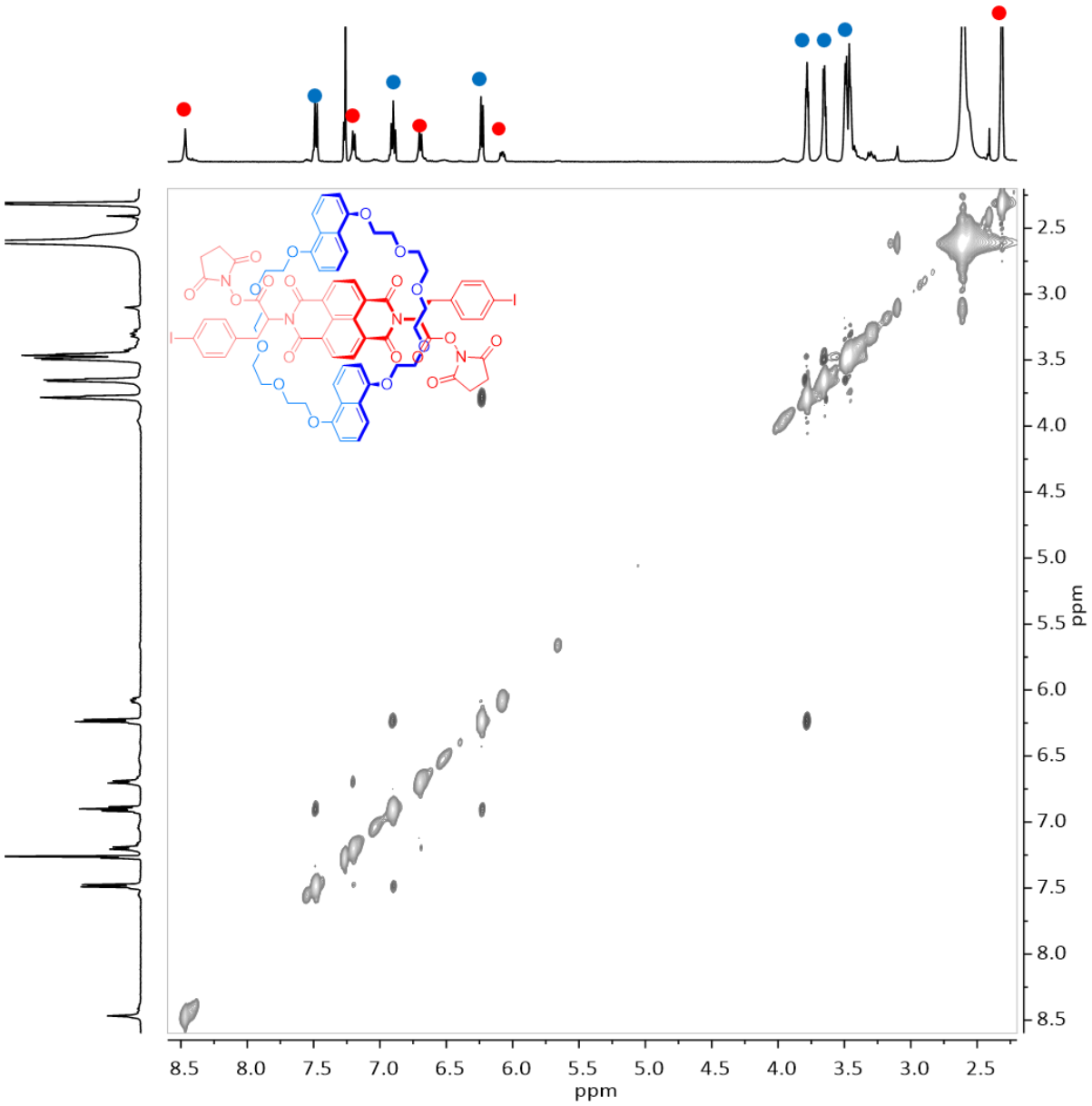

Figure A.35. ^{1}H-^{1}H NOESY-NMR spectrum of *pseudo*rotaxane ***L*-11@7** ($CDCl_3$, 500MHz).

7.2.2. Mass spectroscopy of selected compounds

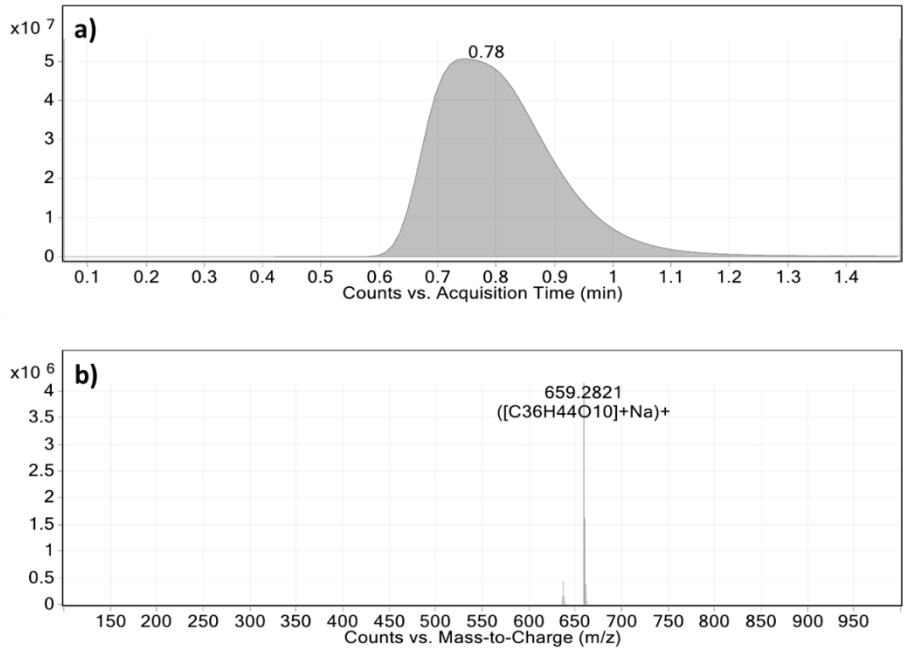

Figure A.36. a) HPLC chromatogram and **b)** ESI$^+$-TOF mass spectrum ([M+Na]$^+$) of compound **7**.

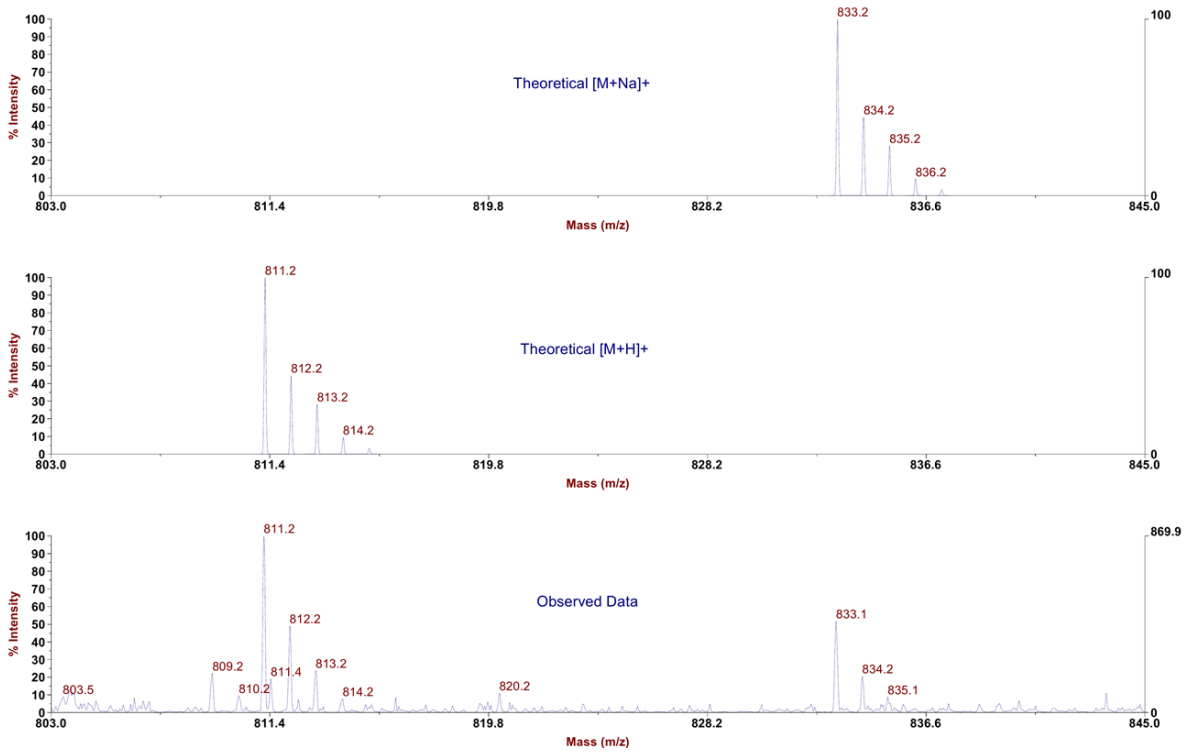

Figure A.37. Solvent-free MALDI mass spectrum of compound **8** (positive mode).

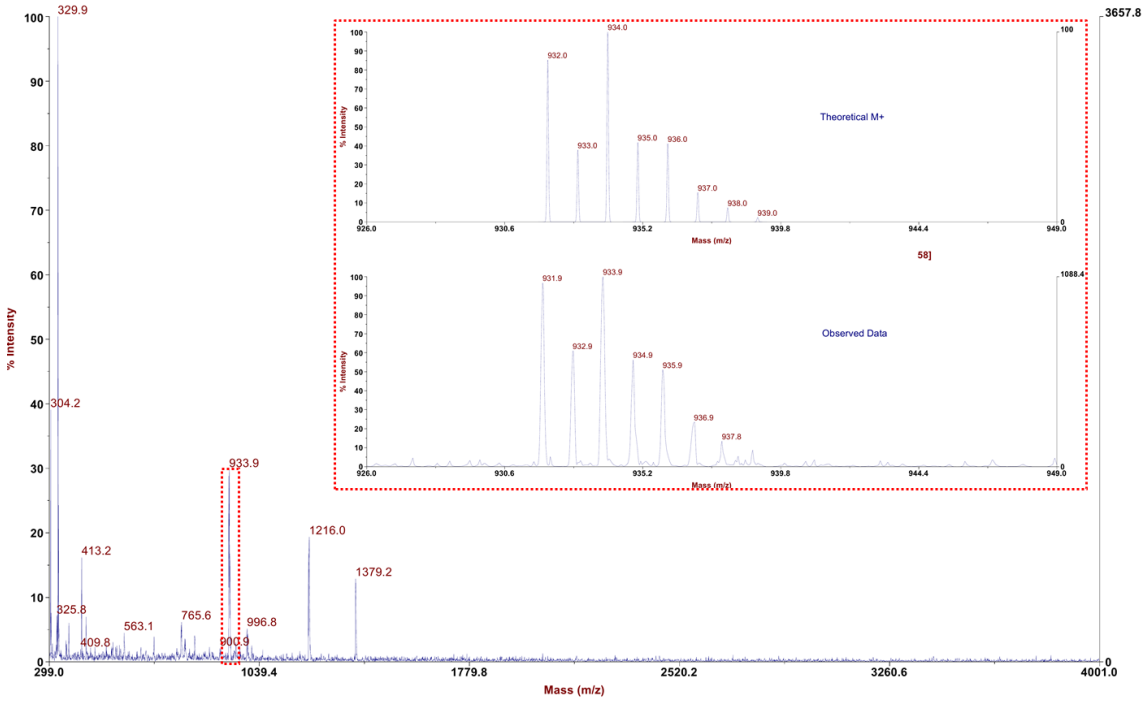

Figure A.38. Solvent-free MALDI mass spectrum of compound **8a** (positive mode).

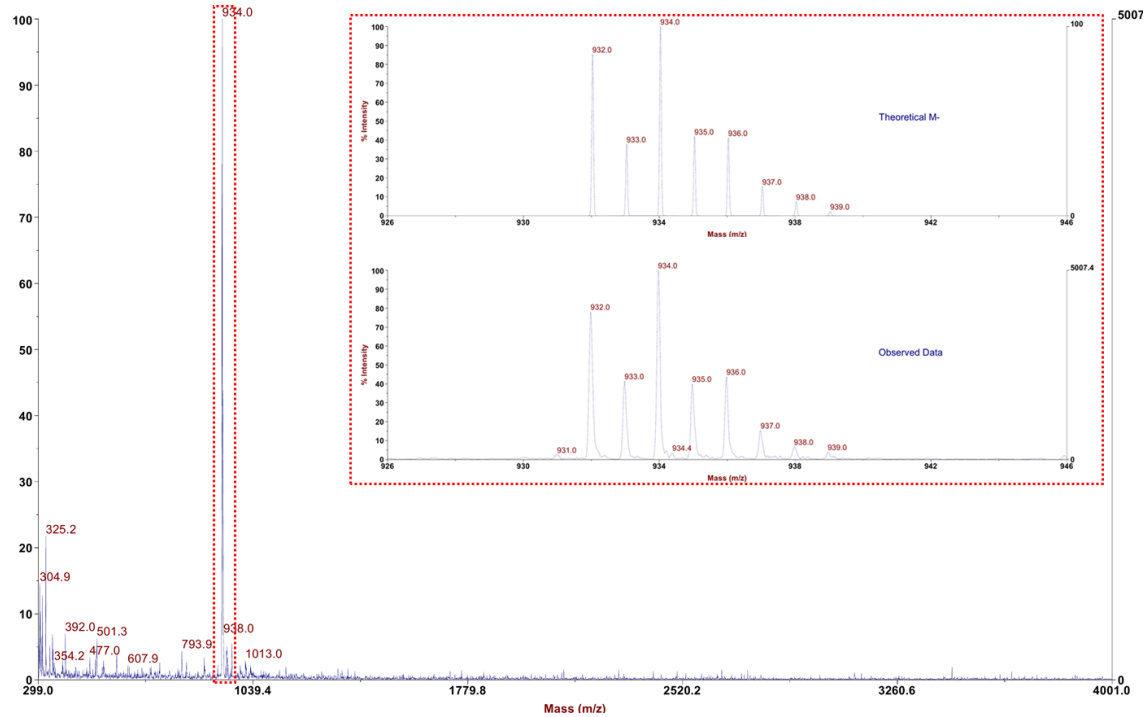

Figure A.39. Solvent-free MALDI mass spectrum of compound **8a** (negative mode).

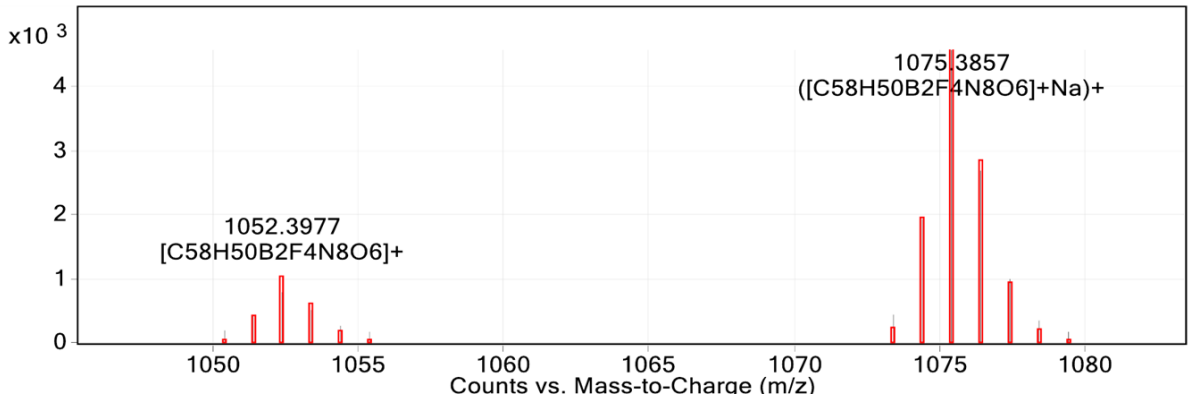

Figure A.40. ESI$^+$-TOF mass spectrum of compound **9** (MeOH) with isotopic patterns of $[M+H]^+$ and $[M+Na]^+$.

7.2.3. UV-visible and fluorescence spectroscopies

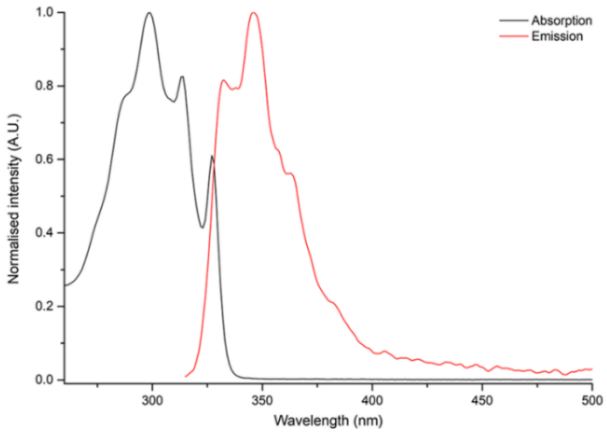

FigureA.41. Normalised absorption(black line) and emission (red line, λ_{ex}=300 nm) spectra of compound **7** (0.025 mM DMSO).

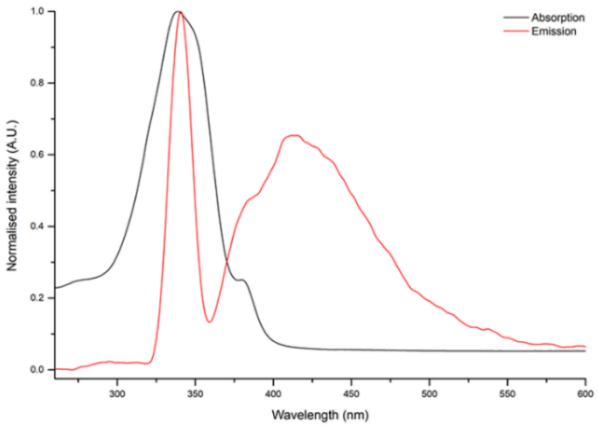

Figure A.42. Normalised absorption(black line) and emission (red line, λ_{ex}=300 nm) spectra of compound **8** (0.025 mM DMSO).

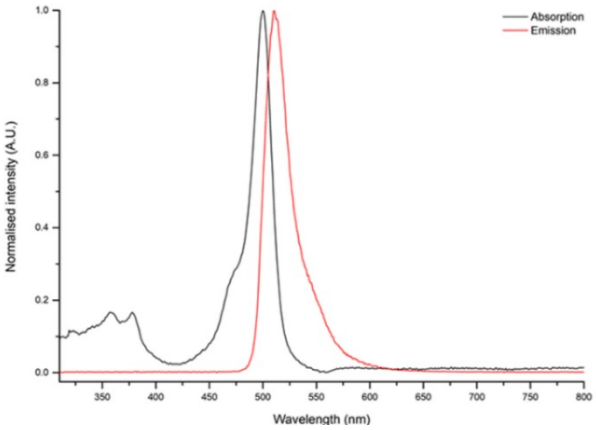

Figure A.43. Normalised absorption(black line) and emission (red line, λ_{ex}=300 nm) spectra of compound **9** (0.025 mM DMSO).

7.2.4. Confocal laser-scanning microscopy

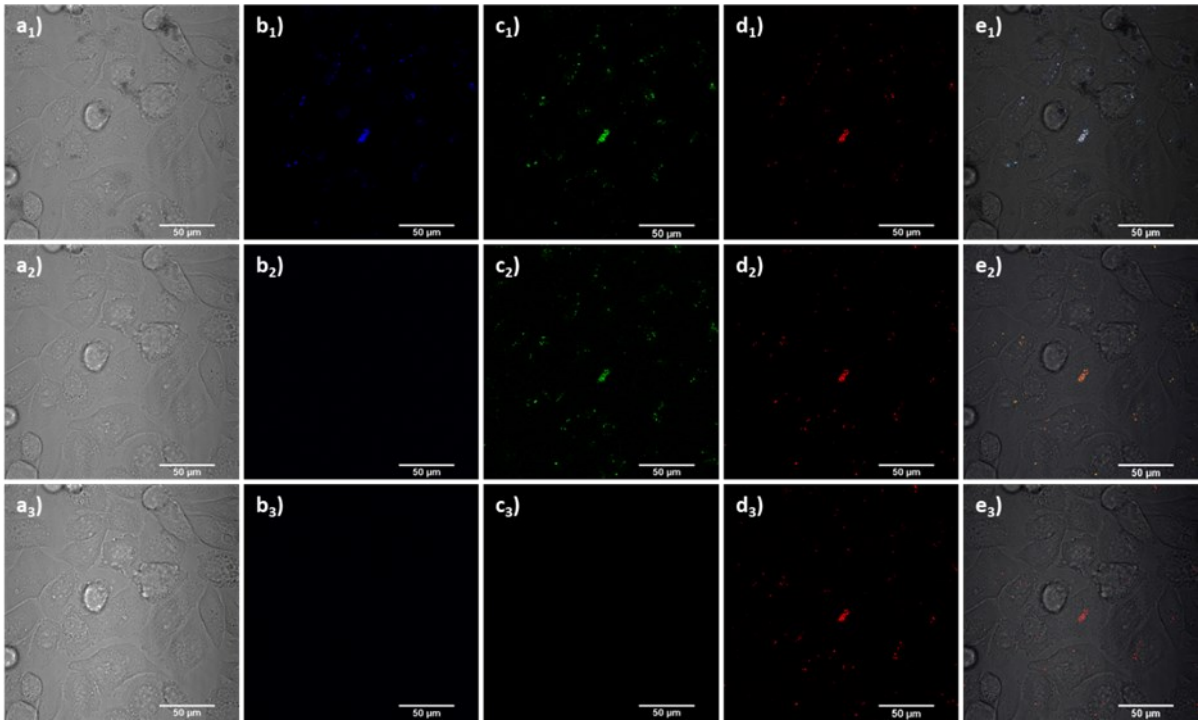

Figure A.44. Single-photon confocal laser-scanning microscopy of PC-3 cells incubated with compound **8** (100 µM, 1:99 DMSO:serum-free medium). **a_1-e_1)** blue channel (λ_{ex}=405 nm; λ_{em}=417-477 nm); **a_2-e_2)** green channel (λ_{ex}=488 nm; λ_{em}=550-650 nm), **a_3-e_3)** red channel (λ_{ex}=561 nm; λ_{em}=570-750 nm). Scale bar: 50 µm.

7.3. Appendices to Chapter 4

7.3.1. NMR spectroscopy of selected compounds

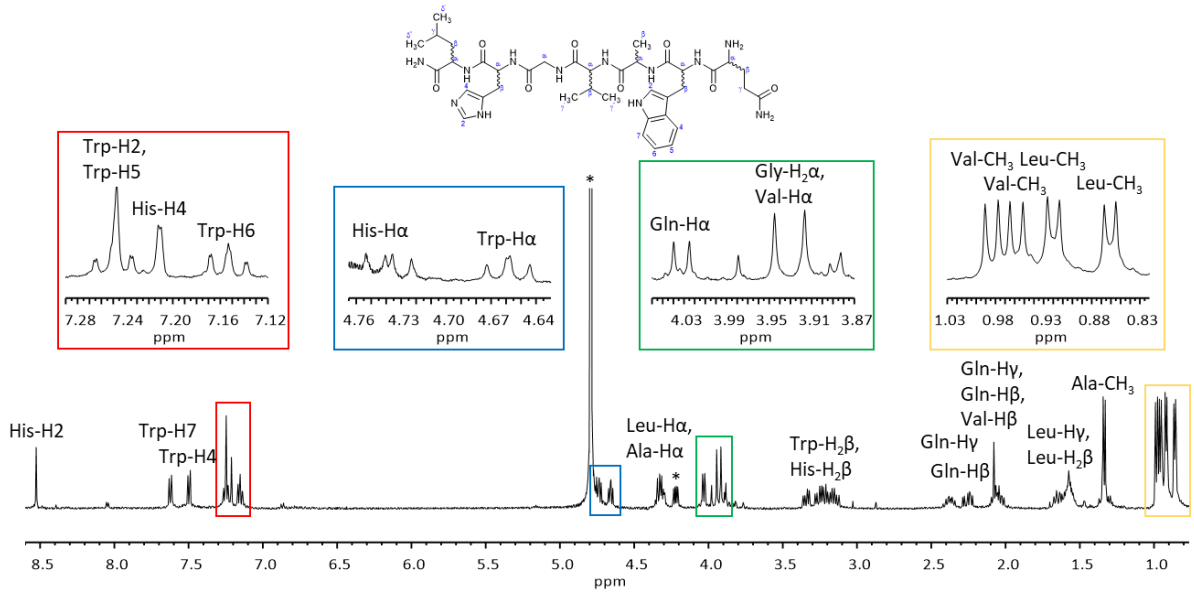

Figure A.45. ^{1}H-NMR spectrum of compound **12** (D_2O, 500 MHz).

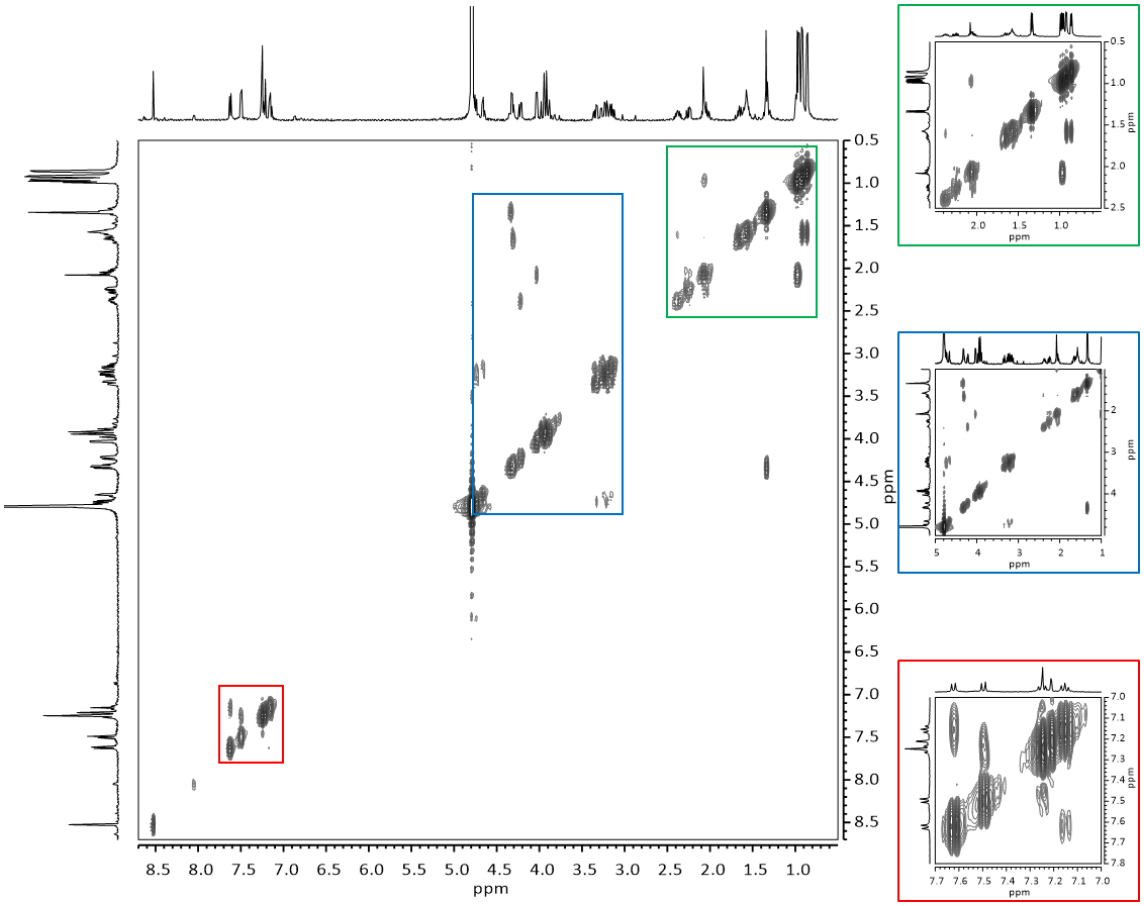

Figure A.46. ^{1}H-^{1}H COSY-NMR spectrum of compound **12** (D_2O, 500 MHz).

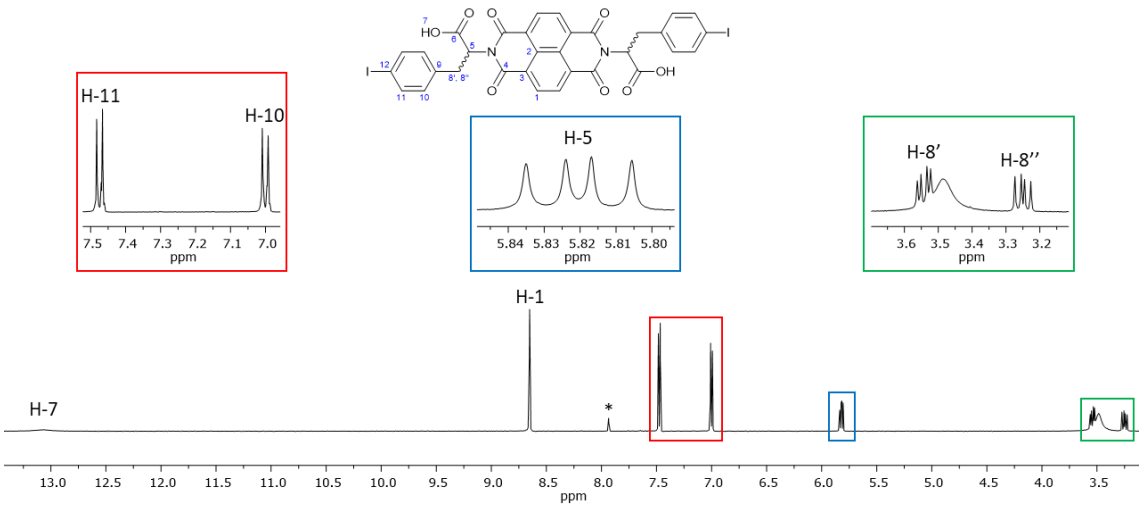

Figure A.43. ^{1}H-NMR spectrum of compound **10** (DMSO, 500 MHz).

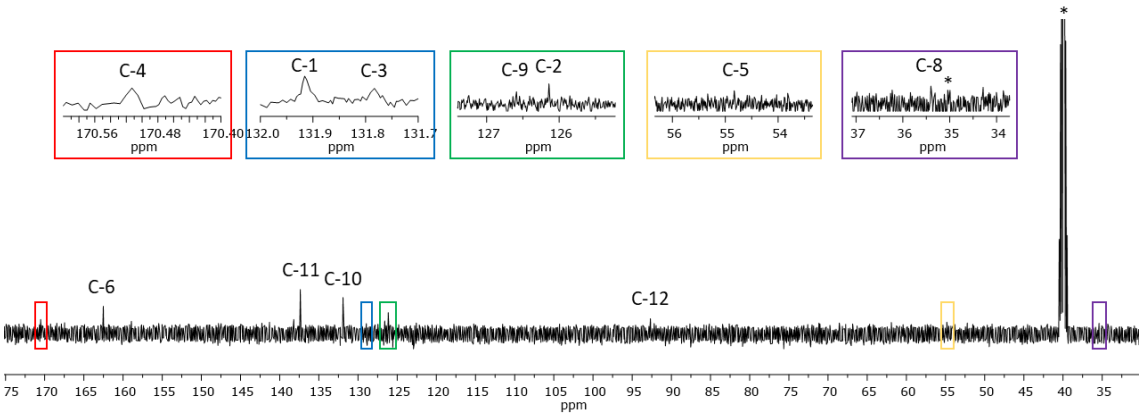

Figure A.47. ^{13}C-NMR spectrum of compound **10** (DMSO, 500 MHz).

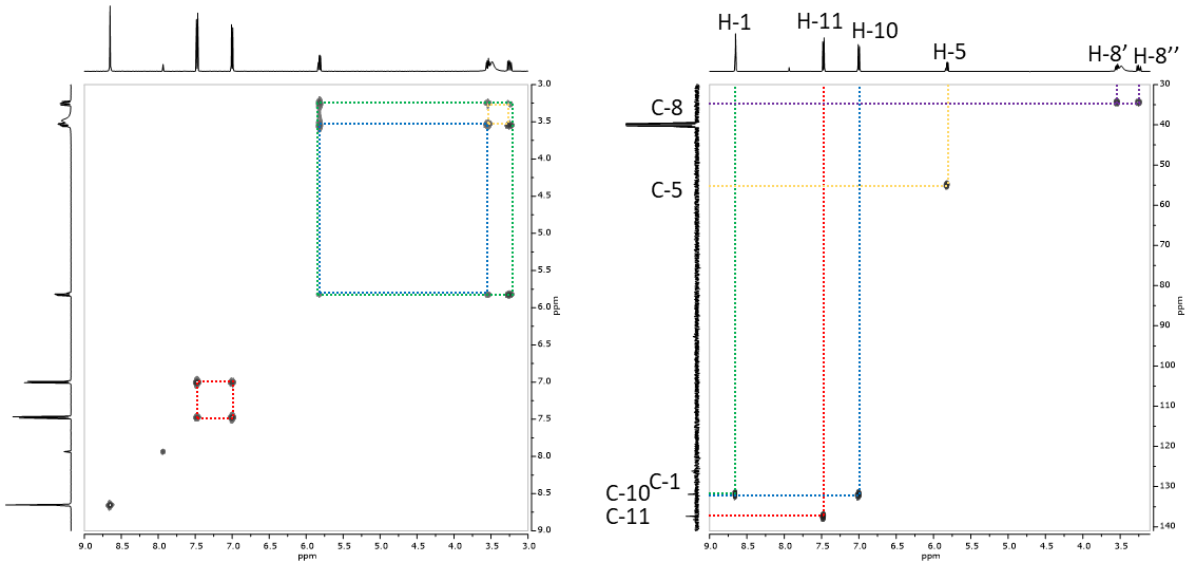

Figure A.48. ^{1}H-^{1}H COSY (left) and ^{1}H-^{13}C HSQC-NMR (right) spectra of compound **10** (DMSO, 500 MHz).

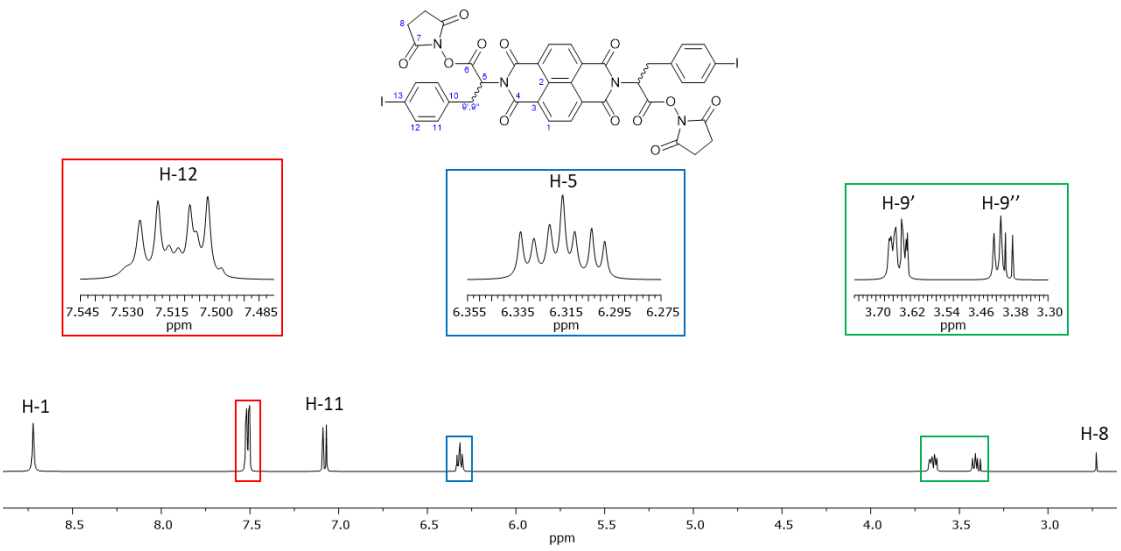

Figure A.49. ^{1}H-NMR spectrum of compound **11** (DMSO, 500 MHz).

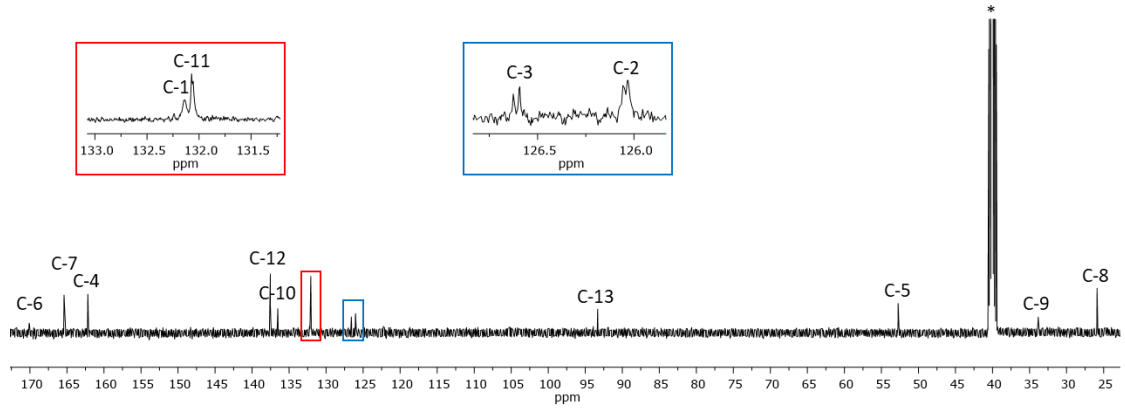

Figure A.50. ^{13}C-NMR spectrum of compound **11** (DMSO, 500 MHz).

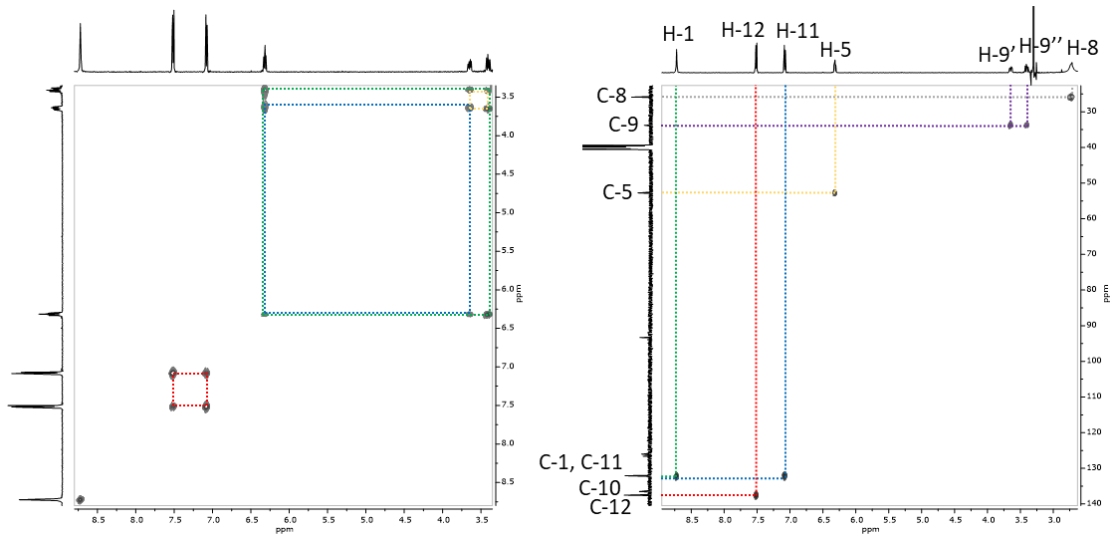

Figure A.51. ^{1}H-^{1}H COSY (left) and ^{1}H-^{13}C HSQC-NMR (right) spectra of compound **11** (DMSO, 500 MHz).

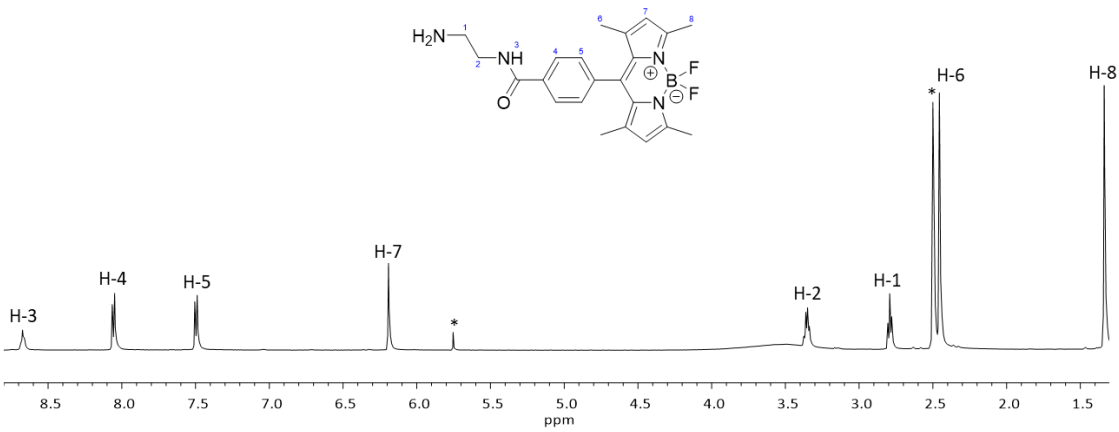

Figure A.52. ^{1}H-NMR spectrum of compound **2** (DMSO, 500 MHz).

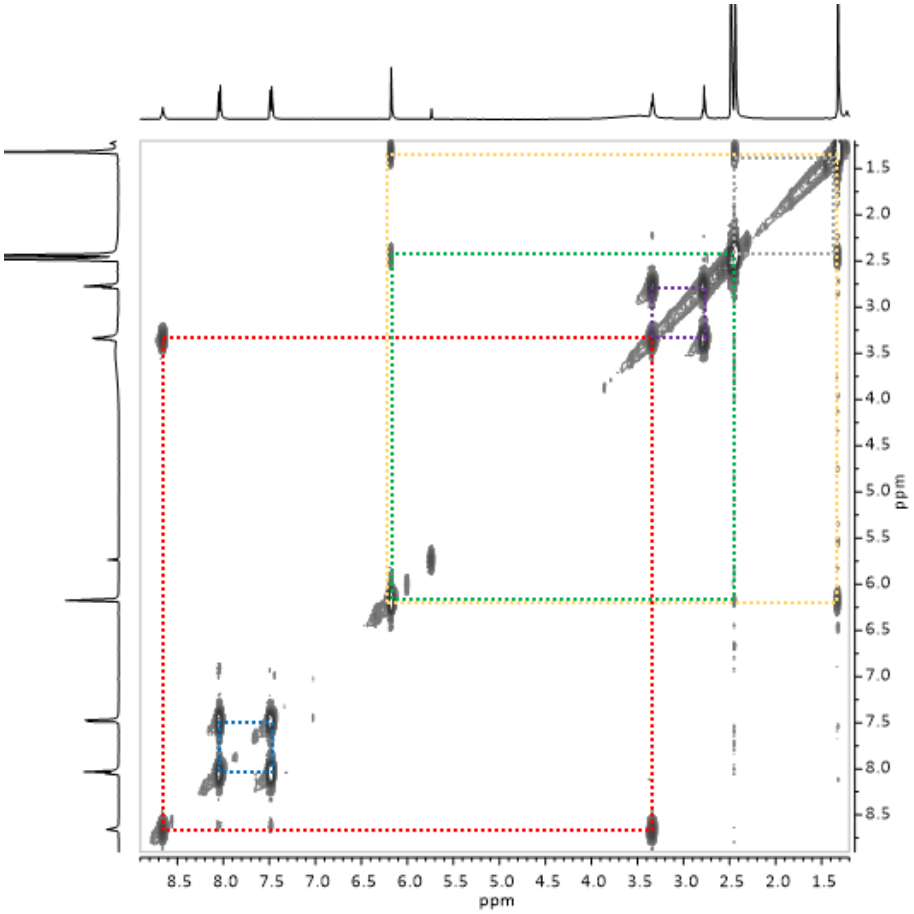

Figure A.53. ^{1}H-^{1}H COSY-NMR spectrum of compound **2** (DMSO, 500 MHz).

7.3.2. Mass spectroscopy of selected compounds

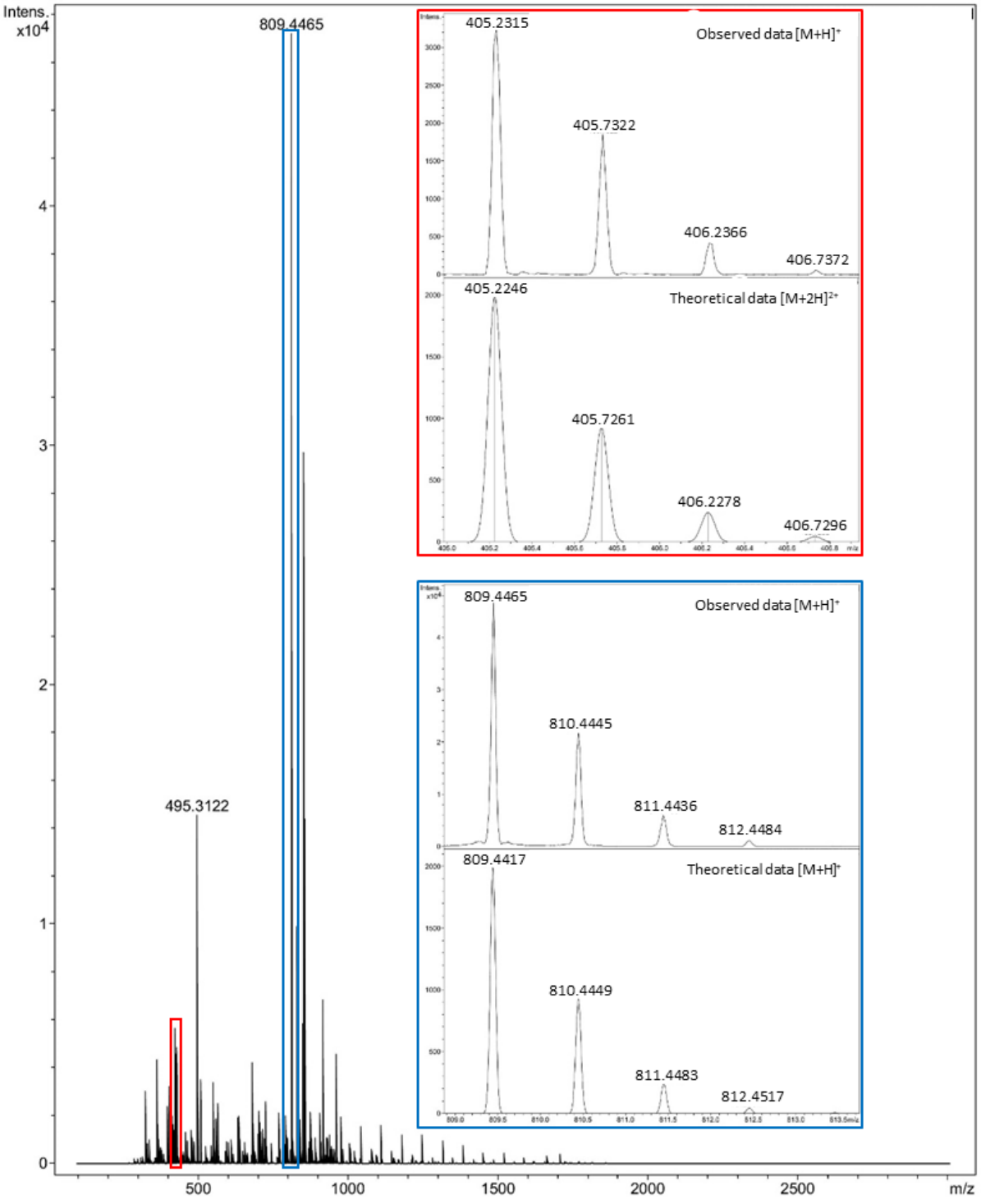

Figure A.54. Mass spectrum of compound **12** (ESI^+-TOF, MeOH).

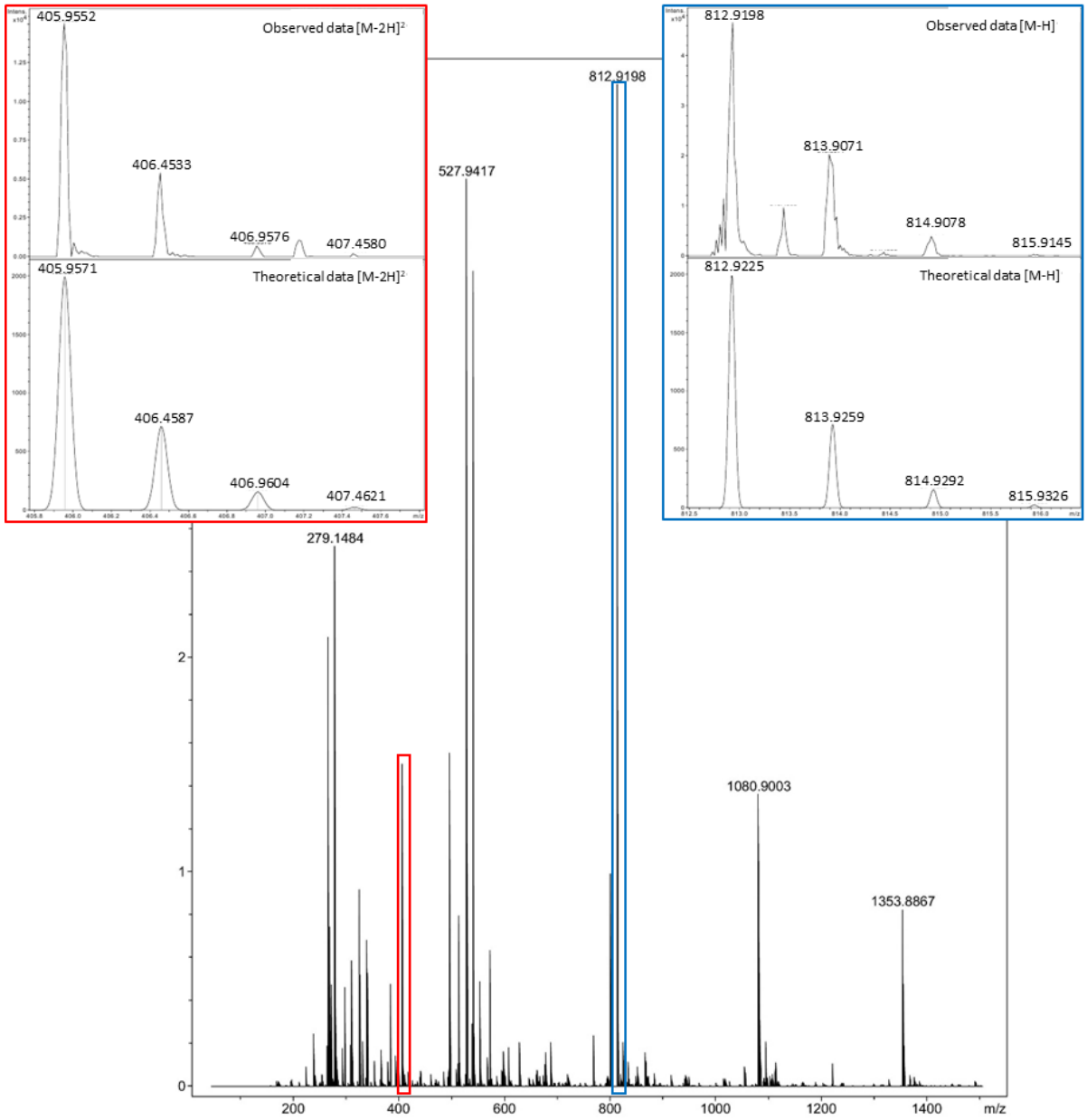

Figure A.55. Mass spectra of compound **10** (ESI^--TOF, MeOH).

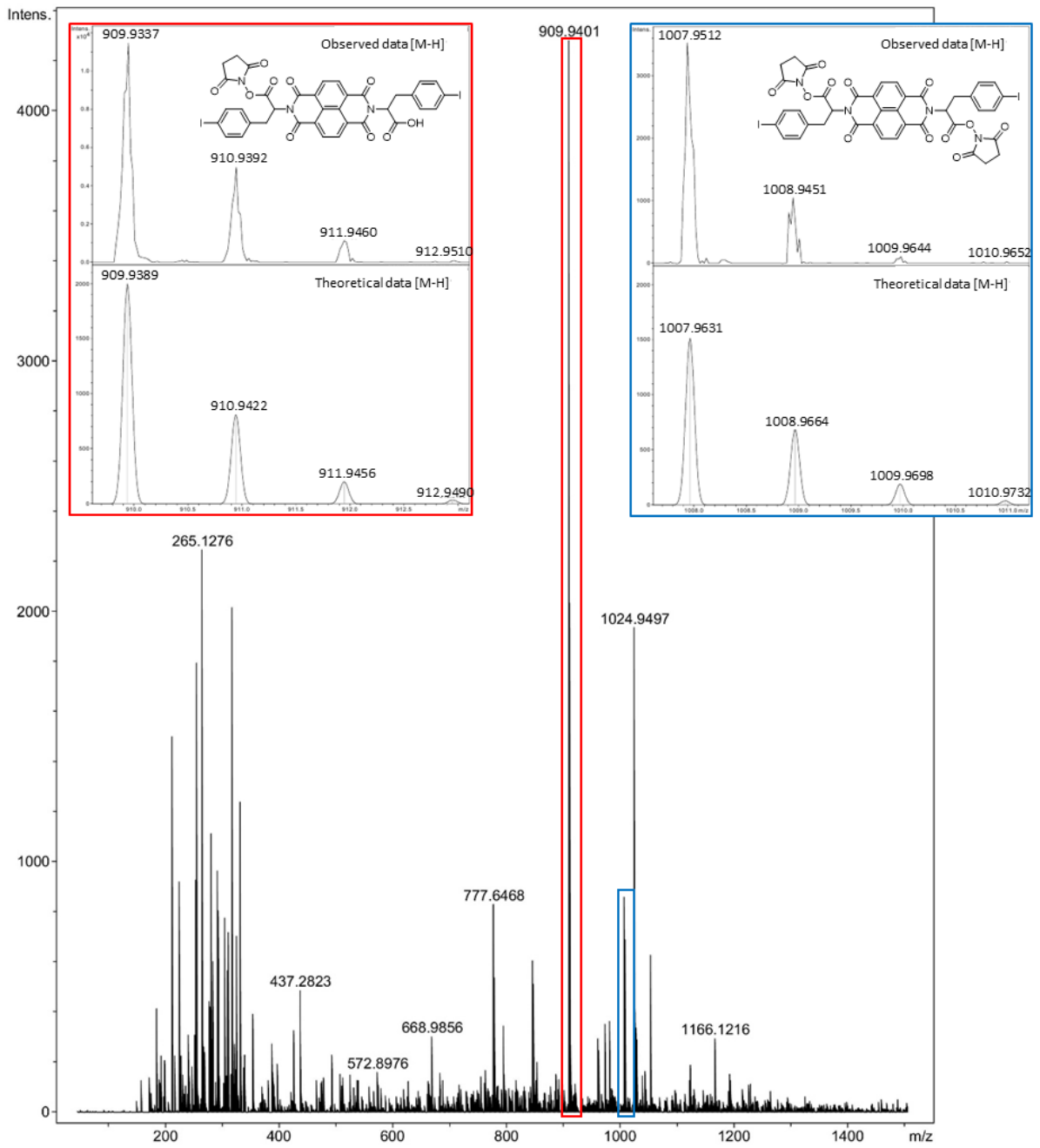

Figure A.56. Mass spectrum of compound **11** (ESI^+-TOF, MeOH).

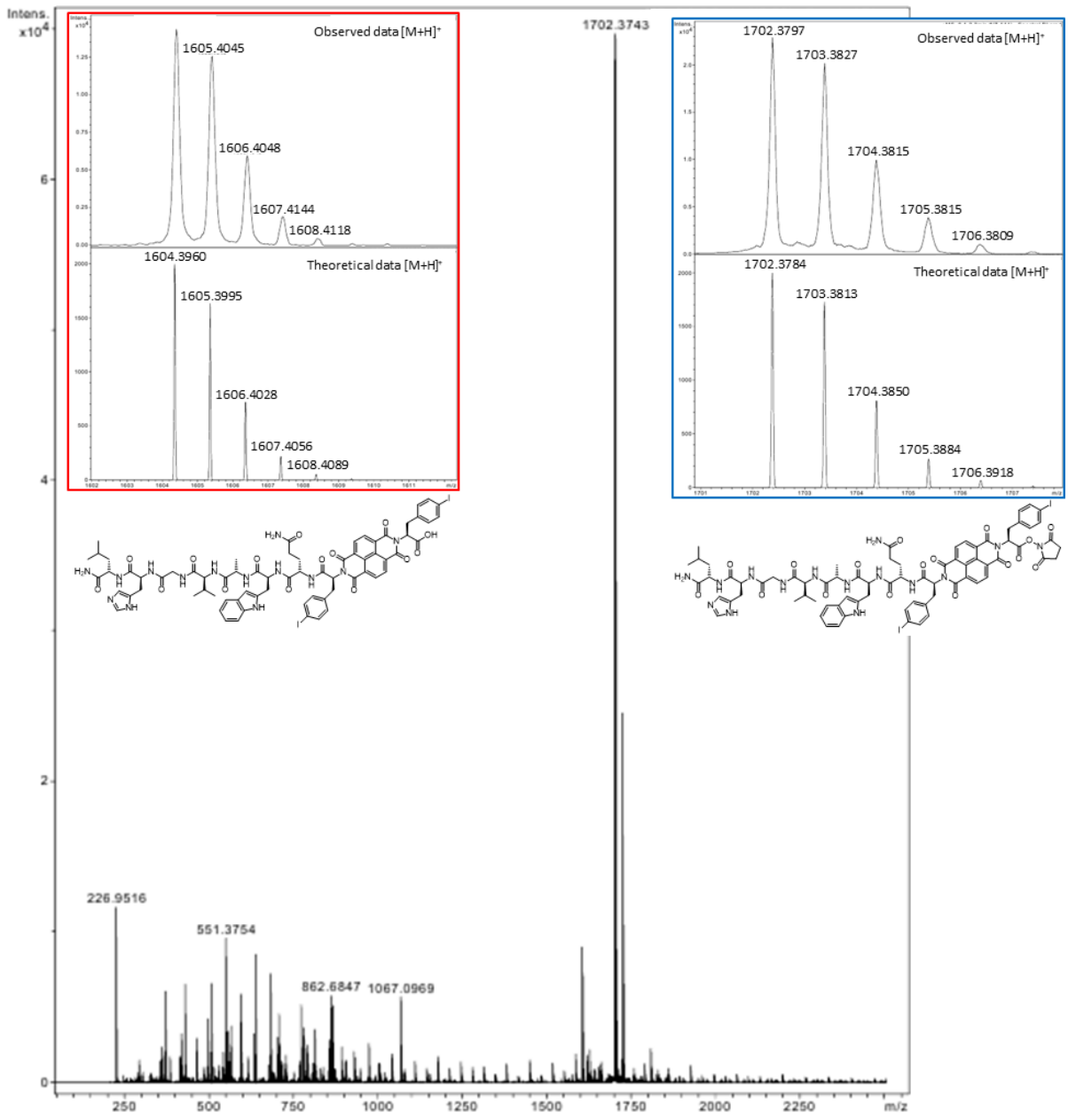

Figure A.57. Mass spectrum of compounds **13** and **13'** (ESI^+-TOF, MeOH).

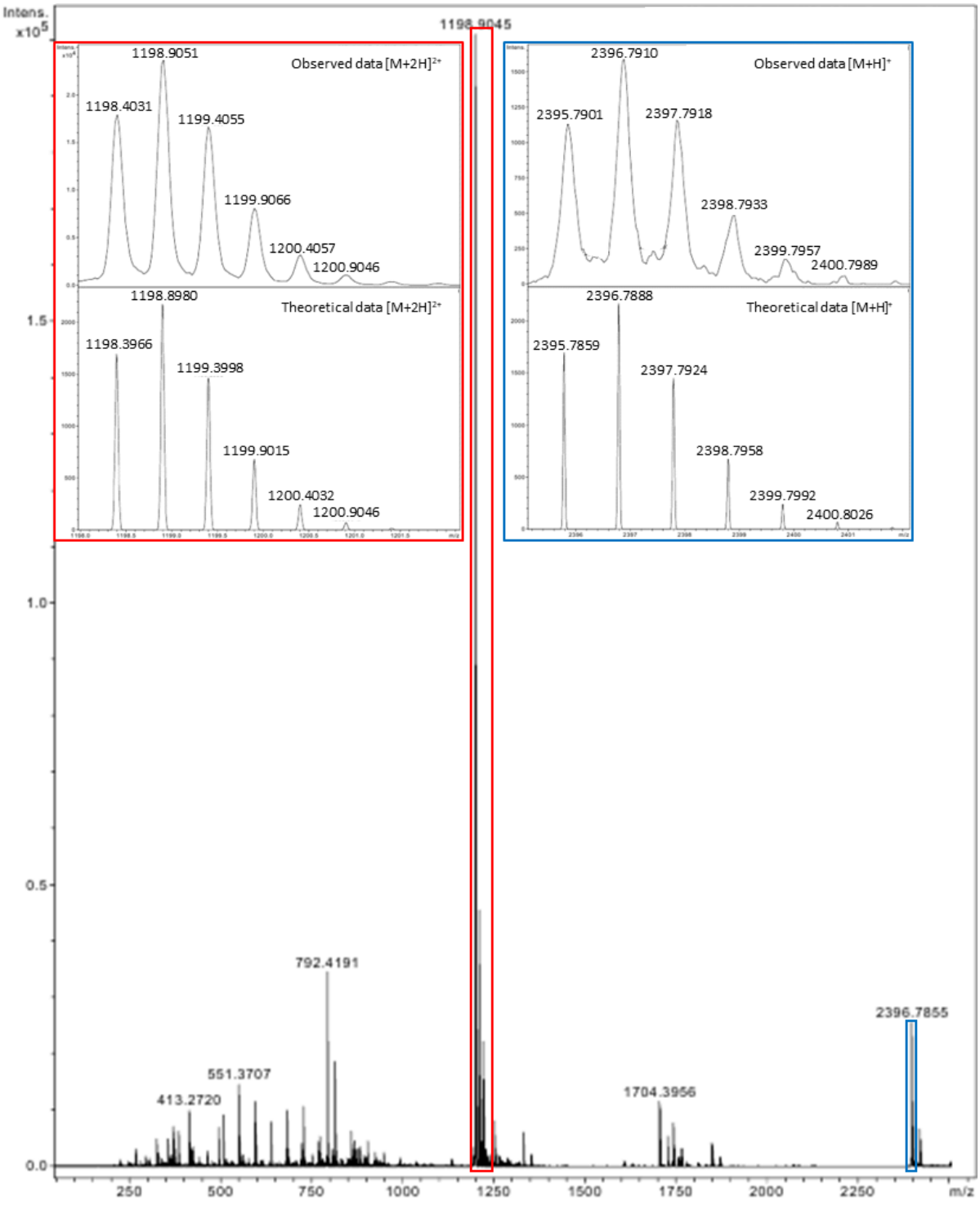

Figure A.58. Mass spectrum of compound **14** (ESI^+-TOF, MeOH).

7.3.3. Circular dichroism spectroscopy

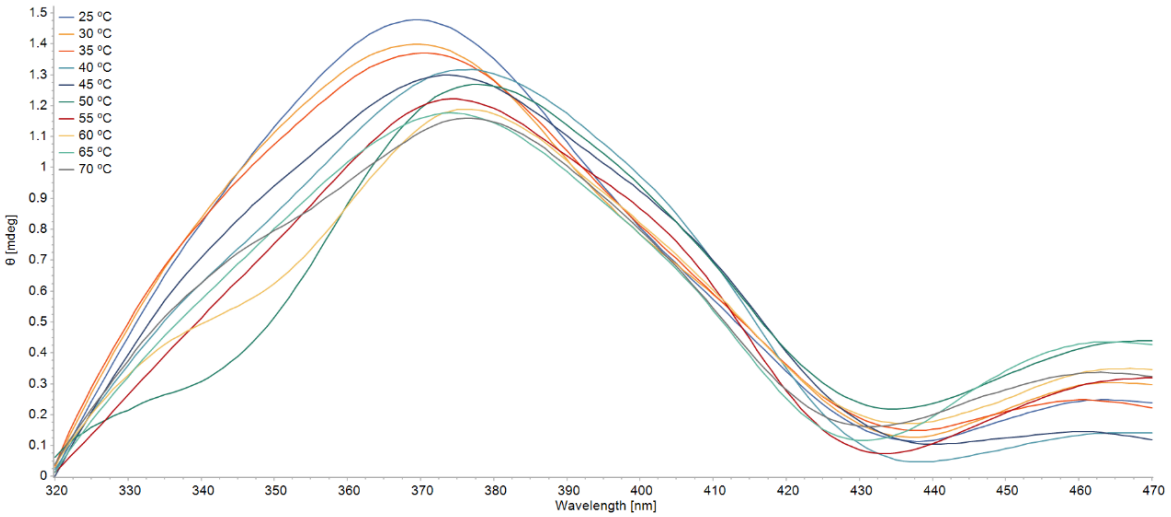

Figure A.59. Variable temperature CD spectra of compound ***L*-13**.

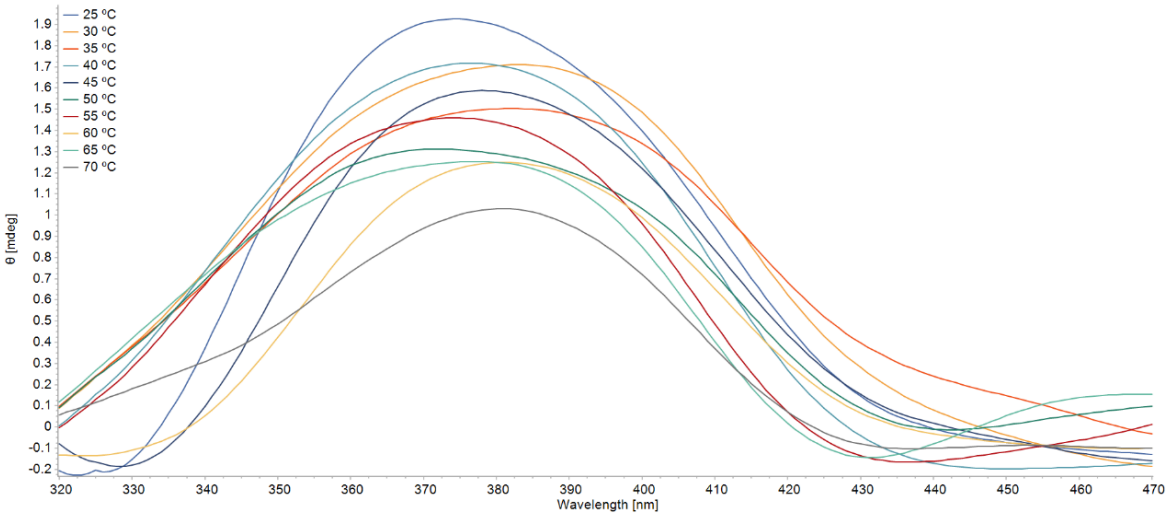

Figure A.60. Variable temperature CD spectra of compound ***L*-14.**

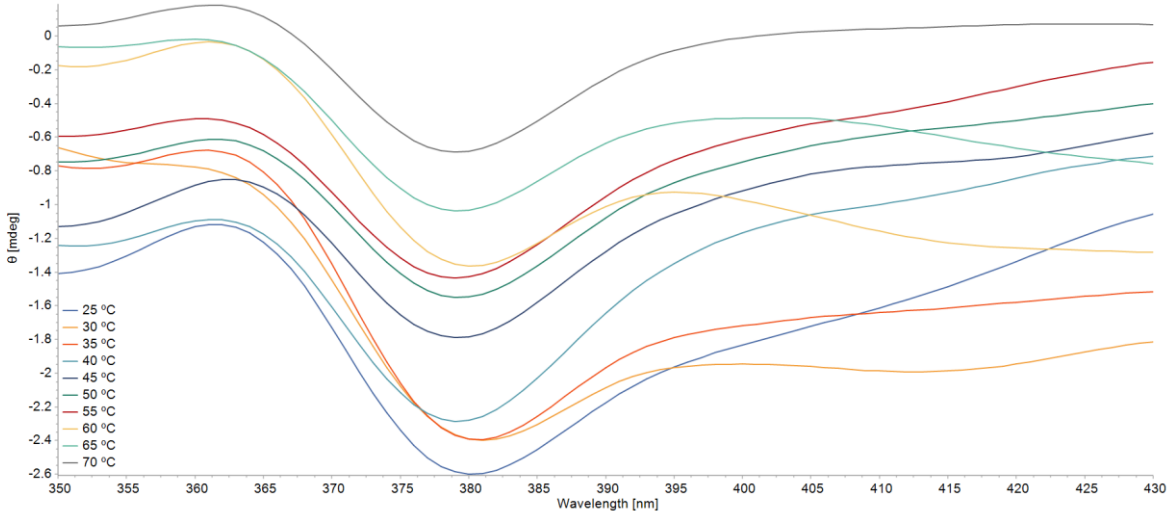

Figure A.61. Variable temperature CD spectra of compound ***D*-13**.

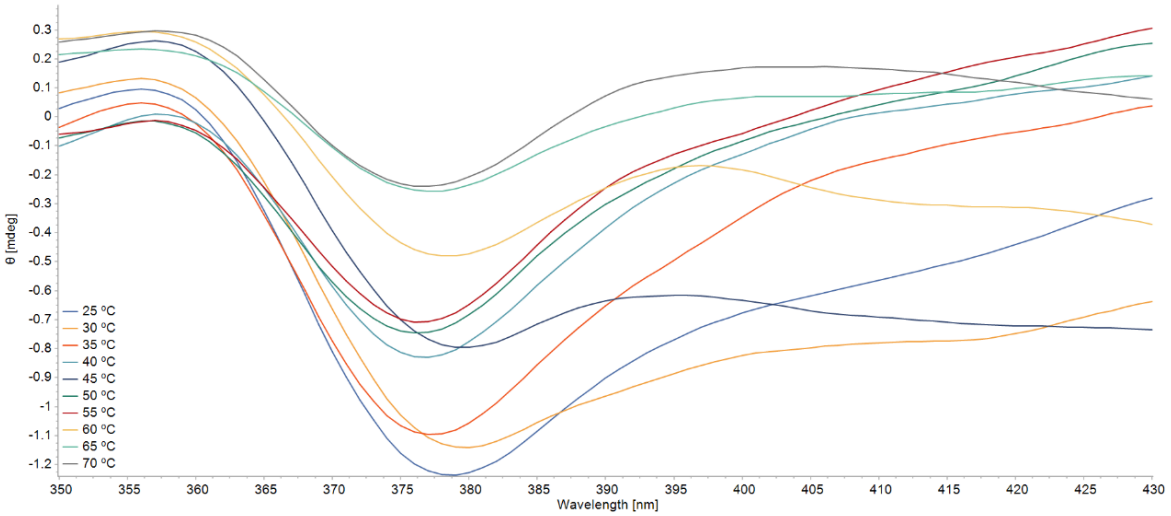

Figure A.62. Variable temperature CD spectra of compound ***D*-14**.

7.3.4. HPLC chromatography

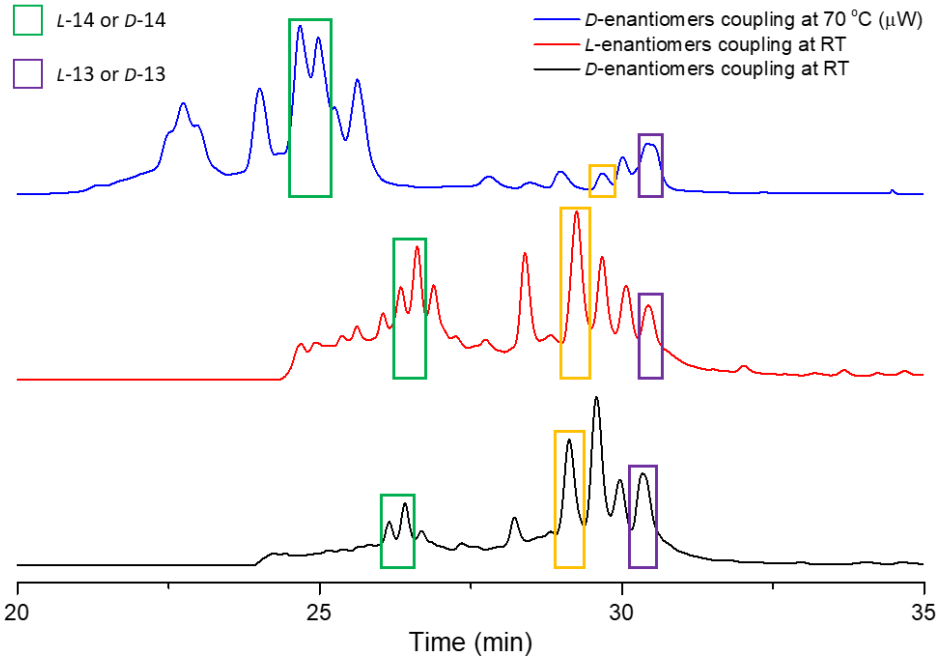

Figure A.63. Comparative semi-preparative HPLC chromatograms of the μW-assisted synthesis of ***D*-13** and ***D*-14** (in blue), the RT syntheses of ***L*-13** and ***L*-14** (in red) and RT synthesis of ***D*-13** and ***D*-14** (in black). The fractions of ***L*-14** (or ***D*-14**) are reported in green; the purple rectangles display the fractions of ***L*-13** (or ***D*-13**). Method B described in Experimental Section.

7.3.5. Investigations into the peptide-NDI aggregation morphologies

The morphology and aggregation behaviour of the proposed imaging probes were analysed by scanning electron microscopy (SEM). In Figures A.64 and A.65, the SEM micrographs of both enantiomers of **13** and **14** are reported in different conditions to assess the effect of the starting solvent on the aggregation of these molecules. Such compounds were freeze-dried overnight from two different solvent systems, *i.e.* H_2O:CH_3CN (1:1) (Figure A.64) and DMSO (Figure A.65), then the obtained solid was placed on mica support and coated by gold.

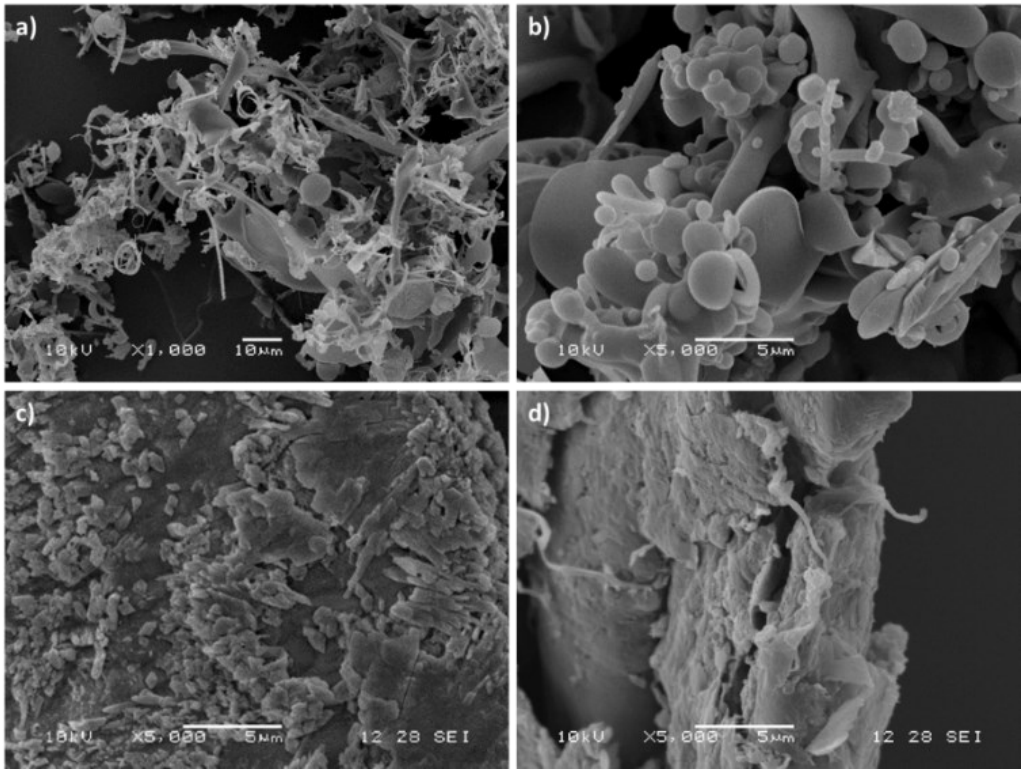

Figure A.64. SEM micrographs of compounds **a)** ***L*-13**, **b)** ***L*-14**, **c)** ***D*-13** and **d)** ***D*-14** after a freeze-drying overnight from a solution of H_2O:CH_3CN (1:1).

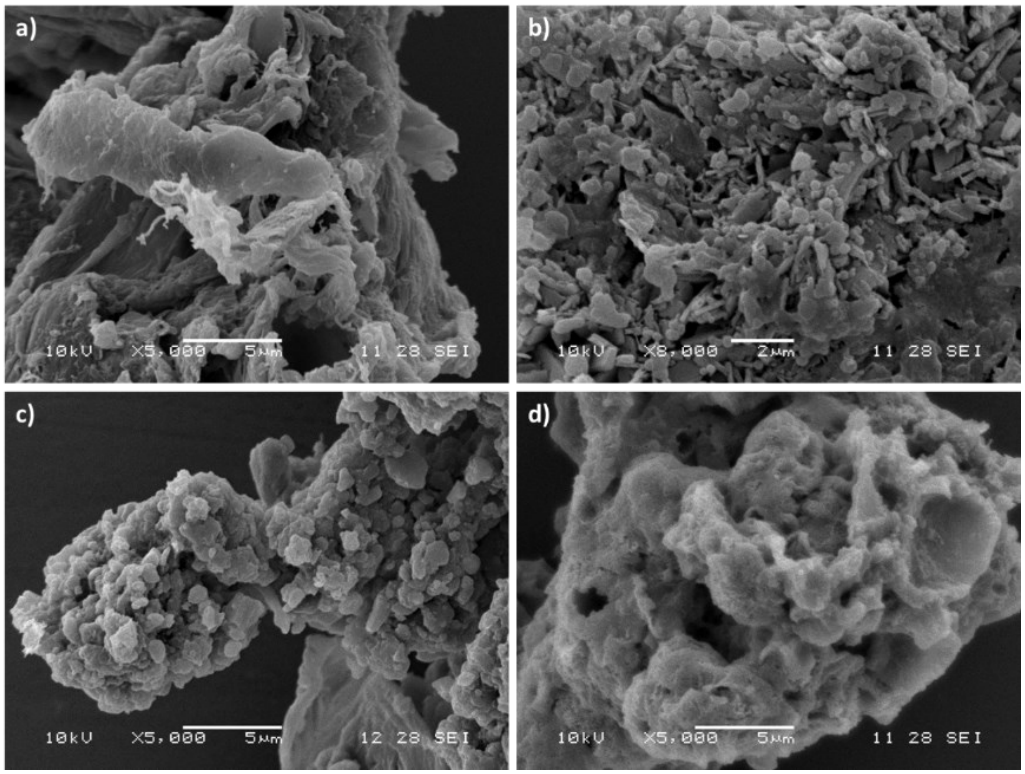

Figure A.65. SEM micrographs of compounds **a)** ***L*-13**, **b)** ***L*-14**, **c)** ***D*-13** and **d)** ***D*-14** after a freeze-drying overnight from a solution of DMSO.

Figure A.64a shows the micrograph of ***L*-13** after freeze-drying overnight from H_2O:CH_3CN mixture in 1:1 ratio. It can be noticed that this molecule prefered to aggregate as coils and long shaped assemblies. Such phenomenon can be attributed to the intermolecular π-π stacking of the aromatic rings of the NDI-core. On the other hand, ***L*-14** (Figure A.64b) presented mainly globular shapes which can be associated with weak intra- and intermolecular interactions among molecules that curled up these species. The morphology and solid-state aggregation behaviour of the *D*-species (***D*-13** and ***D*-14**) are depicted in Figure A.64c and A.64d, respectively. These enantiomers present mainly globular shapes which can be due to their weak interaction among themselves.

In the overnight freeze-drying condition from DMSO (Figure A.65), all four compounds did not show any substantial changes in their morphology and aggregation status. The starting solvent did not affect the organisation of the molecules in solution and, therefore once they were dried, they present the same organisation and morphology as shown previously. This phenomenon can be attributed to the fact that both solvent systems may act in the same manner for organising the structure of the compounds in solution which remain unchanged when they are in solid-state. In this measuring scale, it was not possible to evaluate the effect of the stereochemistry in the morphology of the different couples of enantiomers.

To explore the fluorescence characteristics in the solid-state, the synthesised probes (***L*-13**, ***L*-14**, ***D*-13**, ***D*-14** and **15**) were analysed by confocal laser-scanning microscopy (CLSM), interfaced with the Airyscan technology[1]. This method has been recently used to improve resolution in acquired images of fluorophores, either in living species or solid-state[2]. The Airyscan detection consists of a concentrically arranged hexagonal array of 32 single detector elements which each element acts as a small pinhole.

In a standard confocal microscope, the out-of-focus light, emitted by the specimen, is rejected by the only pinhole set in the microscope. The opening or closing of the pinhole decides how much light reaches the detector. In addition, a minuscule aperture of the pinhole makes the image sharper, increasing the resolution. However, if the pinhole is very small, most of the emitted light can be lost[1]. Airyscan detection has found a balance between resolution and light efficiency. This is possible thanks to its sophisticated arrays of detector elements which allows to all photons to reach the detector, increasing the signal-to-noise ratio, and therefore resolution

[1] J. Huff, *Nat. Methods*, 2015, **12**, 1205.
[2] J. Huff, I. Kleppe, A. Naumann and R. Nitschke, *Na. Methods*, 2018.

(1.7x higher than standard CLSM), sensitivity and speed of detection[1]. In these perspectives, this technology is also known as super-resolution confocal laser-scanning microscopy.

The following figures display the confocal laser scanning micrographs obtained with Airyscan detector of ***L*-13** (A.66a_1-e_1), ***L*-13** (A.66a_2-e_2), ***D*-14** (A.66a_3-e_3), ***D*-14** (A.66a_4-d_4) and **15** (A.66a_5-d_5) in a thin film on Petri dishes, after freeze-drying overnight.

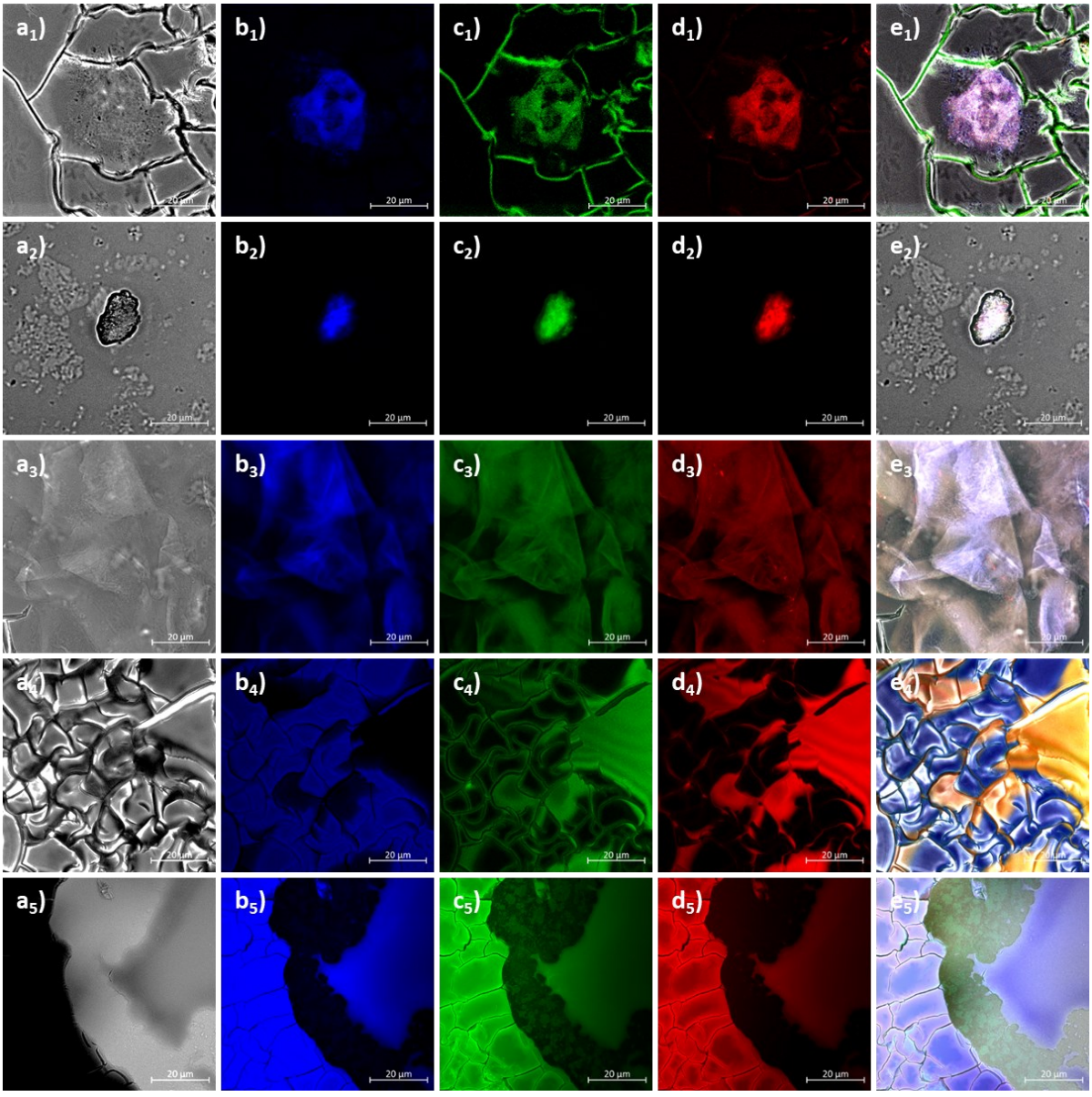

Figure A66. Confocal laser-scanning micrographs (obtained with Airyscan detector) of compounds **a_1-e_1) *L*-13**, **a_2-e_2) *L*-14**, **a_3-e_3) *D*-13**, **a_4-e_4) *D*-14** and **a_5-e_5) 15**. **$a_{1\text{-}5}$)** bright field; **$b_{1\text{-}5}$)** blue channel: λ_{ex}=405 nm, λ_{em}=420-480 nm; **$c_{1\text{-}5}$)** green channel: λ_{ex}=488 nm, λ_{em}=495-550 nm; **$d_{1\text{-}5}$)** red channel: λ_{ex}=561 nm, λ_{em}=555-620 nm; **$e_{1\text{-}5}$)** overlay of blue, green and red channels. The samples were placed in thin film on a Petri dish and freeze-dried overnight. Scale bar: 20 µm.

The fluorescence analysis in a thin film of the proposed probes pointed out that emitted in the expected emission wavelength ranges found in the fluorescence EEM. Particularly, they presented emissions in the blue (λ_{em}=420-480 nm), green (λ_{em}=495-550 nm) and red channels (λ_{em}=555-620 nm). In addition, in this measuring scale, it can be noticed that these species form aggregates in "sheet" and "globular" shapes. These results are consistent with the surface aggregation morphology imaged by SEM. For instance, ***L*-14** shows granular and globular shapes in this measuring scale (Figure A.66a_2-e_2) which can be also noticed in the small-scale measure of SEM (Figures A.64b and A.65b).

7.3.6. Confocal laser-scanning microscopy

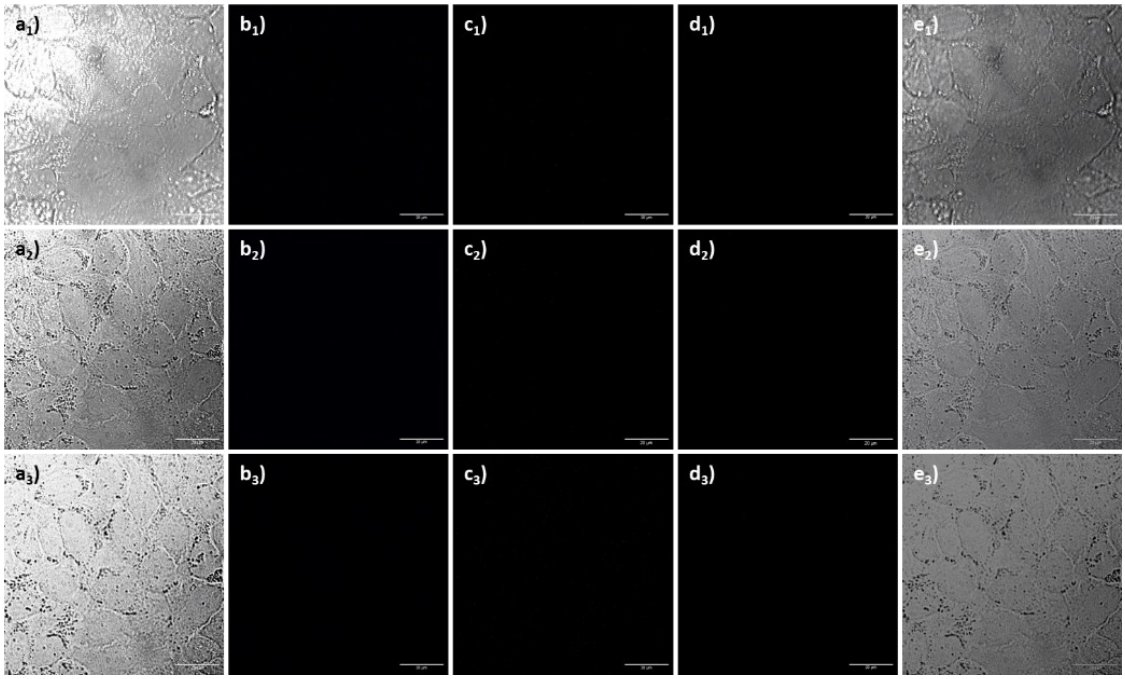

Figure A.67. Single-photon confocal laser-scanning microscopy of A431 cells incubated at 37 °C for 20 min with DMSO (0.1 mM, 1:99 DMSO:serum-free medium). **a_{1-3})** TD channel; **b_{1-3})** blue channel (λ_{em}=417–477 nm); **c_{1-3})** green channel (λ_{em}=500–550 nm); **d_{1-3})** red channel (λ_{em}=570–750 nm); **e_{1-3})** overlay of TD, blue, green and red channels. **a_1-e_1)** λ_{ex}=405 nm, **a_2-e_2)** λ_{ex}=488 nm, **a_3-e_3)** λ_{ex}=561 nm. Scale bar: 20 μm.

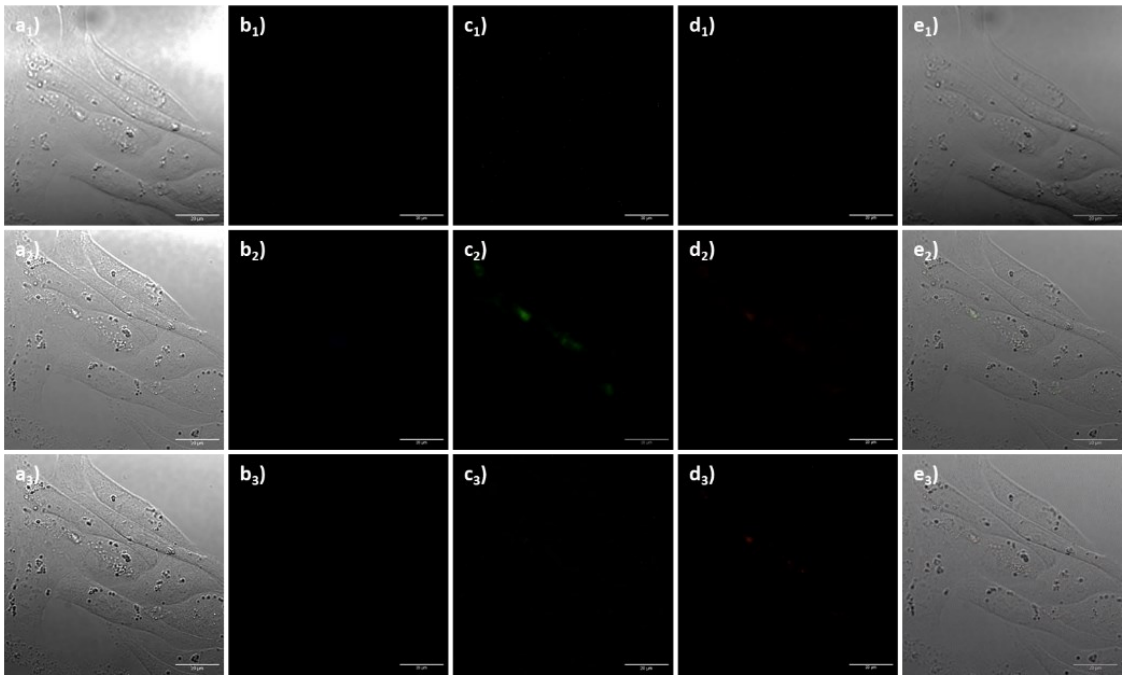

Figure A.68. Single-photon confocal laser-scanning microscopy of CHO cells incubated at 37 °C for 20 min with DMSO (0.1 mM, 1:99 DMSO:serum-free medium). $a_{1\text{-}3}$) TD channel; $b_{1\text{-}3}$) blue channel (λ_{em} = 417–477 nm); **$c_{1\text{-}3}$)** green channel (λ_{em}=500–550 nm); **$d_{1\text{-}3}$)** red channel (λ_{em}=570–750 nm); **$e_{1\text{-}3}$)** overlay of TD, blue, green and red channels. **a_1-e_1)** λ_{ex}=405 nm, **a_2-e_2)** λ_{ex}=488 nm, **a_3-e_3)** λ_{ex}=561 nm. Scale bar: 20 µm.

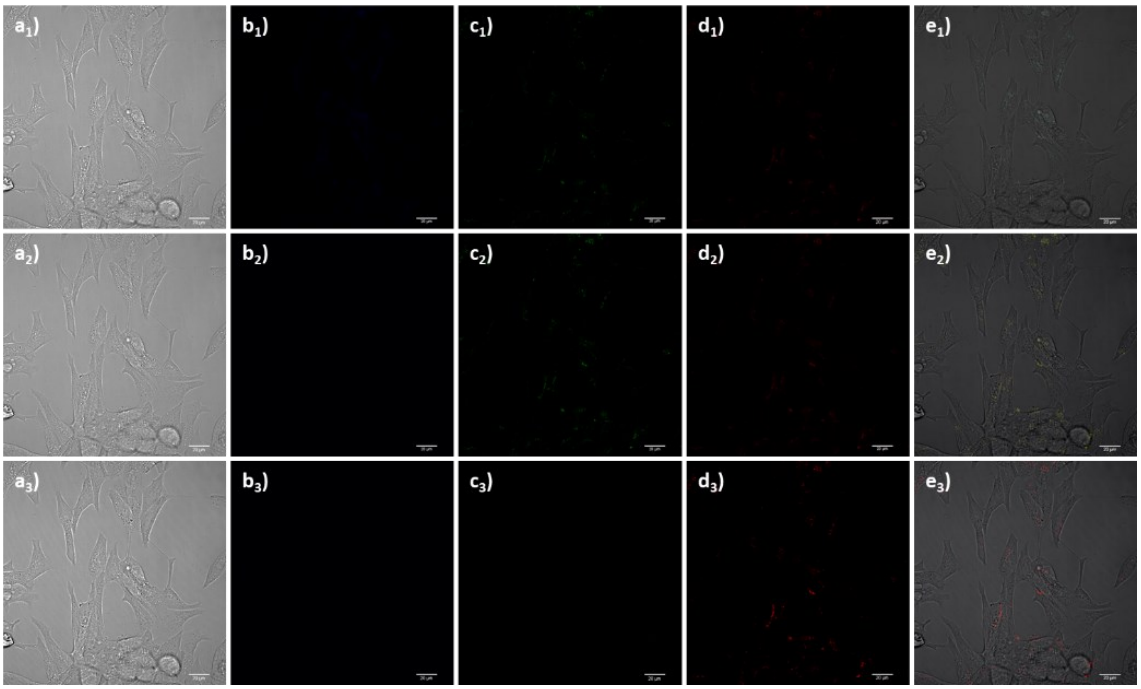

Figure A.69. Single-photon confocal laser-scanning microscopy of LnCaP cells incubated at 37 °C for 20 min with DMSO (0.1 mM, 1:99 DMSO:serum-free medium). **$a_{1\text{-}3}$)** TD channel; **$b_{1\text{-}3}$)** blue channel (λ_{em}=417–477 nm); **$c_{1\text{-}3}$)** green channel (λ_{em}=500–550 nm); **$d_{1\text{-}3}$)** red channel (λ_{em}=570–750 nm); **$e_{1\text{-}3}$)** overlay of TD, blue, green and red channels. **a_1-e_1)** λ_{ex}=405 nm, **a_2-e_2)** λ_{ex}=488 nm, **a_3-e_3)** λ_{ex}=561 nm. Scale bar: 20 µm.

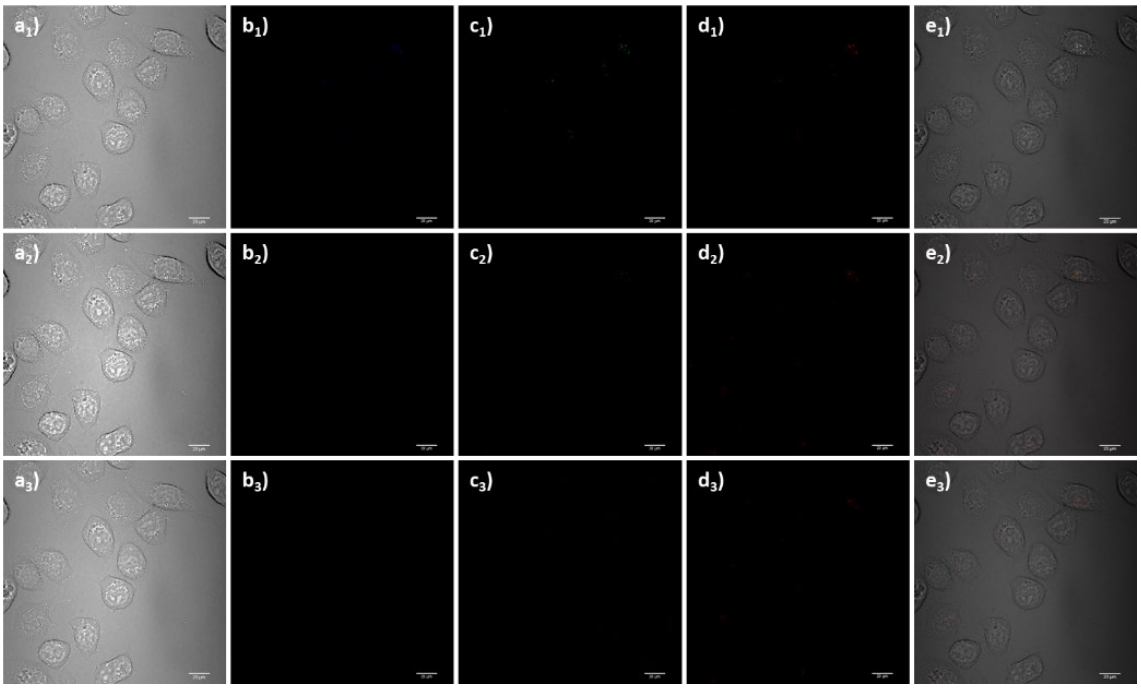

Figure A.70. Single-photon confocal laser-scanning microscopy of PC-3 cells incubated at 37 °C for 20 min with DMSO (0.1 mM, 1:99 DMSO:serum-free medium). **a$_{1-3}$)** TD channel; **b$_{1-3}$)** blue channel (λ_{em}=417–477 nm); **c$_{1-3}$)** green channel (λ_{em}=500–550 nm); **d$_{1-3}$)** red channel (λ_{em}=570–750 nm); **e$_{1-3}$)** overlay of TD, blue, green and red channels. **a$_1$-e$_1$)** λ_{ex}=405 nm, **a$_2$-e$_2$)** λ_{ex}=488 nm, **a$_3$-e$_3$)** λ_{ex}=561 nm. Scale bar: 20 µm.

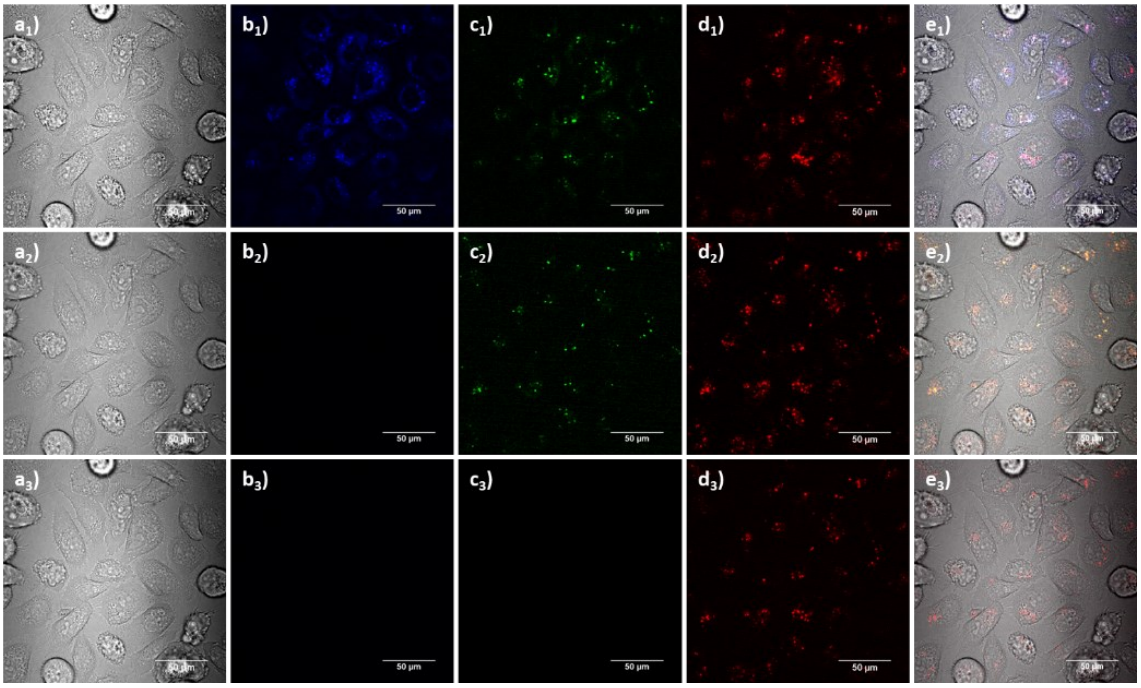

Figure A.71. Single-photon confocal laser-scanning microscopy of PC-3 cells incubated at 37 °C overnight with compound ***L*-12** (0.1 mM, 1:99 DMSO:serum-free medium). **a$_{1-3}$)** TD channel; **b$_{1-3}$)** blue channel (λ_{em}=417–477 nm); **c$_{1-3}$)** green channel (λ_{em}=500–550 nm); **d$_{1-3}$)** red channel (λ_{em}=570–750 nm); **e$_{1-3}$)** overlay of TD, blue, green and red channels. **a$_1$-e$_1$)** λ_{ex}=405 nm, **a$_2$-e$_2$)** λ_{ex}=488 nm, **a$_3$-e$_3$)** λ_{ex}=561 nm. Scale bar: 50 µm.

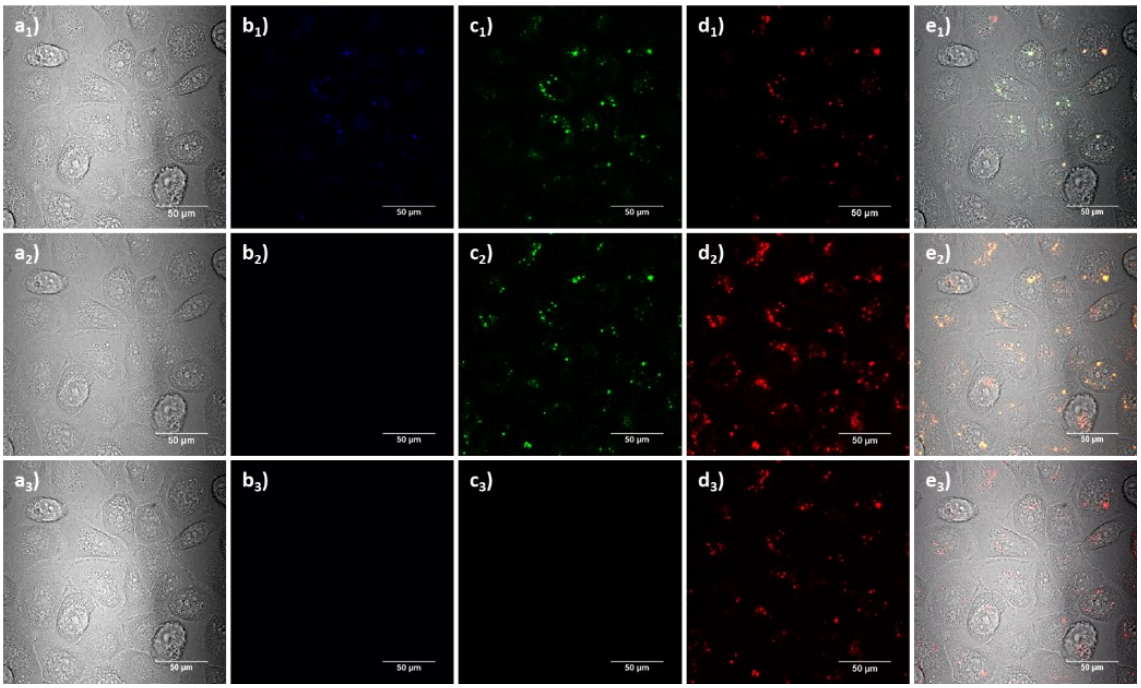

Figure A.72. Single-photon confocal laser-scanning microscopy of PC-3 cells incubated at 37 °C overnight with compound ***D*-12** (0.1 mM, 1:99 DMSO:serum-free medium). **a$_{1-3}$)** TD channel; b$_{1-3}$) blue channel (λ_{em}=417–477 nm); **c$_{1-3}$)** green channel (λ_{em}=500–550 nm); **d$_{1-3}$)** red channel (λ_{em}=570–750 nm); **e$_{1-3}$)** overlay of TD, blue, green and red channels. **a$_1$-e$_1$)** λ_{ex}=405 nm, **a$_2$-e$_2$)** λ_{ex}=488 nm, **a$_3$-e$_3$)** λ_{ex}=561 nm. Scale bar: 50 µm.

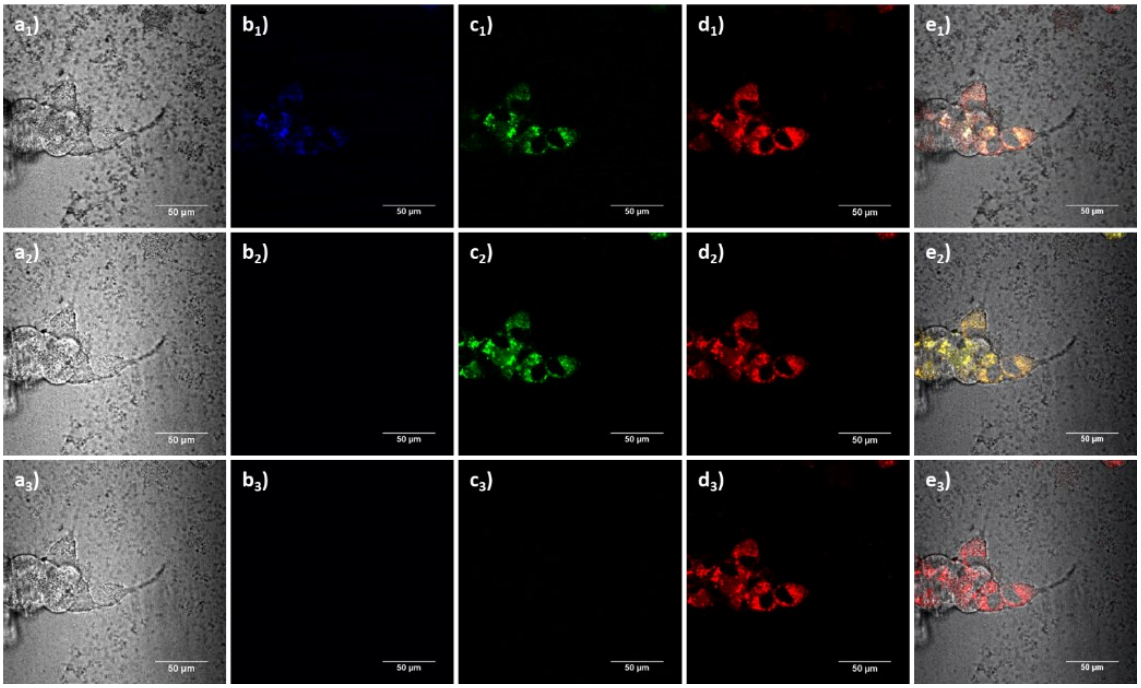

Figure A.73. Single-photon confocal laser-scanning microscopy of LNCaP cells incubated at 37 °C overnight with compound ***L*-11** (0.1 mM, 1:99 DMSO:serum-free medium). **a$_{1-3}$)** TD channel; b$_{1-3}$) blue channel (λ_{em}=417–477 nm); **c$_{1-3}$)** green channel (λ_{em}=500–550 nm); **d$_{1-3}$)** red channel (λ_{em}=570–750 nm); **e$_{1-3}$)** overlay of TD, blue, green and red channels. **a$_1$-e$_1$)** λ_{ex}=405 nm, **a$_2$-e$_2$)** λ_{ex}=488 nm, **a$_3$-e$_3$)** λ_{ex}=561 nm. Scale bar: 50 µm.

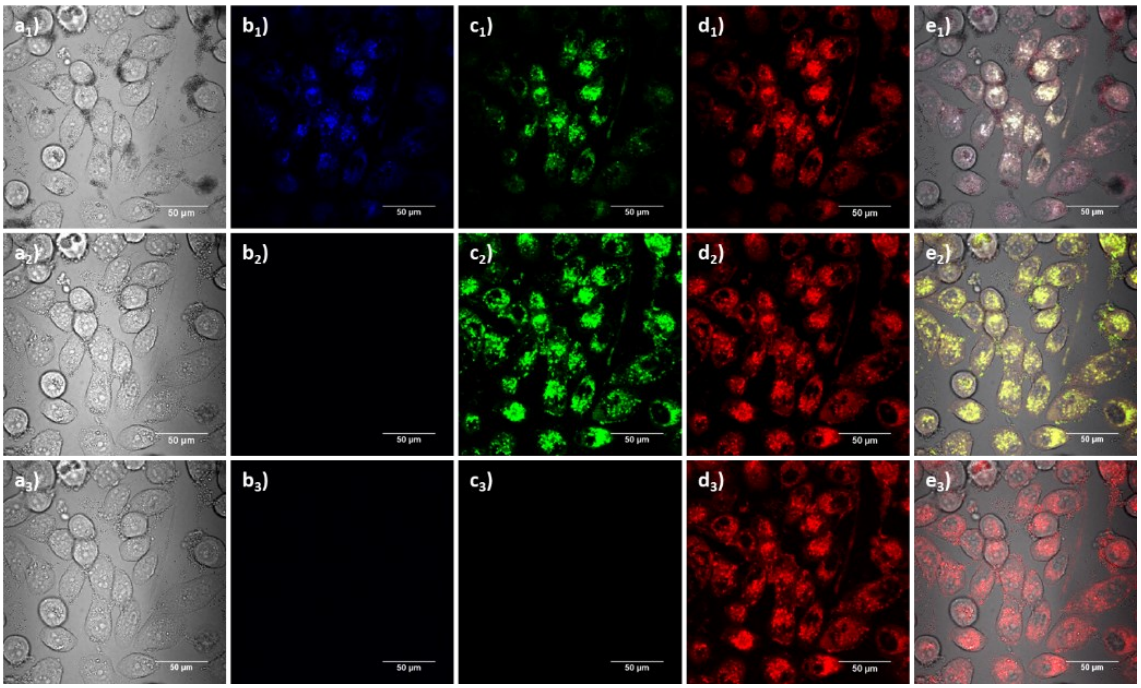

Figure A.74. Single-photon confocal laser-scanning microscopy of PC-3 cells incubated at 37 °C overnight with compound ***L*-11** (0.1 mM, 1:99 DMSO:serum-free medium). **a$_{1-3}$)** TD channel; b$_{1-3}$) blue channel (λ_{em}=417–477 nm); **c$_{1-3}$)** green channel (λ_{em}=500–550 nm); **d$_{1-3}$)** red channel (λ_{em}=570–750 nm); **e$_{1-3}$)** overlay of TD, blue, green and red channels. **a$_1$-e$_1$)** λ_{ex}=405 nm, **a$_2$-e$_2$)** λ_{ex}=488 nm, **a$_3$-e$_3$)** λ_{ex}=561 nm. Scale bar: 50 µm.

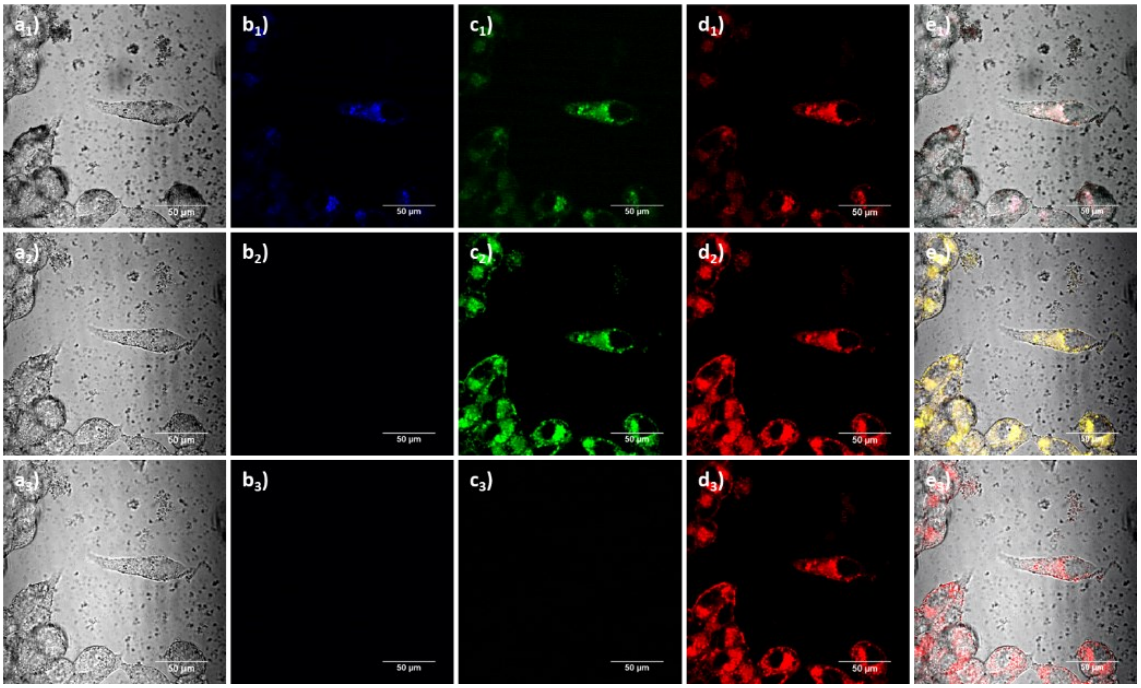

Figure A.75. Single-photon confocal laser-scanning microscopy of LNCaP cells incubated at 37 °C overnight with compound ***D*-11** (0.1 mM, 1:99 DMSO:serum-free medium). **a$_{1-3}$)** TD channel; b$_{1-3}$) blue channel (λ_{em}=417–477 nm); **c$_{1-3}$)** green channel (λ_{em}=500–550 nm); **d$_{1-3}$)** red channel (λ_{em}=570–750 nm); **e$_{1-3}$)** overlay of TD, blue, green and red channels. **a$_1$-e$_1$)** λ_{ex}=405 nm, **a$_2$-e$_2$)** λ_{ex}=488 nm, **a$_3$-e$_3$)** λ_{ex}=561 nm. Scale bar: 50 µm.

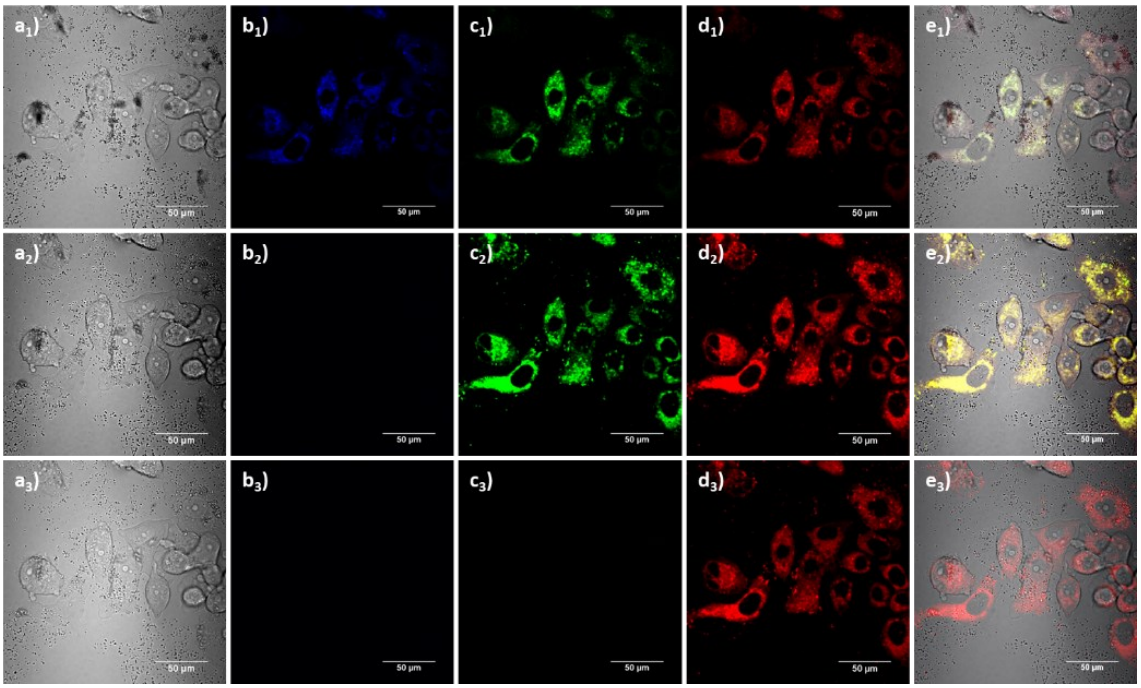

Figure A.76. Single-photon confocal laser-scanning microscopy of PC-3 cells incubated at 37 °C overnight with compound ***D*-11** (0.1 mM, 1:99 DMSO:serum-free medium). **a$_{1-3}$)** TD channel; b$_{1-3}$) blue channel (λ_{em}=417–477 nm); **c$_{1-3}$)** green channel (λ_{em}=500–550 nm); **d$_{1-3}$)** red channel (λ_{em}=570–750 nm); **e$_{1-3}$)** overlay of TD, blue, green and red channels. **a$_1$-e$_1$)** λ_{ex}=405 nm, **a$_2$-e$_2$)** λ_{ex}=488 nm, **a$_3$-e$_3$)** λ_{ex}=561 nm. Scale bar: 50 µm.

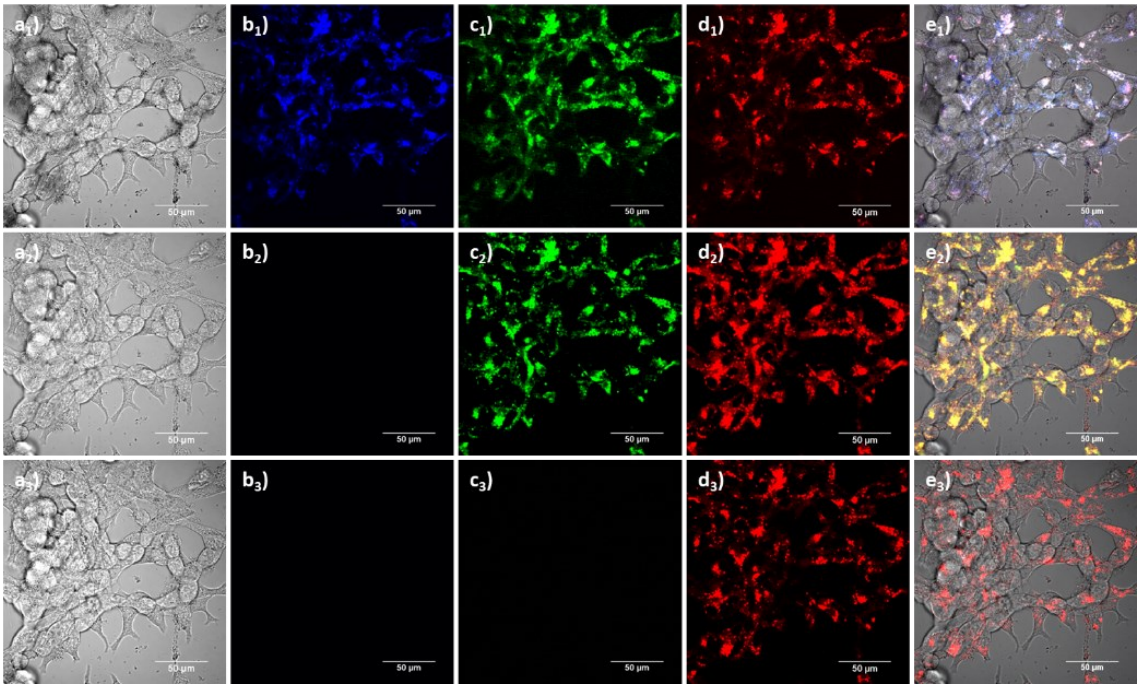

Figure A.77. Single-photon confocal laser-scanning microscopy of LNCaP cells incubated at 37 °C overnight with compound ***L*-13** (0.1 mM, 1:99 DMSO:serum-free medium). **a$_{1-3}$)** TD channel; b$_{1-3}$) blue channel (λ_{em}=417–477 nm); **c$_{1-3}$)** green channel (λ_{em}=500–550 nm); **d$_{1-3}$)** red channel (λ_{em}=570–750 nm); **e$_{1-3}$)** overlay of TD, blue, green and red channels. **a$_1$-e$_1$)** λ_{ex}=405 nm, **a$_2$-e$_2$)** λ_{ex}=488 nm, **a$_3$-e$_3$)** λ_{ex}=561 nm. Scale bar: 50 µm.

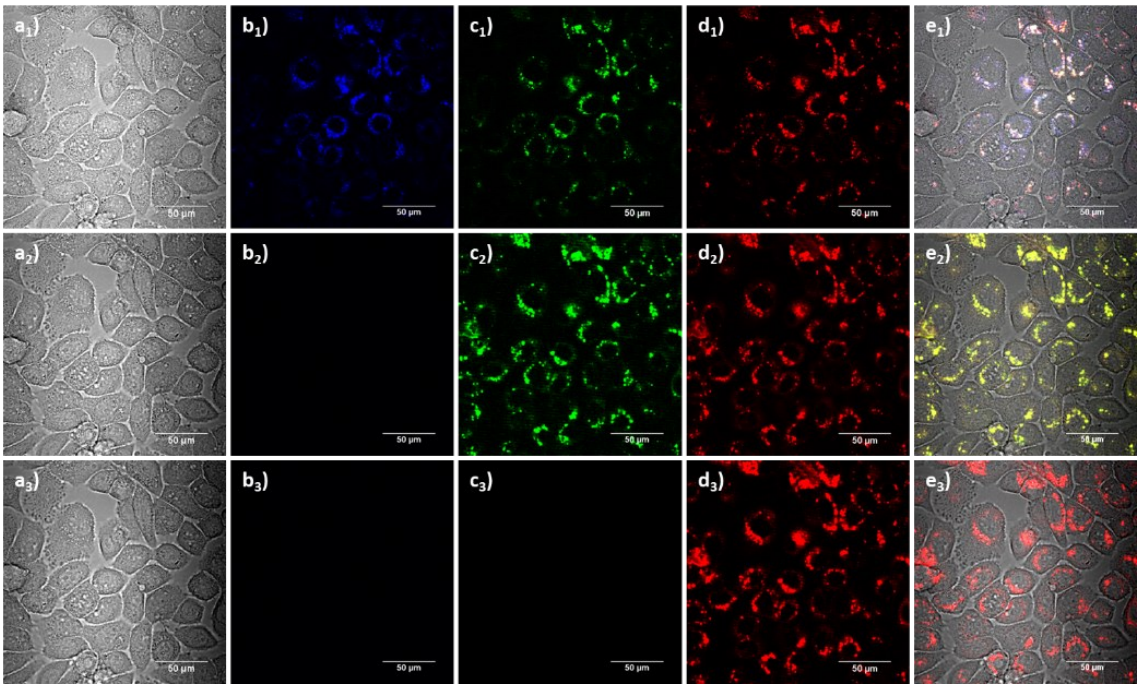

Figure A.78. Single-photon confocal laser-scanning microscopy of PC-3 cells incubated at 37 °C overnight with compound ***L*-13** (0.1 mM, 1:99 DMSO:serum-free medium). **a$_{1-3}$)** TD channel; b$_{1-3}$) blue channel (λ_{em}=417–477 nm); **c$_{1-3}$)** green channel (λ_{em}=500–550 nm); **d$_{1-3}$)** red channel (λ_{em}=570–750 nm); **e$_{1-3}$)** overlay of TD, blue, green and red channels. **a$_1$-e$_1$)** λ_{ex}=405 nm, **a$_2$-e$_2$)** λ_{ex}=488 nm, **a$_3$-e$_3$)** λ_{ex}=561 nm. Scale bar: 50 µm.

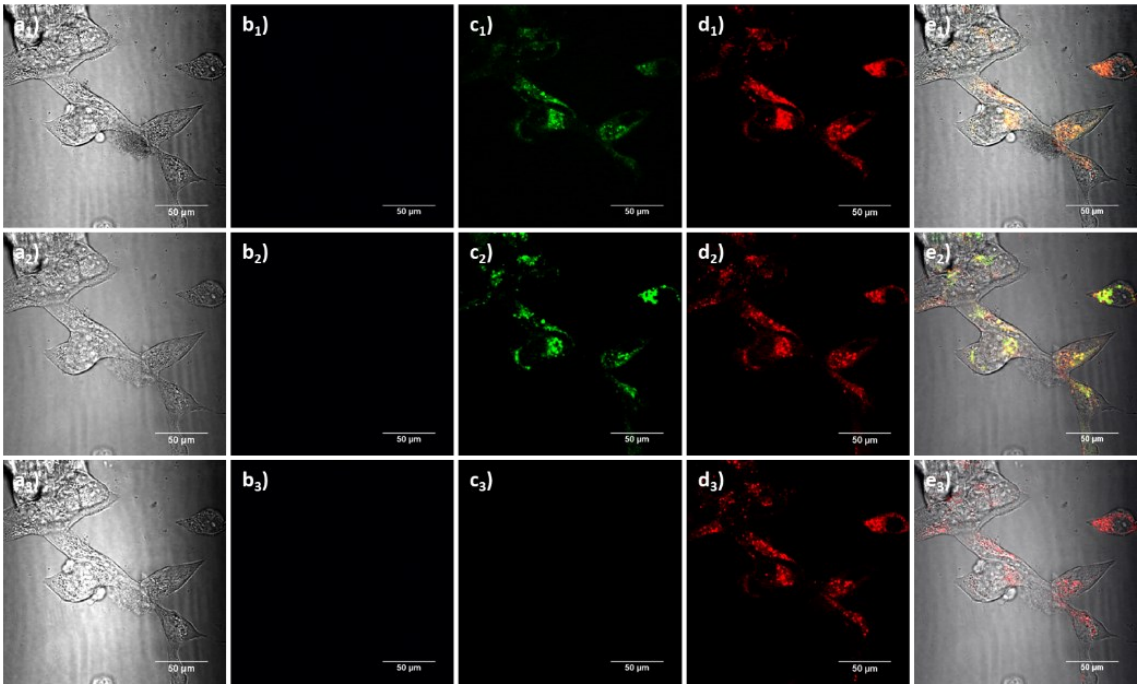

Figure A.79. Single-photon confocal laser-scanning microscopy of LNCaP cells incubated at 37 °C overnight with compound ***D*-13** (0.1 mM, 1:99 DMSO:serum-free medium). **a$_{1-3}$)** TD channel; b$_{1-3}$) blue channel (λ_{em}=417–477 nm); **c$_{1-3}$)** green channel (λ_{em}=500–550 nm); **d$_{1-3}$)** red channel (λ_{em}=570–750 nm); **e$_{1-3}$)** overlay of TD, blue, green and red channels. **a$_1$-e$_1$)** λ_{ex}=405 nm, **a$_2$-e$_2$)** λ_{ex}=488 nm, **a$_3$-e$_3$)** λ_{ex}=561 nm. Scale bar: 50 µm.

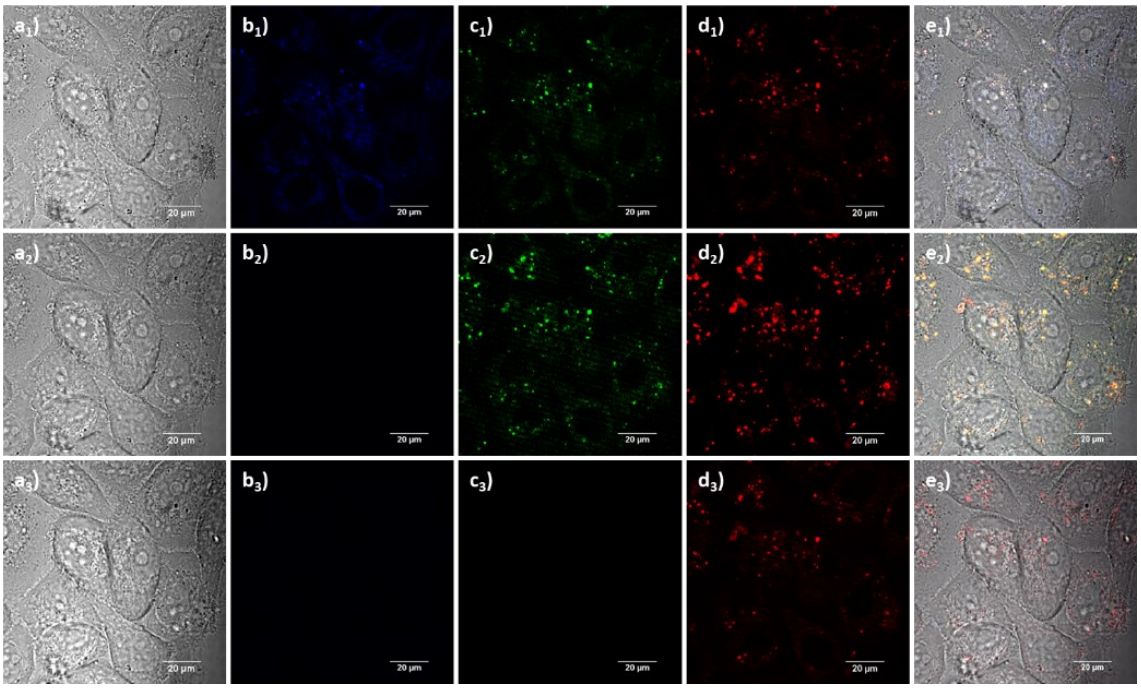

Figure A.80. Single-photon confocal laser-scanning microscopy of PC-3 cells incubated at 37 °C overnight with compound ***D*-13** (0.1 mM, 1:99 DMSO:serum-free medium). **a_{1-3})** TD channel; b_{1-3}) blue channel (λ_{em}=417–477 nm); **c_{1-3})** green channel (λ_{em}=500–550 nm); **d_{1-3})** red channel (λ_{em}=570–750 nm); **e_{1-3})** overlay of TD, blue, green and red channels. **a_1-e_1)** λ_{ex}=405 nm, **a_2-e_2)** λ_{ex}=488 nm, **a_3-e_3)** λ_{em}=561 nm. Scale bar: 50 µm.

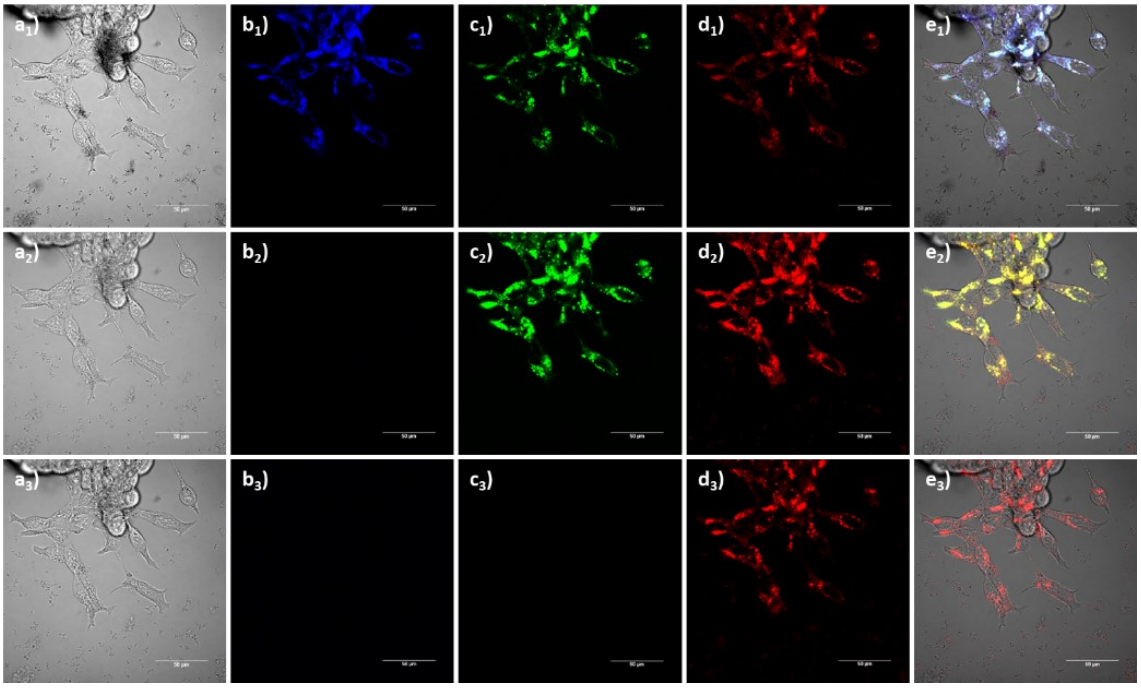

Figure A.81. Single-photon confocal laser-scanning microscopy of LNCaP cells incubated at 37 °C overnight with compound ***L*-14** (0.1 mM, 1:99 DMSO:serum-free medium). **a_{1-3})** TD channel; b_{1-3}) blue channel (λ_{em}=417–477 nm); **c_{1-3})** green channel (λ_{em}=500–550 nm); **d_{1-3})** red channel (λ_{em}=570–750 nm); **e_{1-3})** overlay of TD, blue, green and red channels. **a_1-e_1)** λ_{ex}=405 nm, **a_2-e_2)** λ_{ex}=488 nm, **a_3-e_3)** λ_{ex}=561 nm. Scale bar: 50 µm.

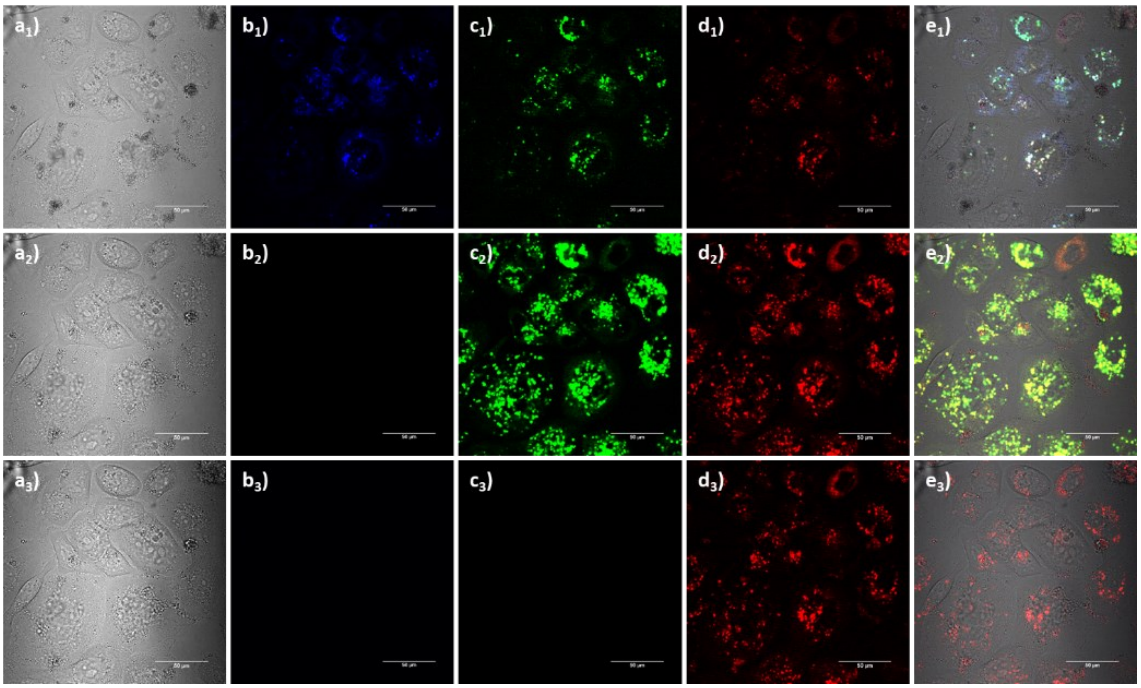

Figure A.82. Single-photon confocal laser-scanning microscopy of PC-3 cells incubated at 37 °C overnight with compound ***L*-14** (0.1 mM, 1:99 DMSO:serum-free medium). **a1-3)** TD channel; b1-3) blue channel (λ_{em}=417–477 nm); **c1-3)** green channel (λ_{em}=500–550 nm); **d1-3)** red channel (λ_{em}=570–750 nm); **e1-3)** overlay of TD, blue, green and red channels. **a1-e1)** λ_{ex}=405 nm, **a2-e2)** λ_{ex}=488 nm, **a3-e3)** λ_{ex}=561 nm. Scale bar: 50 µm.

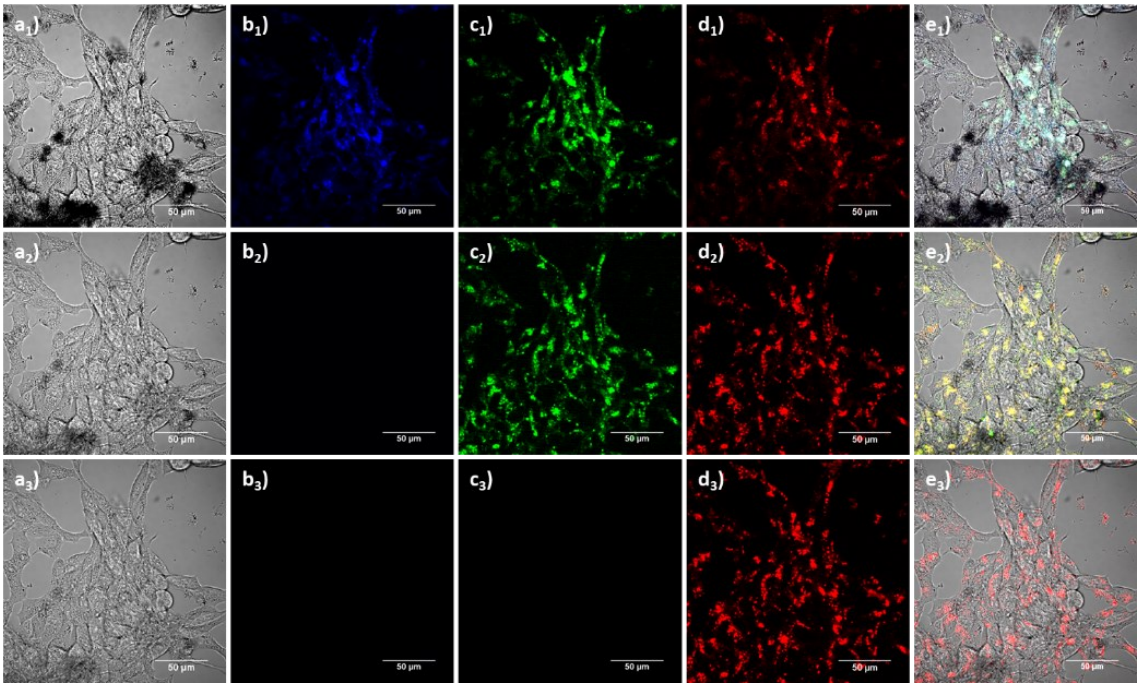

Figure A.83. Single-photon confocal laser-scanning microscopy of LNCaP cells incubated at 37 °C overnight with compound ***D*-14** (0.1 mM, 1:99 DMSO:serum-free medium). **a1-3)** TD channel; b1-3) blue channel (λ_{em}=417–477 nm); **c1-3)** green channel (λ_{em}=500–550 nm); **d1-3)** red channel (λ_{em}=570–750 nm); **e1-3)** overlay of TD, blue, green and red channels. **a1-e1)** λ_{ex}=405 nm, **a2-e2)** λ_{ex}=488 nm, **a3-e3)** λ_{ex}=561 nm. Scale bar: 50 µm.

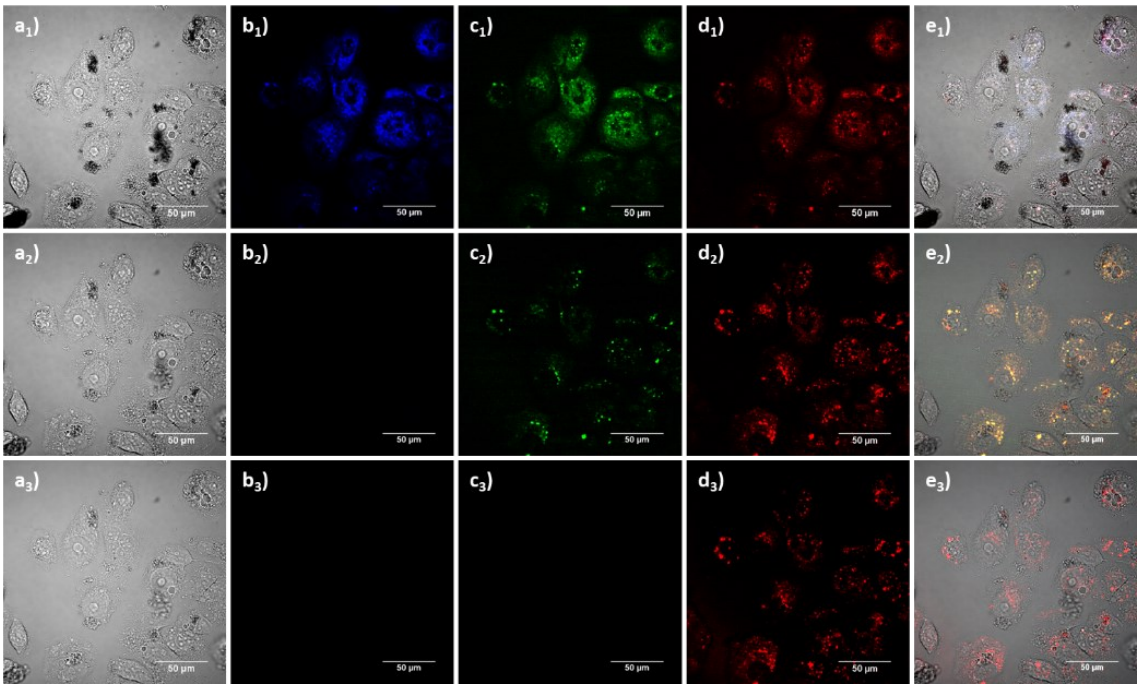

Figure A.84. Single-photon confocal laser-scanning microscopy of PC-3 cells incubated at 37 °C overnight with compound ***D*-14** (0.1 mM, 1:99 DMSO:serum-free medium). **a1-3)** TD channel; b1-3) blue channel (λ_{em}=417–477 nm); **c1-3)** green channel (λ_{em}=500–550 nm); **d1-3)** red channel (λ_{em}=570–750 nm); **e1-3)** overlay of TD, blue, green and red channels. **a1-e1)** λ_{ex}=405 nm, **a2-e2)** λ_{ex}=488 nm, **a3-e3)** λ_{ex}=561 nm. Scale bar: 50 µm.

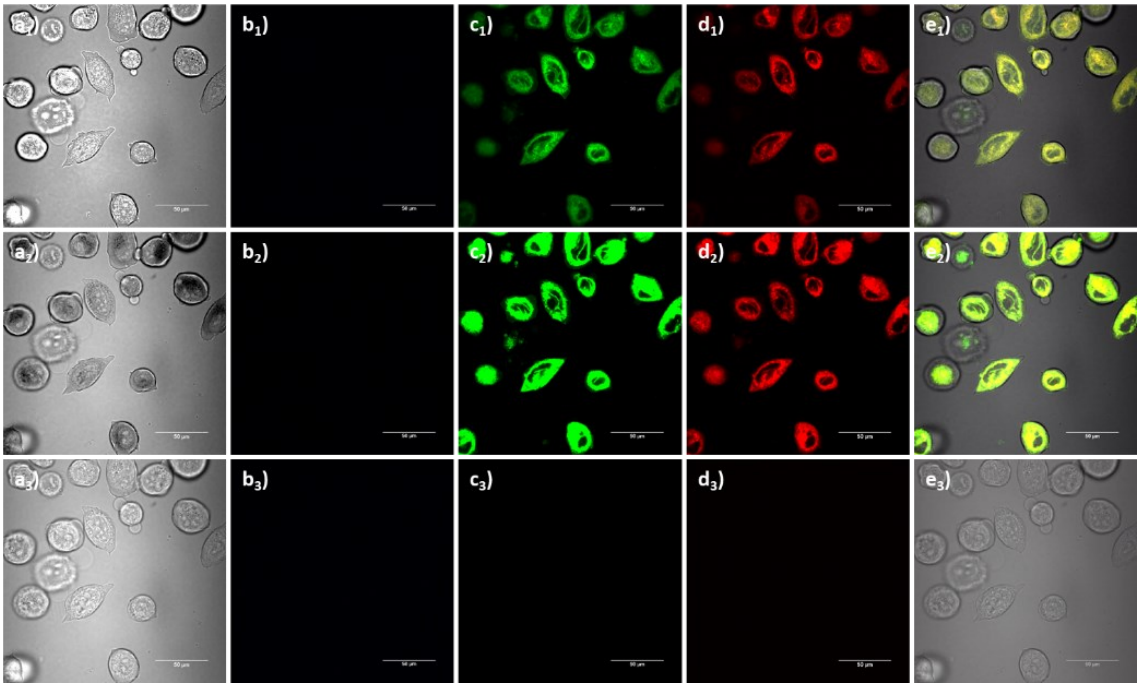

Figure A.85. Single-photon confocal laser-scanning microscopy of PC-3 cells incubated at 37 °C overnight with compound **2** (0.1 mM, 1:99 DMSO:serum-free medium). **a1-3)** TD channel; b1-3) blue channel (λ_{em}=417–477 nm); **c1-3)** green channel (λ_{em}=500–550 nm); **d1-3)** red channel (λ_{em}=570–750 nm); **e1-3)** overlay of TD, blue, green and red channels. **a1-e1)** λ_{ex}=405 nm, **a2-e2)** λ_{ex}=488 nm, **a3-e3)** λ_{ex}=561 nm. Scale bar: 50 µm.

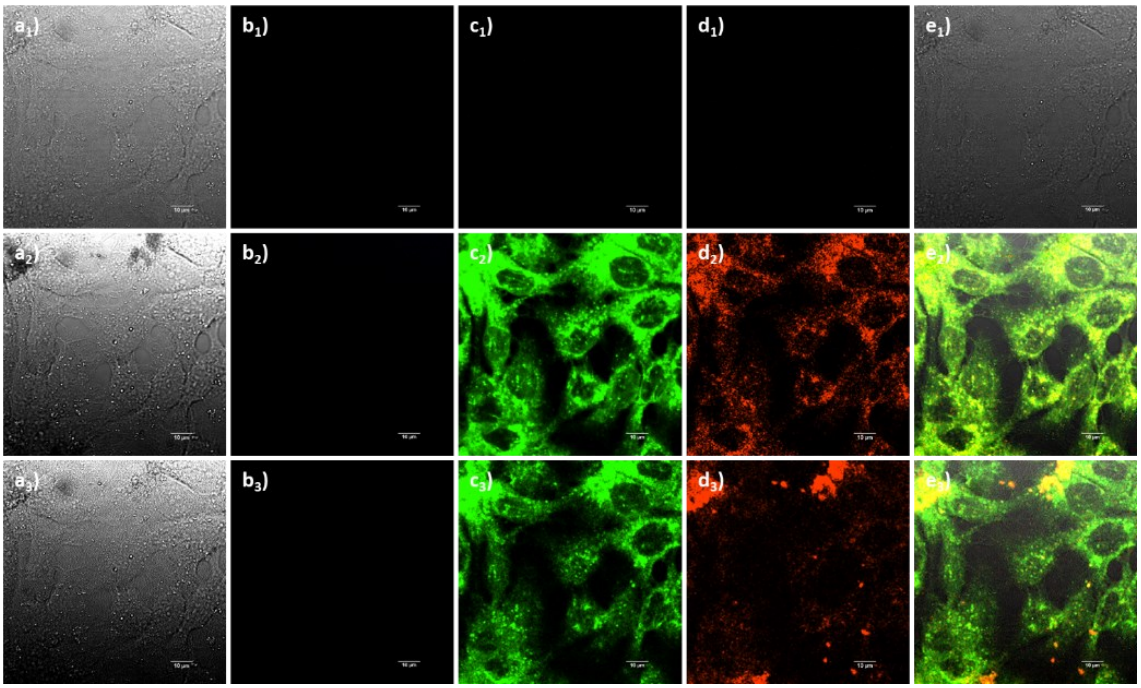

Figure A.86. Single-photon confocal laser-scanning microscopy of A431 cells incubated at 37 °C overnight with compound **15** (0.1 mM, 1:99 DMSO:serum-free medium). **a$_{1-3}$)** TD channel; b$_{1-3}$) blue channel (λ_{em}=417–477 nm); **c$_{1-3}$)** green channel (λ_{em}=500–550 nm); **d$_{1-3}$)** red channel (λ_{em}=570–750 nm); **e$_{1-3}$)** overlay of TD, blue, green and red channels. **a$_1$-e$_1$)** λ_{ex}=405 nm, **a$_2$-e$_2$)** λ_{ex}=488 nm, **a$_3$-e$_3$)** λ_{ex}=561 nm. Scale bar: 50 µm.

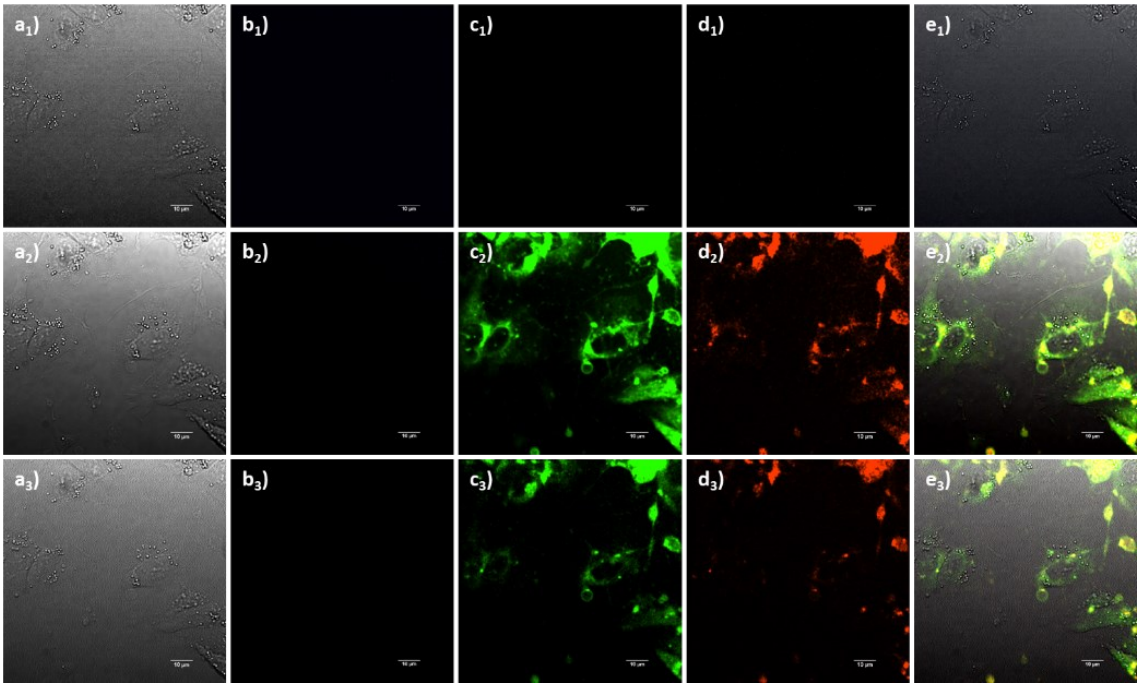

Figure A.87. Single-photon confocal laser-scanning microscopy of CHO cells incubated at 37 °C overnight with compound **15** (0.1 mM, 1:99 DMSO:serum-free medium). **a$_{1-3}$)** TD channel; b$_{1-3}$) blue channel (λ_{em}=417–477 nm); **c$_{1-3}$)** green channel (λ_{em}=500–550 nm); **d$_{1-3}$)** red channel (λ_{em}=570–750 nm); **e$_{1-3}$)** overlay of TD, blue, green and red channels. **a$_1$-e$_1$)** λ_{ex}=405 nm, **a$_2$-e$_2$)** λ_{ex}=488 nm, **a$_3$-e$_3$)** λ_{ex}=561 nm. Scale bar: 50 µm.

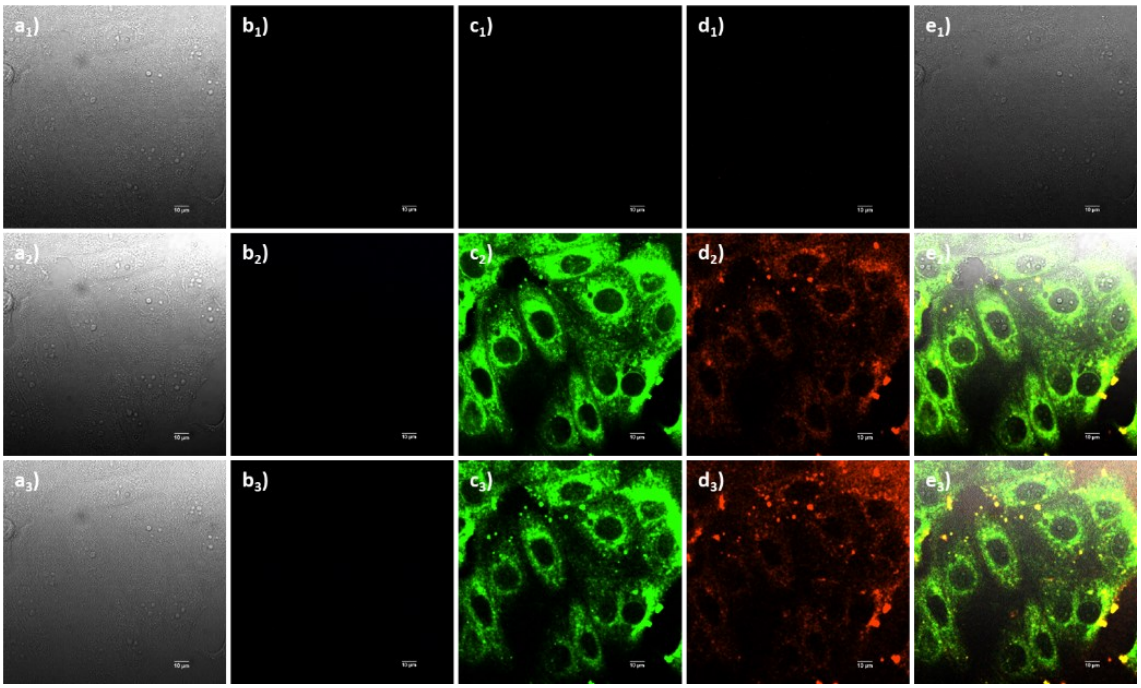

Figure A.88. Single-photon confocal laser-scanning microscopy of MCF-7 cells incubated at 37 °C overnight with compound **15** (0.1 mM, 1:99 DMSO:serum-free medium). **a$_{1-3}$)** TD channel; b$_{1-3}$) blue channel (λ_{em}=417–477 nm); **c$_{1-3}$)** green channel (λ_{em}=500–550 nm); **d$_{1-3}$)** red channel (λ_{em}=570–750 nm); **e$_{1-3}$)** overlay of TD, blue, green and red channels. **a$_1$-e$_1$)** λ_{ex}=405 nm, **a$_2$-e$_2$)** λ_{ex}=488 nm, **a$_3$-e$_3$)** λ_{ex}=561 nm. Scale bar: 50 µm.

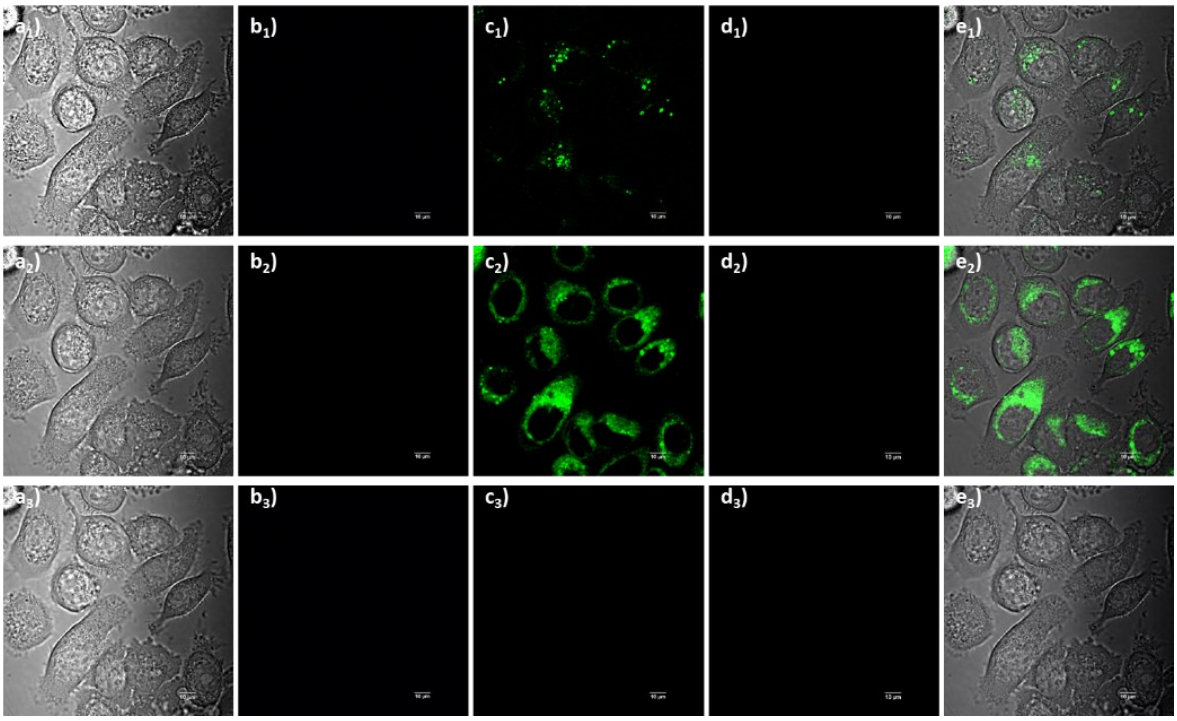

Figure A.89. Single-photon confocal laser-scanning microscopy of PC-3 cells incubated at 37 °C overnight with compound **15** (0.1 mM, 1:99 DMSO:serum-free medium). **a$_{1-3}$)** TD channel; b$_{1-3}$) blue channel (λ_{em}=417–477 nm); **c$_{1-3}$)** green channel (λ_{em}=500–550 nm); **d$_{1-3}$)** red channel (λ_{em}=570–750 nm); **e$_{1-3}$)** overlay of TD, blue, green and red channels. **a$_1$-e$_1$)** λ_{ex}=405 nm, **a$_2$-e$_2$)** λ_{ex}=488 nm, **a$_3$-e$_3$)** λ_{ex}=561 nm. Scale bar: 50 µm.

7.3.7. Confocal laser-scanning microscopy co-localization analysis

Table A.1. PCC and MOC parameters referred to Figure 4.27 in Chapter 4.

Molecule	ROI	PCC	MOC
***L*-12**	1 (red)	0.573	0.606
	2 (green)	0.622	0.677
	3 (bue)	0.488	0.541
***D*-12**	1 (red)	0.465	0.613
	2 (green)	0.522	0.713
	3 (bue)	0.469	0.649
***L*-13**	1 (red)	0.614	0.833
	2 (green)	0.632	0.835
	3 (bue)	0.749	0.791
***L*-14**	1 (red)	0.699	0.739
	2 (green)	0.701	0.679
	3 (bue)	0.826	0.835
***D*-13**	1 (red)	0.161	0.466
	2 (green)	0.428	0.576
	3 (bue)	0.398	0.552
***D*-14**	1 (red)	0.546	0.591
	2 (green)	0.558	0.633
	3 (bue)	0.513	0.616
15	1 (red)	0.247	0.689
	2 (green)	0.454	0.802
	3 (bue)	0.541	0.807

7.3.8. Fluorescence lifetime imaging microscopy

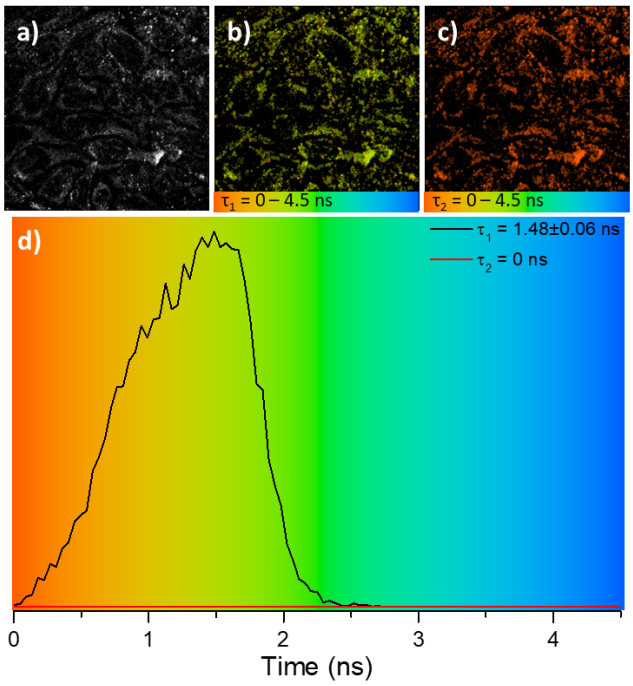

Figure A.90. Two-photon fluorescence lifetime imaging in A431 cells line of DMSO (0.1 mM in 1:99 DMSO:sereum-free medium) including **$a_{1,2}$)** intensity map, **$b_{1,2}$)** lifetime maps in coloured code and lifetime distribution. **a_1-b_1)** τ_1=1.48±0.06 ns and **a_2-b_2)** τ_2=0.00±0.00 ns. λ_{ex}=810 nm; laser power 6. mW; acquisition time 20 s.

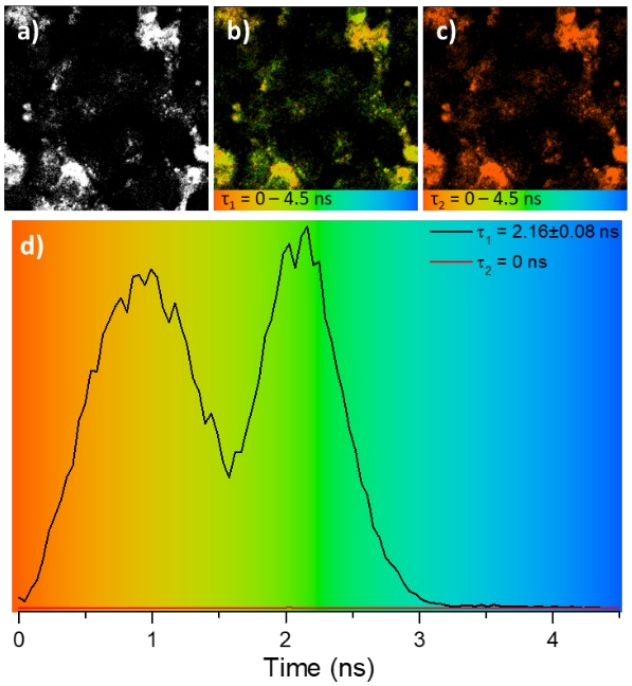

Figure A.91. Two-photon fluorescence lifetime imaging in CHO cells line of compound ***L*-13** (0.05 mM in 1:99 DMSO:sereum-free medium) including **$a_{1,2}$)** intensity map, **$b_{1,2}$)** lifetime maps in coloured code and lifetime distribution. **a_1-b_1)** τ_1=2.16±0.08 ns and **a_2-b_2)** τ_2=0.00±0.00 ns. λ_{ex}=810 nm; laser power 5.0 mW; acquisition time 90 s.

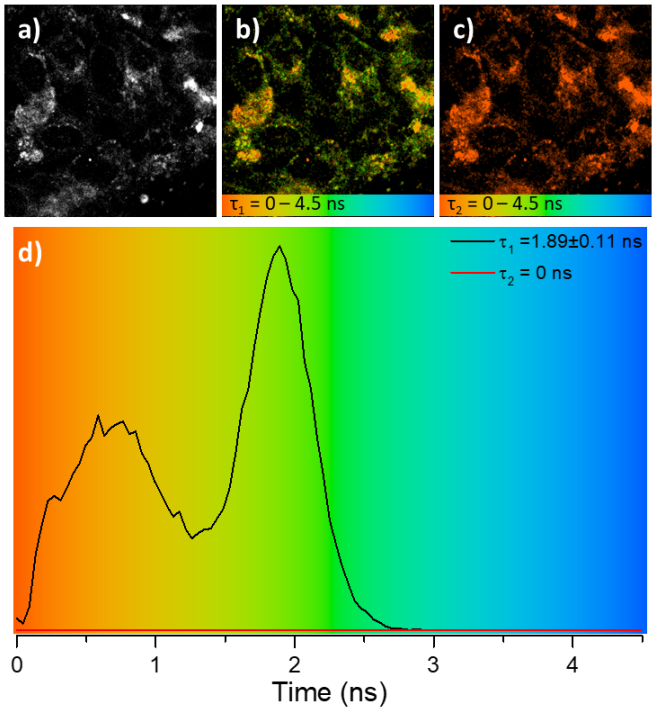

Figure A.92. Two-photon fluorescence lifetime imaging in CHO cells line of compound ***L*-14** (0.05 mM in 1:99 DMSO:sereum-free medium) including **$a_{1,2}$)** intensity map, **$b_{1,2}$)** lifetime maps in coloured code and lifetime distribution. **a_1-b_1)** τ_1=1.89±0.11 ns and **a_2-b_2)** τ_2=0.00±0.00 ns. λ_{ex}=810 nm; laser power 4.7 mW; acquisition time 60 s.

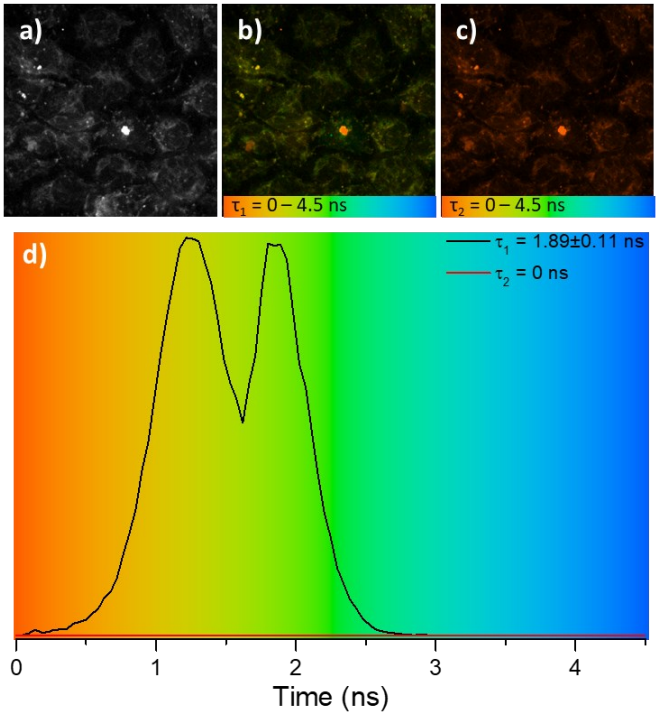

Figure A.93. Two-photon fluorescence lifetime imaging in CHO cells line of compound ***D*-13** (0.05 mM in 1:99 DMSO:sereum-free medium) including **$a_{1,2}$)** intensity map, **$b_{1,2}$)** lifetime maps in coloured code and lifetime distribution. **a_1-b_1)** τ_1=1.89±0.11 ns and **a_2-b_2)** τ_2=0.00±0.00 ns. λ_{ex}=810 nm; laser power 4.9 mW; acquisition time 60 s.

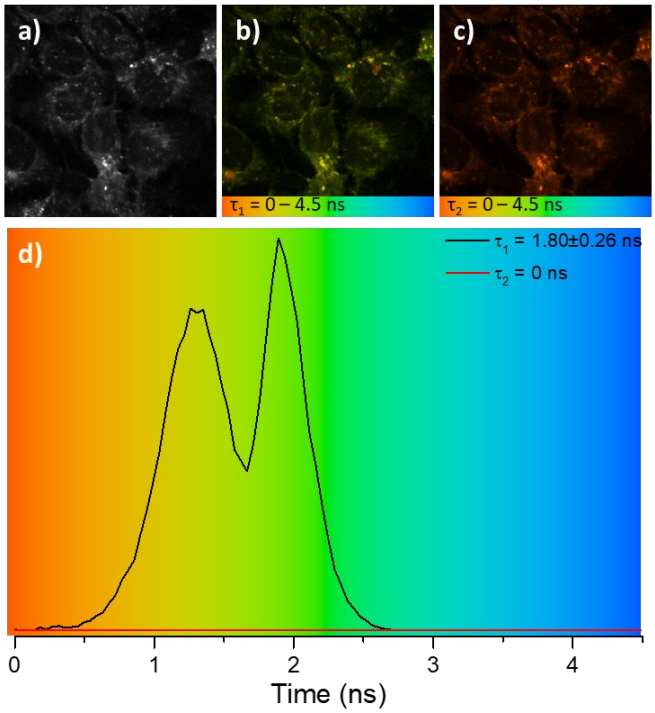

Figure A.94. Two-photon fluorescence lifetime imaging in CHO cells line of compound ***D*-14** (0.05 mM in 1:99 DMSO:sereum-free medium) including **$a_{1,2}$)** intensity map, **$b_{1,2}$)** lifetime maps in coloured code and lifetime distribution. **a_1-b_1)** τ_1=1.09±0.26 ns and **a_2-b_2)** τ_2=0.00±0.00 ns. λ_{ex}=810 nm; laser power 4.9 mW; acquisition time 90 s.

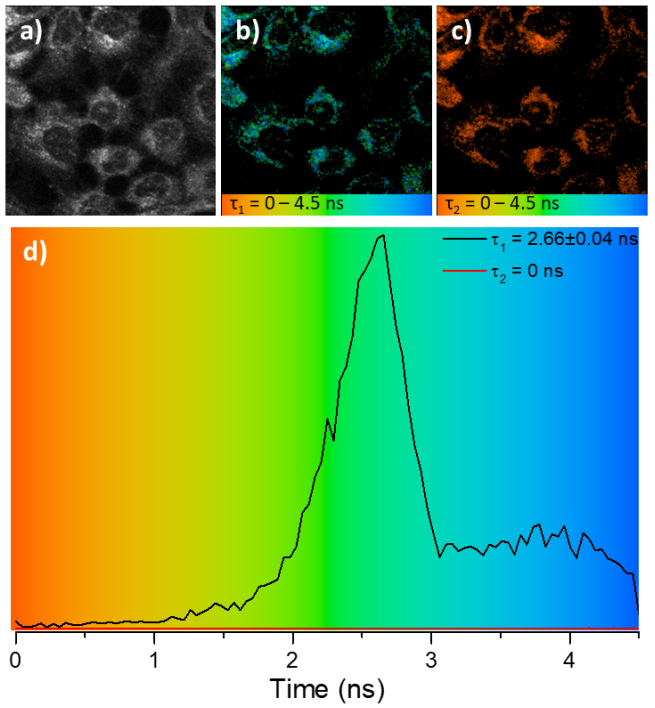

Figure A.95. Two-photon fluorescence lifetime imaging in CHO cells line of compound **15** (0.05 mM in 1:99 DMSO:sereum-free medium) including **$a_{1,2}$)** intensity map, **$b_{1,2}$)** lifetime maps in coloured code and lifetime distribution. **a_1-b_1)** τ_1=2.66±0.04 ns and **a_2-b_2)** τ_2=0.00±0.00 ns. λ_{ex}=910 nm; laser power 1.2 mW; acquisition time 40 s.

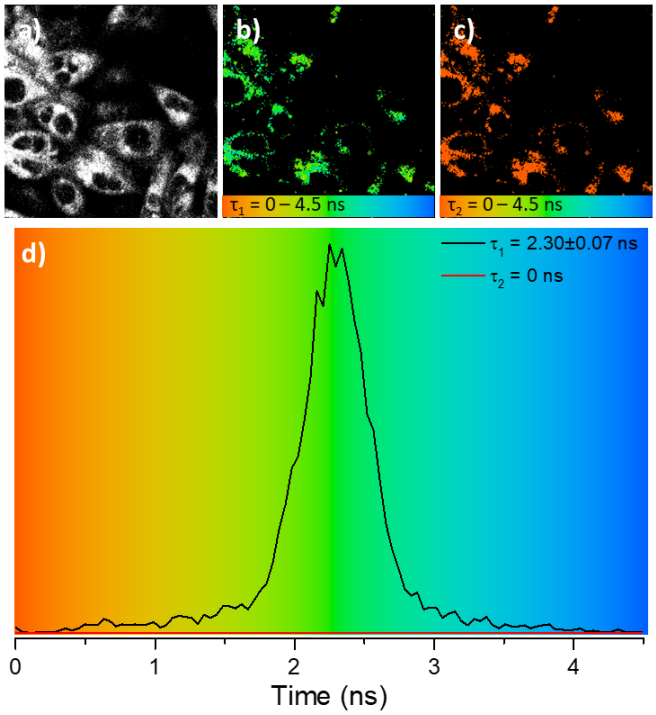

Figure A.96. Two-photon fluorescence lifetime imaging in CHO cells line of compound **2** (0.05 mM in 1:99 DMSO:sereum-free medium) including **$a_{1,2}$)** intensity map, **$b_{1,2}$)** lifetime maps in coloured code and lifetime distribution. **a_1-b_1)** τ_1=2.30±0.07 ns and **a_2-b_2)** τ_2=0.00±0.00 ns. λ_{ex}=910 nm; laser power 0.9 mW; acquisition time 20 s.

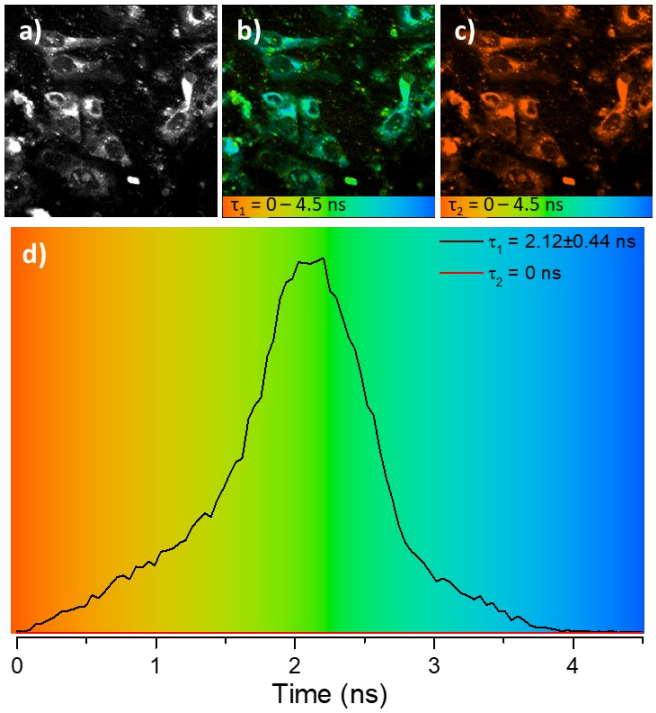

Figure A.97. Two-photon fluorescence lifetime imaging in CHO cells line of compound **15** (0.05 mM in 1:99 DMSO:sereum-free medium) including **$a_{1,2}$)** intensity map, **$b_{1,2}$)** lifetime maps in coloured code and lifetime distribution. **a_1-b_1)** τ_1=2.12±0.44 ns and **a_2-b_2)** τ_2=0.00±0.00 ns. λ_{ex}=910 nm; laser power 3.0 mW; acquisition time 40 s.

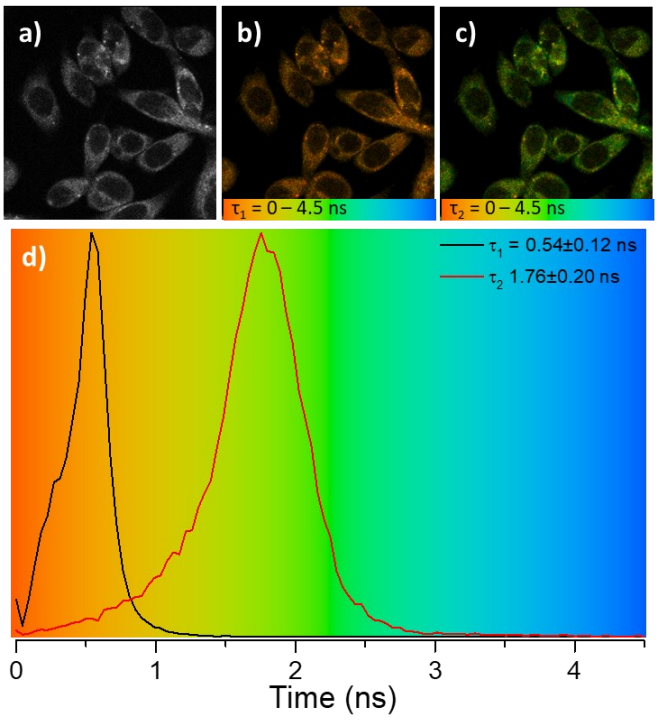

Figure A.98. Two-photon fluorescence lifetime imaging in PC-3 cells line of compound ***L*-14** (0.1 mM in 1:99 DMSO:sereum-free medium) including **$a_{1,2}$)** intensity map, **$b_{1,2}$)** lifetime maps in coloured code and lifetime distribution. **a_1-b_1)** τ_1=0.54±0.12 ns and **a_2-b_2)** τ_2=1.76±0.20 ns. λ_{ex}=810 nm; laser power 3.9 mW; acquisition time 30 s.

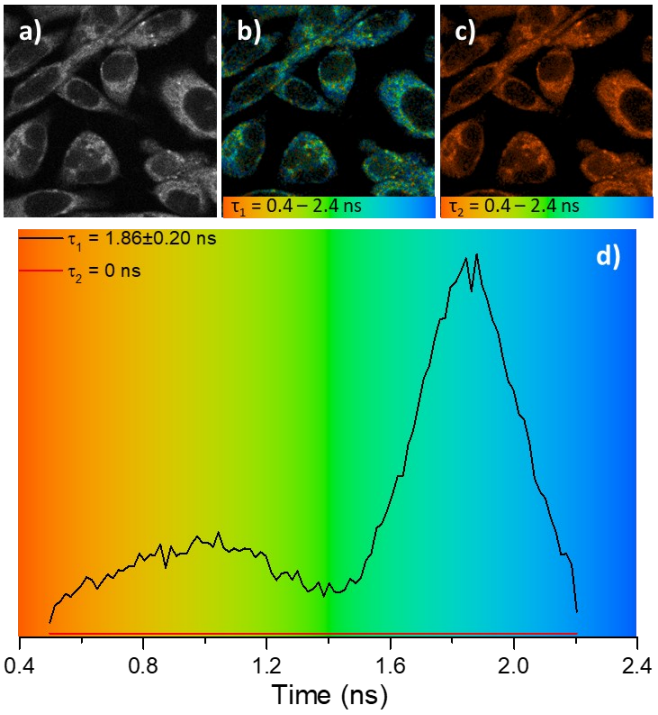

Figure A.99. Two-photon fluorescence lifetime imaging in PC-3 cells line of compound *L*-13 (0.1 mM in 1:99 DMSO:sereum-free medium) including $a_{1,2}$) intensity map, $b_{1,2}$) lifetime maps in coloured code and lifetime distribution. a_1-b_1) τ_1 = 1.86±0.20 ns and a_2-b_2) τ_2 = 0.00±0.00 ns. λ_{ex}=810 nm; laser power 4.9 mW; acquisition time 30 s.

8. Appendices B

8.1. Fluorogenic composite materials for imaging biosensing

The design and synthesis of novel fluorogenic composite materials (FCMs) are presented hereby for biological biosensing as cheap, easy to synthesise and sensitive alternatives to common biosensors. Such materials can be detected by fluorescence emission-based methods, such as fluorescence spectroscopy and confocal microscopy, thanks to their ability to emit fluorescence in the UV-visible range of the light spectrum.

A fluorogenic composite material (FCM) is formed by non-covalent interactions, such as π-π stacking, electrostatic interactions or Van der Waals forces, between a fluorophore and a quenching material[1]. The interaction of the fluorophore and the quenching material generates Förster resonance energy transfer (FRET) in which the fluorophore, acting as a donor, transfers its energy to the quencher, acting as an acceptor[2] with similar resonance energy.

Among the quenching materials, graphene and its congeners have been attracting lots of interest because of their photoluminescence properties. In particular, graphene oxide has been used in different fields, such as medicine, biochemistry and electronics[3] thanks to its low cost, ease of synthesis, mechanical and optical properties, high electron mobility and band gap[3]. Graphene oxide is one of the allotropes of carbon, consisting of sheets of sp^2-bonded carbon atoms with oxidised functionalities (such as epoxy, carboxy and alcoholic groups) arranged in a regular honeycomb-like lattice[4,5]. In recent years, graphene oxide has been studied in different solvents, showing moderate solubility[6]. However, graphene oxide is very well soluble in water and has found several applications in biological conditions[7,8]. Recent studies[9-11] have reported the use of graphene oxide as a platform for biosensing in the biological environment. Thanks to its peculiarity to quench the emission of fluorescent dyes[12], this material has been attracted interest to create FCMs to create fluorescence on-off devices for protein[12], nucleic acids[9,10] and glucose[11]. Thanks to the aforementioned features, graphene oxide has also become an ideal candidate for imaging for different forms of cancer[13-15].

Flat aromatic compounds can be considered ideal candidates as FRET donors in FCMs thanks to their fluorescence emissions in a broad range of wavelengths. In recent years, novel FCM consisting of NDI- and carbon-based materials have been proved to present fluorescence properties for imaging in prostate cancer cells[16].

Novel FCMs will be presented as potential imaging probes for prostate cancer detection. Graphene oxide will be synthesised and investigated as a FRET acceptor.

On the other hand, two different class of FRET donors will be introduced. The first class consists of peptide-targeted NDI scaffolds, previously described in Chapter 4. The rationale of this proposed FCM is to act as a "turn-on/off" biosensor in which the graphene oxide will quench the fluorescence of the peptide-targeted NDI derivative *via* FRET. Once the NDI targeted will interact with the cellular compartments, the FCM will fluoresce because of the FRET between the graphene oxide and the NDI derivative is blocked[45]. The second proposed donors are based on indenyl-core[17]. Scheme B.1 shows the concept of the proposed FCMs, consisting of a fluorescent flat aromatic FRET donor (in red) and a carbon-based FRET acceptor (in black).

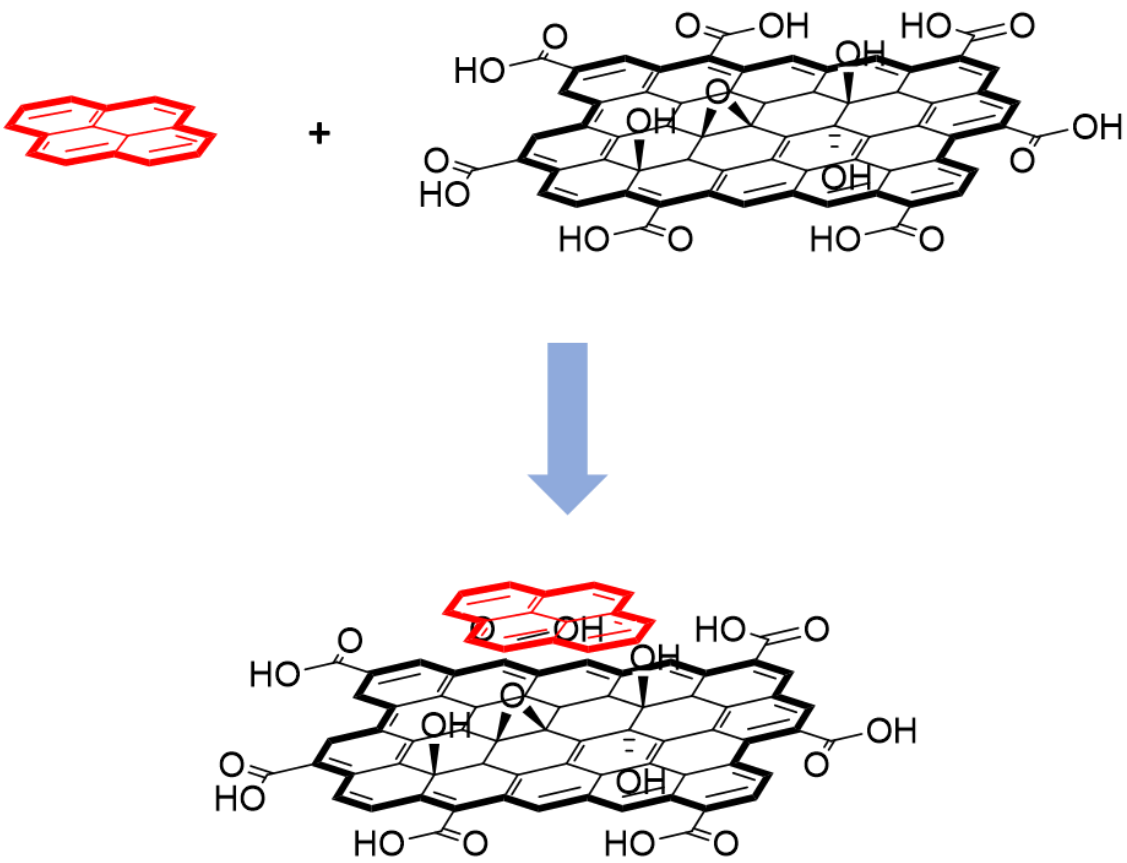

Scheme B.1. Schematic representation of the formation of an FCM with a flat aromatic fluorophore (red) and the quencher graphene oxide layer (**GO**, black diagram).

8.1.1. Synthesis and characterisation of the quenching material

Graphene oxide (**GO**) was chosen as an ideal candidate for the formation of fluorogenic composite material as FRET donor thanks to its facile synthesis, availability and low cost.
GO was synthesised by a modified version of the Hummer's method, reported in 1958[18] and adapted in 2016[19]. Scheme B.2 shows the conditions for obtaining pure GO from graphite.

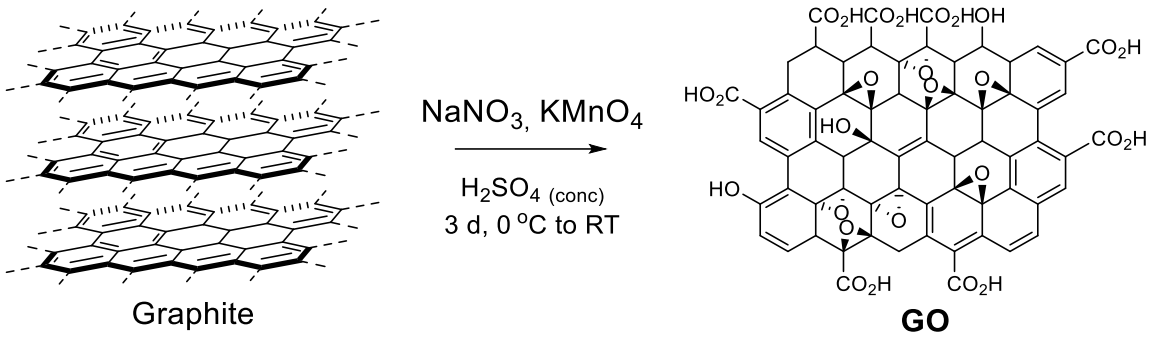

Scheme B.2. Reaction scheme of the synthesis of **GO** from graphite precursor, according to a modified Hummer's method[19].

The following procedure was used to exfoliate the pristine graphite sheets and oxidise the obtained single-layer. Such method involves the treatment of graphite with sodium nitrate and potassium permanganate in concentrated sulfuric acid for 3 days at room temperature. The brown solid (**GO**) was cleaned by dialysis in deionised water and then washed with deionised water and centrifuged.

Raman[20] and FT-IR[21] have been proved to be useful tools to characterise and compare the family of carbon-based materials, such as graphite, graphene and graphene oxide because of such materials show characteristic peaks. In Figure B.1, comparative Raman (a) and FT-IR (b) spectra of graphite (red lines) and **GO** (black lines) are reported with their characteristic bands.

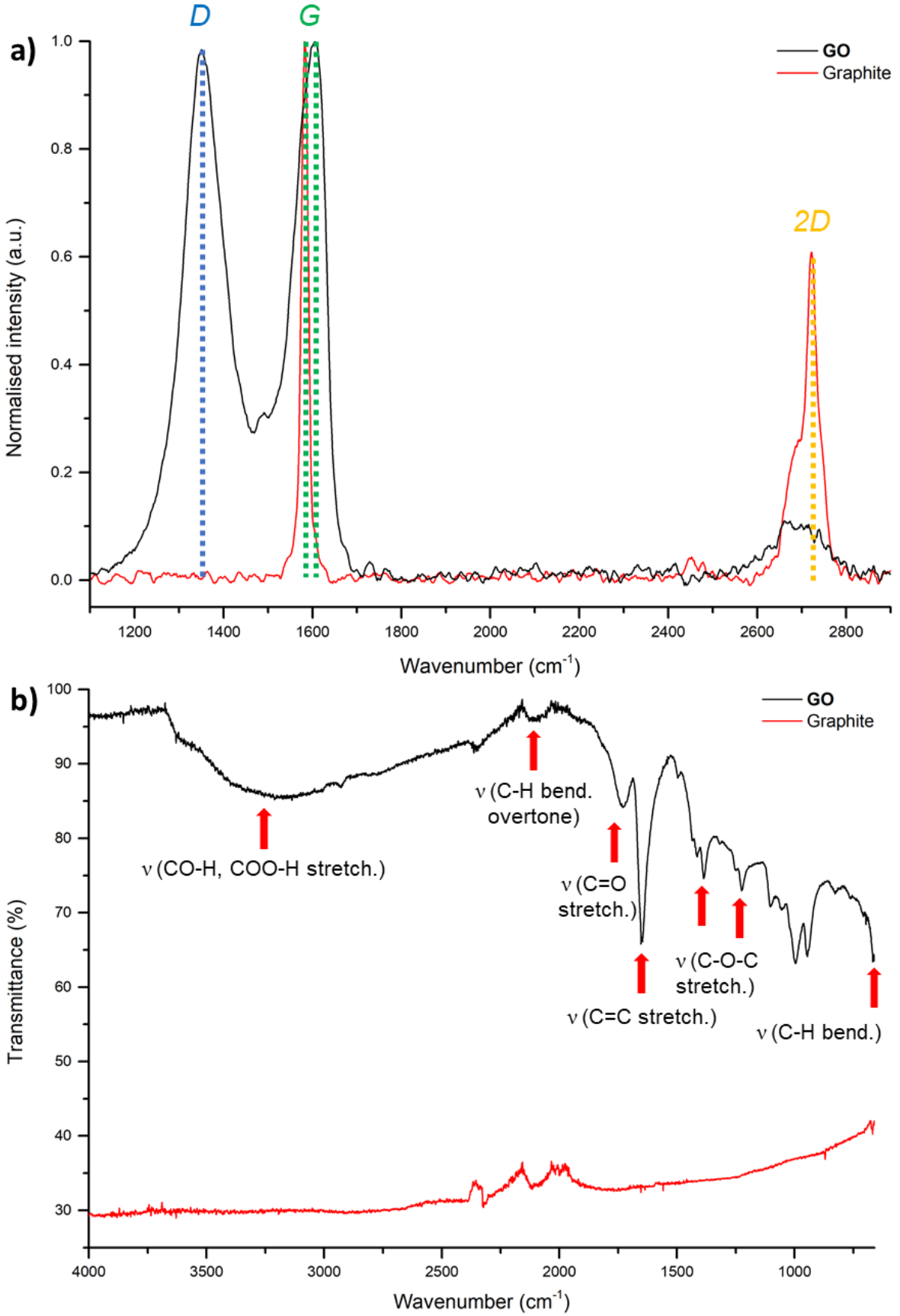

Figure B.1. a) Raman spectra of GO (black line) and graphite (red line); **b)** FT-IR spectra of GO (black line and graphite (red).

Raman spectra (10.1a) show substantial differences between the starting material (graphite) and its congener (graphene oxide). The spectrum of **GO** (black line) presents the band at 1350 cm^{-1} (*D band*), attributed to out-of-plane vibrations of structural defects induced by disruption of sp^2 bonds of carbon atoms due to the existence of oxidised functional groups, such as carboxy, alcoholic and epoxy groups[22-24]. Whilst, the peak at 1610 cm^{-1} (*G band*) derived from in-plane vibrations of the bonded sp^2 carbon atoms. The *2D* band at 2700 cm^{-1} is characteristic for out-of-plane vibrations, attributed to structural defects of material[22,24]. In addition, the intensity ratio of the *D* and *G* bands (I_D/I_G) estimates the quality of the product. Ratios below 1 indicate few oxygen functional groups in the structure[23]; on the other hand, ratios very close to 1 indicate a good degree of oxidation on the material[22,24]. In this case, the calculated I_D/I_G value is 0.98 which is close to the literature values reported for pristine GO[22,24]. The Raman spectrum of pristine graphite (red line) shows the *G band* at 1580 cm^{-1} which is due to the hexagonal lattice of the structure of the carbon-based material. The *2D band* is divided $2D_1$ (2690 cm^{-1}) and $2D_2$ (2720 cm^{-1}) bands. Such a phenomenon is due to a second-order Raman scattering of in-plane optical phonons[25]. The success of the exfoliation and oxidation processes can be noticed from the IR spectra (b) of the two materials.

FT-IR spectrum of **GO** (black line) presents the characteristic peaks of the O-H stretching of carboxylic and alcoholic groups (3255 cm^{-1}). The overtone bands of aromatic C-H bending were found between 2030 and 2000 cm^{-1} which are coupled with the band at 660 cm^{-1} of the aromatic C-H bending. The carboxylic groups presented the C=O stretching band at 1720 cm^{-1} and the C-O stretching band at 1390 cm^{-1}. The band at 1230 cm^{-1} was attributed to the C-O stretching of epoxy and alcoholic groups. On the other hand, the spectrum of graphite (red line) shows two main bands which can be attributed to the aromatic overtones of C-H bending (2160-2035 cm^{-1}) and the corresponding aromatic C-H bending at 669 cm^{-1}.

GO was further investigated by 2D-mapping Raman spectroscopy. A drop of 0.1 mg mL^{-1} in THF of **GO** was deposited in a silicon wafer and, after the evaporation of the solvent, it was irradiated by a laser with energy corresponding to the *G* (λ_{ex}=6246 nm) and *D* (λ_{ex}=7369 nm) bands. In Figure B.2, it is shown the micrograph (a) of the investigated **GO** flake, red-colour scale image, corresponding to the energy of the *G* band (b) and blue-colour scale image, corresponding to the energy of the *D* band (c).

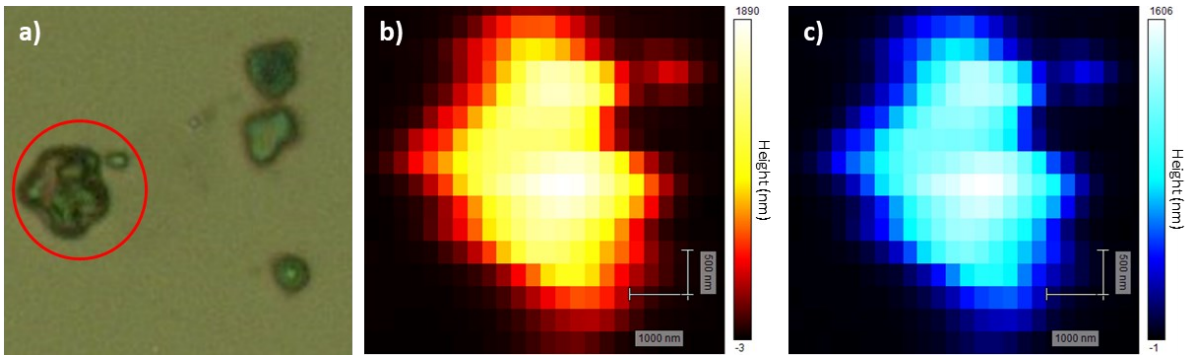

Figure B.2. a) Raman micrograph of the scanned **GO** flake; **b)** red-colour scale images (λ_{ex}=6246 nm); **c)** blue-colour scale images (λ_{ex}=7369 nm) (Scale: length=500 nm, width=1000 nm).

Raman spectra were generated at selected heights of the flake (red circle) from both images in red-scale (B.2b) and blue-scale (B.2c) colours. Such spectra corresponding to 5.2b (λ_{ex}=6246 nm) and 5.2c (λ_{ex}=7369 nm) at different heights of the scanned **GO** flake (red circle) are reported in the Supporting Information (Figures B22 and B.23). The obtained spectra form the analysis were used to evaluate the average ratio between the intensity of the D and G bands ($<I_D/I_G>$) which can approximately quantify the homogeneity and level of oxidation of scanned area[20,26,27] of graphene oxide. Generally, a ratio above 1 indicates that the surface of the material has been oxidised homogeneously[28]. The $<I_D/I_G>$ value found from the analysis was 0.74±0.07 which suggests a good oxidation state of the analysed flake of GO.

GO was analysed by high-resolution TEM and SAED to evaluate its morphology and structure. A solution of **GO** (0.1 mg mL^{-1} in THF) was evaporated in carbon support and analysed by SEM and SAED (Figure B.3).

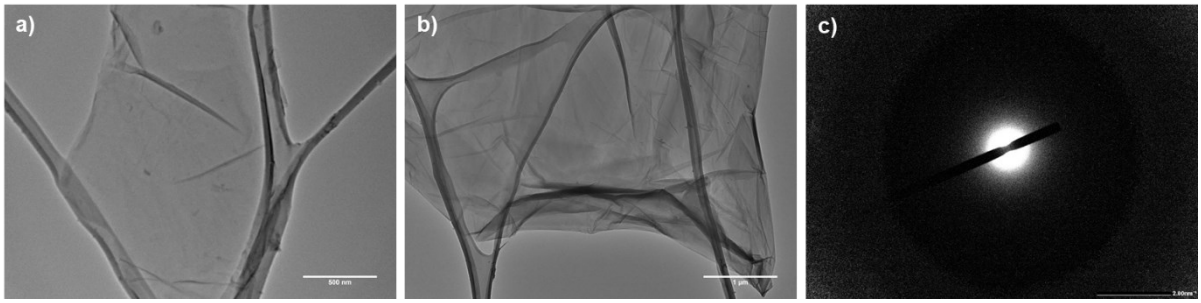

Figure B.3. a and **b**) HR-TEM micrographs of graphene oxide (scale bar: 500 nm and 1 µm, respectively); **c)** SAED pattern obtained for GO (scale bar: 2 nm^{-1}).

The SEM micrographs in Figure B.3a and b show a sheet-like morphology, typical for a 2D-material with different degrees of stacking and sheet sizes. Defects on the material can be noticed by the presence of wrinkling of the sheets[29].

The SAED micrograph (c) suggests that the surface of the sheet produces a typical pattern of an amorphous material due to lack of diffraction spots. This can be attributed to the random oxidation of the surface of the material, occurring during the synthetic process. On the other hand, the typical diffraction pattern of a non-oxidised honeycomb lattice was not observed in the reduced regions of the material.

8.1.2. Investigations into the formation of new fluorogenic composite hybrid nanomaterial

In the last two decades, NDI-based compounds have been explored for their interactions with carbon-based materials to form FCMs[16,30,31]. The rigidity and planarity of these molecules, in addition to their extended π-system, can lead to interact with carbon-based material to create FCM for biosensing and imaging. In Chapter 4, it was explored NDI-targeted compounds (***L*-13** and ***L*-14**) for their optical features and localisation in living cell lines.

Here, the potential application of ***L*-13** with **GO**, as well as ***L*-14**, as FCMs is presented. This peptide-targeted NDIs can be used as signalling and recognition molecules for prostate cancer detection. Preliminary data were obtained by titration of the peptide-tagged NDIs with **GO**, monitored by fluorescence spectroscopy. The starting solution of ***L*-13**, as well as ***L*-14**, was 0.2 mM in DMSO and aliquots of a solution 0.5 mg mL^{-1} in DMSO of **GO** were added.

The fluorescence spectra of ***L*-13** (Figure B.4) and ***L*-14** (Figure B.5) and the plots of their fluorescence emission intensities at 424 and 529 nm *vs* added volume of **GO** are shown. The fluorescence of **GO** is excluded as these carbon-based materials showed fluorescence emissions between 300 and 375 nm.

The points were fitted using the web application *BindFit*[32-34], designed by Prof. Pall Thordarson.

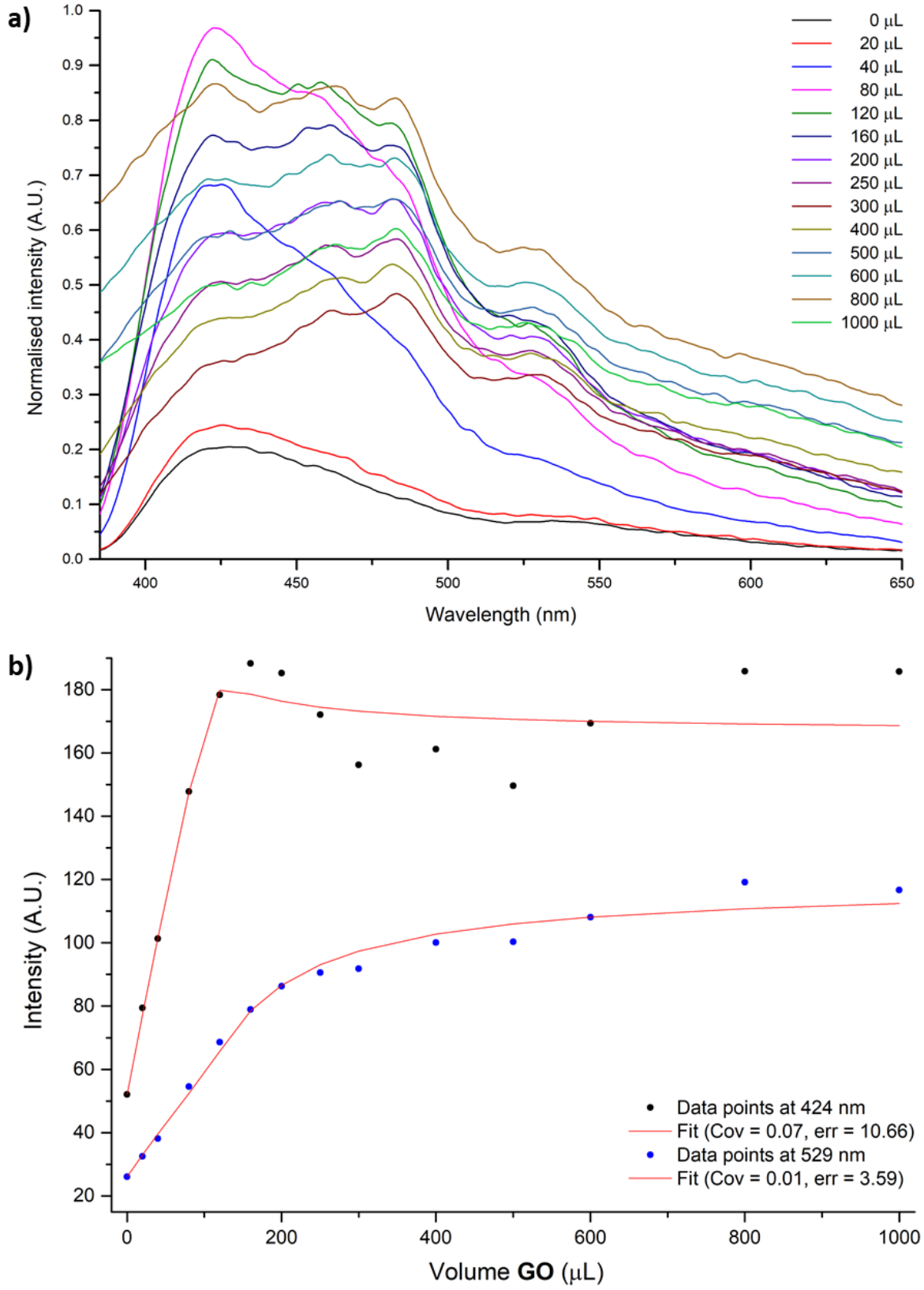

Figure B.4. a) Fluorescence spectra of ***L*-13** titrated with **GO**; **b)** plot with fit of the maxima intensity at 424 nm (black dots) and 529 nm (blue dots) *vs* added volume of **GO**.

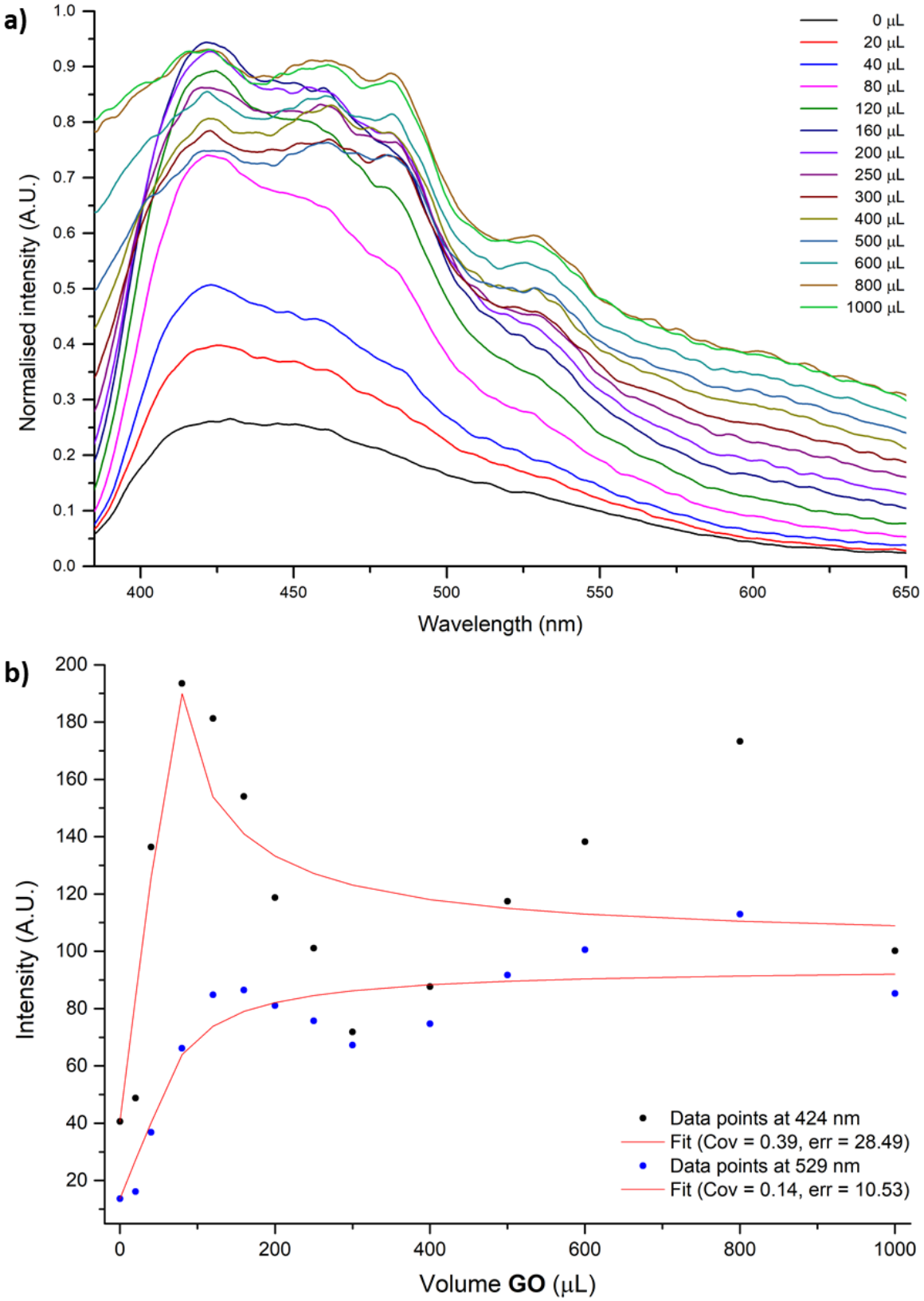

Figure B.5. a) Fluorescence spectra of ***L*-14** titrated with **GO**; **b)** plot with fit of the maxima intensity at 429 nm (black dots) and 529 nm (blue dots) *vs* added volume of **GO**.

The fluorescence spectra of both ***L*-13** and ***L*-14**, titrated with **GO**, presented changes in the fluorescence emission at 424 and 529 nm at λ_{ex}=360 nm.

Both data sets were fitted as 2:1 system of a host-guest complex (hosts: ***L*-13** and ***L*-14**; guest: **GO**). For the system ***L*-13:GO**, the found $K_{1:1}$ was 82 M^{-1} and the $K_{2:1}$ was 2495 M^{-1}; Similarly, the complex ***L*-14:GO** presented a $K_{1:1}$ equals to 126 M^{-1} and the $K_{2:1}$ is 2506 M^{-1}. These values suggested that the NDI-peptide species can interact similarly with the surface of the graphene oxide because of the formation of π-π interactions. In addition, the formation of a 2:1 complex is favourable thanks to the extended surface of **GO** which can host more than one species. Further analysis of the aggregation of these host-guest systems will be carried out to understand their fluorescence characteristics in solution and then be studied in living cells.

8.1.3. Synthesis and characterisation of novel flat aromatic compound for fluorogenic composite material formation

As previously mentioned, flat extended aromatic compounds have become ideal candidates to form FCMs as FRET donors. Here, a potential FRET donor is presented, consisting of a diphenyloxalilimidoyl backbone in which two indenyl moieties are covalently bonded. Scheme 10.3 reports the synthetic pathway of molecule **16**, adapted from a literature procedure[17,35,36].

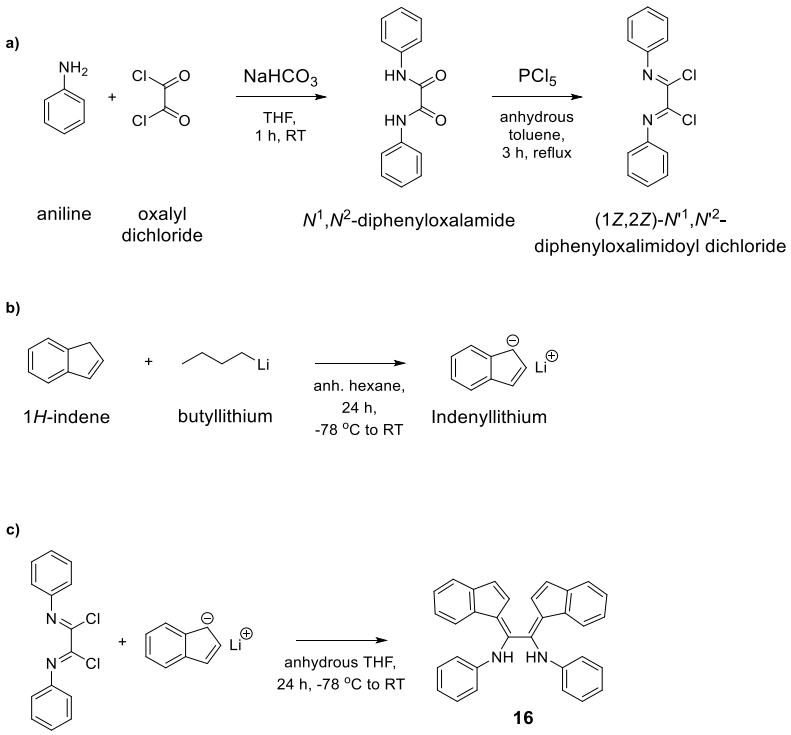

Scheme B.3. a) Reaction scheme for the synthesis of the oxalimidoyl dichloride precursor; **b)** reaction scheme of indenyllithium; **c)** coupling between the oxalimidoyl dichloride precursor and indenillithium.

The path a in Scheme B.3 shows the coupling between aniline and oxalyl chloride, base catalysed, which lead to the pure oxalamide intermediate after neutralising the reaction mixture with deionised water and filtration. This intermediate was treated under anhydrous conditions with phosphorous pentachloride in anhydrous toluene for 3 hours at room temperature. The pure diphenyloxalimidoyl dichloride was obtained after flash chromatography.

In the route b, the synthesis of the indenyl anion is reported which was obtained under anhydrous conditions. Indene was solubilised in anhydrous hexane in a dry ice/acetone bath (*circa* -78 ºC) and *n*-butyl lithium was added dropwise to the solution. The reagents were left to react overnight at room temperature and the product was used without any purification. Path c reports the coupling between the diphenyloxalimidoyl dichloride and the indenyl anion in anhydrous conditions in anhydrous toluene, placed in a dry ice/acetone bath. The pure compound **16** was obtained after 24 hours at room temperature and purified by chromatography. Compound **16** was characterised by mass spectrometry, shown in Figure B.6 with the isotopic patterns of the $[M+H]^+$ (a) and $[M+Na]^+$ (b) with their theoretical data.

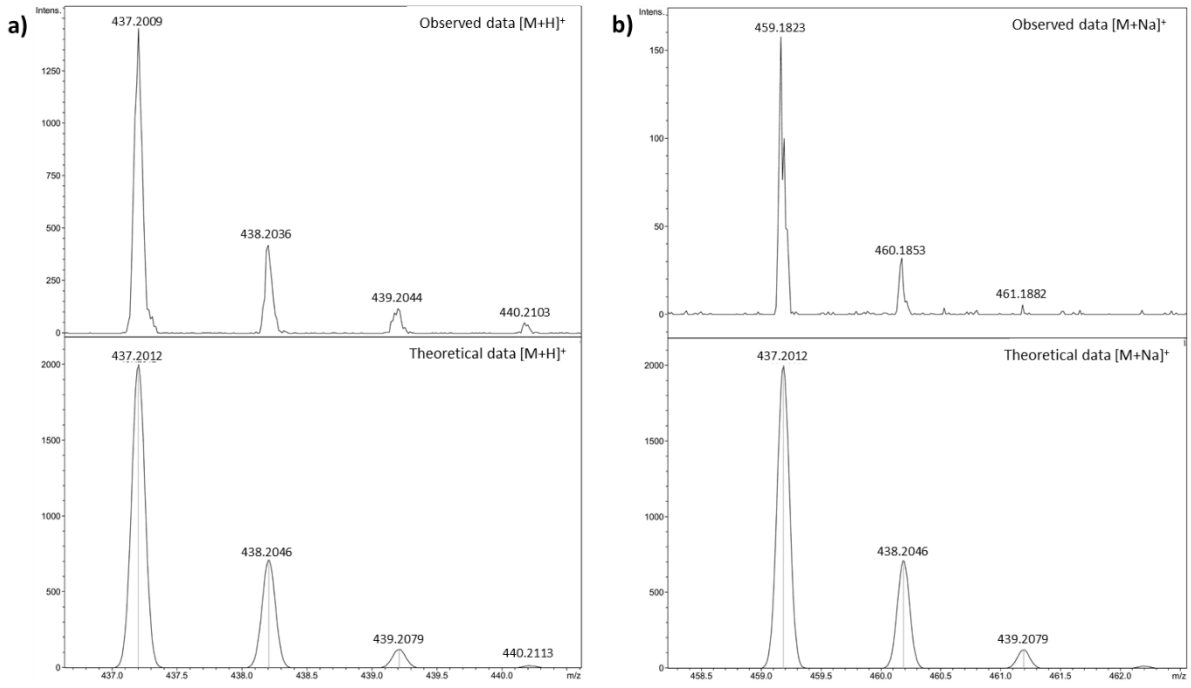

Figure B.6. a) Isotopic patterns of the $[M+H]^+$ ion; **b)** isotopic patterns of the $[M+Na]^+$ ion of compound **16** (exact mass = 436.1936).

Compound **16** was characterised by FT-IR in attenuated total reflectance (ATR) mode which spectrum is shown in Figure B.7.

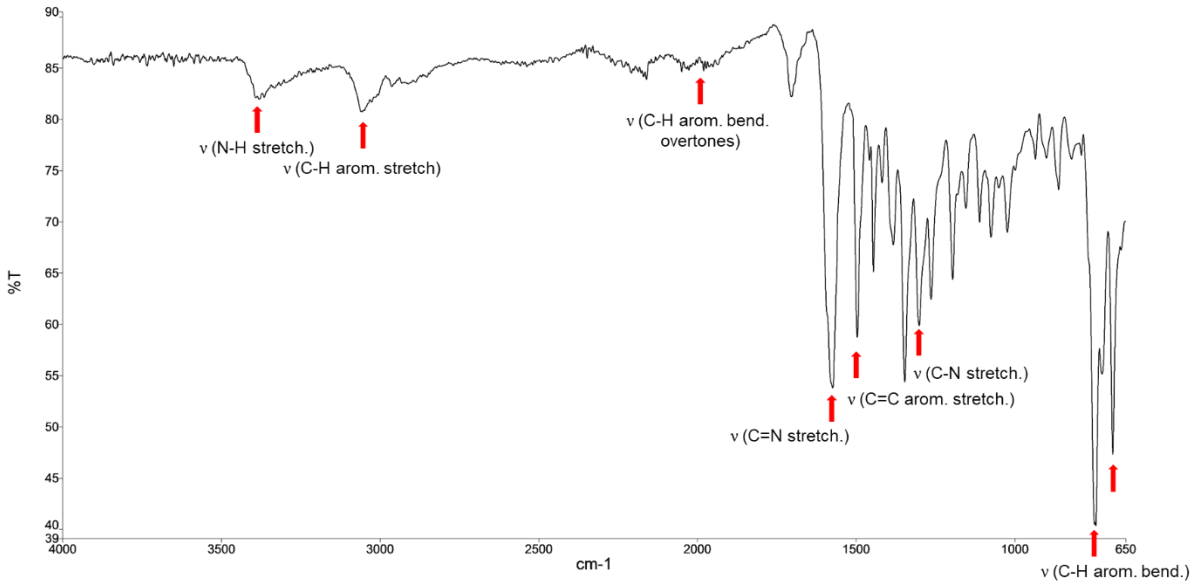

Figure B.7. FT-IR spectrum of compound **16** with main functional group indicated.

FT-IR spectrum shows the characteristic vibrations of the functional groups present on compound **16**. The band at about 3050 cm^{-1} is due to the stretching of the C-H bond in the aromatic rings. Such vibrations are coupled with the aromatic C-H bending bands between 700 and 650 cm^{-1} and their aromatic overtone bands at around 2000 cm^{-1}. In addition, the aromatic C=C stretching can be noticed between 1500 and 1400 cm^{-1}. The stretching of the C-N bond is at 1300 cm^{-1} and the N-H stretching is at 3450 cm^{-1}. Moreover, the stretching of C=N (1570 cm^{-1}) can be noticed in the spectrum suggesting the presence of this functional group in the molecule. An enamine-imine tautomeric equilibrium was hypothesised as shown in Figure B.8 which can be confirmed by the presence of another set of signals in the ^{1}H-NMR spectrum (Supporting Information, Figure B.17).

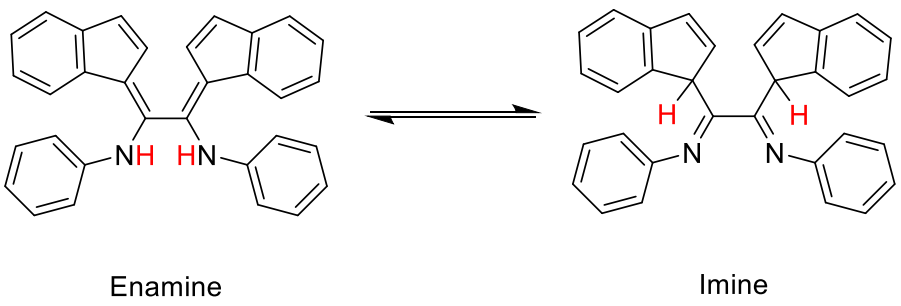

Figure B.8. Proposed enamine-imine equilibrium of compound **16**.

To increase the conjugation and rigidity of **16**, a carbon-carbon coupling between the cyclopentene rings on the indenyl moieties was planned to be created as shown in Scheme B.4. This reaction was previously reported[17] for the complexation of Pt(II) which instead lead to the bridged molecule **17** reported in Scheme B.4.

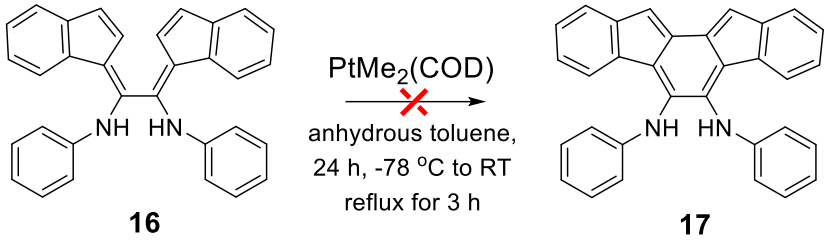

Scheme B.4. Proposed reaction scheme of compound **17**.

A solution of $PtCH_3(COD)$ in toluene was slowly added to the red solution of **16** in anhydrous toluene and left to react for 24 hours. At the end of this period of time, the reaction mixture was warmed under reflux for further 3 hours. The solvent was removed and the obtained solid was analysed by ^1H-NMR which showed any matching signals with the proposed structure. Despite several attempts and care of anhydrous conditions, this reaction did not bring to the desired compound. However, molecule **16** has still considered a valid candidate for the formation of the FCM with **GO**.

8.1.4. Optical characterisation and prostate cancer cells preliminary studies

The optical spectroscopy characteristics of **16** were investigated by UV-visible and fluorescence spectroscopies. These properties were investigated in two solvent systems of equal concentration (0.05 mM) to evaluate the effect of the solvent in their absorption and emission features. Figure B.9 shows the UV-visible spectra of **16** in DMSO (black line) and DCM (red line).

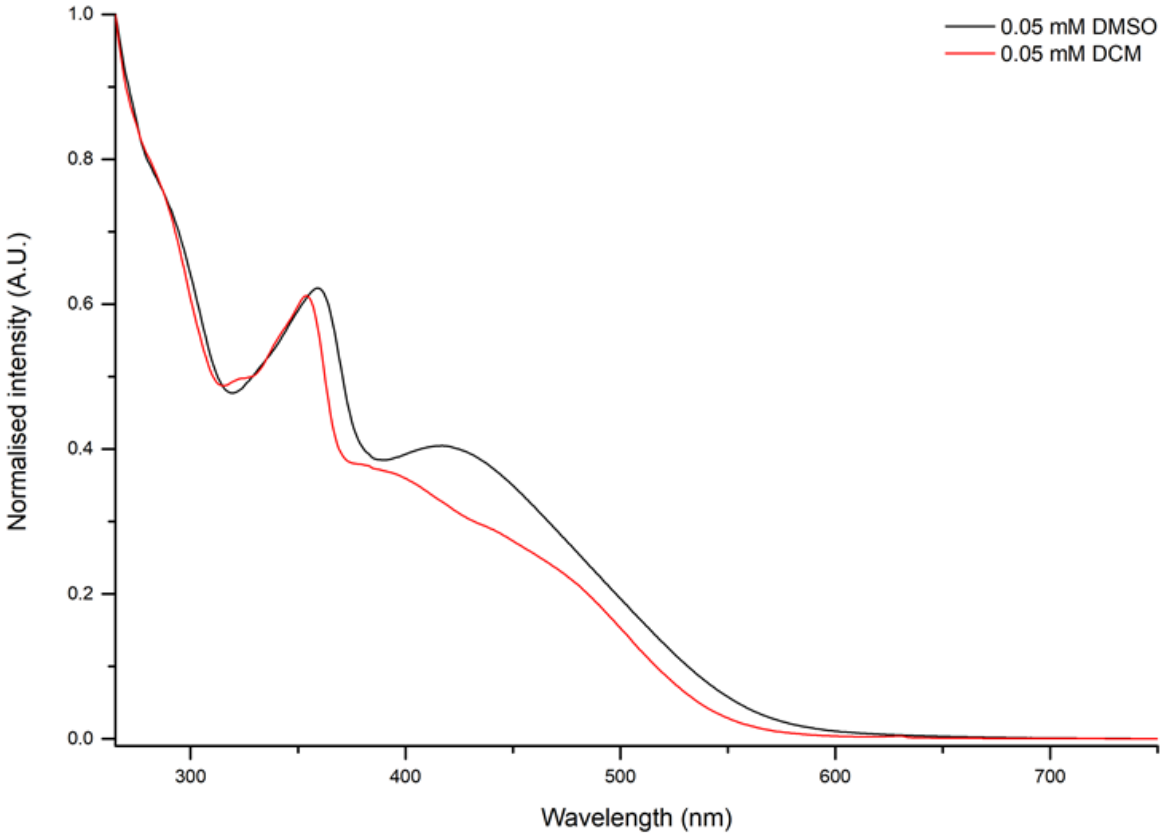

Figure B.9. Normalised UV-visible spectra of compound **16** in 0.05 mM DMSO (black line) and 0.05 mM DCM (red line).

Both spectra show similar bands attributed to the electronic transitions π-π^* and n-π^* due to the aromatic rings. The first absorption appeared at 355 nm in DCM and 359 nm in DMSO. The second transition was found at 420 nm in DMSO. Whilst, such absorption was split in two maxima (389 and 441 nm) in DCM.

The fluorescence emission of compound **16** was evaluated by fluorescence excitation-emission matrix (EEM) maps in both solvent systems. Figure B.10 displays the EEM map in DCM (a) and in DMSO (b).

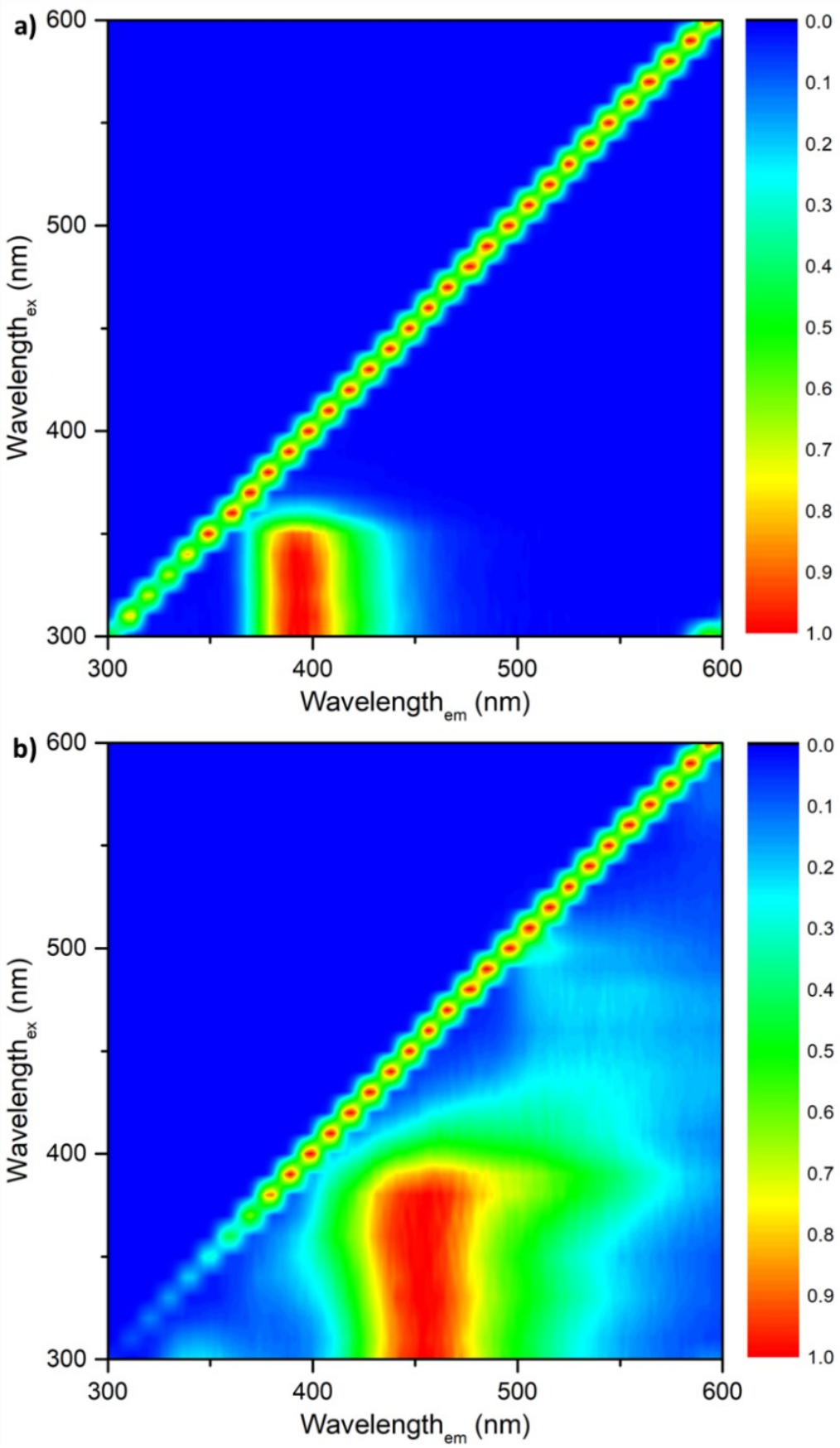

Figure B.10. Normalised fluorescence excitation-emission matrix (EEM) maps of compound **16** in 0.05 mM DMSO (a) and 0.05 mM DCM (b).

Compound **16** shows different fluorescence emissions in the two solvent systems. Particularly, in DCM (a), the emissions are between 360 and 450 nm, when excited between 300 and 360 nm; whilst, the emissions in DMSO are shifted between 400 and 550 nm, in the excitation range of 300 and 430 nm. In addition, weak emissions between 500 and 650 nm (λ_{ex}=450-500) are noticeable. This solvent system will be used to incubate the compound into the cells and all the spectroscopic charactheristic in this solvent will be considered for the confocal laser-scanning microscopy studies.

In Table B.1 the molar extinction coefficient (ε) and the quantum yield (Φ) are summarised in both solvent systems, referred to rhodamine B (2.6 nM, Φ=0.70±0.02, λ_{ex}=348 nm, η=1.33)[37].

Table B.1. Summary table of ε and Φ, referenced to Rhodamine B (2.6 nM, Φ=0.70±0.02, λ_{ex}=348 nm, η=1.33)[37].

Compound 12	**ε_{max} ($\cdot 10^3$ L mol^{-1} cm^{-1})**	**Φ**
0.05 mM DMSO	12.2 (λ_{max}=359 nm)	0.29
0.05 mM DCM	8.4 (λ_{max}=355 nm)	0.10

The fluorescence lifetime of **16** was investigated by TCSPC in 10 mM solution in DMSO. Figure B.11 shows the lifetime distribution of **16**.

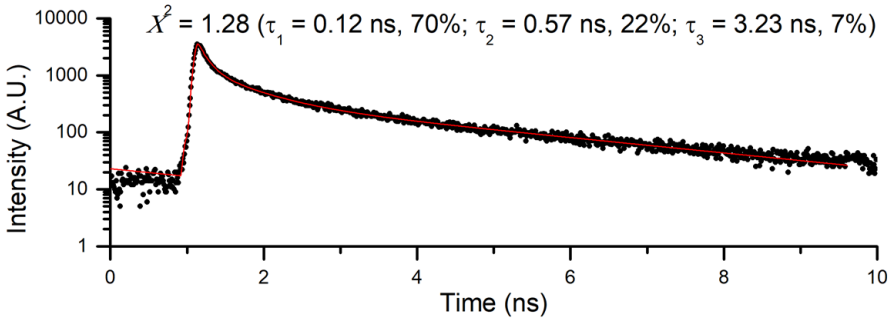

Figure B.11. TCSPC distribution of lifetime decays of compound **16** in 10 mM DMSO.

The lifetime distribution of **16** was fitted as triple-exponential decay with a χ^2 equals to 1.28. The first component represents the major contribution (70%) with 0.12 ns of lifetimes; the second component has a contribution of 22% with 0.57 ns of lifetimes; a minor contribution of 7% has a long-lifetime decay of 3.23 ns.

The distribution and uptake of compound **16** in living prostate cancer cells (PC-3) was evaluated by confocal laser scanning microscopy (CLSM).

Compound **16** was incubated at 37 ºC for 20 minutes in 1:99 DMSO:serum-free medium solution with PC-3 cells (Supporting Information, Figure B.24). Compound **16** showed good distribution and uptake in the cytosol of the cells and its fluorescence emissions are in all three channels of the excitation wavelength of 405 nm.

Such emissions are consistent with the fluorescence EEM map, depicted in Figure B.10b which showed intense emission in the range between 400 and 560 nm at the same excitation wavelength. At the excitation wavelength of 488 nm, **16** showed weak fluorescence emissions only in the green (λ_{em}=500-550 nm) and red (λ_{em}=570-700) channels. The only emission at 561 nm is in the red channel.

The cytotoxicity of **16** was evaluated by MTT assay in PC-3 cells line over 24-, 48- and 72-hours. Figure B.12 shows the normalised cell viability *vs* concentration.

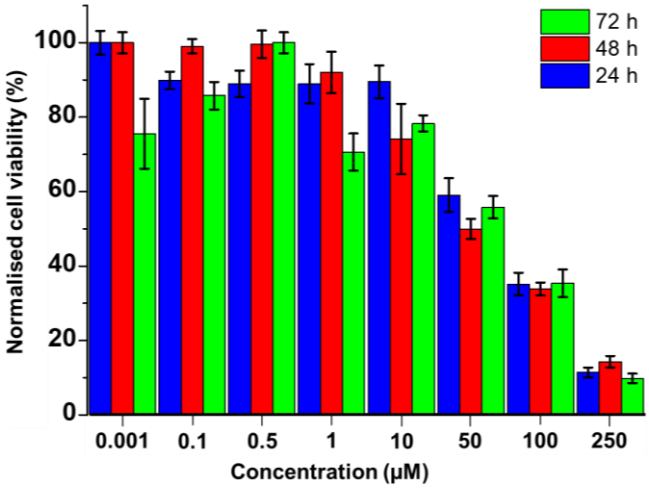

Figure B.12. MTT assay data of compound **16** in PC-3 cells over 24 (blue bars), 36 (red bars) and 72 h (green bars).

Compound **16** showed weak toxicity at 24 hours incubation with the cells until 10 μM. At 50 μM, the compound killed around 40% of the cells, whilst at 100 μM, the viability reached 40%. The 250 μM is the concentration which killed almost the 90% of cells in 24 hours. A similar trend was found at 48 hours incubation. The concentrations of 100 and 250 μM reached 40 and 15% respectively of viable cells. At 72 hours, the cell viability at 0.001 μM started at around 80% which is approximately maintained until 10 μM. The cell viability at 100 and 250 μM reached 40 and 10% respectively. Overall, the compound showed mild toxicity overtime which was accentuated at a concentration greater than 50 μM.

8.1.5. Preliminary analysis of the formation of fluorogenic composite materials in dispersed phase

This part presents a preliminary evaluation of a formed FCM between **16** and **GO**. Such estimation was carried out *via* fluorescence spectroscopy, using the method of titration by successive additions of aliquots of **GO**. The starting solution of **16** was 0.025 mM in DMSO and aliquots of a solution 0.5 mg mL^{-1} in DMSO of **GO** were added. Figure B.13 shows the fluorescence spectra of **16** (a) with the added volumes of **GO**; while the plot b displays the added volumes of **GO** *vs* intensity of the maximum emission (449 nm).

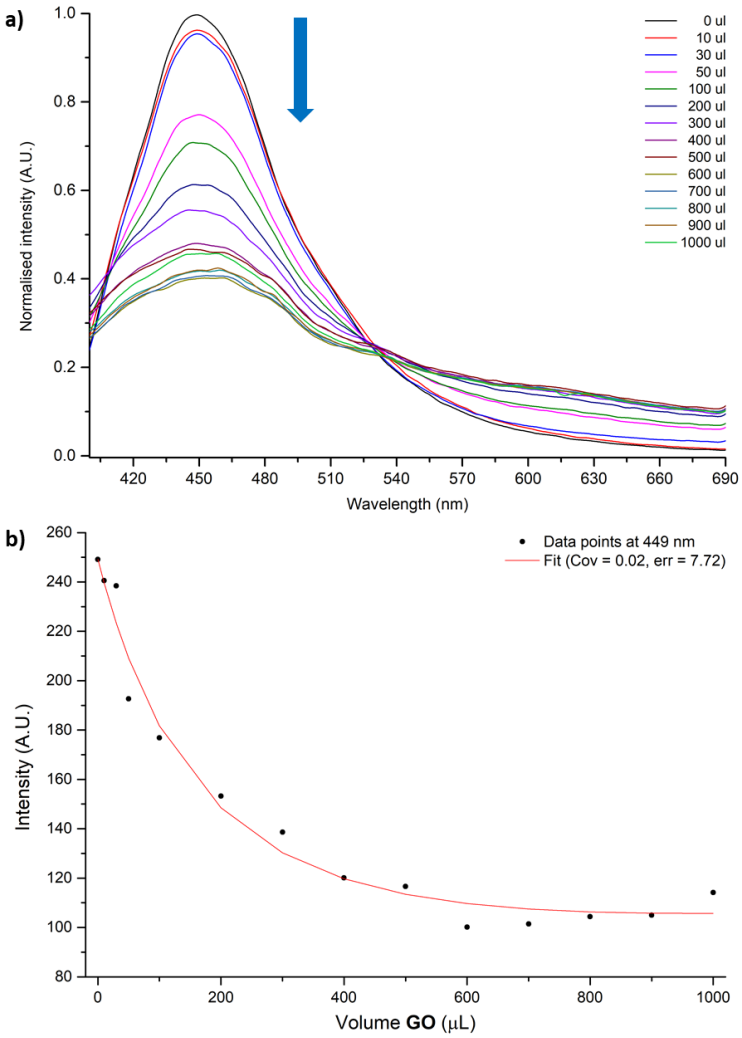

Figure B.13. a) Fluorescence spectra of compound **16** titrated with **GO**; **b)** plot with the fit of the maxima intensity at 450 nm *vs* added volume of GO.

In the spectra in B.13a, a decrease of the fluorescence emission intensity at 449 nm can be noticed at the increase of the volume of **GO** in the solution. The plot in b reports the fluorescence emission intensity at 449 nm *vs* the added volume of **GO** in the solution of **16**.

The points were fitted using the web application *BindFit*[32-34]. The data were fitted for a 2:1 system for a host-guest complex consisting of **16** (host) and **GO** (guest). The association constants found from the fit are 0.07 M^{-1} ($K_{1:1}$, for 1:1 complex) and 3500 M^{-1} ($K_{2:1}$, for the 2:1 complex). The formation of a 2:1 complex of **16** with **GO** is more favourable than the 1:1 complex thanks to the π-π interactions created between the two species.

The fluorescence emissions of **16** at different concentrations were investigated by fluorescence spectroscopy to evaluate if the molecule can itself quench fluorescence. Figure B.14a shows the fluorescence spectra of **16** at different concentrations in DMSO; on the other hand, the plot (b) displays the collected data points at the emission wavelengths of 462 (black dots) and 601 nm (blue dots) *vs* the concentration of **16**.

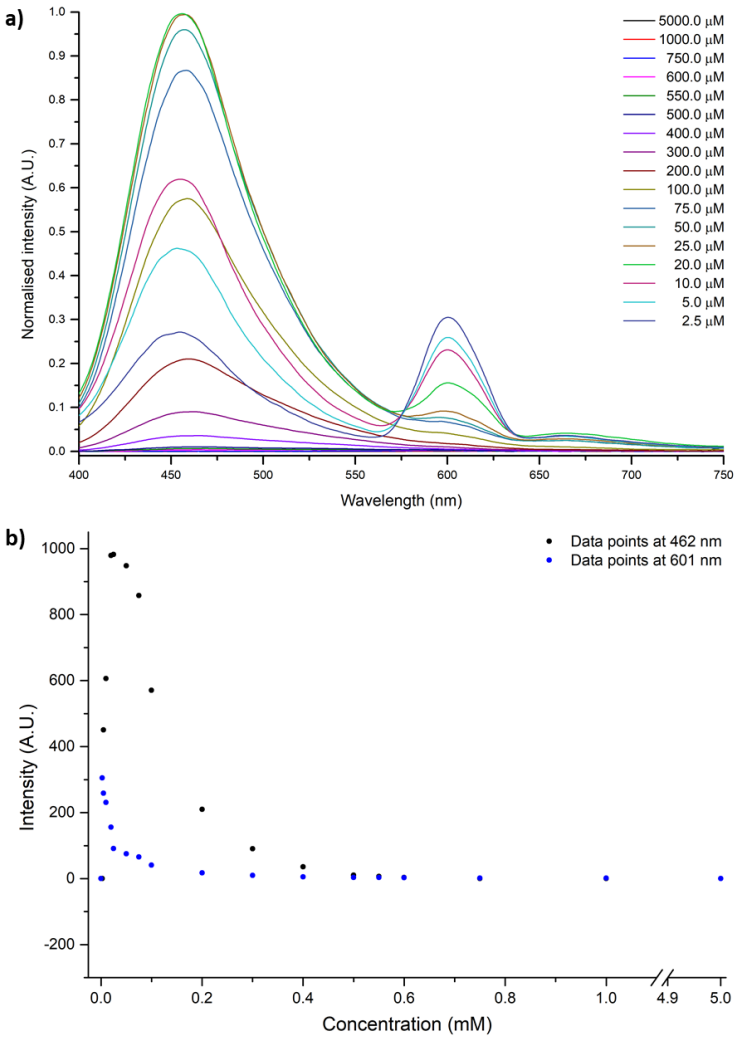

Figure B.14. a) Fluorescence spectra of compound **16** at different concentration; **b)** data points of the maxima intensity at 462 and 601 nm *vs* concentration of compound **16**.

The emission spectra B.14 were obtained by exciting the solutions of compound **16** at 300 nm which is the wavelength where the compound showed intense fluorescence emission. The spectra show a decrease of the fluorescence emission at both emission wavelength (*i.e.* 462 and 601 nm), increasing the concentration. This phenomenon suggests that, at high concentration, the compound can self-aggregate and therefore the fluorescence emission might be quenched. The data points in the plot in Figure B.14b show the maxima fluorescence emission intensities at both 462 and 601 nm of the different concentration of **16**. The data can be fitted as 1:2 system with a $K_{1:1}$ equal to $330 \cdot 10^{12}$ M^{-1} and $K_{1:2}$ of $19 \cdot 10^{12}$ M^{-1}. The data were fitted using the web application *BandFit*[32-34].

8.1.6. Nitro-derivatives for the formation of fluorogenic composite materials for hypoxia selectivity

As described in the Introduction, solid tumoral tissues are under low level of oxygen (hypoxia) which can lead to several effects such as resistance to apoptosis, an increase of invasiveness and metastatic spread[38]. The hypoxic environment has raised a lot of interest in research for the development of compounds which can be activated under low oxygen concentrations to target and kill cancer cells[38] or change fluorescence characteristics in hypoxic conditions[39-41].
Considering such last facts, the aromatic rings (indenyl and aniline moieties) of compound **16** can be considered valid points to derivatise the molecule with a nitro group. This derivatisation can result in a novel imaging biosensor which its fluorescence emission can change under hypoxia condition. Scheme B.5 shows the proposed derivatisation of compound **16**.

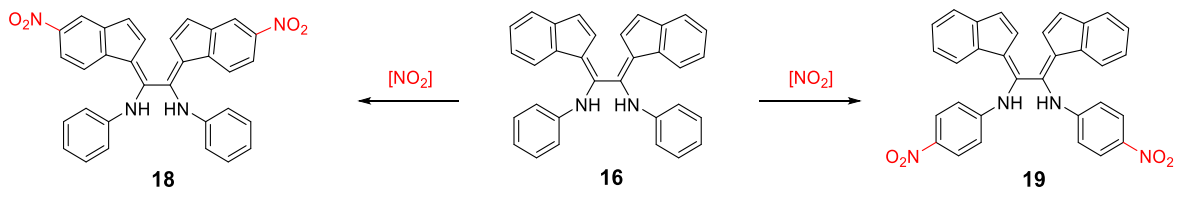

Scheme B.5. Schematic representation of the proposed nitration of the indenyl-based compound.

The proposed derivatisations of **16** with nitro groups were designed to be on the indenyl rings (molecule **18**) or in the aniline ring (molecule **19**).
To attempt the synthesis of molecule **18**, the indenyl derivative should be derivatised with a nitro group. Scheme B.6 shows the synthetic reactions to derivatised the indenyl moiety.

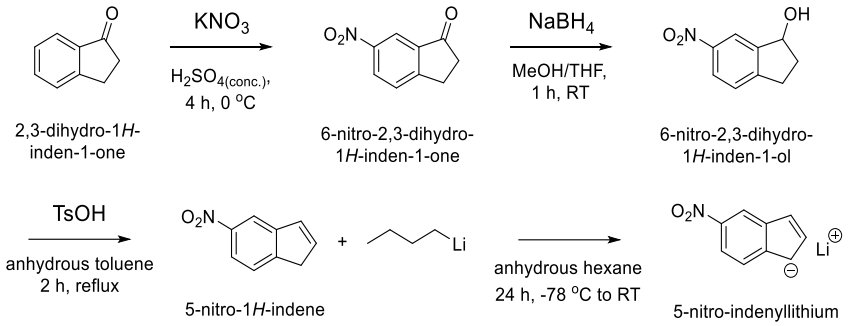

Scheme B.6. Proposed reaction scheme for nitro-indenyllithium.

The first step of this synthetic path was adapted from a previous work[42]. In the first step, indenone was nitrated by sodium nitrate in concentrated sulfuric acid. The obtained nitro-indenone was reduced by sodium borohydride. The corresponding alcohol of nitro-indenone was purified by chromatography and then reduced by using *p*-toluenesulfonic acid and the desired nitro-indene was obtained by chromatography. The fourth step of reaction scheme (*i.e.* the formation of the anionic species of nitro-indene) was attempted in anhydrous condition. Despite the care to respect the anhydrous conditions, the desired product was not obtained.

The second derivatisation to introduce nitro groups on the indenyl backbone was attempted on the aniline moieties. Scheme B.7 reports the synthetic pathway to obtain molecule **19**.

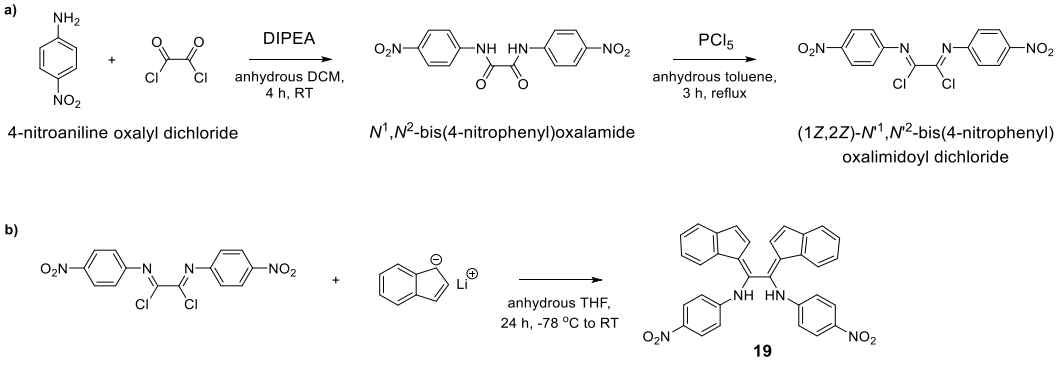

Scheme 10.7. The proposed reaction scheme to obtain *bis*(nitrophenyl)oxalimidoyl dichloride **19**.

The starting material for the synthesis of compound **19** is *p*-nitroaniline. The synthetic procedure was adapted from previous works[17,43] which *p*-nitroaniline was reacted with oxalyl dichloride in basic condition (path a). The obtained dinitrophenyl oxalamide was reacted with phosphorous pentachloride to substitute the ketone groups in chloride, according to the mechanism proposed in literature[44]. The reaction in path b was attempted in Schlenk's line; however, the desired compound **19** was not obtained.

8.1.7. Conclusions

Novel fluorogenic composite materials were assembled and preliminarily studied by fluorescence spectroscopy were performed. The rationale behind this approach is that this synthetic design might be of relevance for potential biosensing and imaging applications using nanomaterials. These materials consisted of a FRET acceptor which generally quenches the fluorescence emission of a FRET donor.

Graphene oxide was chosen as FRET acceptor as it is a well-known fluorescence quencher. This carbon-based material was synthesised from an adapted version of the Hummer's method and characterised by FT-IR and Raman spectroscopies and TEM.

Two different class of FRET donors were investigated by titration with graphene oxide, using fluorescence spectroscopy. The first type of FRET donors is the peptide-tagged NDI which present the aromatic core of the NDI, already investigated with carbon-based materials thanks to π-π interactions established with them. As previously described in Chapter 4, a *mono*- and *bis*-peptide versions were synthesised and characterised. In this Appendices, they were titrated with graphene oxide to evaluate their fluorescence emission changes and estimate their binding constants with the carbon-based materials. Both peptide-tagged NDIs were fitted as 2:1 host-guest systems with graphene oxide with a binding constant of 2500 M^{-1}.
The second type of FRET donor presents a symmetric diphenyloxalilimidoyl backbone with two indenyl moieties. This flat and aromatic compound was synthesised and characterised by NMR and FT-IR spectroscopies and mass spectrometry. The optical characteristics were evaluated by UV-visible and fluorescence spectroscopies in different solvent system. The potential application of this compound was tested by fluorescence spectroscopy *via* titration with graphene oxide. This preliminary result revealed a decrease of the fluorescence emission of the FRET donor, increasing the amount of graphene oxide in solution. In addition, the formed supramolecular aggregate was fitted as a 2:1 host-guest complex with a binding constant of 3500 M^{-1}. Different concentrations of the diphenyloxalilimidoyl compound were investigated *via* fluorescence spectroscopy and this analysis revealed that the compound could quench its fluorescence emission at high concentration.

This diphenyloxalilimidoyl-indenyl compound was planned to be derivatised to incorporate nitro-groups in its structure as a potential FRET donor for hypoxia imaging and/or biosensing. The introduction of nitro-groups on the backbone of the molecule may lead to changes in fluorescence emission properties under hypoxic conditions.

8.1.8. References

1. X.-P. He, Y. Zang, T. D. James, J. Li and G.-R. Chen, *Chem. Soc. Rev.*, 2015, **44**, 4239-4248.
2. P. R. Selvin, *Nat. Struct. Biol.*, 2000, **730-734**.
3. V. Georgakilas, *Functionalization of graphene*, Wiley-VCH, 2014.
4. D. C. Marcano, D. V. Kosynkin, J. M. Berlin, A. Sinitskii, Z. Sun, A. Slesarev, L. B. Alemany, W. Lu and J. M. Tour, *ACS Nano*, 2010, **4**, 4806-4814.
5. E. Morales-Narvàez and A. Merkoçi, *Adv. Mat.*, 2012, **24**, 3298-3308.
6. V. V. Neklyudov, N. R. Khafizov, I. A. Sedov and A. M. Dimiev, *Phys. Chem. Chem. Phys.*, 2017, **19**, 17000-17008.
7. P. Zheng and N. Wu, *Chem. Asian J.*, 2017, **12**, 2343-2353.
8. F. Tian, J. Lyu, J. Shi and M. Yang, *Biosens. Bioelectron.*, 2017, **89**, 123-135.
9. C. Liu, Z. Wang, H. Jia and Z. Li, *Chem. Comm.*, 2011, **47**, 4661-4663.
10. H. Dong, J. Zhang, H. Ju, H. Lu, S. Wang, S. Jin, K. Hao, H. Du and X. Zhang, *Anal. Chem.*, 2012, **84**, 4587-4593.
11. W. Li, T. Jiang, Y. Pu, X. Jiao, W. Tan and S. Qin, *Journal*, 2019, **14**, 344-348.
12. D.-K. Ji, Y. Zhang, X.-P. He and G.-R. Chen, *J. Mater. Chem. B*, 2015, **3**, 6656-6661.
13. C.-H. Lu, H.-H. Yang, C.-L. Zhu, X. Chen and G.-N. Chen, *Angew. Chem.*, 2009, **121**, 4879-4881.
14. Y. Wang, Z. Li, J. Wang, J. Li and Y. Lin, *Trends Biotechnol.*, 2011, **29**, 205-212.
15. J. A. Tyson, D. G. Calatayud, V. Mirabello, B. Mao and S. I. Pascu, *Adv. Inorg. Chem.*, 2016, **68**, 397-440.
16. J. A. Tyson, V. Mirabello, D. G. Calatayud, H. Ge, G. Kociok-Köhn, S. W. Botchway, G. Dan Pantoş and S. I. Pascu, *Adv. Func. Mat.*, 2016, **26**, 5641-5657.
17. C.-T. Chen, M. E. Fischer, C. Windsor, I. C. Vei, D. G. Calatayud, M. L. H. Green and S. I. Pascu, *Polyhedron*, 2016, **119**, 532-547.
18. W. S. J. Hummers and R. E. Offeman, *J. Am. Chem. Soc.*, 1958, **80**, 1339.
19. D. Voiry, J. Yang, J. Kupferberg, R. Fullon, C. Lee, H. Y. Jeong, H. S. Shin and M. Chhowalla, *Science*, 2016, **353**, 1413-1416.
20. J.-B. Wu, M.-L. Lin, X. Cong, H.-N. Liu and P.-H. Tan, *Chem. Soc. Rev.*, 2018, **47**, 1822-1873.
21. V. Ţucureanu, A. Matei and A. M. Avram, *Crit. Rev. Anal. Chem.*, 2016, **46**, 502-520.
22. F. T. Johra, J.-W. Lee and W.-G. Jung, *J. Ind. Eng. Chem.*, 2014, **20**, 2883-2887.
23. S. Muhammad Hafiz, R. Ritikos, T. J. Whitcher, N. Md. Razib, D. C. S. Bien, N. Chanlek, H. Nakajima, T. Saisopa, P. Songsiriritthigul, N. M. Huang and S. A. Rahman, *Sens. Actuators B Chem.*, 2014, **193**, 692-700.

24. S. Perumbilavil, P. Sankar, T. P. Rose and R. Philip, *Appl. Phys. Lett.*, 2015, **107**, 051104.

25. S. Roscher, R. Hoffmann and O. Ambacher, *Anal. Methods*, 2019, **11**, 1224-1228.

26. M. Boutchich, A. Jaffré, D. Alamarguy, J. Alvarez, A. Barras, Y. Tanizawa, R. Tero, H. Okada, T. V. Thu, J. P. Kleider and A. Sandhu, *J. Phys. Conf. Ser.*, 2013, **433**, 012001.

27. S.-G. Kim, O.-K. Park, J. H. Lee and B.-C. Ku, *Carbon Lett.*, 2013, **14**, 247-250.

28. A. A. Dubale, W.-N. Su, A. G. Tamirat, C.-J. Pan, B. A. Aragaw, H.-M. Chen, C.-H. Chen and B.-J. Hwang, *J. Mater. Chem. A*, 2014, **2**, 18383-18397.

29. X. Shen, X. Lin, N. Yousefi, J. Jia and J.-K. Kim, *Carbon*, 2014, **66**, 84-92.

30. F. Würthner, C. Thalacker, S. Diele and C. Tschierske, *Chem. Eur. J.*, 2001, **7**, 2245-2253.

31. G. D. Pantoş, J.-L. Wietor and J. K. M. Sanders, *Angew. Chem. Int. Ed.*, 2007, **46**, 2238-2240.

32. D. Brynn Hibbert and P. Thordarson, *Chem. Comm.*, 2016, **52**, 12792-12805.

33. P. Thordarson, http://supramolecular.org.

34. P. Thordarson, *Chem. Soc. Rev.*, 2011, **40**, 1305-1323.

35. D. Lindauer, R. Beckert, M. Döring, P. Fehling and H. Görls, *J. Prakt. Chem.*, 1995, **337**, 143-152.

36. S. Xia, L. Gan, K. Wang, Z. Li and D. Ma, *J. Am. Chem. Soc.*, 2016, **138**, 13493-13496.

37. A. M. Brouwer, *Pure Appl. Chem.*, 2011, **83**, 2213-2228.

38. A. Nocentini, E. Trallori, S. Singh, C. L. Lomelino, G. Bartolucci, L. Di Cesare Mannelli, C. Ghelardini, R. McKenna, P. Gratteri and C. T. Supuran, *J. Med. Chem.*, 2018, **61**, 10860-10874.

39. K. Yang, K. G. Leslie, S. Y. Kim, B. Kalionis, W. Chrzanowski, K. A. Jolliffe and E. J. New, *Org. Biomol. Chem.*, 2018, **16**, 619-624.

40. R. Kumari, D. Sunil and R. S. Ningthoujam, *Bioorg. Chem.*, 2019, **88**, 102979.

41. B. Ramya Sree, B. Sowjanya and K. Divakar, *Int. Biodeter. Biodegr.*, 2019, **143**, 104737.

42. X. Guan, P. Luo, Q. He, Y. Hu and H. Ying, *Molecules*, 2017, **22**.

43. J. J. Park, Y.-H. Kim, C. Kim and J. Kang, *Tetrahedron Lett.*, 2011, **52**, 3361-3366.

44. R. Bonnett, in *Carbon–Nitrogen Double Bonds* ed. S. Patai, 1970, DOI: 10.1002/9780470771204.ch13, pp. 597-662.7

45. X.-P. He, Q. Deng, L. Cai, C.-Z. Wang, Y. Zang, J. Li, G.-R. Chen, H. Tian, *ACS Appl. Mater. Interfaces*, 2014, **6**, 5379-5382.

8.2. Experimental procedures

8.2.1. Synthesis of graphene oxide (**GO**)

Protocol adapted from literature procedures[18,19]. In a round-bottom flask, 3.01 g of graphite powder were dissolved in 112 mL of $H_2SO_{4\ (conc.)}$ (2.09 mol) and placed in an ice bath. 2.27 g (0.03 mol) of $NaNO_3$ and 6.02 g (0.04 mol) of $KMnO_4$ were slowly added to the solution over 2 h. The mixture was warmed to room temperature and left 3 days to react. 440 mL of 5% $H_2SO_{4(aq)}$ were slowly added to the solution and the reaction was finally terminated by the addition of 30% H_2O_2. The yellow solution was washed with 50 mL of 10% $HCl_{(aq)}$ for removing residual metal ions. The resulting solution was cleaned by dialysis membrane (molecular weight cut-off = 14.000, Sigma-Aldrich) to complete elimination of metal ions and acids. The obtained **GO** was centrifuge at 6000 rpm for 30 min to remove smaller flakes, and then at 12000 rpm for 30 min to concentrate the solution.

Raman spectroscopy (graphene oxide/THF, 0.1 mg/1 mL): 1357cm^{-1} (*D band*); 1595 cm^{-1} (*G band*); 2689 cm^{-1} (*2D band*).

FT-IR spectroscopy (solid phase): $\tilde{\nu}$ = 3255 cm^{-1} (m, CO-H, COO-H and H_2O stretch.); 2030-2000 cm^{-1} (w, C-H aromatic bend. overtones); 1725cm^{-1} (m, C=O str.); 1652.28 cm^{-1} (s, C=C stretch.); 1390 cm^{-1} (w, C-OOH stretch.);1230 cm^{-1} (m, C-O-C or C-OH stretch.), 700 and 650 cm^{-1} (s, C-H arom. bend.).

8.2.2. Synthesis of 1,2-di((Z)-1H-inden-1-ylidene)-*N*1,*N*2-diphenylethane-1,2-diamine (**16**)

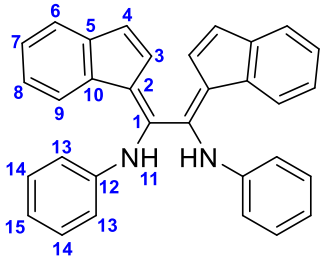

Protocol adapted from literature procedure[17]. In a Schlenk flask, 0.74 mL (8.0 mmol) of aniline were dissolved in 15 mL of THF and 674.3 mg (8.1 mmol) of $NaHCO_3$ were added. 0.34 mL (4 mmol) of oxalyl chloride were added dropwise over 5 min. The reaction was left for 1 h at room temperature. The reaction was quenched with deionized H_2O and the solvents were removed under reduced pressure. The obtained diphenyl oxalamide was filtered and washed with deionized H_2O and dried under *vacuum* and N_2 flux.

The diphenyl oxalamide (1.02 g, 4.2 mmol) and PCl_5 (1.71 g, 8.2 mmol) were dissolved with 30 mL of anhydrous toluene in a Schlenk's flask. The solution was left to reflux for 1 h under stirring. The reaction mixture, still warm, was cannulated in a round-bottom flask. The solvent was removed under reduced pressure and the obtained diphenyloxalimidoyl dichloride was no further purified.

The indenyl anion was obtained by reaction of 0.44 mL (3.7 mmol) of indene were solubilised in 15 mL of anhydrous hexane. The resulting solution was bubbled with Ar for 10 min at -78 ºC under stirring. 1.5 mL (3.7 mmol) of n-BuLi (2.5 M in hexane) was added dropwise over 5 min to the previous solution. The reaction was left for 24 h at room temperature. The solvent was removed by cannulation, the white solid was washed with n-hexane anhydrous twice and then dried with Ar flux.

The obtained indenyllithium species (0.2123 g, 1.4 mmol) was dissolved in 10 mL of anhydrous THF in a Schlenk flask, placed a dry ice/acetone bath. A solution of 202.0 mg (0.72 mmol) of diphenyloxalimidoyl dichloride in 25 mL of anhydrous THF were added dropwise to the indenyl anion solution. The mixture was warmed to room temperature and left to react for 24 h. The solvent was removed under reduced pressure and the obtained compound **12** was purified by column chromatography (silica gel in DCM:hexane, 6:4) to afford a red solid (88.4 mg, 28%).

^{1}H NMR (500 MHz, 298 K, CD_2Cl_2) δ = 7.81 (*d*, 2H, H-9, *J* = 7.5 Hz,), 7.42 (*d*, 2H, H-6, *J* = 7.4 Hz), 7.25-7.22 (*m*, 2H, H-7), 7.19-7.16 (*m*, 2H, H-8), 7.13-7.10 (*m*, 4H, H-14), 6.95 (*t*, 2H, H-15, *J* = 7.4 Hz), 6.69 (*d*, 2H, H-4, *J* = 5.3 Hz), 6.70-6.64 (*m*, 6H, H-3, H-13), 6.50 (*bs*, 2H, H-11).

^{13}C NMR (125 MHz, 298 K, CD_2Cl_2) δ = 143.5 (C-5), 140.5 (C-12) 138.3 (C-1), 134.2 (C-10), 129.6 (C-3), 129.6 (C-2), 128.82 (C-14), 126.3 (C-7), 126.1 (C-4), 124.4 (C-8), 122.6 (C-15), 121.9 (C-9), 121.3 (C-6), 118.4 (C-13).

ESI$^+$-TOF (CH_3OH)**:** m/z = 437.2009 ($[M+H]^+$); 459.1823 ($[M+Na]^+$). Calc.: 436.1939 Da.

FT-IR spectroscopy (solid phase)**:** $\tilde{\nu}$ = 3382 cm^{-1} (w, N-H stretch.), 3055 (w, C-H aromatic stretch.), 2200-2050 cm^{-1} (w, C-H aromatic bend. overtones); 1575 cm^{-1} (s, C=N stretch.); 1496-1382 cm^{-1} (s, C=C stretch.); 1300 cm^{-1} (m, C-N stretch.), 750-685 cm^{-1} (s, C-H aromatic bend.).

8.2.3. Attempt of synthesis of compound **17**

Protocol adapted from literature procedure[17]. A Schlenk flask with a solution of 50.1 mg (0.1 mmol) of **16** in 20 mL of anhydrous toluene was placed in a dry ice/acetone bath. The second solution of $PtMe_2(COD)$ (36.2 mg, 0.1 mmol) in 20 mL of anhydrous toluene were cannulated to the first one. The reaction mixture was warmed at room temperature and left 24 h. The day after, the reaction mixture was refluxed for 3 h. The solvent was removed under reduced pressure and the obtained residue was recrystallised by pentane. The brown crystals were analysed by ^{1}H-NMR spectroscopy and mass spectrometry; however, no corresponding data were found with the desired product.

8.2.4. Attempt of synthesis of compound **18**

Protocol adapted from literature procedure[42]. In a round-bottom flask, 0.60 mL (4.6 mmol) of 1-indanone were dissolved in 5 mL of $H_2SO_{4(conc.)}$ and placed in an ice bath. A solution of $NaNO_3$ (0.8124 g, 7.6 mmol) in 5 mL of $H_2SO_{4(conc.)}$ was added dropwise to the first one over 10 min. The resulting mixture was left in the ice bath for 4 h. The reaction mixture was quenched with iced water and partitioned with DCM. The organic layer was collected and washed with saturated $NaCO_{2(aq)}$ and brine. The organic layer was dried over Na_2SO_4 and the solvent was removed under reduced pressure. 6-nitroinden-1-one was purified by column chromatography in silica gel (hexane:AcOEt, 7:1).

50.2 mg (0.3 mmol) of 6-nitroinden-1-one were dissolved in 3 mL of MeOH:THF (2:1) in a round-bottom flask. 44.2 mg (1.2 mmol) of $NaBH_4$ were added slowly to the solution and the resulting reaction mixture was left for 1 h at room temperature. The mixture was quenched with deionised H_2O and partitioned with AcOEt. The organic layer was washed with brine, dried over Na_2SO_4 and concentrated under reduced pressure. 6-nitroinden-1-ol was obtained by column chromatography in silica gel (hexane:AcOEt, 2:1).

In a round-bottom flask, 6-nitroinden-1-ol (0.6326 g, 3.3 mmol) and *p*-toluenesolfonic acid (0.6125 g, 3.3 mmol) were dissolved in 7 mL of anhydrous toluene. The mixture was left 2h at room temperature. The solvent was removed under reduced pressure and the crude product was partitioned between deionised H_2O and AcOEt. The organic layer was washed with saturated $NaCO_{2(aq)}$ and brine. The obtained organic layer was dried over Na_2SO_4, filtrated and concentrated under reduced pressure. 6-nitro-indene was obtained by flash chromatography in silica gel (hexane:AcOEt, 10:1).

A Schlenk flask with a solution of 6-nitro-indene (0.1023 g, 0.6 mmol) in 5 mL of anhydrous hexane was placed in a dry ice/acetone bath. A solution of 0.30 mL (0.6 mmol) of n-BuLi (2.5 M in hexane) was added dropwise to the first one. The reaction mixture was left to react for 24 h at room temperature. The solvent was removed under reduced pressure. The white solid was analysed by ^{1}H-NMR spectroscopy and mass spectrometry; however, no corresponding data were found with the desired product.

8.2.5. Attempt of synthesis of compound **19**

Protocol adapted from literature procedures[17,43]. In a round-bottom flask, 0.4023 g (2.6 mmol) of *p*-nitroaniline were dissolved in 10 mL of anhydrous DCM. 0.40 mL (2.4 mmol) of DIPEA and 0.10 mL (1.2 mmol) of oxalyl chloride were added dropwise. The reaction mixture was left for 4 h at room temperature. The suspension was filtered and washed with DCM and bis(*p*-nitrophenyl) oxalamide was obtained after removing the solvent under reduced pressure.
In a Schlenk's flask, 0.1053 g (0.3 mmol) of bis(*p*-nitrophenyl) oxalamide and 0.1036 g (0.4 mmol) of PCl_5 were solubilised in 20 mL anhydrous toluene. The reaction mixture was left for 4 h under reflux. Bis(*p*-nitrophenyl) oxalimidoyl dichloride was obtained by removing the solvent under reduced pressure.
Indenyllithium (0.0702 g, 0.6 mmol) was dissolved in 10 mL of anhydrous THF in a Schlenk's flask, placed a dry ice/acetone bath. A solution of 0.1 mg (0.3 mmol) of bis(*p*-nitrophenyl) oxalimidoyl dichloride in 10 mL of anhydrous THF were added dropwise to the indenyl anion solution. The mixture was warmed to room temperature and left to react for 24 h. The solvent was removed under reduced pressure and the crude product was purified by column chromatography (silica gel in DCM:hexane, 6:4). The yellow solid was analysed by ^{1}H-NMR spectroscopy and mass spectrometry; however, no corresponding data were found with the desired product.

8.3. Supporting Information

8.3.1. NMR spectroscopy of selected compounds

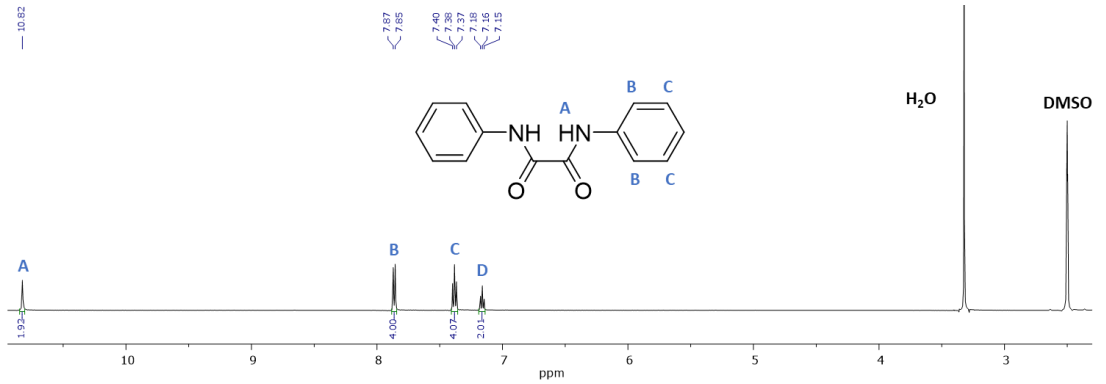

Figure B.15. ^{1}H-NMR spectrum of diphenyloxalimide (DMSO-d_6, 500 MHz).

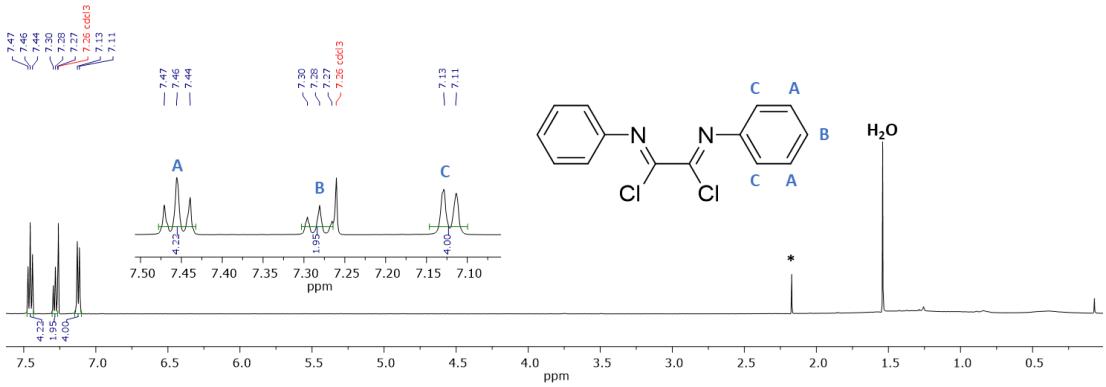

Figure B.16. ^{1}H-NMR spectrum of diphenyloxalimidoyl dichloride ($CDCl_3$, 500 MHz).

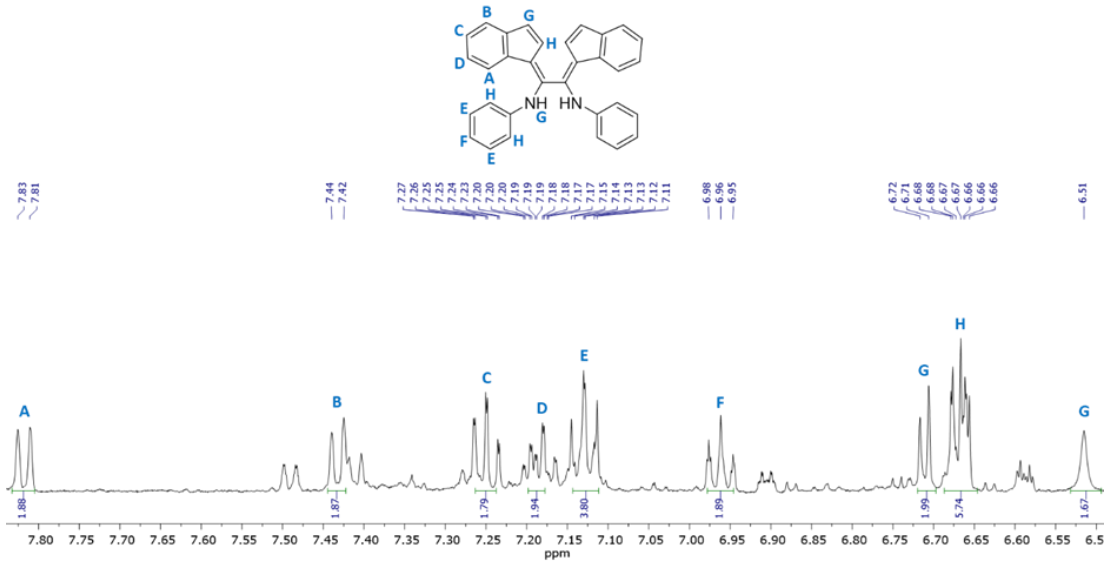

Figure B.17. ^{1}H-NMR spectrum of compound **16** (DMSO-d_6, 500 MHz).

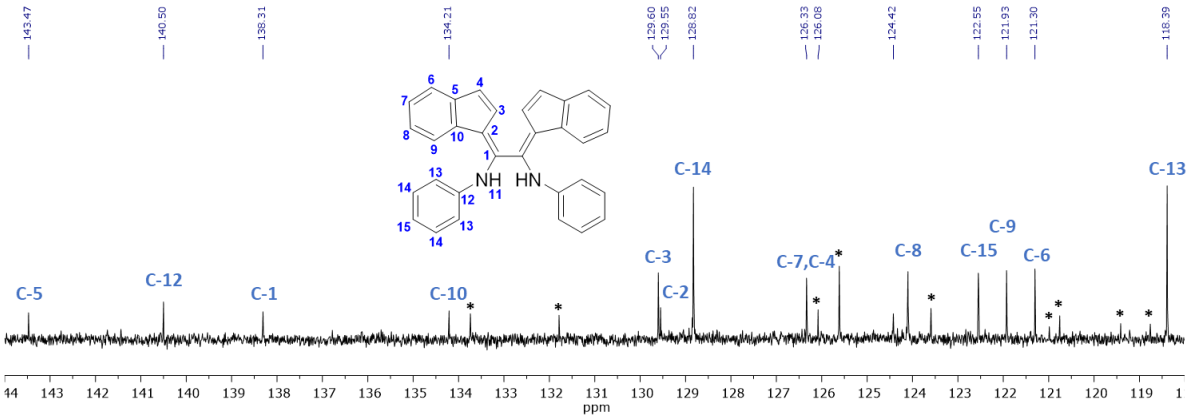

Figure B.18. ^{13}C-NMR spectrum of compound **16** (DMSO-d_6, 125 MHz).

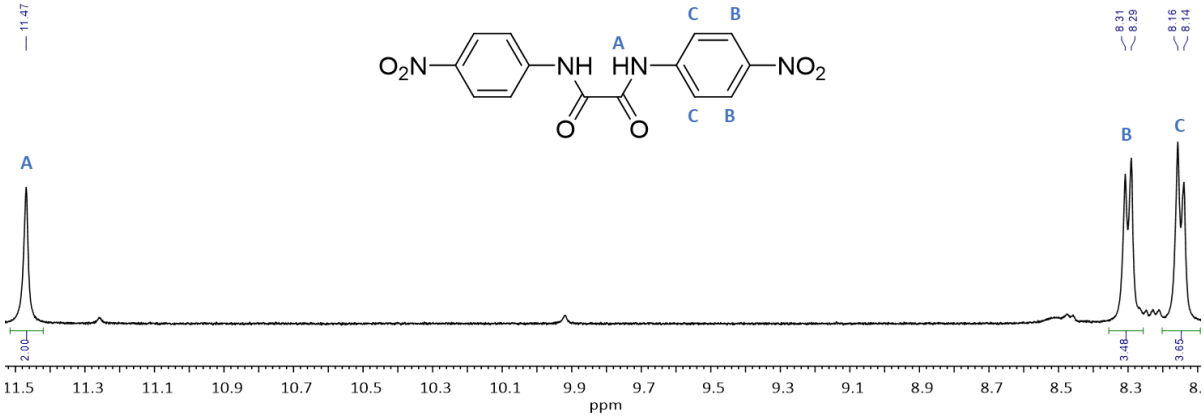

Figure B.19. ^{1}H-NMR spectrum of dinitrophenyl oxalamide ($CDCl_3$, 500MHz).

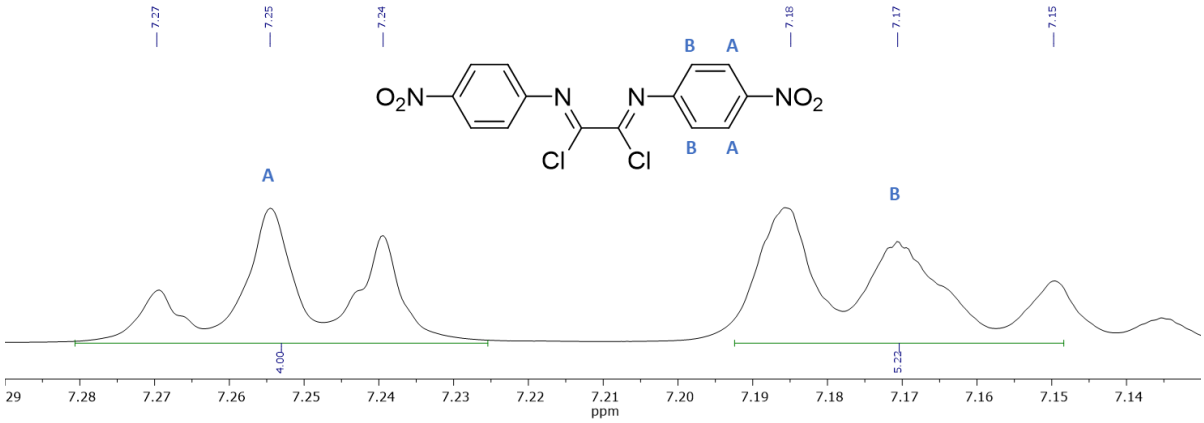

Figure B.20. ^{1}H-NMR spectrum of dinitrophenyl oxalimidoyl dichloride ($CDCl_3$, 500MHz).

8.3.2. Mass spectrometry of selected compounds

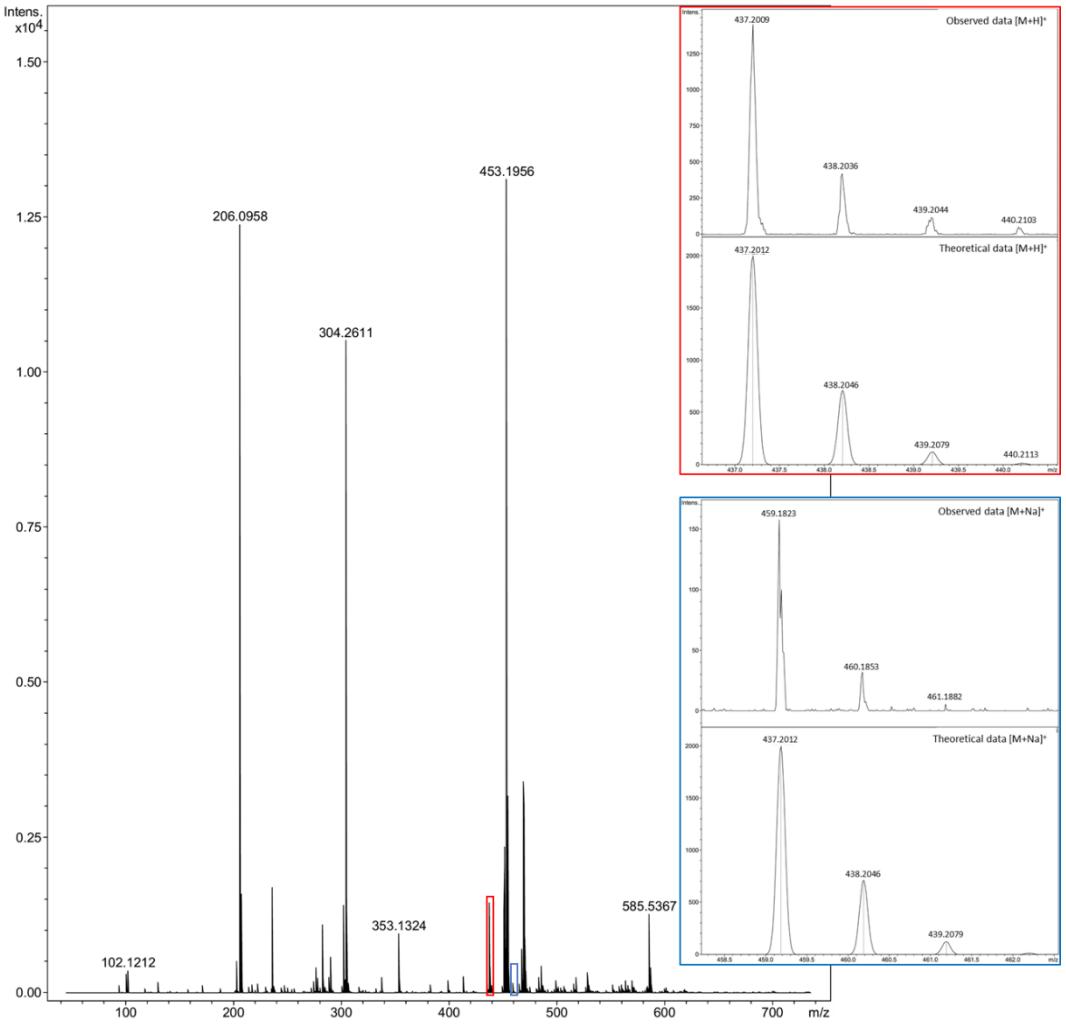

Figure B.21. Mass spectrum of compound **16** (ESI^+-TOF, MeOH).

8.3.3. Raman spectroscopy

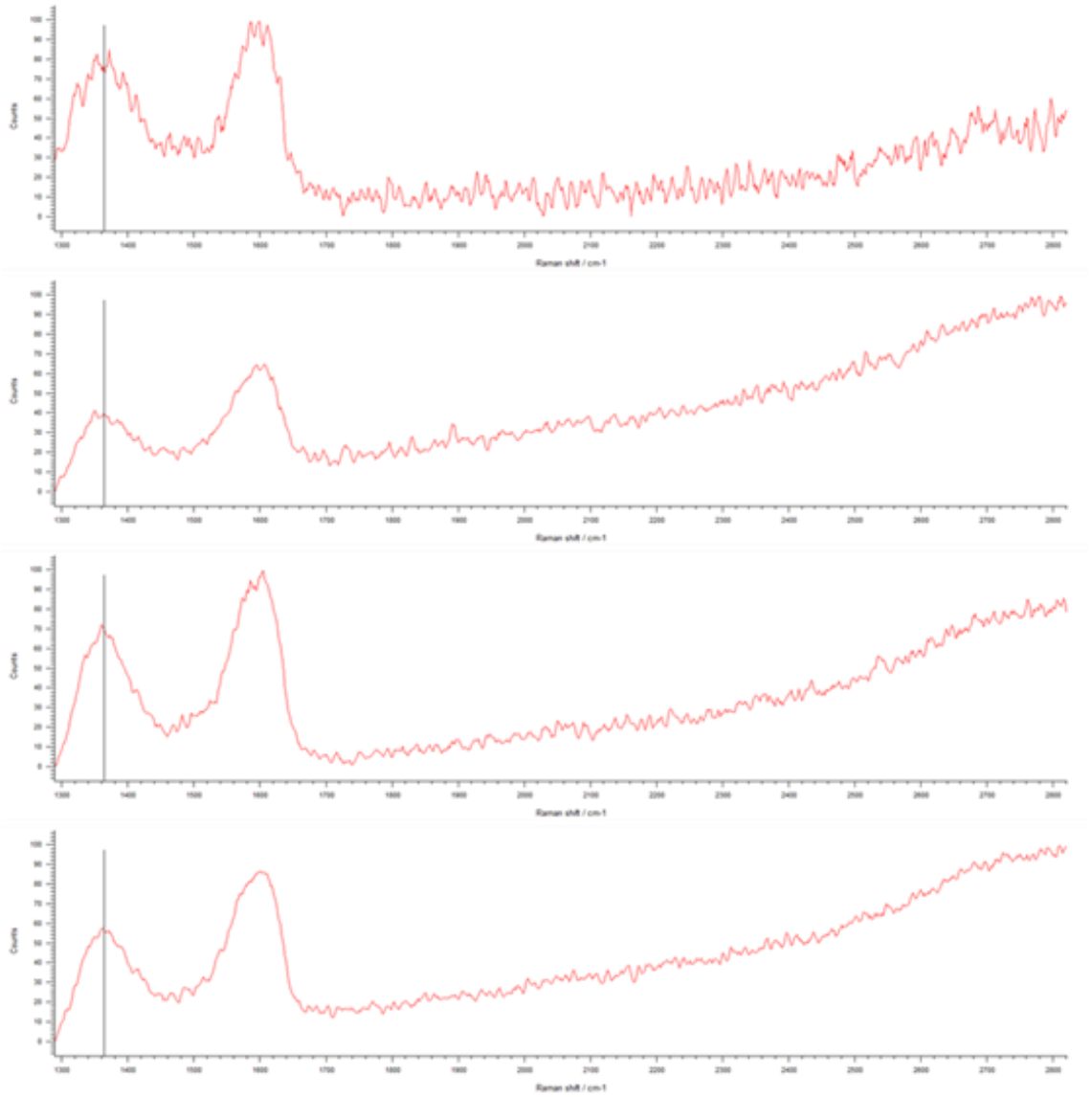

Figure B.22. Raman spectra of the selected flake in the red-colour scale images (λ_{ex}=6246 nm). The corresponding Raman spectra of different depth of the flake are shown from the deepest (the spectrum on the top) to the highest (the spectrum on the bottom). Spectra referred to Figure 5.2b in Chapter 5.

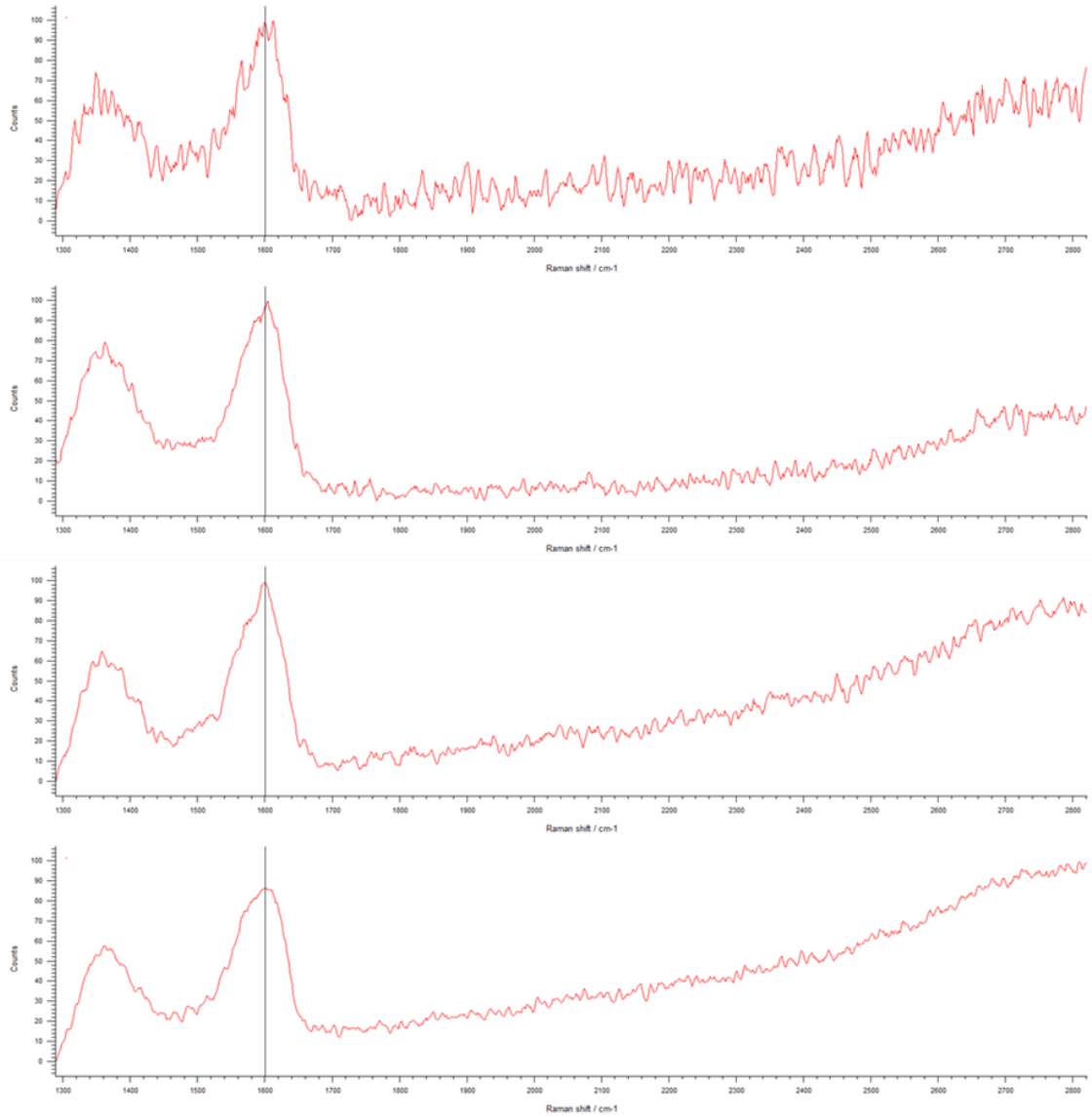

Figure B.23. Raman spectra of the selected flake in the blue-colour scale images (λ_{ex}=7369 nm). The corresponding Raman spectra of different depth of the flake are shown from the deepest (the spectrum on the top) to the highest (the spectrum on the bottom). Spectra referred to Figure 5.2c in Chapter 5.

8.3.4. Confocal laser-scanning microscopy

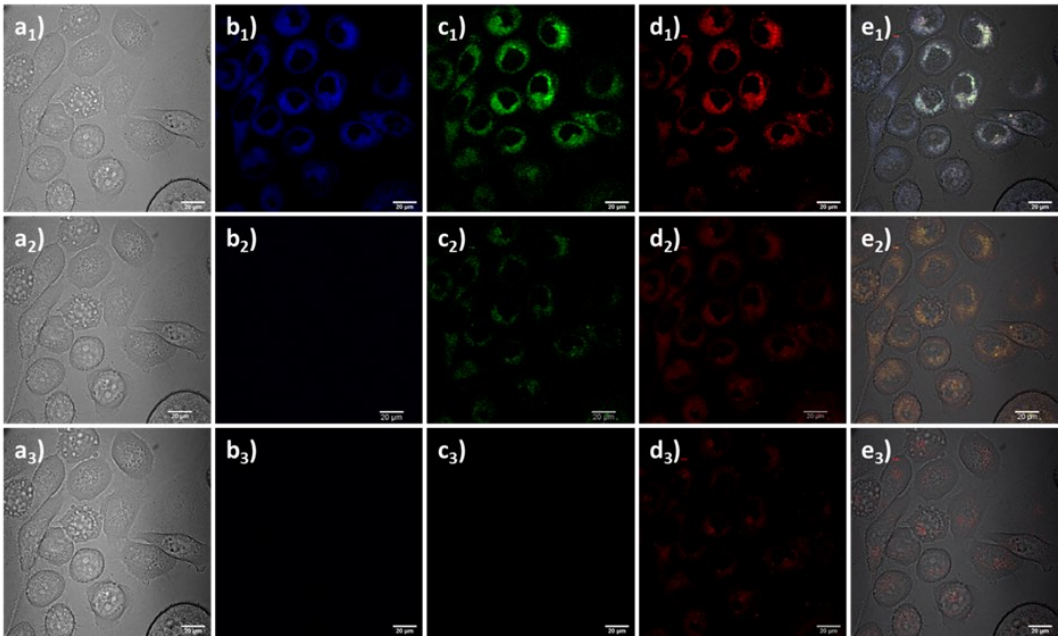

Figure B.24. Single-photon confocal laser-scanning microscopy of PC-3 cells incubated with compound **16** (100 µM, 1:99 DMSO:serum-free medium). **a_1-e_1)** blue channel (λ_{ex}=405; λ_{em}=417-477 nm); **a_2-e_2)** green channel (λ_{ex}=488 nm; λ_{em}=550-650 nm), **a_3-e_3)** red channel (λ_{ex}=561; λ_{em}=570-750 nm). Scale bar: 20 µm.

8.3.5. Confocal laser-scanning microscopy co-localisation analysis

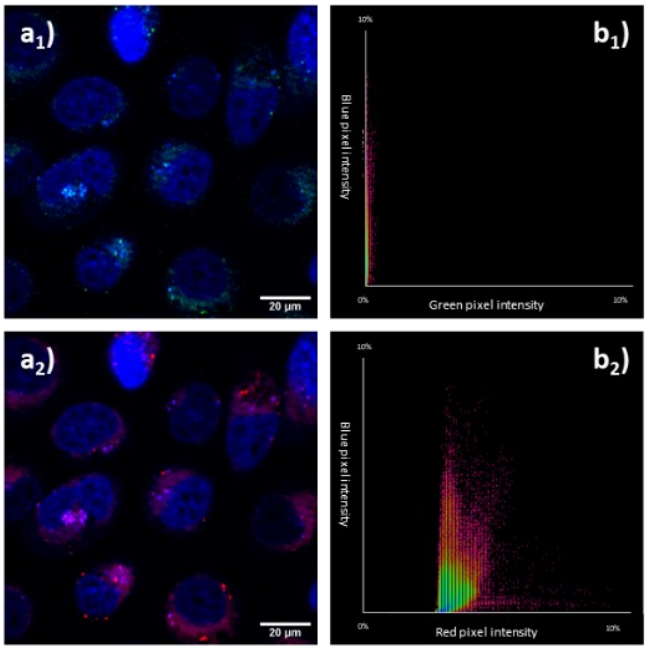

Figure B.25. Confocal laser-scanning microscopy of PC-3 cells incubated at 37 ºC with compound **16** (100 µM, 1:99 DMSO:serum-free medium) and LysoTracker Blue DND-22 (10 µM, 1:99 DMSO:serum-free medium). **a_1)** Superimposed confocal micrographs blue (λ_{em}=417–470 nm) and green channels (λ_{em}=500–550 nm); **a_2)** superimposed confocal micrographs blue (λ_{em}=417–470 nm) and red channels (λ_{em}=570–750 nm). **$b_{1,2}$)** Scatterplots of the micrographs **a_1** and **a_2** respectively.

9. Appendices C

9.1. Investigations into the design optimisation for an electrochemical biosensor for prostate cancer cells detection

This part will explore the design and preliminary tests of an electrochemical biosensor able to discriminate cell lines with a high density of gastrin-realising peptide receptors (GRPRs). Electrochemical impedance spectroscopy (EIS) is used in this work as the analytical method to measure the binding and interactions of the biosensor with different cell lines.

The role of biosensing for detecting and localising cancerous cells in humans has recently found an important position in research worldwide. Biosensing, either electrochemical[1] or optical[2], has recently become crucial for detecting different types of cancer thanks to its reliability, sensitivity, selectivity and low cost.
The general architecture of a biosensor consists of a bio-recognition site, transducer element and electronic system which amplifies, processes and displays the obtained signal. The recognition component is usually a biomolecule modelled after the analyte to interact with. The interaction event generates a measurable signal (*e.g.* change in mass, optical or electrical properties) in the transducer which is proportional to the quantity of analyte in the sample.

As previously described, prostate cancer represents one of the most common malignancies in men and is the third cause of cancer mortality[3]. This could be due to its remarkable ability to spread and invade other organs or tissues specifically and rapidly compared to other forms of cancer[4]. Early detection of prostate cancer is crucial for reducing the spreading and therefore the mortality rate. Prostate-specific antigen (PSA) has been used as a valuable biomarker for the detection of this form of cancer. Despite the improvements of different biosensors[5-7] for sensitive detection, the increase of PSA level may be also due to non-cancerous diseases of the prostate[6]. Targeting specific receptors for prostate cancer with a sensitive, selectively and minimally invasive detection has become a challenge in the research field.

Electrochemical impedance spectroscopy (EIS) has been widely used for characterising biological processes[8]. This technique involves fast data processing, simple instrumentation and low cost and moreover, it is non-destructive for the sample and sensitive[8]. Recent works[9-11] have demonstrated that this electrochemical method has a high potential for future applications in early-stage cancer detection.

Gastrin-releasing peptide receptors (GRPRs) have become the object of study for targeting prostate cancer as they seem upregulated and overexpressed in early and late-stage prostate cancer[12]. GRPR is a 27 amino acids sequence which belongs to the receptor family of the bombesin-related peptides[13]. Bombesin (BBN), a natural 14-amino acids peptide, has recently been studied as a tumour marker thanks to its high affinity to GRPR[13]. The selective binding of BBN to GRPRs has been proven[14], therefore increasing the interest to study it to design new compounds able to localise, detect or treat GRPR-related cancers[15].

The proposed biosensor consists of a gold surface on which a self-assembled monolayer (SAM) is immobilised; the fragment 7-13 of the bombesin peptide is linked to the SAM, which acts as biorecognition element for the GRPRs of prostate cancer cells (Figure 11.1). EIS is used to assess the efficiency of the binding of the bombesin [7-13] peptide with the GRPRs and moreover to guarantee the response of the biosensor in cells lines where GRPRs are overexpressed.

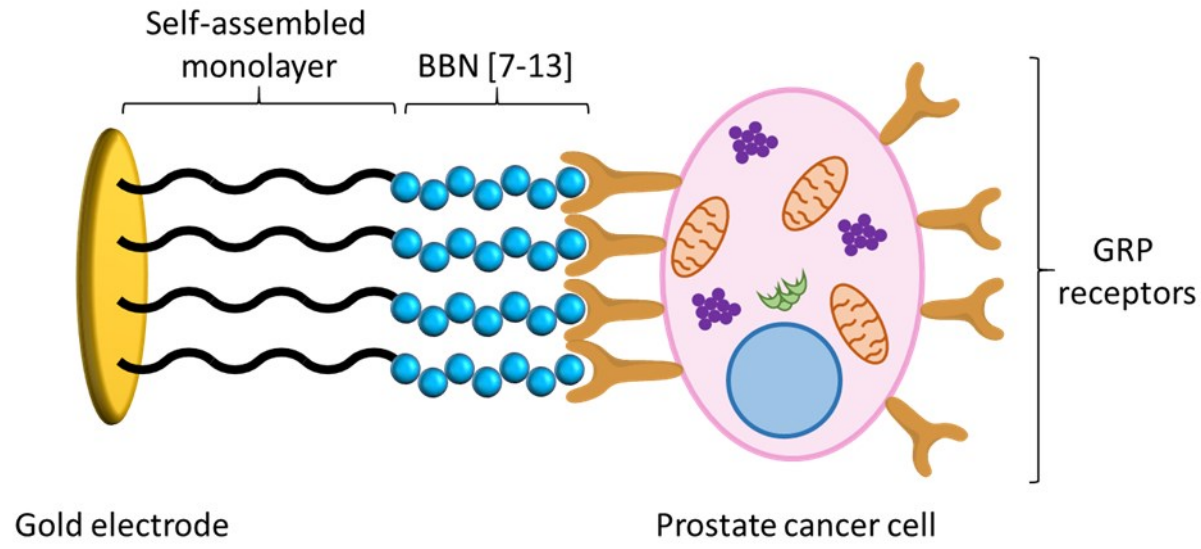

Figure C.1. Representation of the proposed biosensor for prostate cancer cells detection.

9.1.1. Overview of electrochemical impedance spectroscopy

Electrochemical impedance spectroscopy (EIS) has been exploited in different research fields for studying and analysing corrosion mechanisms, charge transport across interfaces and binding events in biological systems[16]. Such a technique has been widely used in the biological field for the detection of microorganisms[17], quality control of food[18] and protein interactions[19]. In recent years, different research groups have focused on the development of biosensors able to detect prostate cancer in the early stage, reducing the rate of biopsies. Early diagnosis could reduce expensive medical treatments and, most importantly, the mortality rate due to this malignancy. Most of these researches[9-11] have been based on the detection of PSA level in men's blood, using EIS. Concentrations below 4 ng mL^{-1} correspond to healthy status, on the other hand, concentrations between 10 and 15 ng mL^{-1} are associated with high probability to prostate cancer[9]. The range between 4 and 10 ng mL^{-1} is not possible to discriminate prostate cancer or benign prostatic hyperplasia (BPH). Despite EIS has proved a minimally invasive, sensitive and cost-saving tool for detecting PSA level, the main challenge could be the specific detection of a unique biomarker which cannot mislead the results.

EIS is based on the measure of the impedance in a certain system. Impedance can be associated with the opposing force to the electrical current as well as the resistance which they share the same unit (Ω). Resistance obeys to the Ohm's law in direct current (DC) circuits, whilst impedance occurs in alternate current (AC) circuits. Impedance (Z) is generally measured in AC potential through the generated current in the cell. The mathematical equations for the sinusoidal potential and current are expressed as below:

$$E_t = E_0 \sin(\omega t) \text{ and } I_t = I_0 \sin(\omega t + \phi)$$

where E_t and I_t are the potential and current at time t, E_0 and I_0 are the amplitude of the signals, ω is the radial frequency and φ is the phase shift. Considering the analogous to Ohm's law, the impedance can be written as:

$$Z = \frac{E_t}{I_t} = \frac{E_0 \sin(\omega t)}{I_0 \sin(\omega t + \phi)} = Z_0 \frac{\sin(\omega t)}{\sin(\omega t + \phi)}$$

where Z_0 is the amplitude of the impedance.

Considering the Euler's relationship, the impedance can be represented as a complex number, where Z' is the real part and Z'' is the imaginary component:

$$Z(\omega) = Z_0(\cos\varphi + j\sin\varphi) = Z' + jZ''$$

In a typical electrical circuit, the impedance is a combination of resistive, capacitive and inductive contributions. The impedance of an ideal resistor is $Z_R = R$; for ideal inductors and capacitors, the impedances are $Z_L = j\omega L$ and $Z_C = 1/(j\omega C)$.

An electrochemical cell can be represented with the Randles' equivalent circuit which is used to model and describe processes in the electrochemical interface (Figure C.2).

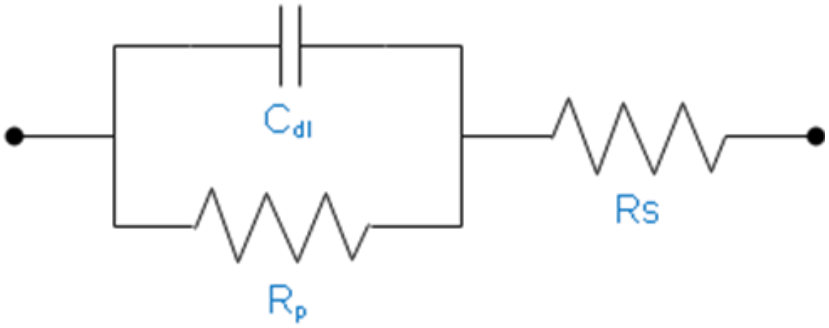

Figure C.2. Schematic representation of the Randle's circuit, modelling the processes in the electrochemical interface.

When an electrochemical reaction (*e.g.* $O + ne^- \rightarrow R$. *O*: oxidant, *n*: number of electrons; *R*: reductant) occurs in solution, a current flow from the electrified interface of the electrode. A Faradaic component is generated from the electron transfer across the interface, producing a polarisation resistance (R_p), along with the solution resistance (R_s). In addition, non-Faradaic currents charge a capacitor (C_{dl}), localised in the double-layer[20].

The analysis of the double-layer has found relevant importance for non-Faradaic processes because the contribution of the charge transfer resistance can be omitted, simplifying the measure of the impedance to only capacitive contribution[21].

Considering this fact, the impedance can be used to estimate a complex capacitance C^* as follow:

$$C^* = \frac{1}{j\omega Z} = C' + jC''$$

From the measure of *Z'* and *Z''*, it is possible to obtain *C'* and *C''*. The data, obtained from the EIS experiments and following the previous assumption, are represented in Nyquist plots, where *C''* values are plotted against *C'* values. A generic Cole-Cole's plot is shown in Figure C.3.

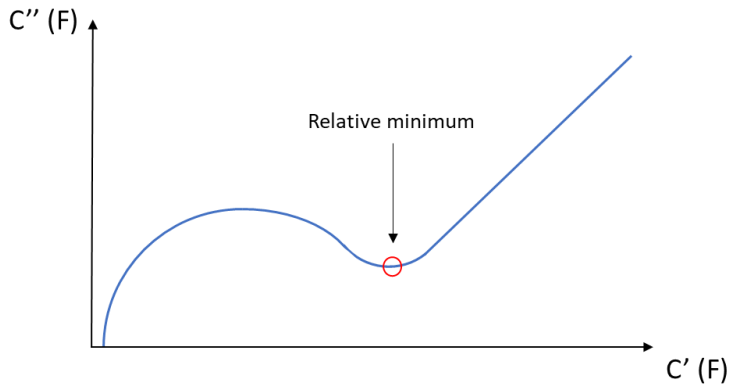

Figure C.3. Generic Cole-Cole's plot with highlighted relative minimum.

The relative minimum of the Nyquist's plot can be associated with the total capacitance of the system as a signal for binding events between, for example, the studied biomolecule and the analyte of target[22].

9.1.2. Construction of the peptide-labelled biosensor and experimental setup

The assessment of the binding of the bombesin [7-13] peptide with the GRPRs and the detection of cellular lines which overexpress these receptors are measured *via* EIS, considering non-Faradaic processes.

This technique uses a typical electrochemical 3-electrode cell which is schematically represented in Figure C.4, adapted from literature[23,24].

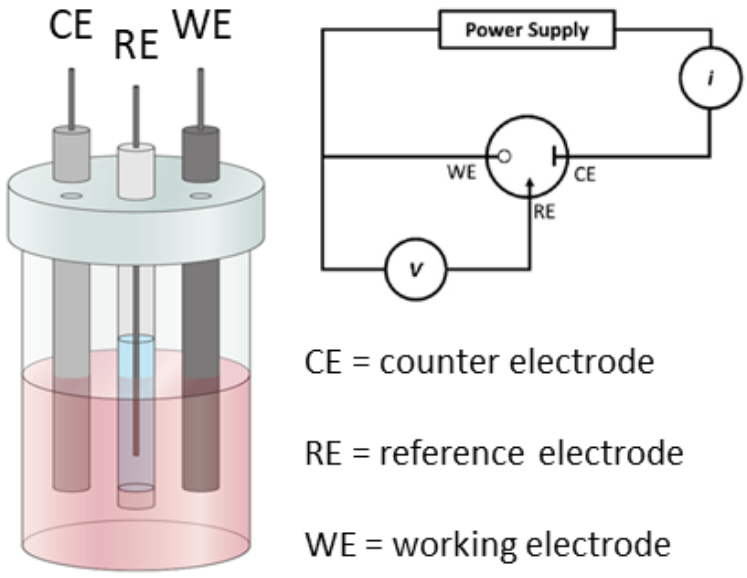

Figure C.4. Electrochemical 3-electrodes cell and its relative electric circuit (figure adapted from literature[24,25]).

This cell consists of a platinum counter electrode-wire (CE), the reference electrode (RE) is a silver/silver chloride (Ag/AgCl) electrode in a solution of potassium chloride (KCl) and the working electrode (WE) is the actual biosensor. The CE closes the circuit and maintains the reference potential ideally constant, whilst the RE is used to obtain the difference between the potentials of WE and RE, which is known. For this purpose, the WE present a gold surface where biological probes are placed on it in order to specifically bind target molecules in the solution. In this setup, a potentiostat applies the desired potential between WE and RE which allow recording the relative currents.

The gold surface used in these experiments were previously cleaned in two different steps in order to obtain a clean and homogeneous surface for the immobilisation of the peptide, avoiding signals due to impurities. The first cleaning step involves manual steps to clean the surface from organic and non-organic compounds from previous experiments. The WE is cleaned with different size of alumina slurry, subsequently by rinsing in ethanol and sonication. The electrochemical polishing removes organic contaminants which could be still absorbed to the gold surface. The electrochemical cell was prepared using a platinum counter electrode, an Ag/AgCl reference electrode and the working electrode which were immersed in a solution of KOH 50 M in H_2O. A potential from -200 to -1200 mV (*vs* Ag/AgCl) with a scan rate of 50 mV/s was applied to the WE, according to the literature procedure[25]. The electrode was rinsed with milliQ-water and ready for the immobilisation of the fragment of bombesin [7-13].
The immobilisation of the peptide was not obtained straightforward on the gold surface. A capacitive sensor based on the interaction between the electrode and the solution could lead to leakage currents. To prevent them, self-assembled monolayers (SAMs) of amphiphilic organic molecules were linked to the gold surface. SAMs have been widely used for the construct different biosensors which also provide strong chemisorption of the target molecule with the gold surface[26]. The alkyl chain should be larger than 8 carbon atoms; however long chains could produce small capacitance which may partially mask the signal because of the binding between the peptide and the receptors.
Scheme C.1 reports the reaction scheme of the immobilisation steps of the bombesin [7-13] on the gold surface.

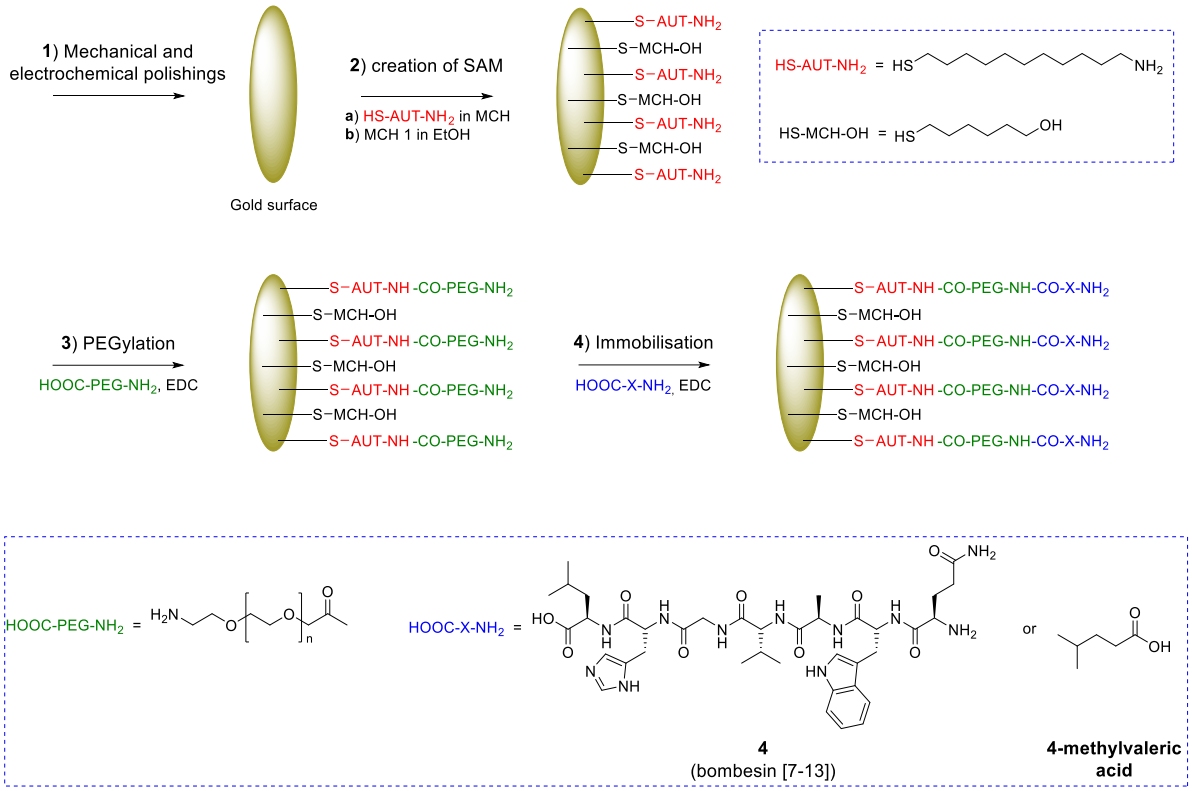

Scheme C.1. Reaction scheme for the immobilisation of the targeting molecules on the gold surface.

The SAM was created using 11-amino-1-undecanethiol (AUT) which provides flexibility and stability for the subsequent modification of the electrode[27] and create a spacer between the peptide and the surface. The clean electrode was immersed in a solution of AUT and 6-mercapto-1-hexanol (MCH) and incubated at room temperature overnight. The following day, the electrode was rinsed with ethanol and incubated in a solution of MCH in ethanol. The last step fills the gap in between chains and prevents that unspecific absorption of the hydroxylic group could interfere with the gold surface[27]. A polyethylene glycol (PEG)-derivative is further covalently linked to the AUT. This derivative presents a carboxylic group on one side and an amino group on the other side. The amino-PEG-carboxylic acid chain is incubated with the electrode and *N*-(3-dimethylaminopropyl)-*N'*-ethylcarbodiimide (EDC) which activates the carboxylic groups on the PEG-derivative, allowing the covalent bond with the amino group of the AUT. The last step involves the bonding of the targeting biomolecule on the electrode. In this study, the experiments were performed using the synthesised bombesin [7-13] as the actual targeting biomolecule and a control molecule (4-methylvaleric acid) which represent a negative response for the binding with the GRPRs. The bombesin [7-13] peptide (**4**), as well as 4-methylvaleric acid, were incubated with EDC in order to activate the carboxylic group of the peptide and react with the amino group of the PEG chain.

9.1.3. Preliminary testing of the biosensing device in different cell lines

The affinity of the BBN [7-13] peptide for GRPRs was tested using EIS in three different cell lines. In particular, PC-3 and LNCaP showed an expression of GRPRs in their cell surface and moreover, it has been demonstrated that PC-3 cells present a higher density of these receptors than in LNCaP[28]. The other cells line, tested as a negative control, is FEK-4 which are non-cancerous cells from normal human dermal fibroblasts tissues and therefore they do not present any expression of GRPRs in their surface.

Preliminary tests on a supramolecular aggregated probe prototype were performed by Dr N. Formisano[29] and Dr J. Tyson[30] which initially focused on evaluating the EIS responses of these cell lines between 30 and 30000 cells mL^{-1}. Figure 11.5b reports their preliminary data in an initial prototype, whereby the difference in capacitance (ΔC') between the measurements with the blank (biosensor immersed in only PBS 0.01 mM) and the different cells concentration in PBS 0.01 mM was plotted. The used peptide still had the BBN [7-13] however this was the non-reactive amide terminated variant: this commercially available peptide (custom-synthesised by EZBiolab, PT030812050) had the amide group on the C-terminus (Figure C.5a) which did not allow the effective coupling and immobilisation within this monolayer. Mass spectrum and HPLC chromatogram are shown in Supporting Information (Figures C.9 and C.11, respectively).

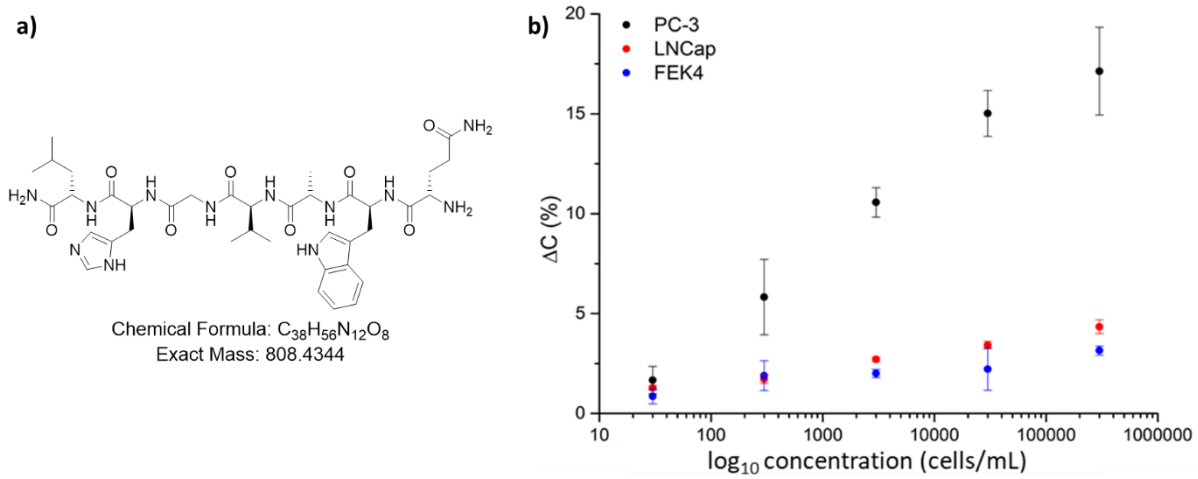

Figure C.5. **a)** Structure, chemical formula and exact mass of the commercially available BBN [7-13] fragment with the amide group in the C-terminus, used in the earlier experiments[29,30]. Preliminary data of the biosensor tested by Dr N. Formisano[29] and Dr J. Tyson[30]. **b)** Percentage difference in capacitance (ΔC') *vs* logarithmic concentration of cells is represented.

Such preliminary tests showed that the biosensor can discriminate cells with different, or none, the density of GRPRs in their membrane. Moreover, this biosensor could discriminate cells lines at a low concentration which can be important for a sensitive device. The reproducibility of the results of this device depends on the success of the SAM formation. In this case, the immobilisation of the peptide on the SAM can be due to non-covalent interactions. This fact may affect the formation of the biorecognition element of the biosensor and therefore the reproducibility of the experiment.

In the following discussion, the immobilisation of the peptide on the SAM was obtained by covalent interactions as shown in Scheme C.1. The BBN [7-13] was obtained by SPPS, as described in Chapter 2, which present the carboxylic group on the C-terminus (Figure C.6) to assure the covalent bond with the SAM on the gold surface of the electrode. Mass spectrum and HPLC chromatogram are shown in Supporting Information (Figures C.10 and C.11).

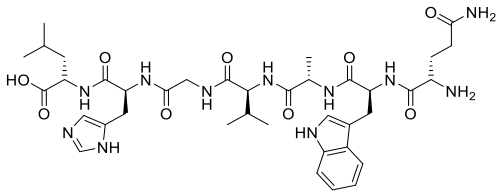

Figure C.6. Structure of the hereby-synthesised fragment BBN [7-13] (**4**) with the carboxylic group in the C-terminus, used in these EIS experiments.

In the first instance, the biosensor was tested in 3 different concentrations of phosphate buffer saline (PBS) which is used as a buffer to simulate the cellular environment (Figure C.7).

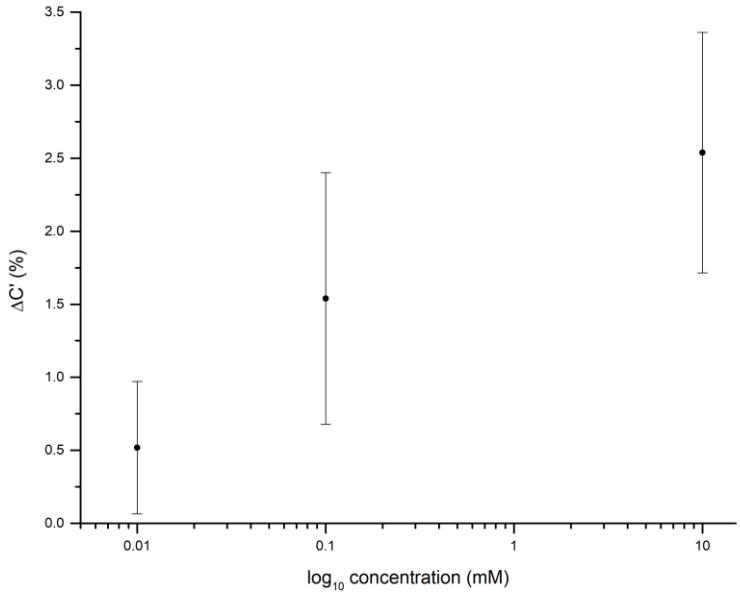

Figure C.7. The plot of percentual of ΔC' *vs* logarithmic concentration of PBS in Milli-Q-water with error bars.

Such test assessed the concentration of PBS that presents the lower signal response in order to not affect further analyses with cells and moreover not damage cells. The concentration of 0.01 mM of PBS showed a lower signal response and standard deviation which makes it a suitable condition for further experiments.

The results of the device consisted of the bombesin [7-13] (**4**), covalently bonded on the SAM, were compared to the data obtained previously by Dr Formisano and Dr Tyson. In the first instance, the device described in this part of the Chapter was compared to another device which presented a non-responsive molecule (4-methylvaleric acid) to assess the specificity of the peptide **4** for the GRPRs. The experiments were carried out on the same cell lines. Figure C.8 shows the results obtained from the biosensor in different cell lines (experimental details shown in Experimental Procedure), tested in different concentration of cells between 10 and 10000 cells/mL in PBS 0.01 mM. The graphs report the ΔC' between the blank and the different cell concentration in PBS 0.01 mM.

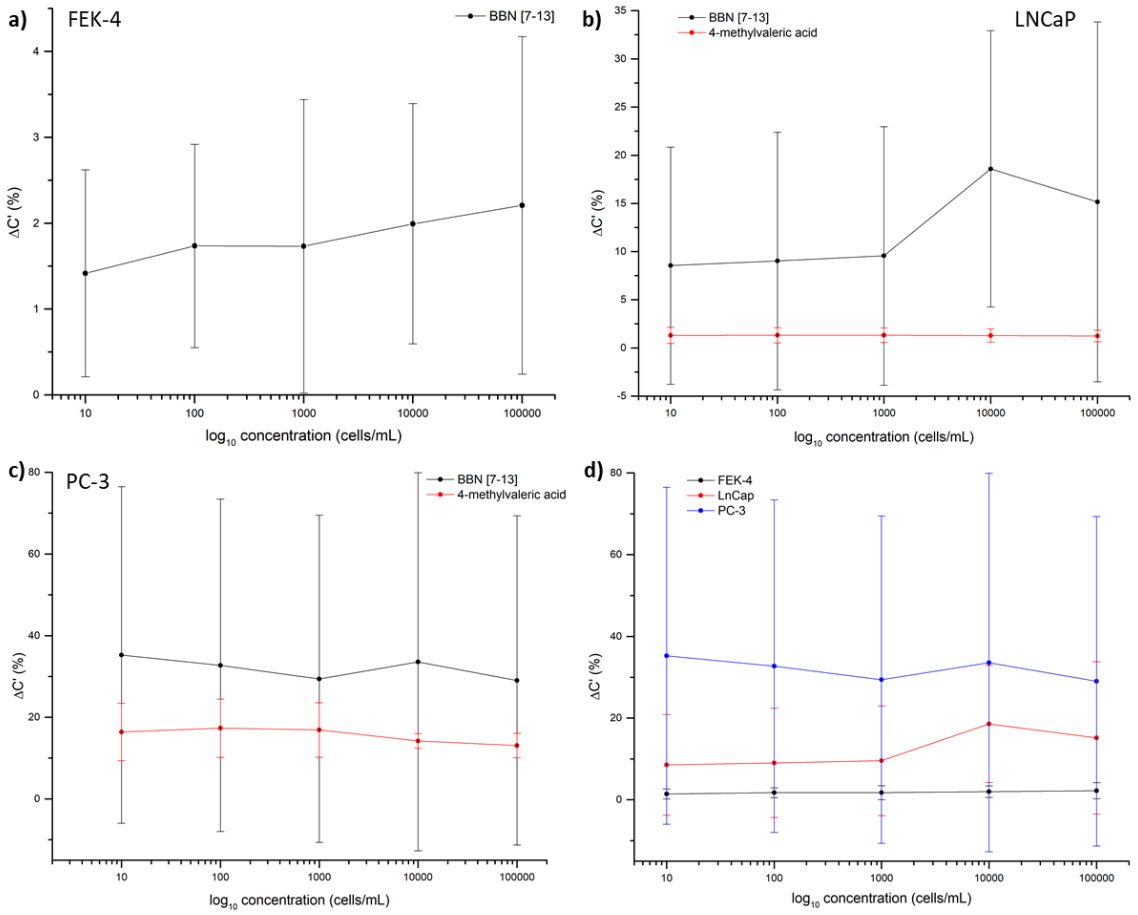

Figure C.8. Plots of percentual of ΔC' *vs* logarithmic concentration of cells. **a)** Data of **4** obtained in FEK-4 cells; b) data of **4** (black dots) and 4-methylvaleric acid (red dots) obtained in LNCaP cells; **c)** data of **4** (black dots) and 4-methylvaleric acid (red dots) obtained in PC-3 cells; d) summary plot of data obtained for **4** in FEK-4 (black dots), LNCaP (red dots) and PC-3 cells (blue dots). (Means and standard deviations were obtained after 3 repetitions on the same day).

Figure C.8a reports the signal response of peptide **4** in FEK-4 cells which showed low signal responses between 1.5 and 2.5%. In Figure C.8b, BBN [7-13] **4** was compared to the 4-methylvaleric acid in LNCaP cells. The peptide showed higher signal responses than the non-responsive molecule which could confirm the specific bind of the peptide with the receptors. In PC-3 cells (Figure C.8c), the signals obtained from the peptide were higher than the 4-methylvaleric acid, confirming the specificity of the peptide for GRPRs responsive cells. Despite the response of the peptide for the cells, the standard deviations of the data of the BBN [7-13] are higher than the 4-methylvaleric acid. This could be due to the complexity of the SAM and peptide, created on the gold surface, and in addition, the difficulty to control the amount of SAM on the surface. Figure C.8d resumes the data obtained from the BBN [7-13] (**4**) in the studied cell lines. It can be noticed that the signal responses increase with the increase of GRPRs density on the cellular surface. This phenomenon could confirm the hypothesis that the peptide is responsive to the GRPRs and moreover it is dependent on the density of them.
Such results, compared with the data obtained by Dr Formisano and Dr Tyson (Figure C.5b), are different likely due to the different immobilisation of the peptide on the SAM. In the previous case, the nature was prevalently non-covalent; in the case discussed in this work, the nature of the bonding interactions within the SAM construction was prevalently covalent. However, it was also striking that the large error bars were obtained on the measurements on PC-3 cells line can be due to the susceptibility of this particular cell line to electrochemical analysis which makes them unreliable. Further studies are necessary for a wider range of cell lines and within different concentration ranges to further validate and then generalise the findings of this biosensing experiment to a range of cancerous and healthy cells.

9.1.4. Conclusions

A novel electrochemical biosensor was designed and constructed to investigate the binding and discrimination of living cell lines with different expression of gastrin-releasing peptide receptors (GRPRs) on their surface. This biosensor presents of the fragment [7-13] of bombesin peptide, well-known targeting molecule for cells which overexpress GRPRs on their surface.

This biosensor consists of the peptide covalently linked by self-assembly monolayer on the gold surface of the working electrode of an electrochemical cell. Electrochemical impedance spectroscopy (EIS) was used as sensitive, low cost and fast method to investigate the biosensor in different cell lines with different concentration of GRPRs on their surface. The obtained results showed that the biosensor and therefore the peptide can discriminate cells with a high concentration of GRPRs on the surface (PC-3 cells) from low concentration (LNCaP cells) and no receptors (FEK-4) on their surfaces.

In the latest works, the circulating tumour cells, found in peripheral blood of men with metastatic prostate cancer, have been reported to be between 1 and 1000 cells/mL[31-33]. The proposed biosensor with the BBN [7-13] peptide, covalently bonded on the gold surface through SAM, can detect and give an appreciable signal in the same range of cells concentration, independently of the cells line in PBS medium. In future experiments, the detection of prostate cancer cells through the biosensor can be explored in human fluids such as blood, blood plasma and/or urine supplied by local hospitals.

In recent years, the targeting and detection of prostate-specific membrane antigen (PSMA), as well as PSA and GRPRs, has increasingly become crucial for imaging and therapy. This antigen presents remarkable characteristics such as wide overexpression on the cell membrane in almost all prostate cancer cells, its expression increases with the stage and grade of the tumour and can increase the deposition and internalisation of radiometals[34]. PMSA represents a potential target for detecting late-stage prostate cancer cells and in the future, its targeting can represent the aim of the design and construction of an electrochemical biosensor.

9.1.5. References

1. L.-H. Pan, S.-H. Kuo, T.-Y. Lin, C.-W. Lin, P.-Y. Fang and H.-W. Yang, *Biosens. Bioelectron.*, 2017, **89**, 598-605.
2. P. Damborský, J. Švitel and J. Katrlík, *Essays Biochem.*, 2016, **60**, 91-100.
3. J. Leal, N. J. Welton, R. M. Martin, J. Donovan, F. Hamdy, D. Neal, S. Noble, A. Lane and J. Wolstenholme, *Cancer Epidemiol.*, 2018, **52**, 99-105.
4. B. D. Hudson, K. S. Kulp and G. G. Loots, *Brief. Funct. Genom.*, 2013, **12**, 397-410.
5. P. Sarkar, P. S. Pal, D. Ghosh, S. J. Setford and I. E. Tothill, *Int. J. Pharm.*, 2002, **238**, 1-9.
6. G. Ertürk, M. Hedström, M. A. Tümer, A. Denizli and B. Mattiasson, *Anal. Chim. Acta*, 2015, **891**, 120-129.
7. R.-M. Kong, L. Ding, Z. Wang, J. You and F. Qu, *Anal. Bioanal. Chem.*, 2015, **407**, 369-377.
8. R. Wang, J. Di, J. Ma and Z. Ma, *Electrochim. Acta*, 2012, **61**, 179-184.
9. M. S. Chiriacò, E. Primiceri, A. Montanaro, F. de Feo, L. Leone, R. Rinaldi and G. Maruccio, *Analyst*, 2013, **138**, 5404-5410.
10. P. Assari, A. A. Rafati, A. Feizollahi and R. Asadpour Joghani, *Microchim. Acta*, 2019, **186**, 484.
11. Y. Yun, Z. Dong, V. N. Shanov and M. J. Schulz, *Nanotechnology*, 2007, **18**.
12. S. M. Elshafae, B. B. Hassan, W. Supsavhad, W. P. Dirksen, R. Y. Camiener, H. Ding, M. F. Tweedle and T. J. Rosol, *The Prostate*, 2016, **76**, 796-809.
13. R. Mansi, R. Minamimoto, H. Mäcke and A. H. Iagaru, *J. Nucl. Med.*, 2016, **57**, 67S-72S.
14. R. P. J. Schroeder, W. M. v. Weerden, C. Bangma, E. P. Krenning and M. d. Jong, *Methods*, 2009, **48**, 200-204.
15. J. Becaud, L. Mu, M. Karramkam, P. A. Schubiger, S. M. Ametamey, K. Graham, T. Stellfeld, L. Lehmann, S. Borkowski, D. Berndorff, L. Dinkelborg, A. Srinivasan, R. Smits and B. Koksch, *Bioconjugate Chem.*, 2009, **20**, 2254-2261.
16. F. Lisdat and D. Schäfer, *Anal. Bioanal. Chem.*, 2008, **391**, 1555.
17. M. Sypabekova, P. Jolly, P. Estrela and D. Kanayeva, *Biosens. Bioelectron.*, 2019, **123**, 141-151.
18. M. Grossi, C. Parolin, B. Vitali and B. Riccò, *Eng. Sci. Technol. Int J.*, 2019, **22**, 102-108.
19. A. Bogomolova, E. Komarova, K. Reber, T. Gerasimov, O. Yavuz, S. Bhatt and M. Aldissi, *Anal. Chem.*, 2009, **81**, 3944-3949.
20. B.-Y. Chang and S.-M. Park, *Annu. Rev. Anal. Chem.*, 2010, **3**, 207-229.
21. V. Tsouti, C. Boutopoulos, I. Zergioti and S. Chatzandroulis, *Biosens. Bioelectron.*, 2011, **27**, 1-11.

22. P. Jolly, M. R. Batistuti, A. Miodek, P. Zhurauski, M. Mulato, M. A. Lindsay and P. Estrela, *Sci. Rep.*, 2016, **6**, 36719.

23. K. J. Lee, N. Elgrishi, B. Kandemir and J. L. Dempsey, *Nat. Rev. Chem.*, 2017, **1**, 0039.

24. R. Raccichini, M. Amores and G. Hinds, *Batteries*, 2019, **5**.

25. L. M. Fischer, M. Tenje, A. R. Heiskanen, N. Masuda, J. Castillo, A. Bentien, J. Émneus, M. H. Jakobsen and A. Boisen, *Microelectron. Eng.*, 2009, **86**, 1282-1285.

26. N. K. Chaki and K. Vijayamohanan, *Biosens. Bioelectron.*, 2002, **17**, 1-12.

27. S. Campuzano, M. Pedrero, P. Yáñez-Sedeño and J. M. Pingarrón, *Int. J. Mol. Sci.*, 2019, **20**.

28. M. G. Dozmorov, R. E. Hurst, D. J. Culkin, B. P. Kropp, M. B. Frank, J. Osban, T. M. Penning and H.-K. Lin, *The Prostate*, 2009, **69**, 1077-1090.

29. N. Formisano, Doctor of Philosophy, University of Bath, 2015.

30. J. A. Tyson, Doctor of Philosophy, University of Bath, 2016.

31. J. Budna-Tukan, M. Świerczewska, M. Mazel, W. A. Cieślikowski, A. Ida, A. Jankowiak, A. Antczak, M. Nowicki, K. Pantel, D. Azria, M. Zabel and C. Alix-Panabières, *Cancers (Basel)*, 2019, **11**, 802.

32. W. Liu, B. Yin, X. Wang, P. Yu, X. Duan, C. Liu, B. Wang and Z. Tao, *Oncol. Lett.*, 2017, **14**, 1223-1232.

33. L.-H. Pan, S.-T. Pang, P.-Y. Fang, C.-K. Chuang and H.-W. Yang, *Theranostics*, 2017, **7**, 4289-4300.

34. T. Maurer, M. Eiber, M. Schwaiger and J. E. Gschwend, *Nat. Rev. Urol.*, 2016, **13**, 226-235.

9.2. Experimental rocedure

The electrodes were immersed in ethanol and sonicated for 5 min, then rinsed with μQ-water. Afterwards, the electrodes were mechanically polished on a pad with alumina slurry 1 μm for 1.5 min, describing an "8"; successively, the electrodes were cleaned on the pad with alumina slurry 0.3 μm for 1.5min; at the end, alumina slurry 0.05 μm was used on the pad for 1.5 min. These mechanical steps were alternated by rinsing with Milli-Q-water and sonicating in EtOH for 5 min. The last sonication step was performed in a solution of KOH 50 mM in Milli-Q-water.

The electrochemical polishing of the electrodes (WE, working electrodes) was performed using a platinum counter electrode and an Ag/AgCl reference electrode immersed in a solution of KOH 50 M in H_2O_2. A potential from -200 to -1200 mV (*vs* Ag/AgCl) with a scan rate of 50 mV/s was applied to the WE, according to the literature procedure[18], using a *CompactStat* potentiostat (*Ivium Technologies*).

The clean electrodes were immersed in 100 μL of AUT:MCH (1:200) and incubated at room temperature overnight. The following day, the electrodes were rinsed with EtOH and incubated for 1.5 h in 100 μL of MCH 1 mM in ethanol. The amino-PEG-carboxylic acid (1mg) is incubated with the electrodes and EDC (80 mM in Milli-Q-water) for 30 min. The immobilisation of the targeting biomolecules (**4** and 4-methylvaleric acid) was performed incubating 35 μM of the species with the electrodes for 2 h.

The EIS measurements with cells were performed in a *PalmSens* potentiostat (*PalmSens*), incubating the electrodes with the cells for 20 min and then leave in the PBS measure solution for 10 min to stabilise. Time of equilibration of 5 s was used before each measure. The frequencies used were between 1 mHz to 10 kHz with 10 points/decade and fixed potentials of E_{dc}=0 V and E_{ac}=0.01 V. Measurements and E_{dc} were *vs* OCP of 15 s.

9.3. Supporting Information

9.3.1. Mass spectrometry of selected compounds

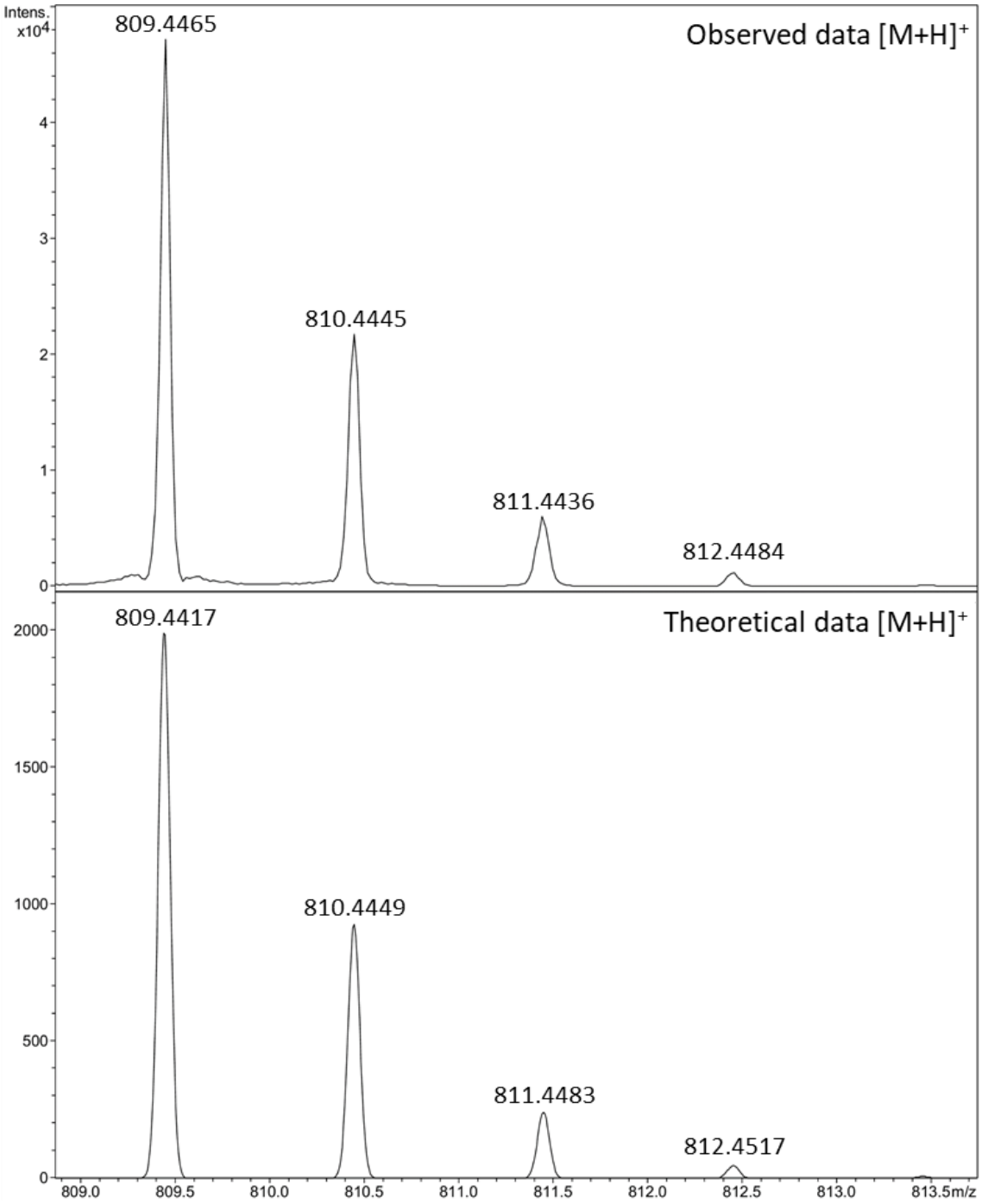

Figure C.9. Observed (top) and theoretical (below) isotopic pattern of the [M+H]+ ion for the bombesin [7-13] peptide, bought from EZBiolab (PT030812050).

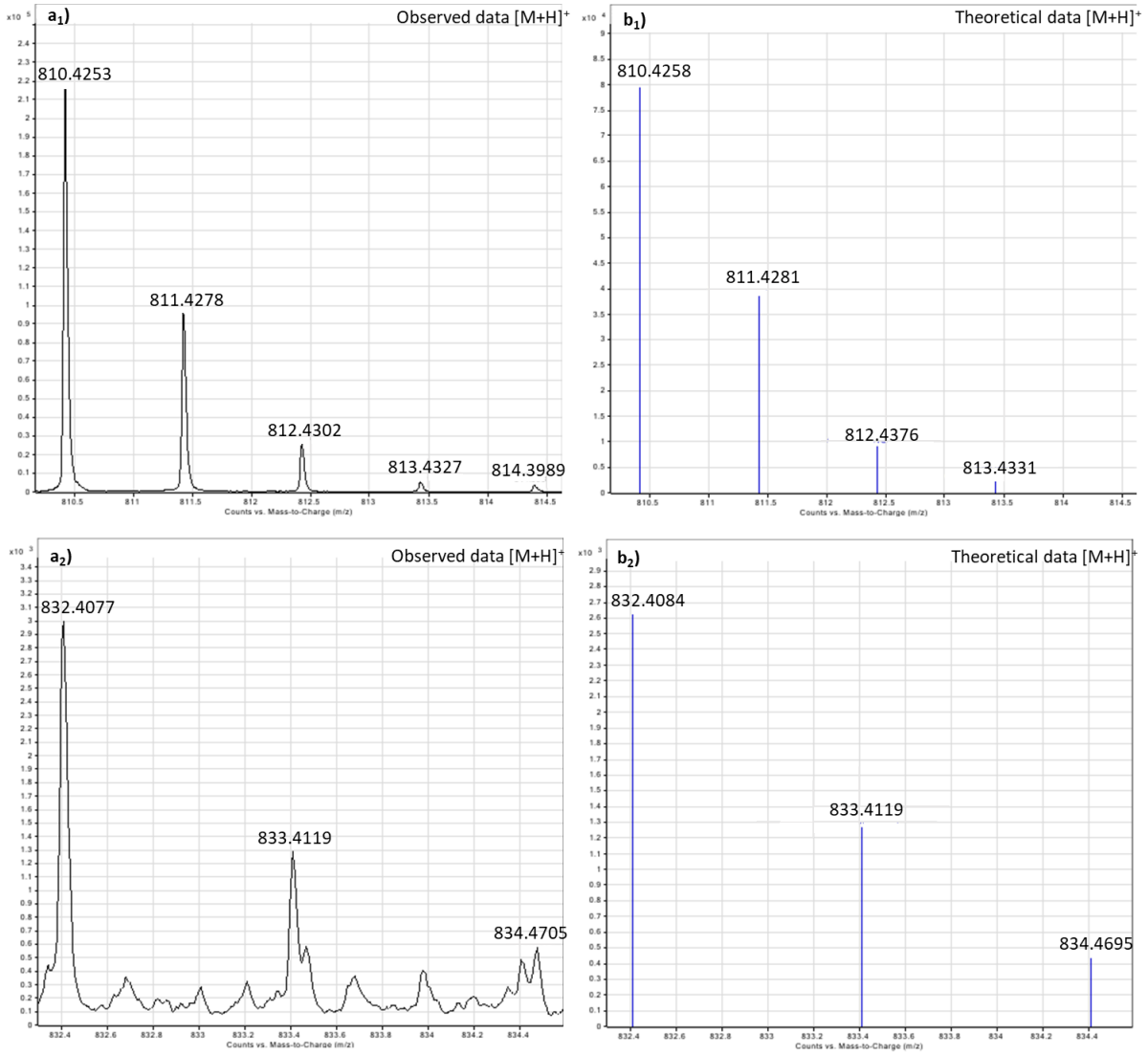

Figure C.10. a1) Observed and **b1)** theoretical isotopic patterns for the ion $[M+H]^+$; **a2)** observed and **b2)** theoretical isotopic patterns for the ion $[M+Na]^+$ of synthesised bombesin [7-13] peptide (**4**).

9.3.2. HPLC chromatography

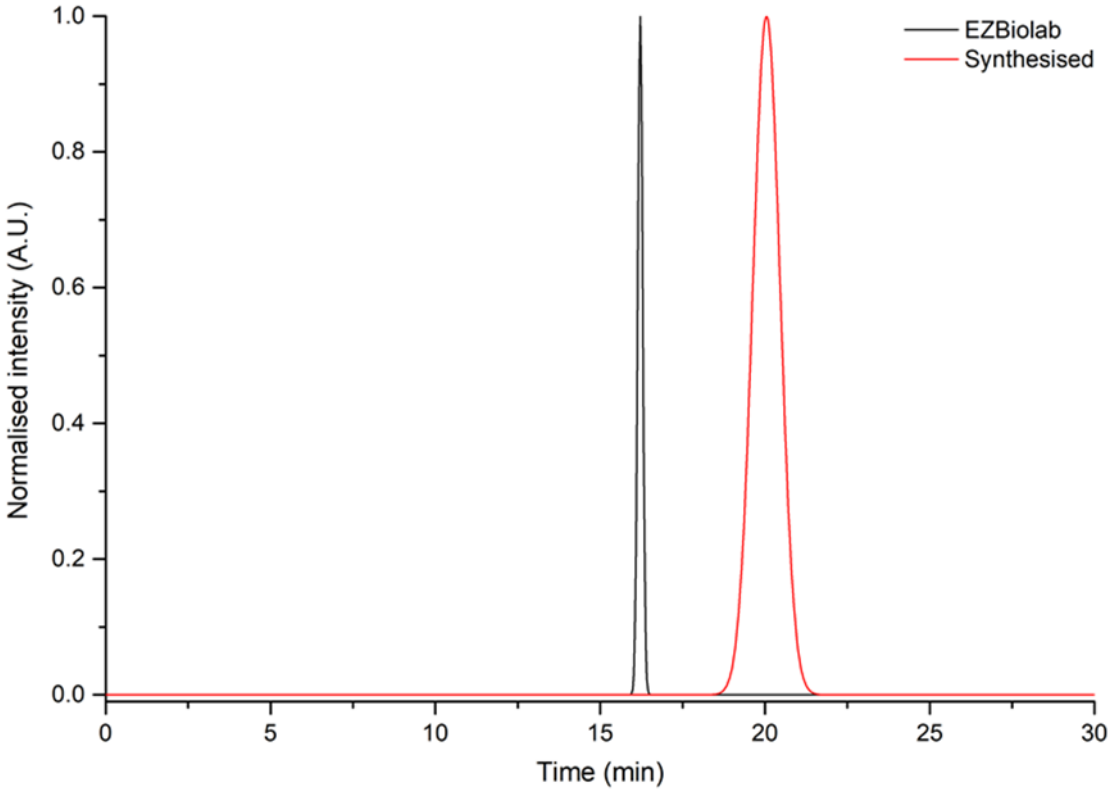

Figure C.11. HPLC chromatograms of the commercially available (EZBiolab, PT030812050) and synthesised (**4**) bombesin [7-13] peptides. Method A in Experimental Section.